TECHNISCHE UNIVERSITÄT MÜNCHEN
Physik-Department
Lehrstuhl für Biomedizinische Physik

Image reconstruction, pre-clinical studies, and signal formation investigations at a dark-field chest radiography setup

Fabio Domenico De Marco

Vollständiger Abdruck der von der Fakultät für Physik der Technischen Universität München zur Erlangung des akademischen Grades eines

Doktors der Naturwissenschaften (Dr. rer. nat.)

genehmigten Dissertation.

Vorsitzender:		Prof. Dr. Martin Zacharias
Prüfer der Dissertation:	1.	Prof. Dr. Franz Pfeiffer
	2.	Prof. Dr. Pierre Thibault

Die Dissertation wurde am 29.01.2021 bei der Technischen Universität München eingereicht und durch die Fakultät für Physik am 02.06.2021 angenommen.

Abstract

The focus of this work is on an imaging setup dedicated to the acquisition of dark-field radiographs of large objects. While conventional radiography measures an object's absorption of X-rays, the dark-field modality detects the amount of radiation that is coherently scattered. Because of this, dark-field radiography can reveal unresolvable inhomogeneities in the microstructure of objects, and thus provide information complementary to normal radiography.

The present setup achieves this with the use of an interferometer-like arrangement of optical gratings. As the required gratings are only available in small sizes, the object field of view was increased by tiling multiple gratings and scanning them across the object. The peculiarities of the employed scanning procedure required the development of suitable algorithms for the retrieval of dark-field radiographs from the setup's scan data.

The first key topic of the thesis is the development of these algorithms and their consolidation into an image processing software package. After analyzing the mathematical structure of the data produced by the setup, several image retrieval algorithms are introduced and their performance is compared. Additionally, several post-processing algorithms are introduced that correct for spectral hardening and improve the visual quality of the images. Finally, the creation of a software module is discussed that unites these functionalities.

Previous small animal studies had shown that dark-field radiography can provide diagnostic benefits for structural pulmonary diseases, and the examined setup previously demonstrated the method's successful transition to large animals. Showing a diagnostic use of dark-field in this setting however required preclinical imaging studies, which are the second main topic of this work. The use of dark-field for the detection of pneumothorax, the signal's relation to inspiration state and lung thickness, and finally the appearance of various clinical features in dark-field radiographs of human cadavers were examined. The aforementioned software package was used for image retrieval in all three imaging studies.

The third main subject of the thesis is the theoretical discussion of several aspects of dark-field signal formation, partly based on imaging experiments. These include the discovery of a visibility-hardening effect, an alternative view on grating-based X-ray imaging based on partial coherence theory, and a comparison of approaches for correcting dark-field estimation bias.

The development of image processing software for the given setup thus enabled the realization of several preclinical imaging studies, which in turn laid the groundwork for the method's further clinical translation. Additionally, the theoretical investigations provide insights into the process of dark-field signal formation, which may be beneficial for various applications of this imaging modality.

Zusammenfassung

Der Schwerpunkt der vorliegenden Arbeit liegt auf einem Bildgebungsgerät für die Aufnahme von Dunkelfeldradiographien großer Objekte. In der konventionellen Radiographie wird der Absorptionsgrad einfallender Röntgenstrahlung gemessen, wohingegen mit der Dunkelfeld-Methode das Maß kohärent gestreuter Strahlung ermittelt wird. Hierdurch kann die Dunkelfeldradiographie nicht direkt auflösbare Inhomogenitäten in der Mikrostruktur von Messobjekten ermitteln, und damit ergänzend zur konventionellen Radiographie wirken.

Das besagte Gerät leistet dies durch den Einsatz einer interferometer-ähnlichen Anordnung optischer Gitter. Da die erforderlichen Gitter aber nur in geringer Größe erhältlich sind, wurde das Sichtfeld des Geräts vergrößert, indem mehrere Gitterkacheln nebeneinander gelegt, und in einer Scanbewegung über das Objekt bewegt werden. Die Eigenheiten der verwendeten Scanverfahrens machte die Entwicklung geeigneter Algorithmen für die Berechnung von Dunkelfeldradiographien aus den Scandaten des Geräts erforderlich.

Das erste Kernthema der Arbeit ist die Entwicklung dieser Algorithmen, und deren Einbindung in ein Bildverarbeitungs-Softwarepaket. Nach einer mathematischen Analyse der im Gerät erzeugten Bilddaten werden mehrere Algorithmen eingeführt und deren Leistungsfähigkeit wird verglichen. Zudem werden mehrere Algorithmen zur Nachbearbeitung der berechneten Bilddaten eingeführt, die dazu dienen, die Quantitativität und den optischen Eindruck der Bilder zu verbessern. Zuletzt wird die Erstellung eines Softwaremoduls erörtert, welches all diese Funktionen miteinander vereint.

Vorausgehende Kleintierstudien haben gezeigt, dass die Dunkelfeldradiographie Vorteile für die Diagnose struktureller Lungenerkrankungen bietet, und am besagten Scangerät wurde zudem die Anwendung der Methode an großen Tieren gezeigt. Der Nachweis eines diagnostischen Nutzens in diesem Kontext setzt allerdings die Durchführung vorklinischer Bildgebungsstudien voraus, welche das zweite Hauptthema der vorliegenden Arbeit bilden.

Der Nutzen der Dunkelfeldmodalität für die Erkennung von Pneumothoraxen, dem Bezug des Signals zum Atemzustand und zur Dicke der Lunge, sowie das Erscheinungsbild diverser klinischer Merkmale in Dunkelfeldradiographien menschlicher Kadaver wurden untersucht. Das obengenannte Softwarepaket wurde für die Gewinnung der Dunkelfelddaten in allen drei Studien eingesetzt.

Das dritte Hauptthema der Arbeit ist die theoretische Diskussion verschiedener Aspekte der Entstehung des Dunkelfeldsignals. Hierzu gehört die Entdeckung eines Aufhärtungseffektes des Interferenzkontrasts, ein Blick auf die Funktionsweise der gitterbasierten Röntgenbildgebung mithilfe von Konzepten der partiellen Kohärenz, sowie ein Vergleich verschiedener Methoden zur Korrektur der Schätzverzerrung des Dunkelfeldsignals.

Zusammenfassend ermöglichte also die Entwicklung von Bildverarbeitungssoftware für ein Dunkelfeldradiographie-Scangerät die Durchführung mehrerer vorklinischer Bildgebungsstudien, die nun eine Grundlage für die weitere klinische Translation der Methode bilden. Zudem gewähren die theoretischen Untersuchungen Einblicke in den Entstehungsprozess des Dunkelfeldsignals, was für vielfältige Anwendungen dieser Modalität von Nutzen sein könnte.

Contents

Chapter 1

Historical context

An X-ray tube is a sphere of glass entirely surrounded by profanity.

– Cuthbert Andrews, about the state of X-ray technology in 1917. [Gutt02]

Contents

The subject of the present thesis is the development of image calculation algorithms for an X-ray dark-field imaging setup and its application for pre-clinical imaging tasks. Like all scientific work, the results presented in this thesis build onto an enormous amount of preceding work. Thus, to place it in its proper context, an overview of important scientific achievements making the present work possible is presented here.

Since the topic of this work intersects with both the discipline of medical X-ray imaging and X-ray imaging physics, the historical development of each is introduced: The discovery of X-rays, early technical developments, and medical radiographic applications are introduced in section 1.1. Although the present work is only remotely connected to tomographic imaging, I believe that an introduction to medical X-ray imaging would be incomplete without X-ray tomography. History and development of X-ray tomography are therefore introduced in section 1.2.

Given that X-rays and visible light are both electromagnetic waves, they both exhibit wave characteristics. The X-ray imaging modalities examined in the present work (phase contrast and dark-field) make explicit use of these wave properties. However, wave properties of visible light had been discovered long before X-rays. Section 1.3 thus introduces these early discoveries, gives an overview of interferometer designs, the most important type of optical setup exploit-

ing phase effects, and introduces the workings of the Zernike phase-contrast microscope, one of the oldest phase-contrast imaging techniques as well as an important inspiration for many subsequently developed methods.

Modern X-ray phase-contrast imaging has benefited greatly from the development of synchrotron X-ray sources, and many imaging methods, including the one employed in this thesis, originated at synchrotron research facilities. A brief description of their history is thus given in section 1.4.

An overview of the X-ray diffraction-based imaging methods themselves is given in section 1.5. X-ray crystallography, the oldest and one of the most important applications of X-ray diffraction, is introduced first. X-ray microscopy, where phase-shifting effects were observed early on and X-ray phase-contrast can be highly beneficial, is introduced in section 1.5.2.

Subsequently (section 1.5.3), the oldest dedicated method for measuring X-ray phase contrast, employing a crystal interferometer, is introduced. Analyzer-based imaging, a related non-interferometric technique, is also presented. The most commonly used method for X-ray phase-contrast, based on free-space propagation of highly coherent X-rays, is introduced (section 1.5.5), followed by the method (or group of methods) employed in the present work, based on optical gratings (section 1.5.6).

Grating-based X-ray phase-contrast measures the distortion of intensity patterns due to refraction or scatter in the sample. Other X-ray phase-contrast imaging methods exists which also employ this principle, such as speckle-based and edge-illumination imaging, are introduced in section 1.5.7.

Finally, more recent developments regarding the medical and pre-clinical application of these various methods are introduced in section 1.6, including references to the present work.

1.1 Early history and medical use

Even though X-rays had been produced in earlier experiments [Thom18], their existence and interaction with matter was first described by W. C. Röntgen in 1895: By ionizing gas in a Crookes tube (a partially evacuated glass bulb containing two electrodes), and accelerating the electrons thus created onto the tube wall, he observed a fluorescence effect on a screen placed behind, although the tube was covered by cardboard. Subsequent experiments revealed that this fluorescence effect was only weakly attenuated when different objects were placed between the tube and the fluorescent screen. He found that the degree of attenuation depends on density, thickness, and type of material. As the fluorescent images yielded sharp projections of the objects, Röntgen concluded the phenomenon to propagate as geometric rays, originating from the point of interaction of the electrons with the tube wall. However, unlike the “cathode rays" discovered shortly before, these were unaffected by magnetic fields, and unlike ultraviolet radiation, they exhibited no noticeable refraction or reflection. Röntgen thus correctly surmised that the observed rays constituted a new discovery and termed them “X-Strahlen” (“X-rays”) to differentiate them from other invisible ray phenomena [Rönt95].

In particular, placing a hand between tube and screen revealed a contrast in transmitted X-ray intensity between bones and the surrounding tissues. The differences in attenuation capability of different materials could thus be exploited to visualize internal structures of the human body and other objects appearing opaque to the naked eye. Röntgen also recognized the sensitivity of photographic plates and films to the newly discovered type of radiation, which allowed the recording of X-ray photographs (*radiographs*) for an objective analysis after acquisition. The response to Röntgen’s discovery was overwhelming: within a year after his publication, over a thousand articles had been produced about the subject [Behl18].

Among the most influential and long-lasting ideas of the many suggested applications was to visualize the interior of human bodies, especially for diagnostic and research purposes. Radiographs could be stored on photographic plates or film and examined later. Fluorescent screens also found clinical use: Since these allow acquisition of a “live,” moving image of the subject, so-called *fluoroscopy* became an important tool for assisting surgeons during interventions. However, before pathological changes could be diagnosed, the appearance of the healthy human body in X-ray images, and normal variations between patients, had to be determined, which was the subject of many early radiographic studies, e.g., concerning skeletal growth [Thom18]. The first clinical X-ray department was already established in 1897 in Glasgow, providing radiography and fluoroscopy services, with demand

exceeding its capacities only six years later [Thom18].

The spectral performance of Crookes tubes is dependent on gas pressure inside the tube, which could not easily be regulated and varied with temperature and the age of the tube. Furthermore, tube voltage and tube current could not be regulated independently [Hofm10]. These issues were resolved with the development of a new tube design by W. Coolidge in 1913, which was not dependent on the presence of ionizable gas. Here, electrons were released using thermionic emission of electrons, e.g. from a heated metal wire, which also works in a vacuum. Spectral hardness and tube current could thus be controlled independently, namely by variation of acceleration voltage and the heating current applied to the metal wire. Furthermore, the performance of Coolidge tubes did not vary as much over their lifetime, and they were easier to operate than Crookes tubes.

Since only a small fraction of the electrons' kinetic energy is converted into X-rays in the anode, the anode is heated significantly during operation (see also section 2.3.2 on page 46). This heating naturally limits the electrical power that may be delivered to the X-ray tube. This limit can be increased by active anode cooling or an increase of anode focal spot size. However, the latter also leads to a decrease in image resolution. This trade-off could be improved with the "line focus" principle by O. Goetze [Behl15]: The achieved resolution depends only on the size of the focal spot as projected into the image plane. Thus, a small angle between anode plane and beam axis decreases apparent focal spot size without increasing demands to tube cooling.

The reduction in acquisition times due to these technical improvements allowed the development of dynamic, contrast-enhancing X-ray imaging methods: In *bronchography*, an agent containing silver, bismuth, or iodine was introduced via the trachea to magnify the contrast of the bronchial tree. Similarly, injection of a contrast agent directly into an artery or via a catheter introduced into a vein allowed highlighting of blood vessel structures near the point of release, e.g., the head or the heart (*cranial / coronary angiography*). Cranial angiography on a patient was successfully performed for the first time in 1927 [Thom18].

Subtraction angiography, a refinement of the technique, was first suggested in 1935: By imaging the investigated region twice, before and after application of the contrast agent, and subsequently subtracting the two images, structures receiving no contrast agent become invisible, and only a map of the distribution of contrast agent remains. Similarly to computed tomography, practical implementations were developed only after the introduction of digital X-ray imaging technology in the 1960s and 70s. *Digital subtraction angiography* (DSA) systems were first commercialized in 1980 [Crum+18]. An important advantage of performing the subtraction digitally is the possibility of correcting the patient's movement between the two images. Nowadays, DSA is most commonly used to identify blood vessel blockages.

In the 1960s, angiography was first combined with a treatment of vascular disease, i.e., by identifying blocked or constricted blood vessels with angiographic methods, guiding a specialized catheter towards the vessel, and using it to dilate the vessel, all during the angiography session. This constituted the first example of *interventional radiography* [Thom18]. The field has since expanded greatly, and a large range of angiographic interventional procedures are now performed routinely.

1.2 Medical X-ray tomography

1.2.1 Conventional tomography

Placing the imaged object between source and film produces a projection of its internal structure, which often leads to an occlusion of features of interest by other structures. Acquisition of a second image from another angle can ameliorate this problem, but naturally, other structures overlap from this new angle. In the 1920s and 30s, an approach was developed to eliminate this problem and produce sectional images of the human body:

A radiographic acquisition was performed while the source and the film were moved along opposite directions. For one particular plane (parallel to the film) within the imaged object, the movement of source and film cancel out. However, features in other regions are blurred by the motion, increasingly so with their distance to the "focus" plane. Thus, they are obscured in the final image, and only features near the focus plane remain visible, producing a sectional image of the object along this plane.

The method was invented at least four times independently in France, Italy, the Netherlands, and Ger-

many. The implementations differed in which elements (source, patient, film) were moved during the acquisition, and in the type of movements performed by these elements. Furthermore, as the optimal plane is always parallel to that of the film, even axial sectional images of the body (as commonly known today from CT and MRI) could be achieved. Different names were used for these variants ("planigraphy", "stratigraphy", "tomography", and others). In 1962, *tomography* was chosen as a generic label for this imaging method [Litt+96].

Movement of these elements on complex trajectories, e.g., circles or spirals, produced better images than linear movement. A very successful device employing this so-called "pluridirectional tomography" was the "Polytome", which was first constructed in 1949 and became commercially available soon after. A large number of medical pluridirectional tomographic devices with increasingly complex movement trajectories was developed until at least 1980 [Litt+96].

1.2.2 Early computed tomography

An alternative, more versatile approach for producing sectional X-ray images took shape with the advent of digital image acquisition and information processing technology in the 1960s. However, its theoretical foundations are far older: In 1917, J. Radon had shown how a function defined on a plane can equivalently be represented by the entirety of its parallel projections from all angles, and how to transform between these two representations [Rado17]. The spatial map of X-ray attenuation strength in a plane of an imaged object can be interpreted as such a function, and its X-ray image as a projection of this function along the direction of the X-rays.

It can be shown that an X-ray image of an object is a projection of the object's spatial distribution of X-ray attenuation coefficients. Radon's publication thus implies that, if X-ray images of an object are acquired from a large number of angles, with the projection rays being oriented in a plane, a sectional image along this plane (a *tomogram*) can be reconstructed from this set of images. Several methods for the calculation, such as iterative, algebraic techniques, or a direct application of Radon's transforms [Broo+76; Buzu08] are possible.

Other than in conventional tomography, no motion blur is desired, and the beam geometry can be such that only the volume of interest is irradiated. However, the need for mathematical operations on imaging data requires information processing technology.

After similar reconstruction problems had been researched in the context of statistics and astrophysics [Buzu08], a sophisticated analytical solution for tomographic reconstruction from a "fan-beam" source, as well as an imaging and tomographic reconstruction method using exclusively analog electronics and X-ray film was presented by B. I. Korenblyum and other researchers from Kyiv Polytechnic Institute [Kore+58; Gust20]: They devised an imaging setup to apply a narrow X-ray fan beam to the imaged object, with the object rotating around an axis orthogonal to the beam. The resulting projections were to be recorded on a roll of X-ray film passing over a drum surrounding the object at some distance, thus encoding intensity as a function of rotation and fan angle (i.e., a so-called *sinogram*). Input of sinogram data for reconstruction of the tomograms was to be achieved by illuminating the film with a cathode ray tube (CRT) focused onto the film and measuring light intensity with a photomultiplier tube. The requisite calculations of the basic arithmetic operations necessary for reconstruction (logarithms, multiplications, integrals, among others) were to be performed by analog electronics. A single evaluation step of the integrand of the reconstruction formula would be translated to light intensity of a second cathode ray tube, projected onto photographic film, thus eventually producing the full tomogram after evaluation of all integrals for all data points of the tomogram. Sampling different points of the sinogram and tomogram films was to be achieved by deflection of the CRT's electron beam as well as rotating the barrel on which the sinogram film was mounted. A total reconstruction time of 5 minutes was estimated for a tomogram consisting of 10^4 data points. It is unclear whether such an apparatus was ever completed. However, this work is one of the earliest studies on the retrieval of tomograms by computational means, i.e., *computed tomography* (CT).

A. M. Cormack developed a solution to the reconstruction problem without knowledge of preceding work [Corm63; Corm64] and successfully verified his method with tomographic measurements of an imaging phantom using a radioactive source: He found the determined attenuation coefficients to be in good agreement with theoretically calculated values [Corm64].

Around the same time, G. Hounsfield began working on the same problem and constructed a tabletop apparatus very similar to Cormack's and, by presenting tomograms acquired with this device, succeeded in convincing a number of influential radiologists of the method's benefits. Funding for the construction of a number of clinical prototypes for head CT scans at EMI, Ltd. could thus be acquired [Beck06].

The first CT scan of a patient was performed in 1971 [Beck06]. The prototypes (then called "EMI scanners") already shared a large number of features with today's CT machines: X-ray source and detector were mounted on a common frame ("gantry") rotating around the patient's head. In this and other "first-generation" CT devices, X-rays were collimated to a pencil beam. In order to produce a parallel-beam geometry, source and detector were translated laterally across the imaged slice, before moving on to the next projection angle. Acquisition of a tomogram thus consisted of alternating translation and gantry rotation steps [Buzu08]. This meant that acquisition for a single 80×80 pixel slice required 4.5 to 20 minutes [Beck06].

Even at this early stage, however, the device achieved a 0.5% accuracy in the determination of absorption coefficients [Houn73], far surpassing the soft-tissue contrasts of other non-invasive brain imaging methods available at the time. Before the introduction of CT, *pneumoencephalography*, an imaging procedure where spinal fluid was drained from the brain and replaced by air or other gasses to enhance soft-tissue contrast for a subsequent radiograph, was commonly used to identify brain lesions. This excruciating procedure induced side effects such as vomiting, headaches, and fever for several days after the examination [Whit+73]. This method was among the first to be nearly entirely replaced by CT.

Unlike the concept by Korenblyum et al., data acquisition and reconstruction were performed with digital technology from the start: X-ray detection was achieved with a sodium iodide scintillation crystal and a photomultiplier tube [Beck06]. A second, identical detector was employed to provide the reference, blank-scan intensity. Output voltages from both detectors were digitized for storage and subsequent reconstruction [Houn73]. For the prototype device, measurement data initially even had to be transported to an external mainframe for reconstruction [Beck06].

1.2.3 Further development of CT

The most straightforward reconstruction algorithm is so-called *back projection*, i.e., a "smearing out" of all projections across the image plane along the reverse direction of projection. However, this leads to significant artifacts. Two better alternatives are *iterative reconstruction* and *analytic reconstruction*. All three are presented and compared in [Broo+76]. Reconstruction of data from the EMI scanner was initially performed using an iterative algebraic reconstruction technique (ART). However, since *filtered back projection* (FBP), one of the algorithmic implementations of the analytic solution for the reconstruction problem, is based on Fourier transforms, its execution speed benefited greatly from applying the *Fast Fourier Transform* (FFT) algorithm for these calculations. Together with general improvements in computer performance, this allowed moving reconstruction of CT data to local computers, and the FBP reconstruction algorithm remains in everyday use for many reconstruction problems even today.

Increasing the number of detector elements in "second-generation" CT devices allowed acquisition of multiple projection rays at a time, significantly reducing acquisition time [Buzu08].

Source translation was finally rendered unnecessary in "third-generation" CT devices, where even larger detector arrays are used, simultaneously acquiring all projection data for a given rotation angle. The resulting acquisition times below 20 s finally allowed performing a complete (axial) trunk scan during a single breathhold [Buzu08]. The radial emission of X-rays motivated the use of curved detector arrays and required adaptation of reconstruction algorithms to the resulting fan-like shape of the radiation field, thus finally replicating the setup geometry proposed by Korenblyum et al. several decades earlier, albeit replacing the X-ray film by a linear array of 400 to 1000 [Buzu08] digital detector modules. This geometry enabled the use of *helical* acquisition techniques, i.e., simultaneous movement of the patient in craniocaudal (head-to-toe) direction and rotation of the source-detector unit ("gantry"), allowing rapid scans of large, multislice volumes.

However, a helical scan would typically require multiple, rapid gantry rotations. This was only possible by replacing the conventional electrical and data connections to the gantry with slip-ring technology [Hurl+09].

A downside of the sharp "fan" collimation is that long, helical scans exert a high heat load to the X-ray tube (since most of the generated X-rays do not contribute to the image) [Gold08]. This was ameliorated by the introduction of detectors consisting of multiple pixel lines ("multislice CT"), since they allowed expanding the radiation field perpendicularly to the axial plane, leading to more efficient use of the X-ray tube by turning the "fan" of X-rays into a wider "cone". The first commercial multislice (2-slice) CT was introduced by Elscint in 1992 [Gold08], but the multislice CT era is mainly understood to begin with the introduction of four-detector row CT setups in 1998/99 [Gold08; Hurl+09].

From then on, CT manufacturers have competed to develop devices with more and more detector lines. This competition produced the first CTs with 16 lines in 2001, 64 lines in 2004 [Hurl+09], and even 256 or 320 slices around 2008.

This increase was largely motivated by the desire to allow imaging of fast, dynamic processes, such as cardiac CT [Hurl+09; Mahe+09] and perfusion studies, but is not as essential for most other medical applications. Naturally, data produced with cone-beam CT require different, more sophisticated reconstruction algorithms to take into account the differences in beam geometry. An overview of such algorithms based on filtered back projection is given in [Turb01].

In 2009, the United States' National Council on Radiation Protection and Measurements (NCRP) released its Report No. 160, which highlighted the significant increase of the general population's exposure to ionizing radiation from medical exams. It showed that, compared to the early 1980s, U.S. residents received more than seven times as much yearly effective dose from medical sources in 2006, thus surpassing the effective dose from natural background sources [NCRP09]. This finding has received widespread attention in U.S. mainstream media, strongly increasing public awareness of radiation risks from CT exams [DeMa17]. Similarly, the number of CT examinations in Germany has increased by 40% from 2007 to 2014, accounting for about 60% of collective effective dose due to medical imaging in 2014 [Neko+17]. Furthermore, nuclear magnetic resonance imaging (MRI), which does not use ionizing radiation, has proven able to replace CT for many imaging tasks.

Consequently, a number of efforts have been taken to reduce ionizing radiation dose. Since reimbursement of CT exams has been partially tied to the availability of dose-reduction features [DeMa17], low-dose capabilities have become a major selling point for CT setups — it has been claimed that by 2009, the "slice war" between manufacturers had given way to a "dose war" [Mahe+09]. Besides the introduction of strict clinical criteria for ordering CT exams, dose reductions have been achieved through improvements in detector technology and the introduction of automatic tube current modulation [DeMa17].

Most prominently however, the demand for dose reduction has lead to a resurgence of iterative reconstruction techniques, specifically in combination with an accurate statistical treatment of measurement data [Thib+07]. Such a *statistical iterative reconstruction* (SIR) promises tomograms with increased signal-to-noise ratios by taking into account certain assumptions about the imaged objects. The iterative approach attempts to solve the reconstruction problem by explicitly minimizing a cost function between data and the system's forward-model applied to the estimate (i.e., the measured sinograms and the forward-projected tomograms). Additional assumptions about imaged objects can then be introduced as additional cost function terms. This so-called *regularization* typically penalizes the presence of sharp edges in tomograms, leading to a smoother appearance of images. However, the magnitude of applied regularization must be chosen carefully so as not to obscure clinically relevant features by excessive smoothing. Furthermore, the statistically accurate treatment of measurement data e.g. leads to a reduction of beam starvation artifacts due to metal objects and much better reconstruction results from measurements with irregularly sampled sinograms. Different variants of iterative reconstruction algorithms have since been introduced by the major CT manufacturers [Flei+11]. However, average yearly effective dose per person in Germany due to CT alone has still increased from 2007 to 2014, meaning that all advances in dose reduction during this time were unable to compensate for the increasing number of CT exams [Neko+17].

A more recent innovation is the development of clinical dual-energy CT devices. In 1976, R. E. Alvarez and A. Macovski proposed a method to combine CT scan data of the same object acquired with two different X-ray spectra and thus obtain a decomposition of linear attenuation coefficients into two independent parameters, approximately representing the fraction of attenu-

ation due to the photoelectric effect and Compton scattering [Alva+76]. Given that these values are material-dependent, the photoelectric and Compton coefficient pairs of any two (sufficiently different) materials can be used as "basis vectors" for virtually decomposing any measured coefficient pair into a fractional mix of both materials. This works especially well for separating bone, metal, or iodine, a commonly-used contrast agent due to its high atomic number, from surrounding soft tissue. The first medical dual-energy CT was introduced by Siemens in 2006, employing two X-ray tubes and detectors operated at different acceleration voltages (e.g., 80 and 140 kV). Other manufacturers have since followed with their own implementations of dual-energy CT capabilities.

There has been rapid progress in the development of solid-state X-ray photon-counting detectors: Due to sophisticated per-pixel readout electronics, thermal noise can be completely suppressed and the lack of an intermediate scintillation step allows a better localization of incident radiation. Furthermore, high readout speeds allow counting and even energy-discrimination of individual X-ray photons (cf. section 2.4.2 on page 49). These properties makes photon-counting detectors ideally suited to use in CT for increasing noise characteristics and implementation of multi-energy spectral acquisition modes. However, their clinical application is still hindered by technological difficulties and photon-counting detector development remains an active field of research.

1.3 Visible-light phase contrast

1.3.1 Discovering the wave properties of light

To confirm the wave nature of light, T. Young performed an experiment in 1803, where a ray of sunlight was split in two by the edge of a thin piece of cardboard, which produced colorful periodic patterns on a screen downstream [Youn04; Sche86]. Young explained this effect by a superposition of the light waves emanating from each slit: Depending on the relative phase of the waves from each slit, they would extinguish or amplify each other. In a similar experiment, Young was also able to estimate the wavelength of red light [Youn02].

A. J. Fresnel further refined this work in 1819: Expanding Huygens' principle of interpreting every point of a wavefront as a new, secondary point source, Fresnel was able to correctly predict the shape of interference patterns from several diffraction geometries [Fres00]. His success further substantiated the wave model of light, which was then still opposed by many notable researchers.

Another arrangement to achieve interference was presented by H. Lloyd in 1834: Using monochromatic radiation impinging on a mirror at a steep angle, interference fringes could be generated on a screen by superposition of direct illumination and light reflected by the mirror. This also proved that light waves experience a half-period phase shift upon reflection from a mirror.

In 1836, H. F. Talbot illuminated a transmission grating with sunlight and observed multicolored periodic patterns at different distances from the grating, essentially reproductions of the grating profile [Talb36]. The relation to diffraction phenomena is not immediately obvious. A theoretical description of this effect was only found in 1881 when J. W. Strutt (Lord Rayleigh) showed it to be a consequence of Fresnel's theory of diffraction when applied to a periodic attenuating object [Rayl81].

Based on the observation that the propagation speed of electromagnetic fields coincided with the speed of light, J. C. Maxwell suggested in 1862 that light is a phenomenon of electromagnetism. He developed a set of 20 "general equations of the electromagnetic field", an early form of what are known today as Maxwell's equations [Maxw65].

Unlike other known wave-like phenomena, however, light waves can traverse the vacuum of space and thus have no obvious medium of propagation. A contemporary hypothesis was the existence of an omnipresent, yet undetectable propagation medium called "luminiferous aether". To determine its existence, A. A. Michelson and E. W. Morley designed an interferometric experiment in 1881, which they subsequently improved and repeated in 1887 [Mich+87]: Assuming the existence of a propagation medium, the speed of light would have to be constant relative to it. Due to the earth's significant speed of movement around the sun, relative differences in the speed of light would have to be observable between propagation in parallel to, and at a right angle with the earth's movement.

Michelson and Morley designed an interferometer using a semi-transparent mirror which split an incident beam into two orthogonal (reflected and transmitted)

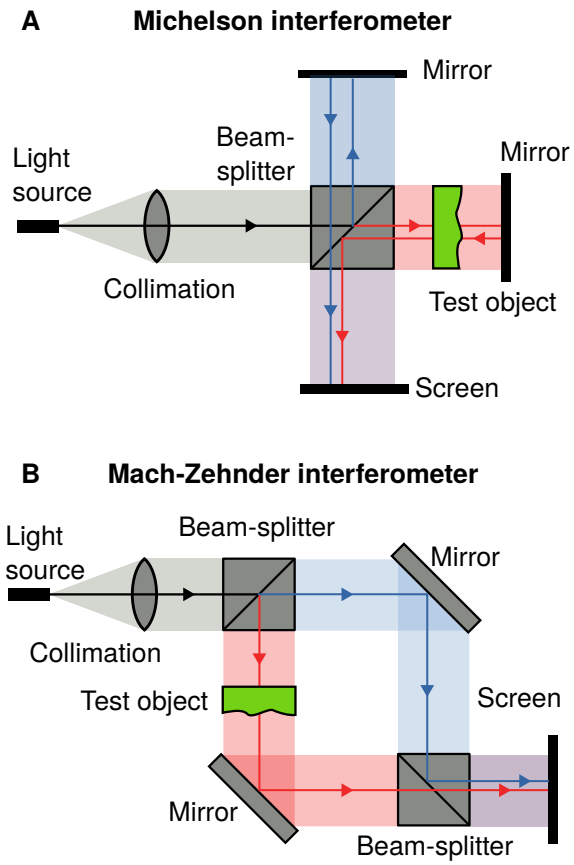

Figure 1.1: Two examples for visible-light two-beam interferometers: the Michelson and the Mach-Zehnder interferometer.

partial beams (cf. Fig. 1.1a). Both beams would then travel at right angles (in parallel with and orthogonal to the earth's movement), reach a conventional mirror, and return to the beam-splitter. The occurring partial reflection and transmission of both beams meant that a superposition of beams traveling in orthogonal directions could be observed. Any deviation in the speed of light for the two directions would lead to a phase delay between both beams. Furthermore, the entire interferometer could be rotated, allowing an interchange of "parallel" and "orthogonal" beams. However, no deviations in phase difference due to rotation could be determined, effectively disproving the aether hypothesis. This finding of a universally constant speed of light (in vacuum) was a cornerstone for the formulation of special relativity by Albert Einstein.

1.3.2 Interferometer designs

Besides basic research, visible-light interferometers are used for many applications, among the most prominent being testing of optical components and microscopic imaging. A large number of visible-light interferometer types exist and can be classified according to beam geometry.

Two-beam interferometers spatially separate two mutually coherent beams, and different optical components are thus used for manipulating each of the two beams.

The spatial separation is most commonly achieved by "amplitude-splitting" a single beam with a beam-splitter, i.e., a semi-transparent mirror. The interferometer used by Michelson and Morley mentioned above is one such example. This type of interferometer can also be adapted for testing optical components, and is then called a "Twyman-Green interferometer". Since either beam traverses the same volume two times (before and after reflection), the wavefront phase is shifted twice by an inserted sample, leading to very high sensitivity.

Tilting both mirrors by 45° and reuniting the beams in a second beam-splitter results in the "Mach-Zehnder" interferometer geometry (Fig. 1.1b). It is often used for to characterize plasmas (variation of refractive index due to temperature and pressure) and air flow [Hari06]. It can be adjusted in such a way that interference fringes and the object under examination are both in focus [Hari06], e.g. allowing imaging an airfoil (the sample) together with its effects on airflow (interference effects). Furthermore, a sample placed in the beam is only traversed once by the wavefront.

However, two-beam interferometers are quite susceptible to external disturbances, since the relative position of optical components manipulating the two beams must be constant down to less than a wavelength. This limitation disappears if the same optical components can be used to manipulate both beams, as is done in so-called **common-beam interferometers**.

One such example is the Newton interferometer (Fig. 1.2a), a design often used for optical components testing due to its simplicity, high stability and moderate coherence requirements. The examined object surface is placed "face-down" onto a corresponding ideal reference. When illuminated with monochromatic light, reflections from the adjacent surfaces reach the screen (or eyepiece) via the same optical path, generating interference fringes. Magnitude and type of

surface deviations can then be inferred directly from the shape of these fringes.

Common-beam interferometers can often be modified to induce a lateral displacement / shear between the two beams. The simplest possible arrangement is a single glass plate with highly parallel surfaces, illuminated at an angle by a collimated, highly monochromatic light source (Fig. 1.2b). Reflection by both surfaces generates mutually coherent beams with a lateral shear dependent on angle and thickness of the glass plate. For small lateral displacements, it can be shown that the resulting phase difference is approximately proportional to the spatial derivative of phase along the shear direction. The resulting fringe pattern thus encodes information about differential phase shift, or equivalently, refraction angle induced by the object.

A shearing interferometer can also be designed by exploiting the Talbot effect (Fig. 1.2c, cf. section 1.3.1): The effect results from coherent superposition of diffraction orders from an optical grating. At certain downstream distances, a self-image of the grating is generated as long as the diffracted fields overlap spatially. An introduced object distorts this image, from which the amount of phase-shift may be estimated. As in the shearing interferometer, the phase shift of the fringe pattern is proportional to differential phase. An analyzer grating may be introduced near the detector if the self-image can not be resolved directly. Of the shown examples, this is the only design not dependent on mirrors, which is especially useful for wavelengths where reflective materials are not readily available.

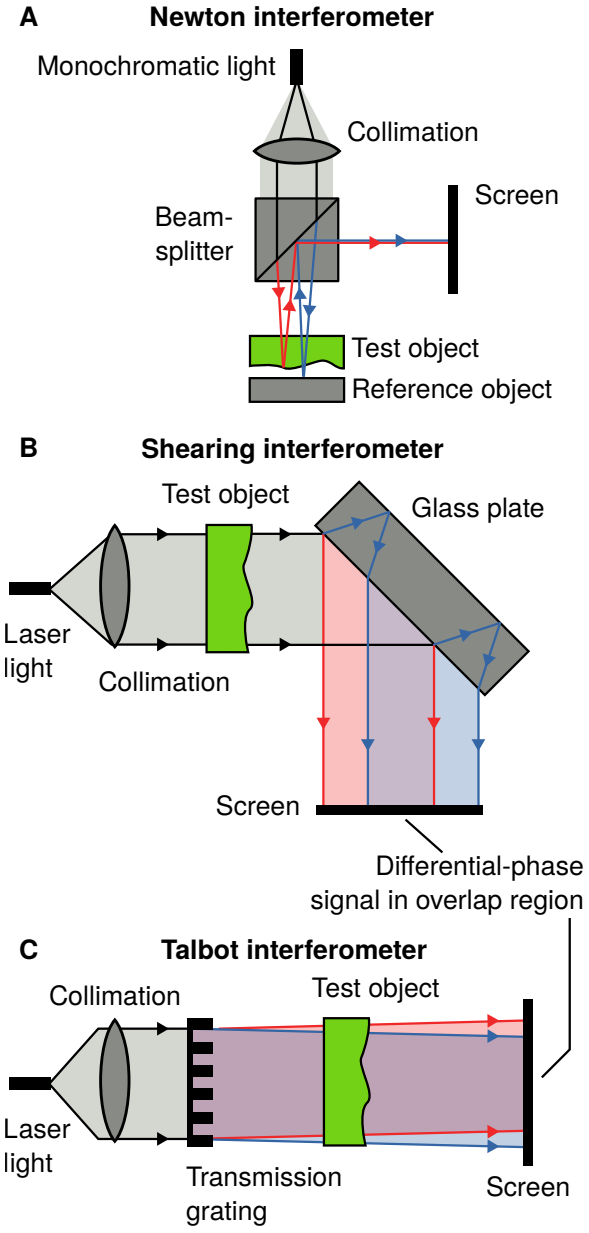

Figure 1.2: Three examples for common-beam interferometers: Newton, shearing, and Talbot interferometer.

1.3.3 Phase-contrast microscopy

An adaptation of interferometric methods for microscopic imaging of phase shifts was first achieved by F. Zernike in 1932: A conventional transmitted-light microscope is modified by insertion of two annular plates, a “condenser annulus” and a “phase plate”. This is illustrated in Fig. 1.3.

The condenser annulus, an aperture that transmits light only in a ring-shaped region, is positioned at the front focal plane of the condenser. The ring-shaped light intensity profile is thus completely defocused in the sample plane (parallel light), and reforms at the back focal plane of the objective. In a ring-shaped region matched with the annular aperture, the phase plate partly attenuates the light and imprints a phase-shift of approximately 1/4 of a wavelength.

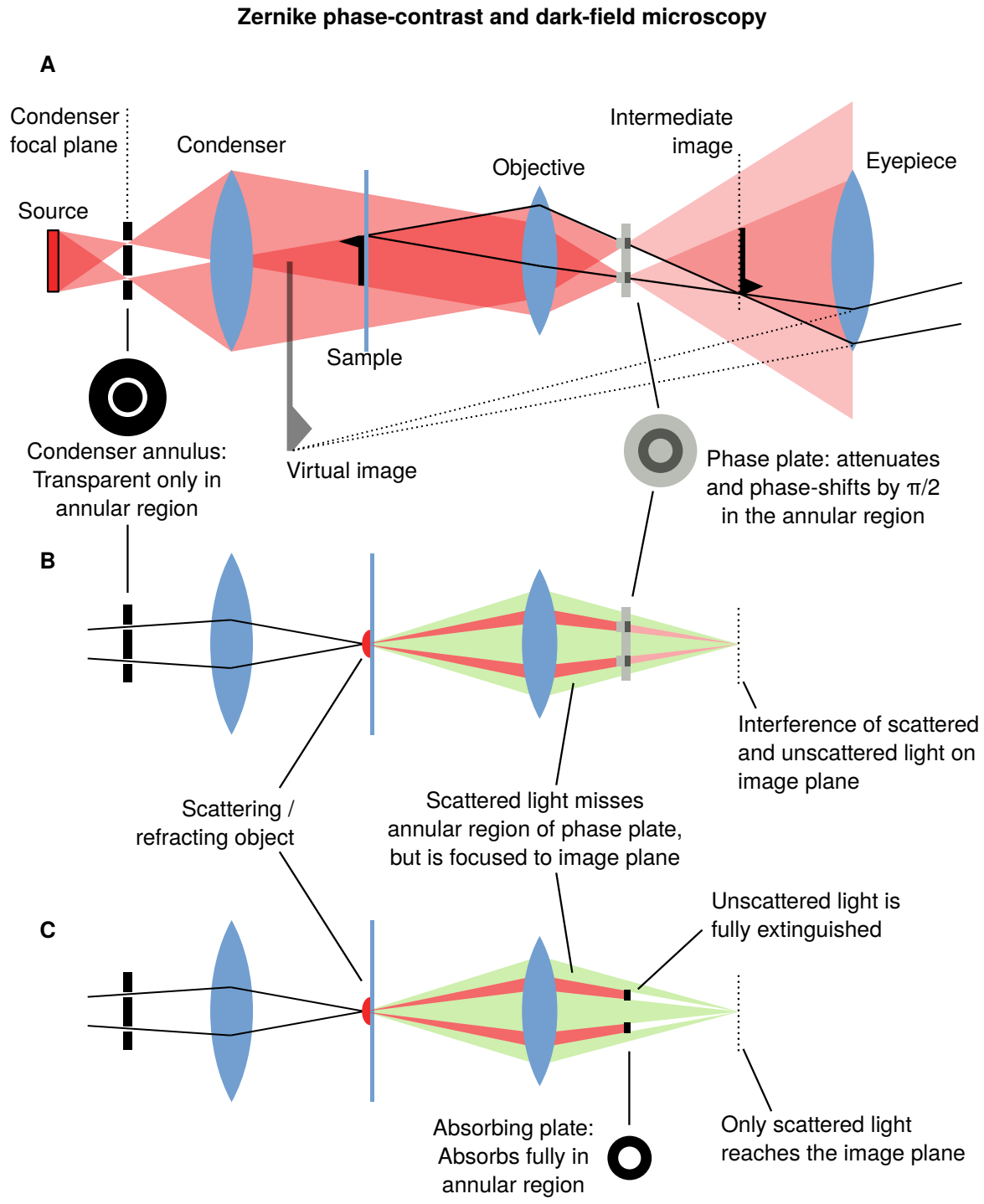

Figure 1.3: Operating principle of the Zernike microscope. (a): The condenser annulus is imaged to the back focal plane of the objective, where the phase plate is located. (b): Scattered and unscattered light passes through different regions of the phase plate, leading to interference effects and a highlighting of phase-shifting structures in the image plane. (c): Replacing the phase plate by an absorbing plate allows blocking all unscattered radiation, producing a dark-field image of the sample.

In the absence of phase-shifting structures in the sample, all light passes through this region and the functionality of a conventional microscope remains unaffected: An intermediate, real image of the sample is generated downstream of the phase plate, and can be further magnified with an eyepiece.

However, in the presence of small structures in the sample, the incident light is partly diffracted. Diffracted and undiffracted light is focused onto the same point in the plane of the intermediate image, but scattered light will not pass through the phase-shifting and attenuating annular region of the phase plate. A spatial separation of diffracted and undiffracted light is thus achieved in the plane of the phase plate (Fig. 1.3b).

In the image plane, diffracted and undiffracted light are out of phase by $\lambda/4$ and, due to the attenuation of the latter in the phase plate, of similar intensity, which maximizes the impact of phase shifts on measured intensity. The general shape of the image thus remains unaffected, but refracting sample regions achieve significantly higher intensity contrast.

Phase-contrast microscopes first became commercially available in 1941. This invention was especially valuable for cell imaging since many types of cells are highly transparent and thus do not generate significant contrast without prior staining.

Alternatively, the phase plate can be replaced by an attenuating disk which blocks all unscattered light (Fig. 1.3c). In this so-called "dark-field illumination", the image is composed only from scattered light. Since no interference occurs, no phase information is retrieved. This is often useful for imaging fibrous structures.

1.4 Synchrotron radiation

X-ray tubes are very inefficient: Only a very small fraction of expended electrical power is converted into X-rays, and these are both highly polychromatic and emitted in a large angular range. This is at odds with the demands of both X-ray crystallography and interferometric methods for highly monochromatic, parallel illumination. Due to a lack of suitable optical elements for X-ray collimation, such conditions could only be achieved by isolating the desired wavelength and propagation direction. This leaves very little flux and leads to long measurement times. In the 1950s however, the potential of using deflecting magnets in particle accelerators as X-ray and UV light sources was recognized.

A *synchrotron* is a ring-shaped particle accelerator: Charged particles (electrons or ions) are alternatingly accelerated by linear accelerator modules, and magnetically deflected and focused to keep them on a closed-loop track. As their kinetic energy increases, the field strength of the deflection and focusing magnets is increased "synchronously", i.e. by the ideal rate to keep the particle trajectory constant.

Such a type of accelerator was first suggested by M. O. Oliphant in 1943, whereas the crucial concept of "phase stability" was developed independently by V. I. Veksler (Soviet Union) and E. M. McMillan (USA). The first demonstration systems were built in 1946, initially for the acceleration of electrons [Wils96].

The synchrotron evolved from a previous circular accelerator design, the *cyclotron*, which uses similar acceleration and deflection principles: it consists of two hollow D-shaped electrodes, in which a constant magnetic field is applied. A high alternating voltage is applied between the electrodes. The particles are thus alternately accelerated (between the electrodes) and deflected by a half-turn while inside an electrode. As the particles gain energy, the radius of their trajectory increases, but—as long as they have nonrelativistic energies—their period remains constant, and the acceleration voltage thus alternates at a fixed frequency [Lawr+32]. However, the period increases when relativistic energies are reached, limiting further acceleration. The concept can be modified by varying acceleration voltage frequency over time (yielding a "synchro-cyclotron"), but this limits operation to the acceleration of single pulses of particles. Due to its method of operation, the synchrotron does not have this limitation. Instead, particle energies are limited primarily by the deflection magnets' maximum field strength, the loss of energy due to bremsstrahlung (cf. section 2.3.2 on page 46), and thus the circumference of the ring.

Like (synchro-)cyclotrons before them, synchrotrons were primarily used for particle collision experiments. Such experiments had lead to many important advancements in particle physics [DiLe93], and the increase in available particle energies now promised the discovery of further elementary particles as well as hitherto unknown particle interaction and decay processes. To this day, the synchrotron remains the state-

of-the-art particle accelerator design for high energy physics research, the most prominent currently being the *Large Hadron Collider* (LHC), featuring the world's largest synchrotron acceleration ring with a 26.7 km circumference [LHC08].

It is well known from radio transmitters that accelerated electric charges (an alternating current in the antenna) emit electromagnetic radiation. In particle accelerators, the much greater accelerations and velocities of particles in an accelerator lead to both higher intensities and lower wavelengths of emitted radiation. In a synchrotron, this effect was first reported in 1948 [Elde+48; Will11]. For the achieved electron energies between 50 and 80 MeV, a significant portion of the radiated spectrum was in the visible range. Spectroscopic measurements through the glass wall of the accelerating tube were found to coincide with theoretical predictions.

A similar study was performed in 1956, now at a synchrotron with electron energies of 233 and 321 MeV. The higher electron energies allowed the generation of ultraviolet and soft X-rays (emitted wavelengths scale approximately with the inverse cube of electron energy [Tomb+56]). Furthermore, the angular distribution of radiated light, which is roughly isotropic for non-relativistic electrons, is focused into the direction of electron movement for high electron energies due to relativistic effects. It was recognized that the resulting high-intensity light source could be exploited for practical uses, such as spectroscopy in the UV and soft X-ray regime [Tomb+56].

In the following years, a number of synchrotrons (now called "first-generation synchrotron sources") thus introduced facilities to use this radiation, while maintaining their main use for collision experiments [Will11]. The hard X-ray regime became accessible with the modification of DESY (Hamburg, Germany) in 1964 [Will11]. Eventually, facilities dedicated entirely to the generation of synchrotron radiation ("second-generation sources") were created, the first one being the Synchrotron Radiation Source (SRS, Cheshire, England) commissioned in 1981 [Will11].

However, although these were among the brightest sources of light in their respective spectral ranges, their spectral bandwidth was still significant and monochromatic beams could only be achieved at the expense of discarding the majority of emitted light [Kita00]. It was realized that the characteristics of the emitted radiation could be improved by employing specially-designed magnet arrays, to be installed in addition to the existing deflection and focusing magnets. These so-called *insertion devices* consist of a series of dipole magnet pairs with alternating polarity. The deflections induced to the beam by two successive magnet pairs cancel out and thus do not disturb the overall electron trajectory. The achieved X-ray power however increases with every magnet pair added to the array (cf. section 2.3.2 on page 46).

Insertion devices can be designed as "wigglers", which feature a greater lateral displacement of the electron beam and a very high overall X-ray output, or as "undulators" with lower lateral displacement, which allows coherent superposition of radiation from individual deflections and results in a spectrum with one or more narrow peaks [Robi09; Kita00]. The first of these so-called "third-generation sources" was the "European Synchrotron Radiation Facility" (ESRF) in Grenoble, France, becoming operational in 1994 [Will11].

The achieved increases in spectral X-ray flux and decreases in source size as well as angular range have allowed to decrease measurement times and accuracy of existing measurement methods, such as X-ray crystallography, but have also enabled the development of entirely new applications, such as propagation-based X-ray phase contrast imaging (section 1.5.5).

1.5 X-ray phase contrast methods

1.5.1 X-ray crystallography

Like all electromagnetic radiation, X-rays exhibit wave properties that can be exploited for experimental purposes. However, since hard X-rays have wavelengths four orders of magnitude smaller than visible light, X-ray diffraction effects are much harder to observe.

Given an optical grating with period p, illuminated by a plane wave at normal incidence with wavelength λ, diffraction maxima are expected in the far-field at angles $\alpha_n = \sin^{-1}(n\lambda/p)$ relative to the normal of the grating plane, n being an integer. Thus, simply replacing a visible-light source in a diffraction experiment with a hard-X-ray source (of sufficient coherence) would produce diffraction angles four orders of magnitude smaller, which would typically not allow resolving individual maxima.

The opposite problem was discussed by P. Ewald and M. von Laue in 1912: Ewald wished to perform diffrac-

tion experiments on a crystal in order to validate a theoretical model of crystal structure, but this was not feasible with visible light due to the wavelengths being much greater than the expected periodicity of the crystal structure. Von Laue suggested using X-rays and was able to produce an X-ray diffraction image of a copper sulfate crystal in the same year, which conclusively proved the wave nature of X-rays [Mart14]. The highly regular atomic arrangement of crystals takes the place of the grating. Since the wavelength of X-rays are in a similar range as dimensions of crystal unit cells, resulting diffraction angles are easy to observe. However, the regularity of crystals in all three dimensions allows for a larger number of diffraction maxima. Their relation to parameters of the crystal lattice are described by the Laue or Bragg relations [AlsN+11, sec. 5.1].

X-rays diffraction experiments have proved to be an ideal tool for examining crystal microstructure and remain an important technique to this day. Acquiring diffraction images for different crystal orientations allows calculation of their internal structure to an extremely high degree of precision. Even molecules not naturally forming crystal structures can be examined, since crystals can often be grown artificially. The structure of a large number of biomolecules has since been discovered with the help of X-ray crystallography. Among the most important findings are the discovery of the double-helix structure of DNA [Wats+53b] and its method of replication [Wats+53a] in 1953, the first determination of a protein's structure (myoglobin) down to an atomic level in 1960 [Kirk14], and the structure determination of a photosynthetic reaction center in 1981 [Mich82; Will11].

1.5.2 X-ray microscopy

Motivated by the invention of the *scanning electron microscope* (SEM) by M. von Ardenne in 1937, a modification of the technique to generate "electron shadow images" was proposed in 1939 [Arde39]: By expanding the electron beam emitted from the probe into a wide cone, a magnified shadow of the object could be generated. This differs from the previously invented *transmission electron microscope* (TEM) by the absence of focusing electron optics. Placing the object very close to the probe would then allow very high sample magnification. The achievable resolution is primarily limited by the size of the electron probe.

Additionally, a geometry was proposed where the TEM electron beam is focused onto a target, and instead using the cone of generated X-rays to image the object at high magnification. Since X-rays are scattered much less than electrons in material, significantly thicker samples could be imaged, while also receiving less radiation damage. This method, later named "X-ray projection microscopy" was realized in the same year [Mals39; Kirz+09]. Conceptually, this is the simplest method to achieve a very high magnification of radiographs, since no X-ray optical elements are required, only the electron beam must be well focused to generate a sufficiently small focal spot. Furthermore, no monochromation is required.

The primary benefit of both electron and X-ray microscopy techniques lies in the higher achievable resolutions: Conventional visible-light microscopes are said to be diffraction-limited, i.e. their resolution is restricted by the light wavelength (which is in the vicinity of 0.5µm). The much smaller X-ray wavelengths (≈ 1 nm) and electron de Broglie wavelengths (≈ 10 pm) used in microscopy shift this fundamental limit to much smaller dimensions.

Besides the finite size of the X-ray focal spot, resolution in X-ray microscopy was limited by diffraction in the sample: The significant propagation distance to the film / detector creates intensity fluctuations around edges. It was only recognized much later that these "artifacts" contain highly valuable information to retrieve X-ray phase-contrast maps. Accordingly, modifications to SEM-based X-ray projection microscopes for the retrieval of phase-contrast information have been presented [Mayo+02].

Over the years, a number of X-ray focusing techniques were developed: P. Kirkpatrick and A. V. Baez suggested the use of a set of two "crossed" grazing-incidence concave mirrors for focusing X-rays [Kirk+48]. It was however recognized that this arrangement can produce significant aberrations when used for X-ray microscopy [Kirz+09]. Similar grazing-incidence focusing optics have however found widespread use in X-ray astronomy.

Additionally, Fresnel zone plates were investigated as alternative focusing elements: Consisting of radially symmetric, attenuating rings, zone plates induce diffraction effects which lead to constructive interference at certain downstream positions, if the incident radiation is sufficiently coherent. However, since the size of the resulting focal spots is deter-

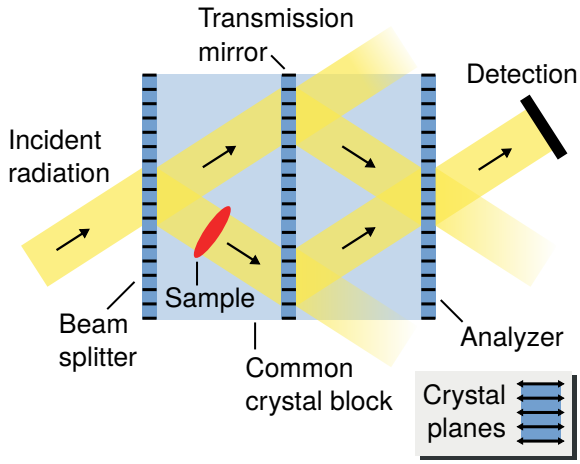

Figure 1.4: Operation of a crystal-based X-ray interferometer. The three crystal layers are produced by cutting grooves into a single ingot.

mined by the smallest features of the zone plate, i.e the width of the outermost zones, construction of Fresnel zone plates with sufficient quality for X-ray microscopy is challenging, especially for use with hard X-rays. The similar behavior of zone plates and optical lenses allowed the imitation of visible-light beam paths for soft X-ray microscopy. X-ray microscopes using zone plates were first implemented for laboratory-based and synchrotron X-ray sources between 1974 and 1983 [Kirz+09].

It was recognized that the achievable contrast due to phase shifts is much higher than the contrast due to attenuation for most X-ray wavelengths [Schm+87]: Based on the phase-contrast generation method in the Zernike microscope, intensity contrasts due to phase shifts were found to be higher for various organic materials and soft X-ray wavelengths. Alternatively, this allows a reduction of dose and associated damage to the sample for comparable image contrast. Thus, the design of the Zernike phase-contrast microscope was successfully adapted to X-rays in this manner [Schm+94].

1.5.3 X-ray crystal interferometers

One of the earliest steps towards X-ray phase contrast imaging was made in 1965 with the development of the first X-ray interferometer [Bons+65]: It consisted of a single, nearly perfect silicon monocrystal into which two grooves of 1 cm width were cut, leaving three 50 µm thin crystal layers with perfect mutual alignment due to being part of the same crystal lattice. Characteristic X-rays from the copper K_α line were selected by Bragg reflection and subsequently diffracted by all three layers (Fig. 1.4): The first layer is illuminated at an angle, and splits the incident beam into two transmitted beams: an undiffracted portion and a reflection on the 220 crystal plane, which is orthogonal to the crystal layers' front surfaces, thus resulting in a reflection symmetric to the longitudinal axis of the setup. The different directions of propagation thus lead to a spatial separation of the two beams. At the second crystal layer, each partial beam is split into a transmitted and a 220 reflection again, and the inherent symmetry of the arrangement causes a pair of spatially separated beams to rejoin and thus to interfere at the third crystal layer. The resulting interferogram is finally observed downstream of the third crystal layer.

The observed type of interferogram is equivalent to what would be observed with a visual-light Michelson or Newton interferometer: The intensity depends sinusoidally on the phase difference between the two beams. A spatial gradient of phase difference thus results in a fringe-like pattern of alternating bright and dark lines, where adjacent bright (or adjacent dark) lines correspond to a phase difference of one wavelength. The fringe pattern can thus be interpreted as contour lines of phase difference.

The authors demonstrated how inserting of a plastic wedge in one of the beams lead to a change in the fringe pattern: The spatial period of these contour lines was increased along the direction of the wedge slope, indicating a spatial phase shift gradient due to the object in this direction. The used wavelength was about three orders of magnitude smaller than visible light (1.54 Å), rendering the setup extremely susceptible to disturbances. Furthermore, the associated beneficial effect on interferometer sensitivity is canceled by the phase shift induced at these wavelengths being five orders of magnitude weaker [1], disqualifying it for use in optical testing.

However, the authors recognized the possibility to differentiate materials with X-ray phase contrast images. Using a very similar setup, this was first realized by M. Ando and S. Hosoya in 1972 [Ando+72]. The significantly higher X-ray energy ($K\alpha_1$ of Molybdenum,

[1] Refractive index of polymethyl methacrylate at $\lambda = 1.54$ Å: $n = 1 - 4.14 \times 10^{-6}$, at $\lambda = 589.3$ nm: 1.4905, thus yielding a phase shift approx. 1.2×10^5 times higher for the latter wavelength.

17.48 keV) allowed measurement of thicker samples: X-ray phase-contrast micrographs of part of a butterfly, a bone sample and a thin granite slice were acquired. The field of view was extended by moving the interferometer, the sample, and the photographic plate relative to the X-ray source. The extremely faint illumination by a single fluorescence line and the high resolution demanded very high acquisition times on the order of 24 h.

Several decades later, the idea to use the X-ray crystal interferometer as a phase-contrast imaging tool was revived by Momose et al. by using it at a synchrotron beamline: The high intensity and narrow bandwidth of synchrotron radiation allowed acquisition of crystal-based phase-contrast images on much shorter timescales and at higher resolutions.

Phase-contrast projections of a biological sample (a slice of rat cerebellum) demonstrated the contrast advantage of phase shifts over attenuation for soft tissues [Momo+95]. Phase-contrast projections were extracted from single images using the Fourier-based method described in [Take+82].

By incorporating a rotating stage to the setup, Momose et al. enhanced the method to generate the first phase-contrast CT measurements [Momo95]. Phase retrieval was refined by introducing a rotatable phase-shifting plate into the reference beam, allowing the acquisition of images at different phase shifts and thus acquire phase-constrast images at the same resolution as the measured data. The first phase-contrast CT measurement of a biological sample was also achieved [Momo+96]. Since the field of view of the Bonse-Hart interferometer is limited by the size of the crystal, alternative interferometer designs with spatially separated crystals were also explored [Yone+99].

1.5.4 Analyzer-based phase contrast

Another method which employs crystals as central optical elements for phase contrast is so-called *analyzer-based imaging*. Here, an incident monochromatic beam is collimated and expanded due to reflection from a first crystal, and then reaches the "analyzer crystal". The latter is pivoted about an axis orthogonal to the beam, and is initially rotated such that it produces a Bragg reflection, which is recorded by a detector.

Deviating the crystal's rotation angle from this position results in a decrease of detected intensity. Since the incident beam usually has nonzero angular divergence, and the crystals' reflectivity changes gradually with the angle of incidence, the intensity does not immediately drop to zero, but decreases gradually [Endr18]. The resulting dependence of intensity on crystal rotation angle is called a "rocking curve".

Upon inserting a phase-shifting object upstream of the analyzer crystal, the beam is refracted, which shifts the angles of radiation incident on the analyzer crystal. Thus, a rocking curve measured with the sample will be shifted relative to a curve from a blank reference measurement. This shift is directly equal to the refraction angle induced by the sample, which is in turn related to a spatial derivative of total phase shift by the sample. Like shearing and Talbot interferometers, the analyzer-based method thus measures differential-phase contrast.

The method has been successfully used with laboratory sources [Davi+95], but benefits greatly from the high brilliance (specifically, the low bandwidth and angular divergence) of synchrotron radiation.

Qualitatively, information about sample attenuation is encoded in the peak height or total area under the rocking curve. In a variation of the analyzer-based method named *diffraction-enhanced imaging*, Chapman et al. presented a method to separately derive both modalities from two images: The undisturbed rocking curve is first measured completely. The angles on either side of the peak, where intensity drops to half of peak intensity, are identified. Upon introducing the sample, one image at each of these two angles is taken. The symmetry of the rocking curve then allows the calculation of maps of attenuation and refraction [Chap+97].

Small-angle scattering information can also be retrieved from the rocking curve, since it leads to an angular spread of the curve. Oltulu et al. presented a model of rocking curve intensity which incorporates it in addition to attenuation and refraction. The effect of small-angle scatter is assumed to be a Gaussian angular spread of (a fraction of) the rocking curve intensity. The model thus describes small-angle scatter as a convolution of the original rocking curve with a sum of a Gaussian and a Dirac delta. Using this approach, attenuation, refraction, and small-angle scatter images of a phantom were successfully retrieved from a set of 24 measured images [Oltu+03].

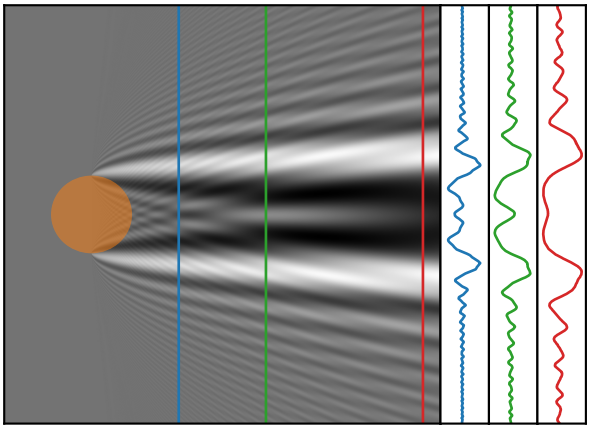

Figure 1.5: Downstream intensity modulations from coherent illumination of a cylindrical phase-shifting sample. The lateral extent of the modulations increases with propagation distance. A map of phase shifts may then be reconstructed from intensity measurements at one or more downstream distances (see line profiles).

1.5.5 Propagation-based phase contrast

A refracting object illuminated with visible light produces shadows on a downstream screen. The amount of refraction can then be evaluated by analysis of these shadows. This so-called "shadowgraph" method can not easily be translated to X-rays because the achievable refraction angles are extremely small. However, a similar approach is feasible if the transverse coherence of the illuminating X-ray source is sufficiently high:

The field at a measurement plane downstream of an object can be thought of as the superposition of spherical waves emanating from each point in the object plane (Huygens-Fresnel principle, cf. section 2.1 on page 33). If the transverse coherence between the different locations in the object's plane is sufficiently high, they may interfere, and thus produce spatial intensity variations in the measurement plane. The spatial extent of these intensity variations is significantly higher than those resulting from mere refraction and increases with the distance between object and measurement plane (cf. Fig. 1.5).

For moderate propagation distances, these intensity variations are most apparent in regions of large spatial gradients of phase-shift. In other words, intensity contrasts at edges and interfaces are highly emphasized. For larger propagation distances, this additional contrast becomes increasingly blurred and the image eventually no longer resembles a conventional projection image.

This type of measurement was first reported in 1995, using highly coherent radiation from the ESRF[2], a third-generation synchrotron source: Intensity fluctuations due to X-ray phase-shifts by very weakly absorbing fibers were observed at multiple propagation distances and X-ray energies [Snig+95]. Soon afterwards, the method was successfully translated to use with a microfocus X-ray tube, which proved that high temporal coherence, i.e. high monochromaticity, is not a requirement [Wilk+96].

For very small specimens, attenuation of hard X-rays is often negligible and all observed intensity modulations can be assumed to arise from phase shifts. In such cases, the map of phase shifts induced by the sample can be reconstructed from a single image [Nuge+96].

In the presence of significant attenuation, this is not possible and imaging data from at least two different propagation distances must be combined to separate attenuation and phase shift. Using a generalized definition of phase, Paganin and Nugent derived an algorithm to perform this retrieval even for partially coherent X-rays [Paga+98]. For a given propagation distance, edge-enhancement contrast depends on feature size, leading to poor visibility of certain features. This may also be ameliorated by joining acquisitions at multiple propagation distances [Cloe+99].

An even simpler approach was developed by Paganin et al. in 2002 [Paga+02]: With the assumption of a constant ratio of phase shift to attenuation everywhere within the sample, a single acquisition is sufficient to retrieve a map of phase shifts. Although this assumption only holds for samples with homogeneous elemental composition, it is often applicable to heterogeneous samples since the ratio of phase shift to attenuation is similar for many biological materials.

The high resolution and image quality as well as the simplicity of the experimental setup and the Paganin phase retrieval method have lead to propagation-based imaging becoming the most popular and widely-used X-ray phase-contrast imaging method. However, the method's high demands to spatial coherence limit its applicability with conventional, non-microfocus X-ray sources.

[2] "European Synchrotron Radiation Facility", Grenoble, France

1.5.6 Grating-based phase contrast

Crystal-based X-ray interferometers, in which a silicon monocrystal takes the place of beam splitters and mirrors from visible-light designs, demonstrated that interferometric techniques could be used to achieve X-ray phase contrast. This type of of interferometer is highly sensitive even to minuscule phase shifts. However, the high sensitivity also means that this approach is highly susceptible to mechanical disturbances and crystal imperfections. Furthermore, object size is severely limited by the size of the crystal.

Another type of diffractive optical element available for use with X-rays are optical gratings. These are objects whose optical properties vary in a highly regular, periodic manner across their surface. Most common are linear gratings, which feature equidistant, parallel lines where attenuation, phase-shift or reflectivity differ from the remaining area. When illuminated with sufficiently coherent light, fields transmitted or reflected by the individual grating structures interfere (constructively or destructively) at different locations, leading to a spatial variation of light intensity in a given measurement plane.

The shape of the achieved intensity distribution depends on multiple parameters, namely: the wavelength λ of the light, the spacing (or pitch) p of adjacent grating lines, and the distance L from the grating at which the intensity is measured. For large distances L (compared to p^2/λ), the so-called *far-field regime* is reached, in which incident light is split into discrete beams at equally-spaced angles. Each beam corresponds to a *diffraction order*, where the relative phase shift between fields from adjacent grating lines equals an integer multiple of the wavelength. This case is easy to achieve if the pitch p is in the vicinity of λ, and can be achieved for X-rays if a crystal serves as a grating, its "pitch" being defined by the lattice spacing, which may be only a few atomic radii.

However, since the width of ordinary grating structures must necessarily be much greater than a single atom, fields from the different diffraction orders from the grating overlap even for large L, and interfere with each other (*near-field diffraction*). As first observed by H. F. Talbot for visible light (section 1.3.1), the intensity modulations resulting from this interference are periodic, and resemble the grating structures themselves (e.g. in pitch). Unlike far-field diffraction beams however, they appear and disappear as L is varied. Furthermore, the distances where contrast is maximal depend on the wavelength. Talbot's experiment was first reproduced with X-rays by Cloetens et al. at the ESRF in 1997, using phase-shifting gratings [Cloe+97].

Introduction of a refracting object before or after the grating equally refracts all diffraction orders, and thus leads to a lateral deflection of the interference pattern (Fig. 1.6b). The amount of refraction can then be inferred directly from this deflection, just as in visible-light shearing interferometers. If the refraction angles are not too large, the interference pattern provides an image of the refracting object. With a grating-based X-ray setup, such images were first achieved by David et al. in 2002 [Davi+02]: In addition to the main (phase-shifting) grating, a combination of a second phase-shifting grating and a Bragg crystal were used to analyze the interference pattern, producing intensity modulations with a much lower spatial period, enabling the visualization of local refraction due to an ensemble of polystyrene spheres.

In 2003, Momose et al. replaced this combination of phase grating and Bragg crystal with an absorption grating, thus assembling the first X-ray Talbot interferometer in the now common design. Furthermore, a method was presented to derive a map of refraction angles from a series of interferograms [Momo+03]. The refraction angle is proportional to the phase shift induced to the wave, differentiated with respect to the coordinate orthogonal to the grating ridges. Maps of refraction angle are therefore also named *differential phase shift* images.

The retrieval of image data was further refined by Weitkamp et al. in 2005 with the *phase-stepping* technique, which allowed a separation of measurement data into maps of attenuation and refraction (cf. section 2.5.6 on page 56). Furthermore, tomographic reconstruction of phase images (retrieved from integrated differential-phase data) were shown to provide volumetric information about the refractive index decrement δ [Weit+05].

Due to the difficulties of manufacturing transmission gratings with low periods and strong attenuation of hard X-rays, the absorption gratings used so far were very small and had limited attenuation capabilities. A combination of techniques to produce larger, and more strongly attenuating gratings were soon examined, among them photolithography, electroplating, evaporation, and anisotropic wet etching [Davi+07]. In particular, a technique abbreviated

"LIGA", developed at the Karlsruhe Institute of Technology (KIT) [Bach+95], later proved to be especially valuable [Mohr+12] (cf. section 3.2.2 on page 73).

Due to its high demands on spatial coherence, the generation of X-ray Talbot images was restricted to measurements at synchrotron beamlines. Illumination of a grating with a conventional X-ray tube does not produce visible Talbot self-images, because the significant size of the source spot leads to a blur of the interferograms, eliminating their contrast (Fig. 1.6a). This could only be circumvented by use of a microfocus X-ray tube, or an extremely narrow collimation of a conventional X-ray tube, either of which severely limited X-ray flux. In 2006, Pfeiffer et al. overcame this limitation by introducing an additional absorption grating near the X-ray tube [Pfei+06]: This *source grating* splits the large source spot into an array of equidistant "source slits". The width of each slit must be narrow enough to limit the aforementioned blur, but the total number of usable slits is unlimited if the period of the source grating is matched to the period of the interferograms at the analyzer grating (the "Lau condition"): in this case, the interferograms from all slits are in phase with each other, and a large fraction of the X-ray tube's flux is used productively. This *Talbot-Lau* approach first introduced X-ray phase contrast to laboratories, and promised a realistic possibility to apply the method for clinical applications[3].

The Talbot-Lau approach was soon extended to tomographic measurements. For the tomographic reconstruction of differential-phase (refraction angle) data, an approach first presented in [Fari+88] was adapted, which combined the integration of differential data with its reconstruction by using a modified kernel for filtered backprojection [Pfei+07].

Although the size and quality of available gratings was increasing thanks to dedicated research efforts, their extent, and thus the field of view of Talbot and Talbot-Lau imaging setups, did not exceed a few centimeters. An alternative to the phase-stepping technique was introduced by Kottler et al. in 2007 [Kott+07]: For this *fringe-scanning* technique, the interferometer would be first slightly detuned so that regularly-spaced moiré fringes were achieved. These arise from the spatial variation of the position of the intensity modulations incident on the analyzer grating, relative to this grating's attenuating structures. In the *phase-stepping* technique, each point of the sample is measured at multiple values of this relative position by laterally moving the analyzer grating. In *fringe-scanning* however, the same set of variations is instead achieved by moving the sample across the moiré pattern (cf. section 3.2.1 on page 71). This has the advantage of allowing the measurement of samples much larger than the grating area with a controlled linear movement of the sample relative to the interferometer. Furthermore, such a scanning setup does not require manipulation of grating positions during the measurement, which allows to assemble the interferometer in a rigid frame and thus reduce its sensitivity to vibration.

The magnitude of differential-phase contrast not only depends on the angle of refraction due to the object, but also on the object's location in the beam. This dependence was thoroughly analyzed by Donath et al. in 2009 [Dona+09] (see section 2.5.8b on page 61). The ratio of image signal and angle of refraction—the angular sensitivity—was found to be greatest when the object was placed directly before or after the modulation grating, and scale linearly with the object's distance to source or analyzer grating, respectively. This means that sample location in grating-based phase contrast not only determines its geometrical magnification, but also the obtained signal magnitude.

A crucial addition to the technique was made by Pfeiffer et al. in 2008. Besides refraction, which leads to a lateral shift of the interferogram, and attenuation, which uniformly decreases its intensity, a third effect could be identified: a decrease of *visibility*, i.e., the interferogram's amplitude, normalized to its mean value [Pfei+08]. It was realized that this effect arises from small-angle scattering in the sample: as in the small-angle X-ray scattering (SAXS) measurement technique, incident radiation is diffracted into a narrow cone by irregular microscopic structures in the sample. This leads to a blur, or irregular displacement of the interferograms, and thus a reduction of visibility when the interferograms are averaged by the analyzer grating. The length scale of the scattering structures is usually far below the spatial resolution. The effect was named *X-ray dark-field* due to its conceptual similarity to the scatter-sensitive, visible-light microscopy technique with dark-field illumination (cf. section 1.3.3). An object's dark-field signal is given by the ratio of reduced and original visibility.

While X-ray dark-field provides per-pixel information

[3] Interestingly, the use of a Talbot-Lau interferometer for X-rays and matter waves had already been suggested in 1992 by Clauser and Reinsch [Clau+92].

about small-angle scatter, a single SAXS measurement provides information only about the ensemble as a whole. On the other hand, SAXS information is much more detailed and complete than the information retrieved from a dark-field image. The relation between X-ray dark-field signal and sample structure was examined in depth by Yashiro et al. [Yash+10] and Lynch et al. [Lync+11]. Furthermore, Strobl has pointed out that these relations are equivalent to the ones for the *spin-echo small-angle neutron scattering* (SESANS) measurement technique [Stro14]. The achieved dark-field signal depends on the autocorrelation function of the object's electron density (normalized to zero mean), evaluated at one "autocorrelation length". This length is a setup-specific value which depends on wavelength, and, like the angular sensitivity, on grating periods and the position of the sample in the beam (cf. section 2.5.8c).

The noise characteristics of differential-phase and dark-field projections differ from those of conventional X-ray. Revol et al. found that, while relative levels of statistical noise for all modalities scale with the inverse square root of detected dose, those of differential phase and dark-field additionally scale with the inverse of (blank-scan) visibility [Revo+10]. This demonstrated that achieving a high visibility is the primary requirement to maximize phase-contrast and dark-field signal-to-noise ratio (SNR) at a given dose level. Subsequently, Chabior et al. demonstrated that the estimation of visibility and dark-field from phase-stepping data is biased, i.e. the expectation value of visibility data increasingly deviates from the true value as SNR decreases [Chab+11]. This suggests caution in the quantitative interpretation of low-SNR dark-field images (see also section 6.3 on page 184 for a discussion of correction methods for this bias).

In 2016, Miao et al. presented an approach to generate low-frequency moiré fringes without the use of an analyzer grating [Miao+16]. Instead, two closely-spaced phase gratings are used in place of a single modulation grating. The combined effect of the two gratings is equivalent to that of one single phase grating with a spatially-varying amplitude (i.e., a beat pattern of the two gratings' slightly differing effective periods). This has a focusing effect which leads to intensity modulations with a sufficiently large period to be detected directly. Besides the increased flux and reduced cost due to the omission of the analyzer grating, this design also allows flexible "tuning" of the setup's angular sensitivity by varying the distance of the two phase gratings. This has been successfully demonstrated to deliver dark-field radiographs with variable angular sensitivity, without a need to adjust the location of the sample in the beam [Kagi+17]. In analogy to the work by Donath et al., angular sensitivity as a function of sample position was recently analyzed for the dual-phase-grating design [Yan+19]. While the dual-phase-grating approach should be compatible with low-coherence sources via the use of a source grating, this has (to my knowledge) not yet been demonstrated experimentally.

1.5.7 Other wavefront-marking methods

In contrast to propagation-based phase contrast, a large number of phase-contrast imaging methods can be classified as "wavefront-marking methods": Optical components are used to generate an intensity modulation on the detector, and information about refraction and/or small-angle scattering by an object is then extracted from the distortion of this pattern. Naturally, grating-based imaging belongs into this category, but other methods besides Talbot self-imaging can be used to produce the modulation pattern:

Grids with a period of at least twice the pixel size can be visualized directly without aliasing. Unlike with finer gratings, the Talbot effect does not occur (at reasonable downstream distances), but as for Talbot images, refracting samples induce a lateral shift of the grid shadow (Fig. 1.6c). The refraction angle can then be retrieved from this shift. Using a signal retrieval method from visible-light interferometry [Take+82], Wen et al. demonstrated the retrieval of phase-contrast and dark-field information from single-shot, *single-grid* X-ray measurements [Wen+08; Wen+09], and also derived a relation of the grid-based dark-field signal to setup parameters, which appears to be identical to the findings by Yashiro et al. for grating-based X-ray [Yash+10], with the grid taking the place of the modulation grating. However, the resolution of the signal retrieval method used by Wen et al. is limited by period of the grid. Morgan et al. therefore developed an alternative processing method, based on the comparison of "interrogation windows", small regions around the pixel of interest, before and after insertion of a sample [Morg+11b; Morg+11a]. This increased the resolution of retrieved differential-phase contrast images far below the grid period, and thus enabled the practical use of grids with

periods much higher than the pixel size for single-shot X-ray phase-contrast.

Propagation-based imaging of rodent lungs typically generates so-called *speckles*, irregular spotty intensity patterns, on the detector. These have been shown to arise due to the lungs' alveolar interfaces acting like unordered clusters of microscopic compound refractive lenses [Kitc+04]. It was recognized that this phenomenon could be used as a wavefront marking mechanism by generating a speckle pattern with a diffuser (such as a piece of sand paper). Since the diffuser structure is usually random and irregular, this is also the case for the generated speckle patterns. Thus, the phase shift induced by an object is not determined with a fit to a known model of measured intensity (e.g. as in grating-based phase-stepping), but is retrieved by measuring the local displacements of the speckle pattern compared to a reference scan measurement [Béru+12], and is thus similar to the "interrogation window" approach by Morgan et al. Due to the lack of translational symmetry in the speckle pattern, the method is intrinsically sensitive to refraction in all directions. Speckle-based imaging has since matured into a versatile imaging technique: the method has been modified to incorporate dark-field information, and is compatible with laboratory sources, high X-ray energies, and tomographic acquisition schemes [Zdor18].

Another approach developed by A. Olivo et al. [Oliv+01] is the *edge-illumination technique*, which is based on the use of an attenuating aperture, or periodic "mask", which splits an incident wave field into one or more narrow "beamlets". In the absence of a sample, these beamlets illuminate an edge, or openings in a co-registered second mask in front of a detector. Introduction of a refracting sample then deflects the beamlet away from this opening, which leads to a reduction in measured intensity (Fig. 1.6d). For weakly attenuating samples, a single measurement is sufficient to encode the angle of refraction. In order to distinguish refraction from attenuation, measurements at two different relative shifts of the masks can be performed, similar to phase-stepping [Munr+12]. By increasing the number of measured relative shifts to three, the method could also be extended to include small-angle scattering information [Endr+14]. Other than grating-based imaging, the beamlets do not interfere and the Talbot effect is not used. Nonetheless, while the method was successfully demonstrated with conventional X-

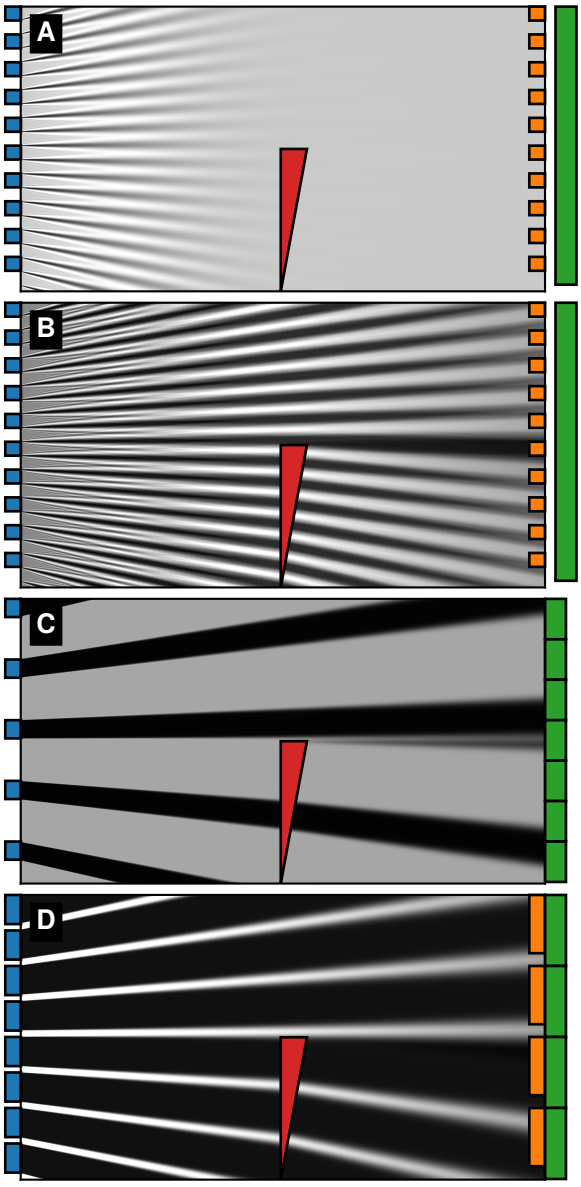

Figure 1.6: Intensity maps for grating-based methods with magnification and source blur. For low transverse coherence, Talbot images can not be observed (a), motivating the introduction of a source grating (b). Grid-based methods directly resolve the grating shadow (c), and edge-illumination employs a set of masks registered to each other and the detector pixels (d). Propagation distance is 0.5 m, but transverse scaling differs: pixel size is 100 µm in all images. For visualization purposes, the refractive power of the wedge (red) in (c) and (d) is greater than in (b).

ray tubes [Oliv+07], its use with large focal spots is limited due to the penumbral blur of the beamlets. Like grating-based imaging however, this method can also benefit from the addition of a source grating, or "source mask" [Bast+16].

1.6 X-ray phase contrast for medical applications

> Without applications, we are just a curiosity.
>
> J. Kirz and C. Jacobsen, about X-ray microscopy [Kirz+09]

The two modalities added by X-ray phase-contrast imaging methods, (differential) phase and dark-field, each offer an important advantage compared to conventional X-ray imaging:

- The phase signal provides greater contrast between objects composed of light elements, whereas
- the dark-field signal provides information about microstructural interfaces below the resolution limit.

Each of these features is beneficial for medical applications, since most biological tissues are composed of light elements, and their performance often rests upon microscopic functional units.

While X-ray phase-contrast imaging methods are not yet part of everyday clinical use, the usefulness and clinical feasibility of such methods has been explored in a large number of experiments, both at synchrotron beamlines and laboratory-based setups. This section provides an overview of some recent developments in this regard.

1.6.1 Breast cancer

Mammography is the most prevalent imaging tool for the detection of cancerous changes in female breast tissue. It is a radiographic method used for diagnosis as well as screening, i.e., preventative early detection [Vogl+11, ch. 20]. The goal of clear distinction between healthy and cancerous tissue is complicated by a number of factors: (Pre-)cancerous growths often have a similar composition as the surrounding tissue, and are superimposed in a projection image by various (healthy) structures, which leads to weak contrast. Detecting the presence of microcalcifications, another important diagnostic marker, additionally requires high resolution. Phase contrast imaging methods have been evaluated to improve this very challenging imaging task.

An early imaging experiment with mammographic samples at an analyzer-based imaging setup yielded high-quality images at acceptable dose levels. However, the use of a fixed-target source and a monochromator lead to measurement times of 10 to 20 minutes [Inga+98].

In [Stam+11], several excised breast samples were imaged in a grating-based setup with a laboratory source. Absorption, phase and dark-field information were fused into a common image by color coding. This revealed additional information compared to preceding conventional *in situ* mammography. These initial findings were later supplemented by a reader study on a total of 33 cases, which found a superior image quality of phase-contrast-supported fusion images, compared to attenuation-only images of equivalent dose [Haus+14].

In [Mich+13], it was demonstrated that microcalcifications may produce a dark-field signal while remaining invisible in conventional mammography. Furthermore, [Wang+14] showed that the chemical composition of microcalcifications could be distinguished by combining attenuation and dark-field image data. However, these findings have been called into question by Scherer et al. [Sche+16a; Wang+16]. An alternative, morphology-based classification of microcalcifications via joint use of attenuation and dark-field data has been presented in [Sche+16b]. Recently, results from an extensive patient study have been presented, which suggest that the ratio of dark-field and attenuation signal can be used to differentiate between benign and malignant microcalcifications [Fort+20].

An adaptation of a clinical mammography system to grating-based imaging was presented in [Koeh+15]. The employed scanning approach sidesteps an important limitation of grating-based imaging, namely the limited area of available gratings. The presented setup achieved a field of view of 160 mm × 196 mm with a scan time of 10 to 15 s, demonstrating the technical feasibility of a clinical phase-contrast mammography system.

The dose efficiency of mammography can be significantly improved if a monochromatic spectrum is used. In [Diem+16], a synchrotron-based edge-illumination

setup was used at the unusually high photon energy of 60 keV to produce high-quality phase-contrast mammograms at a mean glandular dose of only 0.12 mGy (the diagnostic limit is 2.5 mGy). Similarly, mammography with grating-based phase contrast was performed in [Eggl+18] at an inverse Compton source, achieving CNR values superior to clinical images while maintaining similar dose levels.

1.6.2 Joint imaging

Two common diseases affecting joints are *osteoarthritis* and *rheumatoid arthritis* (RA). While osteoarthritis primarily arises from mechanical wear, rheumatoid arthritis is an autoimmune disorder [Sala11, ch. 9]. While RA is much more severe, both conditions are associated with damage to the affected joints' cartilage and underlying bone. Due to the low X-ray absorption contrast of cartilage, and the high demands to spatial resolution, established clinical imaging methods such as radiography, CT, and MRI have limited ability to detect early stages of joint damage from these diseases [Stut+11]. This limits the possibility to monitor disease progression over time.

Because of their advantage in soft-tissue contrast over conventional X-ray, different X-ray phase-contrast techniques have been tested for imaging of cartilaginous structures in joints.

In an early work [Moll+02], an analyzer-based setup was used to image a number of human ankle and knee joints, both with healthy and damaged cartilage. The bone-cartilage interface and damage to the cartilage are apparent in rocking curve images. This work was followed by *in vivo* experiments on guinea pigs [Coan+10], which demonstrated the feasibility of *in situ* phase-contrast imaging of joints. Although the joint anatomy and certain osteoarthritic changes were visualized at low dose, cartilage was not rendered visible.

In another work [Stut+11], grating-based imaging was evaluated for cartilage imaging. Using numerical phantoms, the need for high angular sensitivity was recognized, and cartilage in a human finger joint could be visualized. The authors present design guidelines for a grating-based, lab-source setup dedicated to imaging hand joints.

Such a setup was finally constructed by the Momose group [Tana+13; Momo+14], successfully visualizing cartilage in human finger joints *in vivo* at an average entrance dose of 5 mGy. A clinical imaging study using this device was recently completed, involving 55 healthy participants and 70 RA patients [Yosh+20]. A statistically significant difference between the variation of cartilage thickness between healthy and RA patients could be determined, suggesting potential for early detection of RA.

Furthermore, high-resolution propagation-based phase contrast CT data of human hands [Roug+20] and mouse knees [Roug19, pp. 219–230] recorded at synchrotron beamlines have recently been presented.

1.6.3 Bone imaging and directional dark-field

The microarchitecture of bones can generate a significant X-ray dark-field signal, which has motivated its evaluation for diagnostic imaging of bony structures. However, these structures are also highly ordered. Since dark-field images generated by one-dimensional gratings register only the amount of scattered radiation in one direction, signal magnitude is dependent on the relative orientation of gratings and sample. Retrieval of reliable diagnostic information thus likely requires taking the signal's directional dependence into account.

The use of grating-based phase contrast for imaging entire hands *ex vivo* has been evaluated in [Thür+13]. In this work, the directional dependence of phase-contrast and dark-field signals was taken into account by acquiring radiographs at two orthogonal sample orientations, and combining the individual images to calculate the overall "magnitude" of refraction and scatter. Readers found an improved depiction of soft tissues in the phase contrast modality, while the dark-field image was found to be useful for visualizing calcifications and bony structures.

An alternative approach to quantify the directionally-dependent dark-field signal has been presented in [Jens+10a; Jens+10b], where dark-field values from multiple orientations are fitted to a model incorporating average scattering strength, the degree of anisotropy, and the main direction of scatter.

This method has been demonstrated to visualize a per-pixel-average of bone microstructure orientation [Potd+12; Scha+14]. Since this approach does not require direct resolution of these microstructures, it can be performed at clinically acceptable dose values.

Directional dark-field measurements on human thoracic vertebrae revealed a correlation of mean scatter and anisotropy with "vertebral failure load", i.e., a measure for their mechanical strength [Eggl+14]. This suggests an application for diagnosing osteoporosis, which compromises the mechanical strength of bones.

Using an inverse Compton scattering X-ray source, this approach has recently been applied to a human hand [Jud+17], revealing variations in dark-field anisotropy across different regions of the long bones. Furthermore, microfractures in porcine ribs were found to exhibit an elevated mean scattering strength [Jud19].

A clinical implementation of directional X-ray dark-field imaging is complicated by the demand for measurements at multiple orientations. This limitation might however be resolved by the use of two-dimensional diffracting structures in place of one-dimensional gratings, e.g., as presented in [Kagi+16; Kagi+19].

1.6.4 Lungs and airways

Like bones, lungs have a very complex microstructure that determines their functionality: Air is inhaled via the main airways, which then bifurcate repeatedly into successively finer branches and finally end in alveolar sacs, clusters of microscopic cavities (*alveoli*) surrounded by a network of capillaries [Sala11, ch. 23]. Gas exchange between the air and the blood is then achieved by diffusion across the thin alveolar membranes. In an adult human, the complex hierarchy of airways supplies air to approximately 300 million *alveoli* [Weib63, p. 61], which collectively provide a surface area of approx. 120 m^2 to 140 m^2 [Ochs06]. This enormous area is necessary to allow gas exchange at a sufficient rate despite the very slow underlying diffusive processes.

The mean chord length [Knud+10] of human lungs is approx. 200 µm [Weib63, p. 68], which means that X-rays passing through 10 cm of human lung tissue will traverse approximately 500 alveolar membranes, experiencing refraction at each air-tissue interface.

As mentioned previously, propagation-based [Yagi+99; Kitc+05] and analyzer-based imaging experiments with mouse lungs [Lewi+03; Kitc+05] have shown to produce *speckles*, patchy intensity patterns downstream of the lung. Comparison with simulations showed that this effect is due to multiple refraction on alveolar interfaces, followed by free-space propagation. In particular, the series of subsequently traversed *alveoli* have a similar effect on the X-ray beam as (irregular) compound refractive lenses [Kitc+04].

Propagation-based phase-contrast and other single-image methods have since been used extensively for *in vivo*, real-time airway imaging, e.g. for detection of inhalable substances [Donn+09] or examining drug delivery [Morg+14; Grad+19].

Other analyzer-based experiments on mice have demonstrated so-called extinction contrast, i.e., a broadening of the rocking curve, in the lung region, delivering significant contrast between the lungs and the surrounding area at certain analyzer angles [Zhon+00].

Complex analyzer-based acquisition schemes have been designed to separate attenuation, refraction and small-angle scatter from rocking curves, or even from a single "double-reflection" acquisition with a Laue-geometry analyzer. The mouse lung is very prominent both in the maps of refraction angles and rocking curve width (i.e., the spread of refraction angles, similar to the dark-field modality) [Kitc+10].

The amount of scatter induced by a lung naturally increases with the number of traversed membranes. Since structural lung pathologies such as emphysema affect the number or quality of these membranes, the possibility to detect and quantify such diseases by measuring small-angle scatter was recognized. In emphysema, inflammatory processes destroy alveolar membranes, often "fusing" adjacent alveoli into one larger airspace, leading to a reduction of membranes. An emphysematic lung would thus be expected to scatter less than a healthy lung of comparable size.

However, in order to distinguish pathological changes from normal thickness variations, additional information is necessary, especially for non-tomographic imaging. Since alveolar material occupies only a limited fraction of lung volume (approx. 50% for human lungs [Weib63, p. 54]), and the remaining materials such as airways and connective tissue may not be affected by the pathological changes, the lungs' attenuation signal may be affected differently by pathological changes. This was exploited in one of the first studies of grating-based X-ray dark-field for lung imaging.

In [Schl+12], mouse lungs were imaged *ex situ* in a grating-based imaging setup at an inverse Compton scattering X-ray source. Emphysematic lungs could be distinguished from normal lungs in scatter plots of

dark-field versus transmittance. This was followed up by additional measurements and statistical analyses demonstrated the benefit of using "normalized scatter", the ratio of dark-field and attenuation signal, for emphysema detection [Mein+13].

In a move towards preclinical imaging, Tapfer et al. developed a grating-based phase-contrast CT setup for in vivo small-animal studies [Tapf+11; Tapf+12]. The work in collaboration with SkyScan N.V. (now Bruker microCT N.V., Kontich, Belgium) yielded the "SkyScan 1190" device. A large number of imaging studies for evaluating dark-field for lung pathologies was conducted with two of these devices.

The transferability of emphysema diagnosis capabilities to experiments at this device was demonstrated in [Yaro+13]: healthy and emphysematous lungs *ex situ* could be distinguished via joint analysis of the attenuation and dark-field signals at a range of acceleration voltages. The first *in vivo* dark-field radiographs of a mouse at this device were presented in [Bech+13], and an imaging study for evaluating emphysema detection on living mice was performed in [Mein+14b]. A more extensive imaging study involving 41 animals demonstrated that staging, i.e., a distinction of emphysema severity, could be achieved with the dark-field modality, and with a higher accuracy than using only conventional X-ray [Hell+15].

The range of examined pathologies was then expanded to pulmonary fibrosis. This condition is characterized by a replacement of normal lung parenchyma by scar tissue, which hardens the lung and diminishes its functionality [Sala11, ch. 23]. As treatment options are very limited, patients often have a poor prognosis. In a study with 20 animals, the possibility to diagnose end-stage fibrosis was demonstrated [Yaro+15]. In a later reader study, using dark-field radiographs instead of or in addition to conventional X-ray was found to diagnose pulmonary fibrosis with greater accuracy [Hell+17].

Similar advantages of dark-field radiography for the diagnosis of neonatal lung injury [Yaro+16], pneumothorax [Hell+16], and acute lung inflammation [Hell+18b] were also demonstrated. A reader study examining lung tumor detection of a single *ex situ* specimen which found no clear benefit of dark-field radiography [Mein+14a], was followed by a more extensive investigation on living mice [Sche+17], where a statistically relevant advantage could be identified.

Given the ample evidence of the benefit of X-ray dark-field radiography, an effort was made to transfer the method to larger animals, as an intermediate step to a clinical implementation. Using the setup presented in chapter 3, the first dark-field thorax radiographs of a pig *in vivo* [Grom+17] and of a human *ex vivo* [Will+18] could be acquired. Several of the subsequent findings from experiments with this setup will be the subject of the present thesis, such as: the detectability of pneumothorax in pigs [Hell+18a] (section 5.1), the dependence of dark-field signal on lung thickness at different points in the breath cycle [DeMa+19] (section 5.2 on page 127), the appearance of various imaging features in human cadavers [Fing+19] (section 5.3 on page 145), and a hardening effect of spectral visibility induced by small-angle-scattering objects (section 6.1 on page 159, publication submitted).

Several other scanning dark-field radiography setups with a similar focus have since been developed [Seif+19; Li+20].

Dark-field tomography of mouse thoraxes *in vivo* was first presented in [Velr+15]. Unlike conventional tomograms, which visualize the object's attenuating power, dark-field tomograms display the "linear diffusion coefficient", a measure of small-angle scattering activity. Both emphysematic and fibrotic lungs differ from healthy ones by the numerical values in the dark-field tomograms and the spatial distribution of their variations. Generally, dark-field CT would likely have a high clinical benefit for a wide range of medical conditions. However, achieving measurement times and patient doses compatible with clinical application, as well as achieving sufficient mechanical stability are considerable challenges and an active field of research [Teuf+17].

Chapter 2

Physics and techniques of X-ray imaging

If you wish to make an apple pie from scratch,
you must first invent the universe.

Carl Sagan

Contents

The physical fundamentals for the subsequent content will be introduced in this chapter. A mathematical description of electromagnetic fields as scalar quantities, and their propagation through space, are introduced in section 2.1. We then focus on the different types of interaction of X-rays with matter, and their description in a macroscopic model in section 2.2. The three main mechanisms for the production of X-rays are introduced in section 2.3, and practical, technical implementation of these methods of generation, as well as the detection of X-rays are presented in section 2.4. Section 2.5 introduces the essentials of phase contrast and dark-field in grating-based imaging setups.

2.1 Scalar fields

The interplay between electric fields $\vec{E}$ and magnetic fields $\vec{B}$ was first comprehensively described by a set of differential equations established by J. C. Maxwell [Maxw65] (and formulated in the vector representation known today by O. Heaviside). Two of the four equations show that electric and magnetic

fields are closely tied to each other. In vacuum and an absence of free currents, these are:

$$\nabla \times \vec{E} = -\frac{1}{c}\frac{\partial \vec{B}}{\partial t}, \tag{2.1}$$

$$\nabla \times \vec{B} = \mu_0 \varepsilon_0 \frac{\partial \vec{E}}{\partial t}. \tag{2.2}$$

An oscillating electric field thus generates a magnetic field and vice versa. The ratio between the two is determined by the *permeability* μ_0 and *permittivity* ε_0 of vacuum. Combining Eqs. (2.1) and (2.2) shows that both $\vec{E}(\vec{r},t)$ and $\vec{B}(\vec{r},t)$ fulfill the wave equation:

$$\left(\mu_0 \varepsilon_0 \frac{\partial^2}{\partial t^2} - \nabla^2\right)\vec{E} = 0, \tag{2.3}$$

$$\left(\mu_0 \varepsilon_0 \frac{\partial^2}{\partial t^2} - \nabla^2\right)\vec{B} = 0. \tag{2.4}$$

Comparing this to the standard form of the wave equation, it follows that the phase speed of all solutions to these equations is $c = 1/\sqrt{\mu_0 \varepsilon_0}$. From measurements of μ_0 and ε_0, a value for c was found which was in the vicinity of the previously determined speed of light (about 3×10^8 m/s). Maxwell thus presumed light to be a form of electromagnetic waves.

Furthermore, the phase velocity c defines a *dispersion relation* between the wavenumber $k = 2\pi/\lambda$ and angular frequency ω of any solution:

$$\omega = ck. \tag{2.5}$$

As c is independent of k (in vacuum), the group velocity $v_g = \partial\omega/\partial k$ is also c. One basic solution of Eqs. (2.3), (2.4) is:

$$\vec{E}(\vec{r},t) = \vec{E}_0 \sin\left(\vec{k}\vec{r} - \omega t\right), \tag{2.6}$$

$$\vec{B}(\vec{r},t) = \vec{B}_0 \sin\left(\vec{k}\vec{r} - \omega t\right), \tag{2.7}$$

which corresponds to a plane electromagnetic wave traveling in the direction of the wave vector $\vec{k}$. Furthermore, $|\vec{k}| = 2\pi/\lambda$, $\omega = 2\pi f$, $|\vec{B}_0| = |\vec{E}_0|/c$, and $\vec{B}_0$, $\vec{E}_0$, and $\vec{k}$ are at right angles with each other.

In the case of electromagnetic waves traveling through a homogeneous medium, μ_0 and ε_0 are replaced by $\mu \equiv \mu_r \mu_0$ and $\varepsilon = \varepsilon_r \varepsilon_0$, which results in a change of phase velocity:

$$\omega = \frac{c}{n}k,\ n = \sqrt{\mu_r \varepsilon_r}. \tag{2.8}$$

where n is the *refractive index* of the medium. The calculation of group velocity is more difficult since n is typically a function of k.

It can be shown that the description of electromagnetic waves as two vector fields can be simplified to a single scalar function without loss of precision for most problems of optics. This scalar function may be understood as a vector component of either of the two vector fields [Good05, ch. 3.2]. Additionally, it is often practical to express the scalar field as the real part of a complex-valued analytic signal [Good85, ch. 3.8]. An analytic signal taking the place of Eqs. (2.6), (2.7) is thus

$$U(\vec{r},t) = U(\vec{r})\exp(-i\omega t), \tag{2.9}$$

$$U(\vec{r}) = U_0 \exp(i\vec{k}\vec{r}), \tag{2.10}$$

U_0 being a complex-valued constant. Any such field $U(\vec{r},t)$ must still fulfill the wave equation. The separation of the time dependence allows the formulation of a differential equation for the evolution of $U(\vec{r})$, the Helmholtz equation [Good05, ch. 3.3]:

$$(\nabla^2 + k^2)U(\vec{r}) = 0, \tag{2.11}$$

which may then be solved in place of the complete set of Maxwell's equations.

Propagation of scalar fields Several approaches to do so have been developed, such as the Helmholtz-Kirchhoff integral theorem: Starting from a complete set of boundary conditions, namely all values of U and their normal first derivatives $\partial U/\partial n$ on a closed surface S, the values of $U(\vec{r})$ of all points enclosed by that surface can be retrieved. This is achieved by use of Green's theorem and the use of a suitable Green's function of Eq. (2.11), namely, a spherical wave

$$G(\vec{r}) = \frac{\exp(ikr)}{r}.$$

This function then also appears in the solution [Good05, ch. 3.3]:

$$U(\vec{r}_0) = \frac{1}{4\pi}\iint_S \left\{\frac{\partial U(\vec{r})}{\partial n}G(\vec{r}-\vec{r}_0) - U(\vec{r})\frac{\partial G}{\partial n}(\vec{r}-\vec{r}_0)\right\} d^2\vec{r}. \tag{2.12}$$

The general case of an arbitrary surface S can be simplified to the case of a field emerging from an aperture in a plane: Let S coincide with this plane, and extend into the field downstream of the aperture. If it is ensured that no fields are incident into the volume of S other than through the aperture, the surface integral in Eq. (2.12) can be simplified to cover only the area of this aperture [Good05, ch. 3.4].

Furthermore, an alternative approach exists to solve Eq. (2.11), the Rayleigh-Sommerfeld solution: It is achieved by employing a superposition of two spherical waves as Green's functions G for which $G(\vec{r})$ *or* $\partial G/\partial n(\vec{r})$ are zero in all points $\vec{r}$ in the plane of the aperture, and then applying Green's theorem [Good05, ch. 3.5].

This leads to two separate solutions for $U(\vec{r}_0)$, which are however closely related to Eq. (2.12): they are proportional to the surface integral comprising only the first or only the second summand in Eq. (2.12).

Although the three solutions differ, they have been found to deliver nearly identical results for the case of apertures much larger than the wavelength. The simplest formulation is given by one of the two Rayleigh-Sommerfeld solutions:

$$U(\vec{r}_0) = \frac{1}{i\lambda} \iint_\Sigma U(\vec{r}) G(\vec{r} - \vec{r}_0) \cos\theta \, d^2\vec{r}, \qquad (2.13)$$

with Σ the area of the aperture and θ the angle between $\vec{r} - \vec{r}_0$ and the normal of the area element $d^2\vec{r}$ [Good05, ch. 3.7].

This is very similar to the so-called Huygens-Fresnel principle, according to which every point in a plane of a wavefield can be considered a point source with an amplitude proportional to the field amplitude at this point. The field at any point downstream of this plane can thus be calculated as the superposition of the fields emanating from this array of point sources. However, the cosine term (the obliquity factor) is not consistent with this simple picture and can only be neglected for sufficiently small values of θ.

When expressing Eq. (2.13) in Cartesian coordinates, $|\vec{r} - \vec{r}_0|$ is given by a square root, but can be approximated by a second-order polynomial, which results in the expression [Good05, ch. 4.2]

$$U(x_0, y_0) = \frac{\exp(ikz)}{i\lambda z} \iint_{-\infty}^{\infty} U(x, y) \times \exp\left\{\frac{ik}{2z}\left[(x_0 - x)^2 + (y_0 - y)^2\right]\right\} dx\,dy, \qquad (2.14)$$

where (ξ, η) are coordinates in the aperture plane, (x_0, y_0) coordinates in the measurement plane, and z is the distance between the two planes. This means that the spherical wavefronts emanating from the points in the aperture are approximated as paraboloidal shapes, which is only valid for sufficiently small values of θ [note that $\cos\theta$ from Eq. (2.13) has been set to 1 in Eq. (2.14)]. This is the so-called *Fresnel approximation*.

2.2 Interactions of X-rays with matter

A large number of interaction processes of X-rays with both electrons and atomic nuclei can be distinguished.

They differ in the types of particles participating in the interaction (including particles being destroyed or generated in the interaction), and the amount of energy and momentum exchanged between these particles.

Some interaction types (Thomson and Rayleigh scattering) can be understood and quantitatively described with classical electrodynamics, whereas others (Compton scattering, photoelectric absorption, and others) can only be fully described by a treatment in quantum field theory. The latter category of phenomena will only be introduced phenomenologically.

Several types of X-ray interaction processes with matter can be described as scattering processes. Therefore, a number of physical quantities useful for the characterization of scattering processes will be introduced here.

2.2.1 Scattering by a single, free electron

The effect of an electromagnetic plane wave impinging on a free electron can be understood with classical electrodynamics: The electron is accelerated by the oscillating electric field of the wave, and thus becomes an oscillating electric dipole. The electron itself thus emits an electromagnetic wave at the same frequency as the incident wave (so-called *Thomson scatter*). Given an incident field $U_{\mathrm{in}}(t)$ at the electron, it can be calculated with Maxwell's equations that the emitted electric field amplitude at a distance $\vec{r}$ from the electron is

$$U_{\mathrm{sc}}(t) = -r_0 \frac{e^{ikr}}{r} U_{\mathrm{in}}(t) \cos\alpha, \qquad (2.15)$$

where $r_0 = e^2/(4\pi\varepsilon_0 mc^2)$ is the classical electron radius and α is the angle between $\vec{r}$ and the polarization vector of U_{in} (cf. [AlsN+11, Appendix B]).

The factor e^{ikr}/r merely describes the distance-dependent phase shift and amplitude reduction of a spherical wave. The essential relation between incident and radiated field amplitude is thus given by the factor $-r_0$, which is also called the *scattering length* of a free electron. The negative sign (implying a π phase-shift between $U_{\text{in}}(t)$ and $U_{\text{sc}}(t)$ at $r = 0$) is important: It results from the electron being assumed as free.

This can be understood as the limiting case of an electron trapped in a quadratic potential well, i.e. a harmonic oscillator driven by the incident wave: The phase shift between excitation and response of the oscillator is zero for excitation frequencies ω_{in} far below the oscillator's resonance frequency ω_{res}, $\pi/2$ for $\omega_{\text{in}} = \omega_{\text{res}}$, and approaches π for $\omega_{\text{in}} \gg \omega_{\text{res}}$. For a free electron, the oscillator strength k, and thus the resonance frequency $\omega_{\text{res}} = \sqrt{k/m_e}$ can be said to approach zero, and the response to excitations of all frequencies is thus phase-shifted by π.

In a rough semi-classical view, a bound electron with binding energy ϵ can be interpreted as a harmonic oscillator with $\hbar\omega_{\text{res}} = \epsilon$. For X-rays and the binding energies of most electrons (except from the innermost orbitals), $\omega_{\text{in}} \gg \omega_{\text{res}}$ and the approximation of free electrons is good. This is not the case for lower photon energies, such as UV or visible light. Note however that a harmonic oscillator model is generally not sufficient to describe the behavior of a bound electron.

The difference in phase response between $\omega_{\text{in}} \ll \omega_{\text{res}}$ and $\omega_{\text{in}} \gg \omega_{\text{res}}$ also has an effect on a material's real part of the index of refraction n, cf. section 2.2.4.

2.2.2 Atomic form factor and $\vec{q}$ space

The scattering amplitude of a single free electron from the preceding section can be generalized to an arbitrary spatial distribution of electric charge $\rho(\vec{r})$, such as the electronic configuration of an atom. Note that this is an apparent contradiction:

The electrons are considered "bound" from the perspective of the atom, so that they retain a fixed spatial distribution $\rho(\vec{r})$ (given by the orbitals' wavefunctions), but "free" from the perspective of incident radiation since $\epsilon_{\text{photon}} \gg \epsilon_{\text{bond}}$, i.e. $\omega_{\text{in}} \gg \omega_{\text{res}}$.

In this case, an angular dependence of scattered fields is introduced: Given wave vectors $\vec{k}_{\text{in}}$, $\vec{k}_{\text{sc}}$ of incident and scattered waves, the fields scattered by two point charges of distance $\vec{r}$ are out of phase by $(\vec{k}_{\text{in}} - \vec{k}_{\text{sc}})\vec{r}$, when measured sufficiently far from the scatterer (cf. Fig. 2.1). Generalized to an arbitrary continuous charge distribution $\rho(\vec{r})$ and neglecting polarization effects, the resulting field is proportional to

$$-\frac{r_0}{e}\int_V \rho(\vec{r}) \exp\left[i\left(\vec{k}_{\text{in}} - \vec{k}_{\text{sc}}\right)\vec{r}\right] d^3r.$$

The quantity $\vec{k}_{\text{in}} - \vec{k}_{\text{sc}}$ is often shortened to $\vec{q}$. Since $k = |\vec{k}_{\text{in}}| = |\vec{k}_{\text{sc}}|$ for elastic scattering, the magnitude of $\vec{q}$ can also be written as

$$q = 2k\sin(\theta/2) \underset{\theta \ll 1}{\approx} k\theta, \tag{2.16}$$

where θ is the angle between $\vec{k}_{\text{in}}$ and $\vec{k}_{\text{sc}}$ (cf. Fig. 2.1). Combined with Eq. (2.15), this yields:

$$U_{\text{sc}}(\vec{q}, t) = -r_0 U_{\text{in}}(t)\frac{e^{ikr}}{r} f^0(\vec{q}), \tag{2.17}$$

$$f^0(\vec{q}) = \frac{1}{e}\int_V \rho(\vec{r}) \exp\left(i\vec{q}\vec{r}\right) d^3r. \tag{2.18}$$

with $f^0(\vec{q})$ the *atomic form factor*, which depends on atomic number and the atom's electronic state (ionization, etc.). Note that $f^0(\vec{q})$ is the three-dimensional Fourier transform of $\rho(\vec{r})$. Given Eq. (2.16), the resulting three-dimensional "reciprocal space" of $\vec{q}$ vectors can be sampled by measurements at different scattering angles as well as different wavelengths. Furthermore, $\vec{q} = \vec{0}$ describes forward scattering, where f^0 is equal to the number of electrons in the atom, which is usually given by the atomic number Z. Finally, additional terms can be added to f^0 to describe additional interactions such as resonant scattering and photoelectric absorption. This will be introduced in section 2.2.5.

Conceptually, Eq. (2.18) can be extended to larger volumes than a single atom, so long as limitations due to source coherence can be neglected. Sample ordering beyond the atomic scale must therefore be taken into account. For example, arranging identical objects in a crystal lattice allows coherent addition of scattered radiation from adjacent objects in the lattice at certain diffraction angles. This leads to a powerful amplification of the individual sample's form factor at these angles, which forms the foundation of structure determination via X-ray crystallography (cf. section 1.5.1 on page 20).

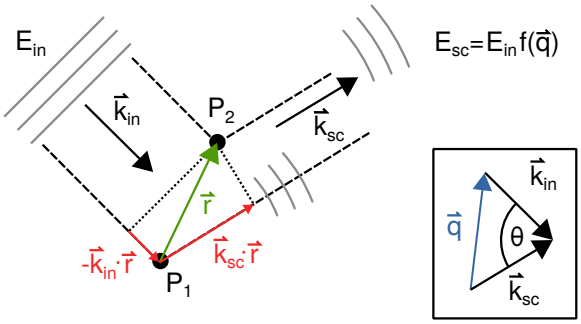

Figure 2.1: Relations between wave vectors and path difference for a scattering object consisting of two point charges P_1, P_2 at a relative location $\vec{r}$. Incident (in phase) and scattered (out of phase) wavefronts are also indicated.

2.2.3 Relation between real-space and $\vec{q}$-space quantities for elastic scattering

Since only intensities are measurable, form factors are not experimentally accessible. A ratio of scattered and incident intensities is thus a more useful experimental quantity.

The *differential cross-section* is defined as the intensity I_{sc} scattered in the solid angle $\Delta\Omega$ per incident flux (photons per second per area) Φ_0, and can be rewritten in terms of incident and scattered field amplitudes [AlsN+11, Ch. 1]:

$$\frac{d\sigma}{d\Omega}(\vec{q}) = \frac{I_{sc}}{\Phi_{in}\Delta\Omega} = \frac{\left|U_{sc}(\vec{q})\right|^2 r^2}{|U_{in}|^2}. \tag{2.19}$$

By inserting Eq. (2.15) in Eq. (2.19), the differential Thomson cross-section results as $d\sigma/d\Omega = r_0^2\cos^2\alpha$, or $r_0^2(1+\cos^2\alpha)/2$ for unpolarized radiation. Taking into account an atomic form factor and using Eq. (2.18),

$$\frac{d\sigma_{coh}}{d\Omega}(\vec{q}) = r_0^2\left|f^0(\vec{q})\right|^2. \tag{2.20}$$

This relates quantities measurable in a scattering experiment to the real-space electric charge density of the specimen. Finally, the inverse Fourier transform of the differential cross-section can be calculated. The correlation theorem shows that it is the autocorrelation function of the charge density:

$$\mathscr{F}^{-1}\left[\frac{d\sigma_{coh}}{d\Omega}(\vec{q})\right] \overset{(2.20)}{=} r_0^2\mathscr{F}^{-1}\left\{f^0(\vec{q})\left[f^0(\vec{q})\right]^*\right\}$$
$$\overset{(2.18)}{=} \frac{r_0^2}{e^2}\mathscr{F}^{-1}\left\{\mathscr{F}\left[\rho(\vec{r})\right]\mathscr{F}^*\left[\rho(\vec{r})\right]\right\} = \frac{r_0^2}{e^2}R_\rho(\vec{r'}),$$

where

$$R_\rho(\vec{r'}) \equiv (\rho\star\rho)(\vec{r'}) = \int \rho(\vec{r})\rho(\vec{r}+\vec{r'})d^3r,$$

since $\rho(\vec{r})$ is a real-valued function. The relation between all four quantities is illustrated below:

$$\begin{array}{ccc} \rho(\vec{r}) & \underset{\mathscr{F}^{-1}}{\overset{\mathscr{F}}{\rightleftarrows}} & e\cdot f^0(\vec{q}) \\ \downarrow\star & & \downarrow|\cdot|^2 \\ R_\rho(\vec{r'}) & \underset{\mathscr{F}^{-1}}{\overset{\mathscr{F}}{\rightleftarrows}} & \frac{e^2}{r_0^2}\frac{d\sigma_{coh}}{d\Omega}(\vec{q}) \end{array} \tag{2.21}$$

Note that the horizontal relations are invertible, but the vertical ones are not. Usually, the goal of a scattering experiment is to retrieve the shape of the object, i.e. $\rho(\vec{r})$, from the measurement data $(d\sigma_{coh}/d\Omega)(\vec{q})$, which is not generally possible (the retrieval of f^0 from $d\sigma_{coh}/d\Omega$ is the so-called "phase problem"). The quantity $R_\rho(\vec{r'})$ is of special importance for the calculation of the X-ray dark-field signal in section 2.5.8c.

2.2.4 Elastic scattering and index of refraction

The properties of an elastic scatterer can be directly related to the real part of the index of refraction of a material composed of these scatterers.

It can be shown that a thin slab of thickness Δ, composed of atoms with a form factor $f^0(\vec{q})$ and a number density ν, if illuminated by a distant monochromatic point source, produces scattered fields adding up to a wave with identical wavelength λ and amplitude

$$U_{sc} = i\lambda\cdot\left[-r_0 f^0(\vec{0})U_0\right]\cdot\nu\Delta, \tag{2.22}$$

where U_0 is the field amplitude at the same point if the thin slab were absent. This result is obtained by integration of scattered fields due to each infinitesimal element of the slab, while taking into account the variation of optical paths from source to slab and slab to detection point [AlsN+11, Ch. 3.1]: Each atom

stimulated by a wave amplitude U_0 emits a wave with amplitude $-r_0 f(\vec{0})U_0$. Most importantly, the collective effect of all scatterers in the slab thus introduces a factor i (or a phase shift of $\pi/2$) and a dependence on wavelength compared to the individual scatterer[1].

The total amplitude at the measurement point is then

$$U_0 + U_{\mathrm{sc}} = U_0\left(1 - i\lambda r_0 f^0(\vec{0})\nu\Delta\right).$$

For sufficiently small values of the imaginary part, this corresponds to a phase shift of $-\lambda r_0 f^0(\vec{0})\nu\Delta$ and a negligibly small change in magnitude. An object with index of refraction n and thickness Δ imparts a phase shift onto an incident plane wave:

$$\begin{aligned} U(z,t) &= U_0 \exp\left[i\left(kz - \omega t\right)\right] \\ &\overset{(2.8)}{=} U_0 \exp\left[i\frac{\omega n}{c}\left(z - \frac{c}{n}t\right)\right]. \end{aligned} \tag{2.23}$$

The position-dependent part of the phase at $z = \Delta$, relative to $z = 0$, is $\omega n\Delta/c$. The phase difference induced by inserting the object is thus $\omega(n-1)\Delta/c$. By comparison:

$$-r_0\lambda\nu f^0(\vec{0})\Delta = \omega(n-1)\Delta/c.$$

Given[2] that $\omega = 2\pi c/\lambda$, rearrangement yields

$$n = 1 - \frac{r_0\lambda^2\nu f^0(\vec{0})}{2\pi}.$$

Furthermore, for a material composed entirely of atoms with atomic number Z, $f^0(\vec{0}) = Z$. Thus, $\nu f^0(\vec{0}) = \nu Z$ can be interpreted as the material's electron density ν_e, and therefore,

$$n = 1 - \frac{r_0\lambda^2\nu_e}{2\pi}. \tag{2.24}$$

This also holds for mixtures of different materials: In this case, $\nu f^0(\vec{0})$ is replaced by a sum over all constituent elements k, i.e. $\sum_k \nu_k f_k^0(\vec{0}) = \sum_k \nu_k Z_k$, which is also equal to ν_e.

The finding in Eq. (2.24) is further generalized to include photoelectric absorption and resonant scattering and in sections 2.2.5 and 2.2.8.

[1] The atomic form factor depends on $\vec{q}$ and therefore on λ, but not for forward scattering. The dependence on λ in Eq. (2.22) results from the relative phase shifts of different scatterers in the slab.

[2] We use here the dispersion relation with $n = 1$ because the above calculation leading to Eq. (2.22) neglects the optical path within the material. Thus, the entire optical path is outside of the medium.

2.2.5 Photoelectric absorption, fluorescence, and resonant scattering

The form factor $f^0(\vec{q})$ can be modified to model additional types of interaction between X-rays and matter, namely resonant scattering and photoelectric absorption. These effects will be discussed below. It should however be noted that these effects can not be understood in the framework of classical electrodynamics. Their contributions to the form factor can thus not be calculated in the same manner as the elastic scattering term f^0, and does not describe the the underlying physics in the same way. They are determined from calculations in quantum field theory, or experimental data. Finally, the contribution of Compton scattering, another important type of interaction, can not be included in the form factor, and must instead be described by its differential cross-section and the angular dependence of the energy of scattered photons.

An *X-ray level* of an atom is defined as its normal state, with one or several electrons removed. It is named according to the quantum numbers of the missing electron's orbital. The first few are named K, L_1, L_2, L_3, M_1, M_2 and M_3, and correspond to states with one vacancy in the $1s$, $2s$,$2p_{1/2}$, $2p_{3/2}$, $3s$, $3p_{1/2}$, and $3p_{3/2}$ orbitals, respectively. Each X-ray level is characterized by its energy. The letter X has been introduced to describe the ground state [Jenk+91].

In *photoelectric absorption*, an incident photon is absorbed by an atom, and its energy is imparted to an atomic electron, which thus leaves the atom. In other words, a transition between two X-ray levels takes place. For this to occur, the photon energy must be at least as high as the energy difference between the two levels. For greater photon energies E, interaction probability approximately scales with E^{-3} (see section 2.2.7). Additionally, the conservation of angular momentum places restrictions on which transitions can occur (the photon has spin 1).

Usually, the final X-ray level has more vacancies than the initial level, i.e. the atom has been ionized in the transition (so-called *photoionization*). The inverse procedure, i.e. a transition to a less energetic X-ray level by emission of a photon, so-called *X-ray fluorescence*, also occurs (typically shortly after a photoabsorption process).

Traditionally, the "allowed" transitions (and their energies) are denoted by the Siegbahn notation ($K\alpha$, $K\beta$, etc.), but are alternatively described by the initial and

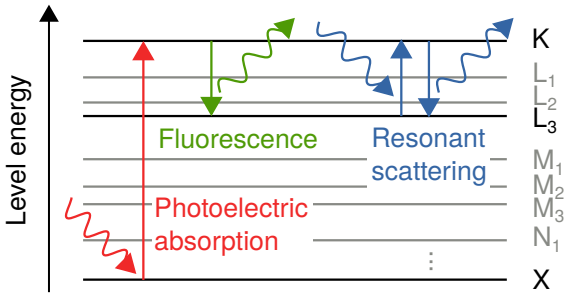

Figure 2.2: Illustration of photoelectric absorption, (X-ray) fluorescence and resonant scattering. The letter X denotes the atomic ground state.

final X-ray level, e.g. X – K for a photoionization process, or K – L_3 for a fluorescence transition (the "$K\alpha_1$" line) [Jenk+91].

In *resonant scattering*, an atom is first raised into an excited state by absorption of an incident photon. This state then decays and in turn releases another photon with the same energy as the original photon [AlsN+11, ch. 8.7]. This mainly occurs for photons with energies near the energy of the atomic transition and leads to a deviation of the index of refraction near these energies. The processes of photoelectric absorption, fluorescence, and resonant scattering are illustrated in Fig. 2.2.

For photoelectric absorption, the quantity $\vec{q}$ is not applicable, since the incident photon is eliminated in the interaction. The angular dependence of resonant scattering is negligible for X-rays, since this interaction mostly takes place with electrons in the innermost orbitals of negligible spatial dimensions (it is thus roughly isotropic) [AlsN+11, ch. 8.4.2]. Both types of interactions however significantly depend on photon energy E.

The atomic form factor can be modified to include both effects:

$$f(\vec{q},E) = f^0(\vec{q}) + f'(E) + i f''(E), \tag{2.25}$$

where $f''(\omega) < 0$ [AlsN+11, Ch. 1.2]. Classically, the imaginary component of f would be understood as an amplitude response of the scatterer, shifted by $\pi/2$ with respect to the incident amplitude. Generalizing Eq. (2.22) from f^0 to f implies that $f'' < 0$ leads to a reduction in scattered amplitude, and thus an attenuation of incident radiation.

As a generalization of Eq. (2.20), the resulting differential cross-section for coherent scattering of unpolarized radiation is [Whit57; Scho+11]

$$\left(\frac{d\sigma_{\text{coh}}}{d\Omega}\right)(\theta, E_\gamma, Z) = \frac{1}{2} r_0^2 \left(1 + \cos^2\theta\right) \left|f(\vec{q}, Z)\right|^2.$$

The modifications to f can also be included in the calculation of the index of refraction n by replacing $f^0(\vec{0})$ in Eq. (2.24) with f from Eq. (2.25):

$$n(E) = 1 - \frac{r_0 \lambda^2 \nu \left[f^0(\vec{0}) + f'(E) + i f''(E)\right]}{2\pi}. \tag{2.26}$$

The real and imaginary parts of n are often denoted with separate symbols:

$$n = 1 - \delta + i\beta_{\text{PE}}, \tag{2.27}$$

where

$$\delta = \frac{r_0 \lambda^2 \nu}{2\pi} \left[f^0(\vec{0}) + f'(E)\right], \tag{2.28}$$

$$\beta_{\text{PE}} = -\frac{r_0 \lambda^2 \nu}{2\pi} f''(E). \tag{2.29}$$

The imaginary part β_{PE} then quantifies the rate of attenuation by the material due to photoelectric absorption.

However, as indicated by the subscript, the quantity thus obtained does not include the attenuating effect of Rayleigh- or Compton scatter. A linear attenuation coefficient (and an effective β) that includes these effects is derived from the total cross-section in section 2.2.7. Finally, the relation of the index of refraction to the effected attenuation and phase-shift of incident radiation is discussed in section 2.2.8.

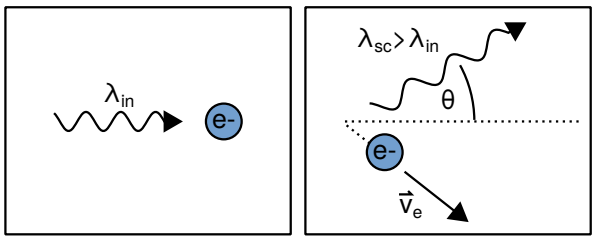

Figure 2.3: Compton scattering by a free electron. Depending on the scattering angle θ, some momentum and energy are transferred to the electron.

2.2.6 Compton scatter

In elastic scattering of X-rays, incident and scattered radiation have the same wavelength. However, experiments showed that the wavelengths of X-rays scattered at large angles are greater than those of the incident radiation. This can not be explained with the classical description of light as an electromagnetic wave, but requires an interpretation of both radiation and scatterer as particles, and the scattering process as an elastic collision of these particles, i.e. an interaction where total energy and momentum are conserved (i.e., an elastic collision[3], cf. Fig. 2.3).

Such a collision necessitates some energy transfer between the photon and the electron, the magnitude of which depends on the collision angle. In order to quantitatively describe the angular dependence of scattered wavelengths, energy and momentum of a the photon must be known. To describe the photoelectric effect, Einstein had also assumed a quantization of electromagnetic radiation, with the energy of these quanta being proportional to frequency, i.e. $E = hf = hc/\lambda$. To calculate the momentum p of such a particle, the famous mass-energy relation $E = mc^2$ can be used together with $p = mv$ (and $v = c$ for light) to arrive at the relation[4] $p = E/c = h/\lambda$. The resulting shift in wavelength is then given by [Thom+09, sec. 3.1]

$$\Delta\lambda \equiv \lambda_{\mathrm{sc}} - \lambda_{\mathrm{in}} = \frac{h}{m_e c}\,(1-\cos\theta)\,,$$

where θ is the scattering angle, λ_{sc} and λ_{in} are the wavelengths of scattered and incident radiation, and m_e is the electron's rest mass. First presented by A. H. Compton in 1923, this description provided further evidence for the quantization of electromagnetic radiation. However, this treatment does not predict the differential cross-section $d\sigma/d\Omega$, i.e. the relative frequency with which a certain scattering angle occurs.

The classical understanding of an elastic collision between solid bodies is not applicable here. Instead, an exact solution was found for a free electron by O. Klein and Y. Nishina in 1928 via quantum electrodynamics calculations which also take relativistic effects into account. The exact equation for the *Klein-Nishina cross-section* is complicated, but can be approximated by

$$\left(\frac{d\sigma_{\mathrm{KN}}}{d\Omega}\right)(\theta,E) \approx \frac{r_0^2\left(1+\cos^2\theta\right)}{2\left[1+\frac{E}{m_e c^2}\,(1-\cos\theta)^2\right]}$$

for photon energies below 100 keV [Thom+09, Sec. 3.1]. Qualitatively, the differential cross-section for Compton scattering is high at all scattering angles for low photon energies (see Fig. 2.4a), and is increasingly focused to the forward direction (small θ) for photon energies exceeding the electron rest mass (approx. 511 keV).

It must be emphasized that the Klein-Nishina cross-section is only applicable to free electrons. Similarly to coherent scatter, deviations occur for the ensemble of electrons bound to an atom, albeit for different reasons: Compton-scattered radiation from different electrons is mutually incoherent and the introduction of a form factor (which implies an addition of amplitudes) is thus not required. However, as described in [Whit57], Compton scattering can be understood as a two-step process: firstly, deflection of the photon by a given angle while transferring the associated momentum to the electron, and secondly, transfer of energy from the photon to the electron. The probability of the first step is given by the Klein-Nishina cross-section, of the latter by the so-called *(incoherent) scattering function* $S(\vec{q},Z)$. The differential cross-section for Compton scatter is thus given by [Scho+11]

$$\left(\frac{d\sigma_{\mathrm{C}}}{d\Omega}\right)(\theta,E,Z) = \left(\frac{d\sigma_{\mathrm{KN}}}{d\Omega}\right)(\theta,E)\cdot S(\vec{q},Z).$$

In particular, S achieves very low values (the second step becomes very improbable) if $\vec{q}$ is much smaller than the root mean square momentum of the electron before the scattering process [Whit57]. Thus,

[3] Confusingly, Compton scattering is also called "inelastic scattering" (to emphasize the change in radiation wavelength), although it is described by an elastic collision process.

[4] The value of the proportionality constant h (the "Planck constant") is $6.62607015 \times 10^{-34}$ Js.

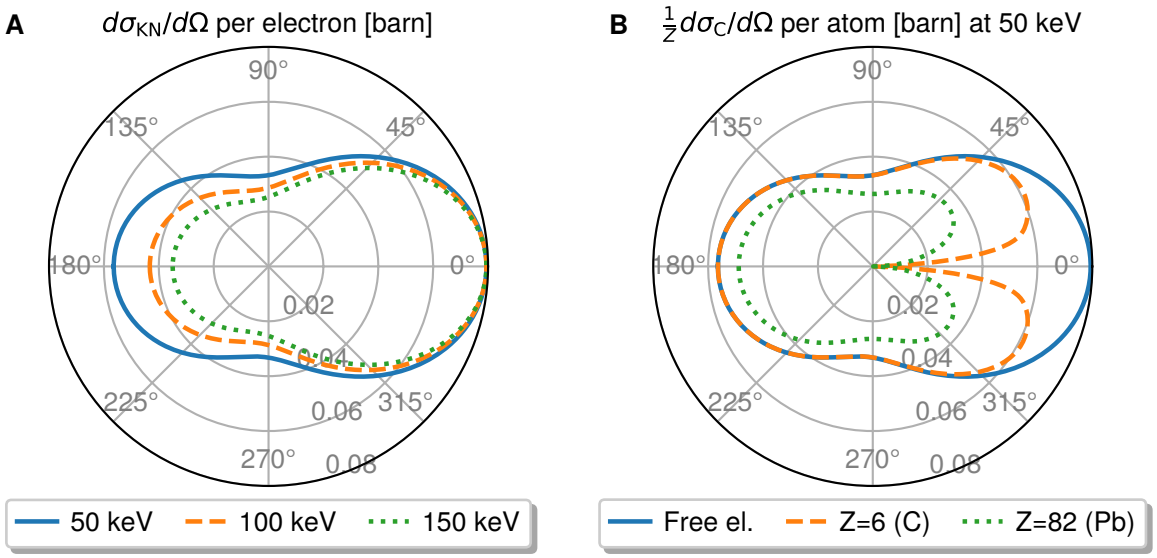

Figure 2.4: Compton scatter cross sections. (a): Differential Klein-Nishina cross-section at different photon energies. (b): Deviation between Compton-scatter differential cross-sections from free electrons (Klein-Nishina) and different atoms (correction by incoherent scattering functions). Values retrieved with the "xraylib" library [Scho+11]. 1 barn = $10^{-28}\,\mathrm{m}^2$.

Compton scatter by bound electrons is much less common for low photon energies or low scattering angles than would be expected by the Klein-Nishina cross-section. This is illustrated in Fig. 2.4b. Similarly, coherent scattering can also be interpreted as a two-step process, allowing an alternative interpretation of $|f(\vec{q},Z)|^2$ [Whit57].

2.2.7 Relative magnitude of interaction types

The overall strength of a given type of X-ray-matter interaction can be characterized by its total cross-section σ, which is simply defined as the integral of the differential cross-section over the entire solid angle:

$$\sigma = \int_{4\pi} \left(\frac{d\sigma}{d\Omega}\right) d\Omega.$$

Like the differential cross-section, the total cross-section gives a measure of interaction probability, albeit without consideration of the scattering angle. Total cross-sections of all interaction types[5] can also be added to provide a probability measure for any interaction type [Hubb82], each with its own dependence on photon energy E:

$$\sigma_{\mathrm{total}}(E) = \sigma_{\mathrm{PE}}(E) + \sigma_{\mathrm{coh}}(E) + \sigma_{\mathrm{C}}(E). \qquad (2.30)$$

The relation of σ, which has the dimensions of an area, to a probability measure is illustrated in Fig. 2.5: An incident particle (photon) interacts with a given atom if its path crosses a normally-oriented surface of area σ located at the atom. For an ensemble of N atoms uniformly distributed in a volume with front surface A and depth z [thus having a number density $\nu = N/(Az)$], the average number of intersections (and thus, interactions) of a normally incident light "beam" composed of M photons is given by the ratio of total interaction area and the front surface, i.e.

$$\langle M_{\mathrm{int}} \rangle = MN\sigma / A = M\nu\sigma z.$$

This equation is generally correct only if incident particles are never deflected or absorbed during an interaction (which is approximately the case for coherent forward scatter). Under the assumption that an incident

[5] Pair production and photonuclear interactions are disregarded in Eq. (2.30) (and generally in this chapter) since they occur only for photon energies beyond 1 MeV, which are not commonly used for imaging.

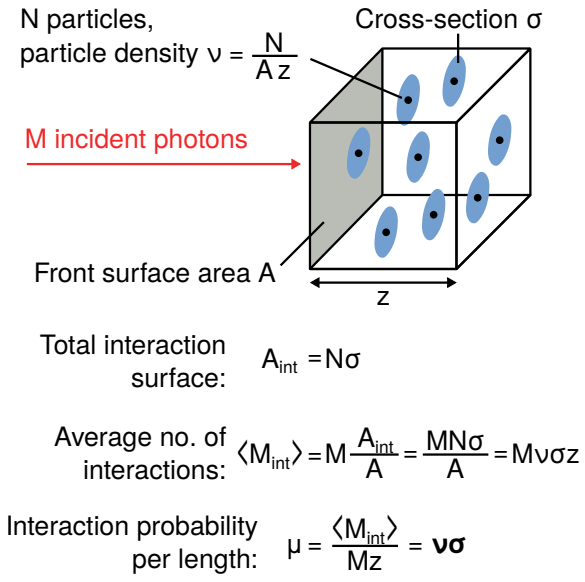

Figure 2.5: Relation between linear attenuation coefficient μ and cross-section σ. The average number of interactions between a narrow light beam with a small volume of material is proportional to the ratio of total cross-sections $N\sigma$ in that volume and the volume's front surface area A.

particle is eliminated after an interaction, the model is only applicable for $\langle M_{\text{int}}\rangle \ll M$. It can however be extended to arbitrary object thicknesses:

The derivative of $\langle M_{\text{int}}\rangle$ with respect to z, i.e., the number of interactions per thickness, is a local measure for the interaction rate and related to the linear attenuation coefficient μ: $d\langle N_{\text{int}}\rangle/dz = \nu\sigma \equiv \mu$. The number of photons detected behind the object is given by $M_{\text{det}} = M - M_{\text{int}}$, and thus,

$$\frac{d\langle M_{\text{det}}\rangle}{dz} = -\nu\sigma M = -\mu M \overset{z \text{ small}}{\approx} -\mu\langle M_{\text{det}}\rangle. \quad (2.31)$$

With the knowledge that $\langle M_{\text{det}}\rangle = M$ for $z = 0$, integration thus yields

$$\langle M_{\text{det}}\rangle(z) = M\exp\left(-\mu z\right). \quad (2.32)$$

As illustrated in Fig. 2.6, the magnitudes of the different types of X-ray-matter interaction differ significantly and depend on both X-ray energy and elemental composition.

The probability for photoelectric absorption roughly scales with the inverse cube of photon energy, but increases sharply when photon energy exceeds the energy of an atomic fluorescence line, since the electronic transition corresponding to that line can now be induced by absorption of a photon.

The total Klein-Nishina cross-section varies only slowly with photon energy. The total Compton cross-section of a bound electron is lower than that of a free electron, due to the relationship characterized by the incoherent scattering function S mentioned in section 2.2.6. This reduction increases for heavier elements (i.e., more strongly bound electrons) and lower photon energies, but at most reduces the atomic total cross-section by a factor of 2 compared to Klein-Nishina, as evident from tabulated values of $S(\vec{q}, Z)$. Roughly speaking, the atomic Compton scattering cross-section thus scales with the number of electrons, i.e. with Z.

The total cross-section for Thomson scatter, i.e., elastic scatter from free electrons, is

$$\sigma_{\text{T}} = \frac{8\pi r_0^2}{3},$$

which follows directly from integration. For coherent forward scattering from atoms, scattered fields from different points in the atomic charge cloud add up constructively. The total forward-scattered field is thus proportional to the total charge, i.e. $f^0(\vec{0}, Z) = Z$. The differential cross-section for coherent forward scatter is then proportional to Z^2, cf. Eq. (2.20). The total cross-section also depends on the dependence of $f^0(\vec{q}, Z)$ on $\vec{q}$ and roughly scales with $Z^{2.5}$.

Even though the differential cross-section in forward direction and the total Thomson cross-section are independent of energy, the total atomic coherent cross-section scales approximately with E^{-2}. This is not related to the proportionality of δ with E^{-2} found in section 2.2.4[6], but arises from the atomic form factor, and thus from the spatial charge density distribution within the atom.

With one exception, the dependence of the total cross-section for each interaction type on photon energy and atomic number approximately follows power laws. This is illustrated in Table 2.1. The exponents have

[6] That result was found with the assumption of a scatter amplitude *independent* of angle and energy, and an integration over scattered fields from all elements in a thin, infinitely extended slab of material. Taking into account the variations of optical path lengths to and from different surface elements in this slab lead to an inverse proportionality of total scattered field strength and photon energy.

$\sigma \propto Z^a E^b$	a	b
σ_{PE} [*]	4.0…4.65 [**]	−2.85…−2.55
σ_{coh}	2.45…2.66	−1.99…−1.56
σ_{C}	0.79…0.96	[***]

Table 2.1: Approximate power-law exponents of total cross-sections for photoelectric absorption, coherent scattering, and Compton scattering on photon energy E and atomic number Z for 20 keV < E < 150 keV and 3 < Z < 89. ([*]): Fits exclude K edge, ([**]): 4.47…4.51 for energies below the K edge. ([***]): Does not follow a power law, σ_{C} is roughly independent of E.

been retrieved via power-law regression to data from the *xraylib* library [Scho+11] for X-ray energies between 20 and 150 keV and all atomic numbers from 3 to 89. More detailed fitting results are also shown in Fig. 1 (Appendix) on page 224.

The relative magnitude of elastic and resonant scattering can be determined by comparing $f^0(\vec{0})$ and f' in the real part of the index of refraction, Eq. (2.28). The scattering factor f' significantly deviates from zero for photon energies in the vicinity of an photoelectric absorption edge, i.e., where f'' sharply increases. This is illustrated for two elements in Fig. 2.7.

For medical imaging purposes, f' is usually negligible since the used photon energies typically far exceed the edge energies of light elements dominant in biological tissues. Tabulated values in *xraylib* show that in the energy range between 20 and 150 keV and for elements with 3 < Z < 89, $f'/f^0(\vec{0}) = f'/Z$ never falls below −11%.

2.2.8 Attenuation and phase shift

We examine the combined effect of all interaction types in a material on its index of refraction, i.e., its attenuating and phase-shifting properties. Using these findings, an approximate relation between an object's index of refraction and its effect on an incident wavefield is then presented.

Generalizing Eq. (2.31), the total attenuation coefficient of a mixture of different elements k is given by each element's total interaction cross-section—as given in Eq. (2.30)—weighted by that element's num-

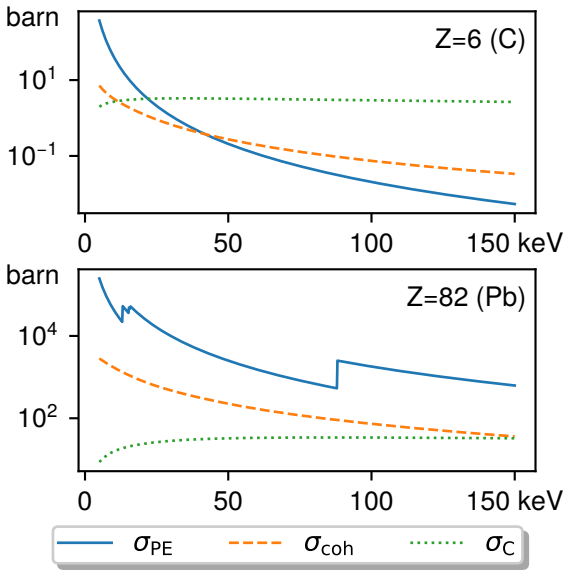

Figure 2.6: Energy-dependence of photoelectric absorption, coherent scattering and Compton scattering for carbon (Z = 6) and lead (Z = 82). 1 barn = $10^{-28}\,\mathrm{m}^2$.

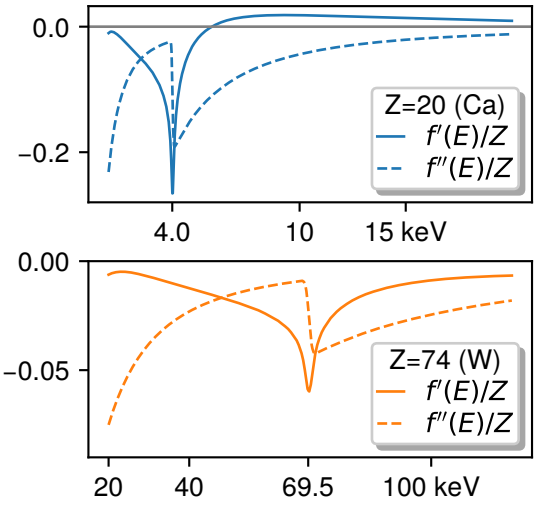

Figure 2.7: Energy dependence of the scattering factors f' and f'', normalized to $f^0(\vec{0}) = Z$, for two elements (calcium and tungsten). The location of the K edge coincides with a drop in f', and an associated change in δ according to Eq. (2.28).

ber density ν_k [AlsN+11, ch. 1.3]:

$$\boxed{\mu_{\text{total}}(E) = \sum_k \nu_k \sigma_{\text{total},k}(E) = \rho N_A \sum_k \frac{\sigma_{\text{total},k}(E)}{A_k},} \tag{2.33}$$

where N_A is the Avogadro constant, ρ is mass density and A_k is the k-th element's molar mass. In a measurement where a narrow, monochromatic beam passes through an object, the dependence of transmitted intensity on object thickness z is typically proportional to $\exp(-\mu_{\text{total}} z)$ [Hubb82]. However, this may differ for other experimental arrangements: Most importantly, Compton-scattered radiation may be measured in the absence of sufficient collimation (downstream of the object), which leads to deviations.

As will be shown below, the imaginary part of the index of refraction is related to the linear attenuation coefficient via $\beta_{\text{total}} = \mu_{\text{total}}/2k$. Similarly to μ_{total} or β_{total}, the real part of the refractive index as given in Eq. (2.28) can also be generalized to an arbitrary mixture:

$$\begin{aligned}\boxed{\delta(E) &= \frac{r_0}{2\pi}\left(\frac{hc}{E}\right)^2 \sum_k \nu_k \left[f_k^0(\vec{0}) + f_k'(E)\right] \\ &= \frac{r_0 \rho N_A}{2\pi}\left(\frac{hc}{E}\right)^2 \sum_k \frac{Z_k + f_k'(E)}{A_k},}\end{aligned} \tag{2.34}$$

where Z_k is the k-th element's atomic number. The *xraylib* library [Scho+11] uses the formulation in Eqs. (2.33) and (2.34) for the calculation of the complex index of refraction.

Given Eqs. (2.33) and (2.34), it would now be interesting to know the effect of an object with known $\mu_{\text{total}}(E)$ and $\delta(E)$ on incident X-rays with photon energy E. In general, the effect of an extended object on an incident wavefield may be difficult to calculate, especially if interaction cross-sections are so high that photons are likely to have multiple successive interactions with the object. Photons may travel in very different directions after being Compton-scattered, and photoabsorption may release electrons which traverse the material and eventually emit another photon when they are reabsorbed. In practice, this "shower" of electrons and X-ray photons resulting from X-ray matter interaction can only be approximated with Monte-Carlo simulation methods, such as EGSnrc [Kawr+20] or Geant4 [Agos+03]. This is necessary e.g. for dose calculations, where the exact location of energy deposition within the material must be known.

For imaging however, only the field downstream of the object is of interest. A number of assumptions and simplifications can be made to determine a relation between the object's interaction cross-sections (or the index of refraction) with its effect on the downstream wavefield.

An approach very useful for X-ray imaging is the *projection approximation*, which assumes that interactions are sufficiently weak (rare) to negligibly perturb the field in directions which are not exactly downstream. This then results in equations which relate the amount of phase shift or attenuation due to an object to projection integrals across the object.

Starting with the Helmholtz equation (2.11), Paganin [Paga06, ch. 2.1] derives a number of useful equations using the projection approximation. His approach and intermediate results will be briefly summarized here.

In matter, the wavenumber k is equal to nk_0, where $k_0 = \omega/c$ is the equivalent wavenumber in vacuum. Eq. (2.11) is thus

$$\left[\nabla^2 + n(\vec{r})^2 k_0^2\right] U(\vec{r}) = 0.$$

By separating a wavefield $U(\vec{r})$ into a product of a plane wave $\exp(ikz)$ and an envelope $\tilde{U}(\vec{r})$, a "product rule" for the application of ∇^2 can be applied which leads to the following relation for $\tilde{U}(\vec{r})$:

$$\left[2ik_0\frac{\partial}{\partial z} + \frac{\partial^2}{\partial x^2} + \frac{\partial^2}{\partial y^2} + k_0^2(n^2-1)\right]\tilde{U}(\vec{r}) = 0. \tag{2.35}$$

The field incident on the object is assumed to be a plane wave propagating in z direction, so that $\partial^2\tilde{U}/\partial x^2$ and $\partial^2\tilde{U}/\partial y^2$ are initially zero. As the projection approximation consists of assuming that the object imparts negligible changes to the wavefield $\tilde{U}$ in all directions other than z, the approximation is applied to Eq. (2.35) by neglecting the $\partial^2\tilde{U}/\partial x^2$ and $\partial^2\tilde{U}/\partial y^2$ terms:

$$\left[2ik_0\frac{\partial}{\partial z} + k_0^2(n^2-1)\right]\tilde{U}(\vec{r}) \approx 0. \tag{2.36}$$

With the object assumed to occupy the volume where $0 < z < z_0$, a solution of Eq. (2.36) can then be given as

$$\tilde{U}(\vec{r}) \approx \exp\left[\frac{-ik_0}{2}\int_0^{z_0} 1 - n^2(x,y,z)\,dz\right]\tilde{U}(\vec{r}_0),$$

where $\vec{r} = [x,y,z_0]^T$ is downstream and $\vec{r}_0 = [x,y,0]^T$ is upstream of the object. Rewriting n as $1-\delta+i\beta$ [as in

Eq. (2.27)], and using the fact that $\delta, \beta \ll 1$ for X-rays,

$$1 - n^2 \approx 2\delta - 2i\beta,$$

and thus (if we omit the dependence of $\tilde{U}$, δ, and β on x and y):

$$\frac{\tilde{U}(z_0)}{\tilde{U}(0)} \approx \exp\Big(-\underbrace{i\,k_0 \int_0^{z_0} \delta(z)\,dz}_{\Delta\Phi}\Big) \times \underbrace{\exp\left(-k_0 \int_0^{z_0} \beta(z)\,dz\right)}_{A}. \tag{2.37}$$

The amount of phase shift $\Delta\Phi$ and the amplitude attenuation factor A can therefore be directly retrieved from projection integrals of the real and imaginary parts of the index of refraction, respectively. As the field intensity I is proportional to $|\tilde{U}|^2$, its attenuation factor is $T = A^2 = \exp(-2k_0 \int_0^{z_0} \beta(z)\,dz)$. By comparison with the linear attenuation coefficient from the Beer-Lambert attenuation law in Eq. (2.32), we find that

$$\mu = 2k_0\beta. \tag{2.38}$$

2.3 X-ray generation

X-rays are electromagnetic radiation with wavelengths in the vicinity of 1 Å [AlsN+11, p. 2] and thus, photon energies in the keV range. Although there is no sharp distinction, the X-ray regime is bounded on the high-wavelength end by extreme ultraviolet (EUV) radiation with photon energies between 30 and 250 eV [Attw99, p. 1]. On the low-wavelength end, a distinction between X-rays and gamma (γ) radiation can be made, although no clear dividing line between the categories exists. Gamma radiation is often understood to originate from radioactive decay processes in atomic nuclei, whereas the term "X-rays" typically describes radiation generated by the acceleration of electrons or fluorescence. Although there is a significant overlap between the energy ranges of photons emitted in both categories, γ radiation typically exhibits very high photon energies beyond 100 keV. The three main mechanisms of γ-ray / X-ray production, as well as their practical implementation, are introduced in this section.

2.3.1 Radioactive sources

Radioactivity describes a phenomenon arising from an instability of some types of atomic nuclei, especially those with an imbalance between the number of protons and neutrons[7]. This instability leads to the decay of the nucleus into one or several "daughter nuclei", as well as a number of elementary particles. Decay processes can be classified according to the types of released particles. Although a large number of decay types exist, most radioactive isotopes decay via the α, β^-, or β^+ processes.

In α decay, a ^{4}He nucleus (the "α particle", composed of two protons and two neutrons), splits off from the main nucleus. The resulting nucleus thus contains two fewer protons and neutrons. This decay process occurs only for heavy nuclei. In β^- decay, a single neutron within the nucleus decays into a proton, while an electron and an antineutrino are released. The β^+ decay process is very similar, but the decay process is inverted: one proton is converted into a neutron, while a positron and a neutrino are emitted.

In neither of these processes, a photon is released directly. The difference in nuclear binding energy of the nucleus before and after decay is mainly transferred to the α or β particle as kinetic energy. In many cases however, the resulting nucleus is in an excited state and decays to its ground state by emission of one or several high-energy photons (the latter if intermediate excitation states exist). Furthermore, the positron released in β^+ decay is annihilated when encountering an electron, producing two gamma photons emitted in opposite directions. These two pathways for the emission of γ rays are illustrated in Fig. 2.8a. For most γ decay processes, decay of excited nuclear states occurs nearly instantaneously, but some elements possess metastable states (nuclides) with a half-life in the range of minutes or hours, thus acting as a source of gamma radiation for an extended period of time.

Gamma radiation from radioactive materials is commonly used for radiotherapy and some imaging applications, such as the inspection of shipping containers. In medical imaging, metastable nuclides (radionuclides) are used extensively: Their inhalation or injection by a patient, and subsequent measurement of

[7] In stable isotopes of light elements, the number of protons and neutrons is nearly identical, but stable isotopes of heavier elements contain an excess of neutrons, which counteracts the protons' electrostatic repulsion. [Open20]

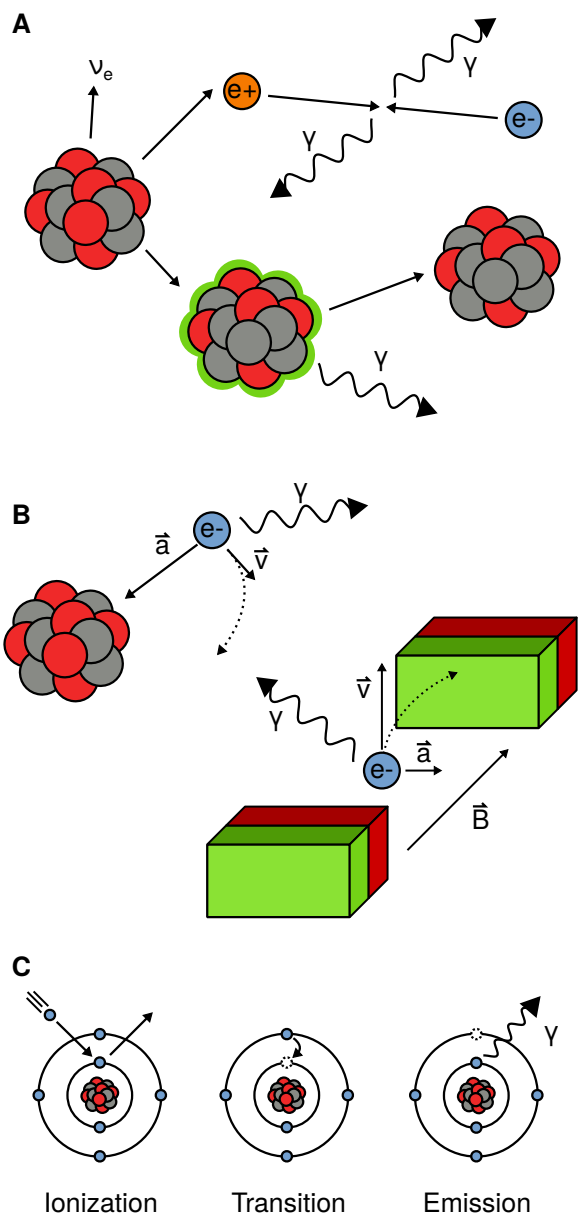

Figure 2.8: Physical origins of X-rays. (a): Radioactive decay (shown: β^+ decay of original nucleus and γ decay of daughter nucleus). (b): Acceleration of charges, by electrostatic forces in material (low velocity, high acceleration) and external magnetic fields (high velocity, low acceleration). (c): X-ray fluorescence. Orbital electron is expelled by high-energy particle (left), vacancy is filled by other orbital electrons (center), and energy difference between states is released as γ photon (right).

gamma radiation emitted from inside the body allows retrieving functional information, e.g. of metabolic activity or blood perfusion. Medical γ-ray imaging techniques include positron emission tomography (PET), scintigraphy, and single-photon emission computed tomography (SPECT).

2.3.2 Accelerated electric charges

As previously mentioned in section 1.4, the emission of radiation by an acceleration of electrical charges is well-known from radio transmitters: An alternating current in a dipole antenna causes the emission of radio waves, their frequency determined by the frequency of the current.

Due to antennas typically being dimensioned in the vicinity of the radiation wavelength, as well as speed limitations of electronic circuits, antennas can usually not be used to detect or generate frequencies greater than those of microwaves.

For the generation of X-rays, free electrons are used instead. The required acceleration or deceleration is achieved either by collision with a material or by magnetic deflection, see Fig. 2.8b.

In synchrotron particle accelerators (cf. section 1.4 on page 19), electrons or protons are alternatingly accelerated by linear accelerator (*linac*) modules, and forced onto a circular path by magnetic fields. The circular beam path allows repeated acceleration by the same linac modules and thus achieves very high electron energies, but requires a synchronous increase of magnetic field strengths.

The magnets used for the deflection of the electron beam in synchrotrons act as X-ray sources if the kinetic energy of the electrons and the "bending power", i.e. the achieved magnetic field strengths are sufficiently high.

For relativistic electrons, the angles of emitted radiation are distorted towards the "forward direction", i.e. the electrons' movement direction. The radiation is thus focused into a narrow cone of high intensity [Will11, ch. 3.5].

With the introduction of third-generation synchrotron sources, this method of X-ray generation has been refined by the use of *insertion devices*, which primarily consist of a lattice of magnets pairs with alternating polarity. The electron beam passes through the space

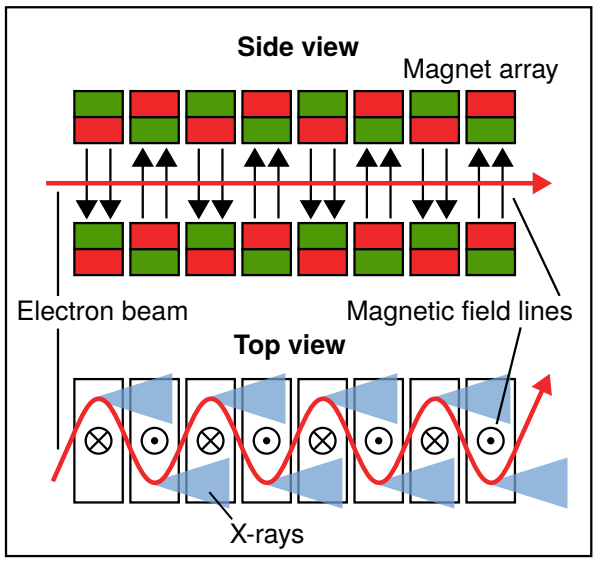

Figure 2.9: Method of operation of a synchrotron insertion device: An array of magnet pairs forces the electron beam onto an oscillating trajectory, which induces the emission of intense X-rays.

between the magnet pairs and is thus deflected in alternating directions, see Fig. 2.9.

An insertion device can be operated in two distinct modes: If the angular deviation of the electron beam exceeds the opening angle of the radiation cone (a *wiggler*), each magnet pair acts as an individual bending magnet, and the total intensity at all wavelength increases linearly with the number of magnet pairs. For smaller angular beam deviations (an *undulator*), interference of radiation from successive magnet pairs occurs, leading to constructive or destructive interference for different wavelengths, resulting in a radiation spectrum consisting of successive narrow peaks [Will11, ch. 3.7].

Acceleration of electrical charges is also an important mechanism of X-ray production in X-ray tubes. In the X-ray tube design by Coolidge, a filament and a target plate are placed in an evacuated vessel (cf. Fig. 2.10a). The filament is electrically heated, which leads to a release of electrons from the material (*thermionic emission*). The electrons are accelerated towards the anode due to a high voltage applied between filament (the cathode) and target (the anode) and are decelerated extremely rapidly by electrostatic repulsion within the anode material.

The electrons' kinetic energy is thus partly converted to electromagnetic radiation with a continuous spectrum of photon energies (*bremsstrahlung*). The high-energy limit of this spectrum is determined by the electrons' acceleration voltage: The highest photon energies E_γ are achieved by the conversion of an electron's entire kinetic energy E_e in a single collision event. Since the kinetic energy of an electric charge e when accelerated by a potential difference U is eU,

$$E_\gamma \leq E_e = eU.$$

Electron energies in the keV range are therefore sufficient for the generation of bremsstrahlung X-rays, compared to electron energies in the GeV range for bending magnets or insertion devices for comparable X-ray energies. However, the efficiency of X-ray generation by X-ray tubes is extremely low: For thin transmission targets, the ratio of X-ray energy and electron energy loss has been found to (approximately) scale as $\eta = 2.8 \times 10^{-6} ZU$, where Z is the atomic number of the anode material and U is given in kV. For thick, non-transmission targets, this is even lower at [Dyso90, section 2.8]

$$\eta = 1.3 \times 10^{-6} ZU\,[\mathrm{kV}]. \tag{2.39}$$

For a tungsten reflection target and $U = 60\,\mathrm{kV}$, this results in an efficiency of $\eta = 0.5\%$. Furthermore, the above efficiency values were derived by integration of X-ray intensities at all emission angles, whereas practical applications utilize only a small cone of radiation. The true efficiency of X-ray tubes is thus even lower.

2.3.3 Fluorescence

The third mechanism of X-ray production was already introduced in section 2.2.5, and is illustrated in both Fig. 2.2 and Fig. 2.8c: Like incident X-rays, electrons of sufficient kinetic energy may also cause ionization of a material and thus induce various non-ground-state X-ray levels. The electrons of an atom or molecule are arranged in a number of orbitals with different binding energies. An incident electron may induce a given X-ray level in an atom if its kinetic energy exceeds the level energy.

In the case of such an event, various transitions to less energetic X-ray levels may occur, often accompanied by the emission of a photon (*X-ray fluorescence*). The photon energy is equal to the energy difference of the transition's initial and final X-ray level.

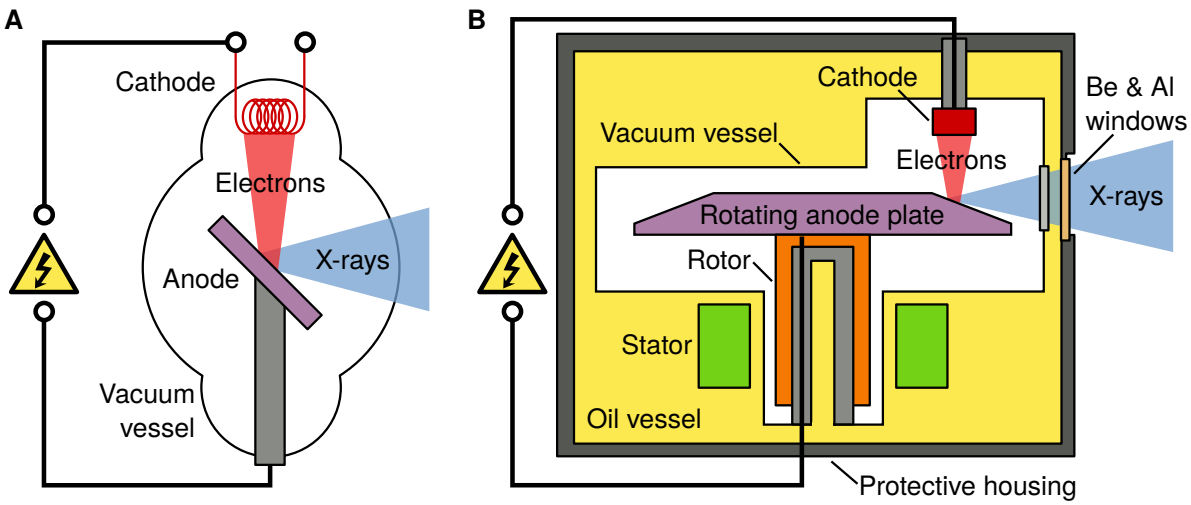

Figure 2.10: X-ray tube designs. (a): Operating principle of a Coolidge-type X-ray tube. (b): Schematic of a modern X-ray tube assembly for medical use. The rotating anode plate with a Goetze line focus is driven by an induction motor (rotor / stator) and supported by a vacuum-compatible bearing. The evacuated vessel (white) is submerged in oil (yellow) and is contained in a housing which acts both as radiation shielding and as protection from mechanical failure. Adapted from [Behl90].

As X-ray level energies are highly specific to the type of atom (or molecule), so is the energy of the photon released in this process. It is therefore also called *characteristic radiation* and measurement of the photon energies of characteristic radiation emitted by a sample (e.g., using an energy-dispersive X-ray detector) can be used to identify its composition to great precision. X-ray levels are usually characterized by one or more vacancies in the atom's innermost shells. Their energies are nearly independent of the atom's chemical configuration and lie in the keV range. X-ray emission spectroscopy is thus well suited to determine the elemental composition of measurement samples.

Characteristic X-rays are produced by X-ray tubes in addition to bremsstrahlung. As illustrated in Fig. 2.11, the spectrum of X-rays produced by X-ray tubes are thus a superposition of a continuous, wide-band component due to bremsstrahlung, and very narrow, high-intensity spectral lines of characteristic X-rays, whose wavelengths are determined by the elemental composition of the tube target.

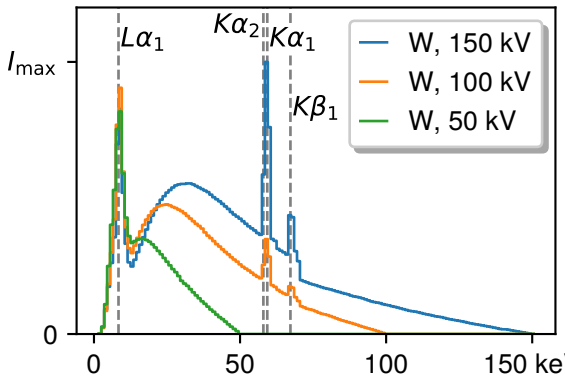

Figure 2.11: Simulated emission spectra [Hern+14] of a tungsten-anode X-ray tube at 50, 100, and 150 kV acceleration voltage. The energies of the most dominant tungsten fluorescence lines are also highlighted. For medical use, this radiation would be filtered by at least 2.5 mm of aluminum, which eliminates nearly all flux for photon energies below approx. 20 keV.

2.4 X-ray imaging hardware

In this section, technical implementations of X-ray generation (discussed in section 2.3) and X-ray detection (discussed in section 2.2 in terms of X-ray-matter interactions) for imaging purposes will be discussed.

2.4.1 X-ray sources

The oldest (and still the most widespread) method to produce X-rays is the use of X-ray tubes. The vast majority of modern X-ray tubes follow the operating principle of the "Coolidge tube" invented in 1913: In an evacuated glass or metal vessel, electrons are emitted via thermionic emission from a heated filament (a "hot" cathode), and accelerated onto a metallic target (the anode) by application of an electric potential. This is illustrated in Fig. 2.10a. On collision with the anode material, the electrons are rapidly decelerated and thus emit a wide spectrum of bremsstrahlung. Additionally, the collisions create vacancies in the electron orbitals of the target material, which leads to an emission of characteristic, material-specific X-ray fluorescence lines.

However, only a small portion of the electrons' kinetic energy is converted to X-rays in either of these processes. The vast majority of this energy is converted to heat in the target material. The *de facto* efficiency of an X-ray tube is even lower since the anode emits X-rays in a large angular range, but only a small portion (rays facing the detection area) are desired. In modern X-ray tube assemblies, the tube is covered by lead shielding in all directions with the exception of an exit window, often made from beryllium. Additional devices are often present to collimate radiation to the area of interest. The low efficiency implies that efficient heat dissipation and a high-power high-voltage generator are required for high X-ray flux and / or long operation times. The anode material may be damaged (molten or evaporated) if heat dissipation is insufficient. This can also spoil the vacuum within the tube and may render the entire device inoperable. Heat dissipation is achieved by submerging the X-ray tube in oil within the tube assembly. Additional heat dissipation may be achieved by circulating the oil through an external cooler.

Another trade-off between beam quality and technical challenges is given by the focusing of the electron beam onto the target: A smaller focus results in X-rays being emitted from a smaller area, which reduces penumbral blurring (and increases spatial coherence). However, the heat is also generated in a smaller area, which further increases demands to heat removal.

This trade-off can be mitigated by the use of suitable electron optics: Focusing electrons to an elongated rectangle on the target (as opposed to a point) leads to a variation of apparent focal spot size on the X-ray emission angle: At low angles, the focal spot is foreshortened, thus appearing much smaller. This so-called "Goetze line focus" thus allows reduced penumbral blurring at high X-ray flux and is very widely used in high-flux X-ray applications. Anode angles in the vicinity of 10° are commonly used, resulting in a reduction of focal spot size by factors between 5 and 10 [Behl15, ch. 6.2.1].

Even greater advances in heat dissipation were achieved by the introduction of the rotating anode: By replacing the fixed target with a rotating circular disk, the heat induced by incident electrons is spread over a much larger area, allowing for a higher flux. However, the combination of rotating parts and vacuum technology is fraught with additional technical challenges: Rotation of the anode disk is achieved with induction motors, which do not require an electrical connection between rotor and stator, and can thus be placed inside and outside of the vacuum vessel, respectively [Behl15, ch. 6.2.3]. Additionally, conventional lubricants can not be used in vacuum, which is why high-precision, silver- or lead-coated ball bearings, or liquid metal spiral-groove bearings are used for the rotor / anode disk [Behl15, ch. 6.2.3]. These technical achievements are visualized in Fig. 2.10b, a simplified schematic of a modern high-performance rotating-anode tube assembly.

2.4.2 X-ray detection

Among the oldest X-ray detection mechanisms is the use of materials that generate visible-light *fluorescence* when irradiated. Since this process does not induce a permanent change to the material, fluorescent screens in an X-ray imaging setup provide object snapshots that update in real time. They are however unable to produce a permanent image, which makes them unsuitable for accurate radiological diagnosis. It was discovered that silver salts used for photography (such as silver bromide and silver chloride) are also sensitive

to X-rays. Thus, photographic plates and films were soon adapted for X-ray imaging.

Similarly to photographic film, *X-ray film* consists of a layer of silver salt emulsion which is applied to one or both sides of a substrate (the eponymous plastic film). As with visible light, exposure to X-rays induces a chemical change to the salt. During the development process, this change is rendered visible as the silver salt exposed to radiation is converted to black metallic silver, the degree of this "blackening" being a function of the received dose. In additional treatment steps, undeveloped silver salts are removed and the image is stabilized. Additionally, the efficiency of the detection process can be increased by combining the film with intensifying screens. These convert a part of the incident X-rays to visible light, which then also contribute to the exposure of the silver salt emulsion [Vogl+11, section 3.2].

Due to the high image quality and comparably low cost, X-ray films were used for the majority of X-ray imaging applications for many decades. However, X-ray imaging methods which require mathematical operations on the image data, such as computed tomography, subtraction angiography, and phase-contrast imaging are largely incompatible with slow, analog film-based technology, instead requiring digital detection.

Early CT devices and some radiography systems used *gas (ionization) detectors*: These consist of an array of ionization chambers, i.e., gas-filled containers with conductive surfaces and a central electrode. By applying a high voltage between electrode and container walls, ionization events by incident X-rays are detected as an electric current [Lanc+16, sec. 2.1.3]. This enables very fast acquisition and digitization, but the use of gas as an absorbing medium limits the efficiency of this approach.

For radiographic applications, systems using *photostimulable phosphor plates* as intermediate storage have been developed (first introduced by Fuji Photo Film Co. in 1983 [Sono+83]). Exposure of a region of the phosphor plate to X-rays creates an excited state in the material which decays only slowly. Illumination of this excited region with an appropriate light source (usually, red light from a HeNe laser) stimulates the emission of blue light. By scanning a "readout laser" over an exposed phosphor plate and measuring the intensity of luminescence in each point, a digital image can be generated. This technique has a higher dynamic range than X-ray film, and the response of the image signal to X-ray intensity is linear, unlike film [Lanc+16, sec. 2.2.2]. However, the readout procedure is slow, and acquisition of images in rapid succession is not feasible, limiting the technique to standard radiographic applications.

Indirect conversion and energy-integrating detection An alternative approach for digital X-ray detection is the combination of X-ray-sensitive phosphors with electronics for the detection of visible light. X-ray intensity is thus encoded first by the intensity of visible-light luminescence, and then by the photodiode current resulting from that luminescence. For imaging purposes, this so-called *indirect conversion* process is employed in *flat-panel detectors*. The operating principle of this design is illustrated in Fig. 2.12. Incident X-rays are received by a phosphor layer. Usually, scintillators such as thallium-doped cesium iodide are used due to their strong X-ray absorption and high light yield [Spah05]. As the intensity of luminescence is proportional to X-ray intensity, light yield is expressed in (visible-light) photons per keV.

Although the efficiency of the scintillator increases with thickness, scattering of scintillation light within the material also increases, which limits the resolution. Scintillator thicknesses usually range from 150 µm for mammographic applications to 600 µm for general radiography [Spah05]. Furthermore, CsI crystals can be grown in columnar structures and thus act as light guides, which reduces scatter.

The scintillator layer is placed on an "active matrix" composed of thin-film-based electronics (Fig. 2.12): a two-dimensional array of photodiodes is placed on charge collector electrodes, which are linked to readout and gate lines via thin-film transistors (TFTs).

During acquisition, each photodiode generates a current which is proportional to the intensity of incident light, and thus to the intensity of X-rays incident on the scintillator. The charge accumulated by the photocurrent is stored by the charge collector electrode [Kott+02]. As the magnitude of this charge is equal to the integrated photocurrent, it is proportional to the integrated X-ray intensity, i.e., the absorbed X-ray energy. This detector design is therefore called *energy-integrating*. After acquisition, detector readout is accomplished by successively activating each gate line, which sends the charges of the associated row of detector elements to an amplifier and an analog-to-digital converter (ADC).

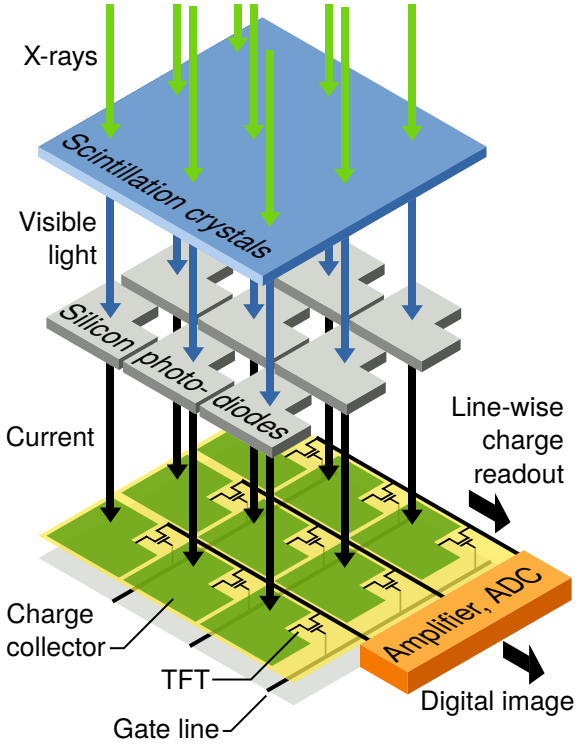

Figure 2.12: Design and operation of a TFT-based flat-panel detector. Incident X-rays reach a layer of scintillation material (often structured CsI crystals), where visible-light photons are produced. These are absorbed by an underlying layer of photodiodes, which induces a current. The total charge accumulated by this current is then stored in a grid of capacitive elements. Readout, i.e. a measurement of these charges, is achieved by a thin-film transistor (TFT) circuit: Sequentially applying a voltage to the series of gate lines discharges one row of capacitive elements at a time.

The fabrication of the necessary TFT electronics uses thin-film deposition techniques used in LCD screen manufacturing, and has profited from the mass-market adoption of this technology [Spah05], enabling large fields of view (beyond 40 cm × 40 cm) as well as pixel sizes in the vicinity of 100 µm.

Direct conversion and photon-counting detection A digital detection technique rapidly gaining in popularity is based on the collection of charges from X-ray-induced ionization events in a semiconductor material. This eliminates the need for a phosphor and can also produce a greater charge, i.e., a stronger signal per X-ray photon, than an indirection detection system [Ball+16]. TFT-based flat-panel detectors have been developed which use a layer of amorphous selenium (a-Se) in place of a scintillator. In these, electron-hole pairs generated by X-ray absorption are separated by applying a voltage to electrodes at the interfaces of the selenium layer [Kasa+02]. Despite the complex interactions in the material, the inherent resolution of an a-Se direct conversion layer is much higher than that of a comparable CsI scintillator layer [Que+95]. On the other hand, the comparably low attenuation coefficient of selenium necessitates a high layer thickness, especially for the high-energy end of medically-used X-rays. Other semiconductor materials, such as cadmium telluride (CdTe), are more suitable for this energy range.

Another important advancement of X-ray detector technology is the development of more sophisticated readout electronics. As the number of generated electron-hole pairs in a direct conversion system is proportional to the absorbed X-ray energy [Ball+16], energy-integrating measurements as with scintillator-based detectors are possible. However, sufficiently fast readout electronics can distinguish the current pulses induced by individual X-ray photons, and thus measure not only the total energy absorbed in an exposure, but also the number of absorption events. The latter quantity provides an improved signal-to-noise ratio, since electronic noise and noise from the energy-integration process [Swan73] are eliminated, and lower-energy X-ray photons, which produce a greater contrast, are weighted as strongly as high-energy photons [Tagu+13]. Furthermore, the shape of the current pulse provides information about the energy of the absorbed X-ray photon, which enables spectral X-ray imaging applications.

However, this comes at the cost of more complex, per-pixel readout electronics which introduces certain limitations. For example, two photons absorbed nearly simultaneously may be interpreted as a single photon with higher energy due to the temporal overlap of current pulses (*pile-up*), and photons arriving during the "dead time" where the previous pulse is processed may not be counted (*dead time losses*) [Ball+16]. This complicates the introduction of photon counting detectors for high-flux applications (e.g., medical CT), where these effects are most prevalent. Nonetheless, the introduction of photon counting detectors is one of the most important recent innovations for many X-ray imaging applications and a very active field of research.

2.5 Principles of grating-based X-ray phase-contrast and dark-field imaging

In this section, the fundamentals of *grating-based X-ray phase contrast*, the imaging method used for all experimental results in this thesis, will be introduced.

After a brief introduction to diffraction gratings in section 2.5.1, the *(fractional) Talbot effect* due to the *modulation grating* (or G_1) is explained in section 2.5.2. Diffraction gratings can be used to imprint a periodic modulation (either in phase or amplitude) onto an incident X-ray wavefield. If this wavefield has sufficient transverse coherence, the *Talbot effect* then causes a reproduction of this periodic pattern at certain downstream distances. In particular, pure phase modulations due to the grating result in amplitude (and thus, intensity) modulations at certain rational fractions of the Talbot distance.

Inserting an object before or after the grating leads to a modification of the detected modulations. Specifically, these modulations can be modified in several different ways, as opposed to conventional X-ray imaging, where only one effect (the reduction in measured intensity) can be determined. This is discussed qualitatively in section 2.5.3, followed by the introduction of the *analyzer grating* (or G_2), which decouples grating periods from detector resolution, in section 2.5.4. The crucial addition of a source grating (or G_0) to enable use of the method with conventional X-ray tubes is explained in section 2.5.5.

Phase stepping, the most common experimental procedure to retrieve data from a grating-based X-ray imaging setup, is introduced in section 2.5.6. Section 2.5.7 explains the effect of replacing parallel-light illumination with point-source illumination (i.e., a light "cone"). Finally, the mathematical relations between the quantities measured in a grating-based setup and the physical properties of the measured object are derived in section 2.5.8.

2.5.1 Diffraction gratings

Diffraction gratings are highly regular, usually planar structures which are characterized mainly by their periodic thickness variation on a microscopic scale. Most optical gratings are periodic only in one direction, although two-dimensional gratings can be manufactured as well. For visible-light applications, gratings can be made to reflect or transmit incident light. Their main purpose is to act as diffracting elements: a monochromatic plane wave incident on a flat transmission grating will be diffracted into regularly-spaced diffraction maxima, whose spacing is determined by the ratio of light wavelength λ and grating period p. Accordingly, white light is spatially separated into its spectral components. Diffraction gratings are thus often used for spectral analysis of visible-light sources.

Most diffraction gratings have a rectangular height profile, i.e., resembling a pulse wave. Equivalently to the definition of the duty cycle of pulse waves, a *duty cycle* $\mathscr{D}$ of the grating's height profile can be defined as the ratio of grating ridge width w and period p: $\mathscr{D} = w/p$. Furthermore, the ratio of grating ridge height h and width w is called the *aspect ratio*.

Gratings can be used for wavelengths beyond the visible spectrum, although their efficiency declines with decreasing wavelength: Lower interaction cross-sections with material at these wavelengths mean that greater amounts of material are required to attenuate incident light. Additionally, as the spacing of adjacent diffraction maxima is proportional to λ/p, low grating periods are especially important to achieve sufficient separation. These extreme demands to period and aspect ratio can only be met by specialized, costly manufacturing methods such as deep X-ray lithography (cf. section 3.2.2 on page 73.)

X-rays have wavelengths in the vicinity of atomic radii. It is thus impossible to achieve similar spatial separation of diffraction maxima as for visible light with

conventional gratings: the grating ridges and grooves would have to have a width of a single atom[8]. Instead, the achieved diffraction angles are very small and fields from all diffraction maxima "overlap". If the transverse coherence of the incident radiation is sufficiently high, they may interfere with each other, which causes the so-called *Talbot effect*.

2.5.2 The Talbot self-imaging effect

As discovered by H. F. Talbot in 1836 and systematically described by Lord Rayleigh in 1881 (cf. section 1.3.1 on page 15), a periodic, fully coherent wavefield with period p and wavelength λ in one plane will be reproduced at certain downstream distances, namely multiples of the *Talbot distance* $z_\mathrm{T} = 2p^2/\lambda$. Furthermore, at downstream distances $z = \frac{1}{2}z_\mathrm{T}, \frac{3}{2}z_\mathrm{T}, \ldots$, the periodic pattern is repeated with a lateral shift of $p/2$ (cf. Fig. 2.14a). This can be verified by Fresnel propagation of an arbitrary periodic wavefield, see e.g. [Good05, ch. 4.5.2]. This applies for purely imaginary or real-valued modulations, i.e. fields transmitted by absorbing gratings as well as phase-shifting gratings.

Closely related to this is the *fractional Talbot effect*: A pure phase modulation is converted into modulations of magnitude (and thus intensity) at downstream distances of certain rational fractions of z_T. Unlike the ordinary Talbot effect, the relevant downstream distances are dependent on specifics of the original modulated pattern, such as the phase-shift amplitude and specific profile of the gratings. A number of such distances for gratings with different duty cycles and amounts of phase shift are compiled in [Sule97].

All of these effects can be understood to emerge from coherent superposition of adjacent diffraction orders generated by the grating. This is illustrated in Fig. 2.13, where the intensity distribution downstream of a coherently-illuminated grating is simulated. For large propagation distances, the diffraction orders are spatially separated, but for shorter distances where they overlap, self-imaging of the periodic grating structure can be observed in regular intervals.

The most commonly-used phase-modulating gratings have a duty cycle of $\mathscr{D} = 0.5$ and achieve a phase shift modulation of π or $\pi/2$ for a given "design energy". For illumination with plane waves, maximum intensity contrast is achieved at $\frac{1}{4}z_\mathrm{T}, \frac{3}{4}z_\mathrm{T}, \frac{5}{4}z_\mathrm{T}, \ldots$ for $\pi/2$-phase-modulating gratings (Fig. 2.14b), whereas for π-phase-modulating gratings, this is the case at $\frac{1}{16}z_\mathrm{T}, \frac{3}{16}z_\mathrm{T}, \frac{5}{16}z_\mathrm{T}, \ldots$ and the resulting intensity modulations have half the grating period (Fig. 2.14c).

In grating-based X-ray phase contrast imaging, an intensity-modulating or a phase-modulating grating may be used. This *modulation grating* is often referred to as G_1, its period accordingly as p_1.

2.5.3 Modification of Talbot images by a sample

Introduction of a sample will lead to a modification of the downstream fields. Usually, three separate effects are distinguished (although more complex modifications have been examined [Modr+12]): Attenuation, refraction, and small-angle scattering. A purely absorbing object uniformly reduces the amplitude of the detected pattern – all intensities of the measured periodic modulation are reduced by a constant factor. Refraction (in the direction of the pattern's periodicity) introduces a deviation between incident and transmitted propagation directions, and thus leads to a lateral shift of the detected pattern. Finally, a variation of electron density on a sufficiently short length scale induces small-angle scattering of the incident beam, which leads to a reduction of amplitude in the detected pattern, relative to its mean intensity. These three cases are illustrated in Fig. 2.15.

Placing an X-ray detector in one of the (fractional) Talbot distances, and analyzing the distortion of the grating self-images by a specimen thus enables the retrieval of its attenuating, phase-shifting, and small-angle scattering properties.

2.5.4 Introduction of an analyzer grating

As conventional X-ray detectors exhibit pixel sizes in the vicinity of 100 µm (cf. section 2.4.2), fringe periods and thus grating periods of at least 200 µm are required to allow directly resolving the grating self-images, which is necessary to allow retrieval of all three image signals (cf. Fig. 2.15). For X-ray wavelengths on the order of 0.5 Å (≈ 25 keV photon energy), this results in an absurd Talbot distance of $z_\mathrm{T} = 1600$ m. X-ray Talbot imaging is thus only feasible in this manner with

[8] Of course, this feat is achieved by X-ray crystallography, where adjacent atoms in the crystal lattice act as grating ridges. Both transmitting and reflecting crystal arrangements are possible, named "Laue reflection" and "Bragg reflection".

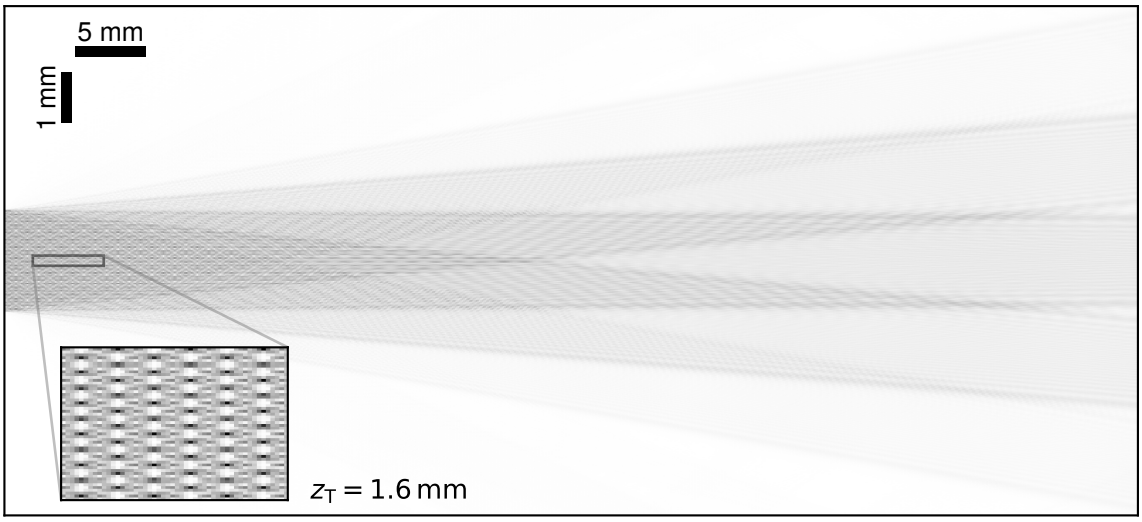

Figure 2.13: Intensity distribution downstream of an absorbing grating illuminated by a plane wave. In regions where the diffraction orders overlap, Talbot self-imaging can be observed, whereas for larger distances, the diffraction orders become spatially separated. Simulated with an angular spectrum representation of an incident wavefield, according to [Good05, ch. 3.10]. $p = 20\,\mu\mathrm{m}$, $\lambda = 500\,\mathrm{nm}$, beam width 2 mm. For X-ray wavelengths and grating periods in the μm range, spatial separation becomes negligibly small.

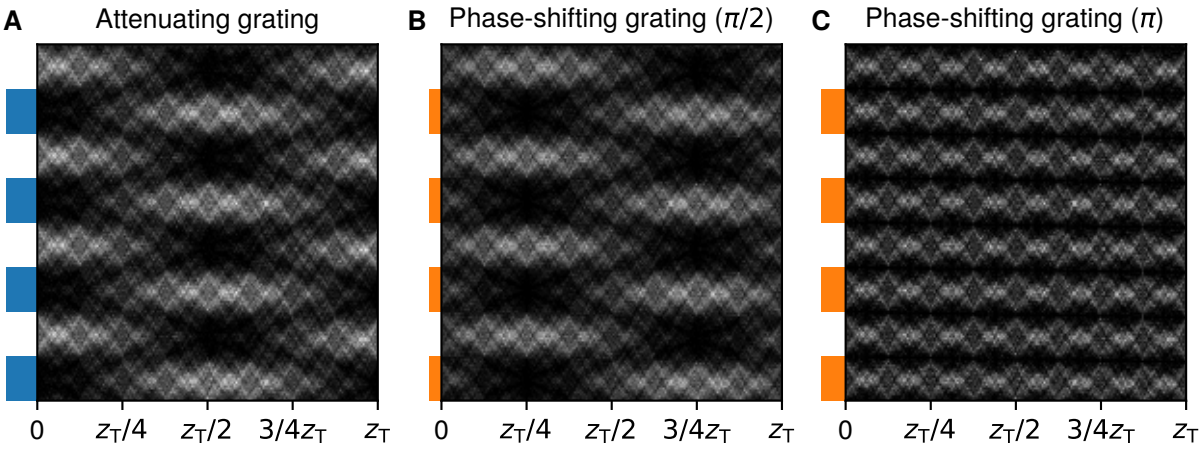

Figure 2.14: Intensity maps downstream of coherently illuminated optical gratings ("Talbot carpets"). (a): Reproduction of periodic wavefield modulations (Talbot effect), (b, c): Conversion of phase modulations to intensity modulations (fractional Talbot effect), assuming a rectangular grating profile with $\pi/2$ (b) and π (c) phase shift. Maximum intensity modulations are achieved at $z = \frac{1}{4}Z_T, \frac{3}{4}Z_T, \ldots$ in (b), and at $z = \frac{1}{16}Z_T, \frac{3}{16}Z_T, \frac{5}{16}Z_T, \ldots$ in (c) with half the grating period.

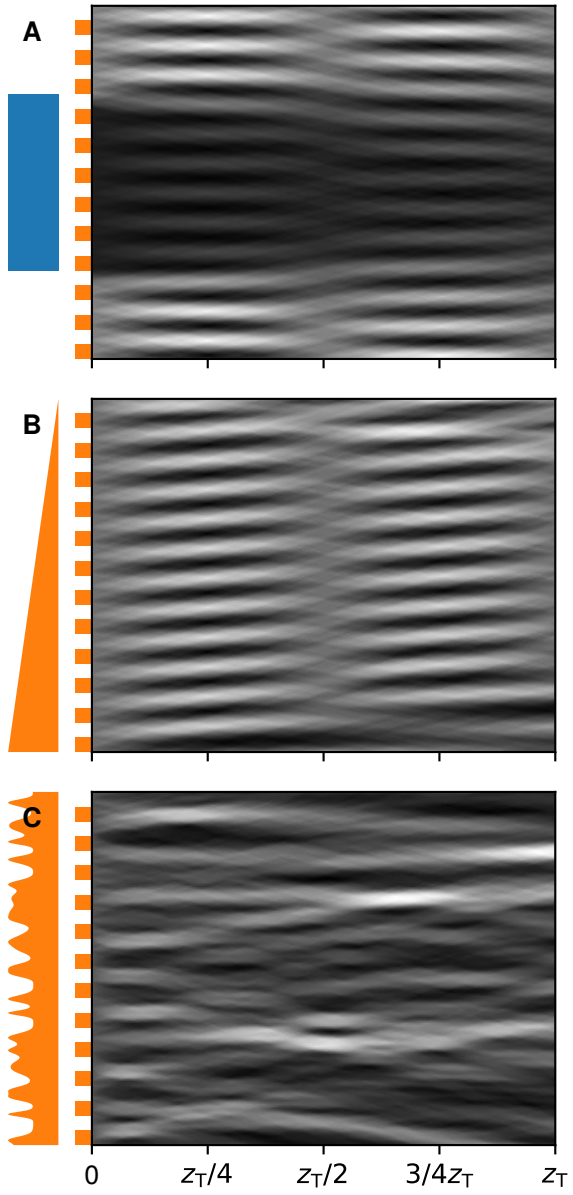

Figure 2.15: Effects of imaging samples on intensity maps downstream of a phase-shifting grating ($\pi/2$). An object from purely attenuating material (a) reduces overall intensity, while a wedge from purely phase-shifting material (b) refracts light and induces lateral shifts to the self-images. Finally, a material from purely phase-shifting material with thickness variations on very small length scales (c) induces small-angle scattering and thus partly destroys the grating self-images. Intensity maps are slightly smoothed.

specialized detectors of much smaller pixel sizes, even when there is no demand for high sample resolution. Furthermore, to achieve a per-pixel detector dose sufficient for the retrieval of image signals with low pixel sizes, large radiation doses must be applied to the imaged sample.

An effective method to decouple detector resolution from grating periods is to introduce an absorbing *analyzer grating* (often abbreviated as G_2) in the measurement plane (just before the X-ray detector). If care is taken that this grating's period p_2 matches the period of the first grating's self-images, the intensity transmitted through each ridge of the second grating is constant, since there is a fixed phase relationship between the self-image and the analyzer grating's transmission function. Since a detector pixel retrieves a signal proportional to light intensity averaged over its area, measured values are approximately independent of pixel size (so long as a pixel is sufficiently larger than one grating period).

2.5.5 Achieving high flux and high spatial coherence

As described above, Talbot self-images arise due to interference between diffraction orders produced by the modulation grating. However, for these effects to occur, there must be a fixed phase relation between the fields at different points in the plane of the modulation grating. In other words, the *transverse coherence length* of radiation must be sufficiently high in the direction orthogonal to the grating lines, namely in the vicinity of p_1 [Momo+10, Fig. 9].

According to the van Cittert-Zernike theorem, the transverse coherence length is inversely related to the size of the source spot, and proportional to the distance from the source spot. The transverse coherence lengths achievable with conventional X-ray tubes are typically very low, which prohibits the direct implementation of an X-ray Talbot interferometer with such sources (see e.g. Fig. 1.6a). Naturally, the coherence length can be increased by collimating the source with a sufficiently small aperture, but this also strongly decreases X-ray flux (roughly in proportion with the area of the collimated spot). Two approaches have been developed to tackle this problem for lab-based setups: maximizing X-ray luminance (flux emitted per unit area) and the use of Talbot-Lau grating arrangements.

An increase in luminance leads to an increase of X-ray flux for a given spot size, and thus a given transverse coherence length. In so-called microfocus X-ray tubes, sophisticated electron emitter and focusing optics, as well as specialized thin transmission targets are used to minimize the size of the source spot [Xray20]. The increased density of thermal power generated in the target during X-ray generation imposes high demands on heat dissipation to avoid damage to the target, and limits the achievable X-ray flux. A higher-flux alternative are so-called liquid metal jet sources [Tuoh+07; Lars+11], where the solid target is replaced by a stream of a liquid metal alloy, which allows rapid heat dissipation into a larger reservoir of liquid metal.

A Talbot-Lau arrangement, on the other hand, is created by the addition of an attenuating grating to a Talbot interferometer. Added near the X-ray source, this *source grating* (G_0) acts as a specialized collimator: A single collimator placed behind the source must be so narrow that a sufficiently high transverse coherence length is achieved at the modulation grating. The X-rays emitted from this collimation then produce Talbot self-images on the analyzer grating or the detector.

A transverse shift of this collimator in the source grating plane leads to a transverse shift of the self-images into the opposite direction. The distance between two such collimators can be matched so that the modulations in the self-images from each collimator are in phase to each other, see Fig. 2.16. This modification thus doubles the detected X-ray flux without detriment to coherence at the modulation grating. Naturally, this principle can then be extended to an array of collimators with a constant spacing. Furthermore, no coherence is required in the direction parallel to the grating lines, allowing the use of line-shaped collimation. A conventional X-ray tube with a large source spot, combined with an intensity-modulating grating is such an array of line sources. The condition of in-phase partial self-images from each grating line is met if

$$\frac{p_0}{p_2} = \frac{L}{D}, \tag{2.40}$$

where p_0 and p_2 are the periods of the source grating and the detected self-images, respectively, L is the distance from source grating to modulation grating, and D is the distance between modulation grating and analyzer grating (Fig. 2.16). Such an arrangement was first presented for use with X-rays in [Pfei+06].

Compared to the use of microfocus sources, the Talbot-Lau approach is able to deliver higher flux (the greater overall tube flux of conventional X-ray tubes usually more than makes up for absorption losses in the source grating) and is directly compatible with clinically-used X-ray hardware.

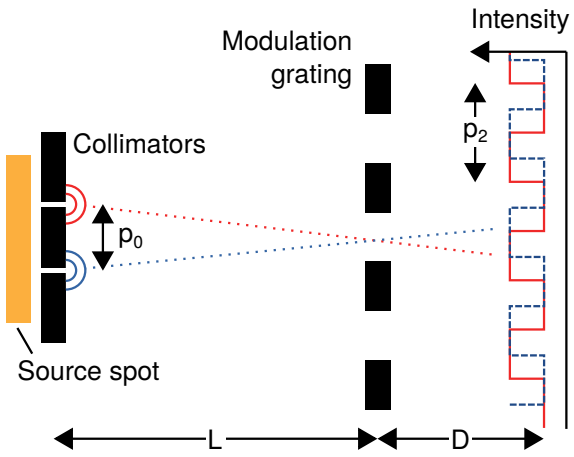

Figure 2.16: Superposition of Talbot self-images generated by adjacent collimators. The highest visibility is achieved if all individual self-image are in phase, which is the case only if Eq. (2.40) is fulfilled.

The choice of source grating duty cycle $\mathscr{D}$ is a trade-off between X-ray flux and transverse coherence: While X-ray flux Φ is proportional to $1-\mathscr{D}$, visibility V is proportional to $\mathscr{D}$ under ideal conditions[9]. It has been shown that the signal-to-noise ratio of visibility and differential phase maps is proportional to $V\sqrt{\Phi}$ [Revo+10; Chab+11] and thus to $\mathscr{D}\sqrt{1-\mathscr{D}}$. This function is maximized for $\mathscr{D} = 2/3$, suggesting that this choice of duty cycle maximizes image quality[10].

2.5.6 Phase stepping

Introducing a specimen leads to distortions of the self-images (Fig. 2.15), which will then become apparent

[9] This is true if stepping curves (cf. section 2.5.6) are assumed as a triangle wave with visibility 1 (convolution of rectangle-wave self-images with rectangle-wave analyzer grating transmission function) are assumed for a point-like source (as shown in Fig. 2.17). The effect of a source grating is modeled by convolution of this stepping curve with the transmission function of the source grating (a third rectangle wave with variable duty cycle), following the approach in [Bech09, ch. 2.4].

[10] Without the use of an analyzer grating, maximum SNR is found for $\mathscr{D} = 1/2$ using the same approach.

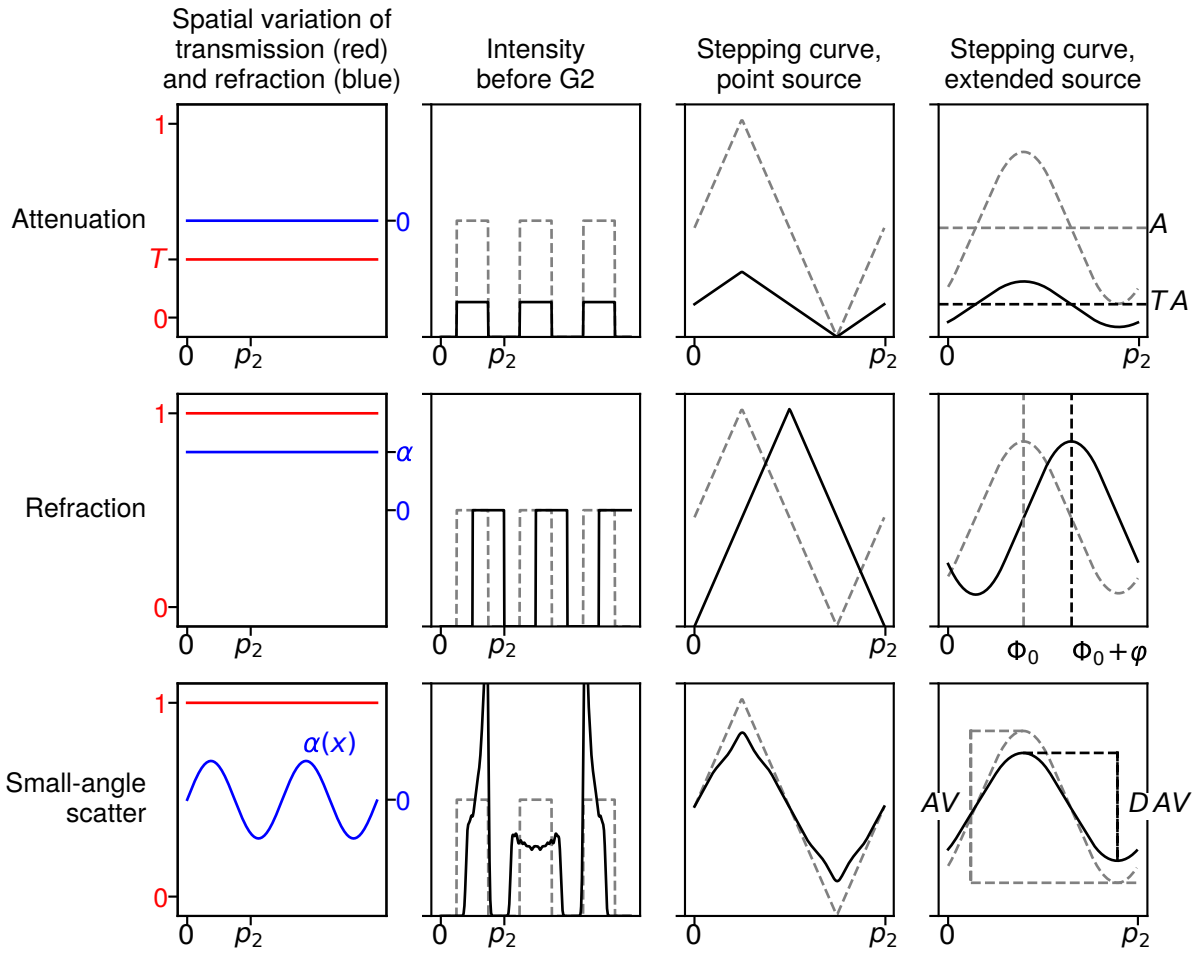

Figure 2.17: Measured intensities for three idealized sample types in a Talbot interferometer. Sample properties are here described by their position-dependent transmission and refraction of radiation over three grating periods (first column): Attenuation and refraction are assumed constant (T, α), whereas the scattering object has a position-dependent refraction angle $\alpha(x)$. The resulting self-images are thus attenuated, shifted, or distorted (second column). Phase-stepping with an analyzer grating and integration of intensity over three grating periods (third column) results in approximately triangular modulations of intensity, if a point source is used. Blur due to a finite size of the source spot (last column) reduces visibility and leads to an approximately sinusoidal shape of stepping curves. While T can be directly retrieved from the change in the stepping curve's mean value, the relations of the curve's lateral shift φ and visibility reduction factor D to the sample properties [α and $\alpha(x)$, respectively] are more complicated and discussed in section 2.5.8.

as deviations from the uniform detected light intensity. Information about the sample can then be inferred from the magnitude of change in light intensity. The resolution with which these changes are detected is determined entirely by detector resolution (and not by grating parameters). In effect, the attenuating, phase-shifting, and scattering properties of the sample are averaged over an area corresponding to the pixel size of the detector.

However, three mutually independent sample properties can not be encoded within a single real-valued number (measured intensity) without loss of information – at least two additional measurements are required. By lateral translation of either of the three gratings, the relative phase of self-image and the analyzer grating's transmission function can be altered, which also leads to a variation of detected light intensity. This intensity must be a periodic function of lateral grating translation for any point in the field of view, whether or not the underlying self-image has been distorted by a specimen. Sampling this function by repeated exposure at different lateral grating positions is called *phase stepping* [Weit+05], the resulting data set for one detector pixel is called a *stepping curve*. Different parameters of a pixel's stepping curve are a measure for average properties of the grating self-image in the area of this pixel: Mean intensity of the stepping curve is proportional to the self-images mean intensity, its lateral shift characterizes the self-image's shift relative to the analyzer grating, and the contrast of the stepping curve is proportional to the self-image's average contrast.

Thus, acquiring a phase-stepping data set with and without the specimen allows retrieving localized information about the self-image's attenuation, deflection and contrast reduction due to the specimen by comparing the change in stepping curve parameters between both measurements.

The full path from sample properties to data measured in a Talbot or Talbot-Lau setup is thus: the modulation of Talbot images by the sample (section 2.5.3), blur of Talbot images due to the finite extent of the source (section 2.5.5), and repeated analysis of Talbot images by analyzer grating and detector (section 2.5.4) for different relative grating positions in the *phase stepping* process.

This is summarized in Fig. 2.17 for three idealized types of samples. For the case of illumination with a point-like monochromatic source and the use of binary gratings, *stepping curves* have a periodic, triangular shape. However, sources with finite transverse coherence introduce a blur which transforms them to an approximately sinusoidal curve shape [Bech09, ch. 2.4]. In the absence of a sample, the measured intensity in the k-th *phase step* can then be described as

$$\boxed{\hat{I}_k^{(\mathrm{r})}(x) = A\left[1 + V\cos\left(\Phi_k - \phi\right)\right],} \tag{2.41}$$

where Φ_k is the lateral shift in radian of the phase-stepped grating. Phase stepping is usually performed over a full period in equidistant intervals, so that $\Phi_k = 2\pi k/N$, $k = 1,\dots N$. The offset ϕ occurs if the gratings are not perfectly matched to each other, resulting in moiré fringes. It is independent of k but may vary across the field of view. A is the mean intensity, and V—the visibility—is the modulation amplitude relative to the mean. A, ϕ, and V are retrieved by regression of Eq. (2.41) to the reference measurements $\{I_1^{(\mathrm{r})},\dots I_N^{(\mathrm{r})}\}$ (performed without a sample in the beam).

The different types of sample interactions shown in Fig. 2.17 each affect one of the three parameters: Attenuation leads to a reduction in A, refraction introduces a shift to ϕ, and small-angle scatter reduces V. These effects can be described by an additional set of three parameters:

$$\boxed{\hat{I}_k(x) = TA\left[1 + DV\cos\left(\Phi_k - \phi + \varphi\right)\right].} \tag{2.42}$$

T is the sample transmittance introduced in section 2.2.8. The shift φ is related to the sample's angle of refraction α, and setup-specific parameters. The factor D quantifies the factor of visibility reduction by the sample. It is primarily a function of the sample's small-angle scattering properties and setup properties, but may also arise due to beam-hardening (see [Yash+15; Pelz+16] and section 4.3.1 on page 101) and other spectral effects (section 6.1 on page 159). The mathematical relations connecting φ and D to sample and setup properties are introduced in section 2.5.8. Regression of Eq. (2.42) to the sample measurements $\{I_1,\dots,I_N\}$ yields values for TA, DV, and $\phi - \varphi$. The sample-specific quantities can then be isolated from these values by division and subtraction with the reference measurement parameters:

$$\boxed{T = \frac{TA}{A},\ \Delta\varphi = \phi - (\phi - \varphi),\ D = \frac{DV}{V}.}$$

2.5.7 Magnification and the Fresnel scaling theorem

For synchrotron imaging setups, distances beyond 100 m between the point of X-ray generation and the imaging experiment are common. Besides very high spatial coherence, this provides a nearly plane-wave illumination of the experiment's optical components. The relations between grating periods and (fractional) Talbot distances introduced so far apply only for this case.

X-ray tubes, on the other hand, emit radiation in a large "cone", which also enables much larger fields of view. In order to use this radiation efficiently, imaging setups must employ a large angular range of this radiation cone, so that plane-wave illumination can not be assumed. As derived e.g. by D. Paganin in [Paga06, Appendix B], the intensity distributions resulting from parallel-light and "cone-beam" illumination of the same object are related to each other via a simple geometrical transformation, if certain conditions are fulfilled, namely: if incident radiation can be assumed as paraxial[11], the projection approximation (see section 2.2.8) can be used for the object, and the conditions to use Fresnel propagation (as discussed in section 2.1) are fulfilled.

In this case, if an object is illuminated by a point source at a finite upstream distance of L, the intensity distribution I^L measured in a plane at a distance d downstream of the object is related to the intensity distribution I^∞ from *parallel* illumination at a downstream distance d/M, where $M = (L+d)/L$, i.e., the geometrical magnification in the case of cone illumination. That is,

$$I^L(x,y,d) \propto I^\infty\left(\frac{x}{M}, \frac{y}{M}, \frac{d}{M}\right), \tag{2.43}$$

where x and y are coordinates orthogonal to the optical axis. This is illustrated in Fig. 2.18. While the magnification in x- and y direction is unsurprising from a geometrical optics perspective, the connection between d and d/M is less obvious.

For a Talbot(-Lau) setup with cone-beam illumination, the relative contrast at a downstream distance d is thus equal to that with parallel-plane illumination at a distance $d/M = Ld/(L+d)$. Since maximum contrast

[11] Paraxial rays are those with a small angle to the optical axis. This condition is thus fulfilled if the angular range of emitted radiation is not too large. However, the resulting conditions on inter-grating distances can be applied even for setups where this is the case.

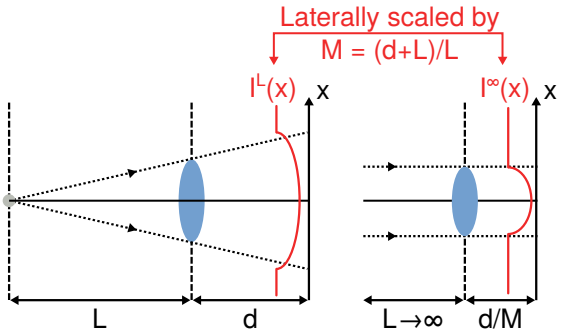

Figure 2.18: Fresnel scaling theorem. Relation between intensity maps from cone-beam illumination (left) and parallel-plane illumination (right) of the same object, see Eq. (2.43).

in parallel-plane illumination is achieved at fractional Talbot distances $D_k = kz_T$ (e.g. $k = 1/16, 3/16, \ldots$ for a π-shifting phase grating), it follows for their cone-beam equivalent d_k that

$$\frac{Ld_k}{L+d_k} = D_k. \tag{2.44}$$

As presented in [Dona+09], solving Eq. (2.44) for d_k yields

$$d_k = \frac{LD_k}{L-D_k}. \tag{2.45}$$

This can also be expressed with normalized distances: $\tilde{d}_k = \tilde{D}_k/(1-\tilde{D}_k)$, where $\tilde{d}_k = d_k/L$, $\tilde{D}_k = D_k/L$. Since $\tilde{D}_k$ usually increases in equal intervals, this means that the distance $\tilde{d}_{k+1} - \tilde{d}_k$ between successive self-imaging distances increases with k, and that no self-images with a parallel-beam equivalent distance of $\tilde{D}_k > 1$ can be observed: as it approaches 1, $\tilde{d}_k$ goes to infinity. This relation is illustrated in Fig. 2.19.

Given this complicated relation between inter-grating distances, it is reasonable to ask which values of D_k are achievable for a given total cone-beam setup length $s = L + d_k$. This has been examined by Donath et al. [Dona+09], who identify three distinct cases:

- Values of $D_k > s/4$ can not be achieved.
- The value $D_k = s/4$ is reached with a symmetric arrangement, i.e. $L = d$, and thus $D = d/2$.
- For values $D_k < s/4$, two solutions for L (and thus, d) exist:

$$L_\pm = \frac{s}{2} \pm \sqrt{\frac{s^2}{4} - sD}.$$

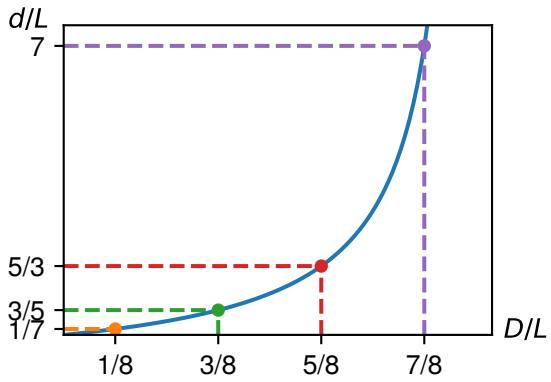

Figure 2.19: Equivalent propagation distances in parallel-plane illumination (*D*) and cone-beam illumination (*d*), normalized with *L*. Highlighted are locations of the first four fractional Talbot distances for a π-shifting phase grating and $L = Z_T/2 = p_1^2/\lambda$. Although they are spaced equidistantly for parallel-plane illumination, their relative distance greatly increases for cone-beam illumination.

The authors name the solution for which $L = L_+ > d$ a *conventional setup*, whereas the solution with $L = L_- < d$ is called an *inverse setup*.

Furthermore, the period of the self-images in cone-beam illumination is increased by the factor M due to the geometrical magnification, i.e.,

$$p_2 = M\frac{p_1}{\eta}. \tag{2.46}$$

Here, p_1/η is the period of the (parallel-beam) self-images of G_1. It is usually identical to p_1 (or in the case of a G_1 grating with a phase modulation of π, to $p_1/2$). The relation between p_0 and p_2 remains unchanged, as in Eq. (2.40):

$$p_0 = p_2\frac{L}{d} = \frac{p_2}{M-1}. \tag{2.47}$$

Because M is greater for the inverse setup, this means that p_2 is larger and p_0 is smaller than for the equivalent "conventional setup" design. Since attenuating gratings with low periods are more difficult to manufacture, the inverse approach is beneficial from a practical standpoint: The more challenging manufacturing process is limited to the G_0 grating, which may be much smaller than the G_2 grating. Furthermore, the inverse design requires a smaller area for the G_1 grating.

On the other hand, the inverse design achieves a lower angular sensitivity (see below) at low levels of geometrical magnification, i.e. if a large field of view is required.

2.5.8 Relation between sample properties and measured quantities

As shown in section 2.2.8, applying the projection approximation shows that the factor T by which a sample attenuates the intensity I_0 of incident monochromatic radiation is determined from the projection integral of the linear attenuation coefficient μ at the given photon energy E, along the direction of light propagation. For parallel-plane illumination with beam propagation in z, and the sample being limited to $0 < z < z_0$:

$$T(E,x,y) = \frac{I}{I_0} = \exp\left[-\int_0^{z_0}\mu(E,\vec{r})\,dz\right], \tag{2.48}$$

with $\vec{r} = [x,y,z]^T$. In grating-based imaging, the transmittance T can be derived directly from the attenuation of measured fringes.

Phase shifts however can only be detected via the fringes' lateral shift, which is dependent on the angle of refraction by the object. Thus, we will first derive the relation between phase shift and refraction angle, and then calculate how the refraction angle determines fringe shift.

2.5.8a Phase shift and angle of refraction

Eq. (2.37) in section 2.2.8 shows that induced phase shift is given by a projection integral of the "refractive index decrement" δ:

$$\Delta\Phi(E,x,y) = k\int_0^{z_0}\delta(E,\vec{r})\,dz. \tag{2.49}$$

In order to determine the relation between refraction angle and phase shift, we can examine the phase of a plane wave with a known direction of propagation: its spatial component is given by $U\exp(i\vec{k}\vec{r})$, i.e. its phase at $z = z_0$ is equal to $\Phi(x,y,z_0) = \vec{k}\vec{r} = k_x x + k_y y + k_z z_0$. If $\vec{k}$ lies in the yz plane, with an angle α_x to the z axis, the phase at any given $z = z_0$ depends linearly on x: $\Phi(x,y,z_0) = k(x\sin\alpha_x + z_0\cos\alpha_x)$. In this case, α_x can be derived directly from the x- dependence of Φ: $\alpha_x = \arcsin[\Phi(x,y,z_0)/(kx)]$. More realistically though, if α_x varies with x, its local value can be retrieved by differentiation:

$$\alpha_x = \arcsin\left(\frac{1}{k}\frac{\partial\Phi(x,y,z_0)}{\partial x}\right).$$

Since the wavefield incident on the sample is assumed to be a plane wave propagating in z direction, we can identify $\Phi(x,y,z_0)$ with $\Delta\Phi$ in Eq. (2.49) except for a phase factor independent of x and y:

$$\Phi(x,y,z_0) = \Phi_0 + \Delta\Phi(E,x,y),$$

and thus:

$$\alpha_x(x,y) = \arcsin\left(\frac{1}{k}\frac{\partial\Delta\Phi(E,x,y)}{\partial x}\right) \tag{2.50}$$

$$= \arcsin\left(\frac{\partial}{\partial x}\int_0^{z_0}\delta(E,\vec{r})\,dz\right) \tag{2.51}$$

$$\overset{\alpha_x\ll 1}{\approx} \frac{\partial}{\partial x}\int_0^{z_0}\delta(E,\vec{r})\,dz. \tag{2.52}$$

The arcsin term can usually be neglected since X-ray refraction angles are very small. α_y (the angle between $\vec{k}$ and the z axis in the xz plane) is retrieved by replacing $\partial/\partial x$ with $\partial/\partial y$. We have assumed here that $\Phi(x,y,z_0)$ can be locally well described by only its first spatial derivatives, which is equivalent to a ray optics view of the problem. This is often appropriate since the spatial variations of δ are on much longer length scales than the X-ray wavelength. However, as grating-based setups "amplify" even very small refraction angles into a large signal, minor deviations from the ray optics view, i.e. due to small-angle scatter, have significant effects on the produced signal (as will be discussed below).

2.5.8b Differential-phase signal and angle of refraction

Refraction leads to a lateral shift of the fringes detected by the analyzer grating. Most commonly, a one-dimensional modulation grating is used, which also produces one-dimensional fringes on the analyzer grating. If the grating lines are assumed to be parallel to the y axis, deflection of resulting fringe patterns in the y direction does not lead to a change in intensity. The setup is thus unable to distinguish any variations in α_y.

The dependence of lateral fringe shift on the refraction angle α_x and its location s in the beam has been derived by Donath et al. [Dona+09] for a Talbot- or Talbot-Lau setup with cone-beam illumination, using ray optics-based arguments. This approach is illustrated in Fig. 2.20.

The path of an undisturbed ray along the optical axis (Fig. 2.20a) is compared to a ray which originates in the same point (S), is refracted by the object at a point D, and ends up in the same point (B) on the analyzer grating as the undisturbed ray (Fig. 2.20b, c). The distance of D to the optical axis (the distance $[DE]$) can be uniquely determined from the setup dimensions (source-G_1 distance L, G_1-G_2 distance d, and sample-G_1 distance s), and the condition that the ray is refracted by the angle α_x:

$$[DE] = (L+s)\tan\beta = (d-s)\tan\gamma, \tag{2.53}$$

$$\alpha_x = \beta + \gamma, \tag{2.54}$$

where $\beta = \angle DES$, $\gamma = \angle DEB$. Furthermore, this is applicable both for sample placement upstream or downstream if s is chosen negative or positive, respectively. Since α_x is small, so are β and γ, so that $\tan\beta \approx \beta$, $\tan\gamma \approx \gamma$. Eqs. (2.53) and (2.54) can be combined to yield

$$[DE] = \alpha_x\frac{(L+s)(d-s)}{L+d}. \tag{2.55}$$

From $[DE]$, we can derive the location of the point C where the ray of interest passes through the modulation grating. Whereas C is the point on G_1 that is mapped to the point B in the measurement plane, its counterpart in the absence of a sample is the intersection of G_1 and the optical axis (i.e., the point A). Therefore, the distance $[CA]$ determines the amount of shift φ the fringe pattern experiences[12]:

$$\frac{[CA]}{p_1} = \frac{\varphi}{2\pi\eta}. \tag{2.56}$$

As in Eq. (2.46), the factor η is 1 for most grating setups, but since a π-phase-modulating G_1 grating produces Talbot images with half the period of other types of modulation grating (Fig. 2.14c), the fringe shift (in radians) is twice as high, so that $\eta = 2$.

$[CA]$ can be geometrically derived from $[DE]$:

$$[CA] = \begin{cases} [DE]\frac{L}{L+s} = \alpha_x L\frac{d-s}{L+d} & (s>0), \\ [DE]\frac{d}{d-s} = \alpha_x d\frac{L+s}{L+d} & (s<0). \end{cases} \tag{2.57}$$

[12] $\Delta\varphi$ is the lateral shift of the (typically sinusoidal) fringe pattern, or alternatively, the lateral shift of the phase-stepping curve, in radian (as shown e.g. in Fig. 2.17). It is not be confused with $\Delta\Phi$ from Eq. (2.49), the (longitudinal) phase shift of the wavefield due to an object.

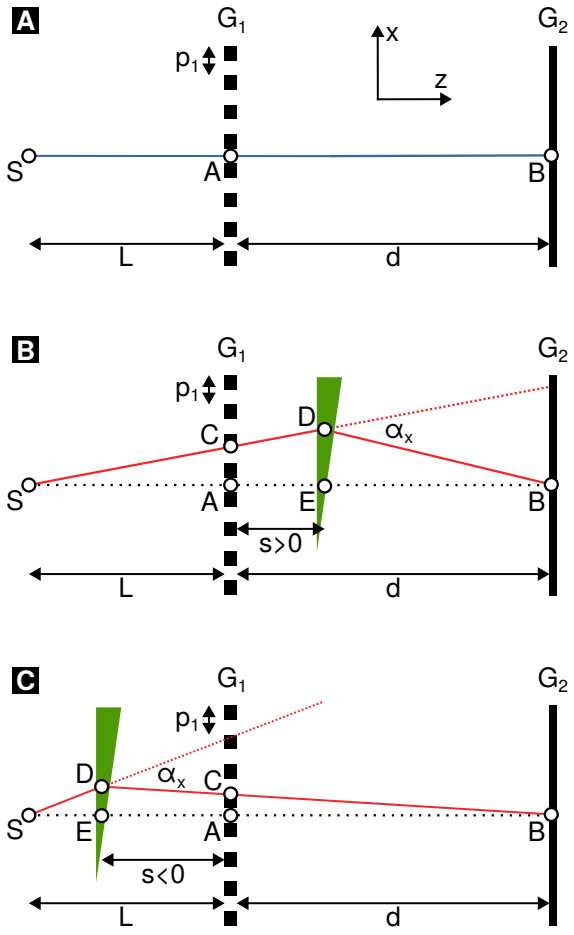

Figure 2.20: Ray optics-based derivation of phase sensitivity by Donath et al. [Dona+09] for a grating-based X-ray setup. (a): In the absence of an object, the source S projects the point A on the G_1 grating onto point B on the G_2 grating (or detector). (b): An object refracts incident radiation by the angle α_x. Intensity at B is now determined by the ray refracted at D. The location of D is given by s, L, d, and the condition that DB is at an angle α to SD. SD intersects the G_1 grating in point C. Since, instead of A, C is now mapped to B, the distance [AC] (in multiples of p_1) determines the phase shift (in multiples of 2π) of the fringe at B. (c): The construction is identical if the sample is placed upstream of G_1 ($s < 0$).

The imaging system's angular sensitivity can be defined as the ratio of the measurable quantity φ (normalized to 2π), and the sample property α_x. Combining this with Eqs. (2.56) and (2.57), we obtain

$$S = \frac{\varphi/(2\pi)}{\alpha_x} = \begin{cases} \frac{\eta}{p_1}\frac{L(d-s)}{L+d} & (s>0), \\ \frac{\eta}{p_1}\frac{d(L+s)}{L+d} & (s<0). \end{cases} \tag{2.58}$$

S is zero at both $s = -L$ (sample directly behind source, or G_0) and $s = d$ (sample directly before G_2). It increases linearly with s and reaches the maximum value $\eta dL/[p_1(L+d)]$ at $s = 0$. Thus, the placement of the sample has implications not only for its geometrical magnification, but also for the achievable amount of differential-phase contrast.

Using Eqs. (2.46) and (2.47), Eq. (2.58) can be simplified to:

$$\boxed{S = \begin{cases} (d-s)/p_2 & (s>0), \\ (d+s)/p_0 & (s<0). \end{cases}} \tag{2.59}$$

2.5.8c Small-angle scatter and dark-field

As shown by Pfeiffer et al. in [Pfei+08], an object's effect on its Talbot image may not always be expressed as a combination of attenuation and phase shift.

It was observed that some objects, such as bone, reduce the measured visibility, i.e. the ratio of fringe contrast and mean fringe intensity. This was attributed to a fluctuation of electron density (and thus, of refraction angles) on microscopic, sub-resolution length scales.

A ray incident on such an object is thus spread out into a narrow cone of radiation. This leads to a distortion of measured self-images, and usually a reduction of measured visibility.

Related effects had been examined quantitatively for propagation-based and analyzer-based phase contrast imaging [Nest08].

Following [Pfei+08], a number of works extended such quantitative analyses to grating-based phase contrast: Yashiro et al. examined the case where the sample was placed upstream of the G_1 grating ($s < 0$) [Yash+10]. Lynch et al. extended this to the sample-after-G_1 case ($s > 0$) [Lync+11]. Finally, Strobl highlighted the mathematical similarity between visibility reduction in grating-based X-ray dark-field imaging, and polarization in the *spin-echo small-angle neutron scattering* (SESANS) imaging technique [Stro14].

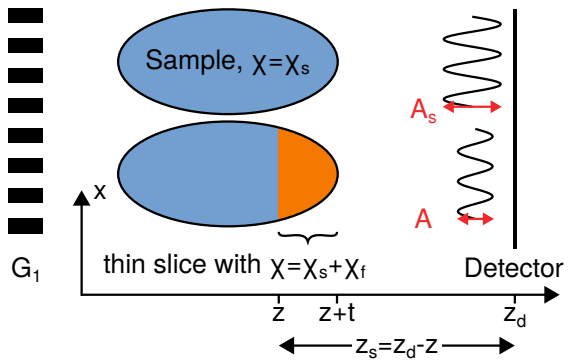

Figure 2.21: Approach by Lynch et al. [Lync+11] to determine the dark-field extinction coefficient: The effect of unresolvable, random fluctuations of the index of refraction (the "fine" part χ_f) in a thin sample slice at z leads to a decrease in the amplitude A of fringes measured at $z = z_d$.

Since some results from [Lync+11] demonstrate the relation between sample properties and measured quantities in an intuitive manner, the calculations are roughly reproduced here, slightly modified, and then discussed.

As in [Nest08; Yash+10], the index of refraction is separated into a "fine" and "smooth" part, i.e. low-frequency and high-frequency components, i.e.:

$$n = 1 + \chi,\ \chi = -\delta - i\beta = \chi_f + \chi_s.$$

The threshold between the two parts is determined by the setup's spatial resolution. Furthermore, the "fine" part is assumed to vary randomly as a function of position, i.e., is uncorrelated to the incident field. This allows simplification of some integrations later on. This step is also performed by [Nest08; Yash+10].

In the following, the impact of χ_f in a thin slice of an object on the observed fringe amplitude A is examined, which leads to an expression of the *dark-field extinction coefficient* (also called the *linear diffusion coefficient* [Bech+10]), the dark-field equivalent of the linear attenuation coefficient. This is illustrated in Fig. 2.21.

The sample slice (of thickness t) is introduced at a position z behind the G_1 grating. A number of approximations are made to justify that, if t is sufficiently small, an angular spectrum representation of the field incident on the slice may instead be replaced by a simple projection in z direction to calculate the phase shift Φ_f due to the fine part χ_f of the index of refraction:

$$\Phi_f(x,y,z) = k\int_0^t d\tau\, \chi_f(x,y,z+\tau). \tag{2.60}$$

Note that Eq. (2.60) includes fine fluctuations of phase shift as well as attenuation, compare e.g. Eq. (2.49) and (2.48) with $\mu = 2k\beta$. Φ_f determines the impact of χ_f on the field downstream of the thin slice:

$$U(x,y,z+t) = \exp\left[-i\Phi_f(x,y,z)\right] U_s(x,y,z+t), \tag{2.61}$$

with U_s being the field if χ_f were zero in the slice.

The amplitude of intensity fringes measured on the detector downstream is derived from $U(x,y,z)$ in three steps:

1. Fresnel propagation of the field U from the slice (z) to the detector (z_d), according to Eq. (2.14).
2. Calculation of intensity from the field at the detector: $I(x_d, y_d) = |U(x_d, y_d)|^2$.
3. Calculation of the fringe amplitude in x direction[13] as a Fourier component of $I(x_d, y_d)$:

$$A = 2\int_D dx_d\, dy_d\, I(x_d, y_d) \exp(-2\pi i x_d/p),$$

with p the fringe period and D the relevant detector area (i.e., one pixel).

These three steps are then combined to yield Eq. (36) in [Lync+11]:

$$A = \frac{2}{\Sigma}\iint_S dx\,dy\, U\left(x+\frac{\xi}{2}, y, z\right) U^*\left(x-\frac{\xi}{2}, y, z\right) \times \exp\left(\frac{-2\pi i x}{p}\right), \tag{2.62}$$

$$\xi = \lambda z_s/p = \lambda(z_d - z)/p, \tag{2.63}$$

where S is the xy plane immediately downstream of the thin slice, Σ is the area of integration, and $z_s = z - z_d$ is the sample-detector distance. This important finding can be interpreted as follows: The fields at every point pair $(x+\xi/2, y)$, $(x-\xi/2, y)$ interfere to produce a fringe component with pitch p in x direction in the detector plane, see Fig. 2.22b, c. Eq. (2.62) could be interpreted as a generalization of

[13] Compared to [Lync+11], we swap x and y coordinates to be consistent with the previous section (grating lines parallel to y).

the double-slit experiment, since the relation of the spacing ξ to the fringe period p is the same. The double-slit experiment would be reproduced e.g. by setting $U(x,y,z) = U_0[\delta(x-\xi/2)+\delta(x+\xi/2)]$ (a double-slit aperture), which then produces a single sinusoidal fringe (Fig. 2.22a).

The exponential term in Eq. (2.62) shows that the fringe from each point pair is phase-shifted shifted according to the x position of the center between the point pair. This can also be understood with the double-slit view: The x position of the central fringe where constructive superposition occurs is located in the middle between both slits.

In a grating-based setup, correlations between $U(x+\xi/2,y,z)$ and $U^*(x-\xi/2,y,z)$ are induced by the modulation grating G_1 and a source with sufficient transverse coherence length. Such correlations can be quantified by concepts from partial coherence theory such as the complex coherence factor or cross-spectral density. The relation of cross-spectral density to the image formation process in a Talbot-Lau setup is examined in section 6.2 on page 173.

Dark-field image contrast is then generated by reducing the degree of correlation between these two points. This is achieved by inducing a random amount of phase shift Φ_f at each of these points. This is quantified by substituting $U(x,y,z)$ in Eq. (2.62) with $U(x,y,z+t)$ as given in Eq. (2.61) , which yields

$$A = \frac{2}{\Sigma}\iint_S dx\,dy \exp\left[-i\Delta\Phi_\mathrm{f}(x,y,z)\right] \times U_\mathrm{s}\left(x+\frac{\xi}{2},y,z\right)U_\mathrm{s}^*\left(x-\frac{\xi}{2},y,z\right)\exp\left(\frac{-2\pi i x}{p}\right), \quad (2.64)$$

where

$$\begin{aligned}\Delta\Phi_\mathrm{f}(x,y,z) &= \Phi_\mathrm{f}\left(x+\xi/2,y,z\right)-\Phi_\mathrm{f}^*\left(x-\xi/2,y,z\right)\\ &= k\int_0^t d\tau\,\chi_\mathrm{f}\left(x+\xi/2,y,z+\tau\right)-\\ &\qquad k\int_0^t d\tau\,\chi_\mathrm{f}^*\left(x-\xi/2,y,z+\tau\right). \quad (2.65)\end{aligned}$$

The variation of the projected refractive index over the distance ξ in the x direction thus determines the thin slice's impact on fringe amplitude. Since $\Delta\Phi_\mathrm{f}$ becomes small with sufficiently small slice thickness t, the term $\exp[-i\Delta\Phi_\mathrm{f}]$ is replaced by its Taylor polynomial $1-i\Delta\Phi_\mathrm{f}-\frac{1}{2}\Delta\Phi_\mathrm{f}^2$. The assumption is then made

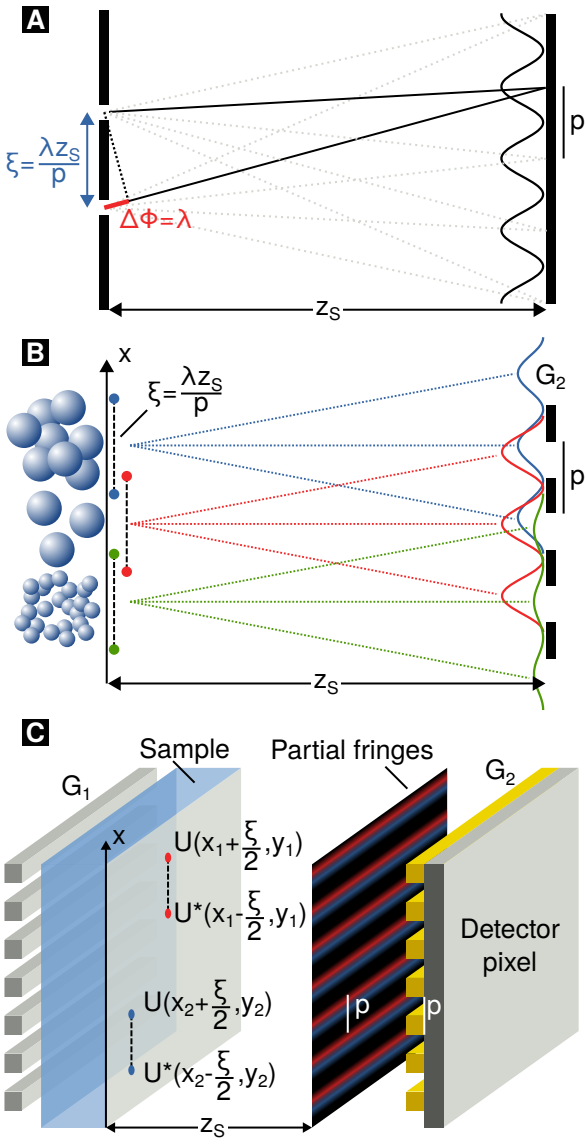

Figure 2.22: Origin of the "scattering length" $\xi = \lambda z_\mathrm{s}/p$ for X-ray dark-field measurements. (a): In the double-slit experiment with slit distance d, the period p of observed fringes is determined by the condition of constructive interference between the fields from both slits ($\Delta\Phi = n\lambda$). (b): In the plane behind the sample of a dark-field measurement, the fields at each point pair $(x-\xi/2,y)$ and $(x+\xi/2,y)$ interfere to create an intensity oscillation with period p. The total amplitude is calculated by integrating the oscillations from all (x,y). (c): Like (b), in perspective view. The individual fringes from each point pair (shown: blue, red) have variable phase and amplitude and their superposition is averaged over the pixel area.

that $\Delta\Phi_\mathrm{f}$—dependent only on χ_f—varies randomly, and independently from the rest of the integral in Eq. (2.64), which depends only on χ_s. The Taylor series terms can thus be extracted from the integral over S:

$$A \approx \left(1 - i\,\langle\Delta\Phi_\mathrm{f}\rangle_S - \frac{1}{2}\left\langle\Delta\Phi_\mathrm{f}^2\right\rangle_S\right) A_\mathrm{s}, \tag{2.66}$$

$$A_\mathrm{s} = \iint_S U_\mathrm{s}\left(x+\frac{\xi}{2}, y, z+t\right) U_\mathrm{s}^*\left(x-\frac{\xi}{2}, y, z+t\right) \times \exp\left(\frac{-2\pi i x}{p}\right) dx\,dy. \tag{2.67}$$

As χ_f was defined to have zero mean, $\langle\Delta\Phi_\mathrm{f}\rangle_S = 0$. However, this term could will be revisited in section 2.5.8e as it can be understood to describe refraction, and thus allows to relate ξ to the setup's angular sensitivity. On the other hand, $\langle\Delta\Phi_\mathrm{f}^2\rangle$ is then equal to the variance, i.e. the "randomness" of $\Delta\Phi_\mathrm{f}$ across the area S, which may be nonzero. It can be seen from Eq. (2.66) that, if $\langle\Delta\Phi_\mathrm{f}^2\rangle$ is found to be proportional to the slice thickness t, an exponential dependence of A on non-infinitesimal sample thickness will result by integration.

This proportionality is not explicitly shown by Lynch et al., but it can be demonstrated that it is plausible for normal-distributed values of χ_f: If the integral over χ_f is discretized, i.e.

$$\int_0^t d\tau\,\chi_\mathrm{f}(x,y,z) \to \sum_{j=0}^{N} \chi_{\mathrm{f},j},$$

and we assume that each $\chi_{\mathrm{f},j}$ is normally distributed with mean 0 and variance σ^2 (we neglect the imaginary part of χ), we find that $\Phi_\mathrm{f}(\xi/2) \equiv k\sum_{j=0}^{N}\chi_{\mathrm{f},j}(\xi/2,y,z)$ is also normally distributed with mean 0 and variance $Nk^2\sigma^2$. If $\Phi_\mathrm{f}(\xi/2)$ and $\Phi_\mathrm{f}(-\xi/2)$ are uncorrelated, the variance of $\Phi_\mathrm{f}(\xi/2) - \Phi_\mathrm{f}(-\xi/2)$ is $2Nk^2\sigma^2$ (and a zero-mean normal distribution). Finally, as $\Delta\Phi_\mathrm{f}^2 = [\Phi_\mathrm{f}(\xi/2) - \Phi_\mathrm{f}(-\xi/2)]^2$, it is equal to $2Nk^2\sigma^2\cdot\chi_1^2$ (χ_1^2 being a chi-square-distributed random variable, which has mean 1). Therefore,

$$\langle\Delta\Phi_\mathrm{f}^2\rangle = 2Nk^2\sigma^2,$$

which is proportional to N and thus to t. Introducing the quantity

$$C(\xi,z) \equiv \frac{\langle\Delta\Phi_\mathrm{f}^2\rangle_S}{2k^2 t}, \tag{2.68}$$

Eq. (2.66) is simplified to

$$A = \left[1 - k^2 C(\xi,z)\,t\right] A_\mathrm{s}. \tag{2.69}$$

The sample microstructure is therefore characterized by the quantity $C(\xi,z)$, separately from slice thickness and wavelength.

Finally, since interferometric visibility depends not only on the fringe amplitude A, but also mean intensity I, the decrease of the latter by the thin object slice must also be taken into account.

By interpreting I as $\lim_{p\to\infty} A = \lim_{\xi\to 0} A$, Lynch et al. reuse the result (2.69) and find that

$$I = \left[1 - k^2 C(0,z)\,t\right] I_\mathrm{s},$$

$$C(0,z) = \frac{2}{t}\left\langle\left[\int_0^t \beta_\mathrm{f}(x,y,z+\tau)d\tau\right]^2\right\rangle_S. \tag{2.70}$$

The term $k^2 t C(0,z)$ is the second-order Taylor polynomial of the Beer-Lambert attenuation factor $\exp[-2k\langle\int_0^t\beta_\mathrm{f}(\tau)d\tau\rangle_S]$. The first-order term is missing due to our definition of χ_f (zero mean). Unintuitively, $C(0,z)$ is not simply zero, even though $\langle\beta(x,y,z)\rangle_S$ is. This is because it constitutes a nonlinear dependence of amplitude reduction on $\Delta\Phi_\mathrm{s}$. $C(0,z)$ increases with the variance of β_f, but is realistically much smaller than $C(\xi,z)$ because only β_f contributes, which should usually be several orders of magnitude smaller than δ_f. However, it is useful as it is below combined with $C(\xi,z)$ to yield an autocorrelation expression:

Eqs. (2.69) and (2.70) can be combined to yield an expression for the change in visibility:

$$V = \frac{A}{I} \approx \left\{1 - k^2\left[C(\xi,z) - C(0,z)\right] t\right\}\frac{A_\mathrm{s}}{I_\mathrm{s}}. \tag{2.71}$$

The term $C(\xi,z) - C(0,z)$ can then be rearranged so that most summands cancel out:

$$\begin{aligned}
&k^2\left[C(\xi,z) - C(0,z)\right] = \\
&= \frac{1}{2t}\left\{\left\langle\left[\Phi_\mathrm{f}\left(x+\xi/2,y,z\right) - \Phi_\mathrm{f}^*\left(x-\xi/2,y,z\right)\right]^2\right\rangle_S - \right. \\
&\quad \left.\left\langle\left[\Phi_\mathrm{f}\left(x,y,z\right) - \Phi_\mathrm{f}^*\left(x,y,z\right)\right]^2\right\rangle_S\right\} \\
&= \frac{1}{t}\left\{\left\langle\Phi_\mathrm{f}\left(x,y,z\right)\Phi_\mathrm{f}^*\left(x,y,z\right)\right\rangle_S - \right. \\
&\quad \left.\left\langle\Phi_\mathrm{f}\left(x+\xi/2,y,z\right)\Phi_\mathrm{f}^*\left(x-\xi/2,y,z\right)\right\rangle_S\right\} \\
&= \frac{1}{t}\left\langle\left|\Phi_\mathrm{f}(x,y,z)\right|^2\right\rangle_S - \\
&\quad \frac{1}{t}\left\langle\Phi_\mathrm{f}(x+\xi/2,y,z)\Phi_\mathrm{f}^*(x-\xi/2,y,z)\right\rangle_S, \\
&\equiv R_{\Phi_\mathrm{f}}(0,0;z) - R_{\Phi_\mathrm{f}}(\xi,0;z).
\end{aligned}$$

with Φ_f as defined in Eq. (2.60). $R_{\Phi_\mathrm{f}}(a,b;z)$ is the autocorrelation function of Φ_f at a relative shift of (a,b) in (x,y) direction for a thin sample slice at z. Integration of Eq. (2.71) then yields

$$V = \exp\left[-\int_0^{z_\mathrm{max}} \mu_\mathrm{d}(z)\,dz\right] V_0, \tag{2.72}$$

with the *dark-field extinction coefficient*

$$\boxed{\mu_\mathrm{d}(z) = R_{\Phi_\mathrm{f}}(0,0;z) - R_{\Phi_\mathrm{f}}(\xi,0;z)\,,} \tag{2.73}$$

where

$$\xi = \lambda \frac{z_\mathrm{d} - z}{p},$$

as previously introduced in Eq. (2.63). Due to the occurrence of ξ in the autocorrelation function R_{Φ_f}, it is also called the *autocorrelation length*.

Note that, over the integration in Eq. (2.72), μ_d varies with z in two ways: Firstly, as the material composition or microstructure may change with z, the shape of $R_{\Phi_\mathrm{f}}(x,0;z)$ as a function of x may vary. Secondly, the sampled autocorrelation length ξ also changes with z, leading to variations of μ_d with z even for objects with constant microstructural parameters. However, since object thickness is usually far below $z_\mathrm{d} - z$, it is often sufficient to assume a constant value for ξ in the integration.

For the entire calculation, monochromatic illumination was assumed. However, the findings may be generalized to polychromatic illumination by decomposing the incident spectrum into a superposition of monochromatic lines of variable intensity, and calculating μ_d separately for each line. However, the calculation of polychromatic visibility from the monochromatic visibility spectrum may be more complicated, as it depends on relative lateral shifts of the monochromatic intensity fringes. One such approach is discussed in section 6.1.

2.5.8d Relation of μ_d to the normalized autocorrelation G and interpretation of R_{Φ_f}

The quantities in Eq. (2.73) can be related to a three-dimensional autocorrelation of χ_f, and thus the quantity $R_\rho(\vec{r}')$ in Eq. (2.21) as follows. Starting with the first term, $R_{\Phi_\mathrm{f}}(\xi,z)$, we swap the order of the xy- and $\tau_1\tau_2$-integrations:

$$\begin{aligned}
&R_{\Phi_\mathrm{f}}(\xi,0;z) = \\
&\quad \frac{1}{t}\left\langle \Phi_\mathrm{f}(x+\xi/2,y,z)\Phi_\mathrm{f}^*(x-\xi/2,y,z)\right\rangle_S \\
&\quad = \frac{k^2}{t}\left\langle \int_0^t d\tau_1 \chi_\mathrm{f}(x+\xi/2,y,z+\tau_1) \right. \\
&\qquad \left. \int_0^t d\tau_2 \chi_\mathrm{f}^*(x-\xi/2,y,z+\tau_2)\right\rangle_S \\
&\quad = \frac{k^2}{\Sigma t}\iint_S dx\,dy \int_0^t d\tau_1 \chi_\mathrm{f}(x+\xi/2,y,z+\tau_1) \\
&\qquad \int_0^t d\tau_2 \chi_\mathrm{f}^*(x-\xi/2,y,z+\tau_2) \\
&\quad = \frac{k^2}{t}\int_0^t d\tau_1 \int_0^t d\tau_2 \left\langle \chi_\mathrm{f}(x+\xi/2,y,z+\tau_1) \right. \\
&\qquad \left. \chi_\mathrm{f}^*(x-\xi/2,y,z+\tau_2)\right\rangle_S .
\end{aligned}$$

We can introduce the variable $\tau' = \tau_2 - \tau_1$ and thus rewrite the integration as

$$\begin{aligned}
R_{\Phi_\mathrm{f}}(\xi,0;z) = \frac{k^2}{t}\int_0^t d\tau_1 \int_{-\tau_1}^{t-\tau_1} d\tau' \\
\left\langle \chi_\mathrm{f}\left(x+\xi/2,y,z+\tau_1\right)\right. \\
\left. \chi_\mathrm{f}^*\left(x-\xi/2,y,z+\tau_1+\tau'\right)\right\rangle_S .
\end{aligned} \tag{2.74}$$

The integrand in Eq. (2.74) is the averaged autocorrelation of χ_f at a relative shift of $\xi\hat{e}_x + \tau'\hat{e}_z$. It is reasonable to assume for unordered materials that this value approaches zero with increasing magnitude of τ', i.e. the contribution to the integral becomes negligible for all τ' with a magnitude greater than some $\delta\tau'$. The τ' integration limits $[-\tau_1, t-\tau_1]$ can be replaced by $[-\delta\tau', \delta\tau']$ if

$$\delta\tau' < \tau_1 < t - \delta\tau'. \tag{2.75}$$

If we assume that $t \gg \delta\tau'$, i.e. the slice thickness is sufficiently greater than the z distance along which correlations of χ_f exist, the relative contribution of τ_1 values to the integral where Eq. (2.75) does not apply becomes negligibly small, and we can write

$$
\begin{aligned}
&R_{\Phi_\mathrm{f}}(\xi,0;z) \approx \\
&\quad \frac{k^2}{t}\int_0^t d\tau_1 \int_{-\delta\tau'}^{\delta\tau'} d\tau' \,\langle \chi_\mathrm{f}(x+\xi/2,y,z+\tau_1) \\
&\qquad \chi_\mathrm{f}^*(x-\xi/2,y,z+\tau_1+\tau')\rangle_S \\
&\quad = \frac{k^2}{t}\int_{-\delta\tau'}^{\delta\tau'} d\tau' \int_0^t d\tau_1 \,\langle \chi_\mathrm{f}(x+\xi/2,y,z+\tau_1) \\
&\qquad \chi_\mathrm{f}^*(x-\xi/2,y,z+\tau_1+\tau')\rangle_S \\
&\qquad = \frac{k^2}{\Sigma t}\int_{-\delta\tau'}^{\delta\tau'} d\tau' \int_0^t d\tau_1 \iint_S dx dy \\
&\quad \chi_\mathrm{f}(x+\xi/2,y,z+\tau_1)\chi_\mathrm{f}^*(x-\xi/2,y,z+\tau_1+\tau') \\
&= \frac{k^2}{V}\int_{-\delta\tau'}^{\delta\tau'} d\tau' \underbrace{\int_{\mathcal{V}} d^3\vec{r}\,\chi_\mathrm{f}\left(\vec{r}+\frac{\xi}{2}\hat{e}_x\right)\chi_\mathrm{f}^*\left(\vec{r}-\frac{\xi}{2}\hat{e}_x+\tau'\hat{e}_z\right)}_{R_{\chi_\mathrm{f}}([\xi,0,\tau'];z)},
\end{aligned}
\tag{2.76}
$$

where $\mathcal{V}$ is the volume (of content $V=\Sigma t$) of a slice at z. The calculation can be repeated equivalently for $R_{\Phi_\mathrm{f}}(0,0;z)$:

$$
R_{\Phi_\mathrm{f}}(0,0;z) = \frac{k^2}{V}\int_{-\delta\tau'}^{\delta\tau'} d\tau' \underbrace{\int_{\mathcal{V}} d^3\vec{r}\,\chi_\mathrm{f}(\vec{r})\,\chi_\mathrm{f}^*\left(\vec{r}+\tau'\hat{e}_z\right)}_{R_{\chi_\mathrm{f}}([0,0,\tau'];z)}.
\tag{2.77}
$$

The general three-dimensional (normalized) autocorrelation function of χ_f for a shift $\vec{r}\,'$ at a location $\vec{r}=[x,y,z]$ is [Ande+08]:

$$
\gamma(\vec{r}\,';z) \equiv \frac{R_{\chi_\mathrm{f}}(\vec{r}\,';z)}{R_{\chi_\mathrm{f}}(\vec{0};z)} = \frac{\int_{\mathcal{V}}\chi_\mathrm{f}(\vec{r})\chi_\mathrm{f}^*(\vec{r}+\vec{r}\,')\,d^3\vec{r}}{\int_{\mathcal{V}}\chi_\mathrm{f}(\vec{r})\chi_\mathrm{f}^*(\vec{r})\,d^3\vec{r}}.
$$

As in Eqs. (2.76) and (2.77), the volume $\mathcal{V}$ is understood to cover only a local area of the thin slice, e.g. the area covered by a single pixel. The denominator serves for normalization, so that $\gamma(\vec{0})=1$ for any $\mathcal{V}$. We can then calculate a projection of $\gamma(\vec{r}\,';z)$ along the z axis:

$$
\begin{aligned}
G(x,y;z) &\equiv \frac{\int d\tau'\,\gamma([x,y,\tau'];z)}{\int d\tau'\,\gamma([0,0,\tau'];z)} \\
&= \frac{\int d\tau'\,R_{\chi_\mathrm{f}}([x,y,\tau'];z)}{\int d\tau'\,R_{\chi_\mathrm{f}}([0,0,\tau'];z)} \\
&= \frac{\int d\tau' \int_{\mathcal{V}}\chi_\mathrm{f}(\vec{r})\chi_\mathrm{f}^*(\vec{r}+x\hat{e}_x+y\hat{e}_y+\tau'\hat{e}_z)\,d^3\vec{r}}{\int d\tau' \int_{\mathcal{V}}\chi_\mathrm{f}(\vec{r})\chi_\mathrm{f}^*(\vec{r}+\tau'\hat{e}_z)\,d^3\vec{r}}.
\end{aligned}
\tag{2.78}
$$

G is also normalized so that $G(0,0)=1$. Comparing Eq. (2.78) with Eqs. (2.76) and (2.77), we find that

$$
G(\xi,0;z) = \frac{R_{\Phi_\mathrm{f}}(\xi,0;z)}{R_{\Phi_\mathrm{f}}(0,0;z)},
$$

where we have generalized the second argument of R_{Φ_f} to an arbitrary location $\vec{r}$. Equivalently, the DFEC is

$$
\begin{aligned}
\mu_\mathrm{d}(z) &= R_{\Phi_\mathrm{f}}(0,0;z) - R_{\Phi_\mathrm{f}}(\xi,0;z) \\
&\boxed{= R_{\Phi_\mathrm{f}}(0,0;z)\,[1-G(\xi,0;z)]\,.}
\end{aligned}
\tag{2.79}
$$

As presented in [Ande+08], G can be directly related to the geometry of the microstructure: Thanks to the normalization, the amount of contrast between different phases in the material—e.g., air and tissue—does not affect the shape or value of $G(\xi,0;z)$.

The energy-dependence of the leading factor $R_{\Phi_\mathrm{f}}(0,0;z)$ can be analyzed if we assume that fluctuations β_f in the imaginary part of χ_f are negligible, i.e that

$$
\chi_\mathrm{f} = -\delta_\mathrm{f} = \frac{-r_0\lambda^2\nu_\mathrm{f}}{2\pi}.
$$

Here, we have also neglected the resonant scattering term f', and define ν_f as the component of electron density leading to δ_f. Equivalently to χ_f, ν_f has zero mean and contains only the high spatial frequencies of ν. Then,

$$
\begin{aligned}
R_{\Phi_\mathrm{f}}(0,0;z) &= \frac{k^2}{t}\left\langle\left|\int_0^t d\tau\,\chi_\mathrm{f}(\vec{r}+\tau\hat{e}_z)\right|^2\right\rangle_S \\
&= \frac{k^2}{V}\int_{-\delta\tau'}^{\delta\tau'} d\tau'\,R_{\chi_\mathrm{f}}([0,0,\tau'];z) \\
&= \frac{k^2}{V}\left(\frac{r_0\lambda^2}{2\pi}\right)^2\int_{-\delta\tau'}^{\delta\tau'} d\tau'\,R_{\nu_\mathrm{f}}([0,0,\tau'];z) \\
&= \frac{r_0^2\lambda^2}{V}\int_{-\delta\tau'}^{\delta\tau'} d\tau'\,R_{\nu_\mathrm{f}}([0,0,\tau'];z).
\end{aligned}
\tag{2.80}
$$

This shows that R_{Φ_f} scales with λ^2. However, since G also depends on λ via ξ, the full dependence of $\mu_\mathrm{d}(z)$ on wavelength is also dependent on particle shape.

Note that $R_{\Phi_\mathrm{f}}(0,0;z)$ can be related to the differential scattering cross-section due to the "fine" fluctuations in electron density.

Eq. (2.21) illustrates the relation between the autocorrelation function of charge density ρ with the differen-

tial scattering cross-section:

$$R_\rho(\vec{r}) = \frac{e^2}{r_0^2}\mathscr{F}^{-1}\left[\frac{d\sigma_{\text{coh}}}{d\Omega}\right] = \frac{e^2}{r_0^2}\frac{1}{(2\pi)^3}\int d^3\vec{q}\,\frac{d\sigma_{\text{coh}}}{d\Omega}(\vec{q})e^{-i\vec{q}\vec{r}}.$$

Since $\rho = e\nu$, $R_\nu(\vec{r}) = R_\rho(\vec{r})/e^2$,

$$R_\nu([0,0,\tau']) = \frac{1}{(2\pi)^3 r_0^2}\int d^3\vec{q}\,\frac{d\sigma_{\text{coh}}}{d\Omega}(\vec{q})e^{-iq_z\tau'},$$

and therefore, with Eq. (2.80),

$$\begin{aligned} R_{\Phi_\text{f}}(0,0;z) &= \frac{r_0^2\lambda^2}{V}\int_{-\delta\tau'}^{\delta\tau'} d\tau'\, R_{\nu_f}([0,0,\tau'];z) \\ &= \frac{\lambda^2}{V(2\pi)^3}\int d^3\vec{q}\,\frac{d\sigma_{\text{coh},f}}{d\Omega}(\vec{q})\underbrace{\int_{-\delta\tau'}^{\delta\tau'} d\tau'\, e^{-iq_z\tau'}}_{2\pi\delta(q_z)} \\ &= \frac{\lambda^2}{V(2\pi)^2}\iint dq_x dq_y \frac{d\sigma_{\text{coh},f}}{d\Omega}(q_x,q_y,0), \\ &= \frac{1}{V}\underbrace{\frac{1}{k^2}\iint dq_x dq_y \frac{d\sigma_{\text{coh},f}}{d\Omega}(q_x,q_y,0)}_{\equiv\,\sigma_{\text{coh},f}}. \end{aligned} \tag{2.81}$$

where $d\sigma_{\text{coh},f}/d\Omega$ is the coherent differential cross-section due to the "fine" part of electron density ρ_f. The term $\sigma_{\text{coh},f}$ in Eq. (2.81) could be interpreted as a total cross-section (q_z must be zero for elastic scattering in the small-angle approximation), but is distinct from the total cross-section of coherent scatter, since only the "fine" parts of electron density variations contribute. It thus depends not only on elemental composition, but also on the microstructure of the sample.

For the example of dilute, monodisperse, homogeneous spheres with radius R, occupying a fraction ϕ of the total volume V, it can be written as $\sigma_{\text{coh},f} = \frac{3}{2}k^2\phi V|\Delta\chi|^2 R$. Here, $\Delta\chi$ is the difference in refractive index between the spheres and the surrounding material. The quantity $\sigma_{\text{coh},f}$ has been described as the *scattering probability per unit length of thickness* [Bouw+02, Eq. 3], although in terms of units, this would be more applicable to the quantity $R_{\Phi_f} = \sigma_{\text{coh},f}/V$ in Eq. (2.81).

2.5.8e Relation between angular sensitivity S and autocorrelation length ξ

The Taylor-approximated equation for the calculation of fringe amplitude in Eq. (2.66) can also be solved to derive the fringe shift induced by a refracting, non-scattering sample. This has the added benefit of delivering a relation between the autocorrelation length ξ from Eq. (2.63) and the angular sensitivity S in Eq. (2.58), which was derived from ray-optics arguments.

Assuming the presence of a thin "wedge" in the interval between z and $z+t$ in Fig. 2.21, and an absence of random, unresolvable variations of χ, we can instead interpret χ_s as the phase shift induced by this wedge. Thus, in Eq. (2.66), $\langle\Delta\Phi_\text{f}^2\rangle_S = 0$. In order to calculate the linear term $\langle\Delta\Phi_\text{f}\rangle_S$, we first determine that

$$\Phi_\text{f}\left(x+\frac{\xi}{2},y,z\right) \approx \Phi_\text{f}\left(x-\frac{\xi}{2},y,z\right) + \xi\cdot\frac{\partial\Phi_\text{f}}{\partial x}\left(x-\frac{\xi}{2},y,z\right) \tag{2.82}$$

(which is exact if Φ_f really is due to a wedge, i.e. changes linearly with x). Further, if an imaginary part of χ_f is negligibly small, we can write

$$\begin{aligned} \Delta\Phi_\text{f} &\equiv \Phi_\text{f}\left(x+\xi/2,y,z\right) - \Phi_\text{f}^*\left(x-\xi/2,y,z\right) \\ &= \Phi_\text{f}\left(x+\xi/2,y,z\right) - \Phi_\text{f}\left(x-\xi/2,y,z\right) \\ &\overset{(2.82)}{=} \xi\cdot\frac{\partial\Phi_\text{f}}{\partial x}\left(x-\frac{\xi}{2},y,z\right). \end{aligned}$$

By comparison of Eq. (2.60) with Eq. (2.52), we find that

$$\frac{\partial\Phi_\text{f}}{\partial x}(x,y,z) = k\frac{\partial}{\partial x}\int_0^t d\tau\,\chi_\text{f}(x,y,z+\tau) = k\alpha_x.$$

Therefore, $\Delta\Phi_\text{f} = k\alpha_x\xi$. Assuming that the area of the wedge is larger than a pixel, $\langle\Delta\Phi_\text{f}\rangle_S = \Delta\Phi_\text{f} = k\alpha_x\xi$, and Eq. (2.66) then becomes

$$A \approx (1 - ik\alpha_x\xi)\,A_\text{s} \overset{k\alpha_x\xi\ll 1}{\approx} \exp(-ik\alpha_x\xi)\,A_\text{s}.$$

Thus, the phase shift introduced to the fringes is

$$\varphi = k\alpha_x\xi.$$

Together with the definition of angular sensitivity from Eq. (2.58), this leads to the relation

$$\boxed{S = \frac{\varphi/(2\pi)}{\alpha_x} = \frac{\xi}{\lambda}.} \tag{2.83}$$

Chapter 3

Fringe-scanning setup for large-FOV dark-field radiography

When a grid's misaligned
with another behind
That's a moiré ...

Randall Munroe, *Color Pattern*
https://xkcd.com/1814

Contents

In this chapter, the design and realization of an X-ray imaging setup for grating-based dark-field radiography of large objects (hereafter referred to as the "*lung-scanning setup*") are presented. The motivation for the construction of such a setup is presented in section 3.1. Important design choices are discussed in section 3.2. Technical details of the most important components are summarized in section 3.3, and their interplay in the full setup is shown in section 3.4, together with an overview of the scanning procedure itself.

Design and construction of this device, as well as the optimization of acquisition parameters are the main subject of the Ph.D. thesis of L. B. Gromann [Grom17]. Furthermore, the functionality and design parameters of the setup have been published in a number of publications [Grom+17; Hell+18a; Saut+19; Fing+19].

3.1 Motivation and history

3.1.1 X-ray phase contrast and dark-field

Methods to image not only attenuation, but also the phase shift of incident X-rays have been developed since at least 1965 (cf. section 1.5 on page 20). With

many of these techniques, it was found that the refraction of X-rays by specimens can provide significant contrast even for nearly transparent objects. The contrast advantage of X-ray phase-contrast imaging methods compared to conventional X-ray is especially high for specimens composed of light elements, i.e., elements with low atomic numbers.

This is the case for most biological materials: The vast majority of biological tissues is primarily composed of oxygen, hydrogen, carbon, and nitrogen. Additionally, adjacent tissues in biological organisms typically have similar elemental compositions. X-ray phase-contrast imaging techniques were found to be especially suitable for imaging of biological tissues, e.g., in microscopy or medical applications [Brav+13].

Beyond imaging phase shifts or refraction angles, it was observed that the visibility of moiré patterns produced by grating-based Talbot-Lau X-ray interferometry (i.e., the pattern's modulation amplitude, normalized with its mean intensity, see section 2.5.6 on page 56) is reduced when introducing certain types of specimen in the beam [Pfei+08]. It was found that this effect arises from small-angle scattering or multiple refraction of X-rays with the sample, and is thus especially prominent for specimens containing a large number of interfaces. The ratio of visibility reduction by the specimen was named "X-ray dark-field" (derived from the dark-field mode of Zernike microscopy, cf. section 1.3.3 on page 17). Later on, other phase-contrast imaging methods were adapted to provide similar information [Beru+12; Endr+14].

Unlike phase contrast, the relation of the X-ray dark-field signal to physical quantities of the specimen is complicated: The salient variable is the autocorrelation function of the sample's electron density, evaluated at a point (the autocorrelation length) determined by parameters of the imaging setup (cf. section 2.5.8c on page 62). In a dark-field projection image, the resulting quantity is integrated along the length of the X-ray path through the sample. Qualitatively speaking, such an image thus quantifies the "amount of coherent scatter" of incident X-rays by the specimen.

3.1.2 Dark-field radiography of the lung

It was recognized that this method of signal generation could be used for medical pulmonary imaging:

Using a Talbot interferometer at an inverse Compton scattering X-ray source, a device with synchrotron-like radiation quality, phase-contrast and dark-field radiographs of *ex situ* healthy and emphysematous mouse lungs were acquired, and a discriminability between the two groups by joint analysis of dark-field and transmission signals was demonstrated [Schl+12]. Furthermore, a small-animal CT device including a Talbot-Lau grating interferometer was developed (SkyScan, Bruker microCT, Kontich, Belgium) in order to evaluate the potential of grating-based X-ray phase contrast and dark-field imaging for medical applications. In a seminal work, the first *in vivo* X-ray phase-contrast and dark-field radiographs of a mouse were acquired with this device [Bech+13]. It was shown that a significant amount of X-ray dark-field signal is generated by the animal's lungs.

This is not surprising considering the microstructural composition of the lung: To enable efficient gas exchange (uptake of oxygen and release of carbon dioxide by the bloodstream), a large surface area between blood vessels and air is required. In the mammalian lung, this is achieved by a very large number of *alveoli*, microscopic air-filled cavities which are connected to the trachea via a branching, hierarchical network of airways. A number of capillaries surrounds each *alveolus* and gas exchange takes place with the alveoli's interior, across the alveolar membranes. X-rays traversing the thorax thus encounter a large number of interfaces between soft tissue and air, which results in repeated refraction and diffraction, and therefore, a reduction of measured visibility.

These findings motivated a series of *in vivo* and *ex vivo* small-animal studies evaluating the method for the detection of many pulmonary pathologies, especially structural lung diseases. The latter affect the composition of the lung at the alveolar length scale and are often irreversible. Among these, studies found benefits of X-ray dark-field imaging for emphysema [Mein+13; Yaro+13; Mein+14b; Hell+15], fibrosis [Velr+15; Yaro+15; Hell+17], and neonatal lung injury [Yaro+16]. Furthermore, X-ray dark-field was found to improve the diagnosis of pneumothorax [Hell+16] and lung cancer [Sche+17].

3.1.3 Limitations for clinical translation

With these findings, a logical next step was to translate the imaging technique to a pre-clinical prototype, i.e. a device capable of acquiring dark-field radiographs of

the human thorax. However, this goal is impeded by a number of technological requirements:

Firstly, the field of view (FOV), i.e., the area of the usable radiation field in a plane orthogonal to the beam, that is achievable with a conventional acquisition technique is limited by the size of the employed gratings. In particular, the analyzer grating (G_2) is located near the detector and must therefore have an area equal to the object's cross sectional area, magnified to the detector plane. In conventional thorax radiography setups, detectors with a size of at least 43 cm × 35 cm are used to cover the entire lung [Kott+02]. To augment such a setup with a Talbot-Lau interferometer, an analyzer grating of similar size would be required.

Secondly, the setup length scales with the squared period of the modulating grating (cf. section 2.5.2). This period (and, by extension, the period of all three gratings) must therefore be very low to allow reasonably short setup lengths. Finally, high visibility, and thus good performance of a Talbot-Lau setup is strongly dependent on the attenuation capabilities of both source and analyzer gratings.

The dose efficiency of X-ray imaging is in large part dictated by the transmittance of the imaged object: The achieved image quality is a function of the radiation dose transmitted by the sample, whereas (roughly speaking) the dose delivered to the object is given by the difference of incident and transmitted radiation.

The attenuation CNR of low-contrast objects, normalized to the square root of patient dose, is highest for a transmittance of $T \approx 20\%$ (cf. Appendix A on page 223). For large objects such as a human thorax, this is achieved at high tube voltages between 70 and 150 kV, far higher than those used for small-animal imaging. The attenuating power of the grating materials is far lower for such high X-ray energies, and greater amounts of absorbing material (and thus, larger grating heights) are required to achieve the same interferometric visibility. This is at odds with the required low periods: The demands for a grating's *aspect ratio*, i.e., the ratio of grating height and period are much higher for high X-ray energies. Only few methods such as the LIGA process can reliably produce such gratings. Even with this process however, the difficulty of grating fabrication sharply increases for high aspect ratios (cf. section 3.2.2).

In summary, a Talbot-Lau X-ray imaging setup requires a large-area analyzer grating with a high aspect ratio, which would be prohibitively expensive and time-consuming to manufacture. An alternative approach is therefore necessary.

3.2 Design concept

This section introduces the most important design features of the *lung-scanning setup*, focusing on three salient points. Section 3.2.1 introduces the measurement technique of *fringe scanning*. Different fringe scanning implementations are compared and their respective advantages are established, motivating the approach used in the setup. The method used for fabrication of the gratings and the motivations for their arrangement in the setup are introduced in section 3.2.2. Finally, section 3.2.3 presents the demands to the imaging hardware, i.e., the X-ray source and detector, for the setup's purpose.

3.2.1 Fringe scanning

The most common method to acquire imaging data with a Talbot- or Talbot-Lau imaging setup is so-called *phase stepping* (cf. section 2.5.6 on page 56): The fringe pattern is analyzed at different relative phases of the fringe pattern and the analyzer grating, by laterally displacing any one of the three gratings. The intensity measured in this way typically has a sinusoidal dependence on shift position, and the three image modalities are encoded in the change of this sinusoidal "stepping curve" when introducing an object: attenuation leads to an overall intensity reduction of the curve, refraction leads to a lateral shift, and small-angle scatter (dark-field) reduces the amplitude of the sinusoidal variation, relative to the curve's mean intensity (cf. Fig. 2.17 on page 57).

These three effects can be quantified by regression of a sinusoidal model function to the measured stepping curve data, or, if phase stepping was performed in equidistant steps over an integer number of periods, by calculating the discrete Fourier transform of the data. Since three values are to be extracted from each pixel, phase stepping must be performed with at least three phase steps in order to yield a unique solution.

As an alternative to phase stepping, a scanning approach has been presented by Kottler et al. [Kott+07]. This approach exploits the fact that a relative displacement between the fringe pattern and the analyzer grating can also be induced by a deliberate "detuning" of

the grating arrangement, i.e., a deviation from the ideal relation of grating periods and inter-grating distances. This leads to a spatial variation of the relative phases of the fringe pattern and the transmission function of the analyzer grating, which results in *moiré fringes*, i.e. a beat pattern of the two periodic functions (Fig. 3.1a). Due to its high sensitivity to small displacements, this effect is commonly observed in grating-based X-ray imaging, even when it is not deliberately introduced.

As explained e.g. in [Chab11, ch. 7], different manipulations of grating position and rotation result in various types of moiré patterns. In particular, displacement of a grating along, or its rotation around the optical axis, results in the formation of linear moiré fringes with a constant period. This means that, if the "crests" of the moiré fringes are parallel e.g. to the x direction, the relative phase of fringe pattern and analyzer grating (i.e., the origin of these fringes) changes linearly with the y coordinate.

The key concept of *fringe scanning* is to replace a microscopic displacement of a single grating by a larger displacement between sample and interferometer: Laterally moving the object to a different location, i.e., a different phase of the moiré pattern, is equivalent to a phase step, if the moiré pattern is sufficiently regular. A full phase-stepping measurement can thus be replaced by continuously moving the object over one full period of the moiré pattern, while intensity is measured at regular intervals (Fig. 3.1b).

This approach has multiple practical advantages: firstly, it eliminates the demand for micron-accuracy, motor-driven grating positioning. Furthermore, since the relative locations of the gratings remain fixed, they may be integrated into a rigid frame, which decreases the setup's sensitivity to mechanical vibration. Finally, fringe-scanning acquisition allows much faster measurement of objects larger than the FOV: as the sample can be moved continuously, no time is lost for sample or grating repositioning.

On the other hand, acquisition during sample movement introduces motion blur, which limits the resolution, depending on movement speed and exposure time per frame. Secondly, acquired data must be shifted so that successive image frames are co-registered. This may necessitate the use of spatial interpolation, which can also lead to a decrease in resolution.

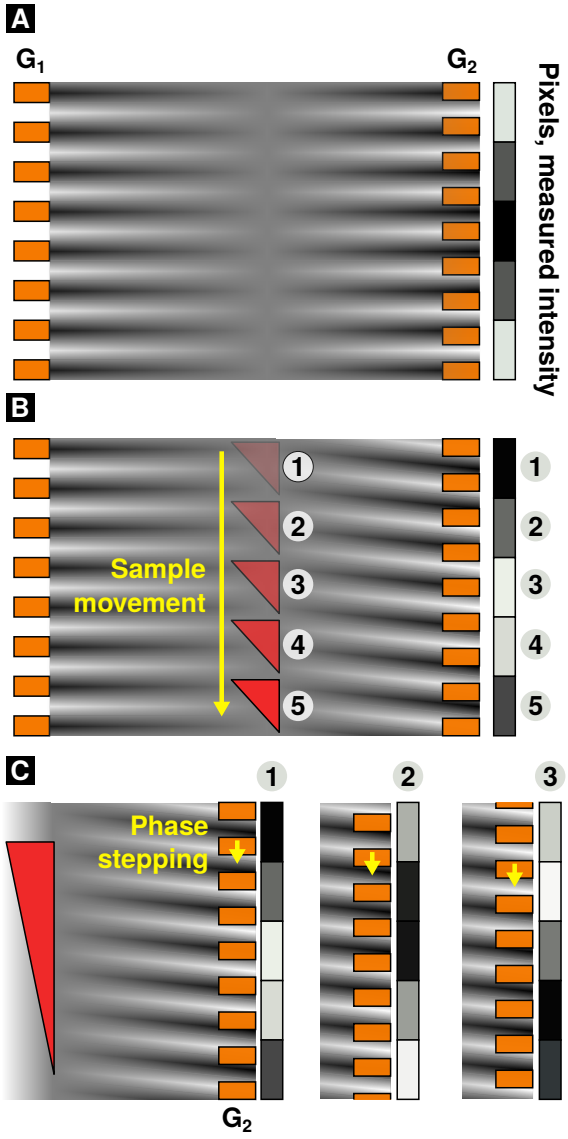

Figure 3.1: Comparison of fringe scanning and phase stepping. (a): Detuning of the interferometer results in the detection of moiré fringes (variation of pixel intensity, right) due to a local phase variation between fringe pattern and G_2 grating. (b): In *fringe scanning*, illumination of a sample feature with different relative fringe-to-G_2 phases is achieved by moving the sample over at least one full period of the moiré pattern. Sample information is retrieved from data acquired at different times and locations ①–⑤. (c): In *phase stepping*, the variation of fringe-to-G_2 phase is instead achieved by measurement at different lateral displacements of one grating (here, G_2: ①–③) and combining data from identical locations.

Fringe-scanning geometries Although a fringe-scanning acquisition must provide relative movement between the moiré pattern and the object, this can be achieved in different ways. While the object may be moved past a stationary interferometer (Fig. 3.2a), a fixed object and mobile interferometer are also possible. This approach may be more practical if the sample is heavy or deforms under movement / acceleration.

However, a linear translation of the interferometer is only feasible if the source is moved with it. This is undesirable due to the significant weight of the tube. Furthermore, rotating-anode tubes may be sources of significant mechanical vibration, which limits the possibility to mechanically connect (and thus jointly move) source and interferometer.

Finally, in a geometry with cone-beam illumination, *linear* scanning movements cause the direction of projection through the object to change over the course of the scan. This results in a slightly different perspective in each frame, similar to a limited-angle tomography (see Fig. 3.2a). On reconstruction of image data, this effect is confounded with the phase modulation from the moiré pattern, which may lead to artifacts.

One alternative is to *rotate* the interferometer around the source's focal spot (Fig. 3.2b, c). This eliminates the need for source movement, and also has the advantage that no variations in projection perspective occur for the same features.

Since the sample is stationary, and all projection rays originate at the focal spot, no rays intersect anywhere else and each location in the sample is thus uniquely mapped to one single projection ray. All measured projection frames in this geometry are thus geometrically consistent. As the interferometer rotates, a different subset of all rays is measured (determined by the interferometer FOV), and each ray is measured multiple times, with different phases of the moiré pattern.

In addition to sample or interferometer, the detector may also be moved during the scan. For a geometry with a mobile interferometer, a stationary detector must cover the entire FOV, while the area of a detector moving with the interferometer can be restricted to the interferometer FOV, as shown in Fig. 3.2c. The latter approach has been successfully demonstrated in [Koeh+15] by modification of a commercial mammographic scanning system.

Note that, among the three designs shown in Fig. 3.2, only the "rotating interferometer, fixed detector" approach in Fig. 3.2b produces spatially co-registered images, as the mapping of pixels $(1, \ldots, 5)$ and rays $(a, \ldots, e)$ is unique at all times.

Fringe-scanning geometry for the *lung-scanning setup* The "fixed detector" geometry in Fig. 3.2b was selected for the *lung-scanning setup*, as it was designed for dark-field radiography of large animals. The critical factors in favor of this geometry are that it prevents the aforementioned projection inconsistencies, while also being compatible with conventional, large-area flat-panel detectors.

The magnitude of projection inconsistencies in the "moving sample" geometry increases with sample thickness. This geometry is thus appropriate e.g. for non-destructive testing applications of thin objects, and could even be integrated into an assembly line for continuous use, as demonstrated in [Bach+17]. For the significant height of a porcine or human thorax however, a higher magnitude of artifacts is to be expected, and continuous sample throughput is less relevant for medical applications.

Although the setup with "moving detector" geometry in [Koeh+15] was also designed on the basis of medical X-ray imaging hardware, the limited width of the built-in detector prohibits its use for a thorax radiography setup. Flat-panel detectors used for general radiography, on the other hand, feature fields of view beyond 40 cm × 40 cm, which is sufficient even if the detector is not moved with the interferometer.

Due to the setup's intended use on pigs, a vertical beam geometry was chosen, with the X-ray tube mounted on the ceiling of the experimental hutch, and the detector being placed on the floor. The animals were to be placed on a horizontal table at a moderate height above the ground.

3.2.2 Grating manufacturing and design of the grating assembly

The LIGA method One of the most suitable techniques for the fabrication of low-period gratings which strongly attenuate X-rays is the so-called (X-ray) LIGA process (*Lithographie, Galvanik und Abformung*, German for "lithography, electroplating, and molding") [Bach+95; Mohr+12]. In this method, a substrate covered by a layer of photoresist polymer is covered by a "mask", i.e., a template of the grating structure (produced e.g. by electron-beam lithography) and exposed

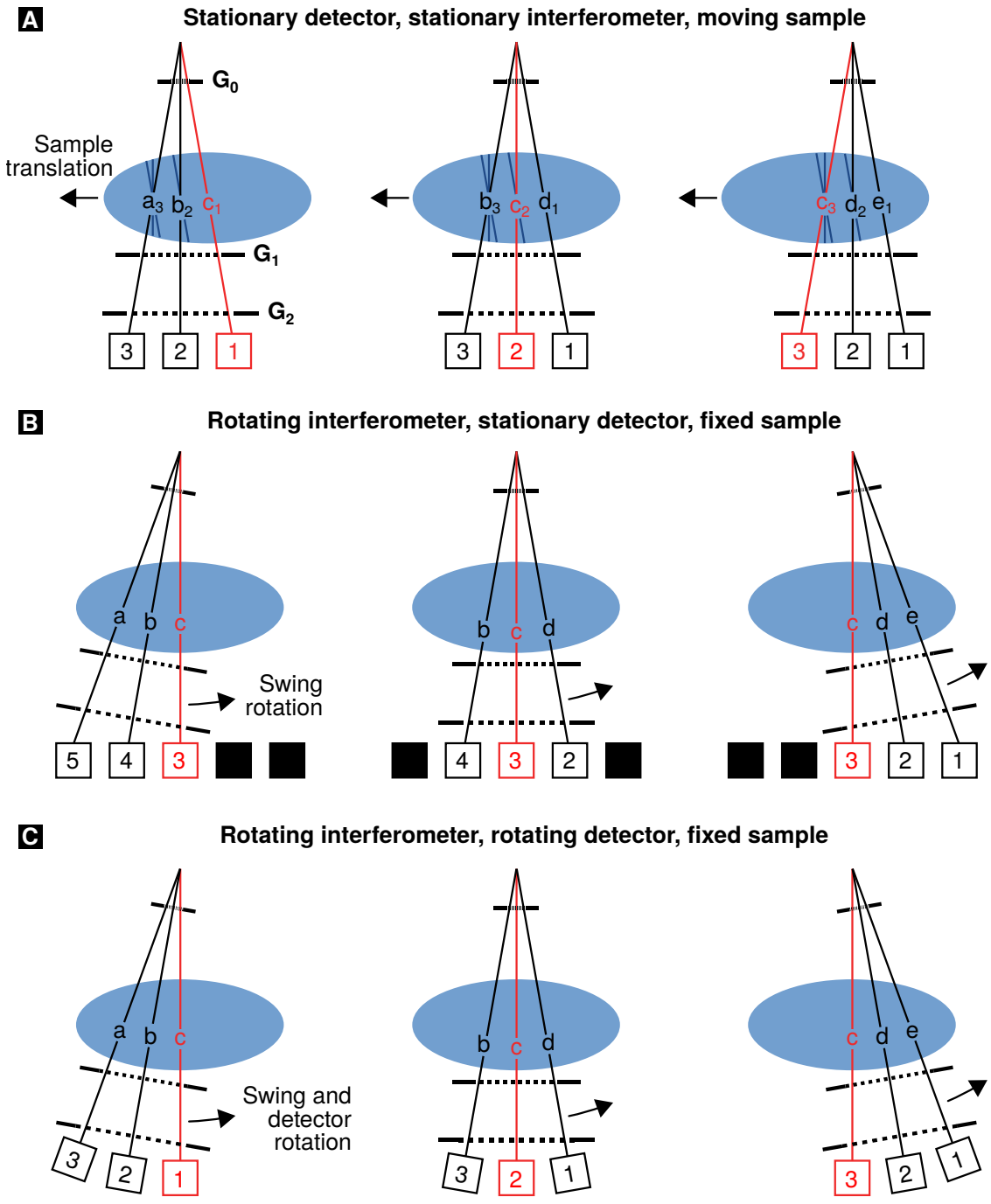

Figure 3.2: Moiré fringe sampling by different fringe-scanning arrangements. Left, middle and right show subsequently recorded frames. X-ray paths through the object are indicated by letters, pixels by numbers. Ray and pixel associated with a feature in the middle of the sample are highlighted in red. (a): Linear translation of the sample (blue oval). (b): Rotation of interferometer around focal spot, stationary detector. (c): Rotation of interferometer and detector around focal spot. Note that the arrangement in (a) produces projections at different angles (e.g.: c_1, c_2, c_3), whereas this does not occur at all in (b), and can be avoided in (c) for well-chosen step sizes. Figure design adapted from [Koeh+15].

to a well-defined dose of X-rays, which induces chemical changes in the regions of resist not obscured by the mask. Depending on the photoresist material, these chemical changes may include cross-linking (and thus solidification) of the polymer, or heat treatment may additionally be necessary to induce the cross-linking process [Mohr+12].

The height of the photoresist layer must be considerable (hundreds of microns), as it limits the height of the final grating. The exposure step is thus classified as a "deep X-ray lithography" process. A key challenge in this step is to achieve a sufficient dose at greater depths in the photoresist, while avoiding overexposure near the surface, as well as an unwanted development of resist due to secondary radiation within the material, or radiation transmitted by the mask [Mohr+12].

The undeveloped resist is then removed, leaving a negative photoresist "image" of the mask pattern on the substrate. (Positive photoresists, which are initially solid and dissolved by exposure to X-rays, can also be used.) Subsequently, the created gaps in the resist pattern are filled with metal (often gold or nickel) in an electroplating process. For this, the substrate must be electrically conductive. In a final step, the unexposed resist between the created gold structures may be removed ("stripped").

The ratio of lamella height and width is called the *aspect ratio*. As low grating periods (narrow lamellae) are required to achieve high angular sensitivity, while high absorption contrast (i.e., tall lamellae) in the analyzer grating are necessary for high visibility and short setup lengths (the Talbot distance is proportional to p_1^2), the achievable aspect ratio is the pivotal technical parameter determining the performance of Talbot- and Talbot-Lau setups. The LIGA approach allows the production of micron-scale gold structures with aspect ratios around 100, significantly higher than those achievable by other fabrication techniques [Mohr+12]. Since high-aspect-ratio gold structures are susceptible to deformation, they tend to stick to each other, requiring the introduction of stabilizing "bridge" structures.

The LIGA method is expensive as it typically requires access to a synchrotron beamline, and is highly sensitive to variations in process parameters. Therefore, experimentation with these parameters is typically necessary to manufacture high-quality LIGA gratings for a desired set of design parameters. Additionally, the maximum area of a single grating is limited by the radiation field achieved by the (synchrotron) X-ray source – typically, a circular area with a diameter of 5 to 7 cm.

Gratings for the *lung-scanning setup* The FOV of a conventional Talbot-Lau setup is determined by the area of the analyzer grating (G_2) and the detector. The limited size of individual LIGA-manufactured gratings can be overcome by removing the edge regions of the substrate, leaving only the rectangular grating area, and tiling multiple gratings side by side. Since the *lung-scanning setup* was required to have a sample FOV in the vicinity of 35 cm × 35 cm, an extraordinary amount of grating tiles would be required to assemble an analyzer grating of adequate area. With a fringe-scanning approach however, the grating area requirement can be greatly reduced in the scan direction, meaning that one-dimensional tiling (orthogonal to the scan direction) is sufficient.

An unusual design was chosen for the initial grating arrangement: Instead of using a phase-modulating G_1 grating and placing the analyzer grating in a fractional Talbot distance for the design energy, an intensity-modulating G_1 grating was to be placed downstream of the sample, with the $G_1 - G_2$ distance far below the distance for the first self-image (as described in [Huan+09]). Since propagation effects at these short distances are minor, the shadow of the modulation grating can be observed in the G_2 plane, comparable to the "beamlets" in the edge-illumination technique (cf. section 1.5.7 on page 27). As these beamlets are nearly achromatic, this design provides high visibility for a very large range of X-ray energies. Additionally, the resulting large $G_0 - G_1$ distance leads to a relatively small gradient of angular sensitivity, which means that the signal due to a scattering or refracting feature depends only weakly on its vertical position.

However, this design requires a large amount of high-aspect-ratio grating tiles, since the required area of G_1 and G_2 is nearly identical. Each grating was assembled from four quadratic tiles, each cut in half and joined into a row of eight half-tiles, thus covering a long rectangular area. The grating ridges were oriented in parallel to the long edge of this rectangle, leading to a direction of phase sensitivity parallel to the rectangle's short edge, and thus parallel to the swing direction.

The G_1 and G_0 gratings were later replaced to form a symmetric geometry with a π phase-modulating G_1 grating, which enabled measurements with higher angular sensitivity, and a tiled G_2 grating assembly with a larger FOV was installed in a third iteration, permitting lower scan times. These modifications are not discussed in detail here, since all of the experimental work

presented here was performed prior to these changes. They will however be featured in in the doctoral thesis of J. Andrejewski.

3.2.3 X-ray imaging hardware

The technical requirements of X-ray imaging hardware are primarily determined by the object under examination, and the imaging task. The dimensions of the imaged sample determine the necessary FOV, as well as required power and spectrum of the X-ray source.

Firstly, the detector FOV should be in the vicinity of the object's region of interest for at least one direction: although radiographs of arbitrary size can in principle be composed from a large number of small-FOV acquisitions, this approach is usually very time-consuming and only practical for specialized, unique experiments. Additionally, the imaging task determines the required image resolution, which is given by the detector's capabilities as well as the focal spot size of the X-ray source.

Secondly, the X-ray spectrum, which is characterized by acceleration voltage, target material, and filtration for laboratory sources, must be selected to achieve sufficient transmittance and contrast. Very soft X-ray spectra are undesirable since the low transmittance leads to high noise levels even when a large dose is applied to the object. At high photon energies, on the other hand, a distinction between materials becomes difficult: attenuation contrast is increasingly due to Compton scatter, which varies less strongly with atomic number than the other interaction types (Table 2.1 on page 43). Furthermore, since visibility depends on the gratings' attenuating power, which decreases at higher photon energies, contrast-to-noise ratios of differential-phase and dark-field images are lower at high photon energies [Revo$^+$10]. Finally, since Talbot distances increase with photon energy and modulation grating period (cf. section 2.5.2 on page 53), adapting a Talbot(-Lau) setup for harder X-rays necessitates reducing grating periods and/or increasing setup length.

The spatial distribution of dose delivered to the object also depends on the spectrum: lower X-ray energies are absorbed closer to the entrance surface. In a medical context, a change in spectrum may thus effect a different distribution of absorbed dose to the organs, and thus a change in effective dose, even if absorbed dose is constant.

Finally, the X-ray flux achieved by the source must be high enough to achieve a sufficient detector dose in a reasonable time. This obviously depends on transmittance (i.e., a thicker object requires a more powerful source), but also on setup length, since detected intensity decreases with the inverse square of distance to the source.

Due to their very low degree of efficiency (cf. section 2.3.2 on page 46), high-flux X-ray tubes require an extraordinary amount of electrical power, the majority of which is converted to heat. This necessitates efficient heat management, such as the use of cooling liquid and air cooling units. The ability of an X-ray tube assembly to store and dissipate heat is a major performance characteristic, especially for applications requiring long operation (e.g., angiography) or high power (e.g., computed tomography).

Requirements for the *lung-scanning setup* As the *lung-scanning setup* was designed to perform thorax radiography on large animals (pigs), its demands to FOV, X-ray spectrum and X-ray flux are similar to those of medical thorax radiography.

The detector FOV must be sufficient to cover the entire lung. In modern digital radiography setups, flat-panel detectors with FOVs of at least 43 cm × 35 cm are therefore used [Kott$^+$02]. However, while the patient is placed directly in front of the detector in conventional radiography, grating-based X-ray imaging requires some distance between object and G_2 grating to achieve a phase-contrast or dark-field signal (both the autocorrelation length ξ and the angular sensitivity S are zero for samples directly in front of the G_2 grating, cf. section 2.5.8 on page 60). The non-negligible magnification thus necessitates a greater detector FOV or accepting a decreased FOV in the patient plane.

As significantly larger digital X-ray detectors are not generally available, multiple detectors would have to be used in parallel to increase the FOV. In a fringe-scanning setup with "moving detector" geometry (Fig. 3.2c), two or more narrow detector modules could be used side-by-side. Since the *lung-scanning setup* was determined to use the "stationary detector" geometry (Fig. 3.2b), the use of multiple detectors was considered impractical and a standard flat-panel detector with a 43 cm × 43 cm FOV was used, resulting in a slightly smaller effective FOV than a conventional radiography system.

The resolution requirements for the *lung-scanning setup* were not known ahead of time. However, as it was known that dark-field radiographs usually exhibit higher noise levels than conventional radiographs, the resolution of a radiography flat-panel detector was expected to be sufficient. However, fringe-scanning acquisition was found to exhaust another aspect of detector capabilities, namely readout rate, which also had implications on resolution (cf. section 3.3.3).

For thorax radiography, acceleration voltages from 125 to 150 kVp are typically used [Vogl+11]. For differential-phase and dark-field radiography however, image CNR strongly depends on visibility, which decreases drastically for high photon energies, primarily due to the decreasing attenuation power of the gratings. This means that optimal tube voltages for human or large-animal dark-field radiography are much lower, in the vicinity of 70 kVp. Nonetheless, conventional medical X-ray tubes can be used since they are compatible with a wide range of acceleration voltages. Their degree of efficiency decreases at lower tube voltages, leading to a greater tube heat load for comparable X-ray flux (see Eq. (2.39) on page 47).

Most importantly, the fringe-scanning approach requires collimating the radiation field to the narrow strip covered by the gratings. This means that the vast majority of X-ray flux is discarded. A fringe scan achieving similar detector dose as an ordinary radiograph without collimation therefore requires much more electrical power.

In conclusion, the X-ray hardware requirements to achieve the design goals of the *lung-scanning setup* necessitated the use of a large-FOV detector as well as a high-flux X-ray tube with good heat management capabilities. In order to achieve this goal, Philips Healthcare (Hamburg, Germany) thus provided a complete medical radiography system, consisting of flat-panel detector, X-ray tube assembly, and high-voltage generator, to the Chair of Biomedical Physics (Technical University of Munich, Munich, Germany). The technical details of each component will be presented in the following section.

3.3 Technical parameters of setup components

3.3.1 X-ray system

The X-ray system employed at the *lung-scanning setup* was developed by Philips Healthcare for use in radiographic and fluoroscopic medical X-ray imaging devices. It synchronizes the operation of a high-voltage generator powering the X-ray tube with image acquisition by a flat-panel detector and data handling on a connected personal computer.

In a flat-panel detector, incident X-rays are converted to visible light by the detector's scintillation crystals. While the detector is in data acquisition mode, visible-light intensity in each pixel is converted into proportional current by a photodiode. The total amount of detected light is represented by an accumulated electric charge in a capacitive element (see also section 2.4.2 on page 49). During readout, these charges are measured and digitized, yielding an integer number (proportional to incident X-ray energy) for each pixel. This image is finally transmitted to the personal computer and all charge counters are reset.

During the readout procedure, the detector is unable to acquire data. In order to avoid unnecessary dose application, no X-rays are produced in this time. This is achieved by providing a pulsed high-voltage signal to the X-ray tube which is synchronized to the detector readout, resulting in an emission of X-ray pulses at a fixed frequency. This synchronization is especially critical for fluoroscopic applications, where a continuous stream of X-ray images is acquired at a constant frame rate.

Detector readout is the slowest step in the acquisition procedure and thus limits the maximum pulse frequency of the X-ray system. In particular, different FOV and binning settings may be selected, resulting in a variable amount of data (pixels) per image, leading to varying readout times, and thus variable maximum pulse frequencies. This is of particular importance for fringe scanning, since acquisition frequency and scanning speed determine the number of exposures of any part of the object during a fringe scan.

The X-ray system is compatible with a number of Philips X-ray tubes and Trixell flat-panel detectors. The devices employed in the *lung-scanning setup* are introduced below.

3.3.2 X-ray tube assemblies

The RO 1750 ROT 360 rotating-anode X-ray tube assembly (Philips Healthcare, Hamburg, Germany) was initially installed in the *lung-scanning setup*. It is a lightweight tube assembly with moderate electrical power and heat capacity and is passively cooled. It is especially suitable for use in medical radiography applications due to the low X-ray flux requirements, compared to digital subtraction angiography or computed tomography.

However, the power requirements at the fringe-scanning setup were shown to exhaust the heat capacity of this assembly. This is mostly due to the collimation of tube radiation into a narrow rectangular fan beam. Because of this, only a small percentage of X-ray flux emitted by the tube contributes to image formation:

As the collimation only illuminates an area on the detector roughly the size of the G_2 grating, which is far more narrow than the full height of the detector, much more electrical power is required to achieve the same detector dose in a fringe scan than in an equivalent uncollimated exposure. The collimation had a width of 24 mm on the detector, whereas the full FOV width was 430 mm. As the collimation must travel a distance of at least 454 mm for a full scan[1], the amount of necessary X-ray tube output (and electrical energy) to achieve the same detector dose is increased by a factor of $454/24 \approx 19$.

Adding to that the significant attenuation of X-ray flux by the gratings, this meant that one fringe-scan with the RO 1750 assembly at maximum tube power was sufficient to heat the assembly from room temperature to just below the emergency shutdown temperature. Due to the limited heat exchange of the tube assembly with the environment, this lead to waiting times between measurements in excess of 30 min.

In order to reduce these waiting times, an X-ray tube assembly with greater heat capacity and active cooling (MRC 200 0310 ROT 1004, Philips Healthcare, Hamburg, Germany) was thus installed in June 2016. In this configuration, heat transfer is supported by circulating the coolant through an external air cooler. This modification almost entirely eliminated waiting times between scans and allowed faster acquisition of multi-scan reference data. Some parameters of the two assemblies are compared in Table 3.1.

[1] For a complete scan, each detector region must be traversed by the full height of the collimation, leading to a travel distance of the detector FOV height plus the height of the collimation.

3.3.3 X-ray detector

The Trixell (Moirans, France) Pixium RF 4343 R1 flat-panel detector was used in the setup since 08/2015. Medical radiographic measurements are usually performed with a minimal distance between patient and detector, which minimizes penumbral blur. In such a case, the detector FOV is nearly identical to the FOV at the location of the patient. With an FOV of 43 cm × 43 cm, the detector is designed to be compatible with chest radiography.

The detector matrix consists of 2874 × 2840 pixels, with a pixel size of 148 µm. With a readout of the full pixel matrix, a maximum frame rate of 4 Hz (i.e., four full-resolution images per second) can be achieved.

However, this was found to be insufficient for fringe-scan acquisition: In order to achieve a reasonably short total measurement time of 40 s, the grating arrangement must rotate at an angular frequency of 5.7 mrad/s. At 4 Hz, this means that subsequent frames are acquired with swing rotation angles 1.4 mrad apart. Given that the grating slot's opening angle is 12.7 mrad, this means that only $12.7/1.4 \approx 9$ different positions of the grating slot can be recorded for any given sample feature. A phase-stepping acquisition with nine phase steps is usually sufficient for signal retrieval. For slot-scanning acquisition in the *lung-scanning setup* however, additional complications arose due to the variation of blank-scan flux and visibility across the grating slot, which must be encoded along with the variation of moiré phase. Given the high amount of artifacts in retrieved images, the sampling was determined to be insufficient for this purpose.

However, higher acquisition frequencies are possible if binning is performed at the hardware level, since a smaller amount of data is generated in each frame. A maximum frame rate of 11.6 Hz can be achieved for 3 × 3 binning, which results in a sampling of 25 or 26 grating slot positions. As phase retrieval was found to produce much fewer artifacts with this setting, it was used for the majority of fringe-scan measurements. On the other hand, the significant readout time limits the X-ray pulse duration to 20 ms at this frame rate, which also restricts the maximum applicable dose in a scan. Furthermore, the resolution of the image is obviously

X-ray tube assembly	RO 1750 ROT 360	MRC 200 0310 ROT 1004
Time of installation	Aug. 2015 – June 2016	since June 2016
Tube voltage	40 kVp–150 kVp	40 kVp–125 kVp
Anode disk diameter	90 mm	200 mm
Focal spot size	0.6 mm / 1.2 mm	0.3 mm / 1.0 mm
Max. anode current at 60 kVp	830 mA	700 mA
Max. heat content	1260 kJ	4000 kJ
Max. heat dissipation	1300 W	3200 W (with air cooler)

Detector	Trixell Pixium RF 4343 R1	
Scintillation layer	CsI(Tl), 600 µm	
	No binning	3 × 3 binning
Pixel matrix	2874 × 2840	957 × 947
Pixel size	148 µm	444 µm
Max. frame rate	4 Hz	11.6 Hz
Max. FOV	43 cm × 43 cm	43 cm × 43 cm

Gratings	$L = \overline{G_0G_1} = 1599$ mm, $d = \overline{G_1G_2} = 231$ mm		
	G_0	G_1	G_2
Pitch, duty cycle	68.7 µm, 0.70	8.73 µm, 0.50–0.58	10 µm, 0.50
Ridge material, height	Au, 240 µm	Au, 150–200 µm	Au, ≈ 180 µm
Substrate material, height	C, 1 mm	Si, 525 µm	Si, 525 µm
Area	50 mm × 50 mm	(48 mm × 24 mm) × 8	(48 mm × 24 mm) × 8

Linear stages	for grating arrangement	for sample bed	for G_0
Type	isel LES 5, 690 mm	isel LES 5, 1090 mm	Newport MFA-PPD
Travel range	540 mm	800 mm	25 mm
Typ. travel speed	11 mm/s	40 mm/s	< 1 mm/s

Other parameters		Source-detector distance	1990 mm
Source-G_0 distance	140 mm	Source-table distance	1683 mm
Used tube voltages	60–70 kVp	Measured visibility	(36 ± 5)% (60 kVp),
Scan duration	40 s		(31 ± 4)% (70 kVp)
Typ. DAP per scan	0.5 Gy cm^2	Sample FOV	36.4 cm × 32.5 cm

Table 3.1: Overview of technical parameters of the *lung-scanning setup*. Parameters of tube assemblies are from the respective service information manuals [RO15; MRC15]. DAP: Dose-area product, i.e., the product of air kerma and FOV in the object plane.

reduced, yielding a matrix of 958 × 947 pixels at a pixel size of 444 µm.

Flat-panel detectors are usually energy-integrating, meaning that the measured signal is proportional to the X-ray energy deposited in the detector's scintillation layer (cf. section 2.4.2 on page 49). It is thus possible to find a factor of proportionality between detector dose and detector signal, which allows a simple conversion of imaging data to maps of detector dose. However, it follows from the detector's energy-dependent quantum efficiency that this conversion factor also depends on the X-ray spectrum incident on the detector.

Three different electronic gain factors are available for the digitization of charge values, mapping a dose range of approximately 5, 20, or 43 µGy to a 16-bit register (all values for 3 × 3 binning). Greater gain values thus provide a more precise quantization (i.e., a higher dose resolution). Due to the low achieved detector dose values per frame, the most sensitive electronic gain setting was used for the majority of measurements.

Spatial variations in spectral X-ray flux due to the *anode Heel effect* lead to deviations from proportional behavior, as well as fluctuations of the factor of proportionality. To correct for this, the detector was calibrated while installed in the *lung-scanning setup*. Prior to performing this calibration, measured detector doses were limited to values below the full dynamic range in order to avoid distortions due to nonlinearities.

3.3.4 Gratings

As the sample table height was chosen to be at a moderate height of 30.7 cm above the detector to achieve a sufficient FOV, the inter-grating distance $d = \overline{G_1 G_2}$ had to be less than that, while the G_1 grating should be as close as possible to the sample table to maximize angular sensitivity. A value of $d = 25$ cm was thus chosen. The height of the experimental hutch limited the total setup length to approximately 2 m.

In order to further maximize angular sensitivity, analyzer and modulation grating pitches were selected as small as possible, while still allowing reliable manufacturing of high-aspect-ratio gold structures with the LIGA process. Given the above boundary conditions, periods of $p_2 = 10$ µm and $p_1 = 8.73$ µm were thus selected.

This highly asymmetric grating geometry required that the width of both the G_1 and G_2 gratings was nearly identical to the detector width. Furthermore, they were both required to have good absorption capabilities for hard X-rays, necessitating LIGA manufacturing to achieve high aspect ratios. Due to the size limit of LIGA structures, this meant that a total of eight grating tiles of a width of 48 mm × 48 mm had to be combined for each grating.

The amount of grating tiles necessary for this approach was deemed to be excessive, and the height of the active grating area was thus halved. Instead of eight full tiles, G_1 and G_2 each required only four tiles, which were cut in half (parallel to the orientation of the grating ridges), and aligned along their short edges, thus providing an area of 384 mm × 24 mm.

The LIGA tiles for the G_2 grating were manufactured by the Micro- and X-ray optics department at the Institute of Microstructure Technology (IMT), Karlsruhe Institute of Technology (KIT, Karlsruhe, Germany), in the framework of a Karlsruhe Nano Micro Facility (KNMF) research proposal. The tiles for the G_1 grating were produced by Microworks GmbH (Karlsruhe, Germany).

Since the feasibility of fringe-scanning acquisition is strongly dependent on fringe period and orientation, both of which react highly sensitively to grating orientation, great care had to be taken in the alignment of grating tiles: Even small changes in tile rotation strongly affect the moiré fringe pattern, and thus the quality of image retrieval. Furthermore, a presence of inter-tile gaps and a phase difference in the ridge pattern of adjacent tiles may lead to inconsistent, unusable data in the threshold areas between the tiles.

Therefore, T. Schröter (Micro- and X-ray optics, IMT, KIT) developed a tiling frame which allows for very precise positioning (translation and rotation) of each individual tile. The design of this device, as well as the boundary conditions and difficulties of the alignment procedure are discussed in [Schr+17]. This approach enabled a rotational alignment to within 1.6 mrad and a grating gap size below 0.4 mm. After alignment, the set of tiles was glued to a polyimide substrate and removed from the tiling frame, allowing the alignment of the next set of tiles.

The high engineering demands to G_1 and G_2 lead to relaxed demands for the source grating G_0 (also produced by Microworks GmbH): as the highly asymmetric design demands a source grating pitch of $p_0 = 68.7$ µm, high absorption power can be achieved even

at a moderate aspect ratio. A high duty cycle of 0.72 was used to achieve good transverse coherence (low slot width) despite the high pitch.

Note that the grating assembly was altered significantly in 09/2017. Since all experimental results shown in this work were achieved prior to this change, it will be discussed in future publications, in particular the dissertation of J. Andrejewski.

3.4 System integration

The assembly of X-ray system, gratings and various other components into the *lung-scanning setup* is described in this section. It must be noted that some components were altered or replaced during the operation of the setup. Instead of the full list of designs, only the most long-lived iteration of each feature prior to 09/2017 is described here, and illustrated in Fig. 3.3.

3.4.1 Mechanical design for the grating assembly

As the entire assembly had to be contained in an existing experimental hutch, the measurements of the assembly were constrained by the interior hutch dimensions. Additionally, some clearance was necessary to allow access to the sample bed for transport and monitoring of anesthetized pigs (and to allow access to all components for maintenance and upgrade).

Since the "fixed detector" fringe-scanning geometry in Fig. 3.2b requires a rotating grating assembly, a design similar to a playground swing set was employed, as illustrated in Fig. 3.3. Both the frame and the grating "swing" itself were assembled with aluminum profiles, carriers, and joints from both the LINOS X 95 and the Bosch-Rexroth systems. Gratings and apertures for beam collimation were mounted on parallel "planes" attached to the swing with LINOS carriers. The use of these carriers allowed for convenient adjustment of planes at arbitrary heights. Cylindrical ball bearing joints were used to achieve the swinging movement. In order to achieve a moiré pattern that is independent of swing position, care was taken that the axis of rotation coincided with the X-ray tube source spot.

Movement of the swing was achieved with the use of a linear translation stage (LES 5, isel Germany AG, Eichenzell, Germany), which translates the rotation of an electric motor to linear movement via the use of a spindle drive. Due to the high sensitivity of the grating assembly to mechanical vibrations, it was connected to the drive via a steel rope: under low tension, this connection partly suppresses vibrations originating from the movement of the drive. However, since this connection is only able to pull a load, not push it, it can only move the swing in one direction from its equilibrium position.

As the detector was placed centrally below the source spot to achieve a vertical projection geometry, the swing's equilibrium position had to be shifted from the vertical to allow scanning the swing over the full detector FOV. As shown in Fig. 3.3, this was achieved by adding lead weights to the swing on horizontal aluminum profiles. The amount of swing torque, and thus tension on the steel rope, could be varied by shifting the counterweights' horizontal position on these profiles.

3.4.2 Sample placement

The requirement to achieve an object FOV similar to a conventional thorax radiography setup restricted the vertical placement of the imaged object (and thus, as described above, the interferometer design). The achievable longitudinal FOV (parallel to swing movement) in the plane of the sample bed surface was limited by the detector length. In the transverse direction, FOV was additionally limited by the width of the tiled gratings, being somewhat more narrow than the detector. With the selected height of the sample bed surface of 30.7 cm above the detector, the achievable FOV of 36.4 cm × 32.5 cm (longitudinal × transverse) at the height of the table surface was deemed acceptable for large-animal thorax imaging.

Like the swing frame, the table was constructed from Bosch-Rexroth aluminum profiles. The table was mounted onto its support via linear rails, which allowed for convenient movement of the imaged body. This enabled a precise selection of the imaged region without a need to directly move the body (and thus inevitably change its posture). As for the swing, a linear translation stage (LES 5, see above) was used for table positioning. A single pane of transparent polycarbonate was used as a table surface, which allowed to see the detector from above, and thus to easily estimate the object FOV.

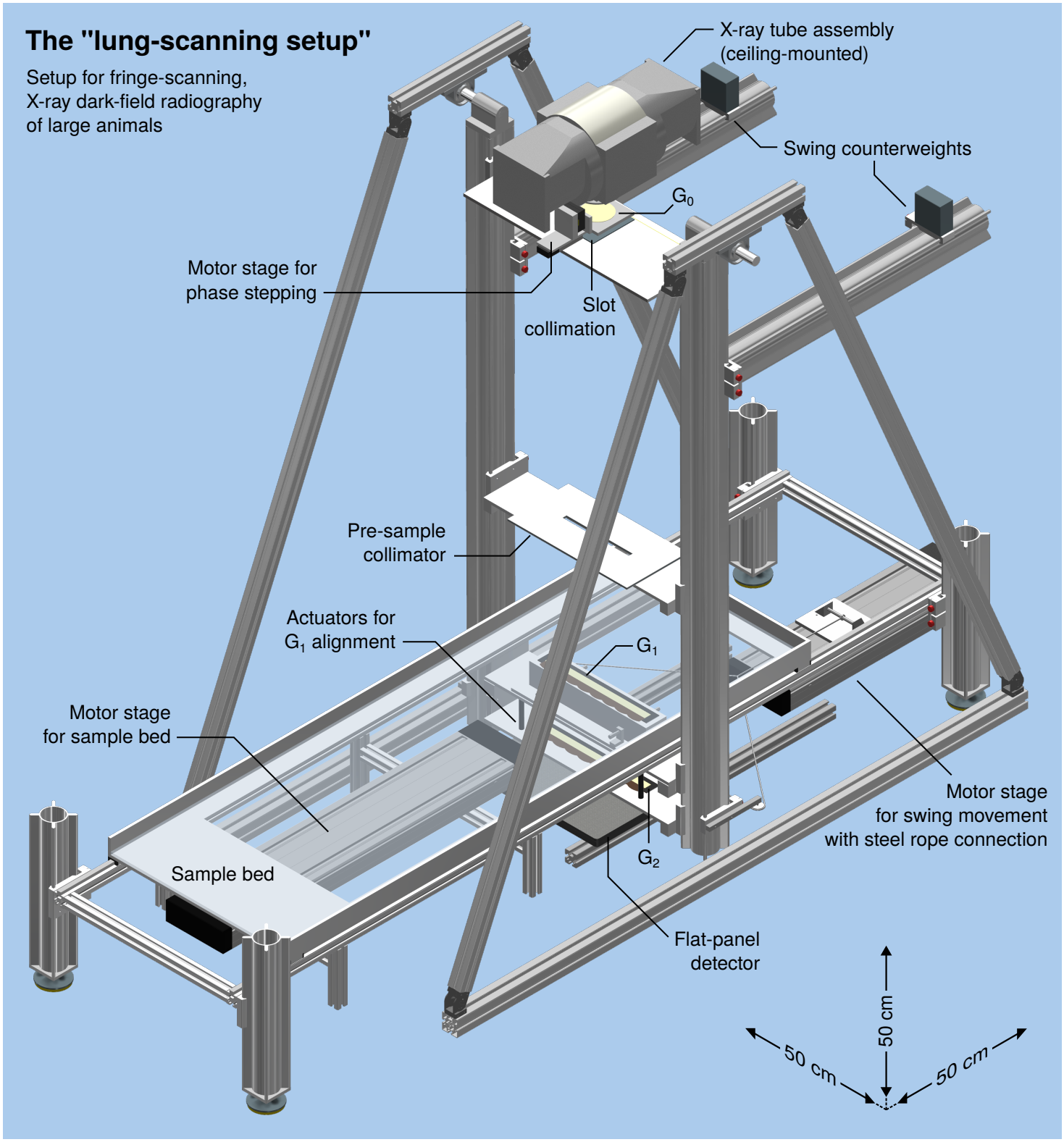

Figure 3.3: Overview of the complete *lung-scanning setup* in isometric perspective.

3.4.3 Slot collimation

The shape of the collimated radiation field was primarily determined by the area of the tiled G_2 grating and its distance to the focal spot. This collimation was achieved by a series of different apertures: first was the set of collimation structures extracted from a medical collimator intended for use with the X-ray tube assembly. Shielding and other structures from the collimator were removed to allow placing the G_0 grating in immediate vicinity to the focal spot.

The general narrow shape of the radiation field was then achieved by a rectangular lead aperture on the plane supporting the G_0 grating (visible in Fig. 3.3). However, the short distance of this collimator to the focal spot—as well as the focal spot's considerable size—resulted in significant penumbral blur of the radiation field: In the sample table plane, the longitudinal extent of the radiation field (neglecting penumbral blur) was 20.5 mm, whereas the penumbral blur amounted to approx. 8 mm (values calculated from measured distances). The collimation width in the G_0 plane was thus set to a value slightly larger than necessary, and then supported by an additional, lead-covered presample collimation plane just above the sample area (also in Fig. 3.3). This avoids a significant drop-off in beam intensity towards the edge of the radiation field due to penumbral blur.

In the imaged object, a significant amount of Compton-scattered radiation is generated, some of which may reach aluminum parts of the G_1 or G_2 planes. In order to ameliorate this problem, some exposed surfaces in this area were covered with lead sheets: as shown in section 2.2.7 on page 41, the relative magnitude of Compton scatter decreases for elements of higher atomic number. Furthermore, collimation in the G_2 plane produces a sharp edge of the radiation field, which is beneficial for data processing (described in chapter 4).

3.4.4 Phase stepping and grating alignment

Despite not being necessary for fringe-scanning, having the option to perform phase stepping is highly beneficial to characterize the setup. For example, this allows the rapid measurement of visibility for a large number of absorption phantoms, and thus to record a lookup table to correct for beam-hardening (cf. section 4.3.1). Additionally, the image retrieval method later found to be most useful for the *lung-scanning setup* requires the possibility to perform phase stepping in combination with fringe scanning (cf. section 4.2.2d on page 96). The G_0 grating was thus mounted onto a motorized linear translation stage with micron-accuracy (MFA-CC, Newport Corporation, Irvine, CA, USA). The comparatively high pitch of the source grating relaxed the demands to positioning accuracy in the phase stepping process. Additionally, a goniometer was installed to adjust the incidence angle, which has a strong effect on grating transmittance.

The ability to perform grating adjustments "live", i.e. to examine moiré fringe shape and visibility while applying changes to grating positions, greatly speeds up the process of aligning the gratings for optimum visibility and fringe shape. This is especially useful for fringe-scanning setups, as the method's feasibility and resulting image quality strongly depend on the correct adjustment of fringes. To achieve this, the tiled G_1 grating was mounted on a plane whose orientation with respect to the "swing" was modified with four motorized actuators. The actuators (visible in Fig. 3.3) were attached to a bottom, fixed aluminum plane, while the screws extended by the actuators served as a support for a second, top plane carrying the G_1 grating. Variation in the positioning of the four screws thus allowed for vertical displacement as well as rotation of the top plane around two axes, enabling a wide range of modifications to moiré fringe shape.

In addition to this, the G_1 grating was not directly attached to the top plane, but was instead placed on a custom, hollow profile on top of this plane. This profile served two functions: firstly, to decrease the distance of the grating to the sample table, and thus increase the setup's angular sensitivity. This could not be achieved by increasing the height of the G_1 planes because this space was obstructed by the base of the sample table. Secondly, the profile allowed for convenient rotation of the G_1 grating around the vertical axis (which was not possible with the actuators). This profile was clamped to the top plane by a set of four laterally-mounted, manual micrometer screws.

3.4.5 Motor and X-ray system control

X-ray system control and image data transfer were achieved via network connection to a personal computer with the Windows 7 operating system, running

control software provided by Philips Medical Systems DMC GmbH (Hamburg, Germany). The control software can be accessed either directly from the computer via a graphical user interface, or from a remote system via a network connection. All exposure parameters, i.e. tube voltage, current, X-ray pulse duration, as well as detector FOV and gain settings, can be controlled via either interface. Additionally, the system can be configured to acquire a fixed total number of pulses.

The linear stages for swing and table positioning were actuated using an XPS-Q8 motion controller, while the G_1 actuators and the G_0 translation stage were connected to an ESP-301 motion controller. Both devices are distributed by Newport Corporation (Irvine, CA, USA) and serve to provide power and relay motion commands to the motors. Such commands can be issued using a web browser interface (XPS) or a key pad (ESP).

In order to perform fringe scanning, synchronized control of both the swing's linear translation stage and the X-ray system was necessary. Separate manual operation of both systems would be impractical, and does not provide consistent results. Control of both systems was thus unified using the *spec* software package by Certified Scientific Software (Cambridge, MA, USA), which is able to interface with a large number of motion controllers and X-ray detectors. Commands are issued either interactively in a console interface, or through the execution of "macros" (scripts) in a dedicated scripting language, which enables the implementation of complex experimental procedures.

As a Unix-based software, *spec* ran on a separate computer with the Ubuntu operating system, and communicated with the Windows computer over a local network connection. Fringe scanning was thus achieved with a *spec* macro combining commands to both the X-ray system and the swing translation stage. The macro initially configures the X-ray system according to user parameters and schedules a fixed number of X-ray pulses which is calculated from the movement speed of the translation stage. After moving the swing to the starting position (and a brief pause to allow mechanical vibrations to decay), swing movement is started and the X-ray system is activated when the motor stage has reached constant speed.

Each X-ray pulse produces a single detector frame, which is then written to a multi-frame binary file. Since both pulse frequency and swing velocity are constant, the location of the collimated radiation field changes by a constant amount between any two frames. When the scan is complete, the X-ray system returns to standby mode, the swing stops, and the output file is closed. Furthermore, Philips Medical Systems DMC GmbH kindly provided functionality for the detector control software to save only a fraction of the full image, cropped to an area slightly larger than the radiation field, which reduced disk space requirements by about 80%.

To use the full length of the detector FOV in scanning direction, the series of X-ray pulses starts before the swing's radiation field enters the detector area, and ends only after the radiation field has completely left the detector. This means that even edge regions of the detector are traversed by the full length of the radiation field (and thus receive the same dose and moiré phase modulation as all other parts of the FOV). The necessary travel range of the linear stage is thus determined by the length of the detector plus the length of the radiation field (in scan direction).

Thanks to the compatibility of both motion controllers with *spec*, arbitrary movement of all motorized stages could be achieved with *spec* macros. For example, in a macro for reference scan acquisition (described in section 4.2.2d on page 96), the phase-stepping capability of the G_0 grating was also incorporated.

3.5 Conclusion and outlook

The *lung-scanning setup*, a grating-based X-ray dark-field imaging device, was designed with the goal of producing thorax radiographs of large animals at sufficient image quality in clinically acceptable measurement times. The necessary FOV was achieved by combining the tiling of LIGA-manufactured gratings with a fringe-scanning acquisition method. Instead of a linear translation, the grating arrangement was rotated to avoid projection artifacts. Grating parameters (periods, heights and distances) were selected to achieve a high visibility at tube voltages in the vicinity of 70 kVp. In order to achieve the high flux necessary for short measurement times, medical X-ray imaging hardware was used. Control of the setup was achieved by synchronously directing the X-ray hardware control application and the motorized movement of the grating arrangement using scientific instrument control software.

The *lung-scanning setup* performed scans of the full field of view (36.4 cm × 32.5 cm in the table plane) in approximately 40 s. Later experiments (cf. [Grom+17; Will+18] and chapter 5) proved that the X-ray flux delivered in this interval was sufficient to allow scanning thoraxes of pigs (22 to 40 kg) and adult humans. Since the achieved patient doses were compatible with clinical application, this demonstrated the feasibility of clinical dark-field radiography.

The lessons learned during the construction and operation of the *lung-scanning setup* were applied to the design of a successor setup, a device situated in the university hospital "Klinikum rechts der Isar" in Munich. At the time of writing, it is used for a clinical study examining COPD detection via dark-field radiography, yielding very promising results.

Assuming a positive study outcome, it remains to be seen whether the fringe-scanning approach employed in both setups is compatible with the demands to a commercial medical X-ray imaging system. An alternative approach for large-FOV, grating-based radiography may be the use of much larger, "full-FOV" gratings. However, the feasibility of this approach is obviously dependent on the possibility to procure large numbers of X-ray-attenuating gratings at competitive prices, which is doubtful given the current state of manufacturing technologies.

Chapter 4

Image processing of fringe-scanning data

> ...I have bought this wonderful machine—a computer. Now I am rather an authority on gods, so I identified the machine—it seems to me to be an Old Testament god with a lot of rules and no mercy.
>
> Joseph Campbell, *The Power of Myth*

Contents

This chapter introduces the methods used for calculating object images from the *lung-scanning setup* described in the previous chapter. For this purpose, the raw data structure is derived from setup geometry and operation in section 4.1. Furthermore, an approach is described to reorder the data into a compact three-dimensional array for digital processing.

A mathematical model for the encoding of the three sample modalities (attenuation, visibility reduction, and refraction) in the raw data is introduced in section 4.2. Four different approaches to extract these modalities from the data are then introduced, and they are compared in terms of bias and variance performance, as well as the required experimental effort. The "full retrieval" method is found to exhibit superior performance (albeit at the expense of a greater required effort for reference scan measurements), which motivates its use for most of the imaging experiments at the *lung-scanning setup*.

A range of post-processing procedures are then introduced in section 4.3: a method for correcting visibility reduction due to beam-hardening is shown, producing dark-field maps that more accurately characterize the small-angle-scattering activity of the imaged object. Subsequently, the origin of artifacts in dark-field images due to the tiling of grating structures is introduced. Two approaches for its correction are compared. Finally, a low-pass filter for dark-field images is introduced, which minimizes the impact of high noise levels while preserving the visibility of important features.

The practical implementation of the above steps into the *lsproc* software package is presented in section 4.4. The fundamental design goals for the package and the

resultant code layout are introduced, and the order of computation steps during a single "run" of the central script is illustrated.

4.1 Structure of data from the *lung-scanning setup*

The technical implementation of the *lung-scanning setup* determines the structure of the acquired data. During the acquisition procedure, the X-ray generator/detector unit is operated in a mode intended for fluoroscopic examinations: X-ray projections are acquired continuously with a constant frame rate, which is achieved by pulsed modulation of the tube acceleration voltage and appropriately-timed detector acquisition and readout intervals. At the same time, the "swing" carrying the grating arrangement is rotated across the field of view via traction from a linear stage moving with constant velocity. A scan data set thus consists of a series of consecutively acquired image frames, i.e., a video of the collimated radiation field traversing the detector.

4.1.1 Angular frequency of the swing

The drive of the swing is illustrated in Fig. 4.1. A rope of length s is attached to the swing at a distance D from its center of rotation, i.e., the location of the focal spot. The other end of the rope is attached to the motor stage at a height difference Δz and horizontal distance y to the attachment of the rope at a vertical swing position. As the stage moves, y varies. The angle α of the swing to the vertical can be calculated as a function of y:

Firstly, the angle $\alpha+\psi$ can be related to the given quantities as $\tan(\alpha+\psi) = y/(D-\Delta z)$. Furthermore, the quantity L in Fig. 4.1 is equal to $\sqrt{y^2+(D-\Delta z)^2}$. This allows calculation of ψ via the law of cosines:

$$\cos\psi = \frac{D^2+L^2-s^2}{2DL} = \frac{D^2+y^2+(D-\Delta z)-s^2}{2D\sqrt{y^2+(D-\Delta z)^2}}.$$

Therefore,

$$\alpha = \arctan\left(\frac{y}{D-\Delta z}\right) - \arccos\left[\frac{y^2-s^2+(D-\Delta z)^2+D^2}{2D\sqrt{y^2+(D-\Delta z)^2}}\right]. \quad (4.1)$$

For the value of $y = y_0 \equiv \sqrt{s^2-\Delta z^2}$, the swing is in a vertical position, i.e., $\alpha = 0$. We can calculate the Taylor polynomial of Eq. (4.1) around $y = y_0$ (cf. Appendix B on page 225):

$$\alpha \approx \frac{y-y_0}{D} - \frac{(y-y_0)^2}{2}\frac{\Delta z}{D^2\sqrt{s^2-\Delta z^2}} + \frac{(y-y_0)^3}{6}\frac{s^2+2\Delta z^2}{D^3(s^2-\Delta z^2)}.$$

Note that the quadratic term disappears for $\Delta z = 0$, i.e., a horizontal adjustment of the connecting rope for a vertical swing position. Finally, the angular frequency ω of the swing can be related to the movement speed of the stage via

$$\omega = \frac{d\alpha}{dt} = \frac{\partial\alpha}{\partial y}\frac{\partial y}{\partial t} = \frac{\partial\alpha}{\partial y}v \approx \frac{v}{D}\left[1 - \frac{\Delta z(y-y_0)}{D\sqrt{s^2-\Delta z^2}} + \frac{(s^2+2\Delta z^2)(y-y_0)^2}{2D^3(s^2-\Delta z^2)}\right]. \quad (4.2)$$

In zero-order approximation, ω is thus given by the ratio of motor speed v and source-rope distance D. A first-order deviation (as a function of swing position y) arises in the presence of a variation Δz in the vertical height of both attachment points of the connecting rope. This deviation occurs since the pulling force from the stage is not perfectly orthogonal to the "lever," i.e., the grating swing.

However, a vertical deviation is introduced even for $\Delta z = 0$ as the swing is displaced from the vertical. Thus, a second-order correction persists in this case.

The magnitude of the corrections in Eq. (4.2) for the *lung-scanning setup* can be evaluated by inserting the variables' numerical values, namely: $\Delta z \approx 0$, $D = 192\,\text{cm}$, and $s = 90\,\text{cm}$. This results in an increase of ω by $\approx 2\%$ at the limits of the scan range ($y-y_0 = \pm 23\,\text{cm}$). This variation is small enough that ω can be assumed as constant for practical purposes.

4.1.2 Size of the radiation field

The movement of the radiation field during the fringe scan is shown schematically in Fig. 4.2: As in Fig. 4.1, α denotes the angle of the interferometer relative to the vertical z axis, and the axis of rotation is parallel to the x axis. The time-dependence of α can be expressed as

$$\alpha(t) = \alpha_0 + \int_0^t \omega(t)\,dt \approx \alpha_0 + \frac{vt}{D}, \quad (4.3)$$

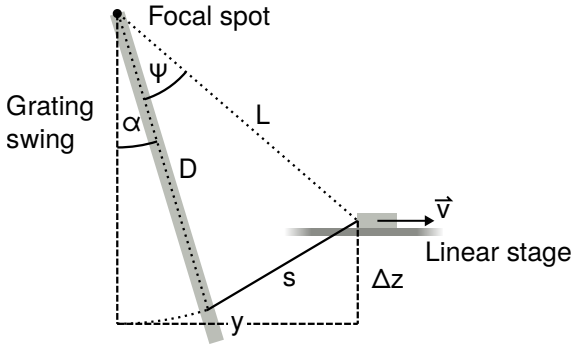

Figure 4.1: Schematic of the swing drive of the *lung-scanning setup*. The rotation of the grating swing is induced by a linear stage, connected via steel rope. The geometry of the attachment leads to slight variations in the swing's angular velocity $\omega = d\alpha/dt$ throughout the scan, despite a constant speed $\vec{v}$ of the linear stage.

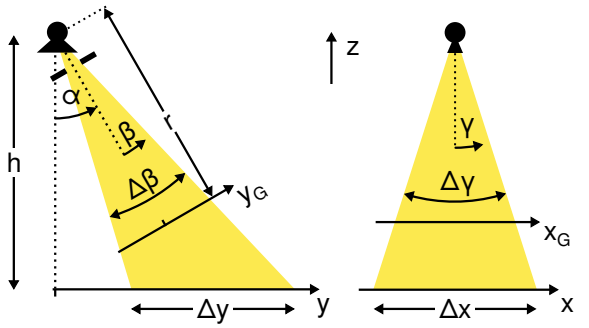

Figure 4.2: Projection of the rotating cone beam onto the planar detector. Despite fixed opening angles $\Delta\beta$, $\Delta\gamma$, the size Δy, Δx of the radiation field on the detector varies with the rotation angle α. For clarity, angles are exaggerated, and gratings are omitted.

where the first- and second-order correction terms in Eq. (4.2) were neglected. Different points in the (rotating) plane of the analyzer grating are denoted by (x_G, y_G). If the interferometer's axis of rotation coincides with the source spot, and variations in the tube intensity profile are neglected, the intensity in this plane is a function of only x_G and y_G, i.e., the intensity map of the moiré fringes is a fixed pattern relative to the interferometer.

Let any point (x_G, y_G) be represented by the angle β in the yz plane, and the angle γ in the xz plane, as shown in Fig. 4.2. The projection of (x_G, y_G) onto the detector plane (vertical distance h from the source spot) is then uniquely described by the angle $\alpha+\beta$ in the yz plane, and γ in the xz plane, namely:

$$x = h\tan\gamma/\cos(\alpha+\beta), \tag{4.4}$$

$$y = h\tan(\alpha+\beta). \tag{4.5}$$

With opening angles $\Delta\beta$, $\Delta\gamma$ of the radiation field in the yz and xz planes, the time during which the field traverses any given point on the trajectory is given by

$$\Delta t \approx \frac{\Delta\beta}{\omega} \approx \frac{\Delta\beta D}{v}, \tag{4.6}$$

and is thus (approximately) *constant* for the entire field of view. On the other hand, the length of the radiation field *in the detector plane* in y direction is given by

$$\begin{aligned}\Delta y &= h\left[\tan(\alpha+\Delta\beta/2) - \tan(\alpha-\Delta\beta/2)\right], \\ &\overset{\Delta\beta\ll 1}{\approx} h\Delta\beta/\cos^2\alpha,\end{aligned} \tag{4.7}$$

and therefore depends on α. The same is true for the extent of the radiation field in the x direction:

$$\begin{aligned}\Delta x &= \frac{h}{\cos(\alpha+\beta)}\left[\tan\left(\frac{\Delta\gamma}{2}\right) - \tan\left(\frac{-\Delta\gamma}{2}\right)\right] \\ &= 2h\tan(\Delta\gamma/2)/\cos(\alpha+\beta).\end{aligned} \tag{4.8}$$

For the given setup however, the dependence of Δx and Δy on α and β is weak since they vary little across the radiation field: The maximum interferometer deflection angle α during a scan is determined by h, as well as the extent y_d of the detector in y direction. For $h = 1.99\,\text{m}$, $y_d = 43.0\,\text{cm}$, $\alpha_{max} = \tan^{-1}(y_d/2h) = 6.2°$. Furthermore, with an extent y_b of the radiation field in y direction of $2.5\,\text{cm}$, $\beta_{max} = \Delta\beta/2 = \tan^{-1}(y_b/2h) = 0.36°$. This corresponds to a relative variation of only 0.6% (0.15 mm) for Δx and of 1.2% (0.3 mm) for Δy, i.e., less than one pixel in 3×3 binning mode.

With $38.4\,\text{cm}\times 2.5\,\text{cm}$, the radiation field area is only 5.2% of the detector's full field of view ($43\,\text{cm}\times 43\,\text{cm}$). Thus, only 5.2% of a single image contains useful information (even less when the radiation field crosses the detector limits at the beginning and end of the scan). Since the detector's active FOV could initially not be limited to the radiation field, the storage of fringe-scan data sets was highly inefficient.

However, Philips Medical Systems later implemented a live image cropping feature to the X-ray system control software: Based on a user-determined width of the crop area in the y-direction (given by the dimensions of the radiation field), an optimal cropping position is calculated on-the-fly by maximizing total intensity

contained within the cropped area. The saved field of view is thus reduced to a rectangle with the selected crop width in the y-direction, and full extent in the x-direction. Crucially, the per-frame cropping coordinates are also saved to allow co-registration of cropped frames.

4.1.3 Data resorting

The key principle of fringe-scanning acquisition is that the sample is measured at different relative grating phases by scanning it through a slightly detuned Talbot- or Talbot-Lau interferometer (see section 3.2.1 on page 71). For the "moving sample" fringe-scanning geometry (Fig. 3.2a on page 74), co-registration of individual image frames requires spatial interpolation. If the movement of the sample projection between two frames is not an integer multiple of pixel size, their registration requires spatial interpolation, which may reduce image resolution in the movement direction and decrease visibility for low moiré fringe periods. This is unnecessary for the *lung-scanning setup*, since both sample and detector remain stationary during acquisition (Fig. 3.2b on page 74).

However, another interpolation step is beneficial for efficient memory usage: Let $I(x_i, y_j, t_k)$ denote the value of the detector pixel (x_i, y_j) acquired in the k-th frame. Since images are acquired at a constant frequency f, the k-th frame of the scan is measured at $t_k = k/f$ (Fig. 4.3a, 4.3b). The duration for which the radiation field covers any given location is given by Δt from Eq. (4.6).

However, the starting and ending times of this interval are dependent on the y coordinate: regions closer to the starting position of the radiation field are reached earlier. For a numerical representation of $I(x_i, y_j, t_k)$ in a 3D array with indices (i, j, k), the range of "useful" k values directly depends on j, and is much smaller than the full range of values (cf. Fig. 4.3c). It is thus a highly inefficient use of memory. Instead, it is more practical to shift pixel values along the k-axis so that this interval starts at zero for all j. This can be achieved by the coordinate transform

$$\tau_{jk} = t_k - \mathcal{T}_+(y_j), \tag{4.9}$$

where $\mathcal{T}_+(y_j)$ is the time at which the collimated radiation field first reaches the coordinate y_j. All values with $\tau_{jk} > \Delta t$ or $\tau_{jk} < 0$ can then be discarded, resulting in a much smaller data set (cf. Fig. 4.3d).

We can calculate $\mathcal{T}_+(y)$ (and $\mathcal{T}_-(y)$, i.e., the time when the radiation field leaves the coordinate y) from the swing's movement parameters. The edges of the radiation field are parameterized by $\beta = \pm\Delta\beta/2$, its y coordinate is thus given by Eq. (4.5):

$$y = h \tan\left(\alpha \pm \frac{\Delta\beta}{2}\right).$$

With α given by Eq. (4.3) and $t = \mathcal{T}_\pm$, we obtain

$$y \approx h \tan\left(\alpha_0 + \frac{v}{D}\mathcal{T}_\pm \pm \frac{\Delta\beta}{2}\right).$$

Rearranging for $\mathcal{T}_\pm$:

$$\begin{aligned}\mathcal{T}_\pm(y) &\approx \frac{D}{v}\left[\arctan\left(\frac{y}{h}\right) - \alpha_0 \mp \frac{\Delta\beta}{2}\right] \\ &\approx \frac{D}{vh}y - \frac{D}{v}\left[\alpha_0 \pm \frac{\Delta\beta}{2}\right].\end{aligned} \tag{4.10}$$

With the small-angle approximation for the inverse tangent function, $\mathcal{T}_\pm(y)$ is a linear function of y plus an intercept.

With $t_k = k/f$, and $y_j = jp$, where p is the pixel size, Eq. (4.10) can be expressed as a direct relation between j and k:

$$k_\pm \equiv f\mathcal{T}_\pm \approx \frac{Dfp}{vh}j - \frac{Df}{v}\left[\alpha_0 \pm \frac{\Delta\beta}{2}\right]. \tag{4.11}$$

Slope and intercept of $\mathcal{T}_\pm(y)$ can be directly determined from a suitable visual representation of the stepping data set: Reverting any cropping applied to the saved data, and subsequent averaging of the full data set $I(x_i, y_j, t_k)$ along the x axis yields a two-dimensional image map

$$\langle I\rangle_x(y_j, t_k) = \sum_i I(x_i, y_j, t_k).$$

The radiation field and its linear movement in the y direction is then represented as a diagonal "bar", as shown in Fig. 4.3c.

For an exact retrieval of limits, Otsu's method [Otsu79] is applied to $\langle I\rangle_x$ to apply a binary thresholding which segments this bar from the background. The top and bottom edges $k_-(j)$, $k_+(j)$ of this segmentation are then retrieved for every column j. They mark the k values of the first and last frame where the coordinate y_j is covered by the radiation field. Based on Eq. (4.11), model functions are defined as

$$\hat{k}_-(j) = aj + b,\ \hat{k}_+(j) = aj + c,$$

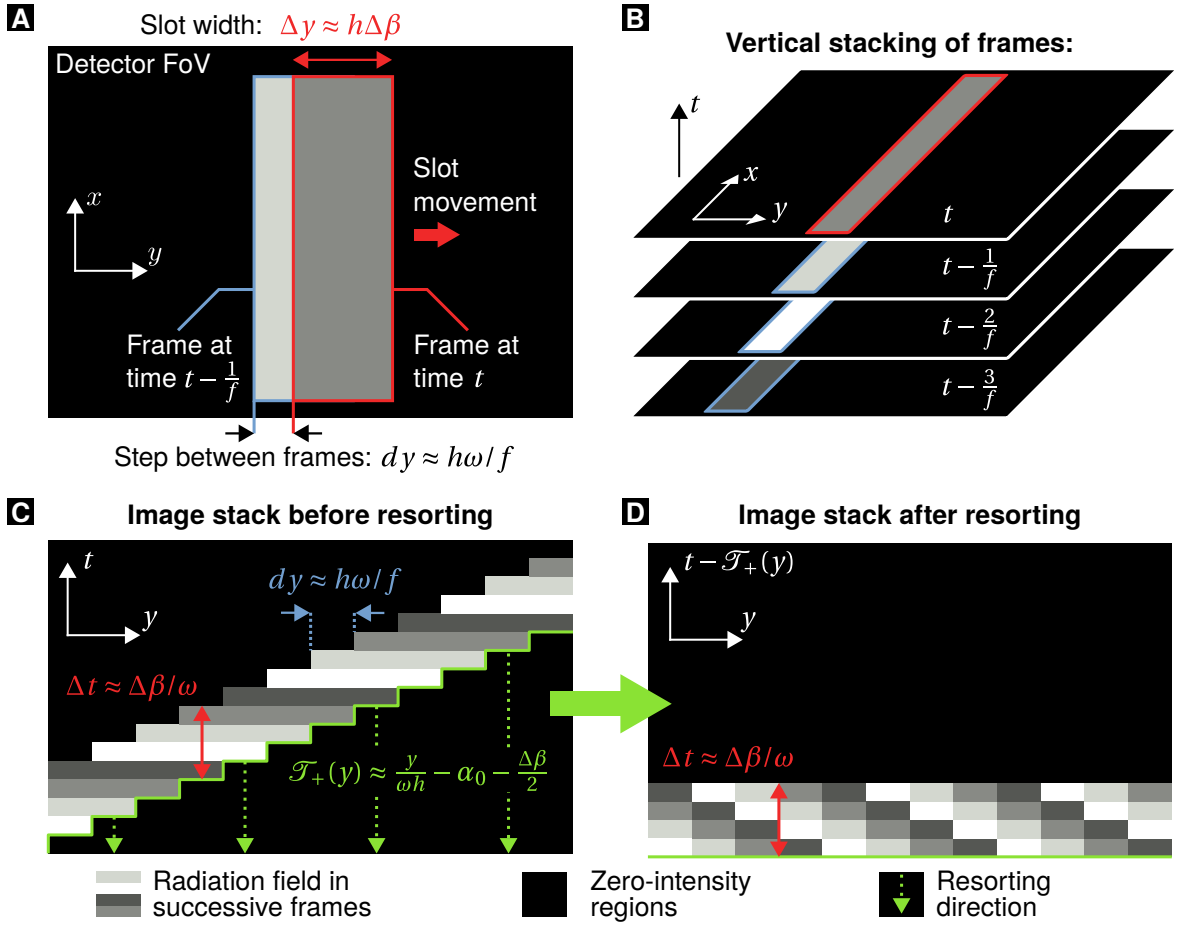

Figure 4.3: Visualization of the data resorting procedure. (a): View of the radiation field in the detector FOV. The field moves a constant amount dy between successive frames. (b): For resorting, all frames are stacked into a 3D array (in chronological order). (c): In a sideways view of the 3D array (achieved e.g. by averaging along the x axis), the movement of the radiation field appears as a diagonal "bar". For each y coordinate, the earliest time $\mathcal{T}_+(y)$ where the radiation field has reached y is apparent as the bar's lower border (green). Resorting is finally achieved by calculating $\tau = t - \mathcal{T}_+(y)$. Note that the y coordinates are not manipulated, interpolation is thus only performed in time, not in space. Furthermore, the number of "useful" frames (i.e., those with nonzero intensity) $\Delta t/f$ remains unaffected by the transform.

and linear regression yields the slope and intercept parameters

$$\tilde{a},\tilde{b},\tilde{c} = \underset{a,b,c}{\arg\min} \sum_j \left[k_+(j) - \hat{k}_+(j)\right]^2 + \left[k_-(j) - \hat{k}_-(j)\right]^2 .$$

Finally, the data is rearranged by shifting each column j by $\lfloor \tilde{a} j + \tilde{b} \rfloor$ pixels, with $\lfloor \cdot \rfloor$ the "floor function", i.e. the argument rounded down to the nearest integer. With the use of sub-pixel interpolation, shifting by $\tilde{a} j + \tilde{b}$ exactly is also possible, albeit potentially at the expense of resolution and/or visibility.

Variations in swing speed or starting point will lead to changes in the parameters $\tilde{a}, \tilde{b}, \tilde{c}$.

Varying swing speed between reference and object scans leads to a change in $\tilde{a}$, and importantly, different sampling intervals of the moiré pattern. Matching such data sets requires more complex interpolation schemes. Although such an algorithm was designed (devised by Lukas Gromann), it was not tested extensively.

A difference in starting point between scans leads only to a change in the offset parameters $\tilde{b}, \tilde{c}$, and could thus be corrected by determining the limits separately for each scan. However, the determination of radiation field limits based on Otsu's method may fail for scans of strongly attenuating objects. Although alternative algorithms were developed to tackle this problem, using identical movement parameters for object and reference scans has proven to be the most reliable approach: in this case, it is sufficient to determine $\tilde{a}, \tilde{b}, \tilde{c}$ from one of the reference scans, and reuse these parameters for the remaining reference scans and the object scan. This is also illustrated in the workflow chart in Fig. 4.17.

Initially, the *spec*-based system control software (cf. section 3.4.5 on page 83) provided only a limited synchronization accuracy between swing movement and the X-ray system, which lead to a slight random deviation in the effective starting point between scans and thus resulted in image artifacts. However, this was solved by Philips Medical Systems DMC GmbH providing an update to the X-ray system control software, allowing synchronization to within one detector clock cycle (i.e., $1/11.6\,\mathrm{Hz} \approx 86\,\mathrm{ms}$).

4.2 Calculation of image signals

Starting with the common model of image formation for phase-stepping measurements of grating-based X-ray phase contrast, an equivalent model for fringe-scanning setups is developed in section 4.2.1. Four different approaches to solve the model (or simplified versions thereof) are introduced in section 4.2.2, and their performance is compared in section 4.2.3.

4.2.1 Modified signal formation model for fringe scanning

As introduced in section 2.5.6 on page 56, a common model for retrieving the image modalities from a phase-stepping data set is

$$\begin{aligned} \hat{I}_k^{(\mathrm{r})} &= A\left[1 + V\cos\left(\Phi_k - \phi\right)\right], \\ \hat{I}_k &= TA\left[1 + DV\cos\left(\Phi_k - \phi - \varphi\right)\right], \end{aligned} \tag{4.12}$$

with $k = 1,\ldots,N$. These equations can also be expressed as:

$$\begin{aligned} \hat{I}_k^{(\mathrm{r})} &= a_0^{(\mathrm{r})} + a_1^{(\mathrm{r})}\cos\left(\Phi_k - \phi_1^{(\mathrm{r})}\right), \\ \hat{I}_k &= a_0 + a_1\cos\left(\Phi_k - \phi_1\right). \end{aligned} \tag{4.13}$$

If all Φ_k are equidistantly spaced over one or several periods, e.g. $\Phi_k = 2\pi k/N$, Eqs. (4.13) are truncated Fourier series with respect to k. Note that all variables in the above equations implicitly depend on detector pixel indices, i.e. a separate instance must be solved for every detector pixel. By least-squares regression of the sample phase-stepping measurement data $I_k\,(k = 1,\ldots,N)$ to this model, values for $[a_0, a_1, \phi_1]$ and $[a_0^{(\mathrm{r})}, a_1^{(\mathrm{r})}, \phi_1^{(\mathrm{r})}]$ can be retrieved. The quantities in Eq. (4.13) are related to those in Eq. (4.12) as

$$\begin{aligned} A &= a_0^{(\mathrm{r})}, & V &= \frac{a_1^{(\mathrm{r})}}{a_0^{(\mathrm{r})}}, & \phi &= \phi_1^{(\mathrm{r})}, \\ T &= \frac{a_0}{a_0^{(\mathrm{r})}}, & D &= \frac{a_1 a_0^{(\mathrm{r})}}{a_0 a_1^{(\mathrm{r})}}, & \varphi &= \phi_1 - \phi_1^{(\mathrm{r})}. \end{aligned} \tag{4.14}$$

This model is usually very accurate for phase-stepping data: The implied assumption that transmittance T, visibility reduction D and sample-induced fringe shift φ are constant throughout the measurement is reasonable since all objects except for the stepped grating remain stationary. Furthermore, the values of Φ_k can be

freely chosen by controlling lateral shift of the stepped grating with a sufficiently precise motorized stage.

For the variant of fringe scanning implemented in the *lung-scanning setup* however (fixed source, sample, and detector, rotating interferometer), this model is unable to fully capture the imaging process: The sampling of different phase values Φ_k is achieved as the grating arrangement passes over a given image region. Thus, the same pixels are imaged by different regions of the gratings. Since the gratings are not perfectly uniform in absorber height and alignment, variations in flux A and visibility V may be introduced which are not due to the sample.

Eqs. (4.13) can be generalized so that they take these variations into account:

$$\begin{aligned} \hat{I}_k^{(\mathrm{r})} &= A_k \left[1 + V_k \cos\left(\Phi_k - \phi\right)\right], \\ \hat{I}_k &= T A_k \left[1 + D V_k \cos\left(\Phi_k - \phi - \varphi\right)\right], \end{aligned} \tag{4.15}$$

or

$$\begin{aligned} \hat{I}_k^{(\mathrm{r})} &= a_{0,k}^{(\mathrm{r})} + a_{1,k}^{(\mathrm{r})} \cos\left(\Phi_k - \phi_1^{(\mathrm{r})}\right), \\ \hat{I}_k &= a_{0,k} + a_{1,k} \cos\left(\Phi_k - \phi_1\right). \end{aligned} \tag{4.16}$$

The fitting parameters A and V (or $a_0^{(\mathrm{r})}$, a_0, $a_1^{(\mathrm{r})}$ and a_1) have gained a dependence on k, which corresponds to a measurement of the sample by different regions of the grating interferometer. However, the parameters in Eqs. (4.16) are linked by the relationships

$$a_{0,k} = T a_{0,k}^{(\mathrm{r})},\ a_{1,k} = D a_{1,k}^{(\mathrm{r})},$$

which ensure that the reduction of flux and visibility due to a sample is still characterized by two parameters independent of k. Compared to the phase-stepping model, the number of unknowns have thus increased from 6 to $3N+3$, where N is the number of measurements per pixel. Effects due to the gratings and the sample are thus distinguished by being dependent or independent of k, respectively.

It should be noted that the independence of T and D from k is an approximation if a polychromatic source is used: the sample modalities then depend on spectral flux and visibility at the detector, which are in turn influenced by grating quality, and are thus dependent on k. Although the model could be modified to allow for such variations, this would require a precise knowledge of spectral properties in different regions of the field of view, and even then, its applicability would depend on the sample's material composition.

Furthermore, grating irregularities may also lead to complex spatial modulations in moiré fringe phase. Let the interferometer be at an arbitrary rotation angle α for time $t = 0$, and let $\Phi(x, y)$ be the resulting map of moiré fringe phases on the detector. By fringe scanning with the radiation field moving over the detector in the y direction with velocity v (for $t > 0$) and an image acquisition frequency f, the fringe phases sampled at (x, y) are

$$\Phi_k(x, y) = \Phi(x, kv/f + y_0).$$

Any deviations from a linearly increasing $\Phi(x, y)$ in the y direction (i.e., a perfectly sinusoidal modulation of intensity) will thus produce a non-equidistant sampling Φ_k of the interval $[-\pi, \pi]$, which may lead to further complications. For phase-stepping, the effects of such an irregular phase sampling have been examined e.g. in [DeMa+18]. Therefore, a number of different image calculation schemes were tested for use with the *lung-scanning setup*.

4.2.2 Evaluated image retrieval methods

4.2.2a Ellipse-based regression

The issue of non-equidistant phase steps and a non-integer number of sampled periods can be tackled with an ellipse-based fitting mechanism: Assuming that interferometer-related variations in flux and visibility are negligible, Eqs. (4.13) are applicable.

So-called Lissajous figures result from a parametric plot of two sinusoidal functions with rational multiples of oscillation frequency. For the case of identical frequencies, an ellipse results, and the phase shift between both functions may be inferred from the shape of the ellipse. For two functions with identical amplitudes and a relative phase shift of $\pm\pi/2$, the ellipse becomes a circle (eccentricity $\varepsilon = 0$). For a phase shift of $\pm\pi$, eccentricity approaches 1 and the ellipse degenerates to a straight line, as shown in Fig. 4.4. Crucially, as long as the two sinusoidal patterns are sampled at the same points, the shape of the ellipse is independent of the sampling pattern.

In calculating a parametric plot of $I_k(\Phi_k)$ versus $I_k^{(\mathrm{r})}(\Phi_k)$, according to Eqs. (4.12), (4.13), this phase shift is described by $\phi_1 - \phi_1^{(\mathrm{r})} = \varphi$. The remaining fit parameters lead to additional modifications of the resultant ellipse: As apparent from Fig. 4.4, the ellipse's center

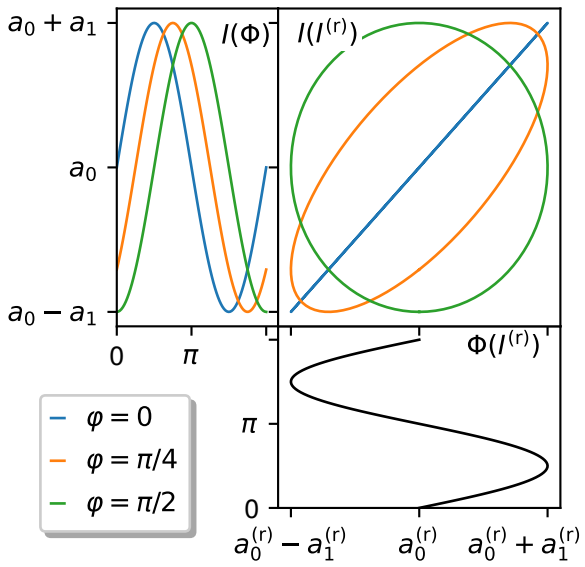

Figure 4.4: Lissajous figures resulting from parametric plots of phase-shifted sinusoidal curves. The relative phase shift φ is uniquely related to the eccentricity of the ellipse.

is determined by a_0 and $a_0^{(r)}$, while a_1 and $a_1^{(r)}$ modify the extent of the ellipse in either direction.

A conic (ellipse, parabola, or hyperbola) in the xy plane can be described as the solution to the equation

$$F(x,y) \equiv ax^2 + bxy + cy^2 + dx + ey + f = 0, \quad (4.17)$$

with the additional condition that $\delta \equiv 4ac - b^2 > 0$ for ellipses. Eqs. (4.13) contain $6+N$ unknowns (N being the number of phase steps). However, the stepping positions $\Phi_1, \ldots \Phi_N$ do not affect the shape of the ellipse, which reduces the effective number of unknowns to 6. Furthermore, the ellipse's eccentricity depends only on the *phase difference* $\phi_1 - \phi_1^{(r)}$ between the two data sets, leaving 5 unknowns to be retrieved by the fit. A unique transform exists between the fit parameters $a, \ldots, f$ and the fit parameters from Eqs. (4.13):

$$\begin{aligned} a_0^{(r)} &= (be - 2cd)/\delta, \\ a_0 &= (bd - 2ae)/\delta, \\ a_1^{(r)} &= 2\sqrt{c\gamma}/\delta, \\ a_1 &= 2\sqrt{a\gamma}/\delta, \text{ and} \\ \varphi = \phi_1 - \phi_1^{(r)} &= \arccos\left(\frac{-b}{2\sqrt{ac}}\right), \end{aligned}$$

where

$$\begin{aligned} \delta &= 4ac - b^2, \\ \gamma &= ae^2 - bde + cd^2 - f\delta. \end{aligned}$$

The expressions can be simplified via Eqs. (4.14) to yield the image modalities T and D:

$$\begin{aligned} T &= \frac{bd - 2ae}{be - 2cd}, \\ D &= \sqrt{\frac{a}{c}} \cdot \frac{be - 2cd}{bd - 2ae}. \end{aligned} \quad (4.18)$$

The added benefit of this approach over simple phase-stepping is its compatibility with non-equidistant phase sampling and a non-integer number of fringe phases. Furthermore, unlike other examined approaches, the ellipse-fitting procedure requires acquisition of only one reference scan.

Different ellipse fitting approaches, i.e. methods to achieve estimates for the parameters $a, \ldots, f$ from a series of point pairs (x_k, y_k), have been developed. The most obvious of these is an iterative minimization of the sum of squared Euclidean distances between data points and fit model. However, iterative approaches are comparatively slow, not guaranteed to converge, and are in this case further impeded by the fact that the orthogonal distance between a point and an ellipse is complicated to calculate [Zhan97].

However, it was discovered that this fitting task can be formulated in such a way that it becomes a linear problem, even when taking into account the ellipse condition that $\delta > 0$. This is achieved by minimizing the sum of squared *algebraic* distances[1] instead of the squared geometric distances between model and data and is formulated as an eigenvalue problem [Fitz+96].

This approach has previously been used for determining phase shifts between vibrational noise from two linked gravimeters (measurement of gravitational acceleration), thus allowing a suppression of such "phase noise" [Fost+02]. Later on, the method in [Fitz+96] was modified to improve numerical stability as well as execution speed [Halí+98].

The latter method was tested for use with data from the *lung-scanning setup*. By interpreting pixel values $(I_k^{(r)}, I_k)$ as points in a plane, and determining an ellipse optimally describing the set of points

[1] The algebraic distance of a point (x, y) to an ellipse with parameters $(a, \ldots, f)$ is equal to $F(x, y)$ from Eq. (4.17). It is obviously zero if the point lies on the ellipse.

$[(I_1^{(\mathrm{r})}, I_1), \ldots, (I_N^{(\mathrm{r})}, I_N)]$, all relevant parameters can be extracted. I.e., using the algorithm described in [Halí+98], we calculate

$$\tilde{a}, \ldots, \tilde{f} = \underset{a,\ldots,f}{\arg\min} \sum_k F(I_k^{(\mathrm{r})}, I_k)^2,$$

with F as defined in Eq. (4.17), and then determine $\tilde{T}$ and $\tilde{D}$ by inserting $\tilde{a}, \ldots \tilde{f}$ for $a, \ldots f$ in Eqs. (4.18).

4.2.2b Linear regression

Another examined approach is based on a simplification of the ellipse fitting method: As shown in Fig. 4.4, the ellipse is reduced to a straight line with positive slope for $\varphi = 0$. If measured samples incur little to no phase shift, linear regression can be attempted. Starting from Eqs. (4.13), assuming $\phi_1^{(\mathrm{r})} = \phi_1$, and setting

$$\hat{I}_k = m\hat{I}_k^{(\mathrm{r})} + b,$$

we find that

$$m = \frac{a_1}{a_1^{(\mathrm{r})}},\ b = a_0 - \frac{a_1 a_0^{(\mathrm{r})}}{a_1^{(\mathrm{r})}} = a_0^{(\mathrm{r})}(T - m).$$

However, the fit coefficients alone are insufficient to retrieve all parameters from Eqs. (4.13). In the absence of phase shift, a total of four parameters must be found, while a straight line is fully defined by two parameters. The remaining information could be retrieved from the maximal and minimal intensities during the measurements, or, as done here, from the mean values $\langle I_k \rangle_k$ and $\langle I_k^{(\mathrm{r})} \rangle_k$, where

$$\langle f_k \rangle_k \equiv \frac{1}{N} \sum_{k=1}^{N} f_k. \tag{4.19}$$

For approximately equidistant sampling of the moiré fringes, the cosine terms in Eqs. (4.13) mostly cancel out, so that

$$\left\langle \hat{I}_k^{(\mathrm{r})} \right\rangle_k \approx a_0^{(\mathrm{r})},\ \langle \hat{I}_k \rangle_k \approx a_0.$$

Therefore,

$$T \approx \frac{\langle \hat{I}_k \rangle_k}{\left\langle \hat{I}_k^{(\mathrm{r})} \right\rangle_k},\ D = \frac{m}{T}.$$

For an approximately equidistant sampling of phases Φ_k, this approach should also be applicable for data with $|\varphi| \ll \pi/2$, since the data points lie on an ellipse which is symmetric to the line which would result for $\varphi = 0$. Note however that negative fit slopes result for $\pi/2 < \varphi < 3\pi/2$. For $\varphi = \pi$: $D = -m/T$.

4.2.2c Basis vector regression

Another approach that was tested is based on the trigonometric identity

$$\cos(\alpha_k - \beta) = \cos\alpha_k \cdot \cos\beta + \sin\alpha_k \cdot \sin\beta. \tag{4.20}$$

Let $\alpha_1, \ldots, \alpha_k, \ldots, \alpha_N$ be an arbitrary set of angles, and define the three vectors

$$\vec{C} = [A_1 \cos\alpha_1, \ldots, A_N \cos\alpha_N],$$
$$\vec{S} = [A_1 \sin\alpha_1, \ldots, A_N \sin\alpha_N],$$
$$\vec{R} = [BA_1 \cos(\alpha_1 - \beta), \ldots, BA_N \cos(\alpha_N - \beta)].$$

It follows from Eq. (4.20) that $\vec{R}$ is a linear combination of $\vec{C}$ and $\vec{S}$, namely:

$$\vec{R} = B(\cos\beta \cdot \vec{C} + \sin\beta \cdot \vec{S}).$$

This can be used to solve the phase retrieval problem while allowing for variable reference scan visibility. By measuring two sets of reference scans with a $\pi/2$ phase shift, achieved e.g. via phase stepping, data following the model

$$\hat{I}_k^{(\mathrm{r},1)} = a_0^{(\mathrm{r})} + a_{1,k}^{(\mathrm{r})} \cos\left(\Phi_k - \phi_1^{(\mathrm{r})}\right)$$
$$\hat{I}_k^{(\mathrm{r},2)} = a_0^{(\mathrm{r})} + a_{1,k}^{(\mathrm{r})} \sin\left(\Phi_k - \phi_1^{(\mathrm{r})}\right). \tag{4.21}$$

is retrieved. Note that Eqs. (4.21) differs from Eqs. (4.16) in that $a_0^{(\mathrm{r})}$ is assumed to be constant. For approximately equidistant placement of $\Phi_1, \ldots, \Phi_N$, its value is approximated by the mean value of all measured intensity values, i.e.

$$a_0^{(\mathrm{r})} \approx \left\langle I_k^{(\mathrm{r},1)} \right\rangle_k \approx \left\langle I_k^{(\mathrm{r},2)} \right\rangle_k,$$

with the definition from Eq. (4.19). This allows calculation of the two zero-mean basis vectors

$$C_k \equiv I_k^{(\mathrm{r},1)} \Big/ \left\langle I_k^{(\mathrm{r},1)} \right\rangle_k - 1 \approx V_k \cos(\Phi_k - \phi),$$
$$S_k \equiv I_k^{(\mathrm{r},2)} \Big/ \left\langle I_k^{(\mathrm{r},2)} \right\rangle_k - 1 \approx V_k \sin(\Phi_k - \phi).$$

The equivalent procedure can be applied to the sample scan data set:

$$R_k \equiv I_k / \langle I_k \rangle_k - 1 \approx DV_k \cos(\Phi_k - \phi + \varphi).$$

Calculation of

$$\tilde{a}, \tilde{b} = \underset{a,b}{\arg\min} \sum_{k=1}^{N} (R_k - aC_k - bS_k)^2 \tag{4.22}$$

yields visibility reduction and phase shift via[2]

$$D = \sqrt{\tilde{a}^2 + \tilde{b}^2},\ \varphi = \arctan2\left(\tilde{b}, \tilde{a}\right),$$

while transmittance is directly calculated as

$$T = \langle I_k \rangle \Big/ \left\langle I_k^{(\mathrm{r},1)} \right\rangle,$$

or $\langle I_k^{(\mathrm{r},2)} \rangle$ in place of $\langle I_k^{(\mathrm{r},1)} \rangle$. This approach allows to take into account variations in measured visibility and is fast to compute, as Eq. (4.22) is a linear minimization problem. On the other hand, no such variations are allowed for the mean intensity a_0. Furthermore, the determination of a_0 by the averaging process is prone to bias, especially when the input data has a highly irregular sampling of phases φ_k.

4.2.2d Full retrieval of reference scan parameters

Finally, a method was tested where the complete set of parameters in the extended model from Eqs. (4.15) is retrieved. This is achieved by a more elaborate acquisition of reference scans:

Similarly to phase stepping, data is acquired between incremental lateral displacements of one of the gratings over one or several grating periods. Instead of a single acquisition frame however, a full reference fringe scan is performed before each displacement. For each detector pixel, this results in a two-dimensional data array $I_{km}^{(\mathrm{r})}$: The intensity at the given pixel is measured not only at multiple relative positions k to the grating arrangement, but also at multiple grating displacements m. In the model from Eqs. (4.15), this can be represented as an additional phase term θ_m:

$$\hat{I}_{km}^{(\mathrm{r})} = A_k \left[1 + V_k \cos\left(\Phi_k - \phi - \theta_m\right)\right]. \tag{4.23}$$

Note that $\hat{I}_{km}^{(\mathrm{r})}$ as a function of m is structurally identical to the model conventionally used for phase stepping [Eqs. (4.12)], since all quantities dependent on k can now be treated as constants. Therefore, the quantities A_k, V_k and $\Phi_k - \phi$ can then be directly calculated *for all* k by least-squares minimization:

$$\boxed{\tilde{A}_k, \tilde{V}_k, \widetilde{\Phi_k - \phi} = \underset{A_k, V_k, \Phi_k - \phi}{\operatorname{argmin}} \sum_m \left(\hat{I}_{km}^{(\mathrm{r})} - I_{km}^{(\mathrm{r})}\right)^2.} \tag{4.24}$$

[2] The function $\arctan2(y, x)$ denotes the angle between the vector $[x, y]^T$ and the x axis.

This enables a determination of T, D, and φ via the model from Eqs. (4.15). Inserting the values retrieved from the reference scans, it reads

$$\hat{I}_k = T\tilde{A}_k \left[1 + D\tilde{V}_k \cos\left(\widetilde{\Phi_k - \phi} - \varphi\right)\right]. \tag{4.25}$$

It can also be expressed as a linear function of parameters P_1, P_2, P_3:

$$\begin{aligned} \hat{I}_k^{(\mathrm{lin})} &= P_1 \cdot \tilde{A}_k \\ &\quad + P_2 \cdot \tilde{A}_k \tilde{V}_k \cos\left(\widetilde{\Phi_k - \phi}\right) \\ &\quad + P_3 \cdot \tilde{A}_k \tilde{V}_k \sin\left(\widetilde{\Phi_k - \phi}\right), \end{aligned} \tag{4.26}$$

where

$$P_1 = T,\ P_2 = TD\cos\varphi,\ P_3 = TD\sin\varphi.$$

Optimal values for P_1, P_2, and P_3 can then be retrieved by another linear least-squares minimization procedure:

$$\boxed{\tilde{P}_1, \tilde{P}_2, \tilde{P}_3 = \underset{P_1, P_2, P_3}{\operatorname{argmin}} \sum_k \left(\hat{I}_k^{(\mathrm{lin})} - I_k\right)^2.} \tag{4.27}$$

Finally, the modalities are calculated from these parameters via

$$\tilde{T} = \tilde{P}_1,\ \tilde{D} = \frac{\sqrt{\tilde{P}_2^2 + \tilde{P}_3^2}}{\tilde{P}_1},\ \tilde{\varphi} = \arctan2\left(\tilde{P}_3, \tilde{P}_2\right). \tag{4.28}$$

The optimization in Eq. (4.27) is slightly more laborious than e.g. the linear regression procedure for phase-stepping data, since the model matrix of independent variables contains $\tilde{A}_k$, $\tilde{V}_k$, and $\tilde{\Phi}_k$, and must therefore be calculated separately for each pixel.

Evidence for the dependence of the regression parameters on k is shown in Fig. 4.5: Here, the values of $\tilde{A}_k$, $\tilde{V}_k$, and $\widetilde{\Phi_k - \phi}$ retrieved with the "full retrieval" method from a phase-stepped series of reference scans are shown for a few pixels. The estimated variations of $\tilde{A}_k$ and $\tilde{V}_k$ with k are considerable.

Overall, this method is more time-consuming and computationally demanding due to the large amount of data acquired, especially for the reference scans. However, it models the behavior of the imaging system quite accurately, and avoids large biases due to its dependence on reference data with equidistantly-sampled fringe phases.

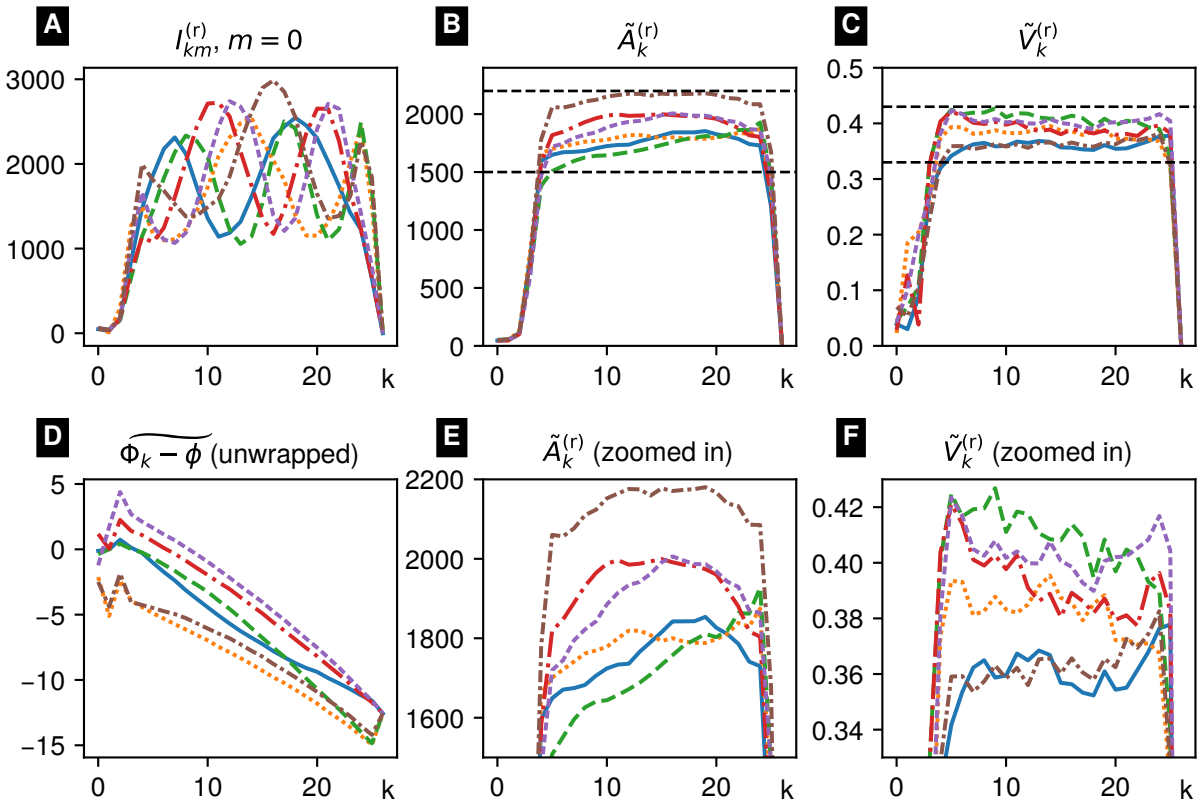

Figure 4.5: Variation of regression parameters of phase-stepped reference scans with the "full retrieval" method. Values from six detector pixels, each covered by different G_1 and G_2 grating tiles, are shown. (a): Measured intensities $I^{(r)}_{km}$ from the first scan ($m = 0$). The decrease in visibility and mean intensity of the moiré fringes towards the edges of the grating (high and low k) is apparent. (b): Retrieved mean intensity $\tilde{A}_k$. (c): Retrieved visibility $\tilde{V}_k$. The limits of the grating and the beam collimation determine the drop-off in both quantities. (d): Retrieved, unwrapped fringe phase $\widetilde{\Phi_k - \phi}$, should vary linearly with k if fringes are perfectly sinusoidal. (e, f): Zoomed-in versions of (b) and (d), respectively, to emphasize variations of the quantities within the grating area. The difference in curve shapes may arise due to a slightly different tilt, and thus, different shadowing behavior of the grating tiles.

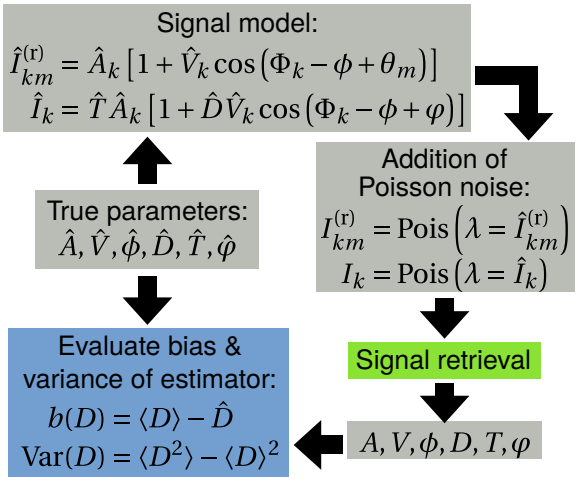

Figure 4.6: Process for the comparison of signal extraction methods. Intensities were calculated from exact parameter values using Eqs. (4.23), (4.25). These were then used as the mean value parameter λ to generate noisy Poisson-distributed data. All four signal retrieval methods were applied to the noisy data and regression results were compared to the exact values.

4.2.3 Comparison of noise and bias performance

In statistical terms, the presented methods of calculating the blank-scan and sample-scan variables from the measured intensities act as different "estimators" of these variables. However, the variables' true values can only be retrieved with limited precision since measured intensities are noisy. In the case of X-ray measurements, the most common source of noise are statistical variations in the number of measured photons, and to a lesser degree, thermal fluctuations in readout electronics.

Two statistical quantities are especially useful to gauge the performance of an estimator: bias and variance (of the estimated quantity).

While the variance $\mathrm{Var}(X) = \left\langle X^2\right\rangle - \langle X\rangle^2$ quantifies the spread of estimated values, the bias $b(X) = \langle X\rangle - \hat{X}$ (with $\langle\cdot\rangle$ representing the expectation value according to the estimator, and $\hat{X}$ the parameter's true value) is a measure for a systematic error in the retrieval process of a parameter X.

Although these quantities can be calculated analytically for some estimators, it is much more practical to perform numerical simulations according to the schematic in Fig. 4.6. For different sets of parameters, expectation values of intensity are calculated either according to the signal formation model in Eqs. (4.13) (constant flux and visibility) or Eqs. (4.15) (variable flux and visibility over the scan). These values then serve as a reference for a set of noise realizations:

If secondary noise sources (e.g., due to electronics) are negligible, and intensity values I_k, $I^{(r)}_k$ are given as a number of detected photons, they are Poisson-distributed. This distribution has only one parameter, which is equal to its expected value, i.e., $\hat{I}_k$ or $\hat{I}^{(r)}_k$.

After generating a large number of noise realizations from the expectation value of each point, the different signal retrieval methods are applied to all of them, and the distribution of resulting parameters is compared to the ground truth, i.e., the input values for the simulation. The first and second moments of all retrieved variables (A,V, ϕ, D, T, φ) were calculated over the values resulting from all noise realizations. Together with the ground truth values, this allowed the calculation of bias and variance of all quantities.

Simulations were thus performed using sets of realistic parameter values for all four signal retrieval methods. In Fig. 4.7, mean and standard deviation (cf. error bars) of retrieved dark-field values are shown as a function of (true) transmittance $\hat{T}$ (for $\hat{D} = 0.02$, $\hat{\varphi} = 0$, middle column), and differential-phase shift $\hat{\varphi}$ (with $\hat{D} = 0.6$, $\hat{T} = 0.02$, lower column). $N = 25$ acquired intensity values per scan were assumed.

Two different curve shapes of $\hat{A}_k$ and $\hat{V}_k$ were examined: the ideal case of $\hat{A}_k, \hat{V}_k = \text{const.}$ (left column), and a more realistic case of shadowing-related fluctuations of both quantities (parabolic profiles with a variation of 25% of their mean values, right column). The mean value $\langle\hat{A}_k\rangle_k = 10^4$ was selected to provide a realistic number of photons per pixel and frame. It was derived from per-frame detector dose levels in a typical reference measurement at the *lung-scanning setup*. The true value $\hat{D}$ is highlighted by a black line, allowing visual assessment of the method's bias.

Since the processing methods employ different types (and amounts) of reference scan data, a set of eight phase-stepped reference scans was simulated. All eight were used in the "full retrieval" method, whereas only two are required for basis vector regression, and one for the remaining two methods. The tested methods did thus not receive completely identical amounts of statistics, but this difference is relatively minor since

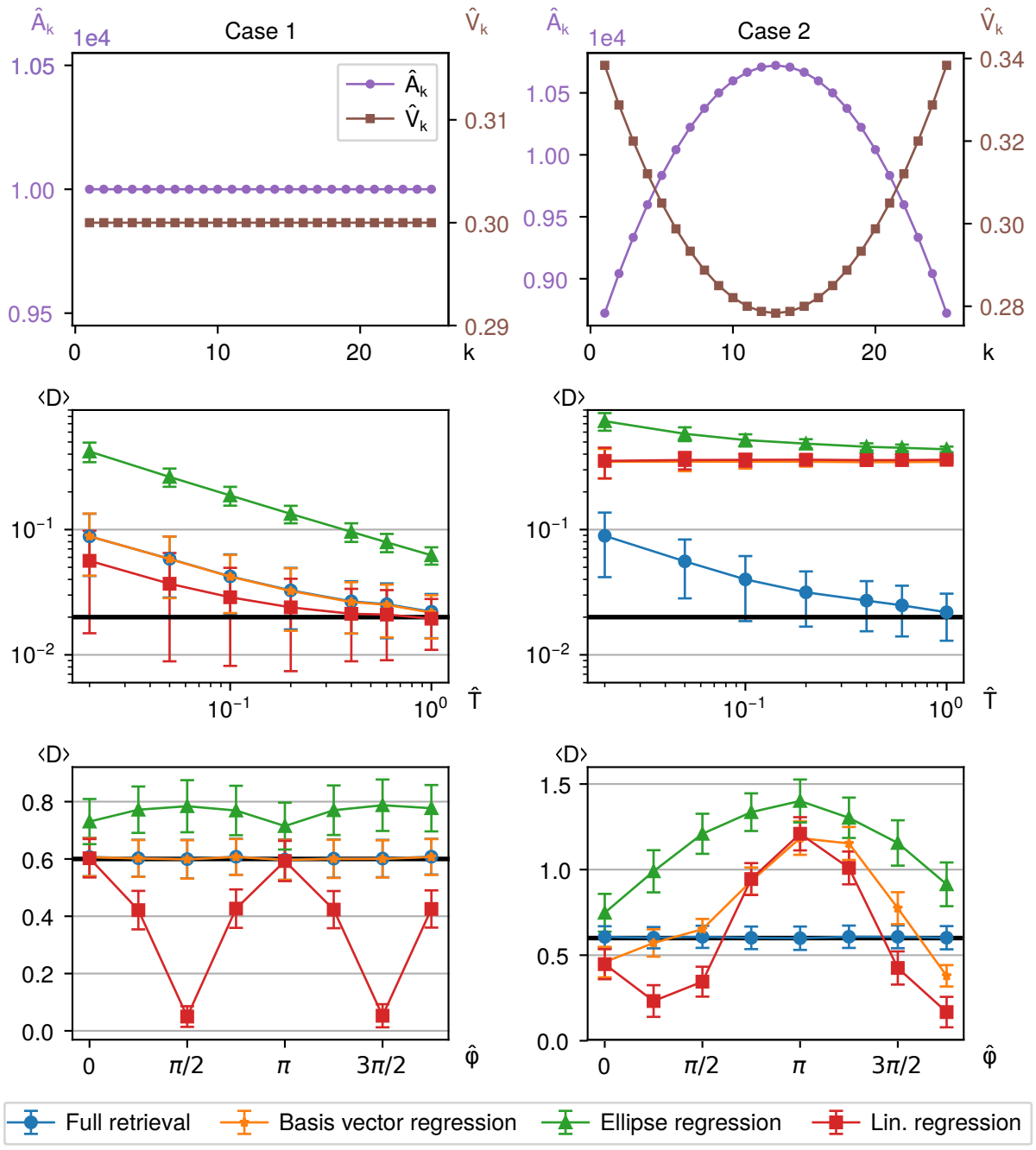

Figure 4.7: Dark-field values retrieved from simulated Poisson-distributed intensities, using each of the four examined signal retrieval methods. Two scenarios are shown, assuming constant (left, case 1) or variable (right, case 2) flux and visibility across the grating area (cf. top row). Middle row: Estimated dark-field values $\langle D \rangle$ as a function of (true) transmittance $\hat{T}$. The true value ($\hat{D} = 0.02$) is highlighted by a black line. The systematic error (bias) is excessive for ellipse regression even in case 1. Bottom row: Estimated values $\langle D \rangle$ as a function of (true) fringe shift $\hat{\varphi}$. Both ellipse and linear regression exhibit a strong φ-dependent bias. As apparent from the right column, only "full retrieval" is able to treat case 2 correctly. Mean and error of each data point are calculated from 900 noise realizations.

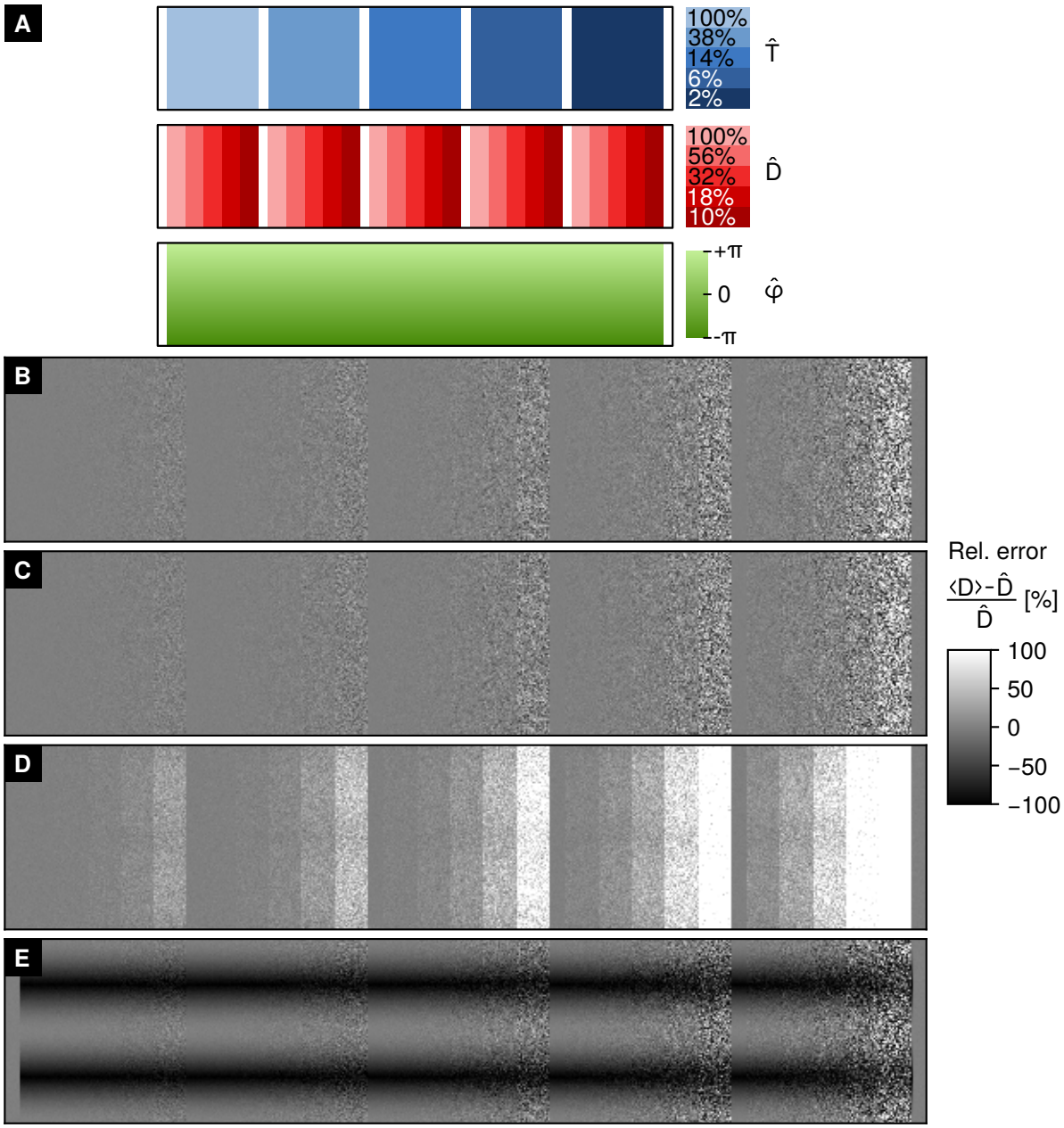

Figure 4.8: Images of relative error in dark-field values retrieved with all four processing methods. (a): Digital phantom consisting of rectangular areas with constant transmittance and dark-field, as well as a vertical gradient of differential-phase values. (b): "Full retrieval", (c): Basis vector regression, (d): Ellipse-based regression, (e): Linear regression. As in Fig. 4.7, the large bias of ellipse-based regression for low values of $\hat{D}$ is apparent. Furthermore, there is a significant φ-dependence of dark-field bias for linear regression.

the reference scan data have much higher statistics than the sample scan and thus contribute little to overall noise and bias levels.

It should be noted that $\hat{D} = 0.02$ (used in the middle column) and $\hat{T} = 0.02$ (bottom column) are extremely low values and, together with $\hat{A} \approx 10^4$, make for very challenging, low-statistics regression problems, well-suited to distinguish the different methods' performance.

Ellipse regression clearly yields much higher dark-field bias values than the other methods. This is not surprising when considering the extreme deformation of a Lissajous ellipse with $\hat{T} = 0.02$ or $\hat{D} = 0.02$. In such cases, the standard deviation of intensity values is in the same range as the intensity variation over the (sample) scan. These values can thus not be unambiguously assigned to either half of the Lissajous ellipse. This method might however be improved by supplementing the existing regression step by a minimization of geometric distances (which must necessarily performed iteratively), or an inclusion of phase-stepped reference scan data (e.g. a comparison of ellipse fits with different phase-stepped reference scans).

Linear regression yields the lowest bias under ideal conditions (constant $\hat{A}$ and $\hat{V}$, $\hat{\varphi} = 0$), but unsurprisingly gives very inaccurate results for $\hat{\varphi}$ values far from 0 or π. Even in the absence of refraction, nonzero fringe shifts φ can occur due to thermal drifts between the acquisition of reference scan and object scan.

Full retrieval and basis vector regression yield nearly identical results for constant $\hat{A}_k$ and $\hat{V}_k$, but basis vector regression is unable to correctly interpret variations in these quantities.

These findings are reiterated in Fig. 4.8, where images of relative deviation between retrieved and true dark-field values are shown. A digital phantom with regions of different amounts of attenuation and visibility reduction, as well as a continuous ramp of differential phase shift was constructed to allow an assessment of each processing method "at a glance".

It is quite apparent that among the examined methods, the "full retrieval" approach yields the best and most consistent results. Its performance was considered worth the additional effort of acquiring phase-stepped reference scan data.

The comparison of the methods presented here is limited in that no application to experimental data was shown. However, the limitations of the "ellipse regression" and "linear regression" methods are so apparent even from simulated data that their practical application can be immediately ruled out. Concerning the "basis vector regression" method, since it appears to work well only if $\hat{A}_k, \hat{V}_k = \text{const.}$, Fig. 4.5 demonstrates that these quantities do actually significantly vary with k in the *lung-scanning setup* implies the method's unsuitability.

Conversely, the good performance of the "full retrieval" method in the simulations does not prove its compatibility with real data. However, it is a logical extension of the experimentally very well-verified sinusoidal phase-stepping model to variable flux and visibility. In particular, the conventional phase-stepping model is contained in the "full retrieval" model as a special case. Furthermore, the quality of the dark-field images produced with this algorithm (as illustrated throughout chapter 5, starting on page 115) does in my opinion serve as sufficient evidence of its performance.

4.3 Post-processing of dark-field image data

Three important post-processing operations for dark-field radiographs are introduced here: a correction of visibility reduction due to beam-hardening (section 4.3.1), a reduction of artifacts due to grating tiling (section 4.3.2), and an improvement of visual impression by low-pass filtering (section 4.3.3).

4.3.1 Beam-hardening correction of visibility

For any grating-based X-ray phase-contrast setup, interferometric visibility is a function of the measured X-ray spectrum (i.e., the spectral intensity). This is due to variations in the gratings' attenuating and phase-shifting capabilities, as well as changes of the self-imaging distances, with photon energy.

The most general way to describe this energy-dependence is a "visibility spectrum". It describes a setup's achieved visibility for illumination with monochromatic radiation, as a function of the radiation's wavelength or photon energy. Thus, the spectrum does not depend on the X-ray source, but only on the used gratings and their arrangement.

Polychromatic illumination can be thought of as a superposition of mutually incoherent monochromatic sources[3]. Thus, the interference fringes observed with polychromatic illumination are composed of monochromatic intensity oscillations that are, in the absence of a refracting object, in phase[4] (Fig. 4.9b, c).

The mean value and relative amplitude of these monochromatic fringes are determined by the spectral intensity and the visibility spectrum. Thus, high fringe amplitudes are achieved for those photon energies where visibility *and* spectral intensity are high. These photon energies therefore contribute strongly to polychromatic visibility (see e.g. E_2 in Fig. 4.9b). Conversely, photon energies with high visibility and low spectral intensity (E_1) or vice versa (E_3) have a lesser impact on overall visibility. Quantitatively, overall visibility can be understood as a mean of monochromatic visibility, weighted by the spectral intensity.[5]

Whereas a small-angle-scattering object modifies the visibility spectrum, a purely attenuating object affects only the detected spectral intensity. As most materials attenuate low-energy X-ray photons more strongly than high-energy photons, spectral intensity behind an attenuating object is shifted towards higher photon energies. This effect is known as *beam-hardening*, and can lead to a change in polychromatic visibility because of the above-mentioned relationships.

This relation is further complicated in the presence of dispersion, i.e. an energy-dependent nonzero amount of refraction: In this case, the monochromatic fringes are no longer in phase, which leads to a further reduction of polychromatic visibility.

In short, visibility reduction in polychromatic measurements can not be unambiguously attributed to small-angle scatter. This is especially problematic for the superposition of scattering and strongly beam-hardening/refracting materials (e.g., lung and bone) in projections. In such a case, the relative impact of the different effects on visibility reduction can not be

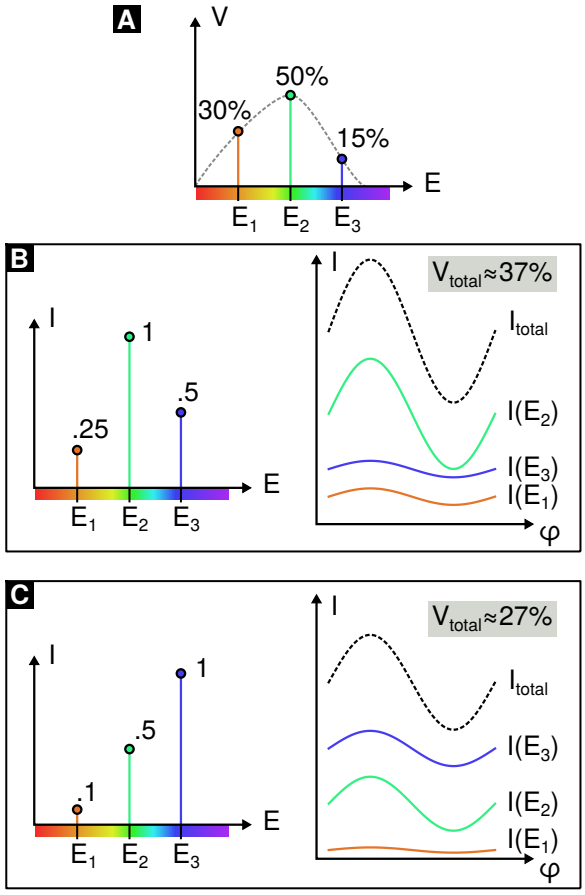

Figure 4.9: Illustration of visibility reduction due to beam-hardening. (a): Visibility spectrum with highlighted values at three photon energies E_1, E_2, E_3. (b): Hypothetical X-ray spectrum composed of narrow lines at these three energies. The intensities of the three monochromatic fringes (right, solid lines) add up to yield the total, polychromatic fringe (dashed line). (c): With a harder spectrum, the resulting polychromatic fringe has lower visibility than in (b) because of the different relative amplitudes of the monochromatic fringes.

[3] Fields with different frequencies are mutually incoherent. The total intensity of the polychromatic field is thus the sum of intensities at the constituent wavelengths, i.e. an integral over the "luminous intensity".[Mand+95, pp. 62–55]

[4] In certain cases, the moiré pattern is inverted as photon energy changes. While this can be interpreted as an abrupt phase shift of the pattern by half a period, it is here viewed as a negative modulation amplitude, i.e. a "negative visibility" (and an absence of phase shifts).

[5] A thorough mathematical model to describe this and related spectral effects is introduced in section 6.1 on page 159.

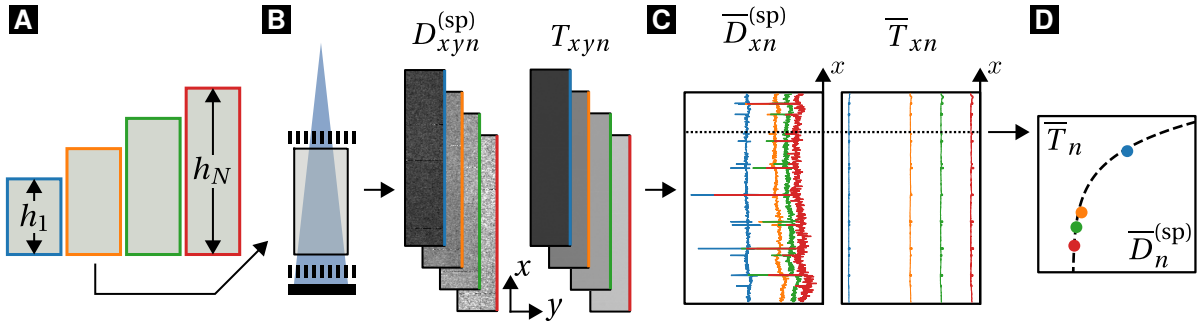

Figure 4.10: Determination of beam-hardening correction functions. (a): A series of POM blocks with gradually increasing heights h_n are selected. (b): Phase-stepping of each block yields maps of transmittance T_{xyn} and visibility reduction $D^{(sp)}_{xyn}$. (c): Averaging these maps along the y axis yields one-dimensional profiles $\overline{D}^{(sp)}_{xn}$, $\overline{T}_{xn}$. (d): A power-law function is fitted to the data for each x value.

uniquely determined. This effect impairs the diagnostic power of polychromatic dark-field imaging, since very different features may produce similar dark-field signal levels.

Beam-hardening correction However, information from the transmittance and differential phase shift images can be used to separate beam-hardening from true small-angle scatter. If the imaged object has uniform elemental composition, the impact of spectral effects on visibility can be derived from the the measured attenuation and differential-phase signals, either via the use of phantom materials or numerical simulations. Such an approach has been presented in [Pelz+16].

In this work, the authors make the assumption that total visibility reduction can be approximated as the product of a small-angle scatter (SAS) factor and a factor due to spectral effects (sp), i.e.

$$D \approx D^{(\mathrm{SAS})}\, D^{(\mathrm{sp})}.$$

For a given material and setup, $D^{(\mathrm{sp})}$ is then a function of transmittance T and fringe shift φ, and the visibility reduction factor due only to small-angle scatter can be approximated as

$$D^{(\mathrm{SAS})} \approx \frac{D}{D^{(\mathrm{sp})}(T,\varphi)}. \tag{4.29}$$

This approach was modified for use with the *lung-scanning setup*: Due to the setup's low angular sensitivity, and thus, the absence of strong differential-phase signals, the dependence of $D^{(\mathrm{sp})}$ on φ was neglected. Other than mammographic applications, for which the correction presented in [Pelz+16] was applied, thorax radiographs contain bony structures as well as soft tissues. This limits the general applicability of a correction approach based on the assumption of a single material. However, since soft and adipose tissues constitute the bulk of attenuating materials in thorax radiographs, the method was designed to correct for these.

For multiple reasons, an approach using experimental measurements was used instead of numerical simulations. Firstly, the variables necessary for a precise calculation of $D^{(\mathrm{sp})}$, namely detected spectral intensity and visibility spectrum, are difficult to measure: Both require the use of spectroscopic measurements, which necessitates elaborate modifications to the experimental setup. Additionally, these measurements would have to be repeated multiple times since the gratings' attenuation properties vary between tiles. Finally, the energy-dependent response of the flat-panel detector would have to be taken into account, which can not be easily measured.

An empirical correction approach, on the other hand, requires only the measurement of different thicknesses of a given phantom material, requiring no changes to the setup. The spatial variability of the correction can easily be taken into account by measuring different heights of the material in a large area, and deriving a position-dependent correction.

The thermoplastic polyoxymethylene (POM) was identified as a suitable reference material for the estimation

of $D^{(\mathrm{sp})}$, since its energy-dependent linear attenuation coefficient is similar to a mixture of soft and adipose tissues in roughly equal parts (cf. Fig. 6.1 on page 162).

The correction procedure is illustrated in Fig. 4.10: POM blocks of different heights h_n ($n = 1, \ldots, N$) were measured, generating maps of attenuation T_{xyn} and visibility reduction $D^{(\mathrm{sp})}_{xyn}$ (x, y being pixel coordinates). Due to the homogeneity of the material at µm length scales, visibility reduction from POM was assumed to be entirely due to spectral hardening effects.

As $D^{(\mathrm{sp})}$ and T both monotonically decrease[6] with n, a unique mapping between the two can be found: By interpolation or regression of a model function to the value pairs $(T_{xy1}, D^{(\mathrm{sp})}_{xy1}), \ldots (T_{xyN}, D^{(\mathrm{sp})}_{xyN})$, the expected value of $D^{(\mathrm{sp})}$ can be retrieved as a function of T. In principle, this could be performed for each pixel (x, y), generating per-pixel correction functions $D^{(\mathrm{sp})}_{xy}(T)$. From values D_{xy}, T_{xy} measured in a real scan, the small-angle-scattering component (or "true dark-field") could then be approximated equivalently to Eq. (4.29):

$$D^{(\mathrm{SAS})}_{xy} \approx \frac{D_{xy}}{D^{(\mathrm{SP})}_{xy}(T_{xy})}. \tag{4.30}$$

However, this approach requires a large amount of measurement data and scanning time. The variance of each per-pixel correction function $D^{(\mathrm{sp})}_{xy}$ is limited by the per-pixel noise levels of the calibration measurements. These are considerable, especially for the dark-field modality and for large POM heights, and can not be arbitrarily decreased without reducing the scanning speed. Therefore, the approach in Eq. (4.30) was simplified: Since $D^{(\mathrm{sp})}$, as a function of T, was found to vary strongly between grating tiles, but much less so with the y coordinate (i.e., along the scan direction), correction functions were only calculated for each x coordinate (the direction orthogonal to the scan direction, Fig. 4.10c).

As the entire range of x values was covered by the collimated slot, a phase-stepping measurement could be performed for each POM thickness in place of a fringe scan, greatly accelerating the calibration procedure. Some image data from this approach is shown in Fig. 4.11a, 4.11b. In order to minimize noise levels, the correction functions were calculated from

[6] This is not generally the case for $D^{(\mathrm{sp})}$, but was found to be accurate in the lung-scanning setup with the range of examined acceleration voltages, i.e., 60 and 70 kVp.

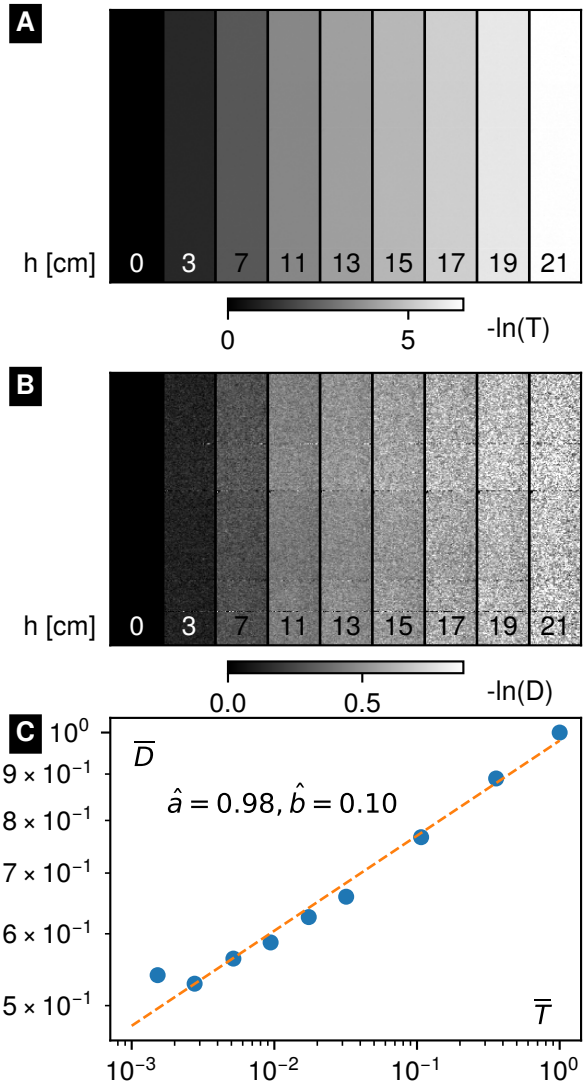

Figure 4.11: Data from phase-stepping measurements for beam-hardening correction. Juxtaposition of logarithmic transmittance (a) and logarithmic visibility reduction (b), for a range of POM phantom heights from 0 to 21 cm. (c): Relation between the two modalities. Data shown here are values for one x value, averaged along the y axis as shown in Eq. (4.31). The power-law fit according to Eq. (4.32) is shown as a dashed line.

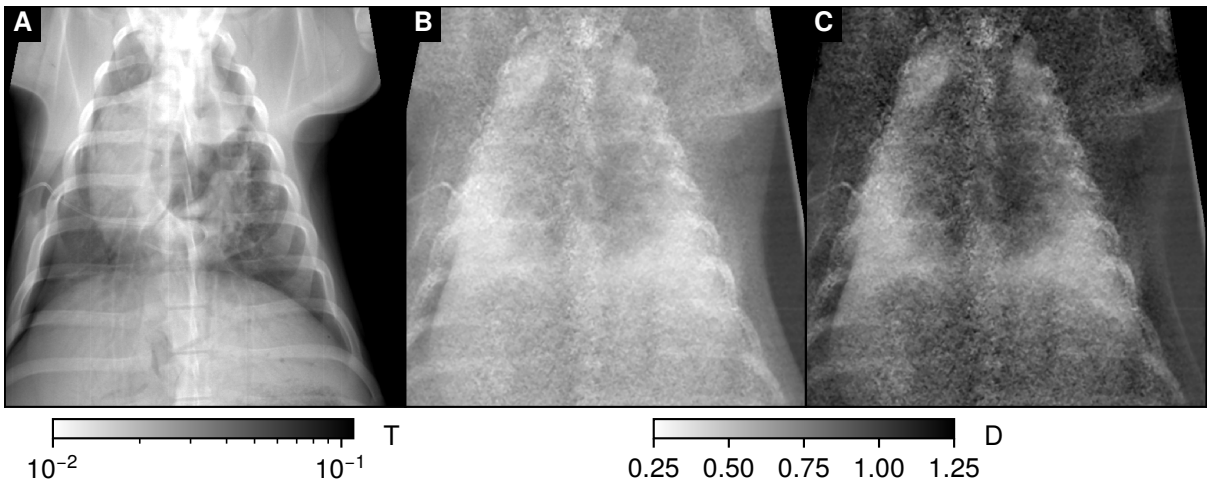

Figure 4.12: Effect of the beam-hardening correction on dark-field projections. Conventional (a) and dark-field (b) radiographs of an *ex vivo* pig thorax. In the beam-hardening-corrected dark-field projection (c), the signal due to spectral hardening (e.g. in the shoulders) disappears, whereas the lungs, being true small-angle-scattering structures, still generate contrast.

data averaged along the y direction, i.e.

$$\overline{D}^{(\mathrm{sp})}_{xn} = \frac{1}{Y}\sum_{y} D^{(\mathrm{sp})}_{xyn},\ \overline{T}_{xn} = \frac{1}{Y}\sum_{y} T_{xyn}, \tag{4.31}$$

with Y the slot width in pixels. Empirically, $\overline{D}^{(\mathrm{sp})}_{xn}$ and $\overline{T}_{xn}$ were found to be correlated by a power-law relationship, so that a function of the form $\overline{D}^{(\mathrm{sp})} = a\overline{T}^{b}$ could be fitted to the data, i.e.:

$$\tilde{a}_x, \tilde{b}_x = \underset{a,b}{\arg\min} \sum_{k=1}^{N} \left(\overline{D}^{(\mathrm{sp})}_{xn} - a\overline{T}^{b}_{xn}\right)^2. \tag{4.32}$$

An example for this regression is shown in Fig. 4.11c. The power-law expression implies that the logarithmic corrected dark-field is simply a linear combination of the measured logarithmic dark-field and transmittance (plus an offset):

$$\ln D^{(\mathrm{SAS})}_{xy} \approx \ln D_{xy} - \ln \tilde{a}_x - \tilde{b}_x \ln T_{xy}.$$

The effect of this correction procedure on real imaging data is illustrated in Fig. 4.12: As intended, the visibility reduction due to spectral hardening is eliminated, and only the lungs (and to a lesser degree, the ribs) remain as sources of dark-field contrast. At least some of the signal originating from the ribs is due to the differing spectral attenuation behavior of bone, but some small-angle scatter may also be present, considering the dark-field imaging studies performed on bony tissues (cf. section 1.6.3 on page 30).

4.3.2 Correction of grating gap artifacts

The quality of dark-field images from the *lung-scanning setup* is affected by gaps between adjacent grating tiles. The minimum gap size achievable during the tiling procedure is limited by mechanical considerations (see [Schr+17] and section 3.3.4 on page 80). The effect of these gaps on the dark-field image depends both on the gap size and the relative phase between the ridge patterns.

For sufficiently large grating gaps, any location on the detector is only reached by rays passing through at most one tile of G_1 and G_2 (Fig. 4.13a). Detector regions in the penumbra of a gap receive some radiation passing through all gratings (and thus have fringe contrast), and some passing through the gap (no fringe contrast). The visibility in this region is thus reduced, according to the relative received intensity of the radiation with and without fringe contrast. As the center of the grating gap shadow is approached, all received radiation passes through the gap and visibility drops to zero.

For smaller gaps on the other hand, the penumbrae of adjacent grating tiles may overlap (Fig. 4.13b), which

means that detector regions in this overlap region receive intensity passing through both tiles. Both intensities carry fringe contrast, but the relative phase of each fringe pattern is determined by the relative phase of the ridge patterns from each tile. Since the intensities from both fringe patterns add up, the total visibility is determined by the phase shift between the tiles (maximal if both are in phase, minimal for a half-period shift).

As given in [Schr+17], the width W of the detector region of reduced visibility shown in Fig. 4.13 is equal to $Mg + (M-1)s$, where g is the gap width, M the magnification factor of the grating onto the detector, and s the lateral extent of the source spot. It can be easily shown that the width W' of the visibility slope is equal to $(M-1)s$. The case of overlapping penumbrae occurs if $2W' > W$, which can be solved for g to yield

$$g < \frac{M-1}{M} s.$$

The magnification of G_1 and G_2 in the *lung-scanning setup* can be calculated from the source-to-grating and grating-to-detector distances (cf. Table 3.1 on page 79). This leads to gap limits of $g(G_2) < 10\,\mu\text{m}$ and $g(G_1) < 126\,\mu\text{m}$. As the gap sizes are only known to be below 400 µm [Schr+17], they are almost certainly larger than $g(G_2)$, and probably also larger than $g(G_1)$. Thus, all observed gaps in the lung-scanning setup are likely to be of the type shown in Fig. 4.13a. With the assumed value $g = 400\,\mu\text{m}$, the value of W, which should correspond to the width of the gap artifacts, is 600 µm for G_1 gaps and 414 µm for G_2 gaps. Given the (binned) pixel size of 444 µm, an artifact width of one to two pixels is expected, which matches experimental observations.

Since the grating tiles in the *lung-scanning setup* were not phase-aligned during tiling, visibility in the tiles' penumbrae is reduced. Although a visibility decrease should not lead to a change in dark-field signal, artifacts arose due to the noise increase associated with a visibility reduction. Since the visibility reduction occurs for all swing positions during the fringe scan, the artifacts appear as thin, nearly perfectly straight lines[7] parallel to the scanning direction.

Although the G_1 and G_2 tiles were of the same size, the images of their gaps on the detector did not overlap

[7] Due to the projection of the circular trajectories of the grating gaps onto the detector plane, the lines are actually hyperbolae, albeit with a very low curvature.

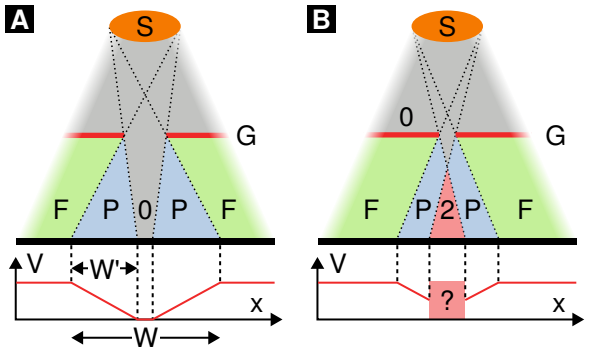

Figure 4.13: Effect of grating gaps on visibility. The grating (G) with a central gap is illuminated by the source spot (S), resulting in areas fully covered by the grating (F), areas not covered by the grating (0), penumbral areas (P), and an overlap of two penumbral areas (2). For sufficiently wide gaps, no overlap occurs and visibility continuously falls to zero (a). If overlap does occur (b), the achieved visibility in this region depends on the relative phase between the ridge patterns of adjacent grating tiles. Figure designed after Fig. 2 in [Schr+17].

(except for the middle) due to the different geometric magnifications of the gratings. As G_1 and G_2 were each composed of eight grating tiles, a total of 13 or 14 lines could usually be observed. These artifacts are highly intrusive since they exhibit large variations in gray values (due to the high noise levels), and are spread roughly equidistantly over the entire field of view.

Filtering-based correction In collaboration with Ingo Maack from Philips Medical Systems DMC GmbH, a correction approach was developed which was based on low- and high-pass filtering operations. In sequence, the image operations are as follows:

First, a high-pass filter is applied to the dark-field projection in the x direction (orthogonal to the line artifacts), producing an image containing primarily the grating line artifacts.

This image is then low-pass filtered in the y direction (parallel to the lines). The result then contains only the isolated gap artifacts, and its subtraction from the original should produce an artifact-free version of the image, without compromising other features. The best filtering results were achieved by convolution with box

kernels. The full operation can thus be formulated as

$$D^{(\mathrm{corr})} = D - B_{1,h} \otimes \left[D - B_{w,1} \otimes D \right], \qquad (4.33)$$

where D is the original image, $\otimes$ denotes convolution, $B_{x,y}$ is a box kernel of $(x \times y)$ pixels, normalized to 1. The best correction results (for 3×3-binned data) were achieved for kernel dimensions in the vicinity of $h = 19$, $w = 81$.

However, it was discovered that gap artifacts could appear in one of two forms. The first kind ("noisy line" type) arises directly from the phenomenon shown in Fig. 4.13: The reduction of visibility in the gap shadow leads to an increase of noise levels in measurement data, and thus in dark-field images, in this region. However, the average value of dark-field signal in this area hardly differs from the neighboring regions, since the visibility reduction occurs both in the reference scans and the object scan (Fig. 4.14a, b).

A slight lateral shift in grating position between reference scans and object scans occurred for a number of measurements. This likely arose due to mechanical disturbances to the setup during measurement preparations. As this introduces a misalignment of the gap between reference and object scans, a different kind of artifact occurs, namely a light-and-dark line pair with relatively low noise levels ("flat line" type, Fig. 4.14a, b).

The effect of these two types of artifacts on the image's frequency-space representation differs significantly. "Flat lines" increase Fourier coefficients at low frequencies in the line direction, and (mostly) high frequencies orthogonal to it. They can therefore be efficiently eliminated with the approach in Eq. (4.33). On the other hand, "noisy lines" contain Fourier coefficients at a large range of spatial frequencies. They are thus only partly removed by the presented correction (Fig. 4.14c, d). An alternative approach was thus developed in order to eliminate both types of artifacts.

Blending-based correction For this method, an overall low-pass-filtered version D_{LP} of the image D is first calculated. This eliminates the gap artifacts, albeit at a significant loss in resolution. Good results were achieved with the operation

$$D^{(\mathrm{LP})} = \mathrm{Binom}_{3,3} \otimes \mathrm{Med}_{5,1}(D), \qquad (4.34)$$

where $\mathrm{Binom}_{x,y}$ is an $(x \times y)$ binomial kernel and $\mathrm{Med}_{x,y}$ is a two-dimensional median filter with an

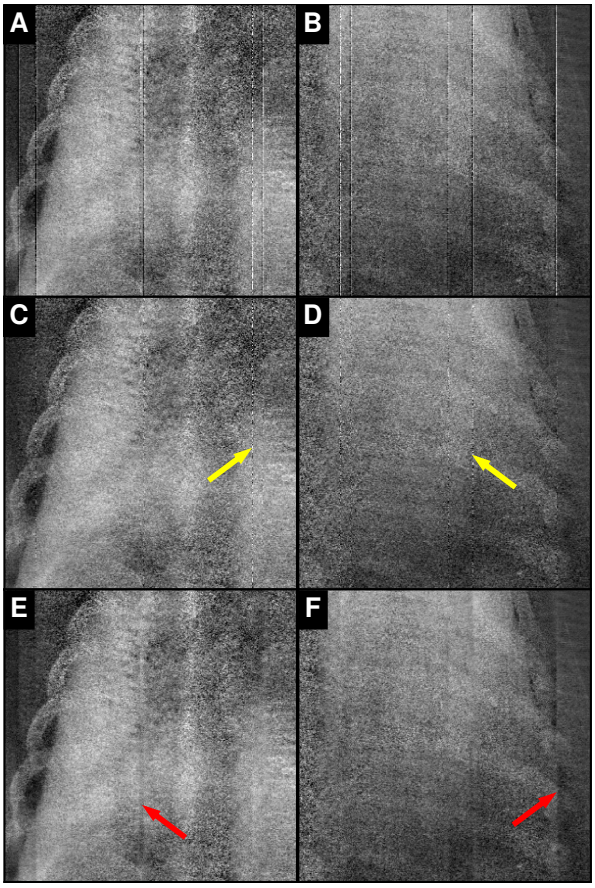

Figure 4.14: Correction methods for grating gap artifacts. (a),(b): Appearance of artifacts in two regions of a beam-hardening-corrected dark-field projection of a porcine thorax measured *in vivo*. (c),(d): Filtering-based correction. "Flat line" artifacts are removed completely, while some "noisy line" artifacts remain (yellow arrows). The transition of dark-field levels across the grating gaps is also smoothed. (e),(f): Blending-based correction. All line artifacts are removed, but tile boundaries partly remain visible due to the variation of signal levels between adjacent tiles (red arrows).

($x \times y$) pixel footprint. The locations of the gap artifacts (in pixel column numbers $x_1, \dots x_{14}$) are then identified, either automatically or manually.

A suitable automatic detection approach works as follows: The standard deviation is calculated for each pixel column x of the dark-field image D. The magnitude of the first derivative of this series of values is then calculated. The artifacts' locations are equal to the locations of the 14 largest values of this array. This approach was found to work robustly for a large range of measurements.

The corrected image is then calculated as a linear combination of the original image D and the low-pass filtered image $D^{(\mathrm{LP})}$, with locally varying scaling factors:

$$D_{xy}^{(\mathrm{corr})} = (1-\alpha_x) D_{xy} + \alpha_x D_{xy}^{(\mathrm{LP})}. \tag{4.35}$$

The coefficient α_x is 0 in the majority of the image, but approaches 1 as the x coordinate reaches that of a gap artifact. The corrected image thus smoothly blends from the original image into its low-pass-filtered version. The shape of α_x was calculated as a Gauss-filtered version of the indicator function for the gap artifacts:

$$\alpha_x = G_1 \otimes \mathscr{I}_x, \mathscr{I}_x = \begin{cases} 1 & \text{if } x = x_1, \dots, x_{14}, \\ 0 & \text{else.} \end{cases}$$

Here, G_1 is a one-dimensional Gauss kernel with mean 1 and standard deviation 1 (in pixels). This approach works independently of the frequency-space representation of the artifacts and only requires knowledge of their location. Although this largely suppresses the artifacts, their locations are still apparent in the corrected image as regions of reduced noise levels due to the low-pass filter.

In order to ameliorate this, the method was extended by the addition of artificial noise in these regions. To add a realistic amount of noise, the approximate noise level in the original dark-field image must be known.

For this purpose, an empirically-determined relation between the noise level in beam-hardening-corrected dark-field projections D and the map of total intensity I detected in the object scan was used. It had been found that

$$\sigma(D) \approx C \cdot I^{-0.6}$$

to a good degree of precision. Although $\sigma(D)$ also depends on blank-scan and object-scan visibility, the variation in detected intensity I varies by a much greater amount in thorax radiography (several orders of magnitude), which makes it the dominant influence.

In order to determine the coefficient C, both D and I were separated into grids of 10px × 10px tiles. $S_{D,k}$, the standard deviation of D, and $\mu_{I,k}$, the mean of I, were calculated in each tile k. C was then estimated via

$$C = \mathrm{median}\left\{ S_{D,1}\mu_{I,1}^{0.6}, S_{D,2}\mu_{I,2}^{0.6}, \dots \right\},$$

which then allowed estimation of per-pixel noise levels

$$\sigma(D_{xy}) \approx C \cdot I_{xy}^{-0.6}.$$

Noise was then added by modifying Eq. (4.35) to

$$D_{xy}^{(\mathrm{corr})} = (1-\alpha_x) D_{xy} + \alpha_x \left[D_{xy}^{(\mathrm{LP})} + \epsilon_{xy} \right],$$

where each ϵ_{xy} is a value drawn from a normal distribution with zero mean and variance $\sigma(D_{xy})^2$. This implicitly assumes that the noise level in $D^{(\mathrm{LP})}$ is negligible. Although this approach is significantly more complicated than the first presented method, it requires little computational power and rarely requires an adjustment of parameters.

An example of the blending-based correction is shown in Fig. 4.14e,f. Other than the filtering-based correction in Fig. 4.14c,d, it also removes type I artifacts. Whereas the filtering-based correction works on the full image, the blending-based approach is restricted to the gap regions.

The latter method highlights slight deviations of (beam-hardening-corrected) dark-field levels between tiles. These are likely due to the limited precision of the used beam-hardening-correction approach. A variation in gold height leads to slightly different beam-hardening behavior, and thus probably slight differences in its deviation from the model in Eq. (4.30), between grating tiles.

4.3.3 Filtering of dark-field images

Noise levels due to photon statistics are generally higher in X-ray dark-field than in conventional attenuation images. Although relative noise levels are (roughly) proportional to the square root of detector dose for both modalities, dark-field noise also strongly depends on visibility [Revo$^+$10; Chab$^+$11].

Since detected dose and visibility vary strongly across the field of view in thorax radiography (cf. chapter 5,

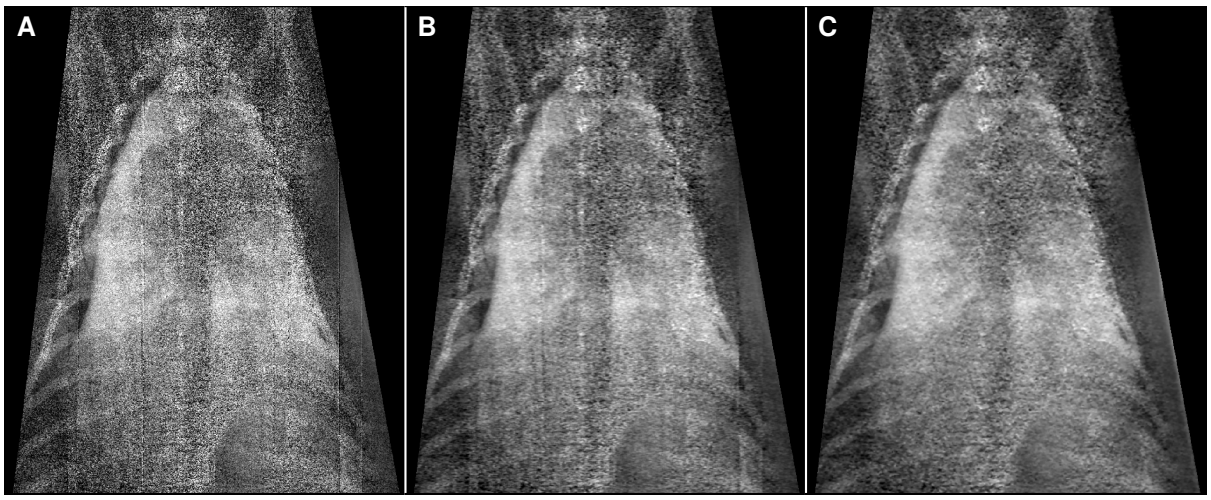

Figure 4.15: Effect of low-pass filtering on visual impression. (a): Beam-hardening-corrected dark-field radiograph (porcine thorax with large pneumothorax, measured *ex vivo*). While windowing is selected to highlight signal contrast between the lung and its surroundings, high noise levels disturb the visual impression. (b): Same image, but median-filtered (5 × 1 footprint), then filtered with binomial kernel (3 × 3 pixels). Noise and gap artifacts are reduced. (c): Combination of (b) with gap correction: 5 × 1 median filter, then filtering-based correction from section 4.3.2, then 3 × 3 binomial filtering. Gap artifacts are fully removed, producing a homogeneous field of view. Identical windowing in all subfigures.

starting on page 115), the same is true for dark-field noise levels. In low-statistics, low-visibility regions of X-ray dark-field projections, noise levels can exceed the range of signal values in the remaining image. This can present a problem for image presentation.

If windowing (i.e., the mapping of pixel values to gray values) is selected so that image information in the important, low-noise image regions (i.e., the lung) is well represented, high-noise regions (e.g., spine or abdomen) may be oversaturated and thus appear as black-and-white noise. This is very prominent and often distracts from central image features (see e.g. Fig. 4.15a).

By applying a low-pass filter to an image, a reduction in noise levels can be achieved at the expense of spatial resolution. Since dark-field thorax radiographs usually do not contain very small features, little diagnostic information is lost by low-pass filtering, especially in regions where contrasts are already obscured by noise.

One simple filtering approach is to use the operation from Eq. (4.34) (5 × 1 median filter, then 3 × 3 binomial filter) for the entire image. The median filtering operation mostly eliminates gap artifacts, and the subsequent application of the binomial filter decreases the overall "patchiness" of the resulting noise structure. The effect on the image is illustrated in Fig. 4.15b.

This can be further improved by applying either one of the gap correction methods *between* the median and binomial filtering steps. As median filtering eliminates most of the "noisy line" structures, the filtering-based correction for gap artifacts eliminates all residual artifacts and creates a smooth transition between the tile areas. This is illustrated in Fig. 4.15c.

A more elaborate filtering approach had been designed in order to produce images with a constant noise level in all subregions. Regions of higher noise are filtered more strongly by using larger filter kernels in this region. Local noise levels were estimated from detector dose, and the dependence of noise suppression on the filter kernel was calculated ahead of time. However, since a change in filter kernel had significant impact on noise structure, resulting images were patchy and uneven, and the approach was thus not pursued further.

4.4 Consolidation of the processing workflow in the Python package *lsproc*

The calculation of image signals from section 4.2 (most importantly, the "full retrieval" method), and the post-processing functionality introduced in section 4.3 were implemented in a common software environment for practical use.

All processing steps were implemented using the *Python* programming language (originally version 2.7, now updated for use with version 3.6 [Pyth20]), making heavy use of the *NumPy* library [NumPy20; Walt+11], which enables efficient numerical computations on large, multidimensional data arrays within *Python*.

All software elements for processing the image data were collected in the *Python* package *lsproc* (short for "**l**ine-**s**canner **proc**essing"). A *Python* package may act as a library, and also contain executable scripts. Both aspects are used in *lsproc*. The code structure is roughly outlined in Fig. 4.16.

The overarching design goals for this module were to achieve

1. a high flexibility and modularity to facilitate changes to the code,
2. good code readability,
3. a reasonably simple user interface, and
4. a reproducibility of results.

These goals are at partly at odds with each other. For example, code readability is improved by providing extensive documentation. However, this limits the ease with which the code can be changed, since all code changes should be accompanied by updates to the documentation. Additionally, reproducibility of old processing results requires maintenance of old software features, which increases code complexity, and thus the difficulty of adding new features while maintaining compatibility with existing ones. This necessitates finding acceptable trade-offs between these competing goals.

Goals 1 and 2 are obviously crucial for collaborative software development, considering that numerous people have contributed to this project. They also facilitate "recycling" code for future, other applications,

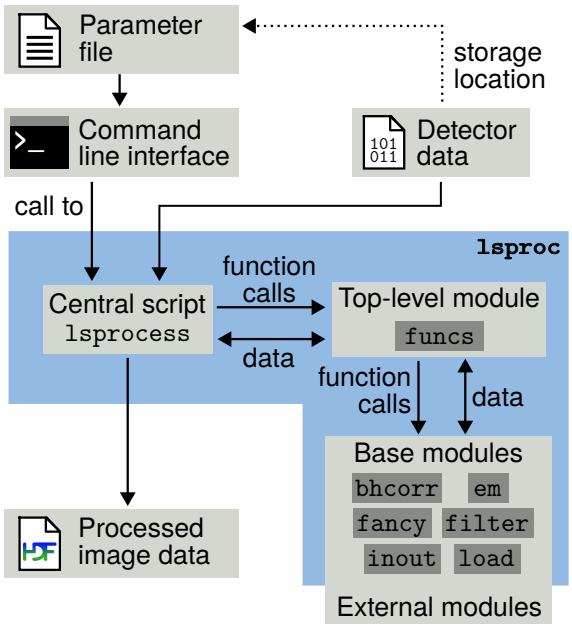

Figure 4.16: Program flow of the processing procedure with the package *lsproc*. The script *lsprocess* is started from the command line, with the path to a parameter file as an argument. It calls a series of functions in the top-level module *funcs*, which in turn consist of simpler work steps defined by functions in the base modules of *lsproc*, as well as external modules.

which helps to reduce redundant code development, i.e., "reinventing the wheel".

Goal 3 is important to ensure smooth everyday operation during experimental work, i.e., outside of code development work. Interrupting experimental work in order to solve software problems can be highly disruptive, especially when working in a small team where dividing computer work and experimental work between people is not feasible.

Finally, goal 4 ensures that image data from the full lifetime of the experimental setup can be processed, despite possible variations in experimental procedure, as well as modifications to the code. This ensures that older measurement data does not become incompatible with code improvements developed long after data acquisition. This is important since several years may pass between data acquisition and scientific publication.

4.4.1 Modularity and structure

The main steps taken to achieve goal 1 was to establish a clear modular code structure. Since the procedure for the calculation of images follows a linear structure, it is implemented as a linear top-to-bottom sequence of commands in an executable script, called *lsprocess*. Individual work steps in this sequence are implemented as *Python* functions. Functions with similar purposes (e.g., different image filters, or input/output functions) are grouped together in sub-modules of *lsproc*. As shown in Fig. 4.16, two hierarchical layers of modules are used. The top-level module *funcs* contains functions which perform relatively complex tasks (e.g., the resorting procedure presented in section 4.1.3). These tasks consist of more fundamental work steps, which are either implemented as functions from the *Python Standard Library*, other *Python* modules such as *NumPy* and *SciPy* [Virt+20], or functions defined in the other, base-level submodules of *lsproc*.

This then leads to a division of tasks between three components of the package:

1. The central script *lsprocess* contains a linear series of calls to high-level functions in *funcs*. All variables on this level are given by user-specified parameters. These may also enable or disable portions of the script.
2. The module *funcs* contains functions that translate complex tasks into a series of simpler tasks, calling on base-level *lsproc* functions as well as external modules.
3. The base-level modules of *lsproc* contain only functions that perform "indivisible", basic tasks.

This division improves overall clarity while keeping the "administrative" effort of organizing the code to a minimum and retaining flexibility for modifications. In addition, all functions from the package can be used in other *Python* scripts or interactively from the interpreter.

4.4.2 User interaction

The behavior of the central script is controlled entirely by a set of user-specified parameters. Among the most important of these are the file paths to the input data (reference scans, sample scan, and beam-hardening-correction data), as well as a series of Boolean parameters (e.g., whether to save processed reference scan data, whether to calculate sample data at all, or whether to apply certain post-processing filters).

In line with goal 1, no graphical interface was implemented for configuring *lsprocess*. Although such an interface may simplify operation, it requires a high amount of work both for the initial design and subsequent maintenance. The script was instead accessed via the command line (i.e., a terminal emulator on a *Linux* distribution). Since passing a large number of configuration parameters in the command line is inconvenient, configuration files were used instead. These were implemented as text files defining a *Python* dictionary.

Due to high demands on working memory (RAM), the central script *lsprocess* is usually used with compute servers accessed remotely. This makes command-line execution inconvenient if the package is not integrated to the local system. For example, the following steps may be necessary to configure one run of the central *lsproc* script:

- Connecting to a compute server via *SSH*
- Editing user parameters in a configuration file
- Adding the path of the *lsproc* package to the *Python* path environment variable
- Navigating to the path of *lsprocess*
- Executing *lsprocess* via *Python* with the configuration file path as a parameter

This is tedious, susceptible to mistakes, and diverts the focus from experimental work. To simplify this, the *lsproc* install routine was modified to integrate the script with the *Bash* shell, allowing its execution in *Bash* from any directory with the command

```
$ lsprocess [-j JOBS] [-t THREADS] PATH
```

where *PATH* is the absolute or relative path to a configuration file, and *THREADS* is the maximum number of threads to use (appropriate values mainly dependent on the number of available CPU cores). Furthermore, in order to perform a series of processing runs (e.g. to process a series of measurements, or the same measurement with different sets of configuration parameters), the option to use Excel spreadsheets as configuration files was introduced. Each line in the

spreadsheet represents one run of the script, and each column contains one parameter value. Not only is this easier to read and compare than a series of text files, but is also faster since multiple instances of the script (maximum number determined by *JOBS*) may run in parallel.

In the spirit of goal 4 (enabling the reproduction of old processing results), older, rarely changed parameters were maintained, which lead to a steady increase in the number of parameters. At the time of writing, a total of 70 parameters can be configured. In order to maintain usability (goal 3) despite this, default values were introduced for most parameters: with this, only those deviating from their default values must be explicitly provided by the user, and typical configuration files contain only about five to ten entries.

Since *lsproc* development uses *Git* versioning, commit numbers ("hashes") can be used to uniquely identify a given version of the package (like version numbers). In order to fully document the origin of a given processed image, all configuration parameters and the *lsproc* commit hash are saved together with the image data. In order to save these very different types of data in the same file, the highly versatile file format *HDF5* [Kozi+18] is used.

4.4.3 Workflow in *lsprocess*

The order of tasks performed by the *lsprocess* script is illustrated in Fig. 4.17. The process usually starts by loading a series of phase-stepped reference scans. Since detector data is usually roughly cropped to the grating area (cf. page 90), this must be reverted to allow determination of slot limits from the data. These limits are then used to re-sort the data (cf. Fig. 4.3), yielding a four-dimensional array $I^{(\mathrm{r})}_{kmxy}$ used for the calculation of reference-scan parameters $\tilde{V}_{kxy}$, $\tilde{A}_{kxy}$, and $\tilde{\Phi}_{kxy}$ via the "full retrieval" method as given in Eqs. (4.23) and (4.24). The resulting three-dimensional arrays are kept in memory, and optionally saved.

The object scan raw data is then loaded from disk. As for the reference scans, reverting the crop and re-sorting are performed, yielding the three-dimensional array I_{kxy} of object-scan intensities. As object and reference scans are performed with identical movement parameters of the interferometer, the time-dependent limits of the radiation field are very nearly identical for both cases. This allows reusing the radiation field limits retrieved from the reference scans for the object scan.

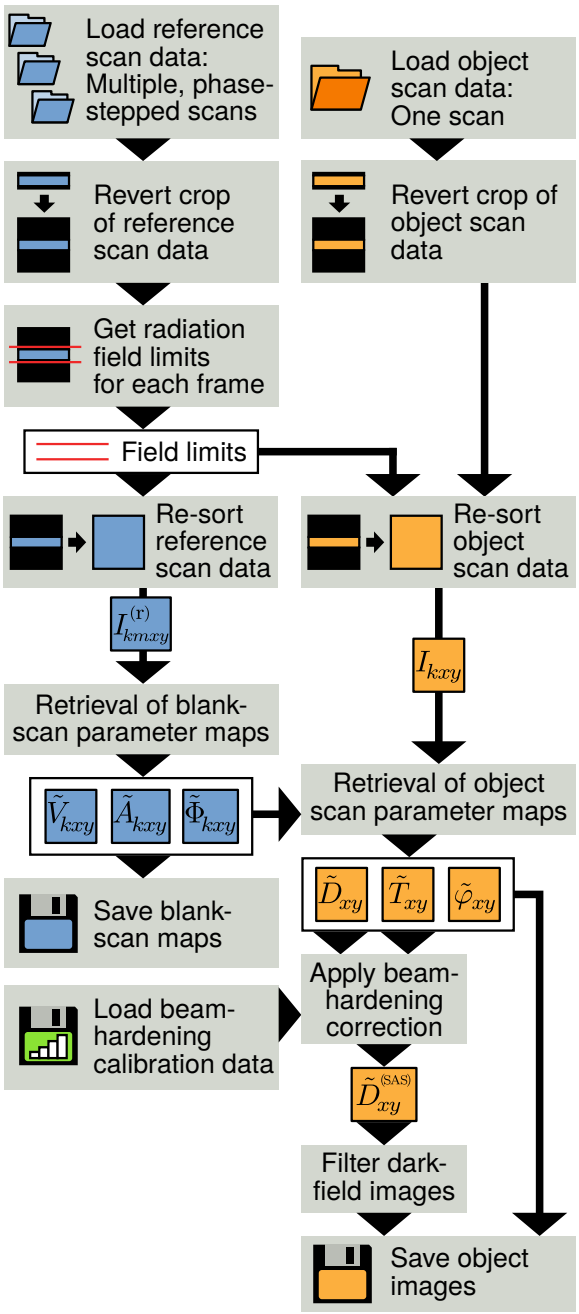

Figure 4.17: Workflow in the central script *lsprocess*. The execution of each work step can be modified with user-supplied parameter values. Object scan data is loaded after the retrieval (and optionally saving) of blank-scan parameters is completed.

The object scan parameters $\tilde{D}_{xy}$, $\tilde{T}_{xy}$, and $\tilde{\varphi}_{xy}$ are then retrieved from both I_{kxy} and the blank-scan parameter arrays via the "full retrieval" method as given in Eqs. (4.27) and (4.28). While no further modifications are necessary for $\tilde{T}$ and $\tilde{\varphi}$, beam-hardening correction (section 4.3.1), grating gap correction (section 4.3.2), and filtering (section 4.3.3) are applied to the dark-field projection $\tilde{D}$. Finally, all modalities (T, φ, and D before and after beam-hardening correction) are saved to disk.

4.5 Conclusion and Outlook

A software module was developed for calculating attenuation and dark-field radiographs from fringe scanning measurements at the *lung-scanning setup*. The module was developed to be easily extendable and simple to use, but also remains "backward compatible" with data acquired throughout several years, and produces reliable, reproducible results. Besides calculation of dark-field radiographs from the data according to a precise signal formation model, a number of post-processing options are available to improve the images' visual impression and quantitativeness. The images produced with this module have been featured in a number of scientific publications [Grom+17; Will+18; Hell+18a; Saut+19; Fing+19; DeMa+19].

However, work on the software is not concluded. With the development of a scanning setup for clinical studies on the basis of the *lung-scanning setup*, new image processing challenges have emerged. A wide range of enhancements, including a complete redesign of signal retrieval to allow for vibration correction, suppression of motion artifacts, estimation of Compton scatter, and visual post-processing have since been developed, which will be critical to demonstrate the clinical feasibility of dark-field thorax radiography. These achievements will soon be featured in a number of journal publications and graduate theses.

Chapter 5

Dark-field imaging studies of porcine and human thoraces

"What does a scanner see? he asked himself. I mean, really see? Into the head? Down into the heart? Does [it] see into me—into us—clearly or darkly?"

Philip K. Dick, *A Scanner Darkly*

Contents

The primary purpose of the *lung-scanning setup* introduced in chapter 3 (page 69) was to produce thorax radiographs of large animals with a grating-based X-ray imaging setup, while operating within parameters compatible with clinical radiography (low dose, short acquisition time, sufficient resolution, and high dark-field contrast from the lung). The success of this endeavor was demonstrated with the first-ever dark-field thorax radiographs of a living pig [Grom+17; Grom17]. This achievement represents the technological foundation for a translation of dark-field radiography to clinical application.

Beyond technical feasibility however, a clinical translation of dark-field imaging must also be justified by its diagnostic benefits. Ample evidence of this benefit had been delivered by numerous studies with small animal models, primarily employing a prototype CT scanner for grating-based imaging [Tapf+11; Tapf+12]. Dark-field radiography was shown to provide benefits for the detection of structural lung diseases such as emphysema [Schl+12; Mein+13; Yaro+13; Mein+14b; Hell+15], fibrosis [Yaro+15; Hell+17], and neonatal lung injury [Yaro+16]), as well as lung tumors [Sche+17] and pneumothoraces [Hell+16]. These pathological changes were found more reliably and at earlier stages when dark-field radiographs were used in addition to conventional X-ray.

However, a transferability of these findings to imaging of larger animals at the *lung-scanning setup* can not be taken for granted, since a large number of technical (X-ray spectrum, visibility, angular sensitivity) and biological parameters (thorax and lung thickness, alveolar microstructure) differs between the two imaging scenarios.

Furthermore, since pig organs are anatomically very similar to human organs [Judg+14], findings from studies on pigs are likely to be more predictive for clinical imaging than small-animal studies. It is therefore advisable to confirm the diagnostic findings from small-animal studies for pigs.

On the other hand, studies involving larger animals are limited due to greater ethical concerns. For example, the artificial induction of a pathology by instillation of a biochemical compound (e.g., *elastase* or *bleomycin* in small-animal models of emphysema and fibrosis, respectively) requires several weeks, and is thus associated with a significant burden for the animals. Longitudinal studies are faced with a similar issue: the repeated transport between animal housing and laboratory, as well as the recuperation from anesthesia after each measurement are likely to be very stressful for the animals. Therefore, all *in vivo* large-animal experiments at the *lung-scanning setup* were performed "terminally", i.e. after completion of the experiment, the animal was euthanized while still under anesthesia, thus limiting suffering as much as possible. The experiments were performed in collaboration with the *Chair for Molecular Animal Breeding and Biotechnology* at the *University of Munich*, based in the university-operated animal farming facility "Lehr- und Versuchsgut Oberschleißheim".

Besides the X-ray dark-field measurements presented in [Grom+17], two imaging studies with pigs have been performed at the *lung-scanning setup*, which will be presented in this chapter:

In order to determine the potential of X-ray dark-field chest radiography for pneumothorax detection, measurements were performed on a total of eight animals (three *in vivo*). Pneumothoraces were artificially induced under anesthesia, and dark-field images were quantitatively compared to the conventional X-ray projections. The CNR between pneumothorax and adjacent lung parenchyma was found to be significantly higher ($p < 0.01$) for dark-field than for transmission, thus confirming the findings in [Hell+16] for newborn mice. This analysis is presented in section 5.1, and has also been published in [Hell+18a].

Section 5.2 evaluates the relation of dark-field signal strength (in healthy lungs) with ventilation pressure, based on *in vivo* measurements on two animals. Although this investigation does not directly involve lung pathologies, it is of relevance for their detection: a variation in the lungs' dark-field signal is due to both microstructural and large-scale anatomical changes. These occur normally during the breathing cycle, or abnormally in the presence of a pathology. In order to determine the effect of abnormal changes to the dark-field signal, it is necessary to first understand its dependence on normal variations. These results have been previously published in [DeMa+19].

In addition to animal experiments, a collaboration with the *Institute of Forensic Medicine* at the *University of Munich* and the *Department of Diagnostic and Interventional Radiology* at the hospital "Klinikum rechts der Isar" allowed the acquisition of the very first human thorax dark-field radiographs. The initial findings, including a reference CT measurement of the body, are documented in [Will+18]. From a large-scale anatomical view, imaging of human cadavers obviously simulates the clinical situation very closely. However, the lung microstructure collapses shortly after death, and is eventually destroyed by autolysis or decomposition. As the dark-field signal is highly dependent on sample microstructure, it is essential that measurements are performed as soon after death as possible. Furthermore, imaging of bodies with major external injuries and infectious diseases were excluded.

Despite these limitations, a total of nine cadavers could be imaged at the fringe-scanning setup over the course of 2 years and 8 months. A reader study was designed to evaluate dark-field and transmission signal strength in different sections of the lungs, and were compared to pathological findings from CT reference measurements. These results are presented in section 5.3, and have been previously published in [Fing+19].

5.1 Improved detection of pneumothorax in pigs via dark-field radiography

The majority of content presented in this section has been previously published in "Depiction of pneumothoraces in a large animal model using x-ray dark-field radiography" by K. Hellbach, A. Bähr, F. De Marco et al. in Scientific Reports, 2018 [Hell+18a]. The presented Figures have been slightly modified, a Figure has been added, and some footnotes were added to explain medical terminology. Technical information about the *lung-scanning setup* has been omitted. The reader is instead referred to chapter 3 (starting on page 69) for this information.

My primary contribution to this work has been the calculation and post-processing of the image data, the design of software tools for (and assistance with) quantitative image analysis, as well as the preparation of the technical aspects of the original manuscript.

5.1.1 Motivation

A pneumothorax is characterized by the presence of air in the pleural cavity[1] that leads to a collapse of the affected lung [Choi14]. Causes may be iatrogenic[2], posttraumatic[3], or idiopathic[4]; pneumothoraces often require immediate treatment in order to avoid severe health consequences [Weis+00]. Medical imaging is usually required to reliably diagnose a pneumothorax, as clinical signs are often unspecific and do not reflect the amount of air in the pleural cavity [Yarm+12].

Chest computed tomography serves as the standard of reference in diagnosing and sizing pneumothoraces [Kell+06]. However, its use is limited in clinical practice due to relatively high cost and radiation dose, as well as inconvenience for critically ill patients [Rank+00]. As conventional chest radiographs are readily available, cost- and time-effective, they are usually the first test ordered for a suspected pneumothorax [Toci+85], although there are limitations resulting in a considerable number of missed pneumothoraces [Brar+10; Moya+07; Neff+00]. Due to the low density of lung tissue, the difference in attenuation between air and lung is very small and can be easily overlooked. In fact, when physicians other than radiologists interpret radiographs, up to 76% of pneumothoraces are missed [Ball+09]. Comparatively high rates of misdiagnosed pneumothoraces have also been reported for inexperienced radiologists [Aitc+93].

If the patient is in an upright position while the radiograph is taken, the air in the pleural cavity usually collects around the lung apices where a thin, sharp line, which might be masked by the rib shadow, indicates the edge of the lung. However, in critically ill patients, chest X-rays need to be acquired in the supine position with air accumulating in the ventral[5] pleural space [Gord80] resulting in an overall sensitivity of only 50% [Omar+10]. Tubes and lines can further reduce the diagnostic sensitivity [Brow+12].

5.1.2 Large animal protocol

All animal procedures were performed with permission of the local regulatory authority, Regierung von Oberbayern (ROB), Sachgebiet 54, approval number AZ 55.2-1-54-2532-61-2015. The ethics committee reviewed the application according to §15 TSchG German Animal Welfare Law. German Landrace Hybrid pigs [wild type, Chair for Molecular Animal Breeding and Biotechnology, Ludwig-Maximilians-University Munich breeding facility; $n = 8$ (*ex vivo* $n = 3$; *in vivo* $n = 5$), weight=(25.8 ± 5.9) kg; age: 2.5 months to 3 months, anterior-posterior thoracic diameter (20.2 ± 2.3) cm] served as experimental animals in this study.

Pigs measured *ex vivo* were euthanized immediately before intubation and image acquisition. Pigs measured *in vivo* were sedated by intramuscular application of ketamine (Ursotamin®, Serumwerk Bernburg, Germany, 20 mg/kg) and azaperone (Stresnil®, Elanco Animal Health, Bad Homburg, Germany, 2 mg/kg). Anesthesia was accomplished by an initial intravenous bolus injection of propofol (Propofol 2%, MCT Fresenius, Fresenius Kabi, Langenhagen, Germany) and continued using a syringe pump (Injectomat® MC Agilia, Fresenius Kabi, Langenhagen, Germany) for permanent application of propofol, quantitatively adjusted to the

[1] Potential space between the membranes (*pleurae*) covering the lung and the chest wall, respectively. These membranes are only connected via a thin liquid film, which allows them to glide against each other during breathing [Sala11, ch. 23].

[2] Caused by medical intervention

[3] Caused by physical injury

[4] Of unknown origin

[5] Towards the front of the body (i.e., the belly)

animals' individual needs. Heart frequency and oxygen saturation were monitored throughout the whole experiment using a pulse oximeter (Palmcare Plus, Medical Econet, Oberhausen, Germany).

Both pigs measured *ex vivo* and *in vivo* were intubated and kept under automated breathing using a mechanical respirator (Fabius® Plus 2, Drägerwerk AG & Co. KGaA, Lübeck, Germany) throughout the experiment. Mechanical ventilation parameters were set to: 12 breaths/min respiratory rate, 15 ml/kg breath volume per body weight, 22 mbar peak airway pressure, 2 mbar PEEP (positive end-expiratory pressure[6]). In order to acquire dark-field and transmission images of the animals' lungs, breathing was stopped for the duration of the measurements with a constant airway pressure of 12 mbar. As the pigs were placed in an abdominal position, all images were acquired in posterior-anterior (p.a.) direction.

The pigs' lungs were imaged before and immediately after induction of a unilateral pneumothorax. Pneumothoraces were induced 10 minutes after intravenous application of 0.05 mg fentanyl for analgesia. The skin was incised at the level of the anterior axillary line[7], between the fifth and seventh intercostal space[8]. The correct intercostal space was identified using sonography. Subsequently, a thin catheter (Central Venous Catheterization Set with Blue FlexTip Catheter, Arrow International, Morrisville, North Carolina, USA) was placed in the pleural cavity. A Heidelberger elongation[9] and a three-way stopcock were attached to the catheter and the pleural space was insufflated with 50 ml to 500 ml air, using a 50 ml perfusion syringe (Perfusion Syringe, Becton, Dickinson and Company, Franklin Lakes, New Jersey, USA) to generate variously sized pneumothoraces [Ovel+12].

After image acquisition, the animals measured *in vivo* were sacrificed under anesthesia by intravenous injection of 0.1 ml/kg body weight T61® (Intervet GmbH, Unterschleißheim, Germany). Subsequently, a computed tomography (CT) scan (GE Discovery CT750, General Electrics Healthcare, USA) of all animals was performed to serve as the standard of reference for the induction of the pneumothorax.

[6] The lowest pressure in the lung during the breath cycle in mechanical ventilation, which is "positive", i.e., greater than ambient pressure.

[7] Imaginary line that runs along the length of the thorax on either side of the body

[8] Space between adjacent ribs

[9] Plastic extension tube

5.1.3 Imaging parameters and post-processing

The X-ray source was operated at 70 kVp and tube currents of 340 to 450 mA. Each part of the field of view received 25 X-ray pulses, resulting in a total scan time of approx. 40 s. The parameters of the used setup are discussed in detail in chapter 3. Dark-field and attenuation images were calculated using the "full retrieval" algorithm described in section 4.2.2d on page 96.

To optimize overall image impression, a set of post-processing filters was used for the dark-field images in Fig. 5.2, 5.3, and 5.4 that is somewhat different from the ones used in the original publication. First, the correction algorithm for moiré fringe artifacts described in [DeMa+18] was selectively applied to affected areas of the field of view. Then, a selective Fourier-based filter was used to detect and low-pass-filter areas with grating tile gaps (cf. section 4.3.2 on page 105), and a 3×3 binomial filter kernel was finally applied to the whole image. For quantitative analysis (see below), these steps were not applied.

5.1.4 Quantitative image analysis and statistical analysis

To calculate CNRs, data from low-pass-filtered dark-field images and unfiltered transmission images were used. Filtering was performed using a 2D Gaussian filter kernel with a FWHM of 3.25 pixels (1.1 mm in the object plane) in both dimensions. This was done to ameliorate the inferior noise characteristics of X-ray dark-field imaging (compared to regular radiography) and trade a CNR increase for a decrease in spatial resolution. Using this filter, very small features (of the order of the filter FWHM) become undetectable, but other features (such as the examined pneumothoraces) are delineated more clearly. This was deemed acceptable because no significant features could be discerned in the unfiltered dark-field images that were lost due to filtering. The filter was not considered useful for the transmission modality because it improved CNR only marginally.

To quantify dark-field and transmission signal intensities in the area of the pneumothorax and the adjacent lung, regions of interest (ROIs) were defined. The ROIs were placed in the air-filled pleural space and in the adjacent lung parenchyma; as illustrated in Fig. 5.1, care was taken to exclude the rib cage as well as me-

diastinal structures[10]. Identical ROIs were used for transmission and dark-field images. As transmission and dark-field images result from the same exposure, they are perfectly registered. The contrast-to-noise ratio (CNR) between the air-filled pleural cavity and the adjacent lung tissue was calculated for dark-field and transmission images according to the equation

$$\mathrm{CNR} = \frac{|\mu_\mathrm{L} - \mu_\mathrm{P}|}{\sqrt{\sigma_\mathrm{L}^2 + \sigma_\mathrm{P}^2}}, \tag{5.1}$$

where μ_L and μ_P represent the mean values of the signals over the lung and pneumothorax ROI, respectively, and σ_L and σ_P are the corresponding standard deviations. To quantify dorsal pneumothoraces[11], the projected area in the object plane of the lung located behind the diaphragm was identified by placing an ROI around the scattering lung before and after a unilateral pneumothorax was induced. The same was done for the side of the lung that was not affected by a pneumothorax, therefore serving as an internal control.

Means and standard deviations for lung sizes and signal intensities from dark-field and transmission images were calculated. Results were tested for statistical significance by using Student's two-tailed t test for paired samples. For the sample size of $n = 6$, a power of $1 - \beta = 99.9\%$ was calculated for a mean paired difference of $\mu_\mathrm{d} = 1.933$ with a standard deviation of $\sigma_\mathrm{d} = 0.734$ and a level of significance of $\alpha = 5\%$. MedCalc® (version 14.12.0, Mariakerke, Belgium) was used for all statistical calculations.

5.1.5 Lateral pneumothoraces: visual & quantitative analysis

As proven by CT, all experimental animals had developed a unilateral pneumothorax. All three pigs measured *ex vivo* and three out of five pigs measured *in vivo* presented with a lateral pneumothorax[12] after instillation of air in the pleural space.

The area of a pneumothorax could be easily identified as a non-scattering space between the lateral portion of the rib cage and the strongly scattering lung

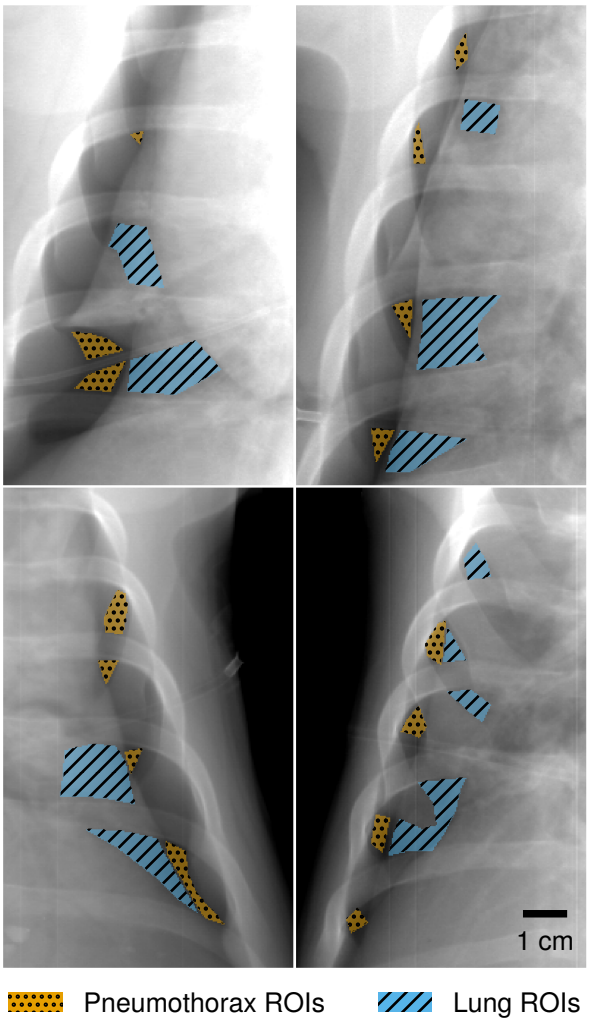

Figure 5.1: Example ROIs selected for the calculation of CNR values, superimposed onto transmission images. All ROI sections are manually drawn polygons, defined with scripts using the *matplotlib* plotting library for *Python* [Hunt07]. Care was taken to exclude ribs and the catheter from the selected regions.

[10] The mediastinum contains e.g. the heart, esophagus, and trachea

[11] Air accumulation in the part of pleural space towards the back of the animal. This may occur if the animal is in an abdominal position since the dorsal region is then the highest point of the pleural space.

[12] Air accumulation along the left or right side of the thorax

parenchyma in dark-field images. Even small pneumothoraces, which were occult in the corresponding transmission images, were visible in the dark-field images because of the high signal contrast between the lung parenchyma and the pleural cavity (Fig. 5.2c and 5.4g).

Major pneumothoraces were visible in both dark-field and transmission images. A thin, sharp pleural line in the peripheral parts of the affected thoracic side marked the area of a pneumothorax in transmission images. The area lateral to this pleural line was more radiolucent than the lung parenchyma, indicating the presence of free air in the pleural cavity. In dark-field images, a non-scattering, dark area next to the scattering lung parenchyma indicated major pneumothoraces. However, the identification of pneumothoraces in transmission images was more challenging compared to the diagnosis in dark-field radiographs, mainly due to a rather small contrast difference between the inflated lung and the air-filled pleural space.

CNRs were calculated to quantitatively evaluate the observations from qualitative image analysis of lateral pneumothoraces. When comparing lung-to-pneumothorax CNRs in the dark-field and transmission modalities, a significantly higher CNR was measured in low-pass-filtered dark-field images (3.65 ± 0.9) than in unfiltered transmission images (1.13 ± 1.1, $p = 0.002$). Several regions of interest determined for CNR analysis are shown in Fig. 5.1. CNR was 1.14 ± 1.1 for low-pass-filtered transmission images and 2.45 ± 0.7 for unfiltered dark-field images.

5.1.6 Dorsal pneumothoraces: visual & quantitative analysis

For two lungs, a lateral pneumothorax could not be detected, although the pleural spaces were inflated with considerable amounts of air (50 and 150 ml). As the pigs were placed in the abdominal position, the pleural line could not be detected laterally, as the air in the pleural space accumulates dorsally, along the space that is located uppermost [Gord80], which—in this study setup—is the posterior basal space, located behind the diaphragm and the organs of the upper abdomen, causing the lung parenchyma in this area to collapse.

When carefully analyzing the dark-field images before pneumothorax induction, the dorsal parts of the lower lung that are located behind the diaphragm showed a weak but still clearly visible dark-field signal (Fig. 5.3). These sections of the lungs appeared considerably smaller after induction of a pneumothorax, indicating a partial collapse of the affected lung due to compression by pleural air located in the uppermost areas of the thorax.

After quantifying the projected area of the lung located behind the diaphragm (which is possible as the scattering lung is directly and exclusively visible in the dark-field images), a significant decrease of inflated lung parenchyma was found after a unilateral pneumothorax was induced [mean area of the affected lung before the induction of a pneumothorax: $(62.8 \pm 7.8)\,\mathrm{cm}^2$, afterwards: $(50.0 \pm 7.2)\,\mathrm{cm}^2$; -20.5%; $p < 0.0001$; $n = 8$]. The area of the unaffected side was analyzed as an internal control, showing no significant difference in size before and after the induction of a pneumothorax [mean area of the affected lung before a pneumothorax was induced: $(57.6 \pm 10.3)\,\mathrm{cm}^2$, afterwards: $(57.0 \pm 7.5)\,\mathrm{cm}^2$; -0.3%; $p = 0.9$; $n = 8$]. This unilateral decrease is illustrated for one animal in Fig. 5.3.

In the corresponding transmission images, a slight increase in transparency with consecutively sharper margins of the basal pleural space was slightly visible, serving as a discrete, indirect sign for a pneumothorax, the so-called deep sulcus sign (Fig. 5.3d) [Gord80].

5.1.7 Discussion

Even initially small pneumothoraces have the potential to dramatically enlarge over a short period of time, making early and reliable diagnosis of this disease essential to prevent serious health consequences, such as a tension pneumothorax, which—if not detected and treated immediately—will result in cardiac failure [Robe+15]. Accurate diagnosis of a pneumothorax is affected by the low contrast between radiolucent lung parenchyma and the air-filled pleural space in conventional transmission images [Auke+12]. As chest radiography is the standard diagnostic tool for the detection of pneumothoraces, adding the information provided by dark-field images may significantly increase the diagnostic sensitivity.

The lung contains a myriad of air-tissue interfaces due to its alveolar microstructure. This leads to a pronounced coherent scatter of X-rays, resulting in a strong dark-field signal, which significantly increases the contrast between the lung and the air-filled pleural space. A previous study in a murine model has

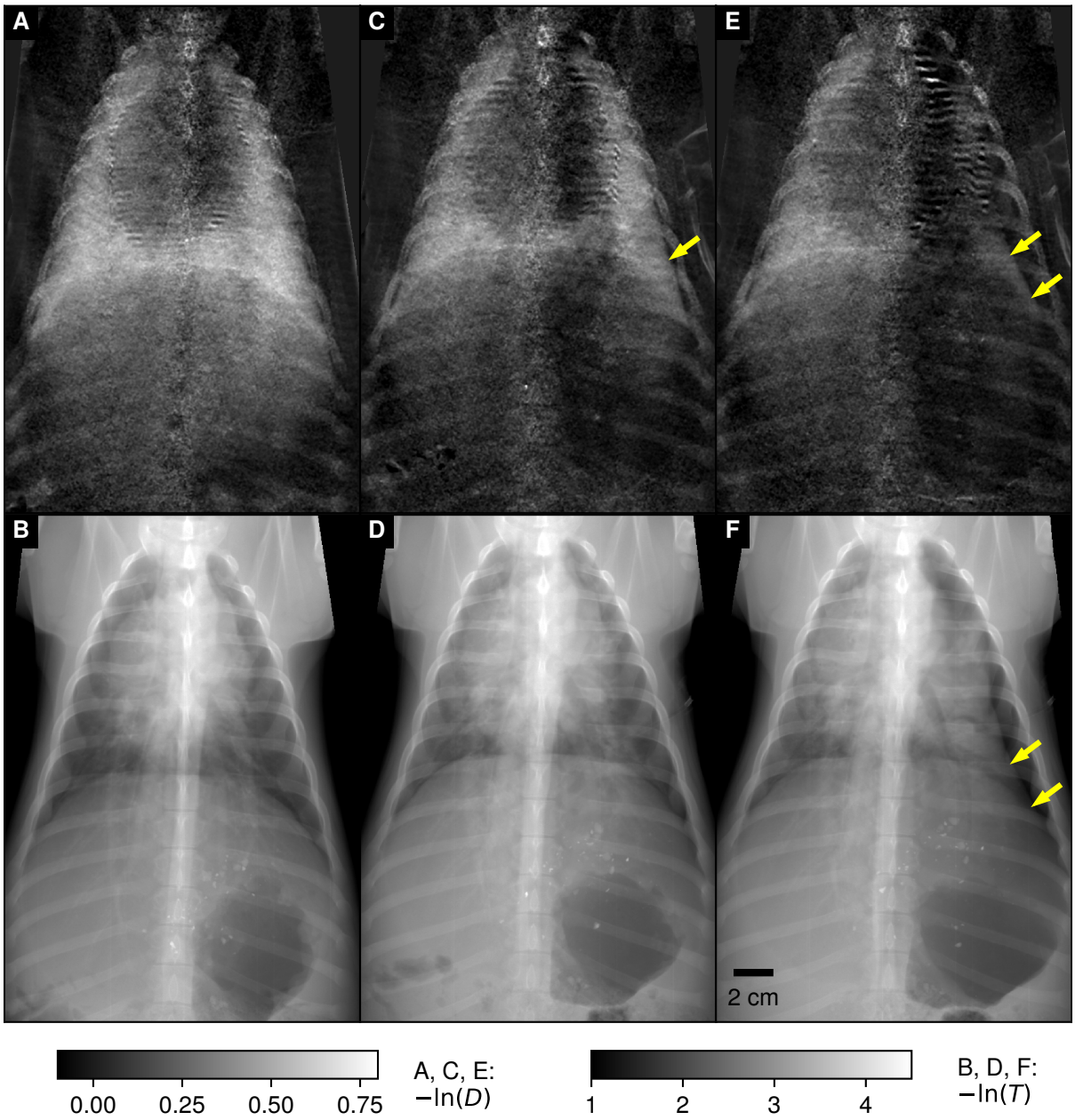

Figure 5.2: Pneumothoraces of different sizes depicted in X-ray dark-field and transmission images. Chest radiographs of the same pig (*in vivo*) just before (a, b) and after application of 250 ml air (c, d) and 500 ml air (e, f) in the left pleural space, comparing transmission images (lower row) with the corresponding dark-field images (upper row). A pneumothorax is indicated in dark-field images as a dark area adjacent to the rib cage on the left side (arrows). After application of 250 ml of air, a small pneumothorax was only visible in the dark-field image, indicated by a discrete widening of the left pleural space.

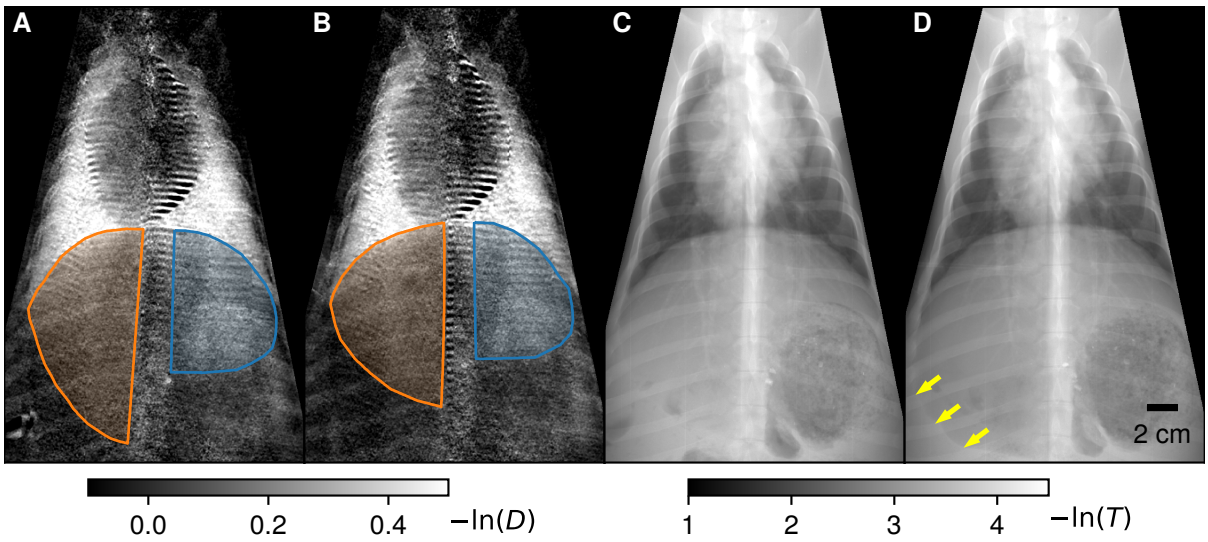

Figure 5.3: Dorsal pneumothorax of a living pig in dark-field and transmission imaging. Scattering lung parenchyma is directly visualized in dark-field images, even if located behind the diaphragm, enabling a quantification of the area of the inflated lung. Before the induction of a pneumothorax (a, c): affected side (orange) 72 cm^2, unaffected side (blue) 55 cm^2. After the induction of a pneumothorax (b, d): affected side (orange) 61 cm^2, unaffected side (blue) 56 cm^2. Indirect signs, such as an increased hyper-transparency in the basal parts of the affected lung and consecutively sharper edges of the pleura, indicate the presence of a pneumothorax in the corresponding transmission image (arrows).

demonstrated the detection of pneumothoraces to be markedly improved when analyzing dark-field compared to transmission images [Hell+16]. We now translated the experimental setup from a small animal to a large animal model in order to identify the potential diagnostic value of dark-field imaging in a setting similar to clinical reality. Using a prototype large-object X-ray dark-field scanner, it is now possible for the first time to depict lungs comparable in size to a human organ.

In line with our hypothesis, we were able to show that diagnosis of pneumothoraces can be facilitated using this new imaging method. Since the CNR between the area of a pneumothorax and the adjacent lung was significantly higher for the dark-field than for the transmission signal, identification of very small, lateral pneumothoraces was exclusively possible in dark-field images. Additionally, diagnosis of dorsal pneumothoraces was facilitated due to the high signal of the lung parenchyma, which was visible even when the basal parts of the lungs were located behind the organs of the upper abdomen.

Clinical relevance of dorsal pneumothorax Especially when thinking of a potential clinical implementation of this imaging technique, facilitated diagnosis of dorsal or (if the images are acquired in supine position) ventral pneumothoraces is of special interest: Severely ill patients, e.g. those in intensive care, have a high risk of suffering from a pneumothorax because they need to undergo various interventions (such as placement of a central venous catheter or thoracentesis[13]) that might result in a pneumothorax [Lois+13]. Supine chest X-rays are routinely ordered to exclude this complication [Eise+12]. As the sensitivity of diagnosing a ventral pneumothorax with conventional transmission imaging is limited, an imaging technique directly visualizing collapsed lung parenchyma is of great advantage. The deep sulcus sign, an indirect and rather unspecific sign for the presence of a ventral/dorsal pneumothorax, is difficult to detect, compared to the direct visualization of lung parenchyma using X-ray dark-field imaging. As transmission and dark-field radiographs are generated at the same time,

[13] Procedure to remove air or fluid from the pleural space via a hollow needle

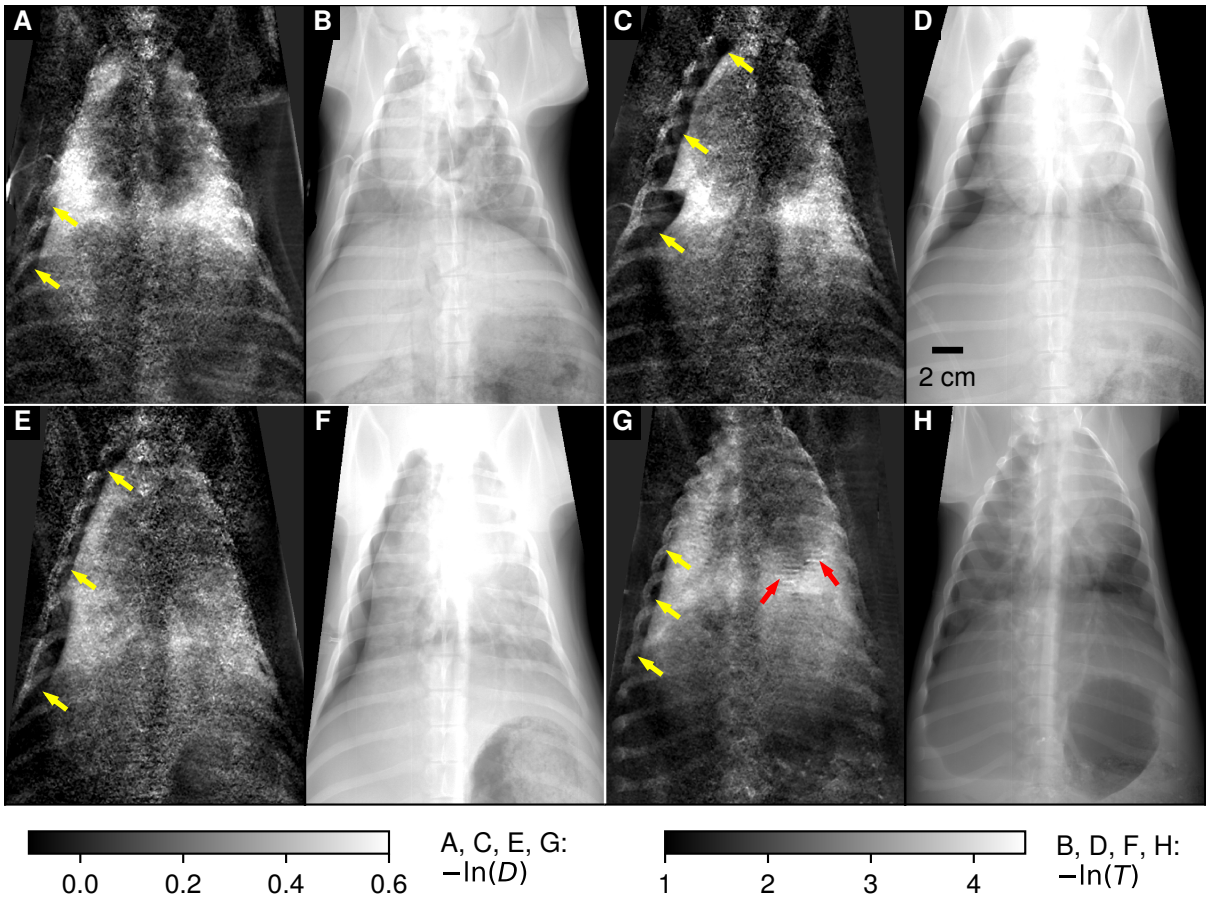

Figure 5.4: Conventional and dark-field chest radiographs of four additional animals (a–f: *ex vivo*, g and h: *in vivo*), after induction of a pneumothorax on the right side (yellow arrows). In the dark-field projection of the animal measured *in vivo* (g), some artifacts originating from the heart beat are visible (red arrows). This Figure is an addition to the content of the original paper.

combining information from both imaging modalities (anatomic details such as margins of the pleural cavity in transmission images, collapse of lung parenchyma in dark-field images) is possible with this imaging setup.

Detection of small lateral pneumothorax The visualization of very small, lateral pneumothoraces was exclusively possible using dark-field imaging in our study setting. Because of the increased CNR between lung parenchyma and pneumothorax in dark-field images, even discrete pleural detachment was visible. As a control image was acquired prior to the induction of a pneumothorax, comparison of both images might lead to an increased visibility of the pneumothorax. To answer the question whether dark-field imaging can actually facilitate the diagnosis of small lateral pneumothoraces, further research, for example by implementation of a reader study, is required.

Motion artifacts A clear distinction between animals measured *in vivo* and *ex vivo* was possible in dark-field images due to motion artifacts appearing as horizontal streaks located at the edges of the heart caused by the heartbeat (Fig. 5.2, 5.3, 5.4g). These artifacts result from organs entering and/or exiting a given image region while the intensity fringe pattern is scanned over it. The intensity modulations from the movement are then misinterpreted during signal extraction as an intensity modulation due to small-angle scatter. The artifacts present as horizontal lines (orthogonal to the scanning direction), similar to the spatial orientation of the fringe pattern, suggesting that artifact magnitude is related to fringe pattern phase.

Sources of noise When calculating the CNRs for transmission images smoothed like the dark-field projections (1.14 ± 1.1, method described in section 5.1.4), CNR for smoothed dark-field images still was significantly higher ($p = 0.002$). The same was found when comparing the CNR for unfiltered dark-field images (2.45 ± 0.7) to that of unfiltered transmission images ($p = 0.03$). We emphasize that the measured standard deviations are (for both modalities) a combination of photon noise and "anatomical noise" (actual variation of signal levels within the ROI due to unresolvable lung structure, i.e. not a truly random effect, see e.g. [Hoes+05]). It is challenging to separate both effects from the limited number of scans. The fact that transmission CNR values are hardly increased by low-pass filtering suggests that they are limited by anatomical noise (of low spatial frequency). This would also suggest that detector dose increase only provides marginal improvements in the attenuation modality: Excluding changes in spatial resolution, the applied filter should be equivalent to a 25-fold dose increase (five-fold CNR increase) in areas where pixel values are uncorrelated and normally distributed with equal mean and variance. For the dark-field modality, the CNR increase is greater, but this may also partly be due to anatomical noise: the high granularity of lung parenchyma may lead to a variation of dark-field signal levels of high spatial frequency. This is currently indistinguishable from photon noise, and would be attenuated more strongly by filtering than low-frequency anatomical noise in the transmission image. Experience from pathologies in small animal models leads us to believe that such a high-frequency signal variation has limited diagnostic value, i.e., moderate low-pass filtering probably does not affect the diagnostic value of dark-field images.

Determining the true spatial dark-field signal variation within the lung would require e.g. a time series of perfectly registered scans. This is not possible with the presented imaging protocol, since ventilation may only be stopped for one scan at a time and ventilation pressure during breath stop cannot be replicated perfectly, limiting registration quality. Since no structures are clearly recognizable within each ROI, anatomical noise appears to affect image quality in the same fashion as true noise. We therefore believe that the combination of both noise sources presents a reasonable measure for quantifying the discriminability of pneumothorax and lung parenchyma.

CT reference data CT scans of the lungs served as the standard of reference in this study to prove the presence of a pneumothorax (cf. Fig. 5.5). The scans can however not be used to draw a conclusion about the size of the pneumothoraces: as the CT device was not located in the same facility as the large-animal X-ray dark-field scanner, the pigs had to be disconnected from the mechanical respirator. Although the animals remained intubated and the aboral part of the laryngeal tube as well as the thoracic puncture site were carefully sealed, an enlargement of the pneumothoraces during transport could not be ruled out.

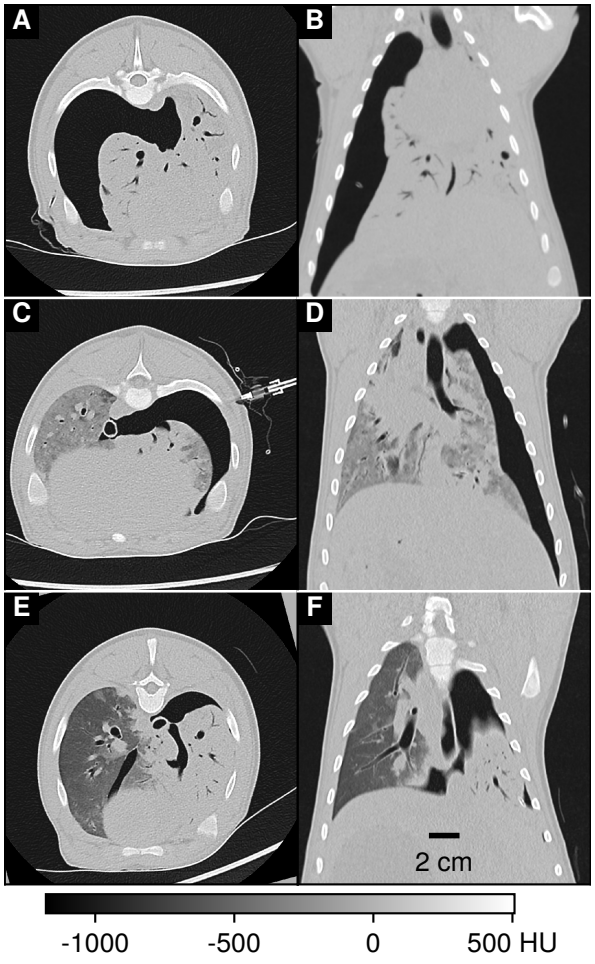

Figure 5.5: Transverse (left) and coronal (right) CT slices of three pigs after pneumothorax induction. The animals were euthanized prior to CT imaging due to the necessary transport. The catheter used for pneumothorax induction is visible in (c). Slice thickness: 2.5 mm (transverse) / 3.0 mm (coronal).

Dose considerations The dose area product (DAP) in our study was determined to be 0.5 Gy cm^2. Assuming a conversion coefficient between DAP and effective dose applicable for clinical chest X-ray in posterior-anterior (PA) orientation (K = 0.16 mSv/(Gy cm^2) [Wall$^+$11]), this would deliver an effective dose of 80 µSv. This is approximately six times as much as that of a conventional PA chest X-ray [Wall$^+$11], which may be acceptable given the additional information provided by the dark-field images.

Limitations and outlook The results of the presented work need to be seen in light of the study design and its limitations. Because this study was designed as a feasibility study, only a small number of animals was used for the experiments. Due to animal welfare reasons, the number of experimental animals also needed to be limited to the utmost minimum. In this study, *ex vivo* as well as *in vivo* animal setups were used to obtain dark-field and transmission images of pneumothoraces. For signal analysis, data of both animal groups was combined. This was possible as no statistically significant difference between *in vivo* and *ex vivo* measurements for transmission and dark-field CNRs was found.

Before dark-field imaging of the lung can be used in a clinical setting, further technical developments are required. The image acquisition time for this setup is 30 to 40 s. Especially for elderly people or patients with impaired lung function, breath-hold times of 30 s are often unachievable [Gay$^+$94]. To avoid breathing artifacts, an image acquisition time of 5 s should not be exceeded.

In conventional chest radiography, tube voltages of up to 125 kV are commonly used [McAd$^+$06], whereas the presented setup was operated at 70 kV. Radiologists' image impression of conventional X-rays produced at these different tube voltages differs significantly. A transition of dark-field radiography to higher voltages would thus be beneficial from a diagnostic point of view. To evaluate whether this is possible while maintaining a sufficient quality of dark-field images, further research is necessary. To simultaneously achieve high visibility and a significant dark-field signal at X-ray energies far beyond 70 keV, gratings with small periods (to achieve high sensitivity) and high absorber heights (to achieve high visibility) are required. Achieving such high aspect ratios may require further advances in grating development.

The optimal trade-off between resolution and dark-field signal levels should also be evaluated: although spatial resolution could be increased by reducing pixel size (e.g., disabling binning), we believe that the associated noise increase may not be desirable from a diagnostic point of view.

This feasibility study is an important step towards future clinical implementation of the X-ray dark-field imaging technique. It was not only possible to visualize lungs comparable to the size of human organs, but the diagnosis of pneumothoraces was also facilitated by the addition of information from dark-field images. Prospectively, this may offer the opportunity to improve clinical care for patients suffering from pneumothoraces.

5.2 Correlation of dark-field signal with lung thickness and ventilation pressure

The findings presented here have previously been published in the article "Contrast-to-noise ratios and thickness-normalized, ventilation-dependent signal levels in dark-field and conventional *in vivo* thorax radiographs of two pigs" by De Marco et al. (2019, Ref. [DeMa+19]). Compared to this work, the Figures and some wordings have been slightly modified, and the notation of dark-field quantities as introduced in section 5.2.2d was changed to be consistent with the rest of the work. Finally, the technical introduction to dark-field imaging and the used setup have been omitted. The reader is instead referred to chapters 2 and 3 for this information.

My main contribution to this work was for the design of the imaging study (measurement at multiple states during the breath cycle, and co-registered placement of the animals during CT measurements), the generation of dark-field and conventional radiographs, data analysis and interpretation, writing the majority of the manuscript, and performing the phantom measurements. The *in vivo* imaging experiments were only possible thanks to the hard work of Dres. Andrea Bähr and Michaela Dmochewitz from the Institute of Molecular Animal Breeding and Biotechnology (University Munich), as well as Dr. Katharina Hellbach from the Department of Radiology at the University Hospital Munich.

5.2.1 Introduction

For pigs—and likely also humans—the magnitude of the dark-field signal varies considerably between different stages of the breathing cycle. Since the medical promise of pulmonary dark-field radiography lies in detecting pathological microstructural changes, it is of major importance to distinguish these from normal changes induced by breathing.

In dark-field radiography, signal strength is described by a line integral through the entire lung, along the direction of projection. The contribution of a given volume element to this integral however depends on local microstructure, specifically on the autocorrelation function values of electron density at a few micrometers or less [Yash+10; Lync+11; Stro14]. Dark-field signal strength is thus a function of structural parameters on multiple length scales.

Lungs consist of hierarchical airway and blood vessel networks, with relevant length scales ranging from centimeters for the bronchi, down to a few micrometers for alveolar walls (*septa*). The forces acting on the lung exert mechanical strain on these structures, leading to structural changes on all length scales during the breathing cycle [Roan+11]. The relationship between breathing state and dark-field signal is thus potentially very complex.

Furthermore, the mechanics of alveolar expansion are not fully understood, as methods for *in vivo* imaging of alveolar structures are limited: For example, optical coherence tomography (OCT) is able to resolve alveolar structures in the living lung, but only in depths up to 2–3 mm below the lung surface [McLa+14].

Multiple models for alveolar dynamics in the breathing cycle have been proposed, such as isotropic alveolar expansion/contraction, (de-)recruitment of alveoli, and alveolar shape change. Although there is evidence in favor of each model, the overall results suggest that a combination of isotropic expansion and alveolar shape changes is at work [Roan+11]. In particular, an *in vivo* time-resolved OCT imaging study on pigs found a predominance of uniformly expanding alveolar clusters [Nama+13].

Although calculations of X-ray dark-field signal from wave-optical simulation of simple models have been performed [Male+12; Vign+18], currently available data is too imprecise and contradictory to develop an accurate three-dimensional model of a breathing lung with sufficiently high resolution.

Thus, the present work seeks to identify individual contributions of microscopic and macroscopic changes in the lung to dark-field signal by experimental means, namely by correlating *in vivo* dark-field radiographs of the porcine lung to several macroscopic parameters retrieved by subsequent *in vivo* imaging of the pigs in a medical CT device.

Furthermore, motivated by results in [Hell+17] (cf. section 5.1), where dark-field CNR of pneumothoraxes were found to exceed those from conventional X-ray, we combine results from the correlation analysis with phantom measurements and calculations. This allows us to compare CNR of dark-field and conventional radiographs in the absence of anatomical structure, and thus, to examine the relative importance of various factors to CNR performance under realistic imaging conditions.

5.2.2 Materials and methods

The goal of the calculation steps presented here is to combine the volumetric data obtained from the CT scans with the dark-field projection data acquired in the radiographic fringe-scanning acquisition, and to compare noise and CNR for the conventional and dark-field radiographs. The relationship between individual calculation steps and procedures, as well as their data output are summarized in Fig. 5.6. Individual procedures or calculations are shown as rectangles, whereas data exchanged between them are shown as ellipses.

Dark-field radiographs retrieved by the fringe-scanning setup (section 5.2.2b) are beam-hardening-corrected using previously acquired dark-field data of plastic absorbers of various heights (section 4.3.1 on page 101). A number of phantom measurements were then performed to reproduce the range of dark-field and attenuation values achieved in the lung region to allow measurement of noise levels (section 5.2.2i).

As detailed in section 5.2.2e, the lung is segmented from the CT data and a renormalized version of the CT data, which is masked to the lung volume, is calculated. These two data sets are then forward-projected, which yields maps of lung thickness and attenuation-equivalent water height. Their registration with data from the dark-field imaging setup is fine-tuned via application of an algorithm which applies elastic transformations to the thickness maps (section 5.2.2f).

Pixel-by-pixel correlation of the thickness and attenuation-equivalent water height maps with appropriate weighting (section 5.2.2g) then yielded mean values for the lungs' dark-field extinction coefficient (section 2.5.8c on page 62), as well as a ratio of dark-field signal per attenuation-equivalent water height. Dividing the latter quantity by the effective linear attenuation coefficient for water retrieved by spectral simulations (section 5.2.2h) retrieves the mean "normalized scatter" value of lung tissue.

Combining this result with the ratio of dark-field and attenuation noise levels (retrieved from calculations and phantom measurements) finally allows calculation of dark-field and attenuation contrast-to-noise ratio (CNR) for any given thickness difference of lung tissue.

5.2.2a *In vivo* imaging procedure

Two German Landrace Hybrid pigs were used (wild type, Institute of Molecular Animal Breeding and Biotechnology, Ludwig Maximilian University Munich breeding facility; animal 1: male, animal 2: female; weight: 25 kg each; age: 3 months; microbiological status not assessed). Animals were kept in conventional housing on continuous solid floor with straw bedding in age-matched groups. Animals were provided commercially-available pig feed and had unlimited access to water. Prior to the experiments, the animals were visually appraised by a veterinarian and no abnormalities were found.

The animals were sedated by intramuscular application of ketamine (Ursotamin®, Serumwerk Bernburg AG, Bernburg, Germany, 20 mg/kg) and azaperone (Stresnil®, Elanco Deutschland GmbH, Bad Homburg, Germany, 2 mg/kg). Anesthesia was continued by intravenous injection with propofol (Propofol 2%, MCT Fresenius, Fresenius Kabi AG, Langenhagen, Germany) using a syringe pump (Injectomat® MC Agilia, Fresenius Kabi AG, Langenhagen, Germany) with dose adjusted to effect. This method of anesthesia was applied to exclude spontaneous breathing during the experiment.

The animals were kept under automated ventilation throughout using an anesthesia machine (Fabius® Tiro, Drägerwerk AG & Co. KGaA, Lübeck, Germany). Heart rate and oxygenation were monitored continuously using a pulse oximeter. Oxygen saturation did not fall below 90% at any point during the experiments. For imaging, ventilation was paused for the duration of dark-field radiographs and CT scans (max. 60 s at a time) with constant pressures of 2, 11, or 20 mbar in the airways, thus simulating expiration, intermediate inspiration, and full inspiration. All constant pressure values were set after achieving peak inspiratory pressure, i.e. during exhalation.

All animal procedures were performed with permission of the local regulatory authority, Regierung von Oberbayern (ROB), Sachgebiet 54, 80534 Munich, approval number AZ 55.2-1-54-2532-61-2015. The application was reviewed by the associated ethics committee according to §15 TSchG German Animal Welfare Law.

To terminate the experiment, the animals were euthanized under anesthesia by intravenous injection of T61® (Intervet GmbH, Unterschleißheim, Germany)

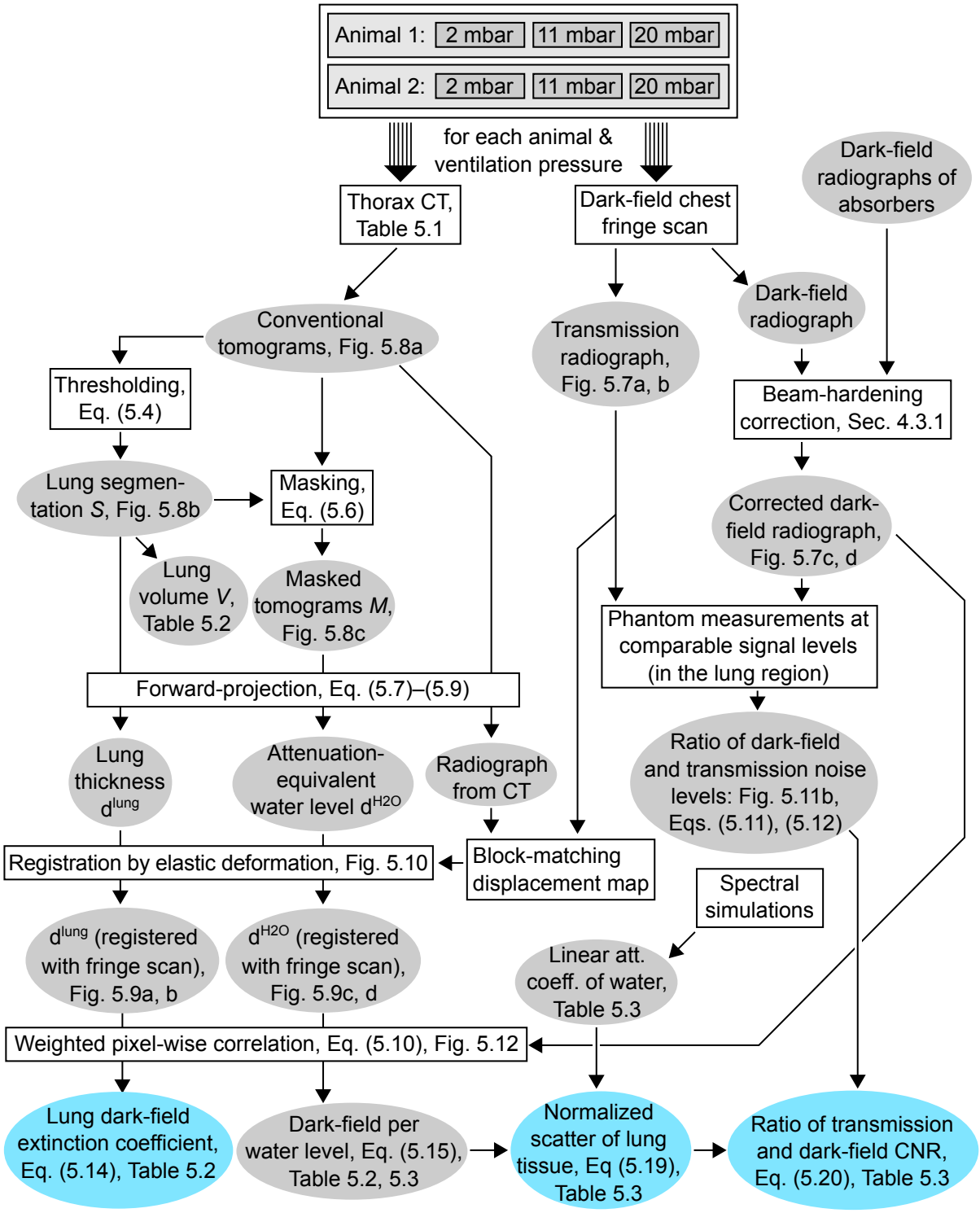

Figure 5.6: Flowchart of all processing and calculation steps. Data sets are shown as ellipses, operations performed on data are shown as rectangles. References to Equations, Figures and Tables are given where possible. Important findings are highlighted in color.

according to the manufacturer's instructions. The examinations were carried out in a non-survival experiment under continuous anesthesia to reduce burden on the animals. Sedation, anesthesia, imaging and termination were performed in two adjacent laboratory spaces. The experiments were conducted on a single day (7 AM until 3 PM) and were performed in sequence, i.e. the above procedure was begun for the second animal after euthanasia of the first animal. No randomization or blinding was performed.

5.2.2b Imaging parameters

To determine a correlation between dark-field signal strength, airway pressure and projected thickness of the porcine lung, the two pigs were subsequently scanned at the dark-field scanning system and a medical 64-slice CT system (iCT SP, Koninklijke Philips N.V., Amsterdam, Netherlands). Two pigs were used instead of only one to allow quantifying the amount of variation of analysis results between animals. With each animal, three dark-field acquisitions and three helical CT scans were performed, at airway pressures of 2, 11, and 20 mbar. In order to allow for accurate registration of image data, care was taken to achieve a similar posture of the pigs and to precisely replicate the ventilation pressures in CT and dark-field measurements.

Detailed parameters of the dark-field scanning system can be found in chapter 3. Each part of the field of view received 25 X-ray pulses, resulting in a total scan time of 40 s. To optimize dark-field image quality, the X-ray system was operated at 60 kVp and a tube current of 600 mA. The achieve entrance surface dose (ESD) per scan was 913 µGy. This is only a slightly higher value than for the acquisition parameters in [Hell+17] (section 5.1): here, an ESD of 720 µGy was achieved at 70 kVp and 340 mA. CT acquisition parameters are given in Table 5.1.

5.2.2c Calculation of dark-field and attenuation values

We distinguish several definitions of "dark-field signal" in this section:

- The measured visibility reduction $D = V/V^{\mathrm{r}}$, with no applied corrections.
- The correction factor $D^{(\mathrm{sp})}(T)$, which is measured in a beam-hardening calibration measurement with transmittance T.
- The beam-hardening-corrected value $D^{(\mathrm{SAS})} = D/D^{(\mathrm{sp})}$, as introduced in Eq. (4.29) on page 103. However, this quantity may still deviate from the true value due to the presence of detected Compton-scattered radiation, or inaccuracies in the beam-hardening correction procedure.
- Finally, the equivalent of $D^{(\mathrm{SAS})}$ in the absence of detected Compton scatter: $D^{(\mathrm{true})}$.

Dark-field and attenuation images of one animal's thorax at two ventilation pressures are shown in Fig. 5.7. They are presented logarithmically, i.e. as $-\ln D^{(\mathrm{SAS})}$, and $-\ln T$, so that the signal values should be proportional to the thickness of a homogeneous absorber or scatterer, respectively. Dark-field projections are beam-hardening-corrected according to the procedure presented in section 4.3.1 on page 101.

5.2.2d Effect of Compton scatter on dark-field signal

At every point on the detector, measured intensity is the sum of Compton-scattered and non-scattered radiation: $I_{\mathrm{total}} = I_{\mathrm{C}} + I_{\mathrm{U}}$. I_{U} depends on relative grating shift ϕ via $I_{\mathrm{U}} = \overline{I_{\mathrm{U}}}(1 + V^{(\mathrm{true})}\cos\phi)$, whereas Compton-scattered radiation is independent of ϕ, as it is incoherent and can thus not carry any visibility. Therefore,

$$I_{\mathrm{total}}(\phi) = \overline{I_{\mathrm{U}}}[1 + V^{(\mathrm{true})}\cos(\phi)] + I_{\mathrm{C}}. \qquad (5.2)$$

The visibility derived from $I_{\mathrm{total}}(\phi)$ is thus

$$V = V^{(\mathrm{true})}(1 + I_{\mathrm{C}}/\overline{I_{\mathrm{U}}})^{-1}.$$

$D = V/V^{\mathrm{r}}$ is also reduced by the same factor $(1 + I_{\mathrm{C}}/\overline{I_{\mathrm{U}}})^{-1}$, since blank-scan visibility values V^{r} are measured without a sample and are thus unaffected by Compton scatter, i.e.:

$$D = D^{(\mathrm{true})}(1 + I_{\mathrm{C}}/\overline{I_{\mathrm{U}}})^{-1}.$$

Data from phantom measurements for beam-hardening correction also contain Compton-scattered radiation, but the ratio of intensities of Compton-scattered and non-scattered radiation ($I_{\mathrm{C}}^{(\mathrm{sp})}/\overline{I_{\mathrm{U}}^{(\mathrm{sp})}}$) may deviate due to the differing spatial distribution

	Tube voltage	Pitch	Scan time	$CTDI_{vol}$	Volume [mm^3]	Voxel size [mm^3]
Animal 1	120 kV	0.609	24.3 s	24.7 mGy	248 × 188 × 255	0.50 × 0.50 × 1.0
Animal 2	120 kV	0.609	25.7 s	24.3 mGy	264 × 182 × 275	0.42 × 0.42 × 1.0

Table 5.1: Acquisition parameters for the CT scans. On each pig, three helical CT scans with the above acquisition and reconstruction parameters were performed at ventilation pressures of 2, 11, and 20 mbar. $CTDI_{vol}$: volume CT dose index as calculated by the CT device (per scan). Volume: smallest rectangular subset of the reconstructed volume containing the entire lung. Dimensions for volume and voxel size: lateral × dorsoventral × craniocaudal. Reconstruction was performed using filtered back projection with "Y-Sharp (YC)" convolution kernel. No noise reduction algorithms were applied.

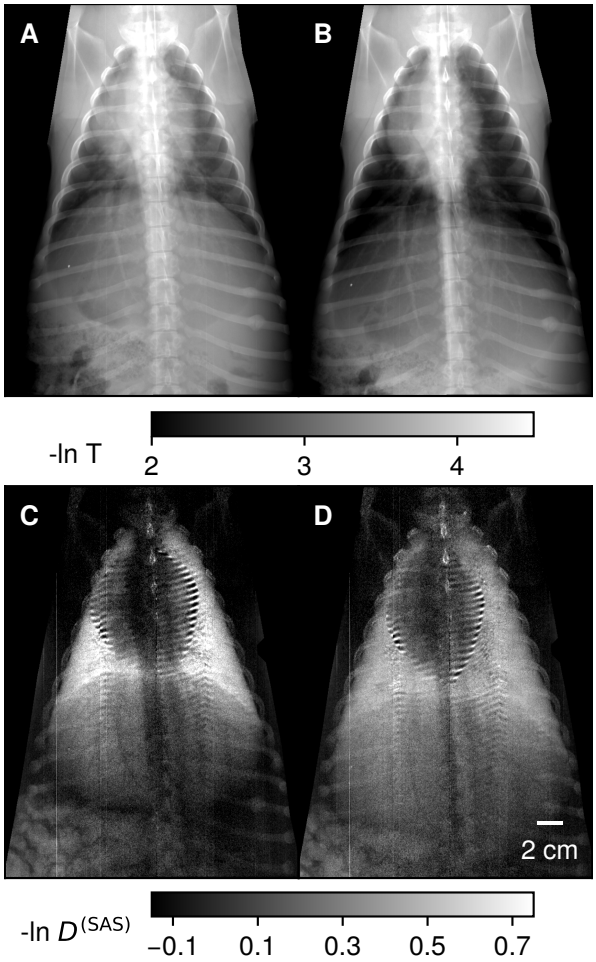

Figure 5.7: Transmission (a, b) and dark-field projections (c, d) from animal 1. (a, c): 2 mbar ventilation pressure (simulated expiration). (b, d): 20 mbar ventilation pressure (simulated inspiration).

of material: Compton scattering occurs nearly isotropically, and scattered radiation detected at a certain position therefore originates from a large area of the sample. The measured visibility reduction $D^{(\mathrm{sp})}$ deviates from its Compton-free equivalent $D^{(\mathrm{sp,true})}$ by

$$D^{(\mathrm{sp})} = D^{(\mathrm{sp,true})}\left(1 + I_{\mathrm{C}}^{(\mathrm{sp})} / \overline{I_{\mathrm{U}}^{(\mathrm{sp})}}\right)^{-1}.$$

The beam-hardening correction then yields

$$\begin{aligned} D^{(\mathrm{SAS})} &\overset{(4.29)}{=} \frac{D}{D^{(\mathrm{sp})}} = \frac{D^{(\mathrm{true})}\left(1 + I_{\mathrm{C}}^{(\mathrm{sp})} / \overline{I_{\mathrm{U}}^{(\mathrm{sp})}}\right)}{D^{(\mathrm{sp,true})}} \\ &= D^{(\mathrm{SAS,true})} \frac{\left(1 + I_{\mathrm{C}}^{(\mathrm{sp})} / \overline{I_{\mathrm{U}}^{(\mathrm{sp})}}\right)}{\left(1 + I_{\mathrm{C}} / \overline{I_{\mathrm{U}}}\right)}, \end{aligned} \tag{5.3}$$

with $D^{(\mathrm{SAS})}$ being the value retrieved with Compton scatter and $D^{(\mathrm{SAS,true})}$ without Compton scatter.

5.2.2e Lung segmentation and masking of CT data

Lung segmentation was performed in the CT image volume via thresholding of Hounsfield unit (HU) values. For each CT volume, L^{low} and L^{high} were determined as HU value bounds of all voxel inside the lung. For the scans with 20 and 11 mbar, $L^{\mathrm{low}} = -922$ HU, $L^{\mathrm{high}} = -512$ HU, for the scans with 2 mbar: $L^{\mathrm{low}} = -870$ HU, $L^{\mathrm{high}} = -410$ HU. For each data set, the corresponding segmentation volume S was defined as

$$S_{x,y,z} = \begin{cases} 1 & L^{\mathrm{low}} < \mathrm{HU}_{x,y,z} < L^{\mathrm{high}} \\ 0 & \text{else} \end{cases} \tag{5.4}$$

for each voxel (x, y, z). Small holes in S were removed via binary closing with a $(3 \times 3 \times 3)$ voxel kernel. The determined thresholds were verified by comparison of the segmented volume with the lung boundaries visible in the original data set.

Furthermore, an attenuation coefficient relative to water was calculated from the Hounsfield unit values h via

$$\frac{\mu}{\mu^{\mathrm{H2O}}} = \frac{h - h^{\mathrm{air}}}{h^{\mathrm{H2O}} - h^{\mathrm{air}}}, \tag{5.5}$$

where $h^{\mathrm{H2O}} = 0\,\mathrm{HU}$ and $h^{\mathrm{air}} = -1000\,\mathrm{HU}$ are the HU values of water and air, respectively. To be able to isolate the portion of the attenuation signal originating from the lung, the volume of relative attenuation values was "masked" by the segmentation S, yielding the data set M:

$$M_{x,y,z} = S_{x,y,z} \cdot \left(\frac{\mu}{\mu^{\mathrm{H2O}}}\right)_{x,y,z} \tag{5.6}$$

The effect of segmentation and masking on one example CT slice are illustrated in Fig. 5.8.

5.2.2f Forward-projection and registration of CT with dark-field radiographs

Forward-projection of the binary segmentation volume S produces a map of its thickness d^{lung} in the direction of projection:

$$d^{\mathrm{lung}}_{x,y} = \int_{R(x,y)} S(\vec{r})\, d\vec{r}, \tag{5.7}$$

with S from Eq. (5.4) interpolated from the discrete to the continuous domain, (x, y) a position in the detector plane, and $R(x, y)$ a straight line from the source to position (x, y) on the detector. This quantity is insensitive to density variations within the lung volume, such as those occurring between different inspiration states. An example is shown in Fig. 5.9a and 5.9b.

Forward-projection of the masked image of relative attenuation coefficients M yields a height of an equivalently absorbing layer of water. This can be seen by equating an arbitrary projection integral with that of a given water layer and solving for its height d^{H2O}:

$$-\ln T_{x,y} = \int_{R(x,y)} S(\vec{r})\mu(\vec{r})\, d\vec{r} \stackrel{!}{=} \mu^{\mathrm{H2O}} \cdot d^{\mathrm{H2O}}_{x,y} \tag{5.8}$$

$$\Rightarrow d^{\mathrm{H2O}}_{x,y} = \int_{R(x,y)} S(\vec{r}) \cdot \frac{\mu(\vec{r})}{\mu^{\mathrm{H2O}}}\, d\vec{r} \stackrel{(5.6)}{=} \int_{R(x,y)} M(\vec{r})\, d\vec{r}, \tag{5.9}$$

with S, μ/μ^{H2O}, and M from Eq. (5.4)–(5.6) interpolated from the discrete to the continuous domain to allow integration. The maps of d^{H2O} values retrieved from two of the CT scans are shown in Fig. 5.9c and 5.9d. For the sake of brevity, we omit the (x, y) pixel subscripts in the following. We use d^{H2O} to interrelate the transmittance values obtained by the dark-field setup and the CT device: Since the two setups use very different X-ray spectra and detectors with differing spectral quantum efficiencies, the retrieved transmittance values are not easily comparable. However, the attenuation spectra of soft tissue and water are very similar in the range of medically-used X-ray energies, which means that the height level d^{H2O} of water, which is equivalent in attenuation to a given amount of lung, is approximately independent of acquisition parameters. Conversion of d^{H2O} to logarithmic transmittance values *of the lung alone* measured at the dark-field setup is then possible by simulating the X-ray spectrum as seen by the detector and calculating the effective linear attenuation coefficient of water μ^{H2O} for this spectrum.

Cone-beam forward-projection [interpolation of S, M to the continuous domain and calculation of the integrals in Eq. (5.7), (5.9)] was performed using a reconstruction software package developed at the Chair of Biomedical Physics, TUM. Projection geometry parameters were selected to match the true geometry of the dark-field setup (as given in [Hell+17]), and projection angles were manually adjusted to optimize registration of the results with data from the dark-field setup.

Lastly, the plugin *bUnwarpJ* [Arga+06] for the image processing software *Fiji* [Schi+12] was used to apply elastic deformations to the projected CT data in order to account for deviations between the positioning of the pigs in CT and dark-field setup, and thus further improve registration with the dark-field radiographs. In a first step, feature pairs from projected CT data and the corresponding attenuation image from the dark-field setup were found by applying a block-matching algorithm in *Fiji*. These pairs of image coordinates were then used as input for *bUnwarpJ*, yielding a slightly distorted version of the projected CT data.

Visual inspection showed a nearly perfect registration of the image pairs, enabling more accurate calculation of pixel-for-pixel correlations. Magnitude and shape of the introduced distortion are visualized in Fig. 5.10 for one of the six data set pairs.

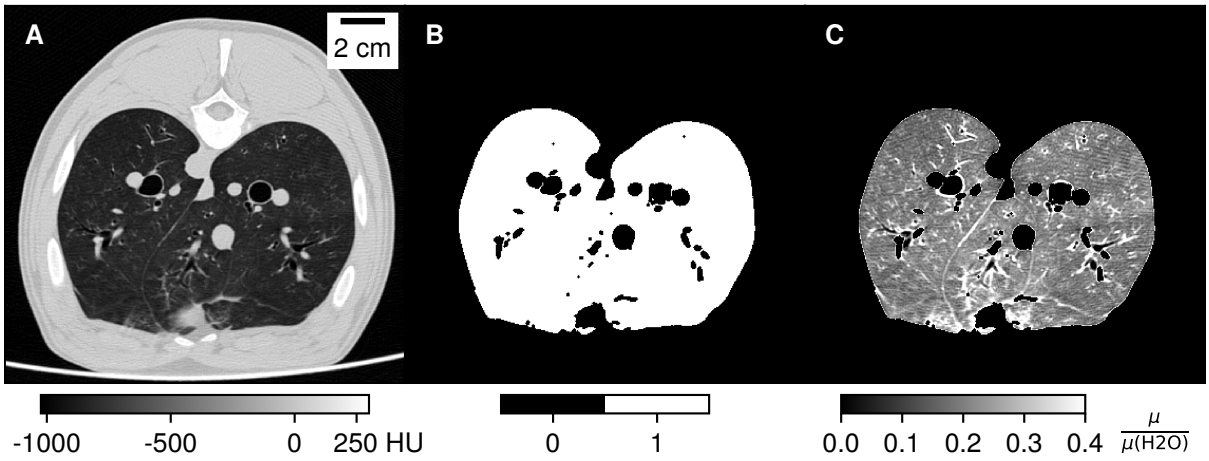

Figure 5.8: CT slice and lung segmentation / masking. (a): Slice from reconstruction of one of the CT scans (animal 2, 20 mbar). (b): Segmentation S of the lung via thresholding as defined in Eq. (5.4), followed by binary closing. Interior of bronchi and more strongly attenuating tissues (HU ≈ 0) are excluded. (c): Masked volume of relative attenuation values M, as defined in Eq. (5.6).

5.2.2g Calculation of weighting coefficients for linear regression

We performed linear regression between $-\ln D^{(\mathrm{SAS})}$ and d^{lung}, as well as between $-\ln D^{(\mathrm{SAS})}$ and d^{H2O}. To account for variable noise levels across different regions in the image, weighting of individual data points was applied in accordance with a simplified version of the model for the propagation of shot noise to the dark-field modality, as presented in [Revo+10]. Specifically, we used the equation

$$\sigma\left[D^{(\mathrm{SAS})}\right]^2 \propto \frac{{D^{(\mathrm{SAS})}}^2}{(V^{\mathrm{r}})^2 I^{\mathrm{r}}}\left[(V^{\mathrm{r}})^2\left(1+\frac{1}{T}\right)+2\left(1+\frac{1}{T{D^{(\mathrm{SAS})}}^2}\right)\right], \tag{5.10}$$

where V^{r} and I^{r} are visibility and detected photon counts in the reference scan. All quantities in Eq. (5.10) are to be understood as functions of pixel indices (x, y). Fit weights were set as $w \propto \sigma(D)^{-2}$. Simplifications with respect to [Revo+10] are in assuming a constant gain for sample and reference scan acquisition, and a proportionality between I^{r} and the signal of the (energy-integrating) detector. Furthermore, the cited equation assumes a phase-stepping acquisition of the images, whereas the presented images were acquired with a fringe-scanning acquisition. Since the model for signal extraction is similar for both acquisition schemes (see e.g. section 4.2.1 on page 92), Eq. (5.10) is reasonably well applicable here.

5.2.2h Spectral simulation of attenuation coefficients for water

The *MATLAB* package *spektr 3.0* [Punn+16] was used to simulate X-ray spectra for two imaging situations, namely the presented three-grating setup operated at 60 kV, and a system without gratings, operated at 125 kV (simulating a setup for conventional thorax imaging, as they are typically operated at 125 to 150 kV [Vogl+11]). The software calculates spectral X-ray flux histograms of tungsten anode X-ray tubes with 1 keV bins.

For both scenarios, tube filtration of 2.5 mm Al was assumed and the spectral fraction of absorbed X-ray flux in a 600 µm detector layer of CsI scintillation material was then calculated. For the first scenario, filtering due to the three gratings is also taken into account (cf. Table 3.1 on page 79 for all setup parameters). The energy-integrating property of the detector signal in a flat-panel detector was modeled by multiplying each energy bin of the spectral absorbed flux with the bin's photon energy before adding up all the products to calculate the detector signal.

An effective linear attenuation coefficient for water was calculated for each scenario by including attenuation due to various heights of water (up to 20 cm) in the spectral calculation, and performing linear regression of logarithmic transmittance with respect to water height. Nonlinearities due to beam-hardening were found to be negligible.

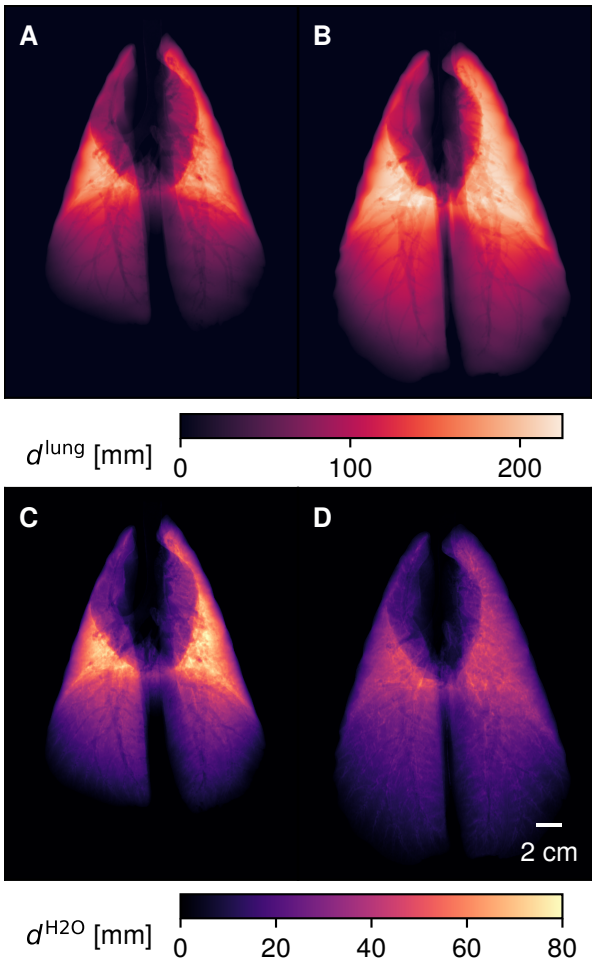

Figure 5.9: Forward-projections of segmented and masked CT data. (a, b): Maps of projected lung thickness d^{lung} [forward-projections of segmentation volumes S, see Eq. (5.7) and Fig. 5.8b]. (c, d): Maps of attenuation-equivalent water level d^{H2O} [forward-projections of relative attenuation volumes M, see Eq. (5.9) and Fig. 5.8c]. Both types of maps are from animal 1, with 2 and 20 mbar ventilation pressure (compare Fig. 5.7). Larger airways are visible in both types of maps, but density variations of lung parenchyma are much more apparent in maps of d^{H2O}.

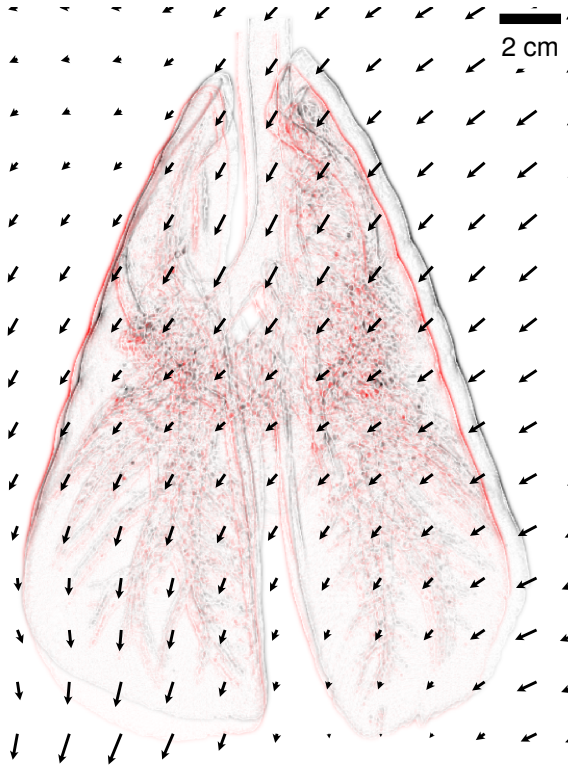

Figure 5.10: Elastic registration of forward-projected CT data with dark-field radiographs. Projected lung thickness d^{lung} (animal 1, 2 mbar), shown with edge-enhancement before (black) and after (red) elastic registration to fringe-scanning data. Arrows indicate the magnitude and direction of local shifts. Minimum and maximum shifts in the area of the lung are 3.2 and 27.0 pixels. Using the effective pixel size of the dark-field setup in a plane 10 cm above the sample table, these correspond to distances of 1.1 and 9.5 mm. Mean displacement in the lung area is 17.3 pixels (6.1 mm).

5.2.2i Noise estimation from phantom measurements and calculations

For the estimation of dark-field and transmission noise levels, a phantom was constructed from polyoxymethylene (POM, Hans-Erich Gemmel & Co. GmbH, Berlin, Germany) and chloroprene (CR-L, W. Köpp GmbH & Co. KG, Aachen, Germany). Four thickness combinations ($d^{\mathrm{POM}}, d^{\mathrm{CRL}}$) were measured to approximate dark-field and attenuation levels achieved in different regions of the pig scans: (6.4 cm, 3.0 cm), (9.6 cm, 2.0 cm), (9.6 cm, 1.0 cm), and (12.8 cm, 0 cm).

Relative noise levels were also calculated from dark-field and transmission signal levels, adapting results from [Revo+10]: It was assumed that detector gain is identical for reference and sample scans, and that standard deviations of logarithmic modalities can be approximated by

$$\sigma(\ln X) \approx \sigma(X) \cdot \left.\frac{\partial \ln x}{\partial x}\right|_{\langle X\rangle} = \frac{\sigma(X)}{\langle X\rangle} \quad (X = D^{(\mathrm{SAS})}, T). \tag{5.11}$$

We thus find that

$$\frac{\sigma\left[\ln D^{(\mathrm{SAS})}\right]}{\sigma\left[\ln T\right]} \approx \sqrt{1 + \frac{2}{(V^{\mathrm{r}})^2}\,\frac{1+\frac{1}{TD^{(\mathrm{SAS})^2}}}{1+\frac{1}{T}}}, \tag{5.12}$$

where V^{r} is the reference scan visibility, for which we assumed the mean measured value of 0.365.

5.2.2j Calculation of attenuation signal fraction due to the lung

Multiplying the water-equivalent map of the pig lung (d^{H2O}, cf. Fig. 5.9c and 5.9d) with the simulated attenuation coefficient of water in the dark-field setup at 60 kV, $\mu^{\mathrm{H2O}}_{\mathrm{eff},60}$, yields a map of the attenuation signal due to the lung alone. This can then be related to the corresponding attenuation image $-\ln T$ of the whole thorax from the dark-field setup (also acquired at 60 kV, cf. Fig. 5.7a and 5.7b) to yield a pixel map of the fraction f of attenuation signal due to the lung:

$$f = \frac{\ln T^{\mathrm{lung}}}{\ln T} = -\frac{d^{\mathrm{H2O}}\mu^{\mathrm{H2O}}_{\mathrm{eff},60}}{\ln T}. \tag{5.13}$$

5.2.3 Results

5.2.3a Magnitude of correction procedures

Beam-hardening correction of dark-field radiographs has a significant influence on signal levels: The logarithmic secondary visibility reduction $-\ln D^{(\mathrm{sp})}$ retrieved from calibration measurements was approximately 10% of logarithmic transmittance $-\ln T$. Given that the latter ranges between 2.0 and 4.0 in the lung area of the radiographs (Fig. 5.11a), the beam-hardening-corrected dark-field values $-\ln D^{(\mathrm{SAS})}$ are about 0.2 to 0.4 below the measured values $-\ln D$, namely in a range between −0.1 and 0.6 (Fig. 5.11a).

The method used for the registration of forward-projected CT data onto the corresponding dark-field radiographs (spline-based elastic deformation) implies that the input data is being slightly distorted. Direction and magnitude of this distortion are illustrated for one pair of images in Fig. 5.10. Displacement of lung features in this data set ranged between 1.1 and 9.5 mm, with a mean displacement of 6.1 mm.

5.2.3b Correlation between ventilation pressure and signal level

For all six pairs of measurements (two pigs, three values of ventilation pressure), the correlations of $-\ln D^{(\mathrm{SAS})}$ with both projected lung thickness d^{lung} and transmission-equivalent water level d^{H2O} were analyzed. In the outermost periphery of the lung, minor discrepancies in registration lead to large errors due to the sharp transition between lung and the surrounding tissue. This region, here defined as all pixels with $0 < d^{\mathrm{lung}} < 3$ mm, was thus excluded from the analysis.

To visualize the correlation of $-\ln D^{(\mathrm{SAS})}$ with d^{lung} and d^{H2O}, we avoided scatter plots because they are unable to visualize details in regions of high plot point density. As shown in Fig. 5.12, we instead present bivariate histograms, where local average point density, i.e. the number of image pixels per hexagonal bin, is color-coded.

The degree of linear correlation between $-\ln D^{(\mathrm{SAS})}$ and d^{lung}, d^{H2O} was quantified by linear regression with weighting according to Eq. (5.10). A superposition of regression results onto the corresponding bivariate histograms is shown in Fig. 5.12.

The slope of the linear regression with respect to d^{lung} is equivalent to the "dark-field extinction coefficient" (the dark-field equivalent to the linear attenuation coefficient μ, named μ_{d} in [Lync+11]), averaged over the entire lung:

$$-\frac{\partial\left[\ln D^{(\mathrm{SAS})}\right]}{\partial d^{\mathrm{lung}}} = \langle\mu_{\mathrm{d}}\rangle_{\mathrm{lung}}. \tag{5.14}$$

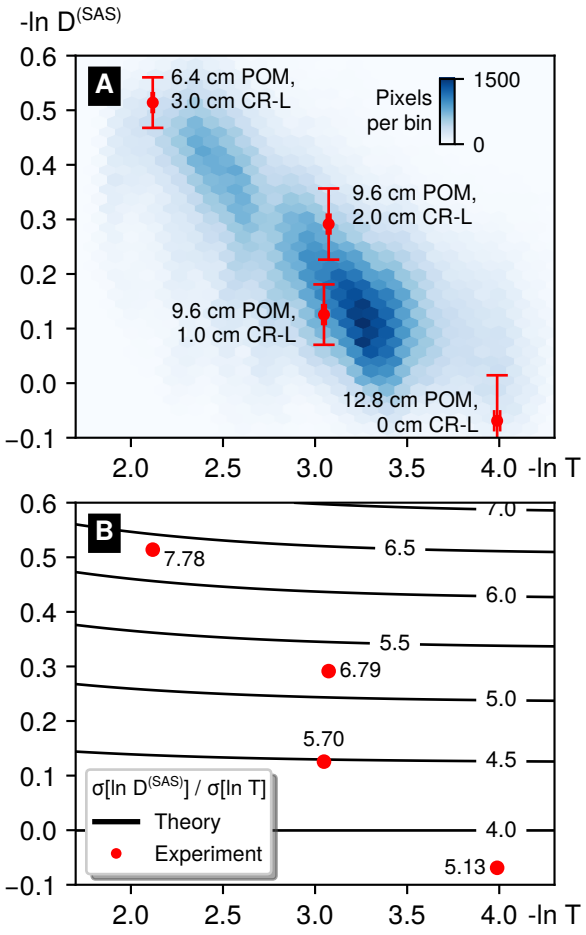

Figure 5.11: Dark-field and attenuation noise levels in the lung area of one pig scan. (a): Bivariate histogram of signal values $(-\ln D^{(\mathrm{SAS})}, -\ln T)$ from *in vivo* dark-field radiography of the pig thorax (animal 1, 20 mbar). Pixels where $d^{\mathrm{lung}} < 3$ mm are excluded. Four phantom measurements were performed at similar signal levels to determine signal standard deviations σ (red markers and error bars), $\sigma[\ln T]$ values are very small. (b): Ratio of standard deviations $\sigma[\ln D^{(\mathrm{SAS})}]/\sigma[\ln T]$ from the phantom measurements (red markers), and theoretically calculated values [Eq. (5.12), black contour lines], displayed as a function of signal levels.

It decreases significantly with rising ventilation pressure (by −33 and −42% from 2 to 20 mbar), cf. Table 5.2.

The observed decrease, both in $-\partial[\ln D^{(\mathrm{SAS})}]/\partial d^{\mathrm{lung}}$, as well as in the lungs' mean linear attenuation coefficient μ for rising pressure is related to the simultaneous increase of lung volume. As μ is proportional to mass density for a given material, the integral of μ over the entire lung volume should be independent of ventilation pressure. In other words, the lungs' mean linear attenuation coefficient should be inversely proportional to lung volume. To verify this, we determined these quantities from the segmented and masked CT volumes (S, M) and plotted μ/μ^{H2O}, as well as $-\partial[\ln D^{(\mathrm{SAS})}]/\partial d^{\mathrm{lung}}$ as a function of lung volume and applied regression of a power-law function $y = aV^b$ (Fig. 5.13). While an inversely proportional relationship is observed for μ/μ^{H2O} ($b \approx -1$), this is not quite the case for $-\partial[\ln D^{(\mathrm{SAS})}]/\partial d^{\mathrm{lung}}$, where we find exponents $b > -1$.

On the other hand, dark-field signal per absorption-equivalent water height is equivalent to the ratio of the lung's mean dark-field extinction coefficient and linear attenuation coefficient normalized to water:

$$-\frac{\partial\left[\ln D^{(\mathrm{SAS})}\right]}{\partial d^{\mathrm{H2O}}} = \frac{\langle\mu_{\mathrm{d}}\rangle_{\mathrm{lung}}}{\langle\mu/\mu^{\mathrm{H2O}}\rangle_{\mathrm{lung}}} = \underbrace{\frac{\langle\mu_{\mathrm{d}}\rangle_{\mathrm{lung}}}{\langle\mu\rangle_{\mathrm{lung}}}}_{\text{Norm. scatter}} \cdot \mu^{\mathrm{H2O}}. \tag{5.15}$$

μ_{d}/μ has been called the "normalized scatter" signal [Mein+14b]. $-\partial[\ln D^{(\mathrm{SAS})}]/\partial d^{\mathrm{H2O}}$ is thus proportional to an average normalized scatter of the entire lung (excluding surrounding tissues).

The results shown in Fig. 5.13 suggest that for increasing ventilation pressure, μ_{d} decreases more slowly than μ, and thus, an increase of $-\partial[\ln D^{(\mathrm{SAS})}]/\partial d^{\mathrm{H2O}}$ should be observed. This is indeed the case: The values for 11 mbar (20 mbar) exceed those for 2 mbar by 4% (1.3%) for animal 1, and by 6.5% (10%) for animal 2. Slopes and coefficients of determination for each regression analysis, as well as lung volumes for all measurements are summarized in Table 5.2.

To estimate the lungs' normalized scatter signal from $-\partial[\ln D^{(\mathrm{SAS})}]/\partial d^{\mathrm{H2O}}$, the effective linear attenuation coefficient of water must be determined [cf. Eq. (5.15)], which was done by simulation. We present calculated values for $\mu_{\mathrm{eff}}^{\mathrm{H2O}}$ in two imaging scenarios (cf. Methods): The first ($\mu_{\mathrm{eff,60}}^{\mathrm{H2O}}$) is valid for the presented dark-field setup when operated at 60 kVp (and thus relevant

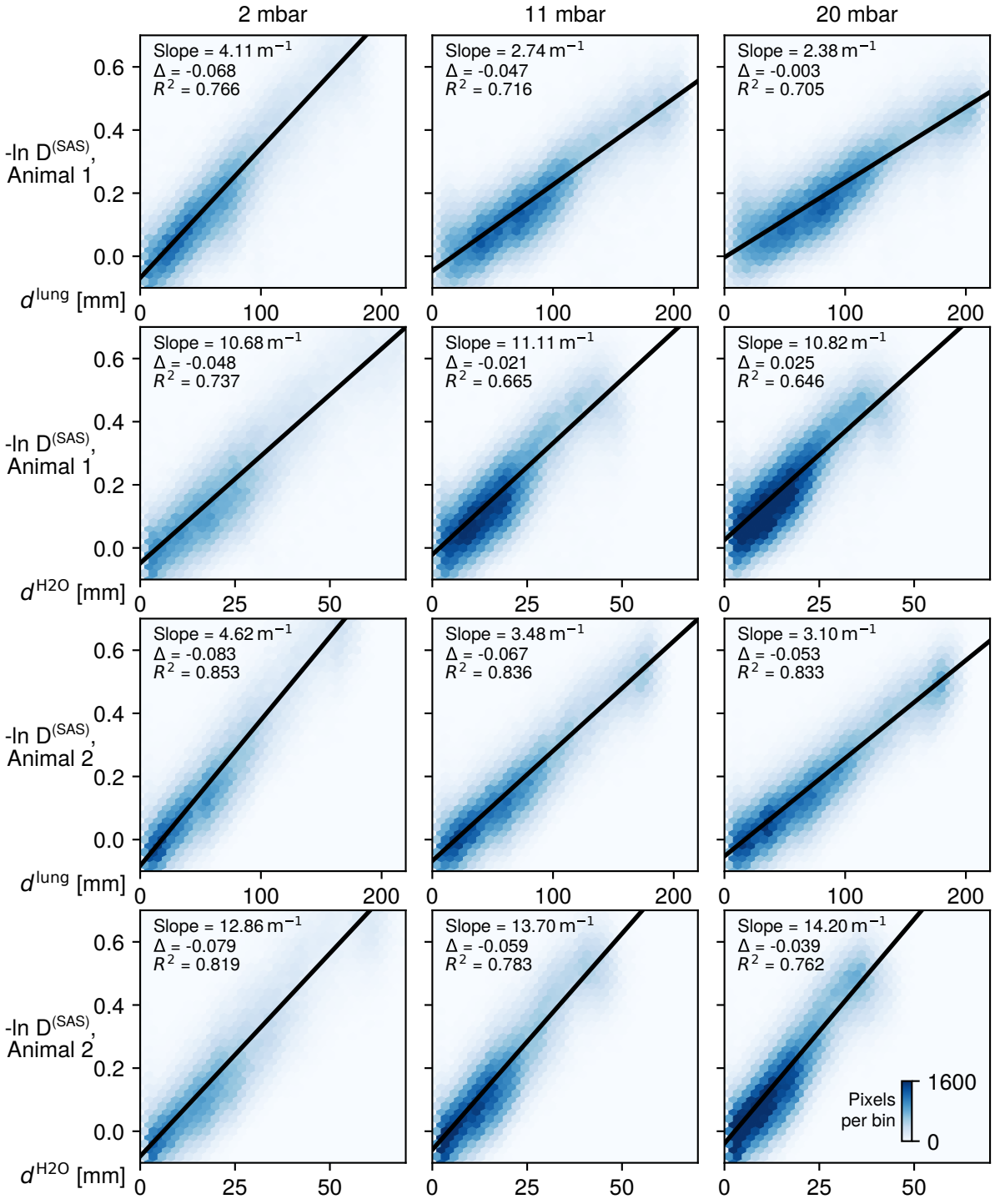

Figure 5.12: Bivariate histograms of logarithmic dark-field signal vs. lung thickness d^{lung} (first and third row) and attenuation-equivalent water level d^{H2O} (second and fourth row), for all measurements in the study. Left / middle / right column: Ventilation pressures of 2 / 11 / 20 mbar. Results from linear regression are superimposed, and also compiled in Table 5.2.

	Animal 1			Animal 2		
Pressure [mbar]	2	11	20	2	11	20
$-\partial\left[\ln D^{(\mathrm{SAS})}\right]/\partial d^{\mathrm{lung}}\,[\mathrm{m}^{-1}]$	**4.11**	**2.74**	**2.38**	**4.62**	**3.48**	**3.10**
Intercept Δ	-0.068	-0.047	-0.003	-0.083	-0.067	-0.053
R^2 of fit	0.766	0.716	0.705	0.853	0.836	0.833
$-\partial\left[\ln D^{(\mathrm{SAS})}\right]/\partial d^{\mathrm{H2O}}\,[\mathrm{m}^{-1}]$	**10.68**	**11.11**	**10.82**	**12.86**	**13.70**	**14.20**
Intercept Δ	-0.048	-0.021	0.025	-0.079	-0.059	-0.039
R^2 of fit	0.737	0.665	0.646	0.819	0.783	0.762
Lung volume [l]	0.76	1.20	1.37	0.78	1.06	1.24

Table 5.2: Results from regression between $-\ln D^{(\mathrm{SAS})}$ and projected lung thickness d^{lung}, as well as between $-\ln D^{(\mathrm{SAS})}$ and d^{H2O}. The quantity $-\partial[\ln D^{(\mathrm{SAS})}]/\partial d^{\mathrm{lung}}$ is a global average of the lungs' dark-field extinction coefficient, cf. Eq. (5.14). The corresponding histograms and regression curves are shown in Fig. 5.12. Lung volumes were retrieved from the segmentation S, cf. Eq. (5.4).

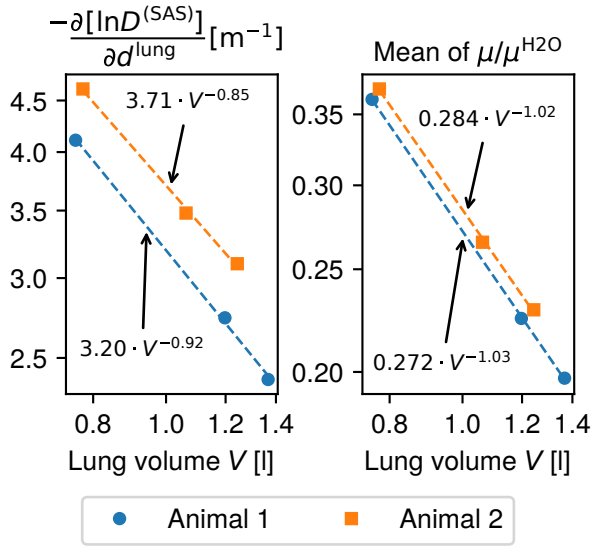

Figure 5.13: Dependence of lungs' average dark-field extinction coefficient ($-\partial[\ln D^{(\mathrm{SAS})}]/\partial d^{\mathrm{lung}}$) and relative linear attenuation coefficient (μ/μ^{H2O}) on lung volume. The three data points correspond to 2, 11, and 20 mbar, respectively. Axes are scaled logarithmically. Mean linear attenuation coefficients are retrieved from HU values in lung segmentation and are inversely proportional to lung volume. Dark-field extinction coefficients decrease more slowly (exponents greater than -1), which could e.g. be due to alveolar recruitment at higher ventilation pressures.

for the calculation of normalized scatter), the second ($\mu^{\mathrm{H2O}}_{\mathrm{eff},125}$) is achieved in a conventional radiographic system operated at 125 kVp, and is provided only for comparison. We find normalized scatter values between 0.4 and 0.5 (cf. Table 5.3). These results will be revisited in the analysis of noise levels further below.

It is apparent that a vertical offset (i.e. nonzero vertical axis intercept) is present in these histograms, which varies between ventilation pressures. We believe that this is primarily due to a deviation between the fraction of Compton-scattered and non-scattered radiation in the sample scan, when compared to the beam-hardening measurement ($I_{\mathrm{C}}/\overline{I_{\mathrm{U}}}$ and $I_{\mathrm{C}}^{(\mathrm{sp})}/\overline{I_{\mathrm{U}}^{(\mathrm{sp})}}$ in Eq. (5.3), respectively):

$I_{\mathrm{C}}^{(\mathrm{sp})}/\overline{I_{\mathrm{U}}^{(\mathrm{sp})}}$ is likely to be very nearly position-independent, since the beam-hardening measurement is performed with homogeneous slabs of POM. We think that $I_{\mathrm{C}}/\overline{I_{\mathrm{U}}}$ can also be assumed to be approximately constant in the area of the lung, since Compton scatter is nearly isotropic and the sample is quite distant from the detector (> 30 cm). Taking the logarithm of Eq. (5.3) and solving for $-\ln D^{(\mathrm{SAS})}$, which is the quantity on the vertical axis in Fig. 5.11a and Fig. 5.12, shows it is the sum of the true signal $-\ln D^{(\mathrm{SAS,true})}$ (which we assume to increase proportionally with d^{lung} and d^{H2O}) and a second term Δ, which should be approximately constant in the whole

$\mu_{\mathrm{eff,60}}^{\mathrm{H2O}}$	$25.42\,\mathrm{m}^{-1}$	
$\mu_{\mathrm{eff,125}}^{\mathrm{H2O}}$	$21.07\,\mathrm{m}^{-1}$	
	Animal 1	Animal 2
$-\partial[\ln D^{(\mathrm{SAS})}]/\partial d^{\mathrm{H2O}}$	$(10.68 \ldots 11.11)\,\mathrm{m}^{-1}$	$(12.86 \ldots 14.20)\,\mathrm{m}^{-1}$
Normalized scatter	$0.420 \ldots 0.437$	$0.506 \ldots 0.559$
$\sigma(\ln D)/\sigma(\ln T)$	$5.1 \ldots 7.8$	
$\mathrm{CNR}(\ln D)/\mathrm{CNR}(\ln T)$	$0.054 \ldots 0.11$	

Table 5.3: Calculation of dark-field-to-attenuation CNR ratios of *in vivo* porcine lung tissue. $\mu_{\mathrm{eff,60}}^{\mathrm{H2O}}$, $\mu_{\mathrm{eff,125}}^{\mathrm{H2O}}$: effective linear attenuation coefficients of water for the dark-field setup at 60 kVp and a setup without gratings at 125 kVp. $-\partial[\ln D^{(\mathrm{SAS})}]/\partial d^{\mathrm{H2O}}$: slopes from linear regression of $-\ln D$ w.r.t. d^{H2O}, cf. Table 5.2. Normalized scatter values are calculated using Eq. (5.15) and inserting $\mu_{\mathrm{eff,60}}^{\mathrm{H2O}}$ for μ^{H2O}. Via Eq. (5.20), we join them with the ratio of standard deviations for realistic signal levels (cf. Fig. 5.11b) to determine ratios of dark-field and transmission CNR due to small differences in lung thickness.

area of the lung:

$$\begin{aligned} -\ln D^{(\mathrm{SAS})} &= -\ln D^{(\mathrm{SAS,true})} - \ln\left(\frac{D^{(\mathrm{SAS})}}{D^{(\mathrm{SAS,true})}}\right) \\ &\overset{(5.3)}{=} \underbrace{-\ln D^{(\mathrm{SAS,true})}}_{\propto\, d^{\mathrm{lung}},\, d^{\mathrm{H2O}}} + \underbrace{\ln\left(\frac{1 + I_{\mathrm{C}}/\overline{I_{\mathrm{U}}}}{1 + I_{\mathrm{C}}^{(\mathrm{sp})}/\overline{I_{\mathrm{U}}^{(\mathrm{sp})}}}\right)}_{\Delta} \end{aligned} \tag{5.16}$$

For $I_{\mathrm{C}}/\overline{I_{\mathrm{U}}}, I_{\mathrm{C}}^{\mathrm{sec}}/\overline{I_{\mathrm{U}}^{\mathrm{sec}}} \ll 1$, $\Delta \approx I_{\mathrm{C}}/\overline{I_{\mathrm{U}}} - I_{\mathrm{C}}^{\mathrm{sec}}/\overline{I_{\mathrm{U}}^{\mathrm{sec}}}$. Values for Δ achieved from linear regression are given in Table 5.2.

5.2.3c Comparison of noise and CNR for dark-field and attenuation radiography

Direct estimation of noise levels from the *in vivo* scans is difficult due to the high spatial variability of both attenuation and dark-field signals. Therefore, dark-field scans of a simple phantom were performed at identical acquisition parameters.

POM was used to simulate attenuation due to soft tissue and fat, whereas the dark-field signal due to the lung was simulated by chloroprene sheets. The amount of phantom material was selected such that similar levels of dark-field and attenuation signal were achieved. Due to the high uniformity of the materials across the field of view, standard deviations of $\ln D^{(\mathrm{SAS})}$ and $\ln T$ could be estimated in manually-defined regions of interest of the phantom measurements.

The phantom materials were selected due to their similarity in spectral X-ray interaction parameters: The linear attenuation coefficients of POM and soft tissue as a function of X-ray energy are approximately proportional for medically-used X-ray energies (see Fig. 6.1 on page 162), and spectrally-resolved X-ray dark-field measurements have shown a comparable energy-dependence as ventilated porcine *ex situ* lung tissue up to about 70 keV. Beam-hardening correction was also applied for the phantom scans.

In order to illustrate the achieved range of signal values in the *in vivo* scans, a bivariate histogram of dark-field and attenuation values from the lung-covered area in one of the measurements is presented in Fig. 5.11a. Four phantom thickness combinations were selected to characterize this range. Mean and standard deviations from these measurements are shown in red (relative errors in $-\ln T$ are very small).

The measured ratios of dark-field and transmission standard deviations are shown side-by-side with theoretically calculated values in Fig. 5.11b (see section 5.2.2i for the calculation).

The experimentally determined values exceed the theoretical values, which may be due to the presence of unresolvable structures within the chloroprene sheets, generating a noise-like pattern ("structural noise"). Assuming statistical independence of shot noise and structural noise, their variances can be added:

$$\sigma^2 = \sigma_{\mathrm{shot}}^2 + \sigma_{\mathrm{struct}}^2. \tag{5.17}$$

For the ratios of dark-field and transmission variances, it thus follows that

$$\frac{\sigma[\ln D^{(\mathrm{SAS})}]}{\sigma[\ln T]} = \sqrt{\frac{\sigma^2_{\mathrm{shot}}[\ln D^{(\mathrm{SAS})}] + \sigma^2_{\mathrm{struct}}[\ln D^{(\mathrm{SAS})}]}{\sigma^2_{\mathrm{shot}}[\ln T] + \sigma^2_{\mathrm{struct}}[\ln T]}} = \frac{\sigma_{\mathrm{shot}}[\ln D^{(\mathrm{SAS})}]}{\sigma_{\mathrm{shot}}[\ln T]} \sqrt{\frac{1+\tilde{\sigma}^2[\ln D^{(\mathrm{SAS})}]}{1+\tilde{\sigma}^2[\ln T]}}, \tag{5.18}$$

where $\tilde{\sigma} = \sigma_{\mathrm{struct}}/\sigma_{\mathrm{shot}}$.

Identifying $\sigma[\ln D^{(\mathrm{SAS})}]/\sigma[\ln T]$ with the measured and $\sigma_{\mathrm{shot}}[\ln D^{(\mathrm{SAS})}]/\sigma_{\mathrm{shot}}[\ln T]$ with the theoretical noise levels ratios, it can be seen that their quotient is equal to $\sqrt{(1+\tilde{\sigma}^2_{\mathrm{D}})/(1+\tilde{\sigma}^2_{\mathrm{T}})}$. Since that quotient is greater than 1 for all measured points (cf. Fig. 5.11b), it must follow that $\tilde{\sigma}_{\mathrm{D}} > \tilde{\sigma}_{\mathrm{T}}$, i.e. "structural" noise is more important compared to shot noise in the dark-field images than in the conventional images of the phantom. This is not too surprising: The absorbing plastic in the phantom is likely very homogeneous, whereas the ability of the chloroprene sheets to generate dark-field signal is intrinsically dependent on the presence of microscopic fluctuations of electron density. For chloroprene, and probably most dark-field-active materials, these fluctuations also extend to much greater length scales (i.e., near the effective pixel size), and thus intrinsically create some level of structural noise. We therefore believe that pure (spatial) dark-field shot noise will rarely be observed, even in measurements of outwardly uniform dark-field phantom materials.

Finally, the estimates for noise level ratios can be combined with the previously determined normalized scatter estimates to determine a combined quantity: Given two regions a, b in a thorax dark-field radiograph, with different (but otherwise arbitrary) levels of lung material in each region, normalized scatter determines the ratio of dark-field and attenuation signal contrast between these regions:

$$\text{Norm. scatt} = \frac{\langle \ln D^{(\mathrm{SAS})} \rangle_a - \langle \ln D^{(\mathrm{SAS})} \rangle_b}{\langle \ln T \rangle_a - \langle \ln T \rangle_b}. \tag{5.19}$$

Dividing this value by the ratio of dark-field and attenuation noise levels then yields the ratio of dark-field and attenuation contrast-to-noise ratios between the two regions:

$$\begin{aligned} &\frac{\text{Norm. scatt}}{\sigma[\ln D^{(\mathrm{SAS})}]/\sigma[\ln T]} \\ &= \frac{[\langle \ln D^{(\mathrm{SAS})} \rangle_a - \langle \ln D^{(\mathrm{SAS})} \rangle_b]/\sigma[\ln D^{(\mathrm{SAS})}]}{[\langle \ln T \rangle_a - \langle \ln T \rangle_b]/\sigma[\ln T]} \\ &= \frac{\mathrm{CNR}_{a,b}[\ln D^{(\mathrm{SAS})}]}{\mathrm{CNR}_{a,b}[\ln T]}. \end{aligned} \tag{5.20}$$

Here, the simplification is used that the noise levels are approximately the same in both regions, which is appropriate if their signal levels deviate only slightly. Other than that, the result is independent of the exact difference in quantity of lung tissue between the regions. This allows comparing the abilities of both modalities to detect small differences in lung tissue.

With experimental values for $\sigma[\ln D^{(\mathrm{SAS})}]/\sigma[\ln T]$ ranging between 5.1 and 7.8, and normalized scatter values in the vicinity of 0.42 to 0.56, it follows that ratios of dark-field and attenuation CNR for *in vivo* lung tissue are surprisingly low with approximately 5.4 to 11%, depending of ventilation level and the position in the thorax (cf. Table 5.3).

Influence of tissue overlap An effect that was ignored in the preceding calculation is that the lung is superimposed by multiple organs in thorax radiography.

This occlusion leads to significant additional contrast not of diagnostic relevance in the conventional image. Very small tissue structures may also appear as "anatomical noise" in the conventional image. A distinction between diagnostically relevant and irrelevant features is then only possible using morphological information, e.g. by a trained radiologist. These effects are however much less relevant for the dark-field modality, as the lung is by far the most prominent source of dark-field signal in the thorax, and other structures are thus rendered nearly invisible. Unfortunately, a quantitative analysis of this effect is difficult due to a high variability of anatomical features between animals, and a strong dependence on the lung region under investigation.

However, we calculated the fraction f of total attenuation signal due to the lung according to Eq. (5.13), which provides an indication for the relative impact of

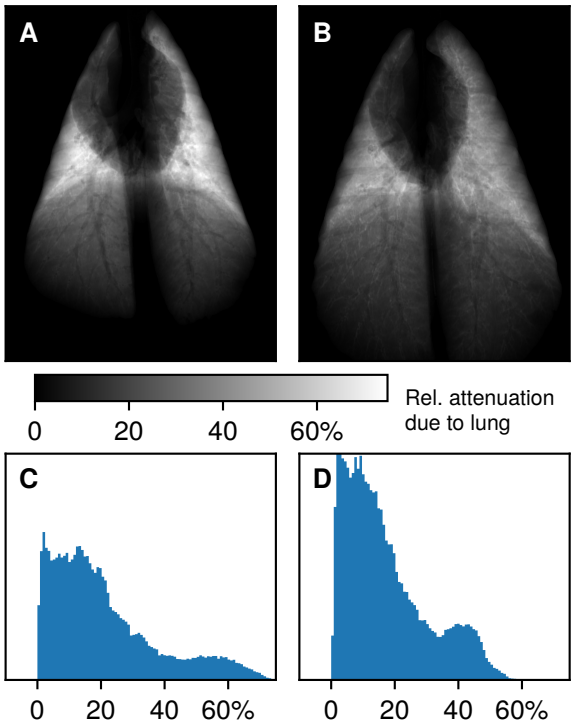

Figure 5.14: Fraction f of the attenuation signal due to the lung in the porcine thorax at 60 kVp (animal 1), shown as spatial maps and histograms for two different values of airway pressure. (a, c): Exhalation (2 mbar). (b, d): Inhalation (20 mbar). In most image areas, the attenuation signal is dominated by organs other than the lung. Calculation of f according to Eq. (5.13).

the lung in conventional radiography of the porcine thorax. For a given value of f, superimposed contrasts from other tissues may exceed the contrast of interest by a factor of $(1-f)/f$. Maps and histograms of f are shown in Fig. 5.14: For the majority of the lung-covered area, less than $f = 25\%$ of the attenuation signal are due to the lung itself.

Note that the pneumothoraxes analyzed in [Hell+17], where CNR values between pneumothorax and adjacent lung were found to be significantly higher in the dark-field modality, were located in distal areas where f is especially low.

Although there are multiple differences for clinical thorax imaging (higher acceleration voltages and higher fractions of detected Compton-scattered intensities, as well as anatomical differences between porcine and human thoraxes), we think that similarly low values for f would be achieved.

5.2.4 Discussion

5.2.4a Previous research

Knowing the dependence of dark-field signal on breathing cycle phase is important for translating the technique to clinical use. This dependence has not yet been systematically examined, however. For small-animal dark-field measurements, breathing was not paused during acquisition, and signal strength was thus effectively averaged over all phases of the breathing cycle. Fringe-scanning dark-field radiographs of pigs and humans, on the other hand, have been acquired with paused ventilation, since thorax motion during fringe-scanning acquisition leads to significant imaging artifacts. This resembles the clinical practice of thorax radiography, where patients are asked to hold their breath during image acquisition to minimize blurring.

Furthermore, observed variations in signal strength can be caused by both variations in projected lung thickness, as well as lung density. Radiographic information alone is unable to distinguish between these effects.

The effect of microstructural size variations in lung- or foam-like materials on dark-field signal has been examined in wave-optical simulations [Male+12; Vign+18], but an experimental verification with a human or large-animal thorax has, to our knowledge, not yet been presented.

In a recent study [Hell+17], lateral pneumothorax in pigs was found to appear in dark-field radiography with a higher CNR than in conventional X-ray. In conventional radiography, the contrast due to features of interest competes with contrasts from other superimposed structures, whereas this effect is largely absent in dark-field radiography. The relative importance of this advantage, compared to "pure" CNR performance was however not examined in that study.

5.2.4b Methodology

In this work, we acquired *in vivo* thorax dark-field radiographs of two pigs. Three different stages in the breathing cycle were simulated by (paused) mechanical ventilation. Position and ventilation pressures were replicated for CT thorax imaging of the same animals. Segmentation, masking, and forward-projection of CT data yielded maps of lung thickness and water-equivalent height of the lung, in registration with the dark-field radiographs.

5.2.4c Results from linear regression

Pixel-for-pixel correlation of logarithmic dark-field signal with both types of thickness maps yielded approximately linear relationships, motivating regression of linear functions, albeit with a non-zero axis intercept. We show that the nonzero intercepts from regression analysis can be explained by a deviation in the fraction of Compton-scattered radiation observed in the sample scans and the calibration scans for correcting visibility-hardening.

Dark-field signal increase per lung thickness retrieved from regression analysis is equivalent to the dark-field extinction coefficient as defined in [Lync+11], averaged over the entire lung. Regression results show that this coefficient is 42% (animal 1) / 33% (animal 2) lower at the highest ventilation pressure (20 mbar) than at the lowest one (2 mbar). Such a behavior is also expected for the logarithmic transmittance of the lung, as the (constant) amount of lung material is distributed over a greater projected area during inspiration. As the linear attenuation coefficient is proportional to mass density, it means that its average value over the entire lung must be inversely proportional to lung volume, which we could verify from CT measurements. The logarithmic dark-field signal however was found to decrease slightly more slowly with increasing lung volume.

We believe that this higher-than-expected dark-field activity may be due to additional alveolar recruitment, or changes of microstructural length scales at higher pressures: As the dark-field signal depends on the sample's autocorrelation function of electron density, thinning alveolar walls or increases in alveolar diameter may affect the dark-field extinction coefficient. Both alveolar recruitment as well as uniform expansion (which is most clearly associated with microstructural length scale changes) are mechanisms involved in alveolar dynamics, and have e.g. been observed with optical coherence tomography [Roan+11; McLa+14].

The second result from linear regression, dark-field signal increase per attenuation-equivalent water height d^{H2O}, is proportional to the ratio of mean dark-field extinction coefficient and linear attenuation coefficient, i.e. an average "normalized scatter" coefficient of the lung. We find a slight increase of this ratio for rising ventilation pressure, which is consistent with the preceding results (slower decrease of dark-field extinction coefficient than linear attenuation coefficient for increasing pressure / lung volume).

In a recent publication [Vign+18], dark-field extinction coefficients of human and murine lung tissue were calculated via wave-optical simulations of a simple lung microstructure model. Using our setup parameters, we converted their results to dark-field extinction coefficients, and find values of 1.94, 1.34, and 1.04 m^{-1} (for 200, 300, and 400 µm alveolar diameter), which are smaller than the values presented here by factors between 1.2 and 4.4.

However, these simulations were performed for a 120 kV tube spectrum. Although a precise conversion to a different flux and visibility spectra would require a new simulation, we can make a simple approximation: Mean energy for the simulations ($E_{\mathrm{mean}} = 64.5\,\mathrm{keV}$) exceed the one used here (42.1 keV) by a factor of 1.53. Given the proportionality of $-\ln D$ with E^{-2}, and ignoring any deviations in both visibility spectrum and autocorrelation length, we expect our signal values to be greater by a factor of 2.35, which is in good agreement with the factors mentioned above.

5.2.4d Results from CNR analysis

The internal structure of the healthy lung causes it to generate a strong dark-field signal and a weak attenuation signal, considering the organ's overall size. It is thus plausible to suspect that the dark-field contrast due to a given amount of lung is so much greater than the attenuation contrast that it is able to compensate the intrinsically greater noise levels in the dark-field modality, and thereby explain the findings from [Hell+17] of greater dark-field CNR for pneumothorax than attenuation CNR.

The ratio of dark-field and attenuation CNR values can be calculated from the "normalized scatter" coefficient and the ratio of noise levels in both modalities, as shown in Eq. (5.20). Noise levels were however not directly measured by analysis of the pig thorax scans. To exclude superposition effects, we constructed a phantom from material slabs of uniform thickness, which generated dark-field and attenuation signal levels comparable to a previously imaged porcine thorax. Noise levels were then measured by ROI analysis in both modalities. The ratio of dark-field and attenuation standard deviations was compared to theoretical calculations (propagation of shot noise to processed modalities).

The measured values for these ratios were found to exceed the theoretical results. We suspect that this is

partly due to the existence of "structural noise" in the dark-field images, even for the uniform chloroprene sheets used in the phantom. As dark-field signal is intrinsically caused by a spatial variation of electron density, we think that structural noise is an inevitable side-effect if this variation extends to the length scale of effective pixel size (as may also be the case for lung tissue).

Contrary to expectations, the ratios of dark-field CNR and attenuation CNR for a given height difference of lung tissue were found to be far below 1 (5.4 to 11%), which stands in contrast to the promising results from [Hell+17]. In chest X-ray however, the lung is superimposed by attenuation contrasts from other, more strongly attenuating materials, which is not simulated by the presented phantom. As the impact of this effect on CNR depends on anatomical structure and is thus highly variable, a precise analysis is difficult. We estimate the magnitude of this effect by calculating the fraction of attenuation signal due to the lung in one of the pig thorax images. The lung is found to contribute less than 25% to total attenuation in the majority of the lung area (whereas it is contributes nearly the entire dark-field signal). It is thus clear that the potential impact of tissue superposition is very high.

5.2.5 Conclusion and outlook

In this work, we have combined imaging data from dark-field chest radiography and thorax CT of two living pigs at three different ventilation pressures. Furthermore, we acquired dark-field radiographs of a simple phantom and performed theoretical calculations to evaluate noise levels in the dark-field and attenuation modalities. The main findings are as follows:

- Correlation of dark-field signal with the lung thickness retrieved from CT showed an approximately **linear dependence**. It allowed calculation of the **lungs' mean dark-field extinction coefficient** and revealed its **strong dependence on lung ventilation** (variation by up to 42%). The numerical values are in good agreement with wave-optical simulations of a simple lung tissue model [Vign+18].
- Correlation of dark-field signal with attenuation-equivalent water height retrieved from CT was also approximately **linear**. Combined with simulated values for the effective linear attenuation coefficient of water, this allowed calculation of the **mean "normalized scatter" value of lung tissue**, which we found to be **nearly independent of ventilation pressure**.
- Measurement of phantom data and theoretical calculations revealed that dark-field noise levels are **five to eight times higher** than those in conventional radiography.
- By combining "normalized scatter" values with the noise levels ratios, we found that **dark-field CNR for a given height difference of lung tissue is only 5 to 10% of the attenuation CNR**. Given contradictory findings in a previous study [Hell+17], we conclude that the **influence of anatomical noise is much higher in conventional radiography** and may significantly improve the relative CNR performance of dark-field radiography.

These findings have a high relevance for the clinical interpretation of dark-field thorax radiographs: The phase in the breathing cycle when the image is acquired may affect its diagnostic benefit due to the variation of signal strength and projected lung size. However, the presented results are also subject to some limitations:

- **Microstructural parameters may differ between human and porcine lungs.** However, the mechanical processes of breathing are very similar. Accordingly, we expect quantitative values to deviate for human lungs measured *in vivo*, but we predict relative trends over the breathing cycle to be comparable. Furthermore, we think the dark-field extinction coefficient's approximate proportionality with inverse lung volume will also apply for human lungs, since the microstructural processes during breathing are likely very similar in human and porcine lungs.
- **Transferability of these results to other setups and imaging parameters may be limited.**
  - The determination of electron density autocorrelation functions of lung tissue at various ventilation pressures would allow prediction of signal levels for arbitrary X-ray energies and phase-sensitivities [Yash+10; Lync+11]. However, this is not currently feasible as there is no universally accepted model of alveolar micromechanics in the living lung [Roan+11].

  - For the present setup and imaging parameters, sampled autocorrelation lengths (named pd in [Yash+10], d in [Lync+11]) are in the vicinity of 0.6 µm. It is important to consider that the range of electron density autocorrelation lengths suitable for human thorax imaging is **limited by SNR considerations**: Much higher values than e.g. 1 µm would achieve very low visibility (and thus, high noise levels) behind a human lung, whereas much lower values yield only a very weak dark-field signal.
  - Since we have not observed abrupt changes in dark-field signal while varying ventilation pressure (and thus, varying dimensions in alveolar microstructure), we think that the autocorrelation function of electron density is smooth in the vicinity of the sampled correlation length values. Furthermore, a large amount of random variation is probably smoothed out due to averaging along the length of the X-ray path through the lung. Thus, we expect setups with similar ranges of sampled autocorrelation lengths to achieve results comparable to the ones presented here.

- In the presented measurements, lung volume at 20 mbar was 60 to 80% higher than at 2 mbar. In a clinical setting with a freely breathing patient however, **much greater relative changes in volume could be achieved**. It is yet to be shown whether the examined correlations still apply for these more extreme levels of inhalation. However, this information could probably only be retrieved from a freely-breathing patient, e.g., in a clinical study of dark-field radiography.

5.3 Reader study in postmortem X-ray dark-field human chest radiographs

Human cadavers are valuable imaging subjects for the evaluation of dark-field chest radiography, since they allow evaluation of the method for realistic human anatomy. At the pre-clinical stage, this would otherwise only be possible using anthropomorphic X-ray phantoms. However, although such phantoms are designed to provide realistic attenuation properties, micro-morphology at a sub-resolution level—and thus the X-ray dark-field signal—is not recreated correctly. In [Will+18], the first X-ray dark-field radiograph of a human cadaver was presented and compared to a CT scan of the thorax. A decrease of dark-field signal could be identified in a region coinciding with the location of a pulmonary edema found in CT.

So far, imaging features of X-ray dark-field radiography have not been described from the perspective of clinical radiology. To allow X-ray dark-field imaging to become a clinical imaging modality, imaging findings have to be reported in a consistent manner and correlated with established imaging modalities to facilitate correct interpretation. Therefore, the purpose of this study on *post mortem* human chest X-ray dark-field radiographs was to address inter- and intra-observer agreement of dark-field signal strength and image quality, and to correlate findings with conventional X-ray and CT.

Chest X-ray dark-field radiography with a tube voltage of 70 kVp was thus performed postmortem on nine humans (three females, six males, age range 52–88 years). Visual quantification of signal strength and image quality of dark-field and transmission data was performed by three radiologists, using grading on ordinal scales. Results were compared to findings from conventional X-ray and CT.

Ordinal data is presented in bar graphs, showing medians and inter-quartile ranges. Intra- and interobserver agreement were determined using weighted Cohen's κ. Differences of signal strength grading between lung regions, and correlations between dark-field and transmission data were also statistically evaluated.

The work presented in this section has been previously published in the article "Imaging features in postmortem x-ray dark-field chest radiographs and correlation with conventional x-ray and CT" by A. Fingerle, F. De Marco et al. in European Radiology Experimental, 2019 [Fing+19]. My primary contribution to the original work has been the generation of dark-field and attenuation images, as well as the preparation of technical sections of the manuscript. Although I participated in the measurements, their realization was only possible thanks to the extensive support by Mr. Fabian Kriner, Dr. Christian Braun and Dr. Florian Fischer from the Institute of Forensic Medicine at the University of Munich. The reader study was carried out by Dres. Felix Meurer, Andreas Sauter and Dominik Deniffel from the Department of Diagnostic and Interventional Radiology at the hospital "Klinikum rechts der Isar", Munich. The majority of work on the manuscript fell to Dr. Alexander Fingerle from the same department. Statistical analyses were performed by Dr. Fingerle and Dr. Bernhard Haller from the Institute of Medical Informatics, Technical University of Munich.

Compared to the original work, several Figures have been added or modified, and a different set post-processing filters was used for the dark-field projections. This means that these projections are not identical to how they appeared in the reader study, but feature fewer artifacts and allow for an improved distinction of small details.

5.3.1 Methods

5.3.1a Human bodies

This prospective study was approved by the Institutional Review Board and was conducted between November 2015 and July 2018. Human bodies were transferred to the Institute of Forensic Medicine at coroner's inquest. Due to the mode of inclusion, no preselection of the human bodies according to certain criteria, e.g., the presence of specific lung diseases, was possible. Externally visible conditions causing a significant impairment of the normal thoracic anatomy and signs of advanced decomposition were exclusion criteria. Imaging was performed before autopsy no longer than 36 h after death with bodies cooled to slow decomposition. The imaging was not part of the forensic analysis. Altogether, nine bodies (three females, age range 52–88 years; six males, age range 60–83 years) were imaged. Airway pressure was kept constant (20 mbar to 25 mbar) during X-ray dark-field imaging by endotracheal intubation[14] and mechanical ventilation.

[14] Insertion of a catheter into the trachea, here for the purpose of mechanical ventilation

5.3.1b X-ray dark-field imaging

Measurements were performed on the setup described in chapter 3. Imaging was performed in supine position with anterior-posterior beam setup. Acquisition time was 40 s. All measurements were performed at 70 kVp and with tube currents ranging from 360 to 700 mA.

5.3.1c CT imaging

Human bodies were imaged in supine position on a 256-slice CT unit (Brilliance iCT, Philips, Amsterdam, Netherlands). High-resolution chest CT was performed in craniocaudal direction with 128×0.625 mm collimation and 0.383 pitch. Tube voltage was 120 kVp. Mean tube current was 537 mA. CT images were reconstructed with "iDose4", a hybrid iterative reconstruction technique (Philips, Amsterdam, Netherlands), at level 2 in axial, coronal, and sagittal view with a slice thickness of 3 mm, 1024×1024 matrix, and 350 mm field of view.

5.3.1d Data acquisition and processing of X-ray dark-field imaging

For their use in the reader study, the dark-field radiographs were low-pass-filtered (2D Gaussian filter kernel, $\sigma = 3.2$ pixels). This reduces noise levels by a factor of ≈ 11.3 for white noise, leading to a visual impression more similar to conventional radiography. Although low-pass filtering obscures small features, these are nearly undetectable in the unfiltered images due to the high noise levels. The used kernel size was found to be an acceptable trade-off between image impression and resolution.

In the Figures presented here however (Figs. 5.19, 5.20, 5.21, and 5.22), a different set of post-processing steps was used: First, a fringe-correction algorithm [DeMa+18] was selectively applied to regions of the dark-field projections strongly affected by fringe artifacts. Due to the occasionally poor convergence of the involved minimization procedure, the required correction factors were determined manually by visual inspection of the corrected projections. Subsequently, a 3×3 median filter, a Fourier-based line suppression filter, and a 3×3 binomial filter were applied to the dark-field radiographs (nearly identical to the approach shown in section 4.3.3 on page 108). No filtering was applied to conventional radiographs.

5.3.1e Reader study

Visual image analysis was independently performed by three residents with three (F. Meurer), five (A. Sauter), and five (D. Deniffel) years of experience in chest imaging on a clinical Picture Archiving and Communication System (PACS) workstation. For training purposes, the dark-field radiograph of human body no. 4 was presented before the reading session to demonstrate low and high dark-field signal intensity. In the first reading session, window settings were fixed to allow optimal comparison of low and high dark-field signal intensities in dark-field radiographs and opacification in conventional chest X-rays to avoid influence of individual windowing.

A linear mapping between gray values and logarithmic visibility reduction ratios, $-\ln(V/V_0)$, was used. Window level and width were set to 8500 and 5000, respectively. Converting these numbers back to physical quantities, this means that a logarithmic visibility reduction ratio of -0.268 corresponds to "black," and a value of 0.343 corresponds to "white[15]." The nine X-ray dark-field radiographs had to be graded separately one after the other without the possibility to compare or change gradings. Next, the conventional X-rays were presented.

On each image, the left and right lung were divided into three regions of equal height: upper, middle, and lower zones, using the apex and the costodiaphragmatic recess as anatomical landmarks, as illustrated in Fig. 5.15. Dark-field signal intensity and degree of transmission (or opacification) of the upper, middle, and lower zones of the left and right lung were graded on a six-point (0–5) ordinal scale as presented in Table 5.4a. For the transmission grading, "0" represents no transmission or hyperattenuation like in the clinical case of a pleural effusion where no ventilated lung parenchyma is visible. "5" represents a normal, healthy lung with high transmission or hypoattenuation.

The reading session was repeated after four weeks. In a separate reading session, the readers independently graded image quality for right and left lung on a 6-point ordinal scale as given in Table 5.4b.

[15] Note that in the Figures presented here, gray level limits are instead set to -0.15 and 0.45.

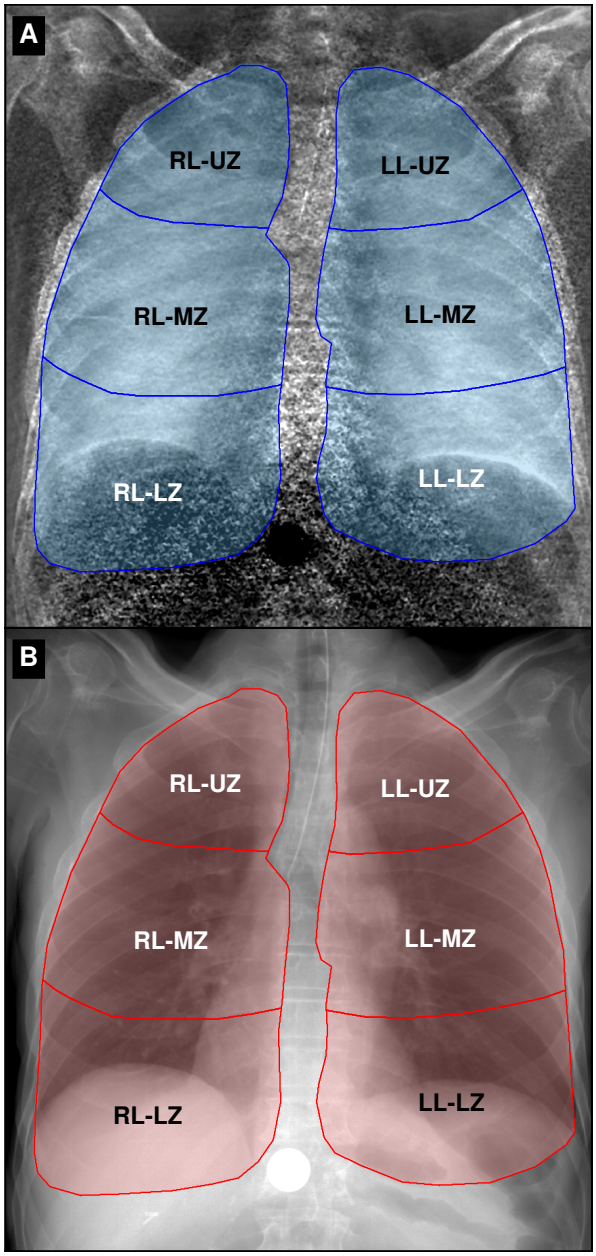

Figure 5.15: Visual evaluation scheme and grading scale for dark-field chest radiographs and conventional X-rays. In both dark-field (a) and conventional (b) chest X-ray, lungs are divided into six regions: upper, middle and lower zone (UZ, MZ, LZ) of the right and left lung (RL, LL), respectively. In each region, dark-field and transmission signals are visually graded using a six-point ordinal scale (Table 5.4a).

	Dark-field	Transmission
a) Signal strength grading (per lung region)		
0	None (dark)	Effusion
1	Low	Consolidation
2	Low to moderate	Between 1 and 3
3	Moderate	Ground glass
4	Moderate to high	Between 3 and 5
5	High (bright)	Normal lung

b) Image quality grading (per lung)	
1	Not diagnostic
2	Sufficient
3	Satisfactory
4	Good
5	Very good
6	Excellent

Table 5.4: Ordinal scales used for grading of signal strength (a) and image quality (b).

As standardized image quality criteria for dark-field radiographs do not exist, the readers were instructed to evaluate the following aspects:

- Symmetrical reproduction of the thorax
- Reproduction of the whole lung
- Presence of artifacts interfering with the grading of pulmonary dark-field signal intensity (e.g., vertical streaking artifacts, dark-field signal from bony structures)

For transmission images, the "European guidelines on quality criteria for diagnostic radiographic images" [Carm+96] were applied wherever possible, considering imaging of a human body in supine position. In this setting, readers were free to change window/level values to optimize individual image impression.

5.3.1f Correlation of dark-field and transmission radiography with CT findings

As there exists no data on X-ray dark-field imaging features of human lung pathologies, we performed a CT scan of each human body to correlate findings in chest CT images with signal changes in dark-field and transmission radiographs. CT images were reviewed by an attending radiologist with ten years of experience in chest radiology (A. A. Fingerle) using axial, sagittal, and coronal reconstructions. Pulmonary findings and extrapulmonary findings with a potential effect on dark-field signal intensity were recorded. Apart from septal thickening, the extent of pulmonary findings was visually quantified for every lobe in 10% intervals. For pleural effusions[16], the maximum width in anterior-posterior direction[17] was measured in centimeters. Other findings were qualitatively recorded. CT findings were correlated with the visual assessment of dark-field signal strength in a descriptive model.

5.3.1g Statistical analysis

Statistical analysis was performed using *GraphPad Prism 7* for Mac OS X (Version 7.0d, GraphPad Software Inc., USA) and *R* (version 3.4.4, R Foundation for Statistical Computing, Vienna, Austria). For ordinal data, bar plots with quartiles[18] are shown.

Intraobserver and interobserver agreement of dark-field signal and transmission grading were evaluated using *weighted Cohen's kappa* (κ) with squared weights. Values of Cohen's κ coefficient were classified as follows: values below 0 were regarded as poor, 0–0.20 as slight, 0.21–0.40 as fair, 0.41–0.60 as moderate, 0.61–0.80 as substantial, and 0.81–1.00 as (almost) perfect agreement, according to Landis et al. [Land+77].

Differences in distributions of dark-field signal and transmission grading for the upper, middle, and lower zones were tested separately for the right and left lung and each reader using the *Friedman test*. If Friedman test indicated a significant ($p < 0.05$) association between region and dark-field signal, *Wilcoxon matched-pairs signed-rank test* was performed for pairwise comparisons of regions of each lung for each reader.

The correlation of dark-field signal with transmission grading was tested with *Spearman's rank correlation coefficient* for each lung region and each reader.

Differences in the grading of image quality between the left and right lung for dark-field and transmission radiographs, respectively, were tested with Wilcoxon matched-pairs signed-rank test.

[16] Accumulations of fluid in the pleural cavity

[17] "Front-to-back", or "belly-to-back" direction

[18] In the original publication: dot plots with medians and 95% confidence interval (based on the Hodges-Lehmann method)

Compared regions		Reader no. 1	2	3
RL-UZ	RL-MZ	0.004	0.004	0.016
RL-UZ	RL-LZ	0.004	0.004	0.008
RL-MZ	RL-LZ	ns	ns	ns
LL-UZ	LL-MZ	0.004	0.004	0.004
LL-UZ	LL-LZ	0.016	0.016	ns
LL-MZ	LL-LZ	ns	ns	ns

Table 5.5: p values for the presence of significant differences of dark-field signal gradings between different lung regions, evaluated with the Friedman test. Non-significant differences ($p > 0.05$) are marked with "ns". All equivalent tests for the transmission images yielded no significant differences for all readers. The distribution of dark-field signal gradings per lung region are illustrated for reader 1 in Fig. 5.17.

5.3.2 Results

5.3.2a Visual grading of dark-field and transmission signals

Statistical analysis of the dark-field and transmission signal strength gradings (Fig. 5.16) indicated a significant (right lung, readers 1–3: $p < 0.0001$; left lung, readers 1–3: $p = 0.001$) association between the lung zones and dark-field signal, which was further investigated by pairwise comparisons of regions of each lung for each reader (Fig. 5.17, Table 5.5). The median dark-field signal grading showed significant differences between the lung upper zones and lung middle zones. The median dark-field signal was also significantly different between the lung upper zones and lung lower zones, except for reader 3 in the left lung.

For transmission radiographs, statistical analysis did not demonstrate significant associations with lung zones (right lung, reader 1: $p = 0.535$, reader 2: $p = 0.482$, reader 3: $p = 0.312$. Left lung, reader 1: $p = 0.568$, reader 2: $p > 0.9999$, reader 3: $p = 0.315$). These results indicate a correlation between the quantity of

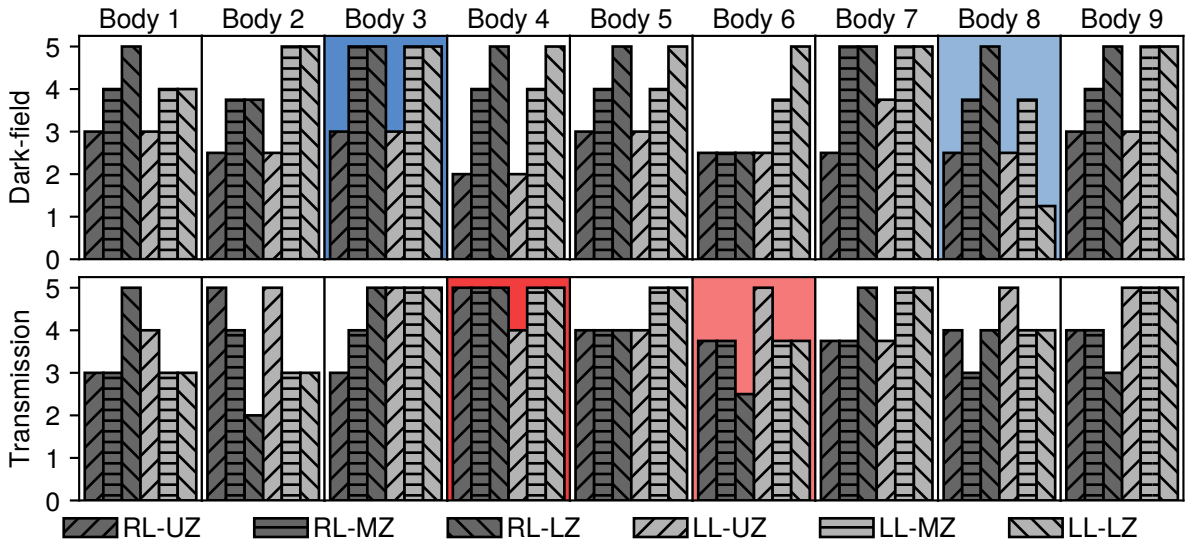

Figure 5.16: Dark-field and transmission signal strength grading of all nine human bodies. For each body and lung region, median of gradings (across readers) is shown. Color indicates cases with highest (blue, red) and lowest (light blue, pink) overall median dark-field or transmission. These four cases are shown as individual Figures (Figs. 5.19, 5.20, 5.21, and 5.22).

Lung region	Reader 1	Reader 2	Reader 3
RL-UZ	>0.9999	0.980	0.827
RL-MZ	0.437	0.929	0.603
RL-LZ	0.329	**0.0079**	**0.0278**
LL-UZ	>0.9999	0.394	0.921
LL-MZ	0.385	0.143	0.185
LL-LZ	0.100	0.077	0.333

Table 5.6: *p* values for the presence of correlations between dark-field and transmission grading in each lung region. Correlations were tested using Spearman's rank correlation coefficient. Statistically significant values ($p < 0.05$) are highlighted.

pulmonary tissue in the beam path (which is lower in lung apex than in middle and lower zones) and dark-field signal magnitude, whereas transmission chest X-rays are indifferent to this aspect. Dark-field signal and transmission grading in each region of the right and left lung for each reader showed significant correlations only in the right lung lower zone for reader 2 ($p = 0.0079$) and reader 3 ($p = 0.0278$). All other tests did not show significant correlations (cf. Table 5.6).

5.3.2b Intra- and interobserver agreement

The intraobserver agreement was substantial to almost perfect for visual grading of dark-field ($\kappa = 0.793$–0.971) and transmission signals ($\kappa = 0.790$–0.918). Comparable results were obtained for interobserver agreement of visual grading of dark-field signal (almost perfect, $\kappa = 0.828$–0.893) and transmission (substantial to almost perfect, $\kappa = 0.700$–0.772) between all three readers. All Cohen's κ values for intra- and interobserver agreement are summarized in Table 5.7.

5.3.2c Image quality

Median image quality grading (Fig. 5.18) assessed by visual evaluation of all nine radiographs and all readers was good for left and right lung of dark-field images (4, interquartile range 1) and very good for left and right lung of transmission images (5, interquartile range 1). Median image quality grading did not show significant differences between the left and right lung for either dark-field ($p = 0.511$) or transmission ($p = 0.688$) radiographs. Median image quality grading was significantly different between dark-field and transmission radiographs for the left and right lung ($p < 0.0001$ for each).

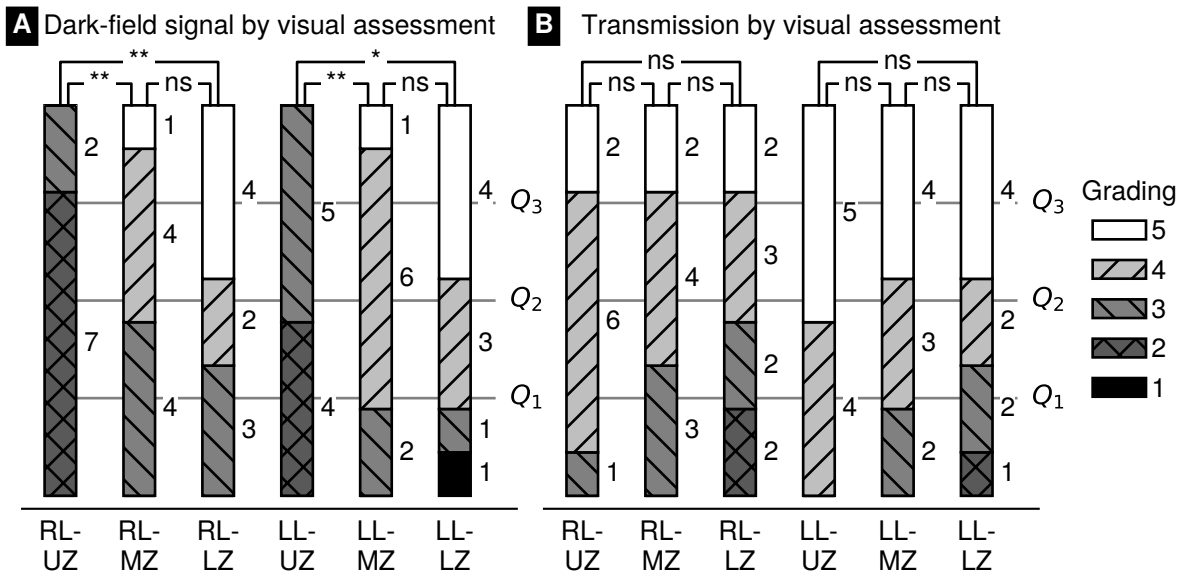

Figure 5.17: Bar graphs of median visual grading of signal strength for dark-field (a) / transmission (b) on a six-point ordinal scale (cf. Table 5.4a) of all nine dark-field and transmission chest X-rays *for reader 1*. Dark-field signal increases from apex to base of the lung (i.e., from UZ to LZ), whereas transmission shows no differences between the zones. Asterisks indicate statistical significance of median dark-field / transmission grading differences between the different zones in the left or right lobe. **: $p \leq 0.01$, *: $p \leq 0.05$, ns: $p > 0.05$ (i.e., not significant). Associated p values in the dark-field modality for all readers are given in Table 5.5. Quartiles of grade distributions are highlighted by the intersections of the bars with the lines marked Q_1, Q_2 (the median), and Q_3.

Intraobserver agreement (κ values)			
	Reader 1	Reader 2	Reader 3
Dark-field	0.959	0.971	0.793
Transmission	0.907	0.918	0.790

Interobserver agreement (κ, dark-field)			
	Reader 1	Reader 2	Reader 3
Reader 1	—	0.848	0.828
Reader 2	0.848	—	0.893
Reader 3	0.828	0.893	—

Interobserver agreement (κ, transmission)			
	Reader 1	Reader 2	Reader 3
Reader 1	—	0.772	0.744
Reader 2	0.772	—	0.700
Reader 3	0.744	0.700	—

Table 5.7: Intra- and interobserver agreement of dark-field and transmission signal grading. Visual grading of dark-field signal and transmission shows substantial (weighted Cohen's $\kappa = 0.61$–0.80) to almost perfect ($\kappa = 0.81$–1.00) intraobserver and interobserver agreement, according to Landis and Koch [Land+77]. Time difference between reading sessions for assessment of intraobserver agreement was 4 weeks.

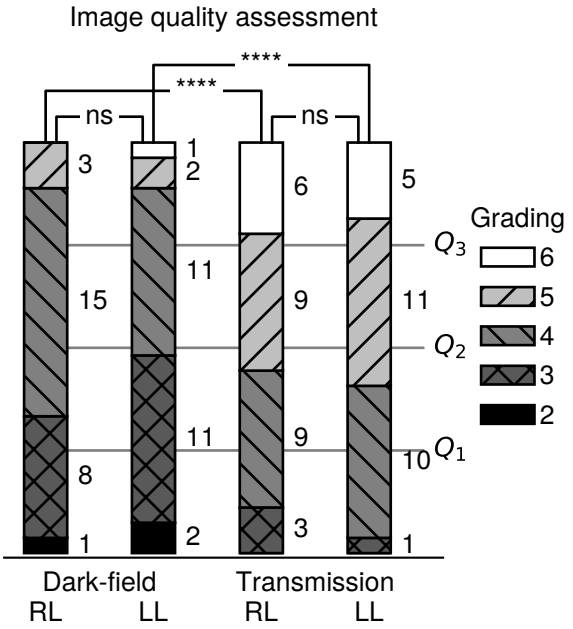

Figure 5.18: Image quality assessment of dark-field and transmission images. Frequencies of image quality gradings for dark-field and transmission radiographs of the left (LL) and right lung (RL) are shown. Image quality is graded on a 6-point ordinal scale (cf. Table 5.4b). Frequencies are accumulated over all images and readers. Quartiles of grade distributions are highlighted by the intersections of the bars with the lines marked Q_1, Q_2 (the median), and Q_3. Asterisks indicate statistical significance of differences: ****: $p \leq 0.0001$, ns: $p > 0.05$ (i.e., not significant).

5.3.2d Correlation of dark-field and transmission radiography with CT findings

In the majority of CT images, ground-glass opacities were present in the lungs to a variable extent (Table 5.8, Figs. 5.19, 5.20, 5.21, and 5.22). Further pulmonary findings included emphysematous changes[19], consolidations[20], tree-in-bud sign[21], and (interlobular) septal thickening [22]. Extrapulmonary findings were pleural effusions[23] and an enlargement of the heart with haemopericardium[24]. In human body no. 4 (Fig. 5.19), we observed only minor (20% of total lobe) emphysematous changes in the parenchyma of all lobes. In the dark-field radiograph, a similar signal increase from the apex to the base of the lung is present in both the left and right lung, whereas transmission radiography shows no differences. The lowest dark-field signal was reported in the lower zone of the left lung in human body no. 8 (Fig. 5.20). The corresponding CT revealed moderate ground-glass opacities[25] affecting 50% of the lower lobe and minor (10%) consolidations. Additionally, an enlarged heart with haemopericardium was extending into the left hemithorax. The highest dark-field signal over all zones of the lungs was present in human body no. 3 (Fig. 5.21), although a

[19] Destruction of lung tissue due to inflammatory processes, caused e.g. by smoking.

[20] Filling of lung tissue with material, e.g. liquid

[21] Radiological finding in lung CT scan indicating airway obstruction

[22] Thickening of connective tissue between *secondary lobules*, small functional sub-units of the lung

[23] Accumulation of fluid in the pleural cavity

[24] Accumulation of blood in the *pericardium*, a volume enclosing the heart

[25] "Radiological term indicating an area of hazy increased lung opacity" [Infa+09]

difference between the apex and the middle and lower zones was still visible. In the corresponding CT images, minor to moderate (20 % to 40 %) ground-glass opacities were observed in all but the middle lobe. In human body no. 6 (Fig. 5.22), the transmission was lowest in the lower zone of the right lung corresponding to widespread (60%) consolidations in the lower lobe and moderate to extensive (50 % to 90 %) ground-glass opacities in the middle or upper lobe, respectively. In addition, extensive emphysematous changes in all lobes were present. Dark-field signal was also low in all zones of the right lung.

5.3.3 Discussion

X-ray dark-field radiography is a novel imaging modality with high potential for lung imaging that has been translated from an experimental method to clinical applicability in recent years. However, so far, its feasibility for imaging of the human lungs has only been demonstrated in a single *post mortem* chest radiograph. Therefore, the purpose of our study was to assess the imaging features of nine *post mortem* dark-field chest radiographs from a clinical point of view as a final step before evaluation of dark-field radiography in clinical studies.

In the visual assessment of *post mortem* dark-field chest radiographs, we observed a gradient of dark-field signal strength from the apex to the base of the lungs. This can be attributed to an increasing amount of lung parenchyma in the X-ray beam path, as small-angle X-ray scattering increases with the amount of scattering material. However, in conventional chest X-rays, the transmission did not correlate with the dark-field signal, demonstrating that this presents a unique imaging feature of dark-field radiography. This finding is in accordance with results of animal studies [Hell$^+$15; Yaro$^+$15; Grom$^+$17]. In a clinical context, this would have to be considered when investigating pathologies that decrease dark-field signal. In centrilobular emphysema, a form of chronic obstructive pulmonary disease that primarily affects the upper lobes, knowledge of this finding will be essential for correct image interpretation.

X-ray dark-field radiography is an imaging modality which we believe will primarily be evaluated by visual assessment. Hence, for its clinical application, it is of major importance that imaging findings are consistently reported. We could demonstrate that visual grading of X-ray dark-field signal in the lungs shows substantial to almost perfect intra- and interobserver agreement, comparable to visual assessment of transmission in conventional chest X-rays. These results confirm outcomes of reader studies performed on X-ray dark-field radiographs of different lung pathologies in small animals [Hell$^+$15; Hell$^+$17] and underline clinical applicability.

Diagnostic image quality is mandatory for reliable reporting of imaging findings and an insufficient image quality may reduce diagnostic confidence of the reporting radiologist [Zhu$^+$17]. The image quality of X-ray dark-field and simultaneously acquired conventional radiographs were graded as good and very good, respectively. Therefore, we deduce that X-ray dark-field imaging provides sufficient image quality for its application and evaluation in clinical trials.

Numerous preclinical animal studies have demonstrated the effect of specific lung pathologies on the dark-field signal. For example, in an animal model of idiopathic pulmonary fibrosis [Yaro$^+$15; Hell$^+$17], X-ray dark-field imaging allowed visualization of early fibrotic changes in the lungs with dark-field images showing circumscribed areas of markedly reduced dark-field signal in lung parenchyma affected by the pathological process next to normal areas with high dark-field signal. In our study, the correlation of pathological findings in conventional X-ray and CT images of individual human bodies with dark-field signal intensity showed comparable results in the human lungs. Areas of pulmonary consolidation may contribute to a major reduction of dark-field signal, whereas ground-glass opacities, representing interstitial and alveolar infiltrates, showed an inconsistent effect on the reduction of dark-field signal.

In one human body, an enlargement of the heart correlated with a strong decrease of the dark-field signal in the left lung lower zone, probably by reducing the amount of lung parenchyma in the X-ray beam path. This is a relevant finding as it shows that extrapulmonary pathologies can also influence the dark-field signal intensity and would have to be considered when interpreting clinical dark-field radiographs.

There are several limitations to our study. The application of X-ray dark-field chest radiography to human bodies limited our control over parameters that potentially alter the dark-field signal. Emphysematous changes, interstitial and alveolar infiltrates, pulmonary consolidation, pleural effusion, and an enlargement of

Right lung (RL)								Left lung (LL)							
		Radiography			CT					Radiography			CT		
Body no.		UZ	MZ	LZ	UL	ML	LL	Body no.		UZ	MZ	LZ	UL	LL	
1	DF	3	4	5	GGO 90%, ST	GGO 40%, ST	GGO 90%, ST	1	DF	3	4	4	GGO 70%, ST	GGO 80%	
	TM	3	3	5					TM	4	3	3			
2	DF	2	3	3	GGO 10%	Tree-in-bud 10%	GGO 50%	2	DF	2	4	4	GGO 20%	GGO 60%	
	TM	5	4	2					TM	5	3	3			
3	DF	3	5	5	GGO 30%	No findings	GGO 40%	3	DF	3	5	5	GGO 20%	GGO 20%	
	TM	3	4	5					TM	5	5	5			
4	DF	2	4	5	Emph 20%	Emph 20%	GGO 10%, Emph 20%	4	DF	2	4	5	Emph 20%	GGO 10%, Emph 20%	
	TM	5	5	5					TM	4	5	5			
5	DF	3	4	5	GGO 80%, ST	GGO 20%	GGO 80%, ST, PE 2 cm	5	DF	3	4	5	GGO 90%, ST	GGO 90%, ST, PE 1 cm	
	TM	4	4	4					TM	4	5	5			
6	DF	2	2	2	GGO 90%, Emph 90%	GGO 50%, Emph 70%, Cons 10%	GGO 10%, Emph 90%, Cons 60%	6	DF	2	3	4	GGO 50%, Emph 60%	GGO 20%, Emph 80%, Cons 20%	
	TM	3	3	2					TM	4	3	3			
7	DF	2	4	4	GGO 10%, Cons 10%	GGO 10%	GGO 10%, Cons 60%	7	DF	3	4	4	GGO 10%, Cons 10%	Cons 70%	
	TM	3	3	4					TM	3	4	4			
8	DF	2	3	4	GGO 30%	GGO 10%	GGO 60%	8	DF	2	3	1	GGO 20%	GGO 50%, Cons 10%, Enlarged heart	
	TM	4	3	4					TM	5	4	4			
9	DF	3	4	5	GGO 20%	GGO 20%	GGO 90%	9	DF	3	5	5	GGO 20%	GGO 80%	
	TM	4	4	3					TM	5	5	5			

Table 5.8: Correlation of dark-field and transmission radiography with CT findings. For all nine human bodies, median dark-field and transmission signal strength gradings for different lung regions are presented next to computed tomography (CT) findings in pulmonary lobes. Color indicates cases with highest (**red**, **blue**) and lowest (**pink**, **light blue**) overall median dark-field signal or transmission grading that are shown as individual figures (Figs. 5.19, 5.20, 5.21, and 5.22). **TM**: Transmission, **DF**: dark-field, **UZ / MZ / LZ**: Upper / middle / lower zone, **UL / ML / LL**: Upper / middle / lower lung lobe. **GGO**: Ground-glass opacities, **Emph**: Emphysematous changes, **ST**: (interlobular) septal thickening, **PE x cm**: Pleural effusion with *x* cm max. width in AP direction, **Cons**: Consolidation, **X%**: Percentage of affected lobe.

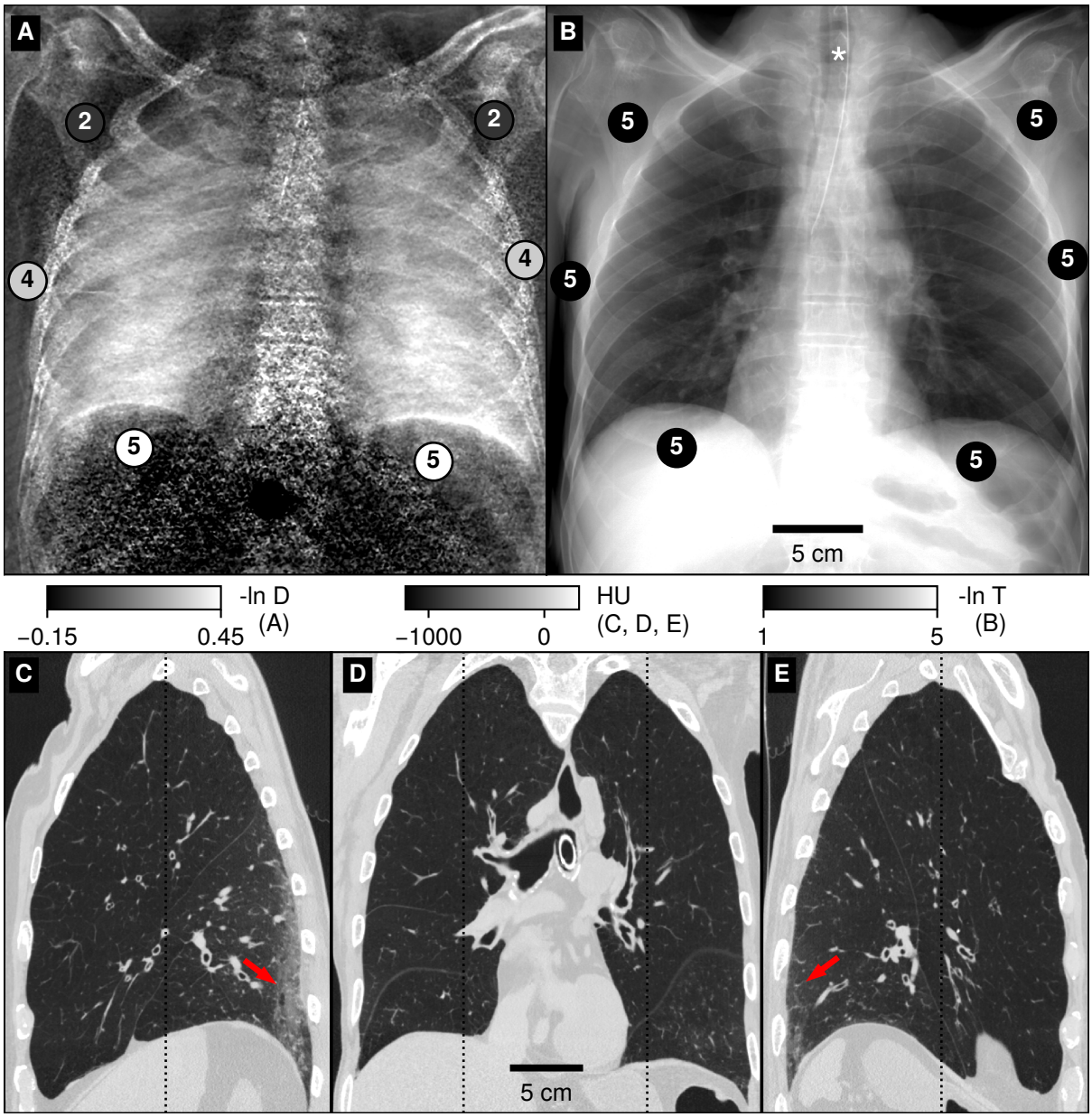

Figure 5.19: Dark-field chest radiograph, conventional X-ray, and CT of human body no. 4. Median visual grading (circled numbers) of dark-field chest radiograph (a) by three independent readers shows increasing dark-field signal from the apex to the base of the lung. Median visual grading of transmission in conventional X-ray (b) shows no difference between upper, middle, and lower zones. Sagittal (c, e) and coronal (d) CT images show regular ventilation of emphysematous lung parenchyma except from some minor subpleural dystelectasis (arrows) in posterior lower lobes. Asterisk in (b) marks the location of the endotracheal tube, which was repositioned between X-ray dark-field/conventional X-ray imaging and CT. Relative location of sagittal and coronal CT slices is indicated by dotted lines.

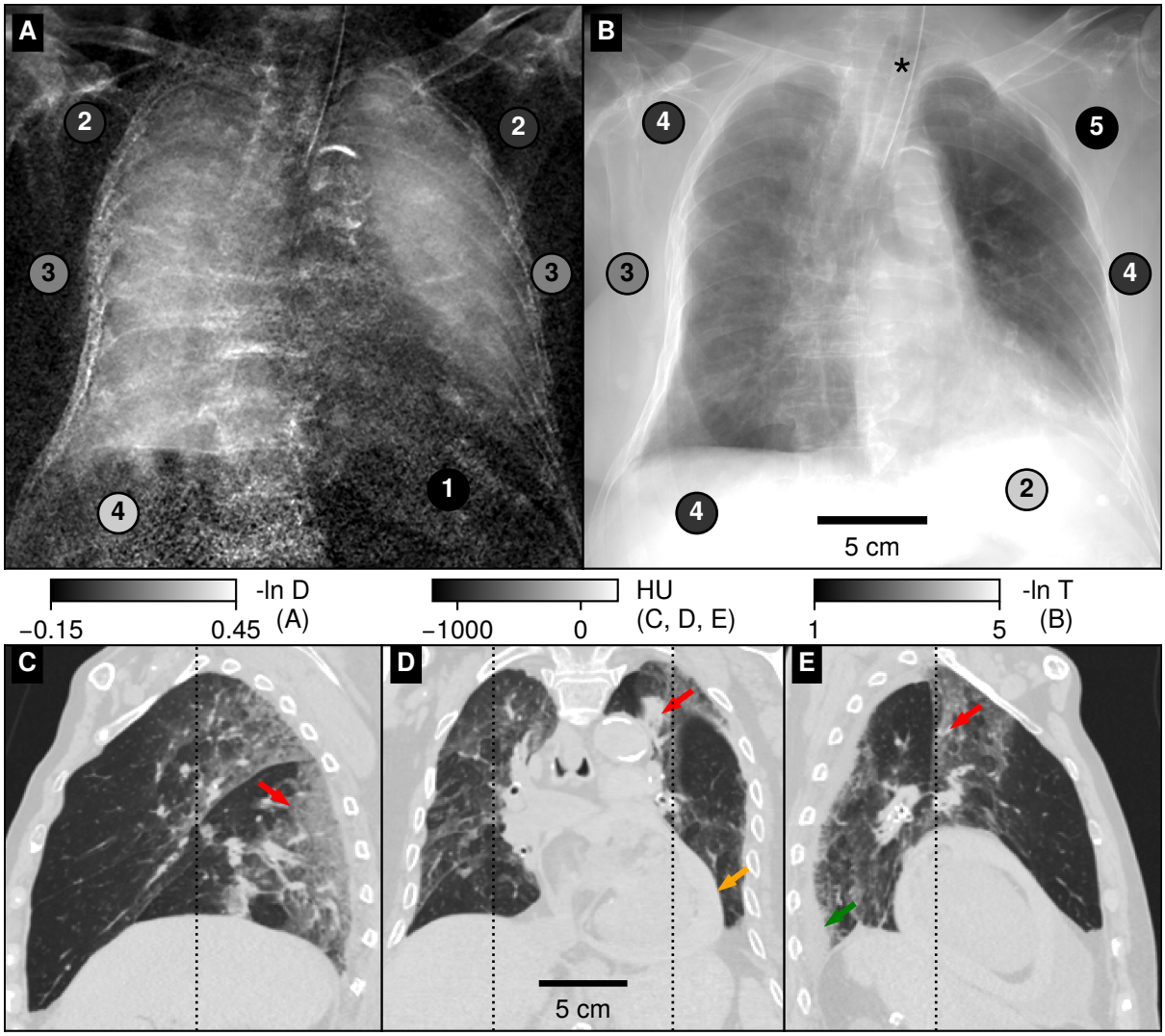

Figure 5.20: Dark-field chest radiograph, conventional X-ray, and CT of human body no. 8. Median visual grading (circled numbers) of dark-field chest radiograph (a) by three independent readers shows a markedly reduced dark-field signal in left lung lower zone and to a minor degree in both middle zones, compared to other regions. Median visual grading of transmission in conventional X-ray (b) shows reduced transmission in the right lung, especially in the middle zone, and a markedly reduced transmission in the lower zone of the left lung. Sagittal (c, e) and coronal (d) CT images show interstitial and alveolar infiltrates (red arrows) in depending parts of the right and left upper and lower lobes. Furthermore, there is an enlargement of the heart with a significant haemopericardium (orange arrow) and small left-sided pleural effusion (green arrow). Asterisk in (b) marks the location of the endotracheal tube. Relative location of sagittal and coronal CT slices is indicated by dotted lines.

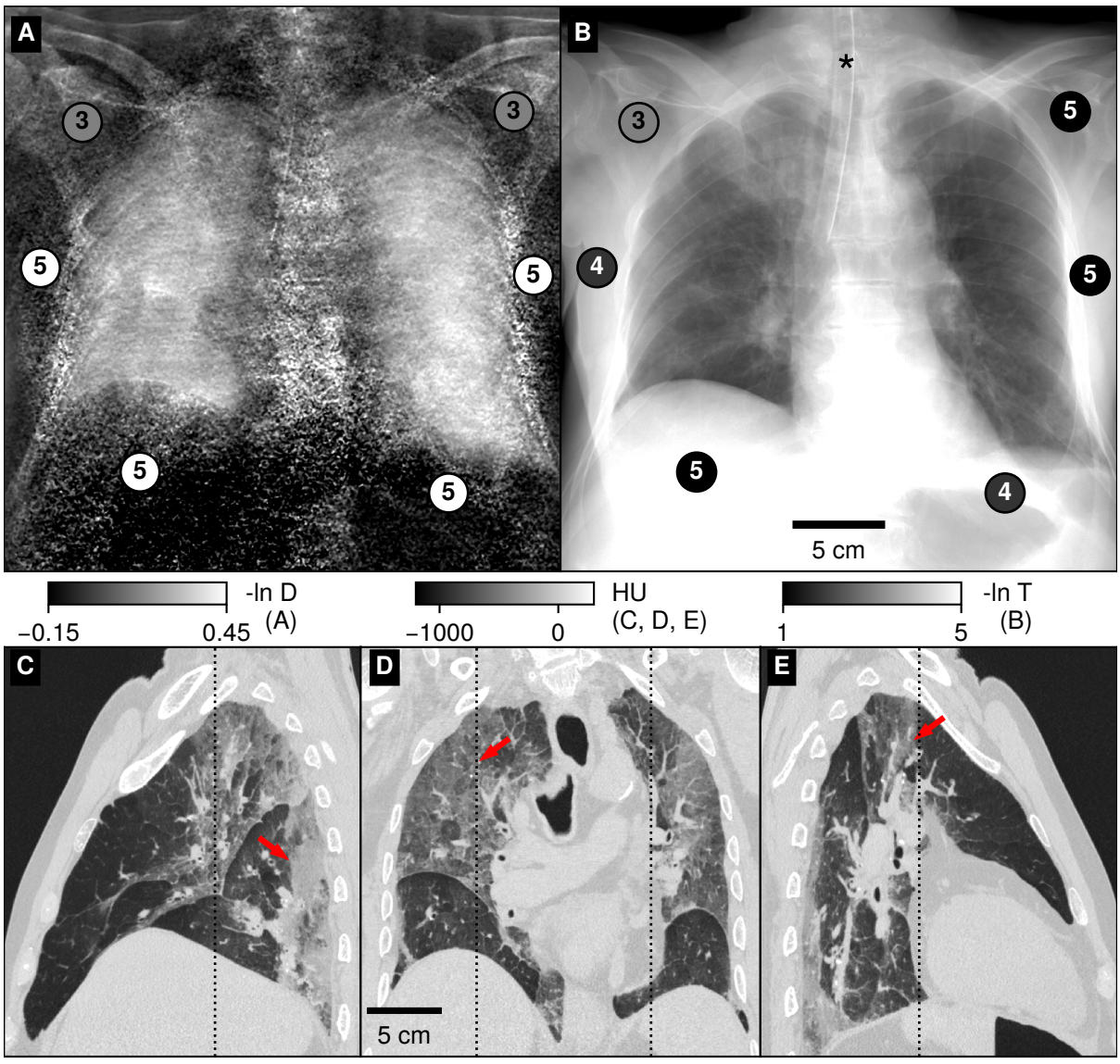

Figure 5.21: Dark-field chest radiograph, conventional X-ray, and CT of human body no. 3. Median visual grading (circled numbers) of dark-field chest radiograph (a) by three independent readers shows highest dark-field signal in the middle and lower zones of the lung. Median visual grading of transmission in conventional X-ray (b) shows reduced transmission in the right lung upper zone and more pronounced in the left lung lower zone. Sagittal (c, e) and coronal (d) CT images show interstitial and alveolar infiltrates (arrows) in dependent parts of right and left upper and lower lobes and right middle lobe. Asterisk in (b) marks the location of the endotracheal tube. Relative location of sagittal and coronal CT slices is indicated by dotted lines.

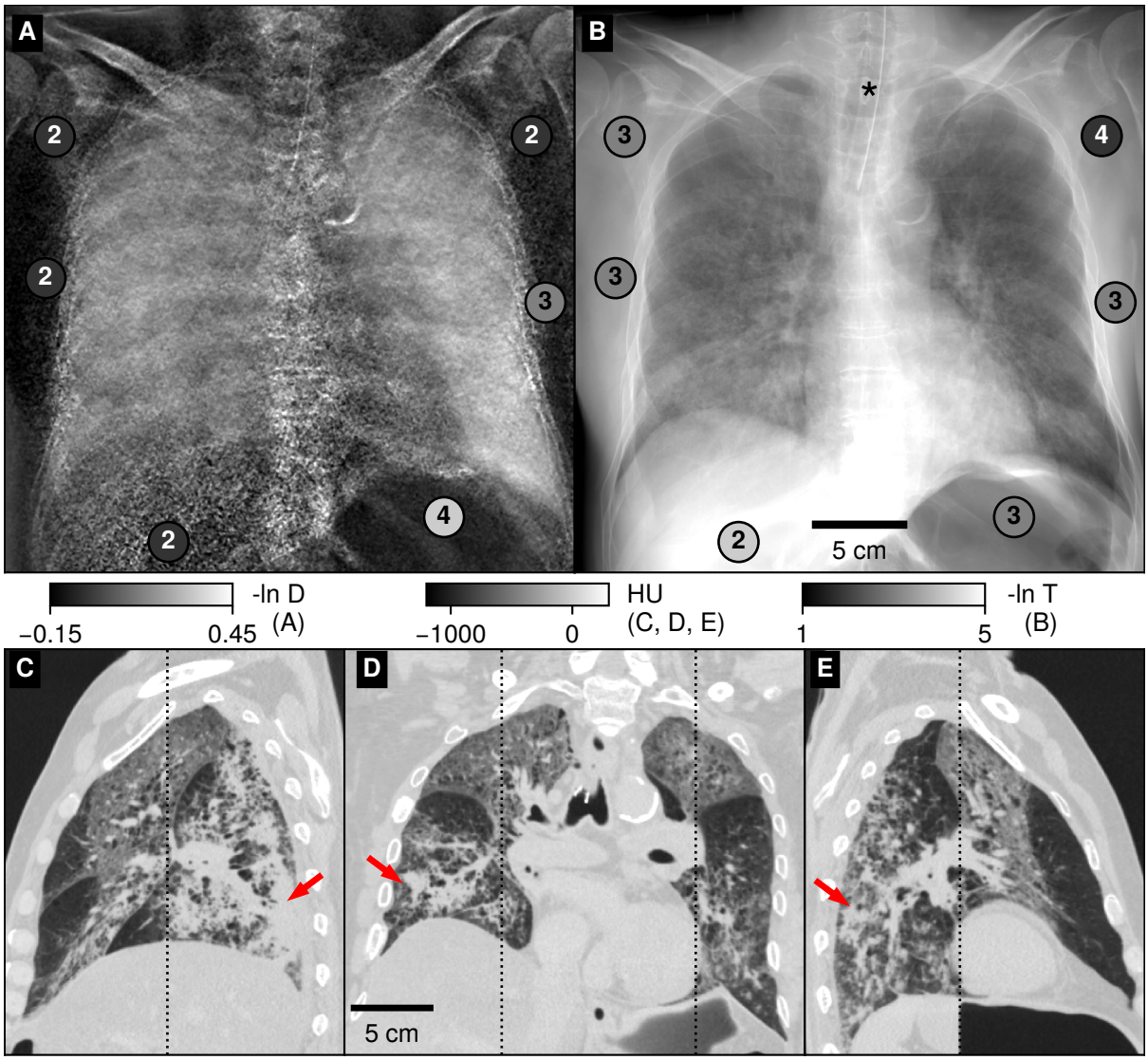

Figure 5.22: Dark-field chest radiograph, conventional X-ray, and CT of human body no. 6. Median visual grading (circled numbers) of X-ray dark-field chest radiograph (a) by three independent readers shows markedly reduced dark-field signal in middle and lower zones of the right lung. Median visual grading of transmission in conventional X-ray (b) shows reduced transmission in the right lung upper zone as well as right and left lung middle zones and is lowest in right-lung lower zone. Sagittal (c, e) and coronal (d) CT images show interstitial and alveolar infiltrates in the right upper lobe, left upper lobe, and right middle lobe, as well as extensive pulmonary consolidation (arrows) in the right lower lobe and, to a lesser extent, in left lower lobe. Asterisk in (b) marks the location of the endotracheal tube. Relative location of sagittal and coronal CT slices is indicated by dotted lines.

the heart are pathologies we observed in the human bodies. Additionally, decomposition processes after death may influence dark-field signal intensity.

In this study, it was not possible to differentiate and quantify the individual contribution of a single finding to the change in dark-field signal strength, because none of the lungs was free of pathologies and could have served as a reference. Furthermore, due to lung anatomy, it is difficult to correlate a CT finding in a pulmonary lobe to dark-field signal changes in a lung zone of a radiograph. However, we gained insight into findings that may have a more pronounced effect on dark-field signal reduction, e.g., pulmonary consolidation, that has not been addressed in animal studies.

X-ray dark-field imaging was performed in supine position, which leads to dystelectasis (improper inflation of the lung) in the dorsal basal parts of the lungs and may influence dark-field signal. To at least partially compensate for this, we performed endotracheal intubation and kept airway pressure constant during X-ray dark-field imaging.

Since X-ray dark-field radiography is a novel imaging modality, the possibility to train the readers for the visual evaluation of the dark-field images was limited. Furthermore, the number of human bodies included in our study is relatively small. Still, our results are in accordance with previous animal studies and demonstrate clinical applicability.

In conclusion, our study on *post mortem* human X-ray dark-field chest radiography demonstrates that X-ray dark-field images provide complementary information of the lungs to conventional X-ray, allow reliable visual quantification of dark-field signal strength, and have reached an image quality warranting an evaluation in clinical trials.

Chapter 6

Theoretical investigations of dark-field signal formation

> Science is made up of so many things that appear obvious after they are explained.
>
> Frank Herbert, *Dune*

Contents

This chapter is a collection of largely theoretical evaluations of the X-ray dark-field signal. Section 6.1 deals with a newly discovered hardening effect: it results in the reduction of an object's dark-field activity if it is preceded by another dark-field active object. It is conceptually similar to beam-hardening familiar from conventional X-ray and CT. This work has been submitted for publication. In section 6.2, concepts from partial coherence theory are used to calculate measured intensities in a Talbot-Lau setup. The approach presented here is straightforward, quite universal, and is useful to understand the dependence of autocorrelation length and angular sensitivity on sample position. Finally, section 6.3 discusses new and existing methods for evaluating and correcting estimation bias of noisy dark-field data. A lookup table representation of each method is presented, and each method's performance is evaluated in terms of residual bias, variance, and mean square error.

6.1 X-ray dark-field signal reduction due to hardening of the visibility spectrum

The content in this section largely follows the manuscript "X-ray dark-field signal reduction due to hardening of the visibility spectrum" submitted to IEEE Transactions on Medical Imaging by F. De Marco,

J. Andrejewski, K. Willer, L. Gromann, T. Koehler, H.-I. Maack, J. Herzen, and F. Pfeiffer. This work has also been published as an electronic preprint [DeMa+20]. The introduction has been largely omitted here; the reader is instead referred to chapter 2 for information about the physics of X-rays phase-contrast imaging, and chapter 3 for an introduction to the *lung-scanning setup*. My contributions to this work are the design and carrying out of the measurements, the theoretical calculations, the design and realization of the numerical optimizations, and writing the manuscript.

Abstract

X-ray dark-field imaging enables a spatially-resolved visualization of small-angle X-ray scattering. Using phantom measurements, we demonstrate that a material's effective dark-field signal may be reduced by modification of the visibility spectrum by other dark-field-active objects in the beam. This is the dark-field equivalent of conventional beam-hardening, and is distinct from related, known effects, where the dark-field signal is modified by attenuation or phase shifts. We present a theoretical model for this group of effects and verify it by comparison to the measurements. These findings have significant implications for the interpretation of dark-field signal strength in polychromatic measurements.

6.1.1 Introduction: Spectral effects in polychromatic dark-field imaging

In analogy to the "linear attenuation coefficient", which is reconstructed by computed tomography (see e.g. section 2.2.8 on page 43), an equivalent volumetric quantity can be defined for the X-ray dark-field: The "linear diffusion coefficient" [Bech+10], or "dark-field extinction coefficient" (DFEC) [Lync+11] characterizes the decrease of the logarithmic dark-field signal per sample thickness. See section 2.5.8c on page 62 for an extensive discussion of the relationships between this quantity and the object's microstructural parameters.

For a grating-based X-ray imaging setup using monochromatic radiation, the interpretation of measured transmittance and X-ray dark-field signals is straightforward: The image signals are directly related to projection integrals of the sample's linear attenuation coefficient or DFEC at the used wavelength, respectively.

With the exception of Compton scatter, the measurement process in a conventional or a grating-based X-ray setup does not change the X-ray wavelength, i.e. for a monochromatic source, the wavelength of detected radiation is equal to that of the source. Unlike conventional X-ray imaging, the image formation process in a grating-based setup is based on interference, and thus the presence of spatial correlations within the wave field. However, it can be shown that different (temporal) Fourier coefficients of a polychromatic wave field are always uncorrelated. (This becomes apparent e.g. when considering the definition of the cross-spectral density of a random process, see e.g. [Mand+95]). This means that no interference effects occur between two fields with different frequencies (i.e., different photon energies).

Because of these two preceding points, it is appropriate both for conventional and grating-based X-ray setups to calculate the measured intensity separately for each photon energy, and finally integrate all intensities. The case of polychromatic illumination can be thus interpreted as a superposition of the intensities at the constituent photon energies. Since the response of a grating-based setup, as well as the attenuating and scattering properties of the sample are dependent on photon energy, this leads to a complex, non-linear dependence of polychromatic transmittance and dark-field on sample thickness.

In conventional X-ray imaging and CT, this is called *beam-hardening*: Since low-energy X-ray photons ("soft" X-rays) are usually attenuated more strongly than high-energy photons ("hard" X-rays), the mean energy of photons transmitted by an object tends to be higher than that of the incident photons. The attenuation properties of structures downstream of such an object are then dominated by the material properties at these higher energies, resulting in a decreased attenuation. In CT, this may become apparent as "cupping" artifacts.

This effect is also present in polychromatic grating-based X-ray imaging. Additionally however, while monochromatic dark-field and phase-contrast are only a function of small-angle scatter and refraction, respectively, their polychromatic counterparts are simultaneously affected by all three basic interactions: attenuation, small-angle scatter and refraction. In particular, the effect of beam-hardening on the dark-field signal has been shown to be significant: Measured visibility in a polychromatic setup is a weighted average of

photon-energy-dependent visibility, and a change in spectral composition of the wave field affects the average's relative weights (harder X-rays are weighted more strongly downstream of an attenuating object). This results in a change—often a decrease—of polychromatic visibility which is not due to small-angle scatter. Multiple approaches for quantifying and correcting this effect have been suggested [Yash+15; Pelz+16] (a correction of this effect for the *lung-scanning setup* is introduced in section 4.3.1 on page 101). Additionally, [Pelz+16] has also examined the influence of photon-energy-dependent refraction (dispersion) on the dark-field signal.

We show here that the aforementioned weights in the calculation of polychromatic visibility are also a function of the (incident) visibility spectrum. This means that different DFEC values may be measured for the same material, located at the same position in the same setup, depending on whether or not it is surrounded by other scattering materials—even if these materials induce minimal attenuation.

Similar to the linear attenuation coefficient, the DFEC is typically higher for "softer" X-rays. Thus, the visibility at these wavelengths is reduced more strongly by a sample, which shifts the mean of the visibility spectrum (downstream of the sample) towards "harder" X-rays. We suggest to call this effect *visibility-hardening*, due to its conceptual similarity to beam-hardening.

We present visibility measurements for a variable number of ethylene-propylene-diene monomer (EPDM) foam rubber sheets and polyoxymethylene (POM) slabs. EPDM foam rubber produces a strong dark-field signal, and attenuates only weakly, whereas POM attenuates strongly and produces no dark-field signal. Two different placements of POM in the beam are used to estimate the influence of detected, Compton-scattered radiation.

A theoretical model for the calculation of polychromatic visibility and dark-field is then introduced, and a regression of this model to one of the data sets is performed to demonstrate the agreement between experiment and theory. The model is then expanded by an estimation of detected, Compton-scattered radiation and successfully applied to both data sets (section 6.1.4).

6.1.2 Experimental procedures

6.1.2a Phantom construction and imaging

An imaging phantom was constructed from uniform slabs of two types of materials: Polyoxymethylene slabs (POM, Hans-Erich Gemmel & Co. GmbH, Berlin, Germany) were used to simulate attenuation by a combination of soft and adipose tissues, whereas sheets of ethylene-propylene-diene monomer cellular foam rubber (EPDM-S, DRG GmbH & CoKG, Neumarkt am Wallersee, Austria) additionally generated small-angle scatter.

Fig. 6.1 shows that the photon-energy-dependence of X-ray interaction cross-sections of POM is comparable to those of standard soft and adipose tissues published by the ICRP (International Commission on Radiological Protection, as tabulated in [NIST17]), in the medically relevant range of X-ray energies. We thus expected POM to exhibit a beam-hardening behavior comparable to those types of tissues. Energy-resolved visibility measurements (unpublished) have shown that POM does not generate small-angle scatter. Any observed visibility reduction is thus entirely due to beam-hardening or Compton scatter.

EPDM is a closed-cell foam rubber. Its highly porous microstructure resembles alveolar structures in the lung and generates a strong dark-field signal. Due to the material's low mass density and high air content, it attenuates X-rays only weakly.

A large, 10 mm thick sheet of EPDM was cut into rectangular pieces to form a "staircase" with five height levels between 10 and 50 mm (plus an adjacent area without any foam rubber). This part of the phantom was placed directly on the sample table in all measurements (cf. Fig. 6.2), with the edges of the foam at a 45-degree angle to the scanning direction.

This was supplemented by a POM layer of uniform thickness over the field of view. In separate measurements, one to four levels of 32 mm POM slabs (i.e., thicknesses of 32 mm to 128 mm) were used. The range of POM and foam rubber thickness levels was selected to produce attenuation and dark-field signal levels comparable to that of a human or porcine thorax. A total of $6 \times 4 = 24$ combinations of material thicknesses were thus examined in a total of four measurements.

Since Compton-scattered radiation is detected at a large range of incidence angles, the detected intensity decreases when the scattering object is moved fur-

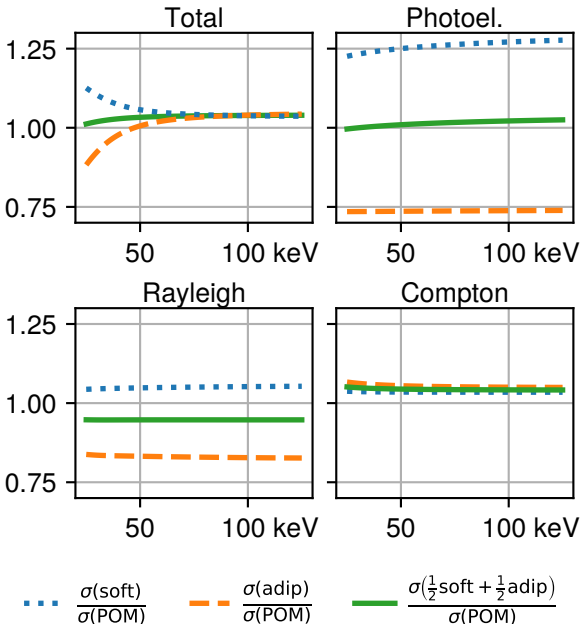

Figure 6.1: Comparison between energy-dependent X-ray interaction cross-sections σ (in cm^2/g) of POM and of ICRP standards for soft tissue (dotted line) and adipose tissue (dashed line). POM corresponds approximately to a mixture of both tissue types with equal mass fractions (solid line). Elemental composition of all materials was taken from [NIST17].

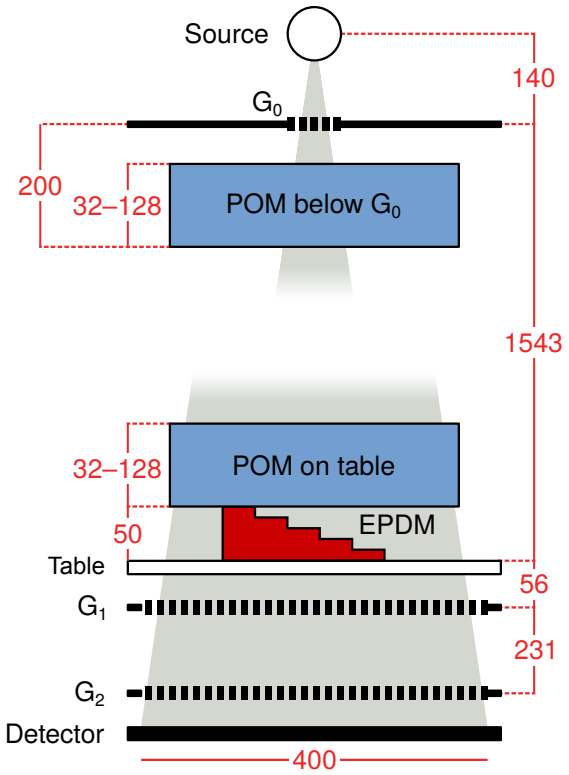

Figure 6.2: Placement of the phantom materials in the imaging setup (front view). In each measurement, POM is placed in only one of the shown locations. Not to scale, numbers are distances in mm. A more detailed overview of the setup is shown in Fig. 3.3 on page 82.

ther from the detector. To evaluate the influence of Compton-scattered radiation on signal levels, two sets of these four measurements were thus performed with different placement of the POM slabs (Fig. 6.2): In the first set, they were placed immediately above the foam rubber staircase. Supports were used to avoid compression of the foam rubber due to the slabs' weight. In the second set, the POM was placed in a mount just below the G_0 grating.

Naturally, other sources of Compton scatter may be present in both measurements, such as the foam rubber and exposed parts of the aluminum frame. However, we assume these factors to be relatively insignificant, due the weak attenuation of the foam rubber, and the X-ray beam being collimated to avoid direct exposure of setup elements other than the gratings.

In order to average out position-dependent spectral effects (such as the anode heel effect), all above-mentioned measurements were repeated with three to five orientations of the foam "staircase" on the table.

6.1.2b Signal retrieval

The three imaging modalities were retrieved using the "Full retrieval of reference scan parameters" approach introduced in section 4.2.2d on page 96. A total of 7 phase-stepped scans were performed to retrieve the reference-scan parameters, and approximately 25 points of the moiré fringe pattern were sampled in each point; i.e., $m = 1,\dots,7$ and $k = 1,\dots,25$ in Eq. (4.23) on page 96.

In the processed images, six regions of interest (ROIs) were defined to coincide with regions of constant foam rubber thickness ($0, 10, \dots, 50$ mm). Mean values of logarithmic transmittance and dark-field $(-\ln T, -\ln D)$ in each ROI were calculated. Results from the different orientations of the foam rubber "staircase" on the table were averaged.

6.1.3 Experimental results

In Fig. 6.3, the resulting mean values of $-\ln D$ are graphed versus mean values of $-\ln T$ for each of the POM / EPDM height combinations. In an ideal scenario with a monochromatic X-ray source and an absence of Compton scatter, the addition of an absorbing and / or scattering slab would lead to a constant additive change in $-\ln T$ and / or $-\ln D$, regardless of the absolute signal levels. The visualization in Fig. 6.3 would thus consist of points on a grid spanned by two vectors $\vec{v}_{\mathrm{POM}} = [\tau_{\mathrm{POM}}, \delta_{\mathrm{POM}}]^T$, $\vec{v}_{\mathrm{EPDM}} = [\tau_{\mathrm{EPDM}}, \delta_{\mathrm{EPDM}}]^T$. Given that POM produces little to no small-angle scattering signal, and EPDM attenuates very weakly, $\vec{v}_{\mathrm{POM}}$ and $\vec{v}_{\mathrm{EPDM}}$ should be nearly orthogonal.

We can observe a number of deviations of the measurement data from this scenario: Firstly, for low amounts of attenuating and scattering materials (i.e., for points in the lower left quadrant of Fig. 6.3), the introduction of additional attenuating POM material significantly increases $-\ln D$. In the presence of a lot of EPDM however, this increase disappears, and partly even turns into a decrease (see upper half of Fig. 6.3, "POM below G_0"). This effect has been examined in [Yash+15; Pelz+16]. It can be understood as a beam-hardening-induced reduction (or increase) in visibility, which results in an increase (or decrease) of $-\ln D$, even though the sample's small-angle-scattering behavior remains unchanged.

Secondly, the magnitude of the previous effect is changed when the absorbing material is placed closer to the detector. As mentioned previously, the detected amount of Compton scatter is significantly higher in this measurement. Since Compton-scattered radiation is incoherent, it does not contribute to fringe modulation, but only increases the mean detected intensity. In a Compton-free measurement, the visibility is given as $V = (I_{\max} - I_{\min})/(I_{\max} + I_{\min})$, where $I_{\max}$ and $I_{\min}$ are the highest and lowest detected intensity during a phase-stepping measurement. Compton scatter contributes some amount ΔI to all measured intensities. Accordingly, the measured visibility is then $V' = (I_{\max} - I_{\min})/(I_{\max} + I_{\min} + 2\Delta I)$, necessarily lower than the true visibility, which is reflected as an increase of $-\ln D$ in Fig. 6.3. A more complete calculation is given in section 6.1.7c.

Finally, the change in $-\ln D$ per added sheet of EPDM decreases with an increasing total number of these sheets. In other words, adding the first sheet of EPDM has a significantly greater impact on $-\ln D$ than adding a fifth EPDM sheet to a stack of four.

This effect can be ascribed only partially to conventional beam-hardening, as the amount of attenuation introduced by the EPDM sheets is very low: Fig. 6.3 shows that the combined attenuation of five layers of EPDM is still much less than that of one POM slab. However, adding the fifth rubber sheet to a one-slab POM layer adds much less dark-field signal than adding the first rubber sheet to a two-slab POM layer, even though the latter arrangement exhibits stronger attenuation. This suggests that attenuation alone is insufficient to parameterize the behavior of polychromatic visibility, and that modifications of the visibility spectrum must also be taken into account.

6.1.4 Theory

In the following, we will introduce a mathematical model to connect the transmission and dark-field signals measured with polychromatic illumination to the spectra of detected intensity and visibility. To demonstrate the compatibility of this model with the measurements, we then perform a regression of the model to the measurement data with the POM material placed directly below the G_0 grating (Fig. 6.3, left). It is then expanded to also include the detection of Compton-scattered radiation.

6.1.4a Calculation of polychromatic signals

The approach for this calculation, as well as the used quantities, are outlined in Fig. 6.4. In conventional X-ray imaging, an object's transmittance is given by the fraction T of incident radiation S_0 which passes through it. This fraction is typically determined from two measurements with identical parameters, one with and one without the object in the beam. For monochromatic radiation, the amount of transmitted radiation S is related to the object's linear attenuation coefficient μ at the used photon energy E via the Beer-Lambert law:

$$T = \frac{S}{S_0} = \exp\left[-\int_0^{z_0} \mu(E,z)\,dz\right], \tag{6.1}$$

with the beam propagating along the z axis (extent of object from $z = 0$ to $z = z_0$). The "amounts" S and S_0 of detected radiation in these measurements can

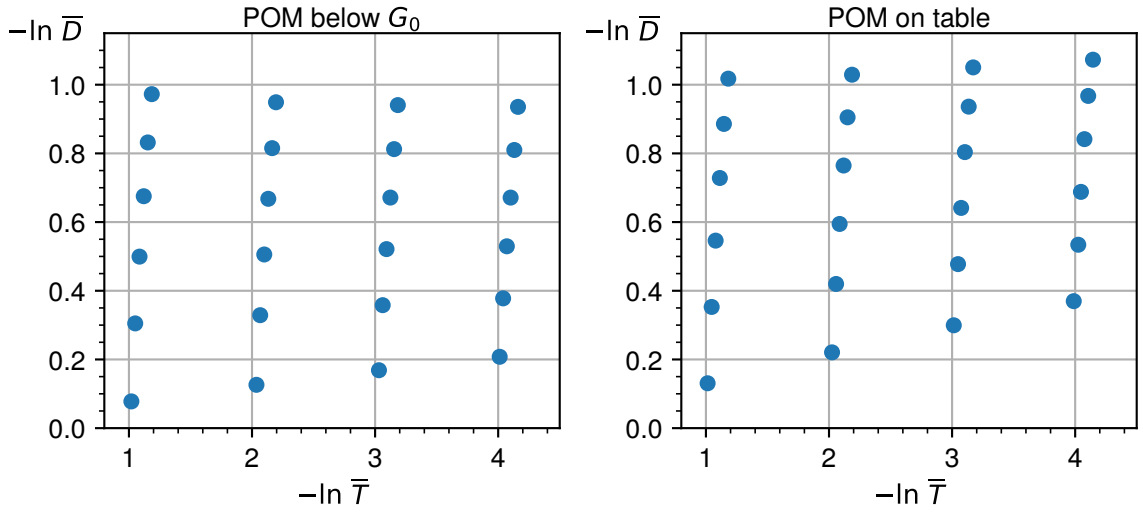

Figure 6.3: Mean measured values of logarithmic visibility reduction $-\ln \mathbf{D}$ and logarithmic transmittance $-\ln \mathbf{T}$ for all examined thickness combinations of the phantom.

be quantified by the radiation energy absorbed, or the number of X-ray photon absorption events registered in a detector. The detector signals S and S_0 are proportional to the number of photons N, N_0 incident on the detector during each measurement, if its response function, i.e. the "signal per photon" $r = dS/dN$ does not depend on N. Then, T is independent of the value of r, and thus of the detection mechanism, for monochromatic measurements. This changes for measurements with polychromatic sources: Again assuming independence of $r(E)$ from $N(E)$, the total measured signal is an integral over the signal from each interval $[E, E+dE]$ of photon energy, i.e.

$$\overline{S_0} = \int_0^\infty \psi_0(E)\,dE,\ \overline{S} = \int_0^\infty \psi(E)\,dE, \tag{6.2}$$

where

$$\psi_0(E) = \frac{\partial N_0(E)}{\partial E} r(E),\ \psi(E) = T(E)\psi_0(E), \tag{6.3}$$

and $(\partial N_0/\partial E)\,dE$ is the number of photons from the energy interval $[E, E+dE]$ incident on the detector in the reference measurement.

For energy-integrating detectors, the response function $r(E)$ is proportional to E and the detector's quantum efficiency (fraction of detected incident photons). For single-photon-counting devices, $r(E)$ depends only on quantum efficiency (when ignoring non-linear effects such as pileup and charge sharing).

Source and detector properties are combined in the quantities $\psi_0(E)$ and $\psi(E)$. They are "detector spectra", i.e. the *detector signal per photon energy interval* $[E, E+dE]$, for the reference and the sample measurement, respectively, and will be used several times in the calculation.

As in Eq. (6.2), we will use an overline to mark quantities (signal levels and effective attenuation coefficients) as they would be measured in a polychromatic grating-based X-ray phase-contrast setup with the detector spectra $\psi_0(E)$, $\psi(E)$. Furthermore, we will use the notation $\langle f \rangle_g$ to denote the mean of $f(E)$, weighted by $g(E)$, i.e.

$$\langle f \rangle_g = \frac{\int_0^\infty f(E)g(E)\,dE}{\int_0^\infty g(E)\,dE}. \tag{6.4}$$

The transmittance in a polychromatic setup is then

$$\overline{T} = \frac{\overline{S}}{\overline{S_0}} \overset{(6.2),(6.3)}{=} \frac{\int_0^\infty T(E)\psi_0(E)\,dE}{\int_0^\infty \psi_0(E)\,dE} \overset{(6.4)}{=} \langle T \rangle_{\psi_0} \tag{6.5}$$

$$\overset{(6.1)}{=} \left\langle \exp\left(-\int_0^{z_0} \mu(E,z)\,dz\right) \right\rangle_{\psi_0(E)}. \tag{6.6}$$

Unlike in Eq. (6.1), $r(E)$ does not cancel out, since it is a function of E.

An effective linear attenuation coefficient $\overline{\mu_0}$ of an additional thin object with linear attenuation coefficient

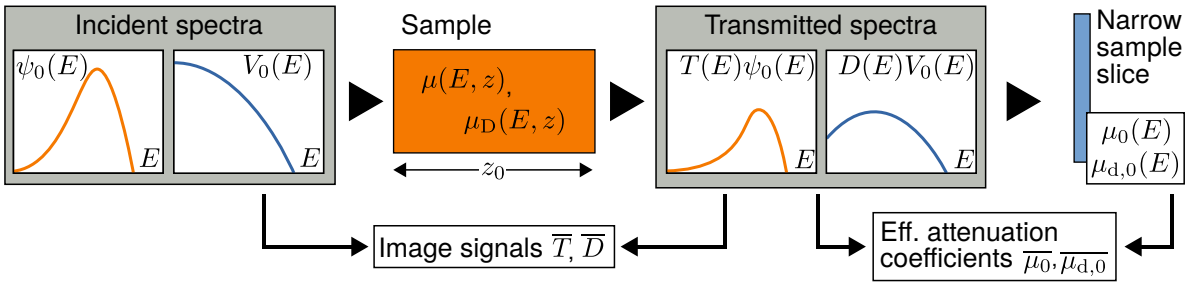

Figure 6.4: Outline of the calculations in section 6.1.4a: A sample with a linear attenuation coefficient $\mu(E,z)$ and DFEC $\mu_d(E,z)$ is illuminated by polychromatic radiation with detector spectrum $\psi_0(E)$ and visibility spectrum $V_0(E)$. The object modifies the spectra according to the Beer-Lambert law, leading to downstream detector and visibility spectra $\psi(E) = T(E)\psi_0(E)$, $V(E) = D(E)V_0(E)$. The spectrally-averaged transmittance and dark-field signals $\overline{T}$, $\overline{D}$ are calculated from incident and transmitted flux and visibility spectra. Finally, the impact of the modified spectra on the effective attenuation coefficients of a downstream object with negligible thickness is examined.

$\mu_0(E)$ behind this object can be derived from Eq. (6.6) via

$$\overline{\mu_0} = -\frac{\partial \ln \overline{T}}{\partial z_0} = \frac{1}{\overline{T}}\frac{\partial \overline{T}}{\partial z_0} = \langle \mu_0 \rangle_{T\psi_0}, \tag{6.7}$$

i.e. it is the object's energy-dependent linear attenuation coefficient $\mu_0(E)$, weighted by the incident detector spectrum $\psi_0(E)$, which has been filtered by the preceding absorber $T(E)$ (for calculation see section 6.1.7a). As lower photon energies are attenuated more strongly, $\psi(E) = \psi_0(E)T(E)$ is increasingly shifted towards higher energies for increasing thickness of the absorber ("beam-hardening"). The lower values of $\mu(E,z_0)$ at these energies lead to an overall decrease of $\overline{\mu_0}$ for increasing thickness of the preceding absorber.

X-ray dark-field imaging enables spatially-resolved visualization of small-angle X-ray scattering of a sample by measuring the ratio of interferometric visibility with and without the sample, $D = V/V_0$. The visibility characterizes the relative contrast of an interferometric fringe pattern. Given the highest and lowest detector signals S_{max}, S_{min} in a given pattern, the visibility is $V = (S_{max} - S_{min})/(S_{max} + S_{min})$. Since the signal modulation of a fringe pattern with fringe phase is typically sinusoidal, i.e. that

$$S_{mod}(E) = S(E)\left\{1 + V(E)\cos[\varphi(E)]\right\}, \tag{6.8}$$

it follows that

$$S_{max}(E) = S(E)[1 + V(E)],\ S_{min}(E) = S(E)[1 - V(E)].$$

For monochromatic radiation, visibility also decreases exponentially as a function of sample thickness [Bech+10; Stro14]:

$$D(E) = \frac{V(E)}{V_0(E)} = \exp\left[-\int_0^{z_0} \mu_d(E,z)dz\right]. \tag{6.9}$$

In analogy to the linear attenuation coefficient $\mu(E,z)$, the dark-field extinction coefficient (DFEC) $\mu_d(E,z)$ characterizes the magnitude of this decrease [Lync+11].

Under the assumption that no phase shift occurs, the visibility $\overline{V}$ measured in a polychromatic setup can be easily calculated from the spectral quantities: In this case, all monochromatic detector signal modulations are in phase, and when interpreting $S_{max}(E)$ and $S_{min}(E)$ as intensities per photon energy interval, their polychromatic equivalents are retrieved by integration:

$$\overline{S_{max}} = \int_0^\infty \frac{\partial S_{max}}{\partial E}dE = \int_0^\infty \psi(E)[1 + V(E)]dE, \tag{6.10}$$

$$\overline{S_{min}} = \int_0^\infty \frac{\partial S_{min}}{\partial E}dE = \int_0^\infty \psi(E)[1 - V(E)]dE. \tag{6.11}$$

An equivalent calculation for non-negligible phase-shift is given in section 6.1.7d. Given that, equivalently to the monochromatic case, $\overline{V} = (\overline{S_{max}} - \overline{S_{min}})/(\overline{S_{max}} + \overline{S_{min}})$, it follows that

$$\overline{V} = \frac{\int_0^\infty V(E)\psi(E)dE}{\int_0^\infty \psi(E)dE} \overset{(6.4)}{=} \langle V \rangle_\psi = \langle V_0 D \rangle_{\psi_0 T}. \tag{6.12}$$

The associated blank-scan visibility $\overline{V_0}$ is found by excluding attenuation and visibility reduction by the

sample. Thus, $T(E) = D(E) = 1$, and $\overline{V_0} = \langle V_0 \rangle_{\psi_0}$. Finally, the spectrally-averaged dark-field signal is given as

$$\begin{aligned}\overline{D} &= \frac{\overline{V}}{\overline{V_0}} = \frac{\langle V \rangle_\psi}{\langle V_0 \rangle_{\psi_0}} \\ &= \frac{\langle V_0 D \rangle_{\psi_0 T}}{\langle V_0 \rangle_{\psi_0}} \overset{(*)}{=} \frac{\langle DT \rangle_{V_0 \psi_0}}{\langle T \rangle_{\psi_0}} \overset{(6.5)}{=} \frac{\langle DT \rangle_{V_0 \psi_0}}{\overline{T}}, \end{aligned} \tag{6.13}$$

with T and D as given in Eq. (6.1) and Eq. (6.9). (The related expression $\langle V_0 \rangle_\psi / \langle V_0 \rangle_{\psi_0}$ is used in [Yash+15] to separately estimate the effect of beam-hardening). The equivalence $(*)$ follows by applying Eq. (6.4) and pairing the four integrals differently. Comparison with Eq. (6.5) demonstrates a direct relation of $\overline{D}$ with $\overline{T}$. The effective DFEC of a thin object at $z = z_0$ with linear attenuation coefficient $\mu_0(E)$ and DFEC $\mu_{\mathrm{d},0}(E)$ is then

$$\begin{aligned}\overline{\mu_{\mathrm{d},0}} &= -\frac{\partial \ln \overline{D}}{\partial z_0} \overset{(6.13)}{=} \left\langle \mu_{\mathrm{d},0} + \mu_0 \right\rangle_{DTV_0\psi_0} - \left\langle \mu_0 \right\rangle_{T\psi_0} \\ &\overset{(6.7)}{=} \left\langle \mu_{\mathrm{d},0} \right\rangle_{DTV_0\psi_0} + \left\langle \mu_0 \right\rangle_{DTV_0\psi_0} - \overline{\mu_0}. \end{aligned} \tag{6.14}$$

(calculation given in section 6.1.7b). The apparent dependence of effective DFEC on $\mu_0(E)$ illustrates the known effect of purely attenuating objects generating an apparent dark-field signal. The quantity $\left\langle \mu_0 \right\rangle_{DTV_0\psi_0} - \left\langle \mu_0 \right\rangle_{T\psi_0}$ characterizes the magnitude of this effect. This term becomes small e.g. if $\mu_0(E)$ or $D(E)V_0(E)$ are approximately constant in the energy region where the detected spectrum $T(E)\psi_0(E)$ is nonzero. That may be the case if $T(E)\psi_0(E)$ has a narrow bandwidth.

Additionally, the first term $\left\langle \mu_{\mathrm{d},0} \right\rangle_{DTV_0\psi_0}$ depends on $D(E)$, i.e. the small-angle-scattering activity of any preceding materials. As $D(E)$ is usually smaller for low energies, a presence of dark-field-active materials will shift the weighting function $D(E)T(E)V_0(E)\psi_0(E)$ towards higher energies, where $\mu_{\mathrm{d},0}(E)$ is usually lower, leading to a decreased effective DFEC $\overline{\mu_{\mathrm{d},0}}$ in the presence of other scattering materials.

6.1.4b Verification with experimental data

In order to verify the findings from the preceding calculations, Eq. (6.5) and Eq. (6.13), which describe the calculation of spectrally-averaged attenuation $\overline{T}$ and visibility reduction $\overline{D}$, were solved numerically for the measurements shown in section 6.1.3.

Since the spectral attenuation and visibility-reduction parameters of the phantom materials were not known exactly, they were formulated as functions of unknown parameters. The values of these parameters were then determined via least-squares regression of the calculated values of $-\ln \overline{D}$ and $-\ln \overline{T}$ to the corresponding experimentally-measured values.

The materials' linear attenuation coefficient can be related to tabulated total cross-sections as

$$\mu(E) = \rho\, \sigma^{(\mathrm{tot})}(E),$$

with ρ being the materials mass density. The values for the total cross-sections $\sigma^{(\mathrm{tot})}$ were retrieved using the *xraylib* library [Scho+11]. For POM, the material composition data tabulated in [NIST17] was used. EPDM is a polymer consisting of ethylene, propylene, and 0 to 12% (weight) of a diene (Dicyclopentadiene, vinyl norbornene, ethylidene norbornene or 1,4-hexadiene) [Ravi12]. In terms of elemental composition, this means EPDM is a mixture of carbon and hydrogen, with a carbon mass fraction between 85.6% and 86.2%. The empirical formula $C_{25}H_{49}$ gives a carbon mass fraction of 85.9%, and was thus assumed here.

Energy-dependent transmittance was then calculated according to Eq. (6.1). The product of thickness and mass density per layer of POM or foam rubber (FR) is subsumed in multiplicative factors A_{POM}, A_{FR}, so that the energy-dependent transmittance of a stack of M POM slabs and N foam rubber sheets is given by

$$T^{(\mathrm{calc})}_{M,N}(E) = \exp\left[-M\, A_{\mathrm{POM}} \sigma^{(\mathrm{tot})}_{\mathrm{POM}}(E) - N\, A_{\mathrm{FR}} \sigma^{(\mathrm{tot})}_{\mathrm{FR}}(E) \right]. \tag{6.15}$$

On the other hand, the materials' energy-dependent dark-field extinction coefficient (DFEC) can not be directly derived from tabulated values: As shown in [Stro14], the logarithmic dark-field is a function of both the macroscopic scattering cross-section Σ and the real-space autocorrelation function $G(\xi)$ of the material's electron density:

$$-\ln D(E) = \int_0^\infty \Sigma(z,E)\,[1 - G(z,\xi)]\, dz, \tag{6.16}$$

where $\xi = hcd_0/(Ep_0)$ if the sample is placed upstream of G_1, at a distance d_0 from the source grating G_0. Thus, both Σ and G have an energy-dependence (Σ is proportional to E^{-2}), but G is additionally dependent on the geometry of the sample's microstructure. $G(\xi)$ has been derived for various types of structures [Ande+08], but is difficult to determine for a foam with multiple

unknown structural parameters (e.g., wall thickness and size distribution of foam cells).

Given the smooth surface and high density of the POM slabs, they were assumed to be homogeneous on the length scale of the sampled ξ values, and thus to generate no dark-field signal ($G_{\mathrm{POM}} \approx 1$).

For the foam rubber, we assumed that $1 - G(\xi)$ in Eq. (6.16) has a power-law dependence on photon energy, i.e. $\propto E^C$, with an unknown exponent $C < 0$. Since the structure-independent term Σ is proportional to E^{-2}, the full integrand then has a photon energy dependence with exponent $C-2$. This fulfills the condition that $\lim_{\xi\to 0}[1 - G(\xi)] = 0$ for any $C < 0$.

The model is less appropriate for the long-wavelength limit, since $\lim_{\xi\to\infty}[1 - G(\xi)] \propto \lim_{E\to 0} E^C = \infty$, instead of the correct value 1. However, $1 - G(\xi)$ only approaches 1 when ξ is near the "characteristic length scale" of the object's microstructure. Although we do not know of an analytical solution of $G(\xi)$ for cellular foams, this holds for many different geometries [Ande+08]. Given that the cell dimensions of the foam rubber are around 1 mm, with cell wall thicknesses on the order of 100 µm, we expect the structure's characteristic length to be in this range. On the other hand, for the used spectrum and filtering, significant flux is only achieved in the interval of photon energies from 25 to 60 keV, which is equivalent to $0.5\,\mu\mathrm{m} < \xi < 1.1\,\mu\mathrm{m}$ (for objects on the sample table), i.e. a very narrow range far below the length scale of the foam structures. Using Eq. (6.9), the dark-field signal of M POM slabs and N foam sheets is thus modeled as

$$D^{(\mathrm{calc})}_{M,N}(E) = \exp\left[-N\,B_{\mathrm{FR}}\left(\frac{E}{E_0}\right)^{C_{\mathrm{FR}}-2}\right], \qquad (6.17)$$

with $E_0 = 40\,\mathrm{keV}$. Thus, B_{FR} encodes the material's overall scattering strength (the logarithmic dark-field per foam sheet at a hypothetical illumination with a photon energy of 40 keV), and C_{FR} determines the signal's dependence on photon energy.

The spectrum produced by the X-ray tube was determined with simulations in PENELOPE / PENEPMA [Llov+16] for a tungsten target and a take-off angle of 11 deg, equal to the X-ray tube's anode angle (i.e., assuming emission of radiation perpendicular to the electron beam). Exact values for tube filtration were not available, but from a schematic in [Behl90], an approximate filtration of 5 mm Al and 9 mm of transformer oil (assumed empirical formula CH_2, $\rho = 0.8\,\mathrm{g\,cm^{-3}}$) was estimated. Filtration due to the gratings was applied, taking their duty cycles and substrate thicknesses into account (see Table 3.1 on page 79). Energy-dependent detection efficiency was modeled using the degree of X-ray attenuation of the used detector's scintillation layer (600 µm of cesium iodide).

Visibility spectra $V_0(E)$ of the setup were simulated using a software module developed at the Chair of Biomedical Physics, Technical University of Munich. The software calculates intensity modulations via Fresnel propagation of coherent wave fields. Additionally, the effects of a finite width of the source grating slots, and of the phase-stepping process are taken into account by appropriate convolution of intensity profiles. Visibility values are calculated from the intensity modulations using Fourier analysis. Fresnel propagation and subsequent calculations are performed with monochromatic radiation, and repeated at equidistantly-spaced X-ray energies (from 0 to 60 keV, at 0.5 keV intervals). Due to the relatively large impact of G_1 absorber height on the visibility spectra (likely due to phase-shifting effects), a series of spectra was generated for the total range of G_1 absorber heights (from 150 µm to 200 µm in steps of 2.5 µm), and then averaged.

Calculation of spectrally-averaged transmittance and dark-field was done by solving Eq. (6.5) and Eq. (6.13), and substituting T and D in these equations with $T^{(\mathrm{calc})}_{M,N}$ and $D^{(\mathrm{calc})}_{M,N}$ from Eq. (6.15) and Eq. (6.17). This was done for all numbers of POM slabs ($M = 1\ldots4$) and rubber sheets ($N = 0\ldots5$), applying the rectangle rule with a discretization of the integrands to 0.5 keV intervals.

The resulting spectrally-averaged, logarithmic transmittance and dark-field values $-\ln\overline{T}^{(\mathrm{calc})}_{M,N}$, $-\ln\overline{D}^{(\mathrm{calc})}_{M,N}$ for each thickness combination (M, N) were then compared to the equivalent experimental values $-\ln\overline{T}^{(\mathrm{m})}_{M,N}$, $-\ln\overline{D}^{(\mathrm{m})}_{M,N}$ (cf. Fig. 6.3), and the sum of squared residuals

$$\mathscr{S} = \sum_{M,N}\left[\ln\overline{D}^{(\mathrm{calc})}_{M,N} - \ln\overline{D}^{(\mathrm{m})}_{M,N}\right]^2 + \left[\ln\overline{T}^{(\mathrm{calc})}_{M,N} - \ln\overline{T}^{(\mathrm{m})}_{M,N}\right]^2$$

was minimized by variation of the parameters A_{POM}, A_{FR}, B_{FR}, C_{FR} (SciPy 1.4.1 [Virt+20], BFGS algorithm). The procedure is illustrated in Fig. 6.5a. The optimized parameters are summarized in the first row of Table 6.1, and a visual comparison of simulated and measured

values is shown in Fig. 6.6 (left). The limited agreement between measurement and simulation was ascribed to a greater than expected presence of Compton scatter, even in the measurements with the absorbing material placed below the G_0 grating.

The large difference of signal levels between the two sets of measurements (cf. Fig. 6.3) suggests that the impact of Compton scatter is significantly higher in the data set with the POM on the table. Regression of the original model to this data set is not shown, since the model's implicit assumption (no impact of Compton scatter) is clearly not applicable (even less than for the other data set).

In order to show that both data sets still conform to the theoretical model at the beginning of this section, we introduce a simple estimation of the effect of a given amount of Compton scatter on signal levels (details given in section 6.1.7c). In this approach, the degree of signal distortion due to Compton scatter is quantified by the ratio γ of detected Compton scatter and non-scattered radiation transmitted by the sample. This fraction is expected to vary both with the number of used POM slabs, as well as their placement in the beam. Thus, the parameter γ_M is assumed to be applicable to all measurements with M POM slabs (transmittance and dark-field for all thicknesses of foam rubber).

Determination of γ_M (for $M = 1,\ldots,4$) is added to the optimization process of the original model, as illustrated in Fig. 6.5b: The sum of squared residuals $\mathscr{S}$ is now calculated from the Compton-corrected and measured signal levels. This optimization was performed for both data sets, resulting in a set of eight optimal parameters each.

6.1.4c Simulation results

The optimized parameters for all variations of the minimization process are summarized in Table 6.1. As expected, the Compton fractions γ increase with the number of POM slabs, and the values are consistently higher when the slabs are placed on the table, i.e. closer to the detector. A_{POM} and A_{FR} are close to the experimentally accessible values of $\rho_{\mathrm{POM}} L_{\mathrm{POM}} \approx 4.51\,\mathrm{g\,cm^{-2}}$ and $\rho_{\mathrm{FR}} L_{\mathrm{FR}} \approx 0.16\,\mathrm{g\,cm^{-2}}$. Furthermore, the dark-field and attenuation values derived from these parameters are shown in an overlay with the measurement values in Fig. 6.6.

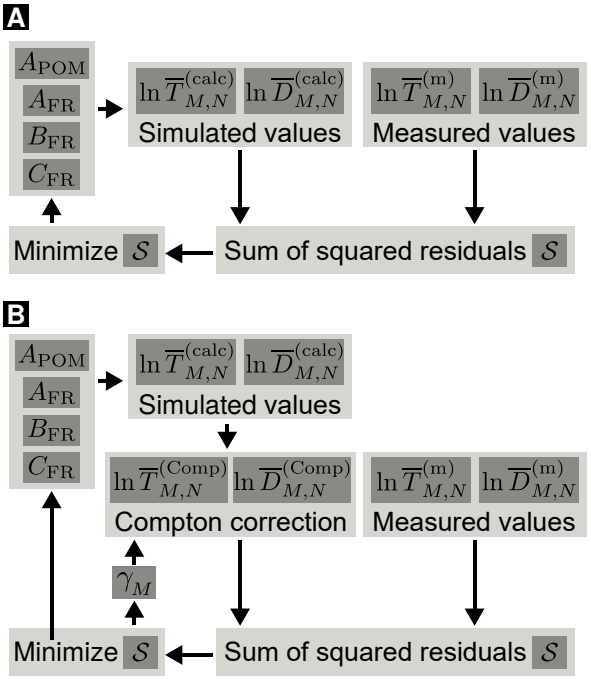

Figure 6.5: Employed minimization procedures for determination of model parameters. (a): The parameters A_{POM}, A_{FR}, B_{FR}, and C_{FR} are found by minimizing the sum of squared residuals between measured and simulated logarithmic transmittance and dark-field. (b): Extended model incorporating Compton scatter. The additional parameters γ_M ($M = 1,\ldots,4$) are used to characterize the amount of detected Compton-scattered radiation for each POM height.

6.1.5 Discussion

In this work, we have shown measurements of attenuation and dark-field signal levels of a phantom with well-defined thicknesses of absorbing and (small-angle) scattering material. We find a nonlinearity in the dark-field signal levels, which we tentatively call *visibility-hardening* and which has not yet been described or explained in literature. We present a theoretical model for spectrally-averaged transmittance and dark-field, and validate this model by comparison to measurement data. The model includes both known effects (the influence of beam-hardening on attenuation and dark-field signal), as well as the observed visibility-hardening effect.

	A_{POM} [g/cm^2]	A_{FR} [g/cm^2]	B_{FR}	C_{FR}	γ_1	γ_2	γ_3	γ_4	$\mathscr{S}$
POM below G_0, no Compton corr.	4.357	0.1348	0.2823	−2.695	—	—	—	—	4.55×10^{-2}
POM below G_0, with Compton corr.	4.462	0.1454	0.2388	−2.203	0.041	0.062	0.082	0.097	3.21×10^{-4}
POM on table, with Compton corr.	4.617	0.1474	0.2465	−2.532	0.088	0.156	0.222	0.286	1.55×10^{-3}

Table 6.1: Parameters of theoretical model providing the best match with measurement data.

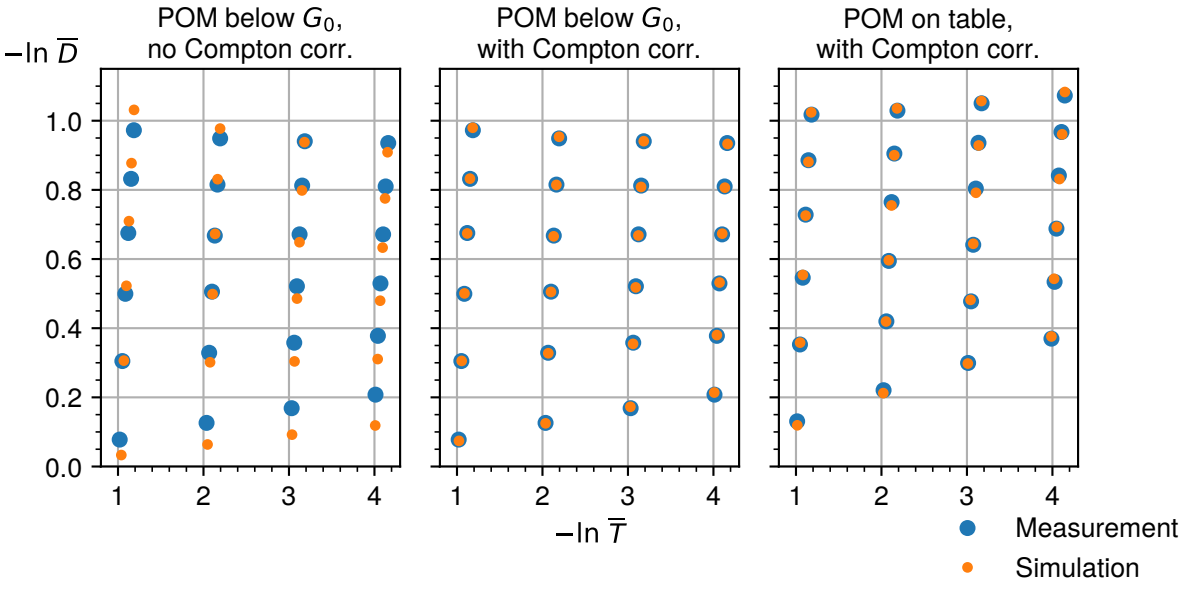

Figure 6.6: Comparison of simulated and measured signal levels (logarithmic transmission, dark-field), after optimization of signal strength and Compton scatter parameters. The determined optimal parameters are summarized in Table 6.1.

We have largely ignored the influence of the differential phase shift signal on the dark-field modality. This was done since the used imaging setup is optimized for large, dark-field-active samples (i.e., animal or human lungs), and therefore has low angular sensitivity, resulting in weak differential-phase signals. We have found the differential-phase modality to carry little useful information in lung imaging, but it is possible that the phase signal from superimposed ribs may distort dark-field signal levels. We are aware of existing work on this issue [Pelz+16], and provide a general equation to calculate spectrally-averaged visibility in the presence of phase shift in section 6.1.7d.

The impact of Compton scatter on the measurements was initially underestimated. Due to changes to the experimental setup, the original arrangement could not be reproduced and the Compton fractions $\gamma_1, \ldots, \gamma_4$ thus could not be measured retroactively, motivating the optimization procedure shown here. The trend of the determined Compton fractions is reasonable: greater values are achieved for larger amounts of absorbing material, and values are higher overall with the material closer to the detector.

The approach is also supported by the good agreement of the remaining fit parameters in the extended model between the two data sets ($< 4\%$ deviation of A_{POM}, A_{FR}, B_{FR}, $\approx 8\%$ of the exponent $C_{\mathrm{FR}} - 2$). Qualitatively, it is clear from the fit without Compton corrections that the observed decrease of DFEC for strong dark-field signal is reproduced by the model, regardless of additional corrections. Furthermore, since the Compton correction applies the same change to $-\ln \overline{D}$ and $-\ln \overline{T}$ for data with identical amounts of POM, it is unable to modify the dark-field signal added by foam rubber, and thus does not encroach upon the visibility-hardening effect.

In principle, the presented findings could be used to correct for *visibility-hardening*: Using measurements from a phantom such as the one used here as calibration, measured dark-field signals could be "relinearized": a quantity could be derived from measured values of $-\ln \overline{D}$ and $-\ln \overline{T}$, which is proportional to the thickness of a (macroscopically homogeneous) small-angle-scattering material. This signal would more accurately express the "scattering power" of the sample, and produce greater contrast between regions of high and low dark-field signal (e.g. healthy and emphysematous regions of the lung).

Additionally, we think that such a correction would be important for dark-field CT measurements: In the presence of strong visibility-hardening, dark-field "cupping artifacts", equivalent to those in conventional CT, would occur due to the decreasing effective DFEC at high sample thickness.

However, such a correction would require the use of phantom materials with an energy-dependent DFEC $\mu_{\mathrm{d}}(E)$ comparable to that of the sample. Finding these may be challenging and probably necessitate comparative spectral dark-field measurements. On the other hand, it may be possible that an approximate similarity (e.g., similar diameter of foam rubber cells and lung *alveoli*) allows a sufficiently precise correction.

Due to the design of the grating arrangement in the *lung-scanning setup*, its visibility spectrum has an unusual shape: visibility peaks for very low photon energies and then continuously decreases. This may lead to a greater magnitude of the "visibility-hardening" effect than in a normal Talbot-Lau setup, where a visibility peak is located at the setup design energy, and typically near the peak of the source spectrum. On the other hand, the effect also increases with the range of achieved dark-field signal levels, implying that setups with high angular sensitivity are especially susceptible. In either case, we suggest that the magnitude of visibility-hardening is estimated [experimentally, or using Eqs. (6.13), (6.14)] when interpreting dark-field signal levels.

6.1.6 Acknowledgment

The authors wish to thank Wolfgang Noichl and Theresa Urban for their help and fruitful discussions. This work was carried out with the support of the Karlsruhe Nano Micro Facility (KNMF, www.kit.edu/knmf), a Helmholtz Research Infrastructure at Karlsruhe Institute of Technology (KIT). We acknowledge the support of the TUM Institute for Advanced Study, funded by the German Excellence Initiative.

6.1.7 Detailed calculations

6.1.7a Calculation of effective linear attenuation coefficient

We find that

$$\frac{\partial\psi(E)}{\partial z_0} \overset{(6.3)}{=} \frac{\partial T(E)}{\partial z_0}\psi_0(E) \overset{(6.1)}{=} -\mu(E,z_0)T(E)\psi_0(E) \overset{(6.3)}{=} -\mu_0(E)\psi(E), \tag{6.18}$$

where we have used the abbreviation $\mu_0(E)$ for $\mu(E,z_0)$. Using this result, we can calculate the derivative of the negative logarithm of Eq. (6.5) w.r.t. z_0:

$$\begin{aligned}\overline{\mu}(z_0) &= -\frac{\partial \ln\overline{T}}{\partial z_0} = -\frac{1}{\overline{T}}\frac{\partial\overline{T}}{\partial z_0} \\ &\overset{(6.5)}{=} -\frac{\int_0^\infty \psi_0(E)dE}{\int_0^\infty \psi(E)dE}\frac{\partial}{\partial z_0}\left[\frac{\int_0^\infty \psi(E)dE}{\int_0^\infty \psi_0(E)dE}\right] \\ &= -\frac{\frac{\partial}{\partial z_0}\left[\int_0^\infty \psi(E)dE\right]}{\int_0^\infty \psi(E)dE} = -\frac{\int_0^\infty \frac{\partial\psi}{\partial z_0}(E)dE}{\int_0^\infty \psi(E)dE} \\ &\overset{(6.18)}{=} \frac{\int_0^\infty \psi(E)\mu_0(E)dE}{\int_0^\infty \psi(E)dE} \overset{(6.4)}{=} \left\langle\mu_0\right\rangle_\psi. \end{aligned} \tag{6.19}$$

6.1.7b Calculation of effective dark-field extinction coefficient

In equivalence to Eq. (6.18), we find that

$$\begin{aligned}\frac{\partial V(E)}{\partial z_0} &\overset{(6.9)}{=} \frac{\partial D(E)}{\partial z_0}V_0(E) \overset{(6.9)}{=} -\mu_{\mathrm{d}}(E,z_0)D(E)V_0(E) \\ &= -\mu_{\mathrm{d},0}(E)V(E). \end{aligned} \tag{6.20}$$

Using Eq. (6.18) and Eq. (6.20), we can calculate the effective dark-field extinction coefficient:

$$\begin{aligned}\overline{\mu_{\mathrm{d},0}} &= -\frac{\partial\ln\overline{D}}{\partial z_0} = -\frac{1}{\overline{D}}\frac{\partial\overline{D}}{\partial z_0} \\ &\overset{(6.13)}{=} \frac{-\overline{T}}{\langle DT\rangle_{V_0\psi_0}}\frac{\partial}{\partial z_0}\left[\frac{\langle DT\rangle_{V_0\psi_0}}{\overline{T}}\right] \\ &= \frac{\partial\overline{T}/\partial z_0}{\overline{T}} - \frac{\partial\langle DT\rangle_{V_0\psi_0}/\partial z_0}{\langle DT\rangle_{V_0\psi_0}}. \end{aligned} \tag{6.21}$$

From Eq. (6.19), we know that $\frac{\partial\overline{T}/\partial z_0}{\overline{T}} = -\left\langle\mu_0\right\rangle_\psi$. Calculation of $\partial\langle DT\rangle_{V_0\psi_0}/\partial z_0$ requires the product rule:

$$\begin{aligned}\frac{\partial\langle DT\rangle_{V_0\psi_0}}{\partial z_0} &= \frac{\partial}{\partial z_0}\left[\frac{\int_0^\infty D(E)T(E)V_0(E)\psi_0(E)dE}{\int_0^\infty V_0(E)\psi_0(E)dE}\right] \\ &= \frac{\int_0^\infty \frac{\partial}{\partial z_0}\left[D(E)T(E)\right]V_0(E)\psi_0(E)dE}{\int_0^\infty V_0(E)\psi_0(E)dE}. \end{aligned} \tag{6.22}$$

The derivative follows from Eq. (6.18) and Eq. (6.20):

$$\begin{aligned}\frac{\partial}{\partial z_0}\left[D(E)T(E)\right] &= \frac{\partial D(E)}{\partial z_0}T(E) + \frac{\partial T(E)}{\partial z_0}D(E) \\ &= -\left[\mu_{\mathrm{d},0}(E)+\mu_0(E)\right]D(E)T(E). \end{aligned} \tag{6.23}$$

Therefore, the second term in Eq. (6.21) is

$$\begin{aligned}\frac{\partial\langle DT\rangle_{V_0\psi_0}/\partial z_0}{\langle DT\rangle_{V_0\psi_0}} &= \frac{-\int_0^\infty V_0(E)\psi_0(E)dE}{\int_0^\infty D(E)T(E)V_0(E)\psi_0(E)dE}\times \\ &\frac{\int_0^\infty\left[\mu_{\mathrm{d},0}(E)+\mu_0(E)\right]D(E)T(E)V_0(E)\psi_0(E)dE}{\int_0^\infty V_0(E)\psi_0(E)dE} \\ &= \frac{-\int_0^\infty\left[\mu_{\mathrm{d},0}(E)+\mu_0(E)\right]D(E)T(E)V_0(E)\psi_0(E)dE}{\int_0^\infty D(E)T(E)V_0(E)\psi_0(E)dE} \\ &= -\left\langle\mu_{\mathrm{d},0}+\mu_0\right\rangle_{DTV_0\psi_0}, \end{aligned} \tag{6.24}$$

and thus, via Eq. (6.21),

$$\overline{\mu_{\mathrm{d},0}} = \left\langle\mu_{\mathrm{d},0}+\mu_0\right\rangle_{DTV_0\psi_0} - \left\langle\mu_0\right\rangle_\psi. \tag{6.25}$$

6.1.7c Effect of Compton scatter on signal levels

Given an object generating attenuation and dark-field signals $\overline{T}$, $\overline{D}$ in the *absence* of Compton scatter, it reduces the mean detector signal $\overline{S_0}$ to $\overline{T}\,\overline{S_0}$, and the visibility $\overline{V_0}$ to $\overline{D}\,\overline{V_0}$ [compare Eq. (6.5) and Eq. (6.13)].

Compton scattering is incoherent, and thus adds only to the detected mean intensity, not the fringe modulation. As Compton-scattered radiation is emitted from materials in a wide angular range, and the whole field of view is covered by an attenuating slab of uniform thickness in all measurements, it is a reasonable approximation to assume a constant intensity $\overline{S_C}$ of detected Compton-scattered radiation across the field of view. In the previous scenario, this leads to an increase of the mean detected signal to $\overline{T}\,\overline{S_0}+\overline{S_C}$, whereas the amplitude of the fringe modulation remains at $\overline{V}\,\overline{T}\,\overline{S_0}$.

This leads to a *decrease* of the relative amplitude, i.e., detected visibility, namely to

$$\overline{V_C} = \frac{\overline{V}\,\overline{T}\,\overline{S_0}}{\overline{T}\,\overline{S_0} + \overline{S_C}} = \frac{\overline{V}}{1+\gamma},$$

where $\gamma = \overline{S_C}/(\overline{T}\,\overline{S_0})$. Furthermore, the measured transmission *increases* to

$$\overline{T_C} = \frac{\overline{T}\,\overline{S_0} + \overline{S_C}}{\overline{S_0}} = \overline{T}(1+\gamma).$$

The logarithmic modalities therefore change as follows:

$$-\ln \overline{T_C} = -\ln \overline{T} - \ln\left(1+\gamma\right), \tag{6.26}$$

$$-\ln \overline{D_C} = -\ln\left(\frac{\overline{V_C}}{\overline{V_0}}\right) = -\ln \overline{D} + \ln\left(1+\gamma\right). \tag{6.27}$$

The two modalities are thus affected by the same additive (subtractive) constant $\ln(1+\gamma)$. This correction function is applied to the simulated signal values, using separate values for γ for each number and placement of POM slabs.

6.1.7d Calculation of visibility reduction with dispersion

The monochromatic signal model in Eq. (6.8) can be expanded by an energy-dependent phase shift $\Phi(E)$, so that

$$S_{\mathrm{mod}}(\varphi, E) = S(E)\{1 + V(E)\cos[\varphi - \Phi(E)]\},$$

and equivalently to Eqs. (6.10), (6.11) in the main text, it follows for the polychromatic case that

$$\begin{aligned}\overline{S_{\mathrm{mod}}}(\varphi) &= \int_0^\infty \frac{\partial S_{\mathrm{mod}}}{\partial E}\,dE \\ &= \int_0^\infty \psi(E)\,dE + \int_0^\infty \psi(E)V(E)\cos\left[\varphi - \Phi(E)\right]dE.\end{aligned} \tag{6.28}$$

The second term on the right-hand side can be expanded:

$$\begin{aligned}&\int_0^\infty \psi(E)V(E)\cos\left[\varphi - \Phi(E)\right]dE \\ &= \cos(\varphi)\int_0^\infty \psi(E)V(E)\cos\left[\Phi(E)\right]dE \\ &+ \sin(\varphi)\int_0^\infty \psi(E)V(E)\sin\left[\Phi(E)\right]dE.\end{aligned} \tag{6.29}$$

Taken as a function of φ, the two terms are in quadrature and the total amplitude is thus

$$\begin{aligned}\mathscr{A} = \Bigg(&\left\{\int_0^\infty \psi(E)V(E)\cos\left[\Phi(E)\right]dE\right\}^2 + \\ &\left\{\int_0^\infty \psi(E)V(E)\sin\left[\Phi(E)\right]dE\right\}^2\Bigg)^{1/2}.\end{aligned} \tag{6.30}$$

To retrieve the effective visibility, this amplitude must be divided by the mean flux, i.e., the first integral on the right-hand side in Eq. (6.28):

$$\begin{aligned}\overline{V} = \frac{\mathscr{A}}{\int_0^\infty \psi(E)\,dE} &= \Bigg(\left\{\frac{\int_0^\infty \psi(E)V(E)\cos[\Phi(E)]dE}{\int_0^\infty \psi(E)dE}\right\}^2 \\ &+ \left\{\frac{\int_0^\infty \psi(E)V(E)\sin[\Phi(E)]dE}{\int_0^\infty \psi(E)dE}\right\}^2\Bigg)^{-1/2} \\ &= \sqrt{\langle V\cos\Phi\rangle_\psi^2 + \langle V\sin\Phi\rangle_\psi^2}.\end{aligned} \tag{6.31}$$

In the presence of non-negligible phase shift, Eq. (6.31) supersedes Eq. (6.12). The calculation of $\overline{V}_0$ should remain unchanged as long as the reference scans are acquired without objects in the beam.

6.2 Description of Talbot-Lau imaging with partial coherence theory

In this section, an alternative mathematical model for the contrast generation in Talbot-Lau imaging setups, based on partial coherence theory, is introduced. In section 6.2.1, the most commonly used approach based on Fresnel propagation, and its limitations, are introduced. Some fundamentals of partial coherence theory are given in section 6.2.2, and a thorough calculation of a three-grating Talbot-Lau system based on the concept of "cross-spectral density" is presented in section 6.2.3.

6.2.1 Fresnel propagation

The conventional method to determine X-ray intensities generated by a grating-based imaging setup is to calculate near-field diffraction patterns generated by the setup's modulation grating G_1 (i.e., self-images) by Fresnel propagation (cf. section 2.1 on page 33) to the detection plane. Results of plane-wave illumination of G_1 may be converted to those resulting from illumination by a point source ("cone-beam illumination") using the Fresnel scaling theorem (see section 2.5.7 on page 59).

The effect of the finite source size is then modeled by convolution of the detected intensity patterns with the source intensity profile, rescaled according to the relative distances of source and detection plane to the modulation grating. The source intensity profile is either defined by the focal spot, or if a source grating (G_0) is used, by the transmission profile of a single period of the source grating.

Finally, given the high-resolution intensity profiles in the detection plane, the detection process itself may be simulated. Most commonly, stepping curves are generated by convolution of these profiles with the transmission function of an analyzer grating. Visibility, flux and phase shift are then evaluated from the parameters of this stepping curve.

In order to characterize the setup as a function of X-ray energy, the entire process must be repeated for each X-ray wavelength of interest. Polychromatic performance can be simulated by summation of intensity values from successive simulations with different wavelengths.

Direct propagation of the field from the source plane to G_1, and from there to the detection plane, is not possible with Fresnel propagation if the source has finite spatial coherence. The reason for this is that a partially coherent field cannot be exhaustively expressed by a scalar field as a function of only one spatial variable. This is why the convolution approach mentioned above is necessary.

However, the theory of partial coherence allows expressing fields of arbitrary coherence and their propagation, allowing the theoretical, direct calculation of grating-based imaging systems with arbitrary illumination.

6.2.2 Partial coherence theory

The introduction presented here roughly follows section 5.2 from [Good85]. The intensity measured at a point $\vec{r}$ and a time near t is determined by the scalar field $U(\vec{r},t)$ as

$$I(\vec{r}) = \left\langle \left| U(\vec{r},t)^2 \right| \right\rangle_t , \tag{6.32}$$

where $\langle\cdot\rangle_t$ denotes an averaging in a small time interval around t. This averaging is relevant even for very short exposure times, since the variation of U with t is extremely fast: We know that $U(\vec{r},t) \propto \exp(-i\omega t)$, where, for example, $\omega = 2\pi c/\lambda \approx 3\cdot 10^{19}\,\mathrm{s}^{-1}$ for radiation with $E = 20\,\mathrm{keV}$. If $U(\vec{r},t)$ is a plane wave, this averaging process does not affect the result. If however, $U(\vec{r},t)$ is the result of illumination by two separate point sources $U_a(\vec{r}_a,t)$, $U_b(\vec{r}_b,t)$, we can write

$$U(\vec{r},t) = c_a U_a\left(\vec{r}_a, t - \frac{d_a}{c}\right) + c_b U_b\left(\vec{r}_b, t - \frac{d_b}{c}\right), \tag{6.33}$$

where $d_a = |\vec{r} - \vec{r}_a|$, $d_b = |\vec{r} - \vec{r}_b|$, and c_a, c_b are constants depending on d_a, d_b. Inserting Eq. (6.33) in Eq. (6.32) yields the relation

$$I(\vec{r}) = I_a + I_b + 2\mathrm{Re}\left[c_a^* c_b \cdot \Gamma_{ab}\left(\frac{d_b - d_a}{c}\right)\right], \tag{6.34}$$

where

$$\begin{aligned} I_a &= |c_a|^2 \left\langle \left| U_a\left(\vec{r}_a, t - \frac{d_a}{c}\right)\right|^2 \right\rangle_t , \\ I_b &= |c_b|^2 \left\langle \left| U_b\left(\vec{r}_b, t - \frac{d_b}{c}\right)\right|^2 \right\rangle_t , \\ \Gamma_{ab}(\tau) &= \left\langle U_a^*(\vec{r}_a,t)\, U_b(\vec{r}_b, t-\tau)\right\rangle_t . \end{aligned} \tag{6.35}$$

Intuitively, I_a and I_b are the intensities which would occur at $\vec{r}$ if only the point source at $\vec{r}_a$ or $\vec{r}_b$ were present. Note that the light travel times d_a/c, d_b/c do not usually affect I_a or I_b, but are crucial for the additional term Γ_{ab}: The average in Eq. (6.35) can be understood as a (temporal) cross-correlation function of U_a and U_b evaluated at a relative shift of $\tau = (d_b - d_a)/c$. $\Gamma_{ab}(\tau)$ is called the *mutual coherence function* and is a measure for the amount of coherence between the fields originating from $\vec{r}_a$ and $\vec{r}_b$:

If $\Gamma_{ab}(\tau) = 0$, the fields are said to be (mutually) completely incoherent, and the measured intensity $I(\vec{r})$ is simply $I_a + I_b$. This would be expected for ordinary, low-coherence light sources. However, if there is a known phase relation between the two light sources, e.g.

$$U_a(\vec{r}_a, t) = U_b(\vec{r}_b, t) = U(t) \text{ and } c_a = c_b = 1,$$

$\Gamma_{ab}(\tau)$ would vary with $\tau = (d_b - d_a)/c$: For $d_b - d_a = 0, \pm\lambda, \pm 2\lambda, \ldots$, the two fields add up constructively, $\Gamma_{ab}(\tau) = \langle |U(t)|^2 \rangle_t$, and $I(\vec{r}) = 4\langle |U(t)|^2 \rangle_t$. Conversely, for $d_b - d_a = \pm\lambda/2, \pm 3\lambda/2, \ldots$, the fields interact destructively, $\Gamma_{ab}(\tau) = -\langle |U(t)|^2 \rangle_t$, and thus $I(\vec{r}) = 0$.

In the double-slit experiment, a light source illuminates a mask with two narrow slits. These slits act as secondary light sources which produce interference fringes on a downstream screen. Replacing the slits by small point-like apertures, we can identify these by the two light sources U_a and U_b at $\vec{r}_a$ and $\vec{r}_b$ in our example. The intensity at a location $\vec{r}$ on the screen is thus given by Eq. (6.34). The observed intensity modulations as a function of $\vec{r}$ thus provide information about $\Gamma_{ab}(\tau)$, i.e. the degree of coherence between fields at $\vec{r}_a$ and $\vec{r}_b$ (I_a and I_b may also vary with $\vec{r}$, but much more slowly).

6.2.3 Application to Talbot-Lau imaging

6.2.3a Cross-spectral density

Since the Talbot-Lau interferometer is commonly used with polychromatic illumination, it is useful to immediately consider the case of wideband polychromatic radiation. Besides the mutual coherence function, a number of other variables for quantifying partial coherence exist, see e.g. [Good85, Table 5-1] for an overview. In the following, we follow an approach used in [Sudo+81] and generalize the calculation presented there. To characterize spatial coherence (i.e. the case of $\vec{r}_a \neq \vec{r}_b$ and $\tau = 0$), the most commonly used quantities is the *complex coherence factor*

$$\mu_{ab} = \frac{\Gamma_{ab}(0)}{\sqrt{\Gamma_{aa}(0)\Gamma_{bb}(0)}},$$

which is however only applicable to quasi-monochromatic radiation. A more general quantity can be introduced by first defining the temporal Fourier transform of $U(\vec{r}, t)$:

$$V(\vec{r}, \omega) = \mathscr{F}[U(\vec{r}, t)] = \frac{1}{2\pi} \int_{-\infty}^{\infty} U(\vec{r}, t)\, e^{i\omega t}\, dt.$$

The similarity of V at different locations $\vec{r}_a$, $\vec{r}_b$ is then characterized by the *cross-spectral density (CSD)* W_{ab} [Mand+76]:

$$\boxed{\left\langle V(\vec{r}_a, \omega)\, V^*\left(\vec{r}_b, \omega'\right)\right\rangle = W_{ab}(\vec{r}_a, \vec{r}_b, \omega)\, \delta\left(\omega - \omega'\right).} \tag{6.36}$$

This allows to describe spatial coherence between any two points $\vec{r}_a$, $\vec{r}_b$, as a function of (angular) frequency $\omega = 2\pi c/\lambda$. Since V is not dependent on time, $\langle\cdot\rangle$ here denotes an *ensemble* average. The Dirac delta in Eq. (6.36) expresses that the Fourier transforms of the fields at two different frequencies are always uncorrelated. In particular, W is the Fourier transform of the mutual coherence function [Mand+95, sec. 4.3]:

$$W_{ab}(\omega) = \int_{-\infty}^{\infty} \Gamma_{ab}(\tau) e^{-i\omega\tau}\, d\tau.$$

Two more pieces of information are required to allow the calculation of intensities in an (idealized) Talbot-Lau interferometer: The effect of a structure (grating) with a spatially variable amplitude transmittance, and the effect of free-space propagation on W.

We assume that the Talbot-Lau setup consists of parallel gratings which are normal to the propagation direction.

In this case, the setup can be assumed to be translationally invariant in the direction parallel to the grating ridges.

The gratings are thus characterized by an amplitude transmittance $t(x)$, where x is orthogonal both to the grating ridges and the axis of propagation.

Amplitude transmittance is taken as the ratio of the *complex* amplitudes just behind and just before the object. It is related to intensity transmittance $T(x)$ and phase shift $\varphi(x)$:

$$t(x) = \frac{U^+(x)}{U^-(x)} = \sqrt{T(x)}\, e^{i\varphi}.$$

In the following, we use the superscripts " + " and " − " to describe the field downstream and upstream of an object, respectively. It can be shown that, for a field passing through an object with transmittance $t(x)$, its cross-spectral density changes according to [Sudo+81]

$$\boxed{W^+(x_a,x_b,\omega) = t(x_a,\omega)\,t^*(x_b,\omega)\,W^-(x_a,x_b,\omega),} \tag{6.37}$$

where the asterisk denotes complex conjugation. Finally, free-space propagation of W can be achieved in an approach similar to Fresnel propagation. However, since cross-spectral density is dependent on two spatial variables, a double integration is necessary. This is derived in [Mand+95, section 4.4.2]: an approximate formula for cases where the propagation distance is much larger than the wavelength is given in Eq. (4.4-18). Adapted to the notation used here, it reads

$$W(\vec{s}_a,\vec{s}_b,\omega) = \left(\frac{k}{2\pi}\right)^2 \iint_{(z=0)} W(\vec{r}_a,\vec{r}_b,\omega)\times \frac{e^{ik(R_b-R_a)}}{R_a R_b}\cos\theta_a\cos\theta_b\, d^2r_a\, d^2r_b\,. \tag{6.38}$$

Here, $\vec{r}_a$ and $\vec{r}_b$ are in the plane $z=0$, $\vec{s}_a$ and $\vec{s}_b$ are arbitrary vectors in the downstream volume $z>0$. $R_a = \|\vec{s}_a - \vec{r}_a\|$, $R_b = \|\vec{s}_b - \vec{r}_b\|$, and θ_a, θ_b are the angles of $\vec{s}_a - \vec{r}_a$ and $\vec{s}_a - \vec{r}_a$ with respect to the plane at $z=0$.

This equation can be simplified using several assumptions: First, that $\vec{s}_a$ and $\vec{s}_b$ are located in the same plane $z=z_0$, and furthermore that W depends only on one component of the spatial coordinates. This allows reducing the four-dimensional integration to a two-dimensional one. Finally, the paraxial approximation gives $\cos\theta_a \approx \cos\theta_b \approx 1$, and a second-order Taylor approximation of $R_b - R_a$ can be performed as for Fresnel propagation. The resulting simplified form of Eq. (6.38) is then given by

$$\boxed{W(u_1,u_2,\omega) \approx \frac{1}{\lambda z_0}\iint_{-\infty}^{\infty} W(x_1,x_2,\omega)\times \exp\left\{\frac{ik}{2z_0}\left[(x_1-u_1)^2-(x_2-u_2)^2\right]\right\} dx_1\,dx_2,} \tag{6.39}$$

which is similar to the form used in [Sudo+81]. Note that x_1, x_2 are coordinates of two different points along the same axis, not orthogonal coordinates.

6.2.3b Calculation steps

The calculation steps and used variable names are illustrated in Fig. 6.7.

We assume the source to be located immediately upstream of the source grating, and to be spatially completely incoherent:

$$W^-_{G0}(x_1,x_2,\omega) = i_\omega(x_1)\,\delta(x_1-x_2). \tag{6.40}$$

The attenuating and/or phase-shifting effect of the source grating is calculated according to Eq. (6.37):

$$W^+_{G0}(x_1,x_2,\omega) = g(x_1,\omega)\,g^*(x_2,\omega)\,W^-_{G0}(x_1,x_2,\omega), \tag{6.41}$$

with $g(x,\omega)$ is the grating's amplitude transmission function. Propagation of W to the G_1 grating is achieved using Eq. (6.39):

$$W^-_{G1}(u_1,u_2,\omega) \approx \frac{1}{\lambda L}\iint_{-\infty}^{\infty} W^+_{G0}(x_1,x_2,\omega)\times, \exp\left\{\frac{ik}{2L}\left[(x_1-u_1)^2-(x_2-u_2)^2\right]\right\} dx_1\,dx_2. \tag{6.42}$$

The amplitude transmission function of the modulation grating $t(u,\omega)$ is then applied:

$$W^+_{G1}(u_1,u_2,\omega) = t(u_1,\omega)\,t^*(u_2,\omega)\,W^-_{G1}(u_1,u_2,\omega), \tag{6.43}$$

and finally, W^+_{G1} is propagated by a distance d to the detection plane:

$$W_F(y_1,y_2,\omega) \approx \frac{1}{\lambda d}\iint_{-\infty}^{\infty} W^+_{G1}(u_1,u_2,\omega)\times \exp\left\{\frac{ik}{2d}\left[(u_1-y_1)^2-(u_2-y_2)^2\right]\right\} du_1\,du_2. \tag{6.44}$$

The measured quantity is an intensity, which is given by:

$$I_F(y,\omega) = W_F(y,y,\omega). \tag{6.45}$$

6.2.3c Calculation

The steps introduced in the previous paragraph are now combined: Inserting Eq. (6.40) into Eq. (6.41) yields

$$\begin{aligned} W^+_{G0}(x_1,x_2,\omega) &= g(x_1)\,g^*(x_2)\,i_\omega(x_1)\,\delta(x_1-x_2) \\ &= \left|g(x_1)\right|^2 i_\omega(x_1)\,\delta(x_1-x_2). \end{aligned}$$

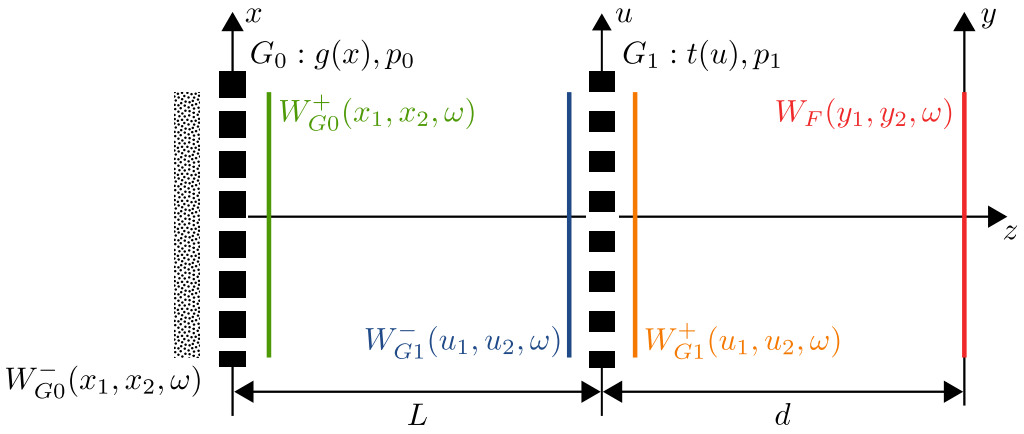

Figure 6.7: Overview of quantities used in the calculation of cross-spectral density (CSD) in the Talbot-Lau geometry. Starting from an completely incoherent wavefield with CSD W^-_{G0} upstream of G_0, the amplitude transmission function $g(x)$ of G_0 is applied to it and the resulting CSD W^+_{G0} is propagated by the G_0–G_1 distance L, yielding W^-_{G1}. Applying the amplitude transmission function $t(u)$ of G_1 results in W^+_{G1}, which is finally propagated by the G_1–detector distance d, yielding W_F. The intensity in the detection plane is finally given by $I_F(y,\omega) = W_F(y,y,\omega)$.

As mentioned in [Sudo+81], the fact that g only shows up as a magnitude square shows that any phase-shifting effects are irrelevant for this kind of illumination. Thus, instead of writing $g(x)$ as a Fourier series, we directly formulate a Fourier expansion of $|g(x)|^2$ with a fundamental period of p_0:

$$|g(x)|^2 =: G(x) = \sum_{n=-\infty}^{\infty} C_n \exp\left[\frac{2\pi i n x}{p_0}\right]. \tag{6.46}$$

Thus,

$$W^+_{G0}(x_1, x_2, \omega) = i_\omega(x_1)\delta(x_1 - x_2) \times \sum_{n=-\infty}^{\infty} C_n \exp\left[\frac{2\pi i n x_1}{p_0}\right]. \tag{6.47}$$

Eq. (6.47) is inserted in Eq. (6.42) to calculate W^-_{G1}:

$$\begin{aligned}
&W^-_{G1}(u_1, u_2, \omega) \approx \\
&\quad \frac{1}{\lambda L} \iint_{-\infty}^{\infty} \exp\left\{\frac{ik}{2L}\left[(x_1 - u_1)^2 - (x_2 - u_2)^2\right]\right\} \times \\
&\quad i_\omega(x_1)\delta(x_1 - x_2) \sum_{n=-\infty}^{\infty} C_n \exp\left[\frac{2\pi i n x_1}{p_0}\right] dx_1 dx_2 \\
&\quad = \frac{1}{\lambda L} \sum_{n=-\infty}^{\infty} C_n \iint_{-\infty}^{\infty} i_\omega(x_1)\delta(x_1 - x_2) \times \\
&\quad \exp\left\{\frac{ik}{2L}\left[(x_1 - u_1)^2 - (x_2 - u_2)^2\right] + \frac{2\pi i n x_1}{p_0}\right\} dx_1 dx_2 \\
&\quad \overset{x_1 \to x}{=} \frac{1}{\lambda L} \sum_{n=-\infty}^{\infty} C_n \int_{-\infty}^{\infty} i_\omega(x) \times \\
&\quad \exp\left\{\frac{ik}{2L}\left[(x - u_1)^2 - (x - u_2)^2\right] + \frac{2\pi i n x}{p_0}\right\} dx.
\end{aligned} \tag{6.48}$$

The exponentials can be simplified:

$$\begin{aligned}
&\frac{ik}{2L}\left[(x - u_1)^2 - (x - u_2)^2\right] + \frac{2\pi i n x}{p_0} \\
&\quad = \frac{ik}{2L}\left(u_1^2 - u_2^2\right) + \frac{ikx}{L}(u_2 - u_1) + \frac{2\pi i n x}{p_0} \\
&\quad = \frac{ik}{2L}\left(u_1^2 - u_2^2\right) + ix\left[\frac{k}{L}(u_2 - u_1) + \frac{2\pi n}{p_0}\right].
\end{aligned} \tag{6.49}$$

Inserting Eq. (6.49) into Eq. (6.48) yields:

$$W^-_{G1}(u_1,u_2,\omega) \approx \frac{1}{\lambda L}\exp\left[\frac{ik}{2L}\left(u_1^2-u_2^2\right)\right]\sum_{n=-\infty}^{\infty} C_n \times \int_{-\infty}^{\infty} i_\omega(x)\exp\left\{ix\left[\frac{k}{L}(u_2-u_1)+\frac{2\pi n}{p_0}\right]\right\}dx. \quad (6.50)$$

The integral can be solved if we assume that $i_\omega(x) =$ const., i.e. that the source grating is homogeneously illuminated:

$$\begin{aligned}\int_{-\infty}^{\infty} dx\, i_\omega(x)\exp\left\{ix\left[\frac{k}{L}(u_2-u_1)+\frac{2\pi n}{p_0}\right]\right\} \\ \rightarrow i_\omega\int_{-\infty}^{\infty} dx\exp\left\{ix\left[\frac{k}{L}(u_2-u_1)+\frac{2\pi n}{p_0}\right]\right\} \\ = 2\pi i_\omega\cdot\delta\left[\frac{k}{L}(u_2-u_1)+\frac{2\pi n}{p_0}\right], \quad (6.51)\end{aligned}$$

where $\delta[\ldots]$ represents the Dirac delta function. Here we have used that $\int_{-\infty}^{\infty}\exp(i\omega t)dt = 2\pi\delta(\omega)$. Thus,

$$W^-_{G1}(u_1,u_2,\omega) \approx \frac{2\pi i_\omega}{\lambda L}\cdot\exp\left[\frac{ik}{2L}\left(u_1^2-u_2^2\right)\right]\times \sum_{n=-\infty}^{\infty} C_n\delta\left[\frac{k}{L}(u_2-u_1)+\frac{2\pi n}{p_0}\right]. \quad (6.52)$$

Writing W^-_{G1} in this manner makes it apparent that it is a Dirac comb as a function of u_2-u_1. In other words, the periodic illumination by G_0 has been translated into a periodic cross-spectral density function. This is in accordance with the van Cittert-Zernike theorem, which states that the mutual intensity function, a quantity closely related to the cross-spectral density, is given by a Fourier transform of the source intensity distribution: The Fourier transform of a periodic function is itself periodic.

The Dirac delta can be rewritten using the knowledge that

$$\delta\left[g(u)\right] = \sum_{g(u_n)=0}\frac{\delta(u-u_n)}{\left|g'(u_n)\right|},$$

where the u_n are the roots of $g(u)$. With the argument of the Dirac delta as a function of u_1, we have only one zero ($u_{1,0} = \frac{2\pi nL}{p_0 k} + u_2$), and $\left|g'(u_{1,0})\right| = \frac{k}{L}$ (k and L are both positive). Thus:

$$\delta\left\{\left[\frac{k}{L}(u_2-u_1)+\frac{2\pi n}{p_0}\right]\right\} = \frac{L}{k}\delta\left[u_1-\left(u_2+\frac{2\pi nL}{p_0 k}\right)\right] \quad (6.53)$$

and inserting Eq. (6.53) into Eq. (6.52) yields:

$$W^-_{G1}(u_1,u_2,\omega) \approx i_\omega\exp\left[\frac{ik}{2L}\left(u_1^2-u_2^2\right)\right]\times \sum_{n=-\infty}^{\infty} C_n\delta\Big[u_1-\Big(u_2+\underbrace{\frac{2\pi nL}{p_0 k}}_{=n\lambda L/p_0}\Big)\Big] \quad (6.54)$$

Replacing k in the argument of the Dirac delta [see annotation in Eq. (6.54)] demonstrates an odd similarity between the propagation of cross-spectral density W from an incoherently illuminated grating, and the propagation of intensity I from a coherently illuminated grating, if we keep one of the spatial variables of W fixed: Both generate peaks at intervals of $\lambda L/p$. This is illustrated in Fig. 6.8.

In order to continue in the calculation, the amplitude transmission function of the modulation grating must be applied by inserting Eq. (6.54) into Eq. (6.43):

$$W^+_{G1}(u_1,u_2,\omega) = i_\omega\cdot t(u_1)t^*(u_2)\times \exp\left[\frac{ik}{2L}\left(u_1^2-u_2^2\right)\right]\sum_{n=-\infty}^{\infty} C_n\delta\left[u_1-\left(u_2+\frac{2\pi nL}{p_0 k}\right)\right] \quad (6.55)$$

We define the amplitude transmission function of G_1, $t(u)$, as a Fourier series with fundamental frequency p_1:

$$\begin{aligned} t(u) &= \sum_{m=-\infty}^{\infty} D_m\exp\left[\frac{2\pi imu}{p_1}\right] \\ \Rightarrow t^*(u) &= \sum_{m'=-\infty}^{\infty} D^*_{m'}\exp\left[\frac{-2\pi im'u}{p_1}\right]. \quad (6.56)\end{aligned}$$

Note that this differs from the Fourier series for the source grating (Eq. (6.46)), which describes the transmission of *intensity*. We insert both parts of Eq. (6.56) into Eq. (6.55):

$$W^+_{G1}(u_1,u_2,\omega) = i_\omega\cdot\sum_{m=-\infty}^{\infty}\sum_{m'=-\infty}^{\infty} D_m D^*_{m'}\times \exp\left[\frac{2\pi i}{p_1}\left(mu_1-m'u_2\right)+\frac{ik}{2L}\left(u_1^2-u_2^2\right)\right]\times \sum_{n=-\infty}^{\infty} C_n\delta\left[u_1-\left(u_2+\frac{2\pi nL}{p_0 k}\right)\right]. \quad (6.57)$$

Then, we propagate this to the detection plane [insert

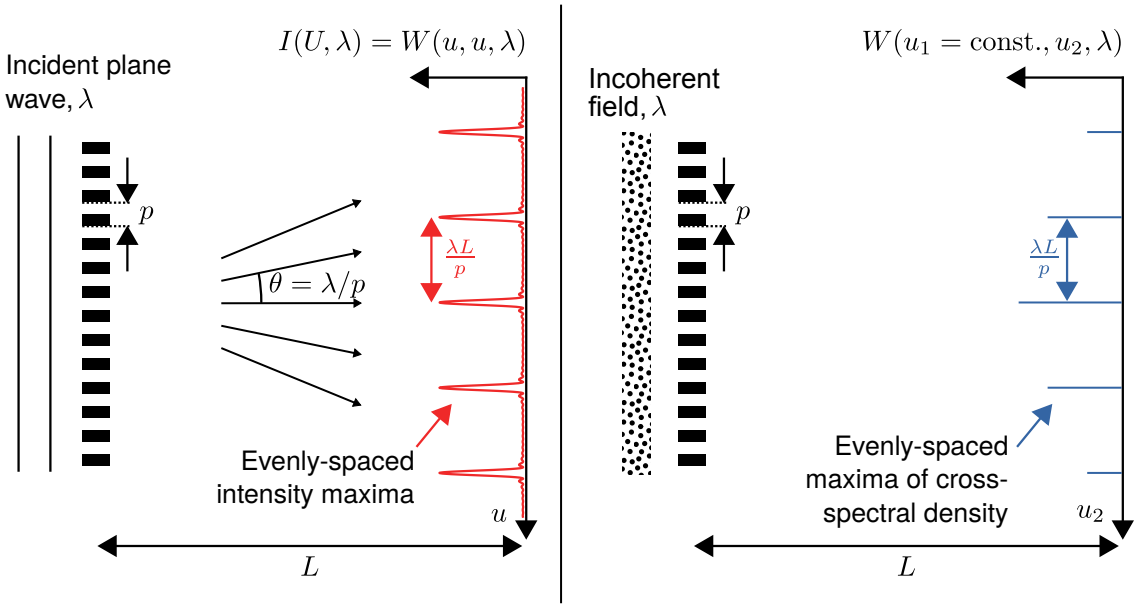

Figure 6.8: Similarity between diffraction peaks and peaks of cross-spectral density. Left: A grating with period p, when illuminated by coherent radiation of wavelength λ, produces intensity maxima with a lateral spacing of $\lambda L/p$ on a screen at a downstream distance L. Right: Replacing the coherent source by an extended, spatially incoherent source directly in front of the grating eliminates all intensity modulations on the screen, but the cross-spectral density, when taken as a function of u_2 with u_1 = const. now has the same periodicity of $\lambda L/p$. I.e., the fields at any two points in this plane are mutually coherent if and only if they are spaced apart a multiple of $\lambda L/p$.

Eq. (6.57) into Eq. (6.44)]:

$$W_F(y_1,y_2,\omega) = \frac{i_\omega}{\lambda d}\sum_{m=-\infty}^{\infty}\sum_{m'=-\infty}^{\infty}\sum_{n=-\infty}^{\infty} D_m D^*_{m'} C_n \times \iint_{-\infty}^{\infty} \exp\left\{\frac{2\pi i}{p_1}\left(mu_1 - m'u_2\right) + \frac{ik}{2L}\left(u_1^2 - u_2^2\right) + \frac{ik}{2d}\left[\left(u_1-y_1\right)^2 - \left(u_2-y_2\right)^2\right]\right\} \times \delta\left[u_1 - \left(u_2 + \frac{2\pi nL}{p_0 k}\right)\right] du_1 du_2. \quad (6.58)$$

Before the Dirac delta is used to eliminate one of the two integrals, the argument in the exponential can be reordered:

$$\begin{aligned}&\frac{2\pi i}{p_1}\left(mu_1 - m'u_2\right) + \frac{ik}{2L}\left(u_1^2 - u_2^2\right) + \frac{ik}{2d}\left[\left(u_1-y_1\right)^2 - \left(u_2-y_2\right)^2\right] \\ &= \frac{ik}{2}\left(\frac{1}{L}+\frac{1}{d}\right)\left(u_1^2-u_2^2\right) + u_1\left(\frac{2\pi im}{p_1} - \frac{iky_1}{d}\right) - u_2\left(\frac{2\pi im'}{p_1} - \frac{iky_2}{d}\right) + \frac{ik}{2d}\left(y_1^2 - y_2^2\right). \quad (6.59)\end{aligned}$$

The integral with respect to u_1 in Eq. (6.58) can simply be evaluated by replacing u_1 with $u_2 + \frac{2\pi nL}{p_0 k}$ in the integrand, thanks to the Dirac delta. After some rearrangement, the exponent in Eq. (6.59) becomes:

$$\begin{aligned}&i\left[\frac{2\pi^2 n^2 L^2}{k p_0^2}\left(\frac{1}{L}+\frac{1}{d}\right) + \frac{k}{2d}\left(y_1^2 - y_2^2\right) + \frac{2\pi nL}{p_0}\left(\frac{2\pi m}{k p_1} - \frac{y_1}{d}\right)\right] + \\ &iu_2\left\{2\pi\left[\frac{m-m'}{p_1} + \frac{n}{p_0}\left(1+\frac{L}{d}\right)\right] + \frac{k(y_2-y_1)}{d}\right\}. \quad (6.60)\end{aligned}$$

We can see that all terms involving u_2^2 have disappeared, thus we have a sum of terms which are linear in u_2 and constant terms. Inserting Eq. (6.60) into Eq. (6.58) yields:

$$\begin{aligned}W_F(y_1,y_2,\omega) = &\frac{i_\omega}{\lambda d}\sum_{m=-\infty}^{\infty}\sum_{m'=-\infty}^{\infty}\sum_{n=-\infty}^{\infty} D_m D^*_{m'} C_n \times \\ &\exp\left\{i\left[\frac{2\pi^2 n^2 L^2}{k p_0^2}\left(\frac{1}{L}+\frac{1}{d}\right) + \frac{k}{2d}\left(y_1^2 - y_2^2\right) + \frac{2\pi nL}{p_0}\left(\frac{2\pi m}{k p_1} - \frac{y_1}{d}\right)\right]\right\} \times \\ &\int_{-\infty}^{\infty}\exp\left(iu_2\left\{2\pi\left[\frac{m-m'}{p_1} + \frac{n}{p_0}\left(1+\frac{L}{d}\right)\right] + \frac{k(y_2-y_1)}{d}\right\}\right) du_2. \quad (6.61)\end{aligned}$$

We can again use the relation $\int_{-\infty}^{\infty}\exp(ikx)dx = 2\pi\delta(k)$ to solve the integral in Eq. (6.61):

$$\begin{aligned}W_F(y_1,y_2,\omega) = &\frac{2\pi i_\omega}{\lambda d}\sum_{m=-\infty}^{\infty}\sum_{m'=-\infty}^{\infty}\sum_{n=-\infty}^{\infty} D_m D^*_{m'} C_n \times \\ &\exp\left\{i\left[\frac{2\pi^2 n^2 L^2}{k p_0^2}\left(\frac{1}{L}+\frac{1}{d}\right) + \frac{k}{2d}\left(y_1^2 - y_2^2\right) + \frac{2\pi nL}{p_0}\left(\frac{2\pi m}{k p_1} - \frac{y_1}{d}\right)\right]\right\} \times \\ &\delta\left\{2\pi\left[\frac{m-m'}{p_1} + \frac{n}{p_0}\left(1+\frac{L}{d}\right)\right] + \frac{k(y_2-y_1)}{d}\right\}. \quad (6.62)\end{aligned}$$

The spectral intensity $I_F(y,\omega)$ is $W_F(y,y,\omega)$, i.e.:

$$\begin{aligned}I_F(y,\omega) = &\frac{2\pi i_\omega}{\lambda d}\sum_{m=-\infty}^{\infty}\sum_{m'=-\infty}^{\infty}\sum_{n=-\infty}^{\infty} D_m D^*_{m'} C_n \times \\ &\exp\left\{\frac{2\pi^2 i n^2 L^2}{k p_0^2}\left(\frac{1}{L}+\frac{1}{d}\right) + \frac{2\pi inL}{p_0}\left(\frac{2\pi m}{k p_1} - \frac{y}{d}\right)\right\} \\ &\times \delta\left\{2\pi\left[\frac{m-m'}{p_1} + \frac{n}{p_0}\left(1+\frac{L}{d}\right)\right]\right\}. \quad (6.63)\end{aligned}$$

We can reorder the sums to obtain a term which is

independent of m and m':

$$I_F(y,\omega) = \frac{2\pi i_\omega}{\lambda d} \times \sum_{n=-\infty}^{\infty} C_n \exp\left\{2\pi i \left[\frac{\pi n^2 L^2}{k p_0^2}\left(\frac{1}{L}+\frac{1}{d}\right) - \frac{nLy}{p_0 d}\right]\right\} \times \sum_{m=-\infty}^{\infty}\sum_{m'=-\infty}^{\infty} D_m D_{m'}^* \exp\left(\frac{4\pi^2 imnL}{k p_0 p_1}\right) \times \delta\left\{2\pi\left[\frac{m-m'}{p_1} + \frac{n}{p_0}\left(1+\frac{L}{d}\right)\right]\right\}. \quad (6.64)$$

The Dirac delta in Eq. (6.64) can be rewritten to make the relation between m and m' apparent:

$$\delta\left\{2\pi\left[\frac{m-m'}{p_1} + \frac{n}{p_0}\left(1+\frac{L}{d}\right)\right]\right\} = \delta\left(-\frac{2\pi}{p_1}\left\{m' - \left[m + \frac{np_1}{p_0}\left(1+\frac{L}{d}\right)\right]\right\}\right) = \frac{p_1}{2\pi}\delta\left\{m' - \left[m + \frac{np_1}{p_0}\left(1+\frac{L}{d}\right)\right]\right\}.$$

Thus, the expression for the intensity in Eq. (6.64) can be reformulated using a single sum and an explicit condition for m':

$$I_F(y,\omega) = \frac{p_1}{\lambda d} i_\omega \sum_{n=-\infty}^{\infty} C_n \times \exp\left\{2\pi i \left[\frac{\pi n^2 L^2}{k p_0^2}\left(\frac{1}{L}+\frac{1}{d}\right) - \frac{nLy}{p_0 d}\right]\right\} \times \sum_{m=-\infty}^{\infty} D_m D_{m+\Delta m}^* \exp\left(\frac{4\pi^2 imnL}{k p_0 p_1}\right), \quad (6.65)$$

where

$$\boxed{\Delta m = \frac{np_1}{p_0}\left(1+\frac{L}{d}\right).} \quad (6.66)$$

If the above equation for Δm does not yield an integer, $D_{m+\Delta m}^* = 0$. It can be seen that I_F is a superposition of complex exponentials with spatial periods $p_0 d/(nL)$. Note that the period p_2 of the analyzer grating G_2 is typically selected such that [Pfei+06]

$$p_2 = p_0 \frac{d}{L}, \quad (6.67)$$

so the intensity fringes effected by the n-th order of the G_0 intensity pattern (with period p_0/n) have a period of p_2/n.

Furthermore, the first exponential can be slightly rephrased and the final exponential term in Eq. (6.65) can be interpreted as a deflection: Rearrangement yields

$$\boxed{I_F(y,\omega) = \frac{p_1}{\lambda d} i_\omega \times \sum_{n=-\infty}^{\infty} C_n \exp\left[\frac{i\pi\lambda n^2 L^2}{p_0^2}\left(\frac{1}{L}+\frac{1}{d}\right)\right] \times \sum_{m=-\infty}^{\infty} D_m D_{m+\Delta m}^* \exp\left[\frac{-2\pi inL}{p_0 d}\left(y - \frac{\lambda m d}{p_1}\right)\right].} \quad (6.68)$$

The m-th term therefore corresponds to a lateral shift of the intensity pattern by $m \cdot \lambda d/p_1$, i.e. the lateral deflection corresponding to the m-th diffraction maximum of G_1 (cf. Fig. 6.8).

6.2.3d Interpretation

The origin of the first exponential in Eq. (6.68), as well as the condition for Δm in Eq. (6.66) is explained visually in Fig. 6.9: For a sinusoidal spatial intensity distribution with a period of p_0/n, cross-spectral density in a plane at a downstream distance of L peaks at $u_1 - u_2 = n\lambda L/p_0$ (Fig. 6.9a). This means that two points in this plane have nonzero mutual coherence if and only if their distance is equal to this value. However, the absolute location of the two points in the plane is arbitrary.

Fig. 6.9b illustrates the angular spectrum of fields transmitted by the modulation grating G_1: When illuminated by a plane wave of normal incidence, the field transmitted by a diffraction grating can be expressed as a superposition of a discrete set of plane waves with different propagation directions (the angular spectrum) [Good05, section 3.10].

The amplitude of the m-th plane wave is related to the Fourier coefficient D_m of the grating's transmission function, and its propagation direction is at an angle $m\lambda/p_1$ to that of the incident wave. At a downstream distance d, this leads to a lateral deflection of the field of $m\lambda d/p_1$ (compared to an absent diffraction grating, or the 0-th plane wave component).

Finally, these two effects are combined in the Talbot-Lau setup in Fig. 6.9c: Illuminated by a periodic intensity modulation of period p_0/n, the field in an arbitrary position in the G_1 plane is partially coherent with another position in this plane at a distance $n\lambda L/p_0$. This

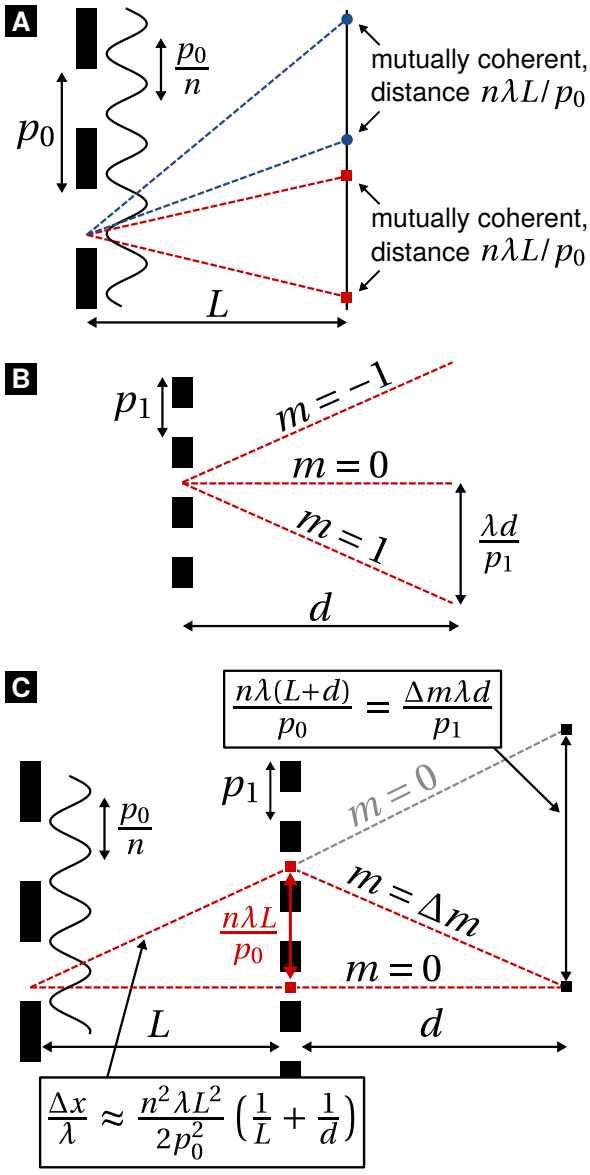

Figure 6.9: Visual interpretation of Eq. (6.68). (a): Sinusoidal illumination with period p_0/n produces at a distance of L a cross-spectral density $W(u_1,u_2,\lambda)$ with a peak at $u_2-u_1=n\lambda L/p_0$. I.e., the fields at any two points at $z=L$ are mutually coherent (and can thus interfere) if they are at a lateral distance of $n\lambda L/p_0$. (b): The field of the m-th diffraction peak of a grating with period p_1 is laterally deflected by $\lambda md/p_1$ at a distance d. (c): A "Talbot-Lau image" is achieved if two diffraction orders of mutually coherent fields coincide, i.e., if the lateral deflection of the paths shown in (a) is compensated by diffraction of one path as shown in (b). See text for a more detailed explanation.

means that the fields at points with these distances can interfere with each other, and diffraction due to the modulation grating occurs.

In order to observe Talbot-Lau images, G_1 *diffraction orders must exist whose difference in lateral deflection exactly cancel the relative distance between mutually coherent points in the* G_1 *plane.* In Fig. 6.9c, this is illustrated by rays originating from an arbitrary point in the G_0 plane and passing through two mutually coherent points in the G_1 plane. In the absence of G_1, the lateral deflection of these rays in the detection plane is equal to $n\lambda\,(L+d)\,/\,p_0$. To cancel out this deflection by combining different G_1 diffraction orders m and $m+\Delta m$, it must be equal to $\Delta m\cdot\lambda d/p_1$. Solving this for Δm provides the result in Eq. (6.66). Note that the relation shown in Fig. 6.9c simultaneously applies for *all* location pairs $(u,\,u+n\lambda L/p_0)$ in the G_1 plane.

Generally, the intensity distribution at the G_0 grating is described by a Fourier series [Eq. (6.46)], and is thus a superposition of sinusoidal functions with different n. Eq. (6.68) shows that the procedure for the calculation of Talbot-Lau images can be performed separately for each harmonic n (the intensities are then summed up).

The first exponential term in Eq. (6.68) describes the path length difference between the two mutually coherent light paths, as shown in Fig. 6.9c. For the case shown in the Figure, the length of the lower path is $L+d$, and that of the upper one is

$$\begin{aligned}&\sqrt{L^2+\left(\frac{n\lambda L}{p_0}\right)^2}+\sqrt{d^2+\left(\frac{n\lambda L}{p_0}\right)^2}\\ =&L\sqrt{1+\left(\frac{n\lambda}{p_0}\right)^2}+d\sqrt{1+\left(\frac{n\lambda L}{p_0 d}\right)^2}\\ \approx&L\left(1+\frac{n^2\lambda^2}{2p_0^2}\right)+d\left(1+\frac{n^2\lambda^2L^2}{2p_0^2d^2}\right).\end{aligned}$$

Therefore, the difference between the two is approximately

$$\Delta x\approx\frac{n^2\lambda^2L}{2p_0^2}+\frac{n^2\lambda^2L^2}{2p_0^2d}=\frac{n^2\lambda^2L^2}{2p_0^2}\left(\frac{1}{L}+\frac{1}{d}\right),$$

and the associated phase difference is $\Delta\phi=k\Delta x$, $k=2\pi/\lambda$.

These findings reproduce the known rules for Talbot-Lau grating periods and inter-grating distances, as presented e.g. in [Dona+09]: For a symmetric Talbot-Lau

setup in the first conventional Talbot order, $L = d = 2Z_T = 4p_1^2/\lambda$, and $p_0 = 2p_1$. In this case,

$$\frac{np_1}{p_0}\left(1+\frac{L}{d}\right) = n,\ \frac{i\pi\lambda n^2 L^2}{p_0^2}\left(\frac{1}{L}+\frac{1}{d}\right) = 2i\pi n^2,$$
$$\exp\left[\frac{-2\pi i n L}{p_0 d}\left(y-\frac{\lambda m d}{p_1}\right)\right] = \exp\left(\frac{-i\pi n y}{p_1}\right).$$

Thus, the phase shift between the mutually coherent light paths (in Fig. 6.9c) is $2\pi n^2$, they are therefore in phase for all n. Furthermore, the lateral shifts between Fourier components disappear for all n. Eq. (6.68) then simplifies to:

$$I_F(y,\omega) = \frac{p_1}{\lambda d} i_\omega \sum_{n,m} C_n D_m D^*_{m+n} \exp\left(\frac{-i\pi n y}{p_1}\right). \tag{6.69}$$

To verify that this is a self-image of G_1, the intensity immediately downstream of G_1 can be calculated as $W^+_{G1}(u,u,\omega)$, with W^+_{G1} given by Eq. (6.57):

$$\begin{aligned} W^+_{G1}(u,u,\omega) &= i_\omega \cdot \sum_{m,m',n} C_n D_m D^*_{m'} \times \\ &\qquad \exp\left[\frac{2\pi i}{p_1}\left(m-m'\right)u\right]\delta\left(-2np_1\right) \\ &\propto i_\omega C_0 \cdot \sum_{m,m'} D_m D^*_{m'} \times \exp\left[\frac{2\pi i}{p_1}\left(m-m'\right)u\right]. \end{aligned} \tag{6.70}$$

With the substitution $m' \to m+n$, the similarity between Eqs. (6.70) and (6.69) becomes apparent. As expected, the fundamental period in Eq. (6.70) is p_1, whereas it is $2p_1$ in Eq. (6.69). However, each summand of Eq. (6.69) contains the additional factor C_n. Since $|C_n|$ decreases with increasing n for typical gratings (cf. Eq. 6.46), the high-frequency summands in in Eq. (6.70) ($|m-m'| \gg 1$) are suppressed in Eq. (6.69), yielding a low-pass-filtered version of Eq. (6.70). Eq. (6.54) illustrates that the C_n characterize the amount of coherence in the plane of the modulation grating: Points in this plane, spaced apart $n\lambda L/p_0$, have a coherence proportional to C_n. Higher orders in the measured intensity profiles are thus generated by higher orders of the G_0 transmission function, which are usually weaker. For typical numerical simulations, this low-pass filtering effect is achieved by convolving the Talbot carpet with the (rescaled) transmission profile of one source grating slot.

Using Eq. (6.68), it can also be shown why the Talbot image of a π-shifting modulation grating must experience frequency doubling. Let the amplitude transmission function $t(u)$ be a rectangular profile with duty cycle of 0.5, so that

$$t(u) = \begin{cases} \alpha & u \bmod p < \frac{p}{2} \\ 1 & u \bmod p \geq \frac{p}{2} \end{cases},\ \alpha \in \mathbb{C}.$$

The Fourier series coefficients according to Eq. (6.56) can then be calculated to be

$$D_m = \begin{cases} \frac{\alpha+1}{2} & m = 0 \\ \frac{\alpha-1}{2\pi i m} & m = \pm 1, \pm 3, \ldots \\ 0 & \text{else.} \end{cases}$$

For a purely phase-shifting grating with shift $\Delta\varphi$, $\alpha = \exp(i\Delta\varphi)$. Thus for $\Delta\varphi = \pi$, $\alpha = -1$ and $D_0 = 0$. Eq. (6.68) shows that for $p_1 = p_0 d/(L+d)$, the m-th Fourier component with $n = \pm 1$ is proportional to $D_m D^*_{m\pm 1}$, which is zero for all m (since D_m is nonzero only for odd m). Therefore, the lowest observed fringe period is $p_2 = p_0 d/(2L)$, i.e. $n = \pm 2$.

Note that the relations between L, d, p_0 and p_1 reproduced here are considered to correspond to "cone-beam illumination" in the literature (cf. [Dona+09]), but this calculation shows that the relation also holds for arbitrarily large sources. The "cone" in the present sense is not defined by the extent of the source spot before the gratings, but the slits of the source grating.

6.2.4 Discussion and Conclusion

An approach was presented to calculate intensities generated by a Talbot-Lau interferometer, by directly incorporating effects of partial coherence in the calculation. The known rules for the selection of grating periods and inter-grating distances are reproduced. However, the partial-coherence view allows an alternative perspective on the relations between the three gratings:

The source grating is illuminated by an extended incoherent source, and thus generates a periodic intensity pattern. This produces a cross-spectral density (CSD) with sharp, equidistantly-spaced peaks in the G_1 plane. This means that fields at any two points in this plane can only interfere if their distance is an integer multiple of the CSD periodicity.

From this partially-coherent field, the modulation grating G_1 produces an angular spectrum of transmitted fields. If grating periods and inter-grating distances are chosen appropriately, some coefficients of the angular spectrum are superimposed coherently:

The components of the angular spectrum differ in the direction of propagation. Fields from spatially separated, mutually coherent points in the G_1 plane can thus be "spatially reunited" in the detection plane, by combining different components of the angular spectrum. This results in intensity modulations, Talbot-Lau images, in the detection plane.

Most commonly, the Talbot-Lau setup is understood as a modification of a Talbot self-imaging setup with coherent illumination: Talbot images are calculated by Fresnel propagation, and Talbot-Lau images are created from these by convolution with the source grating intensity profile. However, this approach does not provide a description of the underlying wavefield.

In contrast, the partial-coherence representation of the Talbot-Lau setup treats the effects of both G_0 and G_1 in a unified way (a modification of the cross-spectral density). The wavefield and its coherence properties may be evaluated for arbitrary locations. Furthermore, objects with arbitrary transmission functions can be added, allowing to e.g. directly calculate the effect of phase-shifting or scattering objects on detected intensity.

Note in particular that *the lateral separation of mutually coherent fields* (vertical distance between the red lines in Fig. 6.9c) *at any location before or after G_1 is identical to the setup's autocorrelation length ξ*, which determines the magnitude of the dark-field signal due to an object. *Since ξ is the spacing between any two points that are mutually coherent, the dark-field activity of an object is determined by its ability to manipulate the field at points with this separation.* This is discussed in depth in section 2.5.8c on page 62. Furthermore, it is shown there that the angular sensitivity S, i.e., the ratio of differential-phase signal and sample refraction, is also directly related to the autocorrelation length via $S = \xi / \lambda$.

Eq. (6.68) can be directly used to calculate intensities and visibility values for a given set of gratings. Arbitrarily complex transmission profiles can be achieved by varying the Fourier coefficients C_n, D_m. For a numerical solution, care should be taken that "ringing artifacts" are not introduced by truncation of the Fourier sums.

With the same approach, other setup designs, such as dual phase-grating setups, could also be evaluated. An adaptation of the partial-coherence approach to numerical simulations may also be possible. This may be of interest e.g. for the case of a finite number of illuminated source grating slits (for which no analytical solution of the cross-spectral density may exist). The computational effort for a propagation of cross-spectral density is greater than for Fresnel propagation of a coherent field, since it requires two spatial integrations. However, this should not prohibit its application, especially since the area integrals may be reduced to a single integration axis for one-dimensional gratings.

6.3 Dark-field bias correction

In grating-based phase-contrast imaging, a bias occurs in the calculation of visibility maps from phase-stepping (or fringe-scanning) data. A number of methods were thus devised to reduce this bias, and compared to existing correction methods. The mathematical foundation for this effect is introduced in section 6.3.1. The different correction methods are then explained, first from a heuristic perspective, and then in a mathematically more rigorous manner in section 6.3.2. The application of each method is illustrated as a function of the biased, noise-normalized input data.

In section 6.3.3, the performance of the different methods is compared in terms of (residual) bias, variance and mean squared error (MSE). The influence of inaccurate knowledge of noise levels on estimation is also discussed.

6.3.1 Mathematical fundamentals

In phase-stepping measurements, the image modalities (as defined in section 2.5.6 on page 56) are typically determined in two steps: A retrieval of fit parameters by solving a linear optimization problem on the measurement data, followed by a conversion of these parameters to the desired modalities.

An optimization problem is understood to be "linear" when the relation between measurement data $\vec{y}$ and the fit parameters $\vec{x}$ – i.e., the "model" – can be expressed by a matrix $\boldsymbol{A}$, so that

$$\vec{y} = \boldsymbol{A}\vec{x} + \vec{\epsilon}, \tag{6.71}$$

where each element of $\vec{\epsilon}$ is a normally-distributed random variable with mean 0. It is often beneficial to phrase a given optimization problem in this form, since its least-squares solution, i.e. the value $\vec{x} = \vec{\xi}$ for which

$$\left\| \boldsymbol{A}\vec{x} - \vec{y} \right\|_2 \tag{6.72}$$

is minimal, can be calculated using the so-called "normal equations" [Punt+13, Eq. 2.18]:

$$\left(\boldsymbol{A}^T\boldsymbol{A}\right)\vec{\xi} = \boldsymbol{A}^T\vec{y}.$$

If $\boldsymbol{A}^T\boldsymbol{A}$ is not singular (i.e., $\boldsymbol{A}$ has full rank), the least-squares solution is directly given as

$$\vec{\xi} = \left(\boldsymbol{A}^T\boldsymbol{A}\right)^{-1}\boldsymbol{A}^T\vec{y}.$$

The matrix $(\boldsymbol{A}^T\boldsymbol{A})^{-1}\boldsymbol{A}^T$ is the so-called "Moore-Penrose inverse" of $\boldsymbol{A}$.

This approach is much faster than other, iterative minimization procedures. For the given application, this is essential as a very large number of regression problems must be solved (one per pixel). Additionally, if the elements of $\vec{y}$ (or $\vec{\epsilon}$) are independent and have equal variance σ^2, the "propagation" of noise from the measurement data $\vec{y}$ to $\vec{\xi}$ can be directly calculated as [Punt+13, Eq. 3.2]

$$\mathrm{Cov}\left(\vec{\xi}\right) = \sigma^2\left(\boldsymbol{A}^T\boldsymbol{A}\right)^{-1}, \tag{6.73}$$

and the elements of $\vec{\xi}$ are also follow normal distributions[1]. In order to rephrase Eq. (4.13) from page 92 as a linear regression problem, the cosine term must be rewritten using the relation

$$\cos\left(\Phi_k - \phi_1\right) = \cos\Phi_k\cos\phi_1 + \sin\Phi_k\sin\phi_1$$

Since the φ_k are known (to some precision), Eq. (4.13) can be rewritten in the form of Eq. (6.71) as

$$\underbrace{\begin{pmatrix} 1 & \cos\Phi_1 & \sin\Phi_1 \\ 1 & \cos\Phi_2 & \sin\Phi_2 \\ \vdots & \vdots & \vdots \\ 1 & \cos\Phi_n & \sin\Phi_n \end{pmatrix}}_{\boldsymbol{A}} \begin{pmatrix} x_1 \\ x_2 \\ x_3 \end{pmatrix} = \underbrace{\begin{pmatrix} I_1 \\ I_2 \\ \vdots \\ I_n \end{pmatrix}}_{\vec{y}},$$

where

$$x_1 = a_0,\ x_2 = a_1\cos\phi_1,\ x_3 = a_1\sin\phi_1$$

(identically for ϕ_1^{r} in place of ϕ_1). If the values I_k can be assumed to be normally distributed, which is usually the case for sufficiently high photon counts, the fit parameters are also normally distributed. However, to retrieve a_1 and ϕ_1, a transform from Cartesian to polar coordinates is necessary:

$$a_1 = \sqrt{x_2^2 + x_3^2},\ \phi_1 = \mathrm{atan2}\left(x_3, x_2\right). \tag{6.74}$$

Since these operations are *not linear* in x_2 or x_3, an undesired effect occurs in the statistical behavior of a_1:

[1] This follows since each element of $\vec{\xi}$ is given by a linear combination of elements of $\vec{y}$: Any linear combination of normally distributed random variables is also normally distributed. Eq. (6.73) does not apply if the variances of the elements of $\vec{y}$ are not identical, but if the problem can be rephrased as a weighted least-squares problem with a suitable selection of weights, a similarly simple relation results.

In a phase-stepping acquisition, a value for x_2 and x_3 is retrieved from the intensity values for each pixel, which are then converted to values of a_1 and ϕ_1 according to Eq. (6.74). If flux, visibility, and fringe phase are (approximately) constant in a given subsection of the image, the retrieved values of x_2 and x_3 can be assumed to be drawn from the same distribution. Their expectation values $\langle x_2 \rangle$, $\langle x_3 \rangle$ can then be approximated by taking their mean over the ensemble of all pixels in this (sufficiently large) region. The correct parameter values $(\hat{a}_1, \hat{\phi}_1)$ can then be calculated from these via Eq. (6.74).

Usually however, spatially-resolved information about a_1 and ϕ_1 is desired, requiring their calculation from x_2 and x_3 for each pixel individually. Due to the nonlinear transforms involved in Eq. (6.74), the resulting distributions of a_1 and ϕ_1 are not normally distributed. In particular, their mean values deviate from their true values. For a_1, this becomes apparent in cases where the "spread" of a_1 values (e.g. the standard deviation) is greater than the true value $\hat{a}_1$: Here, there would be a significant probability of a_1 achieving negative values if the distribution was symmetric. But since a_1 cannot be negative, the distribution must inevitably be skewed towards positive values. This results in a shift of the expectation value towards values greater than $\hat{a}_1$. In other words, the expectation value of the estimator

$$a_1(x_2, x_3) = \sqrt{x_2^2 + x_3^2}$$

is not identical to $\hat{a}_1$. This estimator is thus "biased", i.e.

$$\langle a_1 \rangle = \left\langle \sqrt{x_2^2 + x_3^2} \right\rangle > \sqrt{\langle x_2 \rangle^2 + \langle x_3 \rangle^2} = \hat{a}_1.$$

In other words, a map of a_1 values does not only increase in noise when calculated from fewer photon counts, but also increasingly *overestimates* values.

This effect is illustrated in Fig. 6.10 for the example of $\langle x_2 \rangle = \langle x_3 \rangle = 2^{-1/2}$ and $\mathrm{Var}(x_2) = \mathrm{Var}(x_3) = 1$.

A number of methods to correct for this effect were thus evaluated.

Rician parameter estimation For the case of normally-distributed, independent quantities X, Y with nonzero means μ_X, μ_Y and identical variances σ^2, $Z = \sqrt{X^2 + Y^2}$ follows a so-called "Rice distribution" [Talu+91]. Its probability density function (PDF)

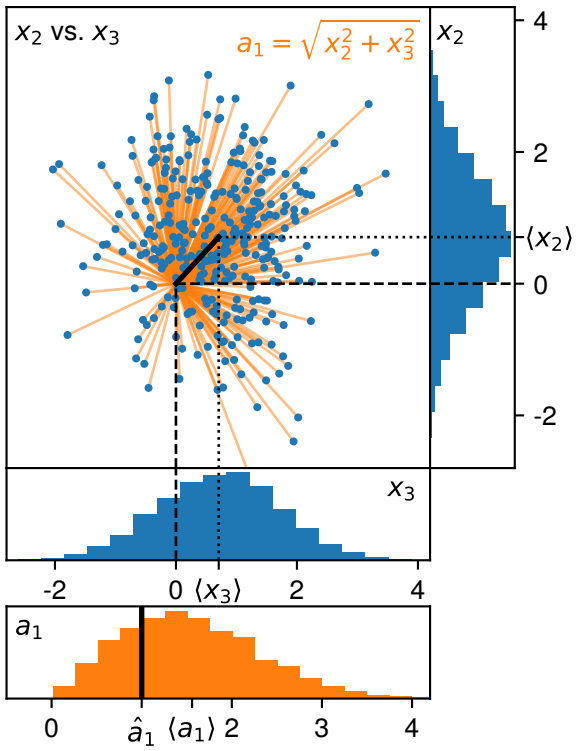

Figure 6.10: Bias in the calculation of magnitudes of normally distributed quantities with nonzero mean. Although the quantities x_2 and x_3 follow independent normal distributions (blue histograms and dots in bivariate histogram), the distribution of magnitudes $a_1 = \sqrt{x_2^2 + x_3^2}$ (i.e., the length of the orange lines) has a positive skew (orange histogram). Its mean value $\langle a_1 \rangle$ is therefore greater than $\hat{a}_1 = \sqrt{\langle x_2 \rangle^2 + \langle x_3 \rangle^2}$ (the solid black line). The quantity a_1 follows a so-called Rice distribution [Talu+91].

is given as

$$p\left(z|\nu,\sigma^2\right) = \frac{z}{\sigma^2}\exp\left[\frac{-\left(z^2+\nu^2\right)}{2\sigma^2}\right] I_0\left(\frac{z\nu}{\sigma^2}\right), \quad (6.75)$$

where I_0 is the zero-order modified Bessel function of the first kind and $\nu = \sqrt{\mu_X^2+\mu_Y^2}$. It was shown in [Chab+11] (and also follows from the previous discussion), that the quantity a_1 approximately follows such a distribution when retrieved from Poisson-distributed photon counts in a phase-stepping measurement (with equidistant phase steps). In particular, for a measurement with N phase steps and a mean number of a_0 detected photons per phase step, [Chab+11] found that $\sigma^2 = 2a_0/N$. Furthermore, noise levels and expectation values of the reconstructed modalities for low- and high-SNR limits are calculated in this publication, providing an envelope for the range of measurable a_1 values.

The "true value" for z in Eq. (6.75), which it approaches for decreasing noise levels, i.e. $\sigma \to 0$, is ν, i.e.: $\lim_{\sigma\to 0}\langle z\rangle = \nu$. Thus, an estimate of ν could be interpreted as a "corrected" version of z. Ideally, the resulting distribution would have no bias, i.e. its expectation value would be equal to the true value. Since every pixel in an image map of a_1 has its own underlying distribution (with values of ν and σ differing between pixels), parameter estimation must be performed from a single sample of z and σ.

In [Talu+91], the authors give an overview of two common methods for estimating the parameters of the Rician distribution: the method of moments, and maximum-likelihood estimation.

6.3.2 Examined bias correction methods

6.3.2a Maximum-likelihood estimation and lookup table representation

In the approach presented in [Talu+91], the "likelihood" (the product of PDFs for each measurement) is maximized by varying the parameters ν and σ, e.g. using an iterative solver. Like the method of moments, this approach is not directly feasible if only a single sample is available: A two-dimensional optimization of the likelihood from a single sample z' will always approach the solution $(\nu,\sigma) = (z',0)$ [Eq. (6.75) tends towards a delta distribution for $\sigma \to 0$ and the likelihood for $z = z'$ approaches infinity].

However, the approach can be modified by derive an estimate for σ ahead of time, e.g. using the above-mentioned relation $\sigma^2 = 2a_0/N$. Maximization of the likelihood function, given this estimate for σ, can then be performed as a function of ν alone.

In order to avoid computationally expensive iterative optimization, this problem can be implemented by a lookup table: With

$$\boxed{\zeta \equiv \frac{z}{\sigma},\ \eta \equiv \frac{\nu}{\sigma},}$$

and the expression

$$q\left(\zeta|\eta\right) = \zeta\exp\left[\frac{-(\zeta^2+\eta^2)}{2}\right] I_0\left(\zeta\eta\right),$$

Eq. (6.75) can be rephrased as

$$p(z|\nu,\sigma) = q(\zeta|\eta)/\sigma.$$

The *maximum-likelihood (ML) solution* of η, i.e.

$$\eta_{\mathrm{ML}}(\zeta) = \underset{\eta}{\operatorname{argmax}}\, q(\zeta|\eta),$$

depends only on the parameter ζ, and can easily be calculated ahead of time for the relevant range of η values. For $\nu \gg \sigma$, i.e. $\eta \gg 1$, bias is negligible and thus, $\eta \approx \zeta$. It is thus sufficient to calculate η_{ML} for "small" values of ζ, e.g. on the interval $[0,10]$, and assume that $\eta_{\mathrm{ML}} = \zeta$ for greater values. The ML solution of ν for an arbitrary z then follows as

$$\nu_{\mathrm{ML}} = \sigma\cdot\eta_{\mathrm{ML}}\left(\frac{z}{\sigma}\right). \quad (6.76)$$

This approach is also useful for the other bias correction methods introduced below.

6.3.2b Method of moments

In [Talu+91], the two-parameter form of the Rician PDF in Eq. (6.75) is simplified to a form dependent on a rephrased variable $y \equiv z/\sqrt{E(z^2)}$ and a single parameter, the signal-to-noise ratio $\gamma \equiv \nu^2/(2\sigma^2)$.

The method of moments is based on the idea that, given a set of measurements $\{y_1,\ldots,y_n\}$ from a given distribution, the expected value of y can be given as an analytical expression of γ [Talu+91, Eq. 5]. The quantity γ can thus be retrieved by calculating the mean of all measured y_i, and solving this analytical expression for γ.

However, the formulation as presented there is not applicable for single-sample measurements: The second moment $E(z^2)$, which is required to calculate y, can not be realistically estimated[2]. In other words, for a set containing one single measurement of z, y is always 1, which implies that no bias correction is applied.

Instead, the transform of $p(z|\nu,\sigma)$ to $q(\zeta|\eta)$ used for the ML solution can also be used here. We are searching for the parameter ν where the distribution's mean $\mu(\nu,\sigma)$ is equal to the observed value z:

$$\nu_{\text{Mean}}(z,\sigma) = \left\{\nu \,\middle|\, \mu(\nu,\sigma) = z\right\}.$$

As we have only one single measured value, it is identical to the mean over all observations. The mean of the Rice distribution is given as

$$\mu(\nu,\sigma) = \int_0^\infty z \cdot p(z|\nu,\sigma)\,dz = \sigma\sqrt{\frac{\pi}{2}}L_{1/2}\left(\frac{-\nu^2}{2\sigma^2}\right), \tag{6.77}$$

where

$$L_{1/2}(\xi) = e^{\xi/2}\left[(1-\xi)\,I_0\left(\frac{-\xi}{2}\right) - \xi\,I_1\left(\frac{-\xi}{2}\right)\right],$$

and I_0, I_1 are modified Bessel functions of the first kind. Therefore, to find ν_{Mean}, it would be necessary to set $\mu(\nu,\sigma)$ in Eq. (6.77) equal to z, and solve for ν. Unfortunately, this is not possible analytically, but the quantity

$$\eta_{\text{Mean}}(\zeta) = \left\{\eta \,\middle|\, \mu(\eta) = \zeta\right\}$$

can be numerically calculated ahead of time for all relevant values of ζ, and a transform equivalent to Eq. (6.76) can be performed to retrieve ν_{EV} for any value of σ.

6.3.2c Mode finding

It can be attempted to estimate ν as the value where z is equal to the *mode* of the Rician distribution $p(z|\nu,\sigma^2)$. The mode of a PDF is given as its "peak", taken as a function of z. Thus,

$$\nu_{\text{Mode}}(z) = \left\{\nu \,\middle|\, \frac{\partial}{\partial z}\,p\left(z|\nu,\sigma^2\right) = 0\right\}.$$

Although this method is similar to the ML approach (in both cases, the parameter ν is estimated to find a maximum of $p(z|\nu,\sigma^2)$, and σ is determined in a separate procedure), they are not identical: The ML solution is given by the position ν_{ML} where

$$\frac{\partial}{\partial \nu}\,p\left(z|\nu,\sigma^2\right)\Big|_{\nu=\nu_{\text{ML}}} = 0,$$

i.e. p is maximal compared to PDFs with identical z, but adjacent values for ν. However, z is kept fixed in both approaches. As for ML optimization, a lookup table approach can be employed by calculating $\eta_{\text{Mode}}(\zeta)$ ahead of time for all relevant values of ζ and applying Eq. (6.76) equivalently.

6.3.2d Correction method by Gudbjartsson and Patz

In [Gudb+95], the authors demonstrate that the values in MR magnitude images also follow a Rician distribution, recognize the associated presence of a bias and present a correction approach based on one single measurement value and an estimate for the noise level. Their approach is thus conceptually very similar to the methods presented so far, but is much more simple to calculate: The authors show that in the high-SNR range, the Rician PDF $p(z|\nu,\sigma)$ is well approximated by a normal distribution with mean $\sqrt{\nu^2+\sigma^2}$. Assuming that the measured value z is equal to this mean, solving for ν yields $\nu = \sqrt{z^2-\sigma^2}$. In order to deliver an estimate for ν even in cases where $\sigma^2 > z^2$, the square root is taken of the argument, i.e.

$$\nu_{\text{GP}} = \sqrt{\left|z^2-\sigma^2\right|}.$$

As for the other methods, this simple function can also be phrased in a σ-independent form:

$$\eta_{\text{GP}} = \sqrt{\left|\zeta^2-1\right|},$$

with conversion from η_{GP} to ν_{GP} according to Eq. (6.76).

6.3.2e Bias correction based on findings from Ji et al.

In [Ji+17], the authors derive approximate values for bias in all three grating-based X-ray phase contrast modalities retrieved from phase-stepping, and validate their findings with experimental data. Although no explicit correction method based on single measurement

[2] Conceivably, the second moment could be estimated from a set of neighboring pixels, but this approach may exhibit problematic behavior in regions of rapidly varying bias levels.

values is given (experimental validation is performed by averaging over regions of interest), the findings can be used to derive such an algorithm: In Eq. 17, the authors derive the bias of a_1 to be approximately $1/(NV)$, where N is the number of phase steps and V is the true visibility. If we assume (as in the "method of moments") that the measured value is equal to the distribution's mean,

$$\begin{aligned} z &= \mathrm{Mean}(a_1) = \text{True value}(a_1) + \mathrm{Bias}(a_1) \\ &= \nu + \frac{1}{NV} \overset{V=\frac{a_1}{a_0}}{=} \nu + \frac{a_0}{N\nu} \overset{\sigma^2=\frac{2a_0}{N}}{=} \nu + \frac{\sigma^2}{2\nu}. \end{aligned} \tag{6.78}$$

Solving Eq. (6.78) for ν yields

$$\nu_\pm = \frac{1}{2}\left(z \pm \sqrt{z^2 - 2\sigma^2}\right).$$

The solution ν_- is clearly incorrect [for example, $\nu_-(z \gg \sigma) \approx 0$], and probably arises due to the equation for the a_1 bias being an approximation.

Like the other methods, the solution ν_+ can be rephrased to a σ-independent form for the calculation of a lookup table:

$$\eta_{\mathrm{Ji}} = \frac{\nu_+}{\sigma} = \frac{1}{2}\left(\zeta + \sqrt{\zeta^2 - 2}\right). \tag{6.79}$$

Note that a real-valued solution for η_{Ji} in Eq. (6.79) only exists for $\zeta \geq \sqrt{2}$. In other words, the assumption that the measured value is equal to the distribution's mean becomes impossible to fulfill for $\zeta < \sqrt{2}$. A continuation of η_{Ji} for this range of values is not apparent.

Alternatively, it is possible to make the (less accurate) assumption that

$$\mathrm{Bias}(a_1) = \frac{\sigma^2}{2\nu} \approx \frac{\sigma^2}{2z},$$

which results in the correction function of

$$\eta^{(2)}_{\mathrm{Ji}} = \zeta - \frac{1}{2\zeta}.$$

This has the advantage of yielding a non-negative estimate for η (and thus, ν) for all $\zeta \geq \sqrt{1/2}$. However, the estimate becomes negative for smaller values of ζ and $\lim_{\zeta \downarrow 0} \eta^{(2)}_{\mathrm{Ji}} = -\infty$. The most obvious modification to rectify this is to clip all negative estimates of $\eta^{(2)}_{\mathrm{Ji}}$ to zero.

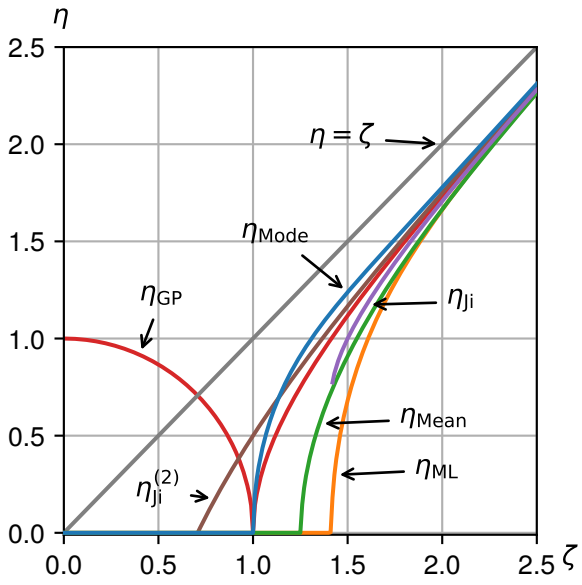

Figure 6.11: Lookup table representation for each of the presented dark-field bias correction methods.

6.3.3 Comparison of methods

6.3.3a Lookup table comparison

The lookup table forms $\eta(\zeta)$ of the presented bias correction functions are displayed in Fig. 6.11, together with the reference line $\eta = \zeta$, which corresponds to no correction.

The application of the correction works as follows: The value for a_1 determined by least-squares estimation is divided by the estimate for σ, e.g. using the relation that $\sigma = \sqrt{2a_0/N}$. Given a lookup table $\eta(\zeta)$, the corrected value is retrieved as

$$a_{1,\mathrm{corr}} = \sigma \cdot \eta\left(\frac{a_1}{\sigma}\right).$$

Of all the curves, the ML solution deviates the strongest from $\eta = \zeta$, i.e. it applies the greatest change to the data. $\eta_{\mathrm{ML}}(\zeta) = 0$ for $\zeta \leq \sqrt{2}$. Thus, all a_1 values which do not exceed their σ estimate by at least $\sqrt{2}$ are set to zero. This results in a significant shift towards lower a_1 values and the appearance of a large number of zero values in low-SNR data. This also applies to η_{Mean}, η_{Mode}, and $\eta^{(2)}_{\mathrm{Ji}}$, albeit to a lesser degree, since they modify a_1 values less strongly than η_{ML}.

Since the Rayleigh distribution is a special case of the Rice distribution ($\nu \to 0$), the values of ζ where

$\eta_{\mathrm{Mean}}(\zeta)$ and $\eta_{\mathrm{Mode}}(\zeta)$ reach zero are given by mean and mode of the Rayleigh distribution for $\sigma = 1$. These are given as $\sqrt{\pi/2}$ and 1, respectively.

The approach by Gudbjartsson and Patz, characterized by η_{GP}, differs from the remaining methods in that $\eta_{\mathrm{GP}}(\zeta)$ achieves a negative slope for $\zeta < 1$. This portion of the histogram is thus essentially "reversed". $\eta_{\mathrm{Ji}}(\zeta)$ behaves similarly to the other methods , but as discussed above, is only defined for $\zeta > \sqrt{2}$, and can thus not be applied to arbitrary Rice-distributed data.

For $\zeta \gtrapprox 2$, all examined correction methods behave very similarly, and the amount of change applied by the corrections is relatively minor.

It should be emphasized that values of η in the vicinity of 1, i.e. those displayed in Fig. 6.11, correspond to a very low-statistics regime: η can be rewritten as

$$\eta = \frac{a_1}{\sigma} = \frac{a_1}{\sqrt{2a_0/N}} = V\sqrt{\frac{a_0 N}{2}}.$$

Note that $a_0 N$ is the total number of detected photons. Thus, $\eta = 1$ is achieved for example at $V = 10\%$ and $a_0 N = 200$ photons.

6.3.3b Quantitative comparison of bias correction methods

The primary criterion by which the correction methods are to be compared to each other is of course the amount of reduction in bias. However, the effect of the corrections on noise levels should also be considered. In particular, both variance and bias are conveniently combined in the so-called mean squared error (MSE), which could thus be interpreted as an overall performance of the estimator.

The bias of an estimator a_1 is the difference of its expectation value $\langle a_1 \rangle$ from the true value $\hat{a}_1$:

$$b(a_1) = \langle a_1 \rangle - \hat{a}_1,$$

The variance of the estimator is given as

$$V(a_1) = \left\langle \left(a_1 - \langle a_1 \rangle\right)\right\rangle^2 = \left\langle a_1^2 \right\rangle - \langle a_1 \rangle^2$$

and gives a measure for the spread of the estimated values around the expectation value. Finally, the mean squared error is defined as

$$\mathrm{MSE}(a_1) = \left\langle (a_1 - \hat{a}_1)^2 \right\rangle.$$

It is also a measure of spread, but the spread around the true value $\hat{a}_1$, not the estimator's expectation value $\langle a_1 \rangle$. It stands to reason that both an increase in $V(a_1)$ or $b(a_1)$ will lead to an increase in $\mathrm{MSE}(a_1)$. In particular, it can be shown that

$$\mathrm{MSE}(a_1) = V(a_1) + b(a_1)^2.$$

The "estimators" that are being compared are composed of the least-squares retrieval of a_1, followed by one (or none) of the lookup-table-based correction methods. Given the Rice PDF $p(z|\nu, \sigma = 1)$, and the lookup table representation $\eta(\zeta)$ of any of the correction methods, the expectation value of a_1 is given as

$$\left\langle a_1^{(\eta)} \right\rangle = \int_0^\infty p\,(z|\nu, \sigma = 1)\,\eta(z)\,dz. \tag{6.80}$$

The second moment is calculated by replacing $\eta(z)$ by $\eta(z)^2$. The performance of the original method, without lookup table corrections, is calculated by setting $\eta(z) = z$. Note that the expected value in Eq. (6.80), and thus bias, variance and MSE calculated from it, are still functions of ν. Calculated in this manner, they describe the estimators' behavior when applied to data drawn from one distribution with fixed $\nu = a_0 V$ (i.e. constant flux and visibility).

The parameters, as shown in Fig. 6.12, are thus given as a function of $\hat{\eta}$, i.e. the true value of η. All methods reduce bias, but η_{ML} and η_{Mean} noticeably overshoot for $1 < \hat{\eta} < 4$. η_{Mode}, $\eta_{\mathrm{Ji}}^{(2)}$, and η_{GP} however achieve nearly complete elimination of bias for $\hat{\eta} > 2$.

All correction methods (except η_{GP} for $\hat{\eta} < 1$) lead to an increase of variance (i.e., noise), especially in the vicinity of $\hat{\eta} = 2$. The shown increase in variance corresponds to an increase of up to 33% in standard deviation (η_{ML}, $\hat{\eta} = 1.43$). In particular, the increase of variance for each method appears to be inversely correlated with the amount of change the method applies to the bias.

The MSE, being a statistic composed of variance and (squared) bias, appears to be dominated by the bias for $\hat{\eta} \lessapprox 1$. All correction methods achieve a decrease in MSE below a certain $\hat{\eta}$ threshold, albeit at the expense of systematically higher MSE values for all $\hat{\eta}$ above that threshold.

6.3.3c Inexact knowledge of σ and a_0

So far, only the change in a_1 due to bias correction with known σ has been analyzed. In real use cases

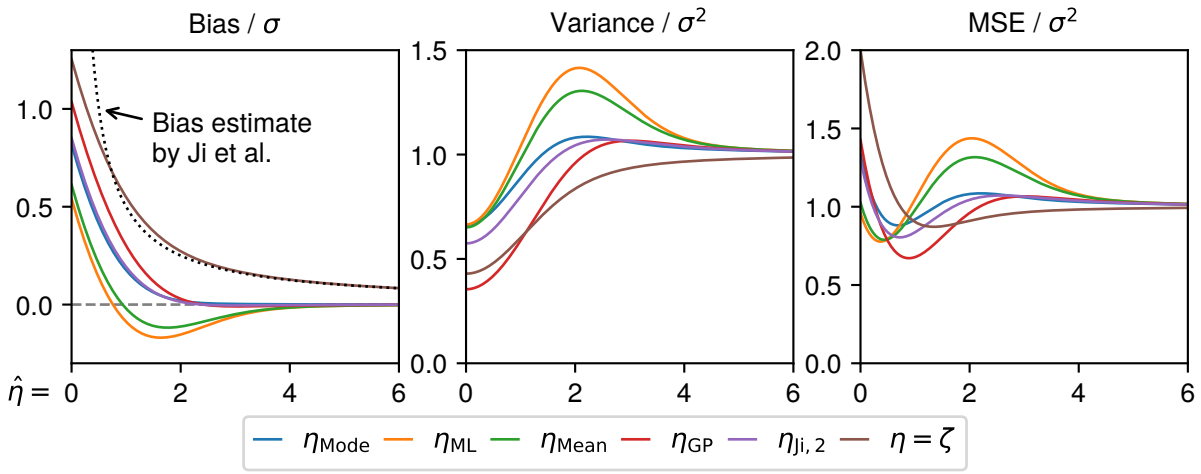

Figure 6.12: Bias, variance, and mean squared error (MSE) of each of the bias correction methods, as well as uncorrected least-squares estimation ($\eta = \zeta$). Values are shown as a function of $\hat{\eta} = \hat{v}/\sigma$. The estimate for the bias as given in [Ji+17, Eq. 17] is also shown.

however, σ must itself be estimated from the measurement data, leading to an additional source of uncertainty for bias correction. Furthermore, the commonly evaluated quantity is not a_1, but $V = a_1/a_0$, where a_0 is another random variable, and thus another source of uncertainty. The impact of these two factors should thus be assessed.

For counts of detected photons, the assumption of Poisson distribution is often justified. Since mean and variance of Poisson-distributed variables are identical, an estimate of the former also serves as an estimate of the latter. For Poisson-distributed phase-stepping data $I_1, \ldots, I_N$ with means $\langle I_k \rangle = a_0 + a_1 \cos(\varphi_k - \Phi_1)$ [cf. Eq. (4.13) from page 92], $I = \sum_{k=1}^{N} I_k$ is also a Poisson-distributed variable with mean $\langle I \rangle = N a_0$ (if the phase steps φ_k are equidistant and cover an integer number of periods).

An estimate of σ may thus be achieved by

$$\sigma = \sqrt{\frac{2a_0}{N}} = \frac{\sqrt{2I}}{N}. \tag{6.81}$$

It can be shown e.g. by numerical simulations that the expectation value of the square root of a Poisson-distributed variable with mean λ is $\sqrt{\lambda}$ to high accuracy. In other words, the bias introduced by the square root is negligible. Furthermore, the variance of the square root is approximately $1/4$ for $\lambda \gtrapprox 50$.

Thus the variance of the σ estimator in Eq. (6.81) is

$$\mathrm{Var}(\sigma) \approx \frac{2}{N^2} \cdot \frac{1}{4} = \frac{1}{2N^2},$$

regardless of the mean value of I.

As shown e.g. in Eq. (6.76) for ML correction, the dependence of the corrected value for v on σ, the uncorrected value z, and the lookup table $\eta(\zeta)$ can be expressed as

$$v = \sigma \cdot \eta\left(\frac{z}{\sigma}\right).$$

Unfortunately, analytical treatment of error propagation from z and σ to v is difficult: Although application of Gaussian error propagation is feasible, it implies that the derivatives $\partial v/\partial z$, $\partial v/\partial \sigma$ are approximately constant over the range of the variables' variation. Fig. 6.11 illustrates that this is not a good approximation: especially for values of $\zeta = z/\sigma$ between 1 and 2, $\eta'(\zeta)$, and thus the partial derivatives, vary very rapidly.

Numerical simulations were thus used to estimate bias and variance of both a_1 and V. Stepping curves with Poisson noise and low statistics were generated ($a_0 = 15$ photons, $N = 5$, variation of V from 0 to 1, thus resulting in $\hat{\eta}$ values between 0 and 6), and estimates for a_0, a_1, and Φ_1 were calculated by least-squares regression, followed by bias correction of a_1. Two different scenarios were distinguished for the correction: Use of the ground-truth value for σ, and estimation

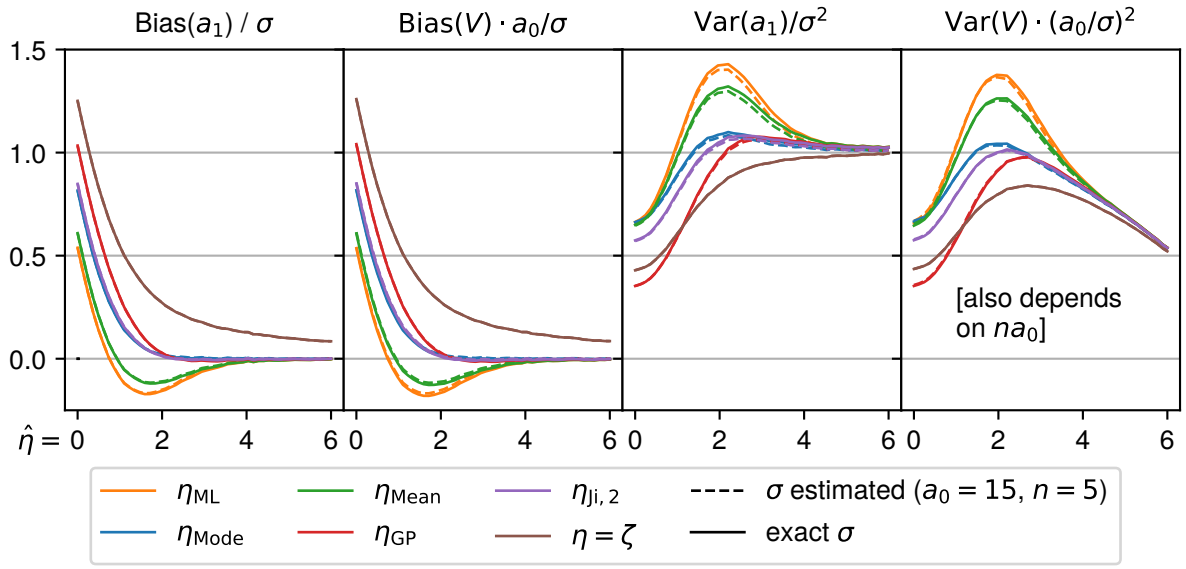

Figure 6.13: Effect of estimation of σ on bias and variance of a_1 and V. Quantities are normalized to allow comparison to Fig 6.12. Values were calculated from simulated phase-stepping data with Poisson noise ($a_0 = 15$ photons, $n = 5$, $\hat{V} = 0\ldots1 \Rightarrow \hat{\eta} = 0\ldots6$). Even for the very low-statistics case shown here, inexact knowledge of σ has very little effect (compare dashed and solid lines). Note that, unlike the other curves, the normalized form of Var(V) also varies with $n \cdot a_0$, especially for high visibility values.

of σ according to Eq. (6.81). Visibility values were calculated by dividing the bias-corrected a_1 values by a_0. Bias and variance were calculated from an ensemble of 5×10^5 stepping curves. The results are shown in Fig. 6.13.

It is apparent that even for the low-statistics case presented here, bias and variance of a_1 and V hardly change when σ is derived from the measurement data. This suggests that the presented bias correction methods can directly be applied to measurement data.

The estimation of σ may be significantly more difficult if energy-integrating detectors are used. Since the detection signal generated by a photon is proportional to its energy, measured intensity values are not Poisson-distributed. The most practical approach in this situation is to develop an empirical relation between mean intensity and variance for the given imaging system, to allow an estimation of σ. Since the underlying distribution of intensity values, and thus the relation of mean and variance, is also a function of the detected spectrum, this empirical model should also parameterize the amount of beam-hardening by the sample, e.g. via sample transmittance. In other words, mean and variance should be measured ahead of time, for many different amounts of exposure time and sample attenuation, so that variance can be reliably retrieved as a function of mean and transmittance.

6.3.4 Discussion

It is not apparent from these results which correction method is generally the most suitable. An overcorrection, as observed for η_{ML} and η_{Mean}, may be undesirable, and the near-perfect correction of bias values by η_{Mode}, η_{GP}, or $\eta_{\mathrm{ji}}^{(2)}$ for $\hat{\eta} > 2$ may be preferable. In cases of very low statistics (i.e., very low values of $\hat{\eta}$), noise in dark-field images will usually be so high that subtle differences in bias correction are imperceptible.

Noisy dark-field data is often low-pass filtered to improve the images' visual impression. This can obfuscate bias problems: while the noise levels is obviously reduced by this operation, the bias remains, possibly leading to an overestimation of visibility (i.e., an *underestimation* of the dark-field activity) of low-SNR image regions. This can be avoided by applying a bias correction prior to low-pass filtering.

Another issue to consider is that the present analysis demonstrates bias and variances as a function of $\hat{\eta}$. In a realistic imaging scenario, noise may however be dominated by spatial fluctuations of $\hat{\eta}$: Dark-field signal generated by foams or lung tissue may exhibit "structural noise", e.g. due to a spatial variation in the number of scattering interfaces, even for constant (macroscopic) sample thickness. This does not limit the validity of the presented approach, but may lead to unexpected behavior, e.g. a differing change of mean and variance by bias correction (compared to simulations) in ROIs of such samples.

Finally, visibility values may be distorted by thse presence of Compton scattering. Image regions strongly affected by Compton scatter will often coincide with those affected by visibility bias. Unfortunately, the correction of Compton scatter is very challenging. An approach based on Monte-Carlo corrections has been presented in [Grom17]. However, this is very time-consuming and requires prior knowledge of the object. For now, a general, fast Compton correction for X-ray dark-field imaging remains an open problem. An adaptation of commercial software-based Compton correction methods for radiography [Ment+14] to grating-based X-ray imaging systems may however be feasible. In terms of order, any Compton scatter corrections should precede bias corrections.

Conclusion and outlook

> In science, each of us knows that what he has accomplished will be antiquated in ten, twenty, fifty years. That is the fate to which science is subjected; it is the very *meaning* of scientific work, to which it is devoted in a quite specific sense [...] Every scientific "fulfilment" raises new "questions"; it *asks* to be "surpassed" and outdated. Whoever wishes to serve science has to resign himself to this fact.
>
> Max Weber, *Wissenschaft als Beruf (Science as a Vocation)*, translated from German

This work discusses the design and use of the lung-scanning setup, a device producing images of the refraction and scattering of X-rays using diffraction gratings. It uses a scanning technique to generate radiographs of large objects despite the limited size of the used gratings.

A brief historical overview of important developments in medical X-ray imaging, interferometry, and X-ray phase contrast is given in chapter 1. This overview provides some historical context for the construction and operation of the *lung-scanning setup*.

The physical fundamentals of X-rays, namely their generation, their propagation through space, and their interaction with matter, are presented in chapter 2. Furthermore, grating-based X-ray imaging fundamentals are introduced, including an extensive discussion of the origin of the dark-field signal.

While design aspects of the lung-scanning setup are summarized in chapter 3, these have been discussed more extensively in the doctoral thesis of my former colleague, Dr. Lukas Gromann [Grom17]. However, the present work adds in-depth information about the calculation of images and its software implementation in chapter 4, which was the focus of the first few years of my doctoral work.

Three dark-field imaging studies on pigs and human bodies (previously published) are presented in chapter 5. These have revealed findings that are of importance for future clinical implementation of dark-field thorax radiography. The first study demonstrates the value of the method for pneumothorax detection, continuing earlier, similar work on small animals. It established a much-improved depiction of pneumothoraxes in the dark-field modality, especially when they were oriented laterally. However, the presence and magnitude of dorsal pneumothoraxes could also be identified.

The second study examines the influence of the dark-field signal from pig lungs on inspiration state and lung thickness. It found that the dark-field per lung thickness is far greater on expiration. In contrast, the ratio of dark-field and attenuation due to the lung is approximately independent of the inspiration state. These findings assist in the distinction between breathing-related and pathological variations in lung dark-field signal strength.

Furthermore, dark-field and attenuation noise levels in the region of the pig lungs were compared with the help of phantom measurements, yielding the result that the CNR achievable for lung tissue in the dark-field modality is far lower than in conventional X-ray. This suggests that any signal strength advantage of the dark-field modality over conventional chest X-ray is mainly due to the absence of superimposed structures from other tissues.

The third work examines a variety of imaging features in dark-field thorax radiographs of several human cadavers. This provided the first visualization of several types of pathologies in this modality and gave evidence of the appearance of dark-field human thorax radiographs in future clinical applications. Furthermore, the performed reader study identified a vertical (*apicobasal*) gradient in the dark-field signal's graded strength. High values for inter- and intra-observer agreement suggest that dark-field radiography is compatible with a traditional, "qualitative" evaluation of

image data by radiologists.

Finally, chapter 6 introduces three theoretical subjects focused on dark-field signal formation. The first of these demonstrates a hitherto unknown phenomenon, *visibility-hardening*. Being mathematically equivalent to *beam-hardening*, this effect implies that the dark-field signal of an object is reduced when it is placed behind other dark-field active materials. This effect thus has significant implications for the correct quantitative interpretation of polychromatic dark-field measurements.

The second theoretical work presents a new perspective on the image formation in a Talbot-Lau setup by calculating the wave fields with partial coherence theory. Other than in the commonly-used approach based on Fresnel propagation, this allows for a full description of the wave field upstream of the modulation grating. Furthermore, the setup's position-dependent *autocorrelation length* is directly related to quantities emerging from this calculation. This analysis promotes a clearer understanding of the physical mechanisms of image formation in the Talbot-Lau setup.

The final work examines different methods for estimating the bias inherent to the calculation of the dark-field signal. Their performance is compared in terms of bias reduction and noise increase. The presented methods are simple to apply to visibility maps with associated noise estimates.

Regarding current and future developments, work on the *lung-scanning setup* is ongoing under the guidance of Ms. Jana Andrejewski and Prof. Dr. Julia Herzen. This work has lead to additional imaging studies ([Saut+19] and other submitted work), as well as an exploration of dark-field tomosynthesis approaches.

Additionally, several of my colleagues, chiefly among them Mr. Konstantin Willer, Mr. Wolfgang Noichl, Ms. Theresa Urban, Ms. Manuela Frank, and Mr. Rafael Schick, have expended an extraordinary amount of work on the development and optimization of a successor of the *lung-scanning setup* for clinical studies. This device has been installed in the Department of Diagnostic and Interventional Radiology at the university hospital "Rechts der Isar" in Munich. It is used in a patient study evaluating dark-field radiography for early detection of COPD. A large amount of experience was gained during the lung-scanning setup's design and operation, thus influencing design decisions for this new clinical setup. Likewise, the software package presented in chapter 4 has been used as a starting point for numerous algorithmic developments for the clinical study setup.

In conclusion, many of the developments and studies from the *lung-scanning setup* presented in this thesis have served as stepping stones to the goal of clinical implementation of dark-field radiography. Furthermore, some of the theoretical findings are also relevant for other applications of X-ray dark-field imaging.

Bibliography

[Agos+03] S. Agostinelli, J. Allison, K. Amako, J. Apostolakis, H. Araujo, P. Arce, M. Asai, D. Axen, S. Banerjee, G. Barrand, et al. "Geant4—a simulation toolkit." In: *Nuclear Instruments and Methods in Physics Research Section A: Accelerators, Spectrometers, Detectors and Associated Equipment* 506.3 (July 2003), pp. 250–303. ISSN: 0168-9002. DOI: 10.1016/S0168-9002(03)01368-8 (cit. on p. 44).

[Aitc+93] F. Aitchison, A. Bleetman, P. Munro, D. McCarter, and A. W. Reid. "Detection of pneumothorax by accident and emergency officers and radiologists on single chest films." In: *Emergency Medicine Journal* 10.4 (Dec. 1993), pp. 343–346. ISSN: 1472-0205. DOI: 10.1136/emj.10.4.343 (cit. on p. 117).

[AlsN+11] Als-Nielsen, Jens and McMorrow, Des. *Elements of Modern X-ray Physics*. 2nd ed. John Wiley & Sons, Ltd, 2011. ISBN: 978-0-470-97395-0 (cit. on pp. 21, 36–37, 39, 44–45).

[Alva+76] R. E. Alvarez and A. Macovski. "Energy-selective reconstructions in X-ray computerized tomography." In: *Physics in Medicine & Biology* 21.5 (Sept. 1976), pp. 733–744. ISSN: 0031-9155. DOI: 10.1088/0031-9155/21/5/002 (cit. on p. 15).

[Ande+08] R. Andersson, L. F. van Heijkamp, I. M. de Schepper, and W. G. Bouwman. "Analysis of spin-echo small-angle neutron scattering measurements." In: *Journal of Applied Crystallography* 41.5 (Oct. 2008), pp. 868–885. ISSN: 0021-8898. DOI: 10.1107/S0021889808026770 (cit. on pp. 67, 166–167).

[Ando+72] M. Ando and S. Hosoya. "An Attempt at X-Ray Phase-Contrast Microscopy." In: *Proceedings of the 6th International Conference on X-Ray Optics and Microanalysis*. Ed. by G. Shinoda, K. Kohra, and T. Ichinokawa. University of Tokyo Press, 1972, pp. 63–68 (cit. on p. 22).

[Arde39] M. von Ardenne. "Zur Leistungsfähigkeit des Elektronen-Schattenmikroskopes und über ein Röntgenstrahlen-Schattenmikroskop." German. In: *Die Naturwissenschaften* 27.28 (July 1939), pp. 485–486. ISSN: 0028-1042. DOI: 10.1007/bf01489234 (cit. on p. 21).

[Arga+06] I. Arganda-Carreras, C. O. S. Sorzano, R. Marabini, J. M. Carazo, C. Ortiz-de-Solórzano, and J. Kybic. "Consistent and Elastic Registration of Histological Sections using Vector-Spline Regularization." In: *Lecture Notes in Computer Science: Computer Vision Approaches to Medical Image Analysis*. Vol. 4241. Springer, 2006, pp. 85–95. ISBN: 978-3-540-46257-6. DOI: 10.1007/11889762_8 (cit. on p. 132).

[Attw99] D. T. Attwood. *Soft X-rays and Extreme Ultraviolet Radiation*. 1st ed. Cambridge University Press, 1999. ISBN: 978-0-521-02997-1 (cit. on p. 45).

[Auke+12] T. S. Aukema, L. F. M. Beenen, F. Hietbrink, and L. P. H. Leenen. "Initial assessment of chest X-ray in thoracic trauma patients: Awareness of specific injuries." In: *World Journal of Radiology* 4.2 (Feb. 2012), pp. 48–52. ISSN: 1949-8470. DOI: 10.4329/wjr.v4.i2.48 (cit. on p. 120).

[Bach+17] S. Bachche, M. Nonoguchi, K. Kato, M. Kageyama, T. Koike, M. Kuribayashi, and A. Momose. "Laboratory-based X-ray phase-imaging scanner using Talbot-Lau interferometer for non-destructive testing." In: *Scientific Reports* 7, 6711 (July 2017). ISSN: 2045-2322. DOI: 10.1038/s41598-017-07032-y (cit. on p. 73).

[Bach+95] W. Bacher, W. Menz, and J. Mohr. "The LIGA Technique and its Potential for Microsystems—A Survey." In: *IEEE Transactions on Industrial Electronics* 42.5 (Oct. 1995), pp. 431–441. ISSN: 0278-0046. DOI: 10.1109/41.464604 (cit. on pp. 26, 73).

[Ball+09] C. G. Ball, K. Ranson, C. J. Dente, D. V. Feliciano, K. B. Laupland, D. Dyer, K. Inaba, V. Trottier, I. Datta, and A. W. Kirkpatrick. "Clinical predictors of occult pneumothoraces in severely injured blunt polytrauma patients: A prospective observational study." In: *Injury* 40.1 (Jan. 2009), pp. 44–47. ISSN: 0020-1383. DOI: 10.1016/j.injury.2008.07.015 (cit. on p. 117).

[Ball+16] R. Ballabriga, J. Alozy, M. Campbell, E. Frojdh, E. Heijne, T. Koenig, X. Llopart, J. Marchal, D. Pennicard, T. Poikela, L. Tlustos, P. Valerio, W. Wong, and M. Zuber. "Review of hybrid pixel detector readout ASICs for spectroscopic X-ray imaging." In: *Journal of Instrumentation* 11.1, P01007 (Jan. 2016). ISSN: 1748-0221. DOI: 10.1088/1748-0221/11/01/P01007 (cit. on pp. 51–52).

[Bast+16] D. Basta, M. Endrizzi, F. A. Vittoria, A. Astolfo, and A. Olivo. "Compact and cost effective lab-based edge-illumination x-ray phase contrast imaging with a structured focal spot." In: *Applied Physics Letters* 108.22, 224102 (June 2016). ISSN: 0003-6951. DOI: 10.1063/1.4953459 (cit. on p. 29).

[Bech+10] M. Bech, O. Bunk, T. Donath, R. Feidenhans'l, C. David, and F. Pfeiffer. "Quantitative x-ray dark-field computed tomography." In: *Physics in Medicine & Biology* 55.18 (Aug. 2010), pp. 5529–5539. ISSN: 0031-9155. DOI: 10.1088/0031-9155/55/18/017 (cit. on pp. 63, 160, 165).

[Bech+13] M. Bech, A. Tapfer, A. Velroyen, A. Yaroshenko, B. Pauwels, J. Hostens, P. Bruyndonckx, A. Sasov, and F. Pfeiffer. "In-vivo dark-field and phase-contrast x-ray imaging." In: *Scientific Reports* 3, 3209 (Nov. 2013). ISSN: 2045-2322. DOI: 10.1038/srep03209 (cit. on pp. 32, 70).

[Bech09] M. Bech. "X-ray imaging with a grating interferometer." PhD thesis. University of Copenhagen, 2009 (cit. on pp. 56, 58).

[Beck06] E. C. Beckmann. "CT scanning the early days." In: *The British Journal of Radiology* 79.937, 29444122 (Jan. 2006). ISSN: 0007-1285. DOI: 10.1259/bjr/29444122 (cit. on p. 13).

[Behl15] R. Behling. *Modern Diagnostic X-Ray Sources: Technology, Manufacturing, Reliability*. CRC Press, June 2015. 423 pp. ISBN: 978-1-4822-4132-7 (cit. on pp. 11, 49).

[Behl18] R. Behling. "History of X-ray Tubes." In: *Handbook of X-ray Imaging*. Ed. by P. Russo. Taylor & Francis Group, LLC, 2018, pp. 139–154. ISBN: 978-1-4987-4152-1 (cit. on p. 10).

[Behl90] R. Behling. "The MRC 200: a new high-output X-ray tube." In: *MedicaMundi* 35.1 (Jan. 1990), pp. 57–64. ISSN: 0025-7664 (cit. on pp. 48, 167).

[Beru+12] S. Berujon, H. Wang, and K. Sawhney. "X-ray multimodal imaging using a random-phase object." In: *Physical Review A* 86.6, 063813 (Dec. 2012). ISSN: 2469-9926. DOI: 10.1103/physreva.86.063813 (cit. on p. 70).

[Béru+12] S. Bérujon, E. Ziegler, R. Cerbino, and L. Peverini. "Two-Dimensional X-Ray Beam Phase Sensing." In: *Physical Review Letters* 108.15, 158102 (Apr. 2012). ISSN: 0031-9007. DOI: 10.1103/physrevlett.108.158102 (cit. on p. 28).

[Bons+65] U. Bonse and M. Hart. "An X-ray interferometer." In: *Applied Physics Letters* 6.8 (Apr. 1965), pp. 155–156. ISSN: 0003-6951. DOI: 10.1063/1.1754212 (cit. on p. 22).

[Bouw+02] W. Bouwman, O. Uca, S. Grigoriev, W. Kraan, J. Plomp, and M. Rekveldt. "First quantitative test of spin-echo small-angle neutron scattering." In: *Applied Physics A: Materials Science & Processing* 74 (Dec. 2002), s115–s117. ISSN: 0947-8396. DOI: 10.1007/s003390101081 (cit. on p. 68).

[Brar+10] M. S. Brar, I. Bains, G. Brunet, S. Nicolaou, C. G. Ball, and A. W. Kirkpatrick. "Occult Pneumothoraces Truly Occult or Simply Missed: Redux." In: *The Journal of Trauma: Injury, Infection, and Critical Care* 69.6 (Dec. 2010), pp. 1335–1337. ISSN: 2163-0755. DOI: 10.1097/TA.0b013e3181f6f525 (cit. on p. 117).

[Brav+13] A. Bravin, P. Coan, and P. Suortti. “X-ray phase-contrast imaging: from pre-clinical applications towards clinics.” In: *Physics in Medicine & Biology* 58.1 (Jan. 2013), R1–R35. ISSN: 0031-9155. DOI: 10.1088/0031-9155/58/1/R1 (cit. on p. 70).

[Broo+76] R. A. Brooks and G. Di Chiro. “Principles of computer assisted tomography (CAT) in radiographic and radioisotopic imaging.” In: *Physics in Medicine & Biology* 21.5 (Sept. 1976), pp. 689–732. ISSN: 0031-9155. DOI: 10.1088/0031-9155/21/5/001 (cit. on pp. 12–13).

[Brow+12] S. E. Brown, M. Macanovic, and M. P. Williams. “Oxygen Reservoir Bags Simulating Chest Pathology: A Case Series.” In: *The Journal of Emergency Medicine* 43.6 (Dec. 2012), pp. 1045–1048. ISSN: 0736-4679. DOI: 10.1016/j.jemermed.2012.01.053 (cit. on p. 117).

[Buzu08] T. M. Buzug. *Computed Tomography*. Springer-Verlag, 2008. ISBN: 978-3-540-39408-2. DOI: 10.1007/978-3-540-39408-2 (cit. on pp. 12–13).

[Carm+96] J. H. E. Carmichael, C. Maccia, B. M. Moores, J. W. Oestmann, H. Schibilla, D. Teunen, R. V. Tiggelen, and B. Wall, eds. *European guidelines on quality criteria for diagnostic radiographic images*. EUR 16260. 1996. URL: https://publications.europa.eu/s/lKRX (cit. on p. 147).

[Chab+11] M. Chabior, T. Donath, C. David, M. Schuster, C. Schroer, and F. Pfeiffer. “Signal-to-noise ratio in x ray dark-field imaging using a grating interferometer.” In: *Journal of Applied Physics* 110.5, 053105 (Sept. 2011). ISSN: 0021-8979. DOI: 10.1063/1.3630051 (cit. on pp. 27, 56, 108, 186).

[Chab11] M. Chabior. “Contributions to the characterization of grating-based x-ray phase-contrast imaging.” PhD thesis. Technische Universität Dresden, 2011 (cit. on p. 72).

[Chap+97] D. Chapman, W. Thomlinson, R. E. Johnston, D. Washburn, E. Pisano, N. Gmür, Z. Zhong, R. Menk, F. Arfelli, and D. Sayers. “Diffraction enhanced x-ray imaging.” In: *Physics in Medicine & Biology* 42.11 (Nov. 1997), pp. 2015–2025. ISSN: 0031-9155. DOI: 10.1088/0031-9155/42/11/001 (cit. on p. 23).

[Choi14] W.-I. Choi. “Pneumothorax.” In: *Tuberculosis and Respiratory Diseases* 76.3 (Mar. 2014), pp. 99–104. ISSN: 0355-5011. DOI: 10.4046/trd.2014.76.3.99 (cit. on p. 117).

[Clau+92] J. F. Clauser and M. W. Reinsch. “New theoretical and experimental results in fresnel optics with applications to matter-wave and X-ray interferometry.” In: *Applied Physics B: Photophysics and Laser Chemistry* 54.5 (May 1992), pp. 380–395. ISSN: 0721-7269. DOI: 10.1007/BF00325384 (cit. on p. 26).

[Cloe+97] P. Cloetens, J. P. Guigay, C. De Martino, J. Baruchel, and M. Schlenker. “Fractional Talbot imaging of phase gratings with hard x rays.” In: *Optics Letters* 22.14 (July 1997), pp. 1059–1061. ISSN: 0146-9592. DOI: 10.1364/OL.22.001059 (cit. on p. 25).

[Cloe+99] P. Cloetens, W. Ludwig, J. Baruchel, D. Van Dyck, J. Van Landuyt, J. P. Guigay, and M. Schlenker. “Holotomography: Quantitative phase tomography with micrometer resolution using hard synchrotron radiation x rays.” In: *Applied Physics Letters* 75.19 (Nov. 1999), pp. 2912–2914. ISSN: 0003-6951. DOI: 10.1063/1.125225 (cit. on p. 24).

[Coan+10] P. Coan, A. Wagner, A. Bravin, P. C. Diemoz, J. Keyriläinen, and J. Mollenhauer. “In vivo x-ray phase contrast analyzer-based imaging for longitudinal osteoarthritis studies in guinea pigs.” In: *Physics in Medicine & Biology* 55.24 (Nov. 2010), pp. 7649–7662. ISSN: 0031-9155. DOI: 10.1088/0031-9155/55/24/017 (cit. on p. 30).

[Corm63] A. M. Cormack. “Representation of a Function by Its Line Integrals, with Some Radiological Applications.” In: *Journal of Applied Physics* 34.9 (Sept. 1963), pp. 2722–2727. ISSN: 0021-8979. DOI: 10.1063/1.1729798 (cit. on p. 12).

[Corm64] A. M. Cormack. “Representation of a Function by Its Line Integrals, with Some Radiological Applications. II.” In: *Journal of Applied Physics* 35.10 (Sept. 1964), pp. 2908–2913. ISSN: 0021-8979. DOI: 10.1063/1.1713127 (cit. on p. 12).

[Crum+18] A. B. Crummy, C. M. Strother, and C. A. Mistretta. "The History of Digital Subtraction Angiography." In: *Journal of Vascular and Interventional Radiology* 29.8 (Aug. 2018), pp. 1138–1141. ISSN: 1051-0443. DOI: 10.1016/j.jvir.2018.03.030 (cit. on p. 11).

[Davi+02] C. David, B. Nöhammer, H. H. Solak, and E. Ziegler. "Differential x-ray phase contrast imaging using a shearing interferometer." In: *Applied Physics Letters* 81.17 (Oct. 2002), pp. 3287–3289. ISSN: 0003-6951. DOI: 10.1063/1.1516611 (cit. on p. 25).

[Davi+07] C. David, J. Bruder, T. Rohbeck, C. Grunzweig, C. Kottler, A. Diaz, O. Bunk, and F. Pfeiffer. "Fabrication of diffraction gratings for hard X-ray phase contrast imaging." In: *Microelectronic Engineering* 84.5-8 (Feb. 2007), pp. 1172–1177. ISSN: 0167-9317. DOI: 10.1016/j.mee.2007.01.151 (cit. on p. 25).

[Davi+95] T. J. Davis, D. Gao, T. E. Gureyev, A. W. Stevenson, and S. W. Wilkins. "Phase-contrast imaging of weakly absorbing materials using hard X-rays." In: *Nature* 373.6515 (Feb. 1995), pp. 595–598. ISSN: 0028-0836. DOI: 10.1038/373595a0 (cit. on p. 23).

[DeMa+18] F. De Marco, M. Marschner, L. Birnbacher, P. Noël, J. Herzen, and F. Pfeiffer. "Analysis and correction of bias induced by phase stepping jitter in grating-based X-ray phase-contrast imaging." In: *Optics Express* 26.10 (May 2018), pp. 12707–12722. ISSN: 1094-4087. DOI: 10.1364/OE.26.012707 (cit. on pp. 93, 118, 146).

[DeMa+19] F. De Marco, K. Willer, L. B. Gromann, J. Andrejewski, K. Hellbach, A. Bähr, M. Dmochewitz, T. Koehler, H.-I. Maack, F. Pfeiffer, and J. Herzen. "Contrast-to-noise ratios and thickness-normalized, ventilation-dependent signal levels in dark-field and conventional in vivo thorax radiographs of two pigs." In: *PLOS ONE* 14.6, e0217858 (June 2019). ISSN: 1932-6203. DOI: 10.1371/journal.pone.0217858 (cit. on pp. 32, 113, 116, 127).

[DeMa+20] F. De Marco, J. Andrejewski, K. Willer, L. Gromann, T. Koehler, H.-I. Maack, J. Herzen, and F. Pfeiffer. "X-ray dark-field signal reduction due to hardening of the visibility spectrum." In: *arXiv.org* (Nov. 2020). arXiv: 2011.03542v1 [physics.med-ph] (cit. on p. 160).

[DeMa17] D. N. DeMaio. "CT Radiation Dose and Risk: Fact vs Fiction." In: *Radiologic Technology* 89.2 (Nov. 2017). PubMed ID: 29298927, pp. 199–205. ISSN: 0033-8397 (cit. on p. 14).

[Diem+16] P. C. Diemoz, A. Bravin, A. Sztrókay-Gaul, M. Ruat, S. Grandl, D. Mayr, S. Auweter, A. Mittone, E. Brun, C. Ponchut, M. F. Reiser, P. Coan, and A. Olivo. "A method for high-energy, low-dose mammography using edge illumination x-ray phase-contrast imaging." In: *Physics in Medicine & Biology* 61.24 (Dec. 2016), pp. 8750–8761. ISSN: 0031-9155. DOI: 10.1088/1361-6560/61/24/8750 (cit. on p. 29).

[DiLe93] L. Di Lella. "Elementary particle physics at the SC." In: *Physics Reports* 225.1 (Apr. 1993), pp. 45–66. ISSN: 0370-1573. DOI: 10.1016/0370-1573(93)90158-A (cit. on p. 19).

[Dona+09] T. Donath, M. Chabior, F. Pfeiffer, O. Bunk, E. Reznikova, J. Mohr, E. Hempel, S. Popescu, M. Hoheisel, M. Schuster, J. Baumann, and C. David. "Inverse geometry for grating-based x-ray phase-contrast imaging." In: *Journal of Applied Physics* 106, 054703 (Sept. 2009). ISSN: 0021-8979. DOI: 10.1063/1.3208052 (cit. on pp. 26, 59, 61–62, 181–182).

[Donn+09] M. Donnelley, K. S. Morgan, A. Fouras, W. Skinner, K. Uesugi, N. Yagi, K. K. W. Siu, and D. W. Parsons. "Real-time non-invasive detection of inhalable particulates delivered into live mouse airways." In: *Journal of Synchrotron Radiation* 16.4 (July 2009), pp. 553–561. ISSN: 0909-0495. DOI: 10.1107/S0909049509012618 (cit. on p. 31).

[Dyso90] N. A. Dyson. *X-Rays in Atomic and Nuclear Physics*. 2nd ed. Cambridge University Press, 1990. 416 pp. ISBN: 978-0-521-26280-4 (cit. on p. 47).

[Eggl+14] E. Eggl, A. Malecki, F. Schaff, G. Potdevin, P. B. Noël, J. S. Bauer, O. Gordijenko, E. Grande García, R. Burgkart, E. J. Rummeny, T. Baum, and F. Pfeiffer. "Prediction of Vertebral Failure Load by Using X-Ray Vector Radiographic Imaging." In: *Radiology* 275.2 (Dec. 2014), pp. 553–561. ISSN: 0033-8419. DOI: 10.1148/radiol.14141317 (cit. on p. 31).

[Eggl+18] E. Eggl, S. Grandl, A. Sztrókay-Gaul, M. Dierolf, C. Jud, L. Heck, K. Burger, B. Günther, K. Achterhold, D. Mayr, J. J. Wilkens, S. D. Auweter, B. Gleich, K. Hellerhoff, M. F. Reiser, F. Pfeiffer, and J. Herzen. "Dose-compatible grating-based phase-contrast mammography on mastectomy specimens using a compact synchrotron source." In: *Scientific Reports* 8, 15700 (Dec. 2018). ISSN: 2045-2322. DOI: 10.1038/s41598-018-33628-z (cit. on p. 30).

[Eise+12] E. Eisenhuber, C. M. Schaefer-Prokop, H. Prosch, and W. Schima. "Bedside Chest Radiography." In: *Respiratory Care* 57.3 (Mar. 2012), pp. 427–443. ISSN: 0020-1324. DOI: 10.4187/respcare.01712 (cit. on p. 122).

[Elde+48] F. R. Elder, R. V. Langmuir, and H. C. Pollock. "Radiation from Electrons Accelerated in a Synchrotron." In: *Physical Review* 74.1 (July 1948), pp. 52–56. ISSN: 0031-899X. DOI: 10.1103/physrev.74.52 (cit. on p. 20).

[Endr+14] M. Endrizzi and A. Olivo. "Absorption, refraction and scattering retrieval with an edge-illumination-based imaging setup." In: *Journal of Physics D: Applied Physics* 47.50, 505102 (Nov. 2014). ISSN: 0022-3727. DOI: 10.1088/0022-3727/47/50/505102 (cit. on pp. 28, 70).

[Endr18] M. Endrizzi. "X-ray phase-contrast imaging." In: *Nuclear Instruments and Methods in Physics Research Section A: Accelerators, Spectrometers, Detectors and Associated Equipment* 878 (Jan. 2018), pp. 88–98. ISSN: 0168-9002. DOI: 10.1016/j.nima.2017.07.036 (cit. on p. 23).

[Fari+88] G. W. Faris and R. L. Byer. "Three-dimensional beam-deflection optical tomography of a supersonic jet." In: *Applied Optics* 27.24 (Dec. 1988), pp. 5202–5212. ISSN: 1559-128X. DOI: 10.1364/AO.27.005202 (cit. on p. 26).

[Fing+19] A. A. Fingerle, F. De Marco, J. Andrejewski, K. Willer, L. B. Gromann, W. Noichl, F. Kriner, F. Fischer, C. Braun, H.-I. Maack, T. Pralow, T. Koehler, P. B. Noël, F. Meurer, D. Deniffel, A. P. Sauter, B. Haller, D. Pfeiffer, E. J. Rummeny, J. Herzen, and F. Pfeiffer. "Imaging features in post-mortem x-ray dark-field chest radiographs and correlation with conventional x-ray and CT." In: *European Radiology Experimental* 3.1, 25 (July 2019). ISSN: 2509-9280. DOI: 10.1186/s41747-019-0104-7 (cit. on pp. 32, 69, 113, 116, 145).

[Fitz+96] A. W. Fitzgibbon, M. Pilu, and R. B. Fisher. "Direct least squares fitting of ellipses." In: *Proceedings of 13th International Conference on Pattern Recognition*. IEEE, Aug. 1996, pp. 476–480. ISBN: 978-0-8186-7282-8. DOI: 10.1109/icpr.1996.546029 (cit. on p. 94).

[Flei+11] D. Fleischmann and F. E. Boas. "Computed tomography—old ideas and new technology." In: *European Radiology* 21.3 (Jan. 2011), pp. 510–517. ISSN: 0938-7994. DOI: 10.1007/s00330-011-2056-z (cit. on p. 14).

[Fort+20] S. Forte, Z. Wang, C. Arboleda, K. Lång, G. Singer, R. A. Kubik-Huch, and M. Stampanoni. "Can grating interferometry-based mammography discriminate benign from malignant microcalcifications in fresh biopsy samples?" In: *European Journal of Radiology* 129, 109077 (Aug. 2020). ISSN: 0720-048X. DOI: 10.1016/j.ejrad.2020.109077 (cit. on p. 29).

[Fost+02] G. T. Foster, J. B. Fixler, J. M. McGuirk, and M. A. Kasevich. "Method of phase extraction between coupled atom interferometers using ellipse-specific fitting." In: *Optics Letters* 27.11 (June 2002), pp. 951–953. ISSN: 0146-9592. DOI: 10.1364/OL.27.000951 (cit. on p. 94).

[Fres00] A. J. Fresnel. "Memoir on the diffraction of light." In: *The wave theory of light. Memoirs by Huygens, Young and Fresnel*. Ed. by H. Crew. 1900, pp. 81–144 (cit. on p. 15).

[Gay+94] S. B. Gay, C. L. Sistrom, C. A. Holder, and P. M. Suratt. “Breath-Holding Capability of Adults.” In: *Investigative Radiology* 29.9 (Sept. 1994), pp. 848–851. ISSN: 0020-9996. DOI: 10.1097/00004424-199409000-00009 (cit. on p. 125).

[Gold08] L. W. Goldman. “Principles of CT: Multislice CT.” In: *Journal of Nuclear Medicine Technology* 36.2 (June 2008), pp. 57–68. ISSN: 0091-4916. DOI: 10.2967/jnmt.107.044826 (cit. on p. 14).

[Good05] J. W. Goodman. *Introduction to Fourier Optics*. 3rd ed. Roberts & Company Publishers, Jan. 2005. 528 pp. ISBN: 978-0-9747077-2-3 (cit. on pp. 34–35, 53–54, 180).

[Good85] J. W. Goodman. *Statistical Optics*. 1st ed. John Wiley & Sons, Inc., 1985. ISBN: 978-0-471-39916-2 (cit. on pp. 34, 173–174).

[Gord80] R. Gordon. “The deep sulcus sign.” In: *Radiology* 136.1 (July 1980), pp. 25–27. ISSN: 0033-8419. DOI: 10.1148/radiology.136.1.7384513 (cit. on pp. 117, 120).

[Grad+19] R. Gradl, M. Dierolf, L. Yang, L. Hehn, B. Günther, W. Möller, D. Kutschke, T. Stoeger, B. Gleich, K. Achterhold, M. Donnelley, F. Pfeiffer, O. Schmid, and K. S. Morgan. “Visualizing treatment delivery and deposition in mouse lungs using in vivo x-ray imaging.” In: *Journal of Controlled Release* 307 (Aug. 2019), pp. 282–291. ISSN: 0168-3659. DOI: 10.1016/j.jconrel.2019.06.035 (cit. on p. 31).

[Grom+17] L. Gromann, F. De Marco, K. Willer, P. Noël, K. Scherer, B. Renger, B. Gleich, K. Achterhold, A. Fingerle, D. Muenzel, S. Auweter, K. Hellbach, M. Reiser, A. Bähr, M. Dmochewitz, T. Schroeter, F. Koch, P. Meyer, D. Kunka, J. Mohr, A. Yaroshenko, H.-I. Maack, T. Pralow, H. van der Heijden, R. Proksa, T. Koehler, N. Wieberneit, K. Rindt, E. Rummeny, F. Pfeiffer, and J. Herzen. “In-vivo X-ray Dark-Field Chest Radiography of a Pig.” In: *Scientific Reports* 7, 4807 (July 2017). ISSN: 2045-2322. DOI: 10.1038/s41598-017-05101-w (cit. on pp. 32, 69, 85, 113, 115–116, 152).

[Grom17] L. Gromann. “Development of a large-animal X-ray dark-field scanner.” Dissertation. Technical University of Munich, 2017 (cit. on pp. 69, 115, 192–193).

[Gudb+95] H. Gudbjartsson and S. Patz. “The Rician Distribution of Noisy MRI Data.” In: *Magnetic Resonance in Medicine* 34.6 (Dec. 1995), pp. 910–914. ISSN: 0740-3194. DOI: 10.1002/mrm.1910340618 (cit. on p. 187).

[Gust20] A. Gustschin. “Translation: About one scheme of tomography.” In: *arXiv:2004.03750 [physics]* (Apr. 2020). arXiv: 2004.03750 (cit. on p. 12).

[Gutt02] D. Guttery. “Cuthbert Andrews.” In: *The Invisible Light* 17 (June 2002). Ed. by A. M. K. Thomas. Retrieved from: http://www.bshr.org.uk/journals/IL17.pdf (2020-09-24). ISSN: 1479-6945 (cit. on p. 9).

[Halí+98] R. Halíř and J. Flusser. “Numerically Stable Direct Least Squares Fitting Of Ellipses.” In: *Sixth International Conference in Central Europe on Computer Graphics and Visualization*. Vol. 98. 1998, pp. 125–132 (cit. on pp. 94–95).

[Hari06] P. Hariharan. *Basics of Interferometry*. 2nd ed. Academic Press, Nov. 2006, p. 248. ISBN: 978-0-12-373589-8 (cit. on p. 16).

[Haus+14] N. Hauser, Z. Wang, R. A. Kubik-Huch, M. Trippel, G. Singer, M. K. Hohl, E. Roessl, T. Köhler, U. van Stevendaal, N. Wieberneit, and M. Stampanoni. “A Study on Mastectomy Samples to Evaluate Breast Imaging Quality and Potential Clinical Relevance of Differential Phase Contrast Mammography:” in: *Investigative Radiology* 49.3 (Mar. 2014), pp. 131–137. ISSN: 0020-9996. DOI: 10.1097/RLI.0000000000000001 (cit. on p. 29).

[Hell+15] K. Hellbach, A. Yaroshenko, F. G. Meinel, A. Ö. Yildirim, T. M. Conlon, M. Bech, M. Mueller, A. Velroyen, M. Notohamiprodjo, F. Bamberg, S. Auweter, M. Reiser, O. Eickelberg, and F. Pfeiffer. "In Vivo Dark-Field Radiography for Early Diagnosis and Staging of Pulmonary Emphysema." In: *Investigative Radiology* 50.7 (July 2015), pp. 430–435. ISSN: 0020-9996. DOI: 10.1097/RLI.0000000000000147 (cit. on pp. 32, 70, 115, 152).

[Hell+16] K. Hellbach, A. Yaroshenko, K. Willer, T. Pritzke, A. Baumann, N. Hesse, S. Auweter, M. F. Reiser, O. Eickelberg, F. Pfeiffer, A. Hilgendorff, and F. G. Meinel. "Facilitated Diagnosis of Pneumothoraces in Newborn Mice Using X-ray Dark-Field Radiography." In: *Investigative Radiology* 51.10 (Oct. 2016), pp. 597–601. ISSN: 0020-9996. DOI: 10.1097/RLI.0000000000000285 (cit. on pp. 32, 70, 115–116, 122).

[Hell+17] K. Hellbach, A. Yaroshenko, K. Willer, T. M. Conlon, M. B. Braunagel, S. Auweter, A. Ö. Yildirim, O. Eickelberg, F. Pfeiffer, M. F. Reiser, and F. G. Meinel. "X-ray dark-field radiography facilitates the diagnosis of pulmonary fibrosis in a mouse model." In: *Scientific Reports* 7, 340 (Dec. 2017). ISSN: 2045-2322. DOI: 10.1038/s41598-017-00475-3 (cit. on pp. 32, 70, 115, 127, 130, 132, 141–143, 152).

[Hell+18a] K. Hellbach, A. Baehr, F. De Marco, K. Willer, L. B. Gromann, J. Herzen, M. Dmochewitz, S. Auweter, A. A. Fingerle, P. B. Noël, E. J. Rummeny, A. Yaroshenko, H.-I. Maack, T. Pralow, H. van der Heijden, N. Wieberneit, R. Proksa, T. Koehler, K. Rindt, T. J. Schroeter, J. Mohr, F. Bamberg, B. Ertl-Wagner, F. Pfeiffer, and M. F. Reiser. "Depiction of pneumothoraces in a large animal model using x-ray dark-field radiography." In: *Scientific Reports* 8, 2602 (Feb. 2018). ISSN: 2045-2322. DOI: 10.1038/s41598-018-20985-y (cit. on pp. 32, 69, 113, 116–117).

[Hell+18b] K. Hellbach, F. G. Meinel, T. M. Conlon, K. Willer, A. Yaroshenko, A. Velroyen, M. Braunagel, S. Auweter, M. F. Reiser, O. Eickelberg, F. Pfeiffer, and A. Ö. Yildirim. "X-Ray Dark-field Imaging to Depict Acute Lung Inflammation in Mice." In: *Scientific Reports* 8, 2096 (Dec. 2018). ISSN: 2045-2322. DOI: 10.1038/s41598-018-20193-8 (cit. on p. 32).

[Hern+14] A. M. Hernandez and J. M. Boone. "Tungsten anode spectral model using interpolating cubic splines: Unfiltered x-ray spectra from 20 kV to 640 kV." In: *Medical Physics* 41.4, 042101 (Mar. 2014). ISSN: 0094-2405. DOI: 10.1118/1.4866216 (cit. on p. 48).

[Hoes+05] C. Hoeschen, O. Tischenko, E. Buhr, and H. Illers. "Comparison of technical and anatomical noise in digital thorax X-ray images." In: *Radiation Protection Dosimetry* 114.1–3 (May 2005), pp. 75–80. ISSN: 0144-8420. DOI: 10.1093/rpd/nch543 (cit. on p. 124).

[Hofm10] J. Hofman. "The art of medical imaging: Philips and the evolution of medical x-ray technology." In: *MedicaMundi* 54.1 (2010), pp. 5–21 (cit. on p. 11).

[Houn73] G. N. Hounsfield. "Computerized transverse axial scanning (tomography). Part I. Description of system." In: *British Journal of Radiology* 46 (Feb. 1973), pp. 1016–1022. ISSN: 0007-1285. DOI: 10.1259/0007-1285-46-552-1016 (cit. on p. 13).

[Huan+09] Z.-F. Huang, K.-J. Kang, L. Zhang, Z.-Q. Chen, F. Ding, Z.-T. Wang, and Q.-G. Fang. "Alternative method for differential phase-contrast imaging with weakly coherent hard x rays." In: *Physical Review A* 79.1, 013815 (Jan. 2009). ISSN: 2469-9926. DOI: 10.1103/PhysRevA.79.013815 (cit. on p. 75).

[Hubb82] J. H. Hubbell. "Photon Mass Attenuation and Energy-absorption Coefficients from 1 keV to 20 MeV." In: *International Journal of Applied Radiation and Isotopes* 33.11 (Nov. 1982), pp. 1269–1290. ISSN: 0020-708X. DOI: 10.1016/0020-708X(82)90248-4 (cit. on pp. 41, 44).

[Hunt07] J. D. Hunter. "Matplotlib: A 2D graphics environment." In: *Computing in Science & Engineering* 9.3 (May 2007), pp. 90–95. ISSN: 1521-9615. DOI: 10.1109/MCSE.2007.55 (cit. on p. 119).

[Hurl+09] G. S. Hurlock, H. Higashino, and T. Mochizuki. “History of cardiac computed tomography: single to 320-detector row multislice computed tomography.” In: *International Journal of Cardiovascular Imaging* 25.S1 (Apr. 2009), pp. 31–42. ISSN: 1569-5794. DOI: 10.1007/s10554-008-9408-z (cit. on pp. 13–14).

[Infa+09] M. Infante, R. F. Lutman, S. Imparato, M. Di Rocco, G. L. Ceresoli, V. Torri, E. Morenghi, F. Minuti, S. Cavuto, E. Bottoni, F. Inzirillo, U. Cariboni, V. Errico, M. A. Incarbone, G. Ferraroli, G. Brambilla, M. Alloisio, and G. Ravasi. “Differential diagnosis and management of focal ground-glass opacities”. In: *European Respiratory Journal* 33.4 (Apr. 2009), pp. 821–827. ISSN: 0903-1936, 1399-3003. DOI: 10.1183/09031936.00047908 (cit. on p. 151).

[Inga+98] V. N. Ingal, E. A. Beliaevskaya, A. P. Brianskaya, and R. D. Merkurieva. “Phase mammography - a new technique for breast investigation.” In: *Physics in Medicine & Biology* 43.9 (Sept. 1998), pp. 2555–2567. ISSN: 0031-9155. DOI: 10.1088/0031-9155/43/9/009 (cit. on p. 29).

[Jenk+91] R. Jenkins, R. Manne, R. Robin, and C. Senemaud. “Nomenclature, symbols, units and their usage in spectrochemical analysis - VIII. Nomenclature system for X-ray spectroscopy (Recommendations 1991).” In: *Pure and Applied Chemistry* 63.5 (May 1991), pp. 735–746. ISSN: 0033-4545. DOI: 10.1351/pac199163050735 (cit. on pp. 38–39).

[Jens+10a] T. H. Jensen, M. Bech, O. Bunk, T. Donath, C. David, R. Feidenhans’l, and F. Pfeiffer. “Directional x-ray dark-field imaging.” In: *Physics in Medicine & Biology* 55.12 (May 2010), pp. 3317–3323. ISSN: 0031-9155. DOI: 10.1088/0031-9155/55/12/004 (cit. on p. 30).

[Jens+10b] T. H. Jensen, M. Bech, I. Zanette, T. Weitkamp, C. David, H. Deyhle, S. Rutishauser, E. Reznikova, J. Mohr, R. Feidenhans’l, and F. Pfeiffer. “Directional x-ray dark-field imaging of strongly ordered systems.” In: *Physical Review B* 82.21, 214103 (Dec. 2010). ISSN: 2469-9950. DOI: 10.1103/PhysRevB.82.214103 (cit. on p. 30).

[Ji+17] X. Ji, Y. Ge, R. Zhang, K. Li, and G.-H. Chen. “Studies of signal estimation bias in grating-based x-ray multicontrast imaging.” In: *Medical Physics* 44.6 (Mar. 2017), pp. 2453–2465. ISSN: 0094-2405. DOI: 10.1002/mp.12235 (cit. on pp. 187, 190).

[Jud+17] C. Jud, E. Braig, M. Dierolf, E. Eggl, B. Günther, K. Achterhold, B. Gleich, E. Rummeny, P. Noël, F. Pfeiffer, and D. Muenzel. “Trabecular bone anisotropy imaging with a compact laser-undulator synchrotron x-ray source.” In: *Scientific Reports* 7, 14477 (Nov. 2017). ISSN: 2045-2322. DOI: 10.1038/s41598-017-14830-x (cit. on p. 31).

[Jud19] C. Jud. “X-ray Vector Radiography for Biomedical Applications.” PhD thesis. Technische Universität München, 2019 (cit. on p. 31).

[Judg+14] E. P. Judge, J. M. L. Hughes, J. J. Egan, M. Maguire, E. L. Molloy, and S. O’Dea. “Anatomy and Bronchoscopy of the Porcine Lung. A Model for Translational Respiratory Medicine.” In: *American Journal of Respiratory Cell and Molecular Biology* 51.3 (Sept. 2014), pp. 334–343. ISSN: 1044-1549. DOI: 10.1165/rcmb.2013-0453TR (cit. on p. 116).

[Kagi+16] M. Kagias, Z. Wang, P. Villanueva-Perez, K. Jefimovs, and M. Stampanoni. “2D-Omnidirectional Hard-X-Ray Scattering Sensitivity in a Single Shot.” In: *Physical Review Letters* 116.9, 093902 (Mar. 2016). ISSN: 0031-9007. DOI: 10.1103/PhysRevLett.116.093902 (cit. on p. 31).

[Kagi+17] M. Kagias, Z. Wang, K. Jefimovs, and M. Stampanoni. “Dual phase grating interferometer for tunable dark-field sensitivity.” In: *Applied Physics Letters* 110.1, 014105 (Jan. 2017). ISSN: 0003-6951. DOI: 10.1063/1.4973520 (cit. on p. 27).

[Kagi+19] M. Kagias, Z. Wang, M. E. Birkbak, E. Lauridsen, M. Abis, G. Lovric, K. Jefimovs, and M. Stampanoni. “Diffractive small angle X-ray scattering imaging for anisotropic structures.” In: *Nature Communications* 10, 5130 (Nov. 2019). ISSN: 2041-1723. DOI: 10.1038/s41467-019-12635-2 (cit. on p. 31).

[Kasa+02] S. Kasap and J. Rowlands. "Direct-conversion flat-panel X-ray image sensors for digital radiography." In: *Proceedings of the IEEE* 90.4 (Apr. 2002), pp. 591–604. ISSN: 0018-9219. DOI: 10.1109/JPROC.2002.1002529 (cit. on p. 51).

[Kawr+20] I. Kawrakow, E. Mainegra-Hing, D. W. O. Rogers, F. Tessier, and B. R. B. Walters. *The EGSnrc code system: Monte Carlo simulation of electron and photon transport*. Tech. rep. PIRS-701. National Research Council Canada, Jan. 2020 (cit. on p. 44).

[Kell+06] A.-M. Kelly, D. Weldon, A. Y. L. Tsang, and C. A. Graham. "Comparison between two methods for estimating pneumothorax size from chest X-rays." In: *Respiratory Medicine* 100.8 (Jan. 2006), pp. 1356–1359. ISSN: 0954-6111. DOI: 10.1016/j.rmed.2005.11.022 (cit. on p. 117).

[Kirk+48] P. Kirkpatrick and A. V. Baez. "Formation of Optical Images by X-Rays." In: *Journal of the Optical Society of America* 38.9 (Sept. 1948), pp. 766–774. ISSN: 0030-3941. DOI: 10.1364/josa.38.000766 (cit. on p. 21).

[Kirk14] R. Kirk. "The first of its kind." In: *Nature Milestones* 511.13 (July 2014). ISSN: 0028-0836. DOI: 10.1038/nature13360 (cit. on p. 21).

[Kirz+09] J. Kirz and C. Jacobsen. "The History and Future of X-ray Microscopy." In: *Journal of Physics: Conference Series* 186, 012001 (Sept. 2009). ISSN: 1742-6588. DOI: 10.1088/1742-6596/186/1/012001 (cit. on pp. 21–22, 29).

[Kita00] H. Kitamura. "Recent trends of insertion-device technology for X-ray sources." In: *Journal of Synchrotron Radiation* 7.3 (May 2000), pp. 121–130. ISSN: 0909-0495. DOI: 10.1107/S0909049500002983 (cit. on p. 20).

[Kitc+04] M. J. Kitchen, D. Paganin, R. A. Lewis, N. Yagi, K. Uesugi, and S. T. Mudie. "On the origin of speckle in x-ray phase contrast images of lung tissue." In: *Physics in Medicine & Biology* 49.18 (Sept. 2004), pp. 4335–4348. ISSN: 0031-9155. DOI: 10.1088/0031-9155/49/18/010 (cit. on pp. 28, 31).

[Kitc+05] M. J. Kitchen, R. A. Lewis, N. Yagi, K. Uesugi, D. Paganin, S. B. Hooper, G. Adams, S. Jureczek, J. Singh, C. R. Christensen, A. P. Hufton, C. J. Hall, K. C. Cheung, and K. M. Pavlov. "Phase contrast X-ray imaging of mice and rabbit lungs: a comparative study." In: *The British Journal of Radiology* 78.935 (Nov. 2005), pp. 1018–1027. ISSN: 0007-1285. DOI: 10.1259/bjr/13024611 (cit. on p. 31).

[Kitc+10] M. J. Kitchen, D. M. Paganin, K. Uesugi, B. J. Allison, R. A. Lewis, S. B. Hooper, and K. M. Pavlov. "X-ray phase, absorption and scatter retrieval using two or more phase contrast images." In: *Optics Express* 18.19 (Sept. 2010), pp. 19994–20012. ISSN: 1094-4087. DOI: 10.1364/OE.18.019994 (cit. on p. 31).

[Knud+10] L. Knudsen, E. R. Weibel, H. J. G. Gundersen, F. V. Weinstein, and M. Ochs. "Assessment of air space size characteristics by intercept (chord) measurement: an accurate and efficient stereological approach." In: *Journal of Applied Physiology* 108.2 (Feb. 2010), pp. 412–421. ISSN: 1522-1601. DOI: 10.1152/japplphysiol.01100.2009 (cit. on p. 31).

[Koeh+15] T. Koehler, H. Daerr, G. Martens, N. Kuhn, S. Löscher, U. van Stevendaal, and E. Roessl. "Slit-scanning differential x-ray phase-contrast mammography: Proof-of-concept experimental studies." In: *Medical Physics* 42.4 (Mar. 2015), pp. 1959–1965. ISSN: 0094-2405. DOI: 10.1118/1.4914420 (cit. on pp. 29, 73–74).

[Kore+58] B. I. Korenblyum, S. N. Tetel'baum, and A. A. Tyutin. "Ob odnoy skheme tomografii [About one tomography scheme]." Russian. In: *Izvestija vyssich ucebnych zavedenij / Radiofizika [News of higher education institutions / Radiophysics]* 1.3 (1958), pp. 151–157. ISSN: 0021-3462 (cit. on p. 12).

[Kott+02] E. Kotter and M. Langer. "Digital radiography with large-area flat-panel detectors." In: *European Radiology* 12.10 (Mar. 2002), pp. 2562–2570. ISSN: 0938-7994. DOI: 10.1007/s00330-002-1350-1 (cit. on pp. 50, 71, 76).

[Kott+07] C. Kottler, F. Pfeiffer, O. Bunk, C. Grünzweig, and C. David. "Grating interferometer based scanning setup for hard x-ray phase contrast imaging." In: *Review of Scientific Instruments* 78.4, 043710 (Apr. 2007). ISSN: 0034-6748. DOI: 10.1063/1.2723064 (cit. on pp. 26, 71).

[Kozi+18] Q. Koziol and D. Robinson. *HDF5*. Computer software. USDOE Office of Science (SC), Advanced Scientific Computing Research (ASCR) (SC-21), Mar. 2018. DOI: 10.11578/DC.20180330.1 (cit. on p. 112).

[Lanc+16] J. L. Lancaster and B. Hasegawa. *Fundamental Mathematics and Physics of Medical Imaging*. CRC Press, Oct. 2016. ISBN: 978-1-4987-5161-2 (cit. on p. 50).

[Land+77] J. R. Landis and G. G. Koch. "The Measurement of Observer Agreement for Categorical Data." In: *Biometrics* 33.1 (Mar. 1977), pp. 159–174. ISSN: 0006-341X. DOI: 10.2307/2529310 (cit. on pp. 148, 151).

[Lars+11] D. H. Larsson, P. A. C. Takman, U. Lundström, A. Burvall, and H. M. Hertz. "A 24 keV liquid-metal-jet x-ray source for biomedical applications." In: *Review of Scientific Instruments* 82.12, 123701 (Dec. 2011). ISSN: 0034-6748. DOI: 10.1063/1.3664870 (cit. on p. 56).

[Lawr+32] E. O. Lawrence and M. S. Livingston. "The Production of High Speed Light Ions Without the Use of High Voltages." In: *Physical Review* 40.1 (Apr. 1932), pp. 19–35. ISSN: 0031-899X. DOI: 10.1103/PhysRev.40.19 (cit. on p. 19).

[Lewi+03] R. A. Lewis, C. J. Hall, A. P. Hufton, S. Evans, R. H. Menk, F. Arfelli, L. Rigon, G. Tromba, D. R. Dance, I. O. Ellis, A. Evans, E. Jacobs, S. E. Pinder, and K. D. Rogers. "X-ray refraction effects: application to the imaging of biological tissues." In: *The British Journal of Radiology* 76.905 (May 2003), pp. 301–308. ISSN: 0007-1285. DOI: 10.1259/bjr/32889803 (cit. on p. 31).

[LHC08] "LHC Machine." In: *Journal of Instrumentation* 3.8, S08001 (Aug. 2008). Ed. by L. Evans and P. Bryant. ISSN: 1748-0221. DOI: 10.1088/1748-0221/3/08/S08001 (cit. on p. 20).

[Li+20] X. Li, Z. Chen, L. Zhang, H. Gao, C. Wu, and X. Zhu. "A preclinical large-field-of-view X-ray multi-contrast lung imaging prototype." In: *Proceedings Volume 11312, Medical Imaging 2020*. Physics of Medical Imaging. Ed. by H. Bosmans and G.-H. Chen. 113121A. Houston, United States: SPIE, Mar. 2020. ISBN: 978-1-5106-3391-9. DOI: 10.1117/12.2549560 (cit. on p. 32).

[Litt+96] J. T. Littleton and M. L. Durizch Littleton. "Conventional Tomography." In: *A History of the Radiological Sciences*. Ed. by R. Gagliardi and B. L. McClennan. https://www.arrs.org/ARRSLIVE/HRS. Radiology Centennial, Inc., 1996, pp. 369–401 (cit. on p. 12).

[Llov+16] X. Llovet and F. Salvat. "PENEPMA: a Monte Carlo programme for the simulation of X-ray emission in EPMA." In: *IOP Conference Series: Materials Science and Engineering* 109, 012009 (Feb. 2016). ISSN: 1757-8981. DOI: 10.1088/1757-899X/109/1/012009 (cit. on p. 167).

[Lois+13] A. Loiselle, J. M. Parish, J. A. Wilkens, and D. E. Jaroszewski. "Managing iatrogenic pneumothorax and chest tubes." In: *Journal of Hospital Medicine* 8.7 (July 2013), pp. 402–408. ISSN: 1553-5592. DOI: 10.1002/jhm.2053 (cit. on p. 122).

[Lync+11] S. K. Lynch, V. Pai, J. Auxier, A. F. Stein, E. E. Bennett, C. K. Kemble, X. Xiao, W.-K. Lee, N. Y. Morgan, and H. H. Wen. "Interpretation of dark-field contrast and particle-size selectivity in grating interferometers." In: *Applied Optics* 50.22 (July 2011), pp. 4310–4319. ISSN: 1559-128X. DOI: 10.1364/AO.50.004310 (cit. on pp. 27, 62–63, 127, 135, 142–144, 160, 165).

[Mahe+09] M. Mahesh and J. M. Hevezi. "Slice Wars vs Dose Wars in Multiple-Row Detector CT." In: *Journal of the American College of Radiology* 6.3 (Mar. 2009), pp. 201–202. ISSN: 1546-1440. DOI: 10.1016/j.jacr.2008.11.027 (cit. on p. 14).

[Male+12] A. Malecki, G. Potdevin, and F. Pfeiffer. "Quantitative wave-optical numerical analysis of the dark-field signal in grating-based X-ray interferometry." In: *Europhysics Letters* 99.4, 48001 (Aug. 2012). ISSN: 0295-5075. DOI: 10.1209/0295-5075/99/48001 (cit. on pp. 127, 141).

[Mals39] F. Malsch. “Erzeugung stark vergrößerter Röntgen-Schattenbilder.” German. In: *Die Naturwissenschaften* 27.51 (Dec. 1939), pp. 854–855. ISSN: 0028-1042. DOI: 10.1007/bf01489432 (cit. on p. 21).

[Mand+76] L. Mandel and E. Wolf. “Spectral coherence and the concept of cross-spectral purity.” In: *Journal of the Optical Society of America* 66.6 (June 1976), pp. 529–535. ISSN: 0030-3941. DOI: 10.1364/JOSA.66.000529 (cit. on p. 174).

[Mand+95] L. Mandel and E. Wolf. *Optical coherence and quantum optics*. 1st ed. Cambridge University Press, 1995. 1194 pp. ISBN: 978-0-521-41711-2 (cit. on pp. 102, 160, 174–175).

[Mart14] L. Martiradonna. “A photograph of crystal order.” In: *Nature Milestones* 511.7 (July 2014). ISSN: 0028-0836. DOI: 10.1038/nature13350 (cit. on p. 21).

[Maxw65] J. C. Maxwell. “VIII. A dynamical theory of the electromagnetic field.” In: *Philosophical Transactions of the Royal Society of London* 155 (Dec. 1865), pp. 459–512. ISSN: 0261-0523. DOI: 10.1098/rstl.1865.0008 (cit. on pp. 15, 33).

[Mayo+02] S. C. Mayo, P. R. Miller, S. W. Wilkins, T. J. Davis, D. Gao, T. E. Gureyev, D. Paganin, D. J. Parry, A. Pogany, and A. W. Stevenson. “Quantitative X-ray projection microscopy: phase-contrast and multi-spectral imaging.” In: *Journal of Microscopy* 207.2 (Aug. 2002), pp. 79–96. ISSN: 0022-2720. DOI: 10.1046/j.1365-2818.2002.01046.x (cit. on p. 21).

[McAd+06] H. P. McAdams, E. Samei, J. Dobbins, G. D. Tourassi, and C. E. Ravin. “Recent Advances in Chest Radiography.” In: *Radiology* 241.3 (Dec. 2006), pp. 663–683. ISSN: 0033-8419. DOI: 10.1148/radiol.2413051535 (cit. on p. 125).

[McLa+14] R. A. McLaughlin, P. B. Noble, and D. D. Sampson. “Optical Coherence Tomography in Respiratory Science and Medicine: From Airways to Alveoli.” In: *Physiology* 29.5 (Sept. 2014), pp. 369–380. ISSN: 1548-9221. DOI: 10.1152/physiol.00002.2014 (cit. on pp. 127, 142).

[Mein+13] F. G. Meinel, F. Schwab, S. Schleede, M. Bech, J. Herzen, K. Achterhold, S. Auweter, F. Bamberg, A. Ö. Yildirim, A. Bohla, O. Eickelberg, R. Loewen, M. Gifford, R. Ruth, M. F. Reiser, F. Pfeiffer, and K. Nikolaou. “Diagnosing and Mapping Pulmonary Emphysema on X-Ray Projection Images: Incremental Value of Grating-Based X-Ray Dark-Field Imaging.” In: *PLOS ONE* 8.3, e59526 (Mar. 2013). Ed. by C. Taube. ISSN: 1932-6203. DOI: 10.1371/journal.pone.0059526 (cit. on pp. 32, 70, 115).

[Mein+14a] F. G. Meinel, F. Schwab, A. Yaroshenko, A. Velroyen, M. Bech, K. Hellbach, J. Fuchs, T. Stiewe, A. Ö. Yildirim, F. Bamberg, M. F. Reiser, F. Pfeiffer, and K. Nikolaou. “Lung tumors on multimodal radiographs derived from grating-based X-ray imaging – A feasibility study.” In: *Physica Medica* 30.3 (May 2014), pp. 352–357. ISSN: 1120-1797. DOI: 10.1016/j.ejmp.2013.11.001 (cit. on p. 32).

[Mein+14b] F. G. Meinel, A. Yaroshenko, K. Hellbach, M. Bech, M. Müller, A. Velroyen, F. Bamberg, O. Eickelberg, K. Nikolaou, M. F. Reiser, F. Pfeiffer, and A. Ö. Yildirim. “Improved Diagnosis of Pulmonary Emphysema Using In Vivo Dark-Field Radiography.” In: *Investigative Radiology* 49.10 (Oct. 2014), pp. 653–658. ISSN: 0020-9996. DOI: 10.1097/RLI.0000000000000067 (cit. on pp. 32, 70, 115, 136).

[Ment+14] D. Mentrup, U. Neitzel, S. Jockel, H.-I. Maack, and B. Menser. *Grid-like contrast enhancement for bedside chest radiographs acquired without anti-scatter grid. Philips SkyFlow*. Whitepaper. https://www.usa.philips.com/healthcare/product/HCNOCTN339/skyflow-scatter-correction-algorithm/documentation. Philips Healthcare, 2014 (cit. on p. 192).

[Miao+16] H. Miao, A. Panna, A. A. Gomella, E. E. Bennett, S. Znati, L. Chen, and H. Wen. “A universal moiré effect and application in X-ray phase-contrast imaging.” In: *Nature Physics* 12.9 (Apr. 2016), pp. 830–834. ISSN: 1745-2473. DOI: 10.1038/nphys3734 (cit. on p. 27).

[Mich+13] T. Michel, J. Rieger, G. Anton, F. Bayer, M. W. Beckmann, J. Durst, P. A. Fasching, W. Haas, A. Hartmann, G. Pelzer, M. Radicke, C. Rauh, A. Ritter, Peter Sievers, R. Schulz-Wendtland, M. Uder, D. L. Wachter, T. Weber, E. Wenkel, and A. Zang. "On a dark-field signal generated by micrometer-sized calcifications in phase-contrast mammography." In: *Physics in Medicine & Biology* 58.8 (Apr. 2013), pp. 2713–2732. ISSN: 0031-9155. DOI: 10.1088/0031-9155/58/8/2713 (cit. on p. 29).

[Mich+87] A. A. Michelson and E. W. Morley. "On the relative motion of the Earth and the luminiferous ether." In: *American Journal of Science* s3-34.203 (Nov. 1887), pp. 333–345. ISSN: 0002-9599. DOI: 10.2475/ajs.s3-34.203.333 (cit. on p. 15).

[Mich82] H. Michel. "Three-dimensional Crystals of a Membrane Protein Complex: The Photosynthetic Reaction Centre from Rhodopseudomonas viridis." In: *Journal of Molecular Biology* 158.3 (July 1982), pp. 567–572. ISSN: 0022-2836. DOI: 10.1016/0022-2836(82)90216-9 (cit. on p. 21).

[Modr+12] P. Modregger, F. Scattarella, B. R. Pinzer, C. David, R. Bellotti, and M. Stampanoni. "Imaging the ultrasmall-angle x-ray scattering distribution with grating interferometry." In: *Physical Review Letters* 108.4, 048101 (Jan. 2012). ISSN: 0031-9007. DOI: 10.1103/PhysRevLett.108.048101 (cit. on p. 53).

[Mohr+12] J. Mohr, T. Grund, D. Kunka, J. Kenntner, J. Leuthold, J. Meiser, J. Schulz, and M. Walter. "High aspect ratio gratings for X-ray phase contrast imaging." In: *AIP Conference Proceedings* 1466 (July 2012), pp. 41–50. ISSN: 0094-243X. DOI: 10.1063/1.4742267 (cit. on pp. 26, 73, 75).

[Moll+02] J. Mollenhauer, M. E. Aurich, Z. Zhong, C. Muehleman, A. A. Cole, M. Hasnah, O. Oltulu, K. E. Kuettner, A. Margulis, and L. D. Chapman. "Diffraction-enhanced X-ray imaging of articular cartilage." In: *Osteoarthritis and Cartilage* 10.3 (Mar. 2002), pp. 163–171. ISSN: 1063-4584. DOI: 10.1053/joca.2001.0496 (cit. on p. 30).

[Momo+03] A. Momose, S. Kawamoto, I. Koyama, Y. Hamaishi, K. Takai, and Y. Suzuki. "Demonstration of X-Ray Talbot Interferometry." In: *Japanese Journal of Applied Physics* 42.7B (July 2003). Part 2, pp. L866–L868. ISSN: 0021-4922. DOI: 10.1143/JJAP.42.L866 (cit. on p. 25).

[Momo+10] A. Momose, W. Yashiro, and Y. Takeda. "X-Ray Phase Imaging with Talbot Interferometry." In: *Biomedical Mathematics: Promising Directions in Imaging, Therapy Planning, and Inverse Problems*. Ed. by Y. Censor, M. Jiang, and G. Wang. Medical Physics Publishing, June 2010, pp. 281–320. ISBN: 978-1-930524-48-4 (cit. on p. 55).

[Momo+14] A. Momose, W. Yashiro, K. Kido, J. Kiyohara, C. Makifuchi, T. Ito, S. Nagatsuka, C. Honda, D. Noda, T. Hattori, T. Endo, M. Nagashima, and J. Tanaka. "X-ray phase imaging: from synchrotron to hospital." In: *Philosophical Transactions of the Royal Society A: Mathematical, Physical and Engineering Sciences* 372.2010, 20130023 (Mar. 2014). ISSN: 1364-503X. DOI: 10.1098/rsta.2013.0023 (cit. on p. 30).

[Momo+95] A. Momose and J. Fukuda. "Phase-contrast radiographs of nonstained rat cerebellar specimen." In: *Medical Physics* 22.4 (Apr. 1995), pp. 375–379. ISSN: 0094-2405. DOI: 10.1118/1.597472 (cit. on p. 23).

[Momo+96] A. Momose, T. Takeda, Y. Itai, and K. Hirano. "Phase-contrast X-ray computed tomography for observing biological soft tissues." In: *Nature Medicine* 2.4 (Apr. 1996), pp. 473–475. ISSN: 1078-8956. DOI: 10.1038/nm0496-473 (cit. on p. 23).

[Momo95] A. Momose. "Demonstration of phase-contrast X-ray computed tomography using an X-ray interferometer." In: *Nuclear Instruments and Methods in Physics Research Section A: Accelerators, Spectrometers, Detectors and Associated Equipment* 352.3 (Jan. 1995), pp. 622–628. ISSN: 0168-9002. DOI: 10.1016/0168-9002(95)90017-9 (cit. on p. 23).

[Morg+11a] K. S. Morgan, D. M. Paganin, and K. K. W. Siu. "Quantitative single-exposure x-ray phase contrast imaging using a single attenuation grid." In: *Optics Express* 19.20 (Sept. 2011), pp. 19781–19789. ISSN: 1094-4087. DOI: 10.1364/OE.19.019781 (cit. on p. 27).

[Morg+11b] K. S. Morgan, D. M. Paganin, and K. K. W. Siu. “Quantitative x-ray phase-contrast imaging using a single grating of comparable pitch to sample feature size.” In: *Optics Letters* 36.1 (Jan. 2011), pp. 55–57. ISSN: 0146-9592. DOI: 10.1364/OL.36.000055 (cit. on p. 27).

[Morg+14] K. S. Morgan, M. Donnelley, N. Farrow, A. Fouras, N. Yagi, Y. Suzuki, A. Takeuchi, K. Uesugi, R. C. Boucher, K. K. W. Siu, and D. W. Parsons. “In Vivo X-Ray Imaging Reveals Improved Airway Surface Hydration after a Therapy Designed for Cystic Fibrosis.” In: *American Journal of Respiratory and Critical Care Medicine* 190.4 (Aug. 2014), pp. 469–472. ISSN: 1073-449X. DOI: 10.1164/rccm.201405-0855LE (cit. on p. 31).

[Moya+07] M. A. de Moya, C. Seaver, K. Spaniolas, K. Inaba, M. Nguyen, Y. Veltman, D. Shatz, H. B. Alam, and L. Pizano. “Occult Pneumothorax in Trauma Patients: Development of an Objective Scoring System.” In: *The Journal of Trauma: Injury, Infection, and Critical Care* 63.1 (July 2007), pp. 13–17. ISSN: 2163-0755. DOI: 10.1097/TA.0b013e31806864fc (cit. on p. 117).

[MRC15] *Service information, MRC 200 0310 ROT 1004 X-ray tube assembly*. 4512-988-00124 REV AA. Philips Healthcare. 2015 (cit. on p. 79).

[Munr+12] P. R. T. Munro, K. Ignatyev, R. D. Speller, and A. Olivo. “Phase and absorption retrieval using incoherent X-ray sources.” In: *Proceedings of the National Academy of Sciences of the United States of America* 109.35 (Aug. 2012), pp. 13922–13927. ISSN: 0027-8424. DOI: 10.1073/pnas.1205396109 (cit. on p. 28).

[Nama+13] E. Namati, W. C. Warger, C. I. Unglert, J. E. Eckert, J. Hostens, B. E. Bouma, and G. J. Tearney. “Four-dimensional visualization of subpleural alveolar dynamics in vivo during uninterrupted mechanical ventilation of living swine.” In: *Biomedical Optics Express* 4.11 (Nov. 2013), pp. 2492–2506. ISSN: 2156-7085. DOI: 10.1364/BOE.4.002492 (cit. on p. 127).

[NCRP09] *Report No. 160 – Ionizing Radiation Exposure of the Population of the United States*. https://ncrponline.org/shop/reports/report-no-160-ionizing-radiation-exposure-of-the-population-of-the-united-states/. National Council on Radiation Protection and Measurements, 2009. ISBN: 978-0-929600-98-7 (cit. on p. 14).

[Neff+00] M. A. Neff, J. S. Monk, K. Peters, and A. Nikhilesh. “Detection of Occult Pneumothoraces on Abdominal Computed Tomographic Scans in Trauma Patients.” In: *The Journal of Trauma: Injury, Infection, and Critical Care* 49.2 (Aug. 2000), pp. 281–285. ISSN: 2163-0755. DOI: 10.1097/00005373-200008000-00015 (cit. on p. 117).

[Neko+17] E. A. Nekolla, A. A. Schegerer, J. Griebel, and G. Brix. “Häufigkeit und Dosis diagnostischer und interventioneller Röntgenanwendungen.” German. In: *Der Radiologe* 57.7 (Mar. 2017), pp. 555–562. ISSN: 0033-832X. DOI: 10.1007/s00117-017-0242-y (cit. on p. 14).

[Nest08] Y. I. Nesterets. “On the origins of decoherence and extinction contrast in phase-contrast imaging.” In: *Optics Communications* 281.4 (Feb. 2008), pp. 533–542. ISSN: 0030-4018. DOI: 10.1016/j.optcom.2007.10.025 (cit. on pp. 62–63).

[NIST17] M. J. Berger, J. S. Coursey, M. A. Zucker, J. Chang, S. M. Seltzer, and P. M. Bergstrom. *Stopping-Powers and Range Tables for Electrons, Protons, and Helium Ions, NIST Standard Reference Database 124*. National Institute of Standards and Technology (NIST), Physical Measurement Laboratory (PML), July 2017. DOI: 10.18434/T4NC7P (cit. on pp. 161–162, 166).

[Nuge+96] K. A. Nugent, T. E. Gureyev, D. F. Cookson, D. Paganin, and Z. Barnea. “Quantitative Phase Imaging Using Hard X Rays.” In: *Physical Review Letters* 77.14 (Sept. 1996), pp. 2961–2964. ISSN: 0031-9007. DOI: 10.1103/physrevlett.77.2961 (cit. on p. 24).

[NumPy20] The SciPy community. *NumPy Manual*. Current version: 1.19. 2020. URL: https://numpy.org/doc/stable/ (cit. on p. 110).

[Ochs06] M. Ochs. “A brief update on lung stereology.” In: *Journal of Microscopy* 222.3 (July 2006), pp. 188–200. ISSN: 0022-2720. DOI: 10.1111/j.1365-2818.2006.01587.x (cit. on p. 31).

[Oliv+01] A. Olivo, F. Arfelli, G. Cantatore, R. Longo, R. H. Menk, S. Pani, M. Prest, P. Poropat, L. Rigon, G. Tromba, E. Vallazza, and E. Castelli. “An innovative digital imaging set-up allowing a low-dose approach to phase contrast applications in the medical field.” In: *Medical Physics* 28.8 (Aug. 2001), pp. 1610–1619. ISSN: 0094-2405. DOI: 10.1118/1.1388219 (cit. on p. 28).

[Oliv+07] A. Olivo and R. Speller. “A coded-aperture technique allowing x-ray phase contrast imaging with conventional sources.” In: *Applied Physics Letters* 91.7, 074106 (Aug. 2007). ISSN: 0003-6951. DOI: 10.1063/1.2772193 (cit. on p. 29).

[Oltu+03] O. Oltulu, Z. Zhong, M. Hasnah, M. N. Wernick, and D. Chapman. “Extraction of extinction, refraction and absorption properties in diffraction enhanced imaging.” In: *Journal of Physics D: Applied Physics* 36.17 (Sept. 2003), pp. 2152–2156. ISSN: 0022-3727. DOI: 10.1088/0022-3727/36/17/320 (cit. on p. 23).

[Omar+10] H. R. Omar, H. Abdelmalak, D. Mangar, R. Rashad, E. Helal, and E. M. Camporesi. “Occult pneumothorax, revisited.” In: *Journal of Trauma Management & Outcomes* 4.1, 12 (Oct. 2010). ISSN: 1752-2897. DOI: 10.1186/1752-2897-4-12 (cit. on p. 117).

[Open20] OpenStax College. *Chemistry. Chapter 21.1: Nuclear Structure and Stability*. May 2020. URL: https://opentextbc.ca/chemistry/ (cit. on p. 45).

[Otsu79] N. Otsu. “A Threshold Selection Method from Gray-Level Histograms.” In: *IEEE Transactions on Systems, Man, and Cybernetics* 9.1 (Jan. 1979), pp. 62–66. ISSN: 0018-9472. DOI: 10.1109/TSMC.1979.4310076 (cit. on p. 90).

[Ovel+12] N. P. Oveland, E. Sloth, G. Andersen, and H. M. Lossius. “A Porcine Pneumothorax Model for Teaching Ultrasound Diagnostics.” In: *Academic Emergency Medicine* 19.5 (May 2012), pp. 586–592. ISSN: 1069-6563. DOI: 10.1111/j.1553-2712.2012.01349.x (cit. on p. 118).

[Paga+02] D. Paganin, S. C. Mayo, T. E. Gureyev, P. R. Miller, and S. W. Wilkins. “Simultaneous phase and amplitude extraction from a single defocused image of a homogeneous object.” In: *Journal of Microscopy* 206.1 (May 2002), pp. 33–40. ISSN: 0022-2720. DOI: 10.1046/j.1365-2818.2002.01010.x (cit. on p. 24).

[Paga+98] D. Paganin and K. A. Nugent. “Noninterferometric Phase Imaging with Partially Coherent Light.” In: *Physical Review Letters* 80.12 (Mar. 1998), pp. 2586–2589. ISSN: 0031-9007. DOI: 10.1103/physrevlett.80.2586 (cit. on p. 24).

[Paga06] D. Paganin. *Coherent X-Ray Optics*. Oxford University Press, Jan. 2006. ISBN: 978-0-19-856728-8. DOI: 10.1093/acprof:oso/9780198567288.001.0001 (cit. on pp. 44, 59).

[Pelz+16] G. Pelzer, G. Anton, F. Horn, J. Rieger, A. Ritter, J. Wandner, T. Weber, and T. Michel. “A beam hardening and dispersion correction for x-ray dark-field radiography.” In: *Medical Physics* 43.6 (May 2016), pp. 2774–2779. ISSN: 0094-2405. DOI: 10.1118/1.4948671 (cit. on pp. 58, 103, 161, 163, 170).

[Pfei+06] F. Pfeiffer, T. Weitkamp, O. Bunk, and C. David. “Phase retrieval and differential phase-contrast imaging with low-brilliance X-ray sources.” In: *Nature Physics* 2.4 (Mar. 2006), pp. 258–261. ISSN: 1745-2473. DOI: 10.1038/nphys265 (cit. on pp. 26, 56, 180).

[Pfei+07] F. Pfeiffer, O. Bunk, C. Kottler, and C. David. “Tomographic reconstruction of three-dimensional objects from hard X-ray differential phase contrast projection images.” In: *Nuclear Instruments and Methods in Physics Research Section A: Accelerators, Spectrometers, Detectors and Associated Equipment* 580.2 (Oct. 2007), pp. 925–928. ISSN: 0168-9002. DOI: 10.1016/j.nima.2007.06.104 (cit. on p. 26).

[Pfei+08] F. Pfeiffer, M. Bech, O. Bunk, P. Kraft, E. F. Eikenberry, C. C. Brönnimann, C. Grünzweig, and C. David. "Hard-X-ray dark-field imaging using a grating interferometer." In: *Nature Materials* 7.2 (Jan. 2008), pp. 134–137. ISSN: 1476-1122. DOI: 10.1038/nmat2096 (cit. on pp. 26, 62, 70).

[Potd+12] G. Potdevin, A. Malecki, T. Biernath, M. Bech, T. H. Jensen, R. Feidenhans'l, I. Zanette, T. Weitkamp, J. Kenntner, J. Mohr, P. Roschger, M. Kerschnitzki, W. Wagermaier, K. Klaushofer, P. Fratzl, and F. Pfeiffer. "X-ray vector radiography for bone micro-architecture diagnostics." In: *Physics in Medicine & Biology* 57.11 (May 2012), pp. 3451–3461. ISSN: 0031-9155. DOI: 10.1088/0031-9155/57/11/3451 (cit. on p. 30).

[Punn+16] J. Punnoose, J. Xu, A. Sisniega, W. Zbijewski, and J. H. Siewerdsen. "Technical Note: spektr 3.0 – A computational tool for x-ray spectrum modeling and analysis." In: *Medical Physics* 43.8 (July 2016), pp. 4711–4717. ISSN: 0094-2405. DOI: 10.1118/1.4955438 (cit. on p. 133).

[Punt+13] S. Puntanen, G. P. H. Styan, and J. Isotalo. *Formulas Useful for Linear Regression Analysis and Related Matrix Theory*. SpringerBriefs in Statistics. Berlin, Heidelberg: Springer Science+Business Media, 2013. ISBN: 978-3-642-32930-2. DOI: 10.1007/978-3-642-32931-9 (cit. on p. 184).

[Pyth20] Python Software Foundation. *The Python Language Reference*. Version 3.6. 2020. URL: https://docs.python.org/3.6/reference/ (cit. on p. 110).

[Que+95] W. Que and J. A. Rowlands. "X-ray imaging using amorphous selenium: Inherent spatial resolution." In: *Medical Physics* 22.4 (Apr. 1995), pp. 365–374. ISSN: 0094-2405. DOI: 10.1118/1.597471 (cit. on p. 51).

[Rado17] J. Radon. "Über die Bestimmung von Funktionen längs gewisser Mannigfaltigkeiten." German. In: *Berichte der mathematisch-physikalischen Kl. Sächsischen Gesellschaft der Wissenschaften* 69 (1917), pp. 262–277. ISSN: 0365-6470 (cit. on p. 12).

[Rank+00] J. J. Rankine, A. N. Thomas, and D. Fluechter. "Diagnosis of pneumothorax in critically ill adults." In: *Postgraduate Medical Journal* 76.897 (July 2000), pp. 399–404. ISSN: 0032-5473. DOI: 10.1136/pmj.76.897.399 (cit. on p. 117).

[Ravi12] P. S. Ravishankar. "Treatise on EPDM." In: *Rubber Chemistry and Technology* 85.3 (Sept. 2012), pp. 327–349. ISSN: 0035-9475. DOI: 10.5254/rct.12.87993 (cit. on p. 166).

[Rayl81] Lord Rayleigh. "XXV. On copying diffraction-gratings, and on some phenomena connected therewith." In: *Philosophical Magazine Series 5* 11.67 (1881), pp. 196–205. ISSN: 1478-6435. DOI: 10.1080/14786448108626995 (cit. on p. 15).

[Revo+10] V. Revol, C. Kottler, R. Kaufmann, U. Straumann, and C. Urban. "Noise analysis of grating-based x-ray differential phase contrast imaging." In: *Review of Scientific Instruments* 81.7, 073709 (July 2010). ISSN: 0034-6748. DOI: 10.1063/1.3465334 (cit. on pp. 27, 56, 76, 108, 133, 135).

[RO15] *Service information, RO 1750 ROT 360 X-ray tube assembly*. 4512-988-00984 REV AC. Philips Healthcare. 2015 (cit. on p. 79).

[Roan+11] E. Roan and C. M. Waters. "What do we know about mechanical strain in lung alveoli?" In: *American Journal of Physiology. Lung Cellular and Molecular Physiology* 301.5 (Nov. 2011), pp. L625–L635. ISSN: 1040-0605. DOI: 10.1152/ajplung.00105.2011 (cit. on pp. 127, 142–143).

[Robe+15] D. J. Roberts, S. Leigh-Smith, P. D. Faris, C. Blackmore, C. G. Ball, H. L. Robertson, E. Dixon, M. T. James, A. W. Kirkpatrick, J. B. Kortbeek, and H. T. Stelfox. "Clinical Presentation of Patients With Tension Pneumothorax: A Systematic Review." In: *Annals of Surgery* 261.6 (June 2015), pp. 1068–1078. ISSN: 0003-4932. DOI: 10.1097/SLA.0000000000001073 (cit. on p. 120).

[Robi09] A. L. Robinson. "History of synchrotron radiation." In: *X-ray data booklet*. Ed. by A. C. Thompson. 3rd ed. http://xdb.lbl.gov. Oct. 2009. Chap. 2.2 (cit. on p. 20).

[Rönt95] W. C. Röntgen. “Ueber eine neue Art von Strahlen. Vorläufige Mittheilung.” German. In: *Sitzungsberichte der Würzburger Physik.-medic. Gesellschaft* 137 (1895), pp. 132–141 (cit. on p. 10).

[Roug+20] H. Rougé-Labriet, S. Berujon, H. Mathieu, S. Bohic, B. Fayard, J.-N. Ravey, Y. Robert, P. Gaudin, and E. Brun. “X-ray Phase Contrast osteo-articular imaging: a pilot study on cadaveric human hands.” In: *Scientific Reports* 10, 1911 (Feb. 2020). ISSN: 2045-2322. DOI: 10.1038/s41598-020-58168-3 (cit. on p. 30).

[Roug19] H. Rougé-Labriet. “Développement de l’imagerie X biomédicale en contraste de phase par tavelures [Development of speckle based X-ray imaging for biomedical applications].” French. PhD thesis. Université Grenoble Alpes, Dec. 2019 (cit. on p. 30).

[Sala11] K. S. Saladin. *Human anatomy*. 1st ed. New York: McGraw-Hill, 2011. ISBN: 978-0-07-111187-4 (cit. on pp. 30–32, 117).

[Saut+19] A. P. Sauter, J. Andrejewski, F. De Marco, K. Willer, L. B. Gromann, W. Noichl, F. Kriner, F. Fischer, C. Braun, T. Koehler, F. Meurer, A. A. Fingerle, D. Pfeiffer, E. Rummeny, J. Herzen, and F. Pfeiffer. “Optimization of tube voltage in X-ray dark-field chest radiography.” In: *Scientific Reports* 9, 8699 (June 2019). ISSN: 2045-2322. DOI: 10.1038/s41598-019-45256-2 (cit. on pp. 69, 113, 194).

[Scha+14] F. Schaff, A. Malecki, G. Potdevin, E. Eggl, P. B. Noël, T. Baum, E. G. Garcia, J. S. Bauer, and F. Pfeiffer. “Correlation of X-Ray Vector Radiography to Bone Micro-Architecture.” In: *Scientific Reports* 4, 3695 (Jan. 2014). ISSN: 2045-2322. DOI: 10.1038/srep03695 (cit. on p. 30).

[Sche+16a] K. Scherer, L. Birnbacher, K. Willer, M. Chabior, J. Herzen, and F. Pfeiffer. “Correspondence: Quantitative evaluation of X-ray dark-field images for microcalcification analysis in mammography.” In: *Nature Communications* 7, 10863 (Apr. 2016). ISSN: 2041-1723. DOI: 10.1038/ncomms10863 (cit. on p. 29).

[Sche+16b] K. Scherer, E. Braig, S. Ehn, J. Schock, J. Wolf, L. Birnbacher, M. Chabior, J. Herzen, D. Mayr, S. Grandl, A. Sztrókay-Gaul, K. Hellerhoff, and F. Pfeiffer. “Improved Diagnostics by Assessing the Micromorphology of Breast Calcifications via X-Ray Dark-Field Radiography.” In: *Scientific Reports* 6, 36991 (Dec. 2016). ISSN: 2045-2322. DOI: 10.1038/srep36991 (cit. on p. 29).

[Sche+17] K. Scherer, A. Yaroshenko, D. A. Bölükbas, L. B. Gromann, K. Hellbach, F. G. Meinel, M. Braunagel, J. von Berg, O. Eickelberg, M. F. Reiser, F. Pfeiffer, S. Meiners, and J. Herzen. “X-ray Dark-field Radiography – In-Vivo Diagnosis of Lung Cancer in Mice.” In: *Scientific Reports* 7, 402 (Mar. 2017). ISSN: 2045-2322. DOI: 10.1038/s41598-017-00489-x (cit. on pp. 32, 70, 115).

[Sche86] W. Scheider. “Bringing One of the Great Moments of Science to the Classroom.” In: *The Physics Teacher* 24.4 (Apr. 1986), pp. 217–219. ISSN: 0031-921X. DOI: 10.1119/1.2341987 (cit. on p. 15).

[Schi+12] J. Schindelin, I. Arganda-Carreras, E. Frise, V. Kaynig, M. Longair, T. Pietzsch, S. Preibisch, C. Rueden, S. Saalfeld, B. Schmid, J.-Y. Y. Tinevez, D. J. White, V. Hartenstein, K. Eliceiri, P. Tomancak, and A. Cardona. “Fiji: An open-source platform for biological-image analysis.” In: *Nature Methods* 9.7 (June 2012), pp. 676–682. ISSN: 1548-7091. DOI: 10.1038/nmeth.2019 (cit. on p. 132).

[Schl+12] S. Schleede, F. G. Meinel, M. Bech, J. Herzen, K. Achterhold, G. Potdevin, A. Malecki, S. Adam-Neumair, S. F. Thieme, F. Bamberg, K. Nikolaou, A. Bohla, A. O. Yildirim, R. Loewen, M. Gifford, R. Ruth, O. Eickelberg, M. Reiser, and F. Pfeiffer. “Emphysema diagnosis using X-ray dark-field imaging at a laser-driven compact synchrotron light source.” In: *Proceedings of the National Academy of Sciences of the United States of America* 109.44 (Oct. 2012), pp. 17880–17885. ISSN: 0027-8424. DOI: 10.1073/pnas.1206684109 (cit. on pp. 31, 70, 115).

[Schm+87] G. Schmahl and D. Rudolph. “Proposal for a Phase Contrast X-ray Microscope.” In: *X-ray Microscopy*. Ed. by P.-C. Cheng and G.-J. Jan. Springer-Verlag, 1987, pp. 231–238. DOI: 10.1007/978-3-642-72881-5_16 (cit. on p. 22).

[Schm+94] G. Schmahl, D. Rudolph, P. Guttmann, G. Schneider, J. Thieme, B. Niemann, and T. Wilhein. "Phase Contrast X-ray Microscopy." In: *Synchrotron Radiation News* 7.4 (July 1994), pp. 19–22. ISSN: 0894-0886. DOI: 10.1080/08940889408261282 (cit. on p. 22).

[Scho+11] T. Schoonjans, A. Brunetti, B. Golosio, M. Sanchez del Rio, V. Armando Solé, C. Ferrero, and L. Vincze. "The xraylib library for X-ray–matter interactions. Recent developments." In: *Spectrochimica Acta Part B: Atomic Spectroscopy* 66.11-12 (Nov. 2011), pp. 776–784. ISSN: 0584-8547. DOI: 10.1016/j.sab.2011.09.011 (cit. on pp. 39–41, 43–44, 166).

[Schr+17] T. J. Schröter, F. J. Koch, P. Meyer, D. Kunka, J. Meiser, K. Willer, L. Gromann, F. De Marco, J. Herzen, P. Noel, A. Yaroshenko, A. Hofmann, F. Pfeiffer, and J. Mohr. "Large field-of-view tiled grating structures for X-ray phase-contrast imaging." In: *Review of Scientific Instruments* 88.1, 015104 (Jan. 2017). ISSN: 0034-6748. DOI: 10.1063/1.4973632 (cit. on pp. 80, 105–106).

[Seif+19] M. Seifert, V. Ludwig, S. Kaeppler, F. Horn, P. Meyer, G. Pelzer, J. Rieger, D. Sand, T. Michel, J. Mohr, C. Riess, and G. Anton. "Talbot-Lau x-ray phase-contrast setup for fast scanning of large samples." In: *Scientific Reports* 9, 4199 (Mar. 2019). ISSN: 2045-2322. DOI: 10.1038/s41598-018-38030-3 (cit. on p. 32).

[Snig+95] A. Snigirev, I. Snigireva, V. Kohn, S. Kuznetsov, and I. Schelokov. "On the possibilities of x-ray phase contrast microimaging by coherent high-energy synchrotron radiation." In: *Review of Scientific Instruments* 66.12 (Dec. 1995), pp. 5486–5492. ISSN: 0034-6748. DOI: 10.1063/1.1146073 (cit. on p. 24).

[Sono+83] M. Sonoda, M. Takano, J. Miyahara, and H. Kato. "Computed radiography utilizing scanning laser stimulated luminescence." In: *Radiology* 148.3 (Sept. 1983), pp. 833–838. ISSN: 0033-8419. DOI: 10.1148/radiology.148.3.6878707 (cit. on p. 50).

[Spah05] M. Spahn. "Flat detectors and their clinical applications." In: *European Radiology* 15.9 (Apr. 2005), pp. 1934–1947. ISSN: 0938-7994. DOI: 10.1007/s00330-005-2734-9 (cit. on pp. 50–51).

[Stam+11] M. Stampanoni, Z. Wang, T. Thüring, C. David, E. Roessl, M. Trippel, R. A. Kubik-Huch, G. Singer, M. K. Hohl, and N. Hauser. "The First Analysis and Clinical Evaluation of Native Breast Tissue Using Differential Phase-Contrast Mammography." In: *Investigative Radiology* 46.12 (Dec. 2011), pp. 801–806. ISSN: 0020-9996. DOI: 10.1097/RLI.0b013e31822a585f (cit. on p. 29).

[Stro14] M. Strobl. "General solution for quantitative dark-field contrast imaging with grating interferometers." In: *Scientific Reports* 4, 7243 (Nov. 2014). ISSN: 2045-2322. DOI: 10.1038/srep07243 (cit. on pp. 27, 62, 127, 165–166).

[Stut+11] D. Stutman, T. J. Beck, J. A. Carrino, and C. O. Bingham. "Talbot phase-contrast x-ray imaging for the small joints of the hand." In: *Physics in Medicine & Biology* 56.17 (Aug. 2011), pp. 5697–5720. ISSN: 0031-9155. DOI: 10.1088/0031-9155/56/17/015 (cit. on p. 30).

[Sudo+81] R. Sudol and B. J. Thompson. "Lau effect: theory and experiment." In: *Applied Optics* 20.6 (Mar. 1981), pp. 1107–1116. ISSN: 1559-128X. DOI: 10.1364/AO.20.001107 (cit. on pp. 174–176).

[Sule97] T. J. Suleski. "Generation of Lohmann images from binary-phase Talbot array illuminators." In: *Applied Optics* 36.20 (July 1997), pp. 4686–4691. ISSN: 1559-128X. DOI: 10.1364/AO.36.004686 (cit. on p. 53).

[Swan73] R. K. Swank. "Absorption and noise in x-ray phosphors." In: *Journal of Applied Physics* 44.9 (Sept. 1973), pp. 4199–4203. ISSN: 0021-8979. DOI: 10.1063/1.1662918 (cit. on p. 51).

[Tagu+13] K. Taguchi and J. S. Iwanczyk. "Vision 20/20: Single photon counting x-ray detectors in medical imaging." In: *Medical Physics* 40.10, 100901 (Sept. 2013). ISSN: 0094-2405. DOI: 10.1118/1.4820371 (cit. on p. 51).

[Take+82] M. Takeda, H. Ina, and S. Kobayashi. "Fourier-transform method of fringe-pattern analysis for computer-based topography and interferometry." In: *Journal of the Optical Society of America* 72.1 (Jan. 1982), pp. 156–160. ISSN: 0030-3941. DOI: 10.1364/JOSA.72.000156 (cit. on pp. 23, 27).

[Talb36] H. Talbot. "LXXVI. Facts relating to optical science. No. IV." In: *Philosophical Magazine Series 3* 9.56 (Dec. 1836), pp. 401–407. ISSN: 1941-5966. DOI: 10.1080/14786443608649032 (cit. on p. 15).

[Talu+91] K. K. Talukdar and W. D. Lawing. "Estimation of the parameters of the Rice distribution." In: *Journal of the Acoustical Society of America* 89.3 (Mar. 1991), pp. 1193–1197. ISSN: 0001-4966. DOI: 10.1121/1.400532 (cit. on pp. 185–186).

[Tana+13] J. Tanaka, M. Nagashima, K. Kido, Y. Hoshino, J. Kiyohara, C. Makifuchi, S. Nishino, S. Nagatsuka, and A. Momose. "Cadaveric and in vivo human joint imaging based on differential phase contrast by X-ray Talbot-Lau interferometry." In: *Zeitschrift für Medizinische Physik* 23.3 (Sept. 2013), pp. 222–227. ISSN: 0939-3889. DOI: 10.1016/j.zemedi.2012.11.004 (cit. on p. 30).

[Tapf+11] A. Tapfer, M. Bech, B. Pauwels, X. Liu, P. Bruyndonckx, A. Sasov, J. Kenntner, J. Mohr, M. Walter, J. Schulz, and F. Pfeiffer. "Development of a prototype gantry system for preclinical x-ray phase-contrast computed tomography: Prototype gantry system for preclinical x-ray phase-contrast CT." In: *Medical Physics* 38.11 (Oct. 2011), pp. 5910–5915. ISSN: 0094-2405. DOI: 10.1118/1.3644844 (cit. on pp. 32, 115).

[Tapf+12] A. Tapfer, M. Bech, A. Velroyen, J. Meiser, J. Mohr, M. Walter, J. Schulz, B. Pauwels, P. Bruyndonckx, X. Liu, A. Sasov, and F. Pfeiffer. "Experimental results from a preclinical X-ray phase-contrast CT scanner." In: *Proceedings of the National Academy of Sciences of the United States of America* 109.39 (Sept. 2012), pp. 15691–15696. ISSN: 0027-8424. DOI: 10.1073/pnas.1207503109 (cit. on pp. 32, 115).

[Teuf+17] M. v. Teuffenbach, T. Koehler, A. Fehringer, M. Viermetz, B. Brendel, J. Herzen, R. Proksa, E. J. Rummeny, F. Pfeiffer, and P. B. Noël. "Grating-based phase-contrast and dark-field computed tomography: a single-shot method." In: *Scientific Reports* 7, 7476 (Aug. 2017). ISSN: 2045-2322. DOI: 10.1038/s41598-017-06729-4 (cit. on p. 32).

[Thib+07] J.-B. Thibault, K. D. Sauer, C. A. Bouman, and J. Hsieh. "A three-dimensional statistical approach to improved image quality for multislice helical CT." In: *Medical Physics* 34.11 (Oct. 2007), pp. 4526–4544. ISSN: 0094-2405. DOI: 10.1118/1.2789499 (cit. on p. 14).

[Thom+09] A. Thompson, D. Attwood, E. Gullikson, M. Howells, K. Kim, J. Kirz, J. Kortright, I. Lindau, Y. Liu, P. Pianetta, A. Robinson, J. Scofield, J. Underwood, G. Williams, and H. Winick. *X-Ray Data Booklet*. Ed. by A. C. Thompson. 3rd ed. https://xdb.lbl.gov/. Berkeley: Lawrence Berkeley National Laboratory, University of California, 2009 (cit. on p. 40).

[Thom18] A. M. K. Thomas. "History of Radiology." In: *Handbook of X-ray Imaging*. Ed. by P. Russo. Taylor & Francis Group, LLC, 2018, pp. 331–353. ISBN: 978-1-4987-4152-1 (cit. on pp. 10–11).

[Thür+13] T. Thüring, R. Guggenberger, H. Alkadhi, J. Hodler, M. Vich, Z. Wang, C. David, and M. Stampanoni. "Human hand radiography using X-ray differential phase contrast combined with dark-field imaging." In: *Skeletal Radiology* 42.6 (Apr. 2013), pp. 827–835. ISSN: 0364-2348. DOI: 10.1007/s00256-013-1606-7 (cit. on p. 30).

[Toci+85] I. M. Tocino, M. H. Miller, and W. R. Fairfax. "Distribution of pneumothorax in the supine and semirecumbent critically ill adult." In: *American Journal of Roentgenology* 144.5 (May 1985), pp. 901–905. ISSN: 0361-803X. DOI: 10.2214/ajr.144.5.901 (cit. on p. 117).

[Tomb+56] D. H. Tomboulian and P. L. Hartman. "Spectral and Angular Distribution of Ultraviolet Radiation from the 300-Mev Cornell Synchrotron." In: *Physical Review* 102.6 (June 1956), pp. 1423–1447. ISSN: 0031-899X. DOI: 10.1103/physrev.102.1423 (cit. on p. 20).

[Tuoh+07] T. Tuohimaa, M. Otendal, and H. M. Hertz. "Phase-contrast x-ray imaging with a liquid-metal-jet-anode microfocus source." In: *Applied Physics Letters* 91.7, 074104 (Aug. 2007). ISSN: 0003-6951. DOI: 10.1063/1.2769760 (cit. on p. 56).

[Turb01] H. Turbell. "Cone-Beam Reconstruction Using Filtered Backprojection." PhD thesis. Department of Electrical Engineering, Linköpings Universitetet, 2001 (cit. on p. 14).

[Velr+15] A. Velroyen, A. Yaroshenko, D. Hahn, A. Fehringer, A. Tapfer, M. Müller, P. B. Noël, B. Pauwels, A. Sasov, A. Ö. Yildirim, O. Eickelberg, K. Hellbach, S. D. Auweter, F. G. Meinel, M. F. Reiser, M. Bech, and F. Pfeiffer. "Grating-based X-ray Dark-field Computed Tomography of Living Mice." In: *EBioMedicine* 2.10 (Oct. 2015), pp. 1500–1506. ISSN: 2352-3964. DOI: 10.1016/j.ebiom.2015.08.014 (cit. on pp. 32, 70).

[Vign+18] J. Vignero, N. W. Marshall, G. Vande Velde, K. Bliznakova, and H. Bosmans. "Translation from murine to human lung imaging using x-ray dark field radiography: A simulation study." In: *PLOS ONE* 13.10, e0206302 (Oct. 2018). Ed. by R. Zhang. ISSN: 1932-6203. DOI: 10.1371/journal.pone.0206302 (cit. on pp. 127, 141–143).

[Virt+20] P. Virtanen, R. Gommers, T. E. Oliphant, M. Haberland, T. Reddy, D. Cournapeau, E. Burovski, P. Peterson, W. Weckesser, J. Bright, S. J. van der Walt, M. Brett, J. Wilson, K. Jarrod Millman, N. Mayorov, A. R. J. Nelson, E. Jones, R. Kern, E. Larson, C. Carey, İ. Polat, Y. Feng, E. W. Moore, J. VanderPlas, D. Laxalde, J. Perktold, R. Cimrman, I. Henriksen, E. A. Quintero, C. R. Harris, A. M. Archibald, A. H. Ribeiro, F. Pedregosa, P. van Mulbregt, and SciPy 1.0 Contributors. "SciPy 1.0: Fundamental Algorithms for Scientific Computing in Python." In: *Nature Methods* 17 (Feb. 2020), pp. 261–272. ISSN: 1548-7091. DOI: 10.1038/s41592-019-0686-2 (cit. on pp. 111, 167).

[Vogl+11] T. J. Vogl, W. Reith, and E. J. Rummeny, eds. *Diagnostische und Interventionelle Radiologie*. Vol. 1. Springer Medizin, 2011. ISBN: 978-3-540-87668-7. DOI: 10.1007/978-3-540-87668-7 (cit. on pp. 29, 50, 77, 133).

[Wall+11] B. F. Wall, R. Haylock, J. T. M. Jansen, M. C. Hillier, D. Hart, and P. C. Shrimpton. *Radiation Risks from Medical X-ray Examinations as a Function of the Age and Sex of the Patient*. https://www.gov.uk/government/publications/medical-x-rays-radiation-risks-by-age-and-sex-of-patient. Health Protection Agency, Centre for Radiation, Chemical and Environmental Hazards, 2011. ISBN: 978-0-85951-709-6 (cit. on p. 125).

[Walt+11] S. van der Walt, S. C. Colbert, and G. Varoquaux. "The NumPy Array: A Structure for Efficient Numerical Computation." In: *Computing in Science & Engineering* 13.2 (Mar. 2011), pp. 22–30. ISSN: 1521-9615. DOI: 10.1109/MCSE.2011.37 (cit. on p. 110).

[Wang+14] Z. Wang, N. Hauser, G. Singer, M. Trippel, R. A. Kubik-Huch, C. W. Schneider, and M. Stampanoni. "Non-invasive classification of microcalcifications with phase-contrast X-ray mammography." In: *Nature Communications* 5, 3797 (May 2014). ISSN: 2041-1723. DOI: 10.1038/ncomms4797 (cit. on p. 29).

[Wang+16] Z. Wang, N. Hauser, G. Singer, M. Trippel, R. A. Kubik-Huch, C. W. Schneider, and M. Stampanoni. "Correspondence: Reply to 'Quantitative evaluation of X-ray dark-field images for microcalcification analysis in mammography'." In: *Nature Communications* 7, 10868 (Apr. 2016). ISSN: 2041-1723. DOI: 10.1038/ncomms10868 (cit. on p. 29).

[Wats+53a] J. D. Watson and F. H. C. Crick. "Genetical Implications of the Structure of Deoxyribonucleic Acid." In: *Nature* 171.4361 (May 1953), pp. 964–967. ISSN: 0028-0836. DOI: 10.1038/171964b0 (cit. on p. 21).

[Wats+53b] J. D. Watson and F. H. C. Crick. "Molecular Structure of Nucleic Acids: A Structure for Deoxyribose Nucleic Acid." In: *Nature* 171.4356 (Apr. 1953), pp. 737–738. ISSN: 0028-0836. DOI: 10.1038/171737a0 (cit. on p. 21).

[Weib63] E. R. Weibel. *Morphometry of the Human Lung*. Springer-Verlag Berlin Heidelberg, 1963. ISBN: 978-3-642-87553-3. DOI: 10.1007/978-3-642-87553-3 (cit. on p. 31).

[Weis+00] D. Weissberg and Y. Refaely. "Pneumothorax: Experience with 1,199 patients." In: *Chest* 117.5 (May 2000), pp. 1279–1285. ISSN: 0012-3692. DOI: 10.1378/chest.117.5.1279 (cit. on p. 117).

[Weit+05] T. Weitkamp, A. Diaz, C. David, F. Pfeiffer, M. Stampanoni, P. Cloetens, and E. Ziegler. "X-ray phase imaging with a grating interferometer." In: *Optics Express* 13.16 (Aug. 2005), pp. 6296–6304. ISSN: 1094-4087. DOI: 10.1364/OPEX.13.006296 (cit. on pp. 25, 58).

[Wen+08] H. Wen, E. E. Bennett, M. M. Hegedus, and S. C. Carroll. "Spatial Harmonic Imaging of X-ray Scattering—Initial Results." In: *IEEE Transactions on Medical Imaging* 27.8 (Aug. 2008), pp. 997–1002. ISSN: 0278-0062. DOI: 10.1109/TMI.2007.912393 (cit. on p. 27).

[Wen+09] H. Wen, E. E. Bennett, M. M. Hegedus, and S. Rapacchi. "Fourier X-ray Scattering Radiography Yields Bone Structural Information." In: *Radiology* 251.3 (June 2009), pp. 910–918. ISSN: 0033-8419. DOI: 10.1148/radiol.2521081903 (cit. on p. 27).

[Whit+73] Y. S. White, D. S. Bell, and R. Mellick. "Sequelae to pneumoencephalography." In: *Journal of Neurology, Neurosurgery, and Psychiatry* 36.1 (Feb. 1973), pp. 146–151. ISSN: 0022-3050. DOI: 10.1136/jnnp.36.1.146 (cit. on p. 13).

[Whit57] G. White Grodstein. *Circular of the Bureau of Standards no. 583: X-ray Attenuation Coefficients From 10 kev to 100 Mev*. https://apps.dtic.mil/dtic/tr/fulltext/u2/a278139.pdf. National Bureau of Standards, 1957 (cit. on pp. 39–41).

[Wilk+96] S. W. Wilkins, T. E. Gureyev, D. Gao, A. Pogany, and A. W. Stevenson. "Phase-contrast imaging using polychromatic hard X-rays." In: *Nature* 384.6607 (Nov. 1996), pp. 335–338. ISSN: 0028-0836. DOI: 10.1038/384335a0 (cit. on p. 24).

[Will+18] K. Willer, A. A. Fingerle, L. B. Gromann, F. De Marco, J. Herzen, K. Achterhold, B. Gleich, D. Muenzel, K. Scherer, M. Renz, B. Renger, F. Kopp, F. Kriner, F. Fischer, C. Braun, S. Auweter, K. Hellbach, M. F. Reiser, T. Schroeter, J. Mohr, A. Yaroshenko, H.-I. Maack, T. Pralow, H. van der Heijden, R. Proksa, T. Koehler, N. Wieberneit, K. Rindt, E. J. Rummeny, F. Pfeiffer, and P. B. Noël. "X-ray dark-field imaging of the human lung—A feasibility study on a deceased body." In: *PLOS ONE* 13.9, e0204565 (Sept. 2018). ISSN: 1932-6203. DOI: 10.1371/journal.pone.0204565 (cit. on pp. 32, 85, 113, 116, 145).

[Will11] P. Willmott. *An Introduction to Synchrotron Radiation*. 1st ed. Wiley, 2011. ISBN: 978-0-470-74579-3. DOI: 10.1002/9781119970958 (cit. on pp. 20–21, 46–47).

[Wils96] E. J. N. Wilson. "Fifty years of synchrotrons." In: *EPAC 96: Fifth European Particle Accelerator Conference: Sitges (Barcelona), 10 to 14 June 1996*. Ed. by S. Myers, A. Pacheco, R. Pascual, C. Petit-Jean-Genaz, and J. Poole. Vol. 1. Bristol: Institute of Physics Publishing, 1996, pp. 135–139. ISBN: 978-0-7503-0387-3 (cit. on p. 19).

[Xray20] *Microfocus X-ray tubes - technology*. X-RAY WorX GmbH. Sept. 2020. URL: https://web.archive.org/web/20200928203942/https://www.x-ray-worx.com/index.php/en/microfocus-x-ray-tubes-overview/microfocus-technology (visited on 09/28/2020) (cit. on p. 56).

[Yagi+99] N. Yagi, Y. Suzuki, K. Umetani, Y. Kohmura, and K. Yamasaki. "Refraction-enhanced x-ray imaging of mouse lung using synchrotron radiation source." In: *Medical Physics* 26.10 (Oct. 1999), pp. 2190–2193. ISSN: 0094-2405. DOI: 10.1118/1.598735 (cit. on p. 31).

[Yan+19] A. Yan, X. Wu, and H. Liu. "Sample phase gradient and fringe phase shift in dual phase grating X-ray interferometry." In: *Optics Express* 27.24 (Nov. 2019), pp. 35437–35447. ISSN: 1094-4087. DOI: 10.1364/OE.27.035437 (cit. on p. 27).

[Yarm+12] L. Yarmus and D. Feller-Kopman. "Pneumothorax in the Critically Ill Patient." In: *Chest* 141.4 (Apr. 2012), pp. 1098–1105. ISSN: 0012-3692. DOI: 10.1378/chest.11-1691 (cit. on p. 117).

[Yaro+13] A. Yaroshenko, F. G. Meinel, M. Bech, A. Tapfer, A. Velroyen, S. Schleede, S. Auweter, A. Bohla, A. Ö. Yildirim, K. Nikolaou, F. Bamberg, O. Eickelberg, M. F. Reiser, and F. Pfeiffer. "Pulmonary Emphysema Diagnosis with a Preclinical Small-Animal X-ray Dark-Field Scatter-Contrast Scanner." In: *Radiology* 269.2 (Nov. 2013), pp. 427–433. ISSN: 0033-8419. DOI: 10.1148/radiol.13122413 (cit. on pp. 32, 70, 115).

[Yaro+15] A. Yaroshenko, K. Hellbach, A. Ö. Yildirim, T. M. Conlon, I. E. Fernandez, M. Bech, A. Velroyen, F. G. Meinel, S. Auweter, M. Reiser, O. Eickelberg, and F. Pfeiffer. "Improved In vivo Assessment of Pulmonary Fibrosis in Mice using X-Ray Dark-Field Radiography." In: *Scientific Reports* 5, 17492 (Dec. 2015). ISSN: 2045-2322. DOI: 10.1038/srep17492 (cit. on pp. 32, 70, 115, 152).

[Yaro+16] A. Yaroshenko, T. Pritzke, M. Koschlig, N. Kamgari, K. Willer, L. Gromann, S. Auweter, K. Hellbach, M. Reiser, O. Eickelberg, F. Pfeiffer, and A. Hilgendorff. "Visualization of neonatal lung injury associated with mechanical ventilation using x-ray dark-field radiography." In: *Scientific Reports* 6, 24269 (Apr. 2016). ISSN: 2045-2322. DOI: 10.1038/srep24269 (cit. on pp. 32, 70, 115).

[Yash+10] W. Yashiro, Y. Terui, K. Kawabata, and A. Momose. "On the origin of visibility contrast in x-ray Talbot interferometry." In: *Optics Express* 18.16 (Aug. 2010), pp. 16890–16901. ISSN: 1094-4087. DOI: 10.1364/OE.18.016890 (cit. on pp. 27, 62–63, 127, 143–144).

[Yash+15] W. Yashiro, P. Vagovič, and A. Momose. "Effect of beam hardening on a visibility-contrast image obtained by X-ray grating interferometry." In: *Optics Express* 23.18 (Sept. 2015), pp. 23462–23471. ISSN: 1094-4087. DOI: 10.1364/OE.23.023462 (cit. on pp. 58, 161, 163, 166).

[Yone+99] A. Yoneyama, A. Momose, E. Seya, K. Hirano, T. Takeda, and Y. Itai. "Operation of a separated-type x-ray interferometer for phase-contrast x-ray imaging." In: *Review of Scientific Instruments* 70.12 (Sept. 1999), pp. 4582–4586. ISSN: 0034-6748. DOI: 10.1063/1.1150116 (cit. on p. 23).

[Yosh+20] H. Yoshioka, Y. Kadono, Y. T. Kim, H. Oda, T. Maruyama, Y. Akiyama, T. Mimura, J. Tanaka, M. Niitsu, Y. Hoshino, J. Kiyohara, S. Nishino, C. Makifuchi, A. Takahashi, Y. Shinden, N. Matsusaka, K. Kido, and A. Momose. "Imaging evaluation of the cartilage in rheumatoid arthritis patients with an x-ray phase imaging apparatus based on Talbot-Lau interferometry." In: *Scientific Reports* 10, 6561 (Apr. 2020). ISSN: 2045-2322. DOI: 10.1038/s41598-020-63155-9 (cit. on p. 30).

[Youn02] T. Young. "XIV. An account of some cases of the production of colours, not hitherto described." In: *Philosophical Transactions of the Royal Society of London* 92 (Dec. 1802), pp. 387–397. ISSN: 0261-0523. DOI: 10.1098/rstl.1802.0016 (cit. on p. 15).

[Youn04] T. Young. "I. The Bakerian Lecture. Experiments and calculations relative to physical optics." In: *Philosophical Transactions of the Royal Society of London* 94 (Dec. 1804), pp. 1–16. ISSN: 0261-0523. DOI: 10.1098/rstl.1804.0001 (cit. on p. 15).

[Zdor18] M.-C. Zdora. "State of the Art of X-ray Speckle-Based Phase-Contrast and Dark-Field Imaging." In: *Journal of Imaging* 4.5, 60 (Apr. 2018). ISSN: 2313-433X. DOI: 10.3390/jimaging4050060 (cit. on p. 28).

[Zhan97] Z. Zhang. "Parameter estimation techniques: a tutorial with application to conic fitting." In: *Image and Vision Computing* 15.1 (Jan. 1997), pp. 59–76. ISSN: 0262-8856. DOI: 10.1016/S0262-8856(96)01112-2 (cit. on p. 94).

[Zhon+00] Z. Zhong, W. Thomlinson, D. Chapman, and D. Sayers. "Implementation of diffraction-enhanced imaging experiments: at the NSLS and APS." In: *Nuclear Instruments and Methods in Physics Research Section A: Accelerators, Spectrometers, Detectors and Associated Equipment* 450.2-3 (Aug. 2000), pp. 556–567. ISSN: 0168-9002. DOI: 10.1016/S0168-9002(00)00308-9 (cit. on p. 31).

[Zhu+17] H. Zhu, L. Zhang, Y. Wang, P. Hamal, X. You, H. Mao, F. Li, and X. Sun. "Improved image quality and diagnostic potential using ultra-high-resolution computed tomography of the lung with small scan FOV: A prospective study." In: *PLOS ONE* 12.2, e0172688 (Feb. 2017). Ed. by L. Zeng. ISSN: 1932-6203. DOI: 10.1371/journal.pone.0172688 (cit. on p. 152).

List of Figures

List of Tables

Appendices

A Calculation of transmittance for maximum dose-normalized CNR

We assume two adjacent objects with identical linear attenuation coefficient μ and projected thicknesses x_1 and x_2. They are illuminated by an amount of X-rays that would, in the objects' absence, result in an average of N photons being detected. According to the Beer-Lambert law, the average number of photons detected behind the objects are $\langle N_1\rangle = N\exp(-\mu x_1)$ and $\langle N_2\rangle = N\exp(-\mu x_2)$. Since N_1 and N_2 are Poisson-distributed random variables, their variances are equal to their mean values $\langle N_1\rangle$, $\langle N_2\rangle$, and the contrast-to-noise ratio (CNR) between the two quantities is then

$$\mathrm{CNR}_{1,2} = \frac{\langle N_1\rangle - \langle N_2\rangle}{\sqrt{\langle N_1\rangle + \langle N_2\rangle}} = \sqrt{N}\frac{\exp(-\mu x_1) - \exp(-\mu x_2)}{\sqrt{\exp(-\mu x_1) + \exp(-\mu x_2)}},$$

assuming without loss of generality that $N_1 > N_2$. The total number of photons absorbed by the two objects (which is a measure of the total absorbed dose) is given as

$$\begin{aligned} A &= N\left[1 - \exp(-\mu x_1)\right] + N\left[1 - \exp(-\mu x_2)\right] \\ &= N\left[2 - \exp(-\mu x_1) - \exp(-\mu x_2)\right]. \end{aligned}$$

Since A is proportional to N, the N-dependence of $\mathrm{CNR}_{1,2}$ is eliminated with the normalization

$$\mathrm{NCNR}_{1,2} \equiv \frac{\mathrm{CNR}_{1,2}}{\sqrt{A}} = \frac{e^{-\mu x_1} - e^{-\mu x_2}}{\sqrt{(e^{-\mu x_1} + e^{-\mu x_2})\,(2 - e^{-\mu x_1} - e^{-\mu x_2})}}.$$

The quantity optimized here is the change in $\mathrm{NCNR}_{1,2}$ with the deviation between x_1 and x_2. For small differences, this can be approximated by

$$\left.\frac{\partial\,\mathrm{NCNR}_{1,2}}{\partial x_2}\right|_{x_2=x_1} = \frac{\mu\, e^{\mu x_1/2}}{\sqrt{2e^{2\mu x_1} - 2e^{\mu x_1}}}.$$

This quantity does not have a local maximum when viewed as a function of x_1 (and fixed μ), but it does as a function of μ (and fixed x_1): It becomes maximal if

$$\mu x_1 = 2(1 - e^{-\mu x_1}),$$

which is fulfilled for $\mu x_1 = 0$ and $\mu x_1 \approx 1.594$, but only the latter yields a local maximum. It corresponds to a transmittance of $T_1 = \exp(-\mu x_1) \approx 0.203$.

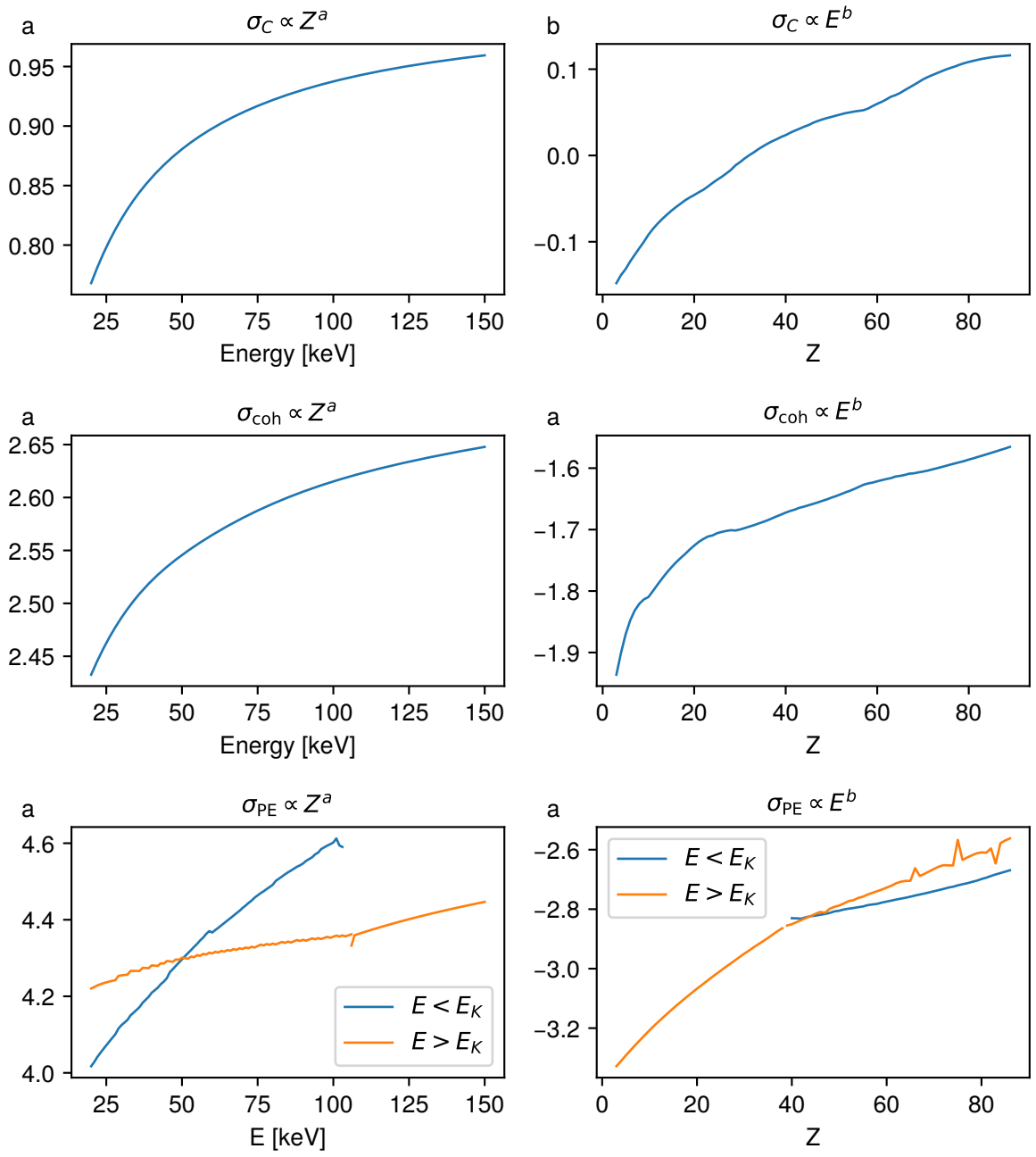

Figure 1 (Appendix): Power-law regression results for the dependence of total interaction cross-sections of Compton scattering, coherent scattering and photoelectric absorption, as a function of photon energy *E* and atomic number *Z*. For photoelectric absorption, regression analyses were performed separately for energies below and above the K-edge energies of the respective elements.

B Calculation of Taylor coefficients of Eq. (4.1)

The first three coefficients of the Taylor polynomial of Eq. (4.1) were calculated using the Maxima software (Maxima 5.41.0, http://maxima.sourceforge.net/). The used commands and their outputs are listed below.

Definition of Eq. (4.1), written as a function of L (as shown in Fig. 4.1):

(% i1) `alpha:atan(y/(D-dz)) - acos((L^2+D^2-s^2)/ (2*D*L));`

$$\operatorname{atan}\left(\frac{y}{D-dz}\right)-\operatorname{acos}\left(\frac{-s^2+L^2+D^2}{2DL}\right) \tag{alpha}$$

Definition of L:

(% i2) `Lfull:sqrt(y^2+(D-dz)^2);`

$$\sqrt{y^2+(D-dz)^2} \tag{Lfull}$$

Substitution of (Lfull) into (alpha):

(% i3) `alphafull:subst(Lfull, L, alpha);`

$$\operatorname{atan}\left(\frac{y}{D-dz}\right)-\operatorname{acos}\left(\frac{y^2-s^2+(D-dz)^2+D^2}{2D\sqrt{y^2+(D-dz)^2}}\right) \tag{alphafull}$$

Definition of y_0, the y coordinate where the swing is vertical:

(% i4) `y0:sqrt(s^2-dz^2);`

$$\sqrt{s^2-dz^2} \tag{y0}$$

Substitution of y for y_0 in (alphafull). Although not apparent from the output, this value is zero:

(% i5) `radcan(subst(y0,y,alphafull));`

$$\operatorname{acos}\left(\frac{dz-D}{\sqrt{s^2-2D\,dz+D^2}}\right)-\operatorname{atan}\left(\frac{\sqrt{s-dz}\sqrt{s+dz}}{dz-D}\right)-\pi \tag{% o5}$$

Calculation of the first derivative of (alphafull) with respect to y at $y = y_0$:

(% i6) `radcan(subst(y0,y,diff(radcan(alphafull),y,1)));`

$$\frac{1}{D} \tag{% o6}$$

Calculation of the second derivative of (alphafull) with respect to y at $y = y_0$:

(% i7) `radcan(subst(y0,y,diff(radcan(alphafull),y,2)));`

$$-\frac{dz}{D^2\sqrt{s-dz}\sqrt{s+dz}} \tag{% o7}$$

Calculation of the third derivative of (alphafull) with respect to y at $y = y_0$:

(% i8) `radcan(subst(y0,y,diff(radcan(alphafull),y,3)));`

$$\frac{s^2+2dz^2}{D^3\,s^2-D^3\,dz^2} \tag{% o8}$$

C Software used for the preparation of this document

- Typesetting: *LyX*, versions 2.3.2 and 2.3.5 (https://www.lyx.org) and *TeX Live 2017* (https://www.tug.org/texlive/)
- Data visualization: *Python*, versions 3.5, 3.6, and 3.8 (https://www.python.org/)
  - *matplotlib*, version 3.2.0 (https://matplotlib.org/)
  - *NumPy*, version 1.18 (https://numpy.org/)
  - *SciPy*, version 1.4.1 (https://www.scipy.org/)
  - *xraylib*, versions 3.3.0 and 4.0.0 (https://github.com/tschoonj/xraylib/wiki)
- Illustrations: *Inkscape*, version 0.92 (https://inkscape.org/). Fig. 3.3: Autodesk Inventor 2019 (https://www.autodesk.com/)

Scientific contributions

Publications with first or shared first authorship

- **F. De Marco**, J. Andrejewski, K. Willer, L. Gromann, T. Koehler, H.-I. Maack, J. Herzen, and F. Pfeiffer. "X-ray dark-field signal reduction due to hardening of the visibility spectrum." *Submitted to IEEE Transactions on Medical Imaging*. 2020.

- A. A. Fingerle*, **F. De Marco***, J. Andrejewski, K. Willer, L. B. Gromann, W. Noichl, F. Kriner, F. Fischer, C. Braun, H.-I. Maack, T. Pralow, T. Koehler, P. B. Noël, F. Meurer, D. Deniffel, A. P. Sauter, B. Haller, D. Pfeiffer, E. J. Rummeny, J. Herzen, and F. Pfeiffer. "Imaging features in post-mortem x-ray dark-field chest radiographs and correlation with conventional x-ray and CT." In: *European Radiology Experimental* 3.1, 25 (July 2019). ISSN: 2509-9280. DOI: 10.1186/s41747-019-0104-7.

- **F. De Marco**, K. Willer, L. B. Gromann, J. Andrejewski, K. Hellbach, A. Bähr, M. Dmochewitz, T. Koehler, H.-I. Maack, F. Pfeiffer, and J. Herzen. "Contrast-to-noise ratios and thickness-normalized, ventilation-dependent signal levels in dark-field and conventional in vivo thorax radiographs of two pigs." In: *PLOS ONE* 14.6, e0217858 (June 2019). ISSN: 1932-6203. DOI: 10.1371/journal.pone.0217858.

- **F. De Marco**, M. Marschner, L. Birnbacher, P. Noël, J. Herzen, and F. Pfeiffer. "Analysis and correction of bias induced by phase stepping jitter in grating- based X-ray phase-contrast imaging." In: Optics Express 26.10 (May 2018), pp. 12707–12722. ISSN: 1094-4087. DOI: 10.1364/OE.26.012707.

- L. Gromann*, **F. De Marco***, K. Willer, P. Noël, K. Scherer, B. Renger, B. Gleich, K. Achterhold, A. Fingerle, D. Muenzel, S. Auweter, K. Hellbach, M. Reiser, A. Bähr, M. Dmochewitz, T. Schroeter, F. Koch, P. Meyer, D. Kunka, J. Mohr, A. Yaroshenko, H.-I. Maack, T. Pralow, H. van der Heijden, R. Proksa, T. Koehler, N. Wieberneit, K. Rindt, E. Rummeny, F. Pfeiffer, and J. Herzen. "In-vivo X-ray Dark-Field Chest Radiography of a Pig." In: *Scientific Reports* 7, 4807 (July, 2017). ISSN: 2045-2322. DOI: 10.1038/s41598-017-05101-w.

Publications with co-authorship

- K. Taphorn, **F. De Marco**, J. Andrejewski, T. Sellerer, F. Pfeiffer, and J. Herzen. "Grating-based spectral X-ray dark-field imaging for correlation with structural size measures." In: *Scientific Reports* 10, 13195 (Aug. 2020). ISSN: 2045-2322. DOI: 10.1038/s41598-020-70011-3.

- A. P. Sauter*, J. Andrejewski*, **F. De Marco**, K. Willer, L. B. Gromann, W. Noichl, F. Kriner, F. Fischer, C. Braun, T. Koehler, F. Meurer, A. A. Fingerle, D. Pfeiffer, E. Rummeny, J. Herzen, and F. Pfeiffer. "Optimization of tube voltage in X-ray dark-field chest radiography." In: *Scientific Reports* 9, 8699 (June 2019). ISSN: 2045-2322. DOI: 10.1038/s41598-019-45256-2.

- K. Willer*, A. A. Fingerle*, L. B. Gromann, **F. De Marco**, J. Herzen, K. Achterhold, B. Gleich, D. Muenzel, K. Scherer, M. Renz, B. Renger, F. Kopp, F. Kriner, F. Fischer, C. Braun, S. Auweter, K. Hellbach, M. F. Reiser, T. Schroeter, J. Mohr, A. Yaroshenko, H.-I. Maack, T. Pralow, H. van der Heijden, R. Proksa, T. Koehler, N. Wieberneit, K. Rindt, E. J. Rummeny, F. Pfeiffer, and P. B. Noël. "X-ray dark-field imaging of the human lung—a feasibility study on a deceased body." In: *PLOS ONE* 13.9, e0204565 (Sep. 2018). ISSN: 1932-6203. DOI: 10.1371/journal.pone.0204565.

- K. Hellbach*, A. Baehr*, **F. De Marco**, K. Willer, L. B. Gromann, J. Herzen, M. Dmochewitz, S. Auweter, A. A. Fingerle, P. B. Noël, E. J. Rummeny, A. Yaroshenko, H.-I. Maack, T. Pralow, H. van der Heijden, N. Wieberneit, R. Proksa, T. Koehler, K. Rindt, T. J. Schroeter, J. Mohr, F. Bamberg, B. Ertl-Wagner, F. Pfeiffer, and M. F. Reiser. "Depiction of pneumothoraces in a large animal model using x-ray dark-field radiography." In: *Scientific Reports* 8, 2602 (Feb. 2018). ISSN: 2045-2322. DOI: 10.1038/s41598-018-20985-y.

- T. J. Schröter, F. J. Koch, P. Meyer, D. Kunka, J. Meiser, K. Willer, L. Gromann, **F. De Marco**, J. Herzen, P. Noel, A. Yaroshenko, A. Hofmann, F. Pfeiffer, and J. Mohr. "Large field-of-view tiled grating structures for X-ray phase-contrast imaging." In: *Review of Scientific Instruments* 88.1, 015104 (Jan. 2017). ISSN: 0034-6748. DOI: 10.1063/1.4973632.

* Shared first authorship

Presentations

- "Imaging features of dark-field human chest X-rays" – Oral presentation at the 8^{th} *International Symposium on biomedical applications of X-ray phase contrast imaging (IMXP 2019),* Jan. 2019, Garmisch-Partenkirchen, Germany.

- "X-ray dark-field radiographies of *in vivo* pig and *ex vivo* human" – Oral presentation at the 7^{th} *International Symposium on biomedical applications of X-ray phase contrast imaging (IMXP 2018),* Jan. 2018, Garmisch-Partenkirchen, Germany.

- "Systematic analysis of *in vivo* dark-field signal in pig lungs" – Poster presentation at the 4^{th} *International Conference on X-ray and Neutron Phase Imaging with Gratings (XNPIG2017),* Sep. 2017, Zürich, Switzerland.

- "Improving image quality in laboratory x-ray phase-contrast imaging" – Oral presentation at *SPIE Medical Imaging 2017,* Feb. 2017, Orlando (FL), USA.

  – Associated proceedings paper: **F. De Marco**, M. Marschner, L. Birnbacher, M. Viermetz, P. Noël, J. Herzen, and F. Pfeiffer. "Improving image quality in laboratory X-ray phase-contrast imaging." In: *Proceedings Volume 10132, Medical Imaging 2017: Physics of Medical Imaging.* Vol. 10132. 2017. DOI: 10.1117/12.2255537.

Acknowledgments

During my graduate work at the Chair of Biomedical Physics, I have received generous help and support from a large number of people. The present work could not exist without them, and I am indebted to them all.

First and foremost, I am extremely grateful to my doctorate supervisor, Prof. Dr. Franz Pfeiffer, for taking me on as a graduate student and including me in a very engaging project, while also giving me the space and opportunity to pursue my own ideas. And not least of all, for funding me throughout all this time, including the lengthy phase of writing down this work.

I would also like to express my deep gratitude to Prof. Dr. Julia Herzen, for a huge amount of helpful discussions, for providing valuable guidance and mentoring, and for including me in several of her group's interesting projects.

I would like to thank Konstantin Willer for a lot of valuable discussions, the crucial contribution of his technical expertise during the construction and operation of the *lung-scanning setup*, and for his special ability to create a positive and comfortable working atmosphere.

A big thanks also to Dr. Lukas Gromann, for lively discussions about all kinds of topics, for contributing many ingenious ideas, and for keeping our work at a fast and challenging pace.

Special thanks go to Jana Andrejewski for many interesting conversations and discussions, for her reliable contributions especially to lengthy, difficult, and often thankless tasks (such as proofreading large parts of this work), and for being a great colleague.

Thanks should also go to Wolfgang Noichl. His contributions to image processing algorithms and the corresponding, very engaging discussions are greatly appreciated.

I am also very grateful to Dr. Martin Dierolf for providing his vast expertise in all things X-ray on many occasions.

The joys and/or burdens of maintaining the chair's IT infrastructure were also largely borne by Wolfgang and Martin. Thank you for your service!

A big thank you also to Dr. Bernhard Gleich and the staff of the Munich School of BioEngineering for always ensuring the functionality and safety of the laboratory and office facilities.

A major part of the success of the *lung-scanning setup* was due to the support by Philips

Medical Systems. I would especially like to thank Dr. Thomas Koehler, Ingo Maack, and Dr. Andre Yaroshenko for contributing many great ideas and providing a lot of insight in a large number of in-person and remote discussions. Furthermore, I am very grateful for the in-depth technical support by Thomas Pralow and Hendrik van der Heijden.

I also gratefully acknowledge the work of Dr. Tobias Schröter, Dr. Pascal Meyer, and many other members of the X-ray optics group at the KIT Institute of Microstructure Technology, whose work greatly contributed to the success of the *lung-scanning setup*.

I am greatly indebted to the radiologists Dr. Alexander Fingerle and Dr. Katharina Hellbach for their crucial contributions and insights during our collaboration.

In addition, I owe my thanks to the veterinarians Dr. Andrea Bähr and Dr. Michaela Dmochewitz for their work during the large-animal studies. These experiments would have been impossible without their skills and dedication.

I am also very grateful to Dr. Christian Braun, Fabian Kriner, and Dr. Florian Fischer from the Institute of Forensic Medicine in Munich, whose great commitment has made the human cadaver studies possible.

Many thanks as well to Kirsten Taphorn, Manuela Frank, Theresa Urban, Dr. Lorenz Hehn, Alex and Niko Gustschin, Manuel Viermetz, Benedikt Günther, Dr. Christoph Jud, Dr. Yash Sharma, and Rafael Schick for engaging discussions, valuable ideas, and practical support.

I would like to offer my special thanks to Nelly de Leiris and Dr. Klaus Achterhold for their—often underappreciated—support in all things administrative and bureaucratic.

More generally, I am grateful to everyone at the Chair of Biomedical Physics and the Group for Biomedical Imaging Physics for their solidarity and for turning two research groups into a community!

And finally, I would of course like to thank my friends and family for their steady support and encouragement throughout the years.